1

Executive Summary

Authors:
Aurel Florian Moise, Sandeep Sahany, Muhammad Eeqmal Hassim, Chen Chen, Xin Rong Chua, Venkatraman Prasanna, Gerald Lim, Jianjun Yu, Shipra Jain, Anupam Kumar, Pavan Harika Raavi, Fei Luo, Trina Ng, Nidheesh Gangadharan

METEOROLOGICAL SERVICE SINGAPORE
Centre for Climate Research Singapore

1.1 Background to Singapore's Third National Climate Change Study

The challenge of climate change presents an existential threat to both humanity and the Earth's ecosystems, underscoring the need for a strategic understanding and a proactive response to mitigate its associated risks. Small island nations like Singapore, confronted with increasing evidence of climate change impacts, urgently need reliable and actionable information to effectively prepare for and adapt to the multifaceted risks associated with this global challenge.

Every 6-7 years, the Intergovernmental Panel on Climate Change (IPCC) issues Assessment Reports that provide current insights into the scientific, technical, and socio-economic aspects of climate change. The latest IPCC assessment cycle, featuring reports on the Physical Science Basis, Impacts, Adaptation and Vulnerability, and Mitigation of Climate Change, along with a Synthesis Report and a Climate Change Atlas, contributes valuable information on a global scale. However, these reports, primarily based on global climate models, lack the granularity needed for regional and local assessments and adaptation planning.

Building on the foundation of Singapore's Second National Climate Change Study (V2), the Third National Climate Change Study (V3) addresses this gap by providing high-resolution climate change projections for Singapore and the broader Southeast Asian region. By dynamically downscaling global climate model simulations, the study offers a new dataset crucial for informed adaptation planning, enhancing Singapore's resilience to the adverse effects of climate change.

Led by the National Environment Agency (NEA), and with the Meteorological Service Singapore's Centre for Climate Research Singapore (CCRS) at the forefront of developing high-resolution downscaled climate projections, V3 contributes to Singapore's national endeavors by enhancing understanding of climate change effects and aiding in the formulation of comprehensive, long-term plans for national resilience.

The V3 study comprises a Stakeholder Report and an accompanying Technical Report. The Stakeholder Report provides a succinct overview of V3's key findings, tailored for diverse audiences. This includes Singaporean Government agencies and Southeast Asian counterparts involved in downstream impact studies, policy development, and adaptation planning. It is also designed for researchers in local Institutes of Higher Learning and beyond, along with the general public interested in climate change and sustainability. For a comprehensive understanding, the Technical Report delves into V3's methodology, global and regional projections derived from Global Climate Models (GCMs), the evaluation and sub-selection of GCMs, the setup of the SINGV-RCM, assessment of downscaled simulations, bias adjustment, regional climate change projections, and sea level projections over Singapore and the broader region. Please see Chapter 2 Introduction for more details.

Moreover, to enhance the interpretation and comprehension of the V3 study, individuals can explore specific data visualizations from V3 at https://www.mss-int.sg/V3-climate-projections.

1.2 Recent Climate Trends in Singapore

The global mean temperature for 2022 exceeded the 1850–1900 average by 1.15°C. In Singapore, the average daily mean temperature has shown a steady increase, rising at a rate of 0.24°C per decade over the past four decades since 1984. This temperature rise persists despite substantial year-to-year variability, influenced by large-scale climate drivers like the El Niño-Southern Oscillation (ENSO). El Niño events generally lead to higher annual mean temperatures across Singapore, while La Niña events tend to moderate them. The natural modulations contribute to varying warming rates across decades, e.g., an increase of 0.52°C per decade between 1984 and 1993, contrasting with an increase of 0.07°C per decade between 2013 and 2022. Alongside the mean temperature increase, observations in

Singapore also indicate an upward trend in daily minimum and maximum temperatures.

In terms of rainfall trends, Singapore's annual rainfall has experienced a slight upward trend of 83mm per decade from 1980 to 2022. However, this trend is overshadowed by significant year-to-year variations. It's essential to emphasize that the ENSO has a significant influence on Singapore's rainfall patterns, causing increased rainfall during La Niña years and reduced rainfall during El Niño years. Singapore is known for its humid tropical rainforest climate. Between 1985 and 2020, there has been a slight decline in the annual mean near-surface relative humidity in Singapore.

Situated between two monsoon systems, Singapore experiences the Southwest Monsoon from June to September and the Northeast Monsoon from November to early March. The average wind speeds are generally mild over Singapore, with even lighter and variable winds during the inter-monsoon period. The annual mean wind speed exhibits inter-annual and multi-decadal variability. In recent decades, observations suggest a potential increasing trend, which could be part of the multi-decadal variability.

Please see Chapter 3 Observed Climate Change for more details.

1.3 Methodology to Produce Climate Change Projections for Singapore and Southeast Asia

The initial stage in crafting high-resolution climate change projections for Singapore involved the assessment and sub-selection of 49 global climate models employed in the IPCC AR6 for dynamical downscaling. This evaluation adhered to established practices within the international scientific community engaged in dynamical downscaling, led by the World Climate Research Programme (WCRP) Coordinated Regional Downscaling Experiment (CORDEX) community. A thorough examination of key climate variables, including temperature, rainfall, winds, relative humidity, and sea level pressure, was conducted. Relevant climate drivers for the Maritime Continent (MC), such as monsoons, El-Nino Southern Oscillation (ENSO) and its teleconnections, Indian Ocean Dipole (IOD), Northeast Monsoon surges, and Madden-Julian Oscillation (MJO), were also considered. This rigorous evaluation aimed to identify and flag any models deemed implausible for climate change projections in the region.

The sub-selection process extends beyond global model evaluation. Additional dimensions for sub-selection encompass (i) availability of relevant 6-hourly data to drive the regional climate model, (ii) coverage of a broad spectrum of model families, (iii) inclusion of a diverse range of climate sensitivities, and (iv) representation of a comprehensive range of future outcomes from the global models. Please see Chapter 5 GCM Evaluation and Sub-selection for more details.

The regional climate model chosen for dynamical downscaling was the SINGapore Variable resolution model (SINGV), re-configured from a numerical weather prediction model to operate in a climate mode. This conversion exemplifies a seamless modeling framework, allowing the same system to be employed for both numerical weather prediction (hours to days) and climate change projections (decades). To ensure successful configuration as a regional climate model, the SINGV model underwent customization for climate mode through multiple sensitivity studies at different resolutions and domain sizes over the MC. For further details, please refer to Chapter 6 SINGV-RCM.

V3 downscaling simulations include one historical simulation driven by the latest ERA5 reanalysis and multiple simulations driven by sub-selected CMIP6 GCMs. In total, V3 carried out dynamical downscaling from 6 GCMs for the historical period (1955-2014) and the future (2015-2099) under 3 IPCC AR6 global warming scenarios (Shared Socioeconomic Pathway 1-2.6, SSP2-4.5, and SSP5-8.5) at 8km horizontal resolution over the Southeast Asia (SEA) domain. Additional high-resolution simulations at 2km horizontal resolution were carried out over the western MC domain, which encompassed the period of 1995-2014 and the same 3 SSP scenarios, utilizing 5 GCMs for two 20-year time slices in the future (2040-2059 and 2080-2099).

Our investigation has demonstrated that high-resolution regional climate model (RCM) downscaling simulations, conducted at both 8km and 2km resolutions, contribute value across various aspects when compared to coarse resolution Global Climate Models (GCMs). The SINGV-RCM downscaling consistently aligns with the parent driving model, faithfully tracking the long-term trends and variability of the parent model. Notably, the downscaled simulations accurately replicate crucial meteorological parameters, including precipitation, temperature, relative humidity, and wind speed, across different time scales from diurnal to seasonal and their annual cycles.

The variables simulated by the SINGV-RCM exhibit strong agreement with high-resolution regional observations, such as ground-based stations and satellite merged products. This alignment underscores the RCM's skill in representing historical climate conditions. Additionally, the RCM demonstrates abilities in capturing regional climate drivers, such as remote ENSO-teleconnection, and processes like cold surges specific to this region.

For thorough evaluation, the RCM simulations over Singapore are analyzed at each land grid using high-resolution observations. Notably, the 2km resolution simulations show improvements over the 8km resolution simulations and provide a more detailed representation of the climate within the island nation. Further details are available in Chapter 7 Evaluation of Dynamically Downscaled Simulations.

One more thing worth highlighting here is the HPC aspect of the V3 study. Approximately 2000 model years of dynamical downscaling simulations at 8 km resolution, covering nearly the entire Southeast Asia (SEA), and ~750 model years at 2 km resolution focusing on the western Maritime Continent, were conducted for both current and future climates as part of V3. Due to computing resource constraints and V3 timelines, the simulations were distributed across three High-Performance Computing (HPC) systems on two continents: NSCC Koppen and A2A in Singapore, and NCI Gadi in Australia. Throughout the simulation period, computing and storage requirements fluctuated, reaching peak computing levels exceeding ~35 million core-hours per month and storage capacities reaching ~12 PB. Furthermore, approximately 4 PB of data was efficiently transferred from Australia to Singapore at peak speeds of ~1 Gbps, facilitated by NSCC and SingAREN. The HPC journey for V3 simulations was both challenging and adventurous, demanding significant efforts from CCRS and dedicated time for resource and simulation management. Through collaborative teamwork within MSS/CCRS and support from NSCC, NCI, and SingAREN, coupled with the diligent efforts of the V3 team at CCRS, challenges were successfully navigated, and the desired outcomes were achieved, meeting the V3 delivery timelines. More details are available in Chapter 13 High Performance Computing Aspects.

1.4 CMIP6-informed Global to Regional Climate Projections

CMIP6 models (utilized in the IPCC AR6), offer a comprehensive understanding of climate change at both global and regional scales. In contrast to their CMIP5 counterparts, CMIP6 models boast higher spatial resolution, enhanced model physics through improved parameterization schemes, and an increased incorporation of earth system models featuring carbon cycle and biogeochemistry components. Additionally, CMIP6 models introduce a socioeconomic storyline (SSP1-2.6, SSP2-4.5, SSP3-7.0, and SSP5-8.5) in conjunction with radiative forcing levels, as opposed to the CMIP5 models' Representative Concentration Pathways (RCP) 2.6, 4.5, 6.0, and 8.5. This inclusion enriches future warming scenarios. Consequently, the utilization of CMIP6 models enhances confidence in projecting future climate variables and processes compared to the earlier CMIP5 models.

The projected global mean surface air temperature is expected to rise by 0.4 to 1.0°C relative to the period 1995-2014 across most scenarios in the near term (2021-2040). Additionally, during the same period, land surface temperatures are anticipated to increase by at least 1.0°C more than ocean temperatures. In the near term, land precipitation is projected to

increase under both low emission (-0.2 to 4.7%) and high emission (0.9 to 12.9%) scenarios, with certain regional uncertainties stemming from internal variability, model uncertainty, and aerosol emission uncertainties.

Besides mean state variables, tropical climate drivers are also expected to undergo warming-induced changes. Global monsoon precipitation is anticipated to increase, despite a reduction in circulation strength both in the mid and end century. The El Niño-Southern Oscillation (ENSO) response to warming remains uncertain across different scenarios, but a robust signal of ENSO-induced precipitation variability is evident over the tropical Pacific. Although the frequency of strong positive Indian Ocean Dipole (IOD) events is expected to rise, the IOD response remains uncertain due to the lack of strong evidence and dependence on mean state biases in the model. In a future warmer climate, the Madden-Julian Oscillation (MJO) is projected to intensify, accompanied by an increased magnitude of associated precipitation.

For the Southeast Asia (SEA) region, CMIP6 Global Climate Models (GCMs) indicate a temperature increase slightly below the global average. Daily mean surface temperatures are projected to rise over both land and oceans, with a more pronounced land-sea temperature contrast in high Equilibrium Climate Sensitivity (ECS) models at annual and seasonal time scales. During the hot summer periods in March to May (MAM) and June to August (JJA) seasons over the northern parts of SEA, temperatures are expected to increase by up to 5°C or more. Mean annual rainfall projections indicate increased values over most land regions of SEA, with higher increases over northern SEA, Borneo, and New Guinea. Under the high warming scenario (SSP5-8.5), there is a strong ENSO-rainfall signal over the MC in JJA with strong drier conditions during El Niño and strong wetter conditions during La Niña.

The frequency of Northeast monsoon surges is anticipated to increase to 19% (from the current 18%), resulting in heightened rainfall over Borneo, Sulawesi, south Sumatra, New Guinea, and east of the Philippines. Conversely, there is a projection of reduced rainfall around the Maluku islands. The combined impacts of climate change, land subsidence, and regional human activities contribute to a higher level of confidence in the escalation of floods and prolonged inundation across the Mekong Delta region.

In summary, the CMIP6 future projections indicate increased global and regional surface air temperatures, enhanced global precipitation (regional differences; wet gets wetter, dry gets drier), increased monsoon land precipitation, and enhanced ENSO-rainfall teleconnections. In addition to the mean changes, extremes in temperature and rainfall are projected to increase, especially under SSP5-8.5 over many parts of the globe, including SEA. Please see Chapter 4 From Global to Regional Projections – insights from CMIP6 for more details.

1.5 Regional Climate Change Projections for Southeast Asia

In the V3 study, we utilized SINGV-RCM driven by selected CMIP6 GCMs to assess climate changes across Southeast Asia, examining key variables such as temperature, rainfall, and large-scale drivers crucial to the region.

In terms of rainfall, projections indicate an increase in annual-mean domain-average rainfall over Southeast Asia towards the end of the 21st century. The multi-model mean projects a higher end-century change compared to mid-century changes for each scenario, but the inter-model spread is notable. Such slight increase in the annual mean rises from spatially complex changes across individual seasons. For instance, substantial rainfall increases occur in the northern Maritime Continent throughout all seasons, while western and central equatorial Maritime Continent experiences drying, particularly during dry months (JJA). Extreme rainfall events, measured by maximum 1-day rainfall (RX1day) and (RX5day), are expected to rise across most Southeast Asian land regions during all seasons.

As for temperature, the multi-model mean indicates projected temperature increases of 3.3°C over the Southeast Asian domain by the end of the century under the high emission scenario. Land areas in Southeast Asia are

expected to experience even higher warming, reaching 4°C by the century's end, consistent with the understanding that land regions warm more than ocean regions. Changes in annual maximum (tasmax) and annual minimum near-surface air temperatures are qualitatively similar to those in annual mean temperature. Temperature extremes, represented by changes in the seasonal maximum of daily maximum temperatures (TXx), show consistent warming trends over the Southeast Asian domain, with larger increases over land areas, exceeding 6oC in parts of Indochina during JJA and SON. The seasonal minimum of daily minimum temperatures (TNn) also increases across much of the domain.

Regarding relative humidity (hurs), seasonal mean near-surface relative humidity changes are generally small or negative over land (ranging from 0 to -1.9%), while increases are observed over oceans. The largest decreases are evident in JJA, particularly over Indochina, Borneo, and New Guinea. This reduction in land relative humidity aligns with existing studies and is accompanied by enhanced land warming.

Examining regional climate drivers, a weakening of the monsoonal flow with anomalous easterlies over the Indian Ocean is observed. Notably, JJA experiences a strengthening of the monsoon flow over Indochina. Changes in the northeast monsoon surge align with the parent GCMs in terms of increased frequency and anomalous easterlies over Indochina and west of Sumatra, as well as anomalous westerlies north of New Guinea. Note that, the magnitude of rainfall changes in the downscaled simulations are enhanced relative to the parent GCMs, with slight differences in the spatial distribution of rainfall.

CMIP6 GCMs indicate that the negative ENSO teleconnection over Southeast Asia (SEA) is expected to expand geographically and intensify with warming. Specifically, SEA is projected to experience heightened aridity during El Niño events, leading to prolonged drying and drought conditions. Conversely, La Niña events are anticipated to bring increased precipitation, resulting in more heightened flood risks. The zonal dipole pattern of the ENSO teleconnection across the Indo-Pacific Ocean is projected to shift eastward. These anticipated changes align consistently between RCMs and their parent GCMs, and the downscaled models offer additional fine-scale spatial details. These climate driver projections carry significant implications for water resource management and agriculture in the region. The potential for prolonged droughts during El Niño events and intensified flooding during La Niña events underscores the importance of adapting water resource strategies and agricultural practices to effectively respond to these anticipated shifts in climate patterns.

It is important to emphasize the added value of future projections derived from high-resolution RCMs compared to coarse-resolution driving GCMs. Note that GCMs often exhibit smoothed spatial changes due to their coarse resolutions. In contrast, high-resolution (8km) RCMs consistently reproduce large-scale changes similar to driving GCMs but offer a more detailed representation of high rainfall variability in the high mountain areas of Java and Papua New Guinea. These enhancements are crucial for advancing regional climate impact studies, and further details can be found in Chapter 8 Regional Climate Change Projections.

1.6 High-resolution Climate Change Projections for Singapore

Our high-resolution regional climate model (RCM) simulations, conducted at resolutions of 8km and 2km, have demonstrated excellent performance over the Maritime Continent. However, these high-resolution RCMs exhibit minor model biases when compared to local observations specifically within Singapore. To ensure that we provide appropriate simulation data for local climate change impact studies, we have conducted bias adjustments for key climate variables. By applying bias adjustments to these selected variables, we aligned the RCM simulations more closely with the observed local climate conditions in Singapore. The bias adjustments conducted in our study have demonstrated very good performance to remove the model biases in the historical period. We consider bias adjustment to be a crucial step in the post-processing of regional downscaling simulations, as it significantly improves the

realism and accuracy of the RCM outputs. The successful implementation of bias adjustments enhances our confidence in the climate projections and their suitability for assessing and addressing the impacts of climate change in Singapore. For further details, please refer to Chapter 9 Bias adjustments.

Singapore is projected to experience varying levels of temperature increase under low to high emission scenarios. V3 projections show that the daily mean temperatures over Singapore could increase by 0.6°C - 5.0°C by the end of the century and the daily maximum temperature could increase by 0.5°C - 5.3°C. Notably, the estimated upper limits of potential temperature increase in V3 are higher than V2. Furthermore, the daily mean Wet Bulb Globe Temperature (WBGT) - a key indicator for assessing heat stress - is expected to increase by 0.5°C - 4.3°C. The daily maximum WBGT could increase by 0.5°C - 4.0°C. This shift implies an increase in the frequency of days experiencing high heat stress, with an estimated 54 to 326 days featuring WBGT exceeding 33°C for an hour or more during daylight hours.

Singapore rainfall undergoes a transition from wet to dry across Monsoon seasons. The rainy months are from November to January, which marks the wet phase of the Northeast Monsoon season. On the contrary, Singapore is relatively dry in the months of June – August, which is the dry phase of the Southwest Monsoon. V3 study projects diverging changes in Singapore rainfall across different seasons. An intensification of precipitation is anticipated during the traditionally wet months (i.e., “wet gets wetter”) with an increase in mean rainfall of up to 58%. Conversely, the dry months may experience a potential rainfall decrease of up to 42% (i.e., “dry gets drier”).

The projections also indicate a heightened likelihood of extreme rainfall events throughout all seasons and scenarios, potentially escalating by as much as 92% during April and May. Additionally, the frequency of dry periods is expected to rise, occurring approximately every ten months, and extending for a maximum duration of around 3 weeks.

According to V3 projections, the near-surface wind speed over Singapore has the potential to increase by up to 20% during the Northeast (Dec-Mar) and Southwest monsoon (Jun-Sep) seasons. Additionally, in the intermonsoon months of April and May, under the high emissions scenario, there could be an increase of up to 11% by the end of the century.

For further details, please refer to Chapter 10 Singapore Climate Change Projections.

1.7 Past and Future Sea Level Change in Singapore and Southeast Asia

In conjunction with the downscaling simulations, another aspect of the V3 study centers on observed changes and projections of mean sea level around Singapore and the region. Sea level projections in V3 are derived from the state-of-the-art IPCC AR6 projections. For Singapore, V3 employed the IPCC AR6 methodology to generate relative mean sea level projections using corrected tide-gauge data to produce the most updated vertical land movement projections.

Relative mean sea level has been rising at a rate of 3.6 mm/yr off Singapore (average rate across four tide-gauges with rate varies between 3.27 - 3.77 mm/yr) for the 1993 - 2021 period. The contemporary mass redistribution between the oceans and the land, which refers to ocean’s exchange of water between ice sheets, glaciers, and other terrestrial water storages, is the main driver of observed sea-level rise around Singapore during the last three decades (~70% of the total rise). On the other hand, the ocean internal mass redistribution dominates the sterodynamic sea-level rise (~23% of the total rise) with a very weak contribution from local steric changes. These findings hence indicate that nearly 90% of the observed sea-level rise off Singapore is “mass-driven” and highlights the importance of having a bottom pressure recorder in the shelf region of Singapore to assist future studies and monitoring of mean sea-level rise.

By the year 2100, Singapore is expected to undergo a relative mean sea level rise of 0.45 ± 0.03 m under the SSP1-2.6 scenario, 0.57 ± 0.04 m under SSP2-4.5, and 0.79 ± 0.04 m under

SSP5-8.5. These are median values across six locations in Singapore. In the high emission scenario (SSP5-8.5), particularly at Sultan Shoal, Singapore may face a relative sea-level rise of up to 1.15m by 2100.

Looking further into the future, by the year 2150, the projected rise in relative sea level is estimated at 0.72 ± 0.05 m under SSP1-2.6, 0.95 ± 0.06 m under SSP2-4.5, and 1.37 ± 0.06 m under SSP5-8.5. These represent the average estimates of median values at six different locations in Singapore. In particular, at Sultan Shoal, the relative sea level could likely reach up to 2.12 m under SSP5-8.5 by 2150. Additional information is available in Chapter 12 Sea Level Projections.

1.8 Science Communications on Climate Changes and Uncertainty

Projecting future climate changes for Singapore presents a unique set of challenges. Located in between two significantly larger regions where opposing trends in rainfall are projected for most seasons, Singapore faces the intricate and seasonally variable influences of regional climate drivers within the Southeast Asia (SEA) region. The city-state's small size further complicates the task of predicting changes in rainfall, adding to the complexity.

Recognizing the inherent uncertainties in climate projections, the V3 study endeavors to offer valuable insights to users relying on bias-adjusted projections for Singapore, emphasizing the reliability and robustness of the projections. Through our analysis, we observe an escalation in scenario uncertainty over time, particularly from mid-century to end-century. Additionally, this uncertainty is contingent on the chosen climate model. For instance, in a specific model, the scenario uncertainty in precipitation change over Singapore can be as high as 25% during the end-century, and similarly the scenario uncertainty in temperature projections during the end-century can be as high as 3.5°C.

Model uncertainty follows a similar trajectory, amplifying over time and exhibiting greater variability in the end-century compared to the mid-century. Model uncertainty is highest for the SSP5-8.5 scenario. For Singapore during the end-century, the model uncertainty in projected precipitation change under SSP5-8.5 could be as high as 30%, and that for projected temperature change could be as high as 2.2°C. Dynamical downscaling also introduces uncertainty, influencing the sign of precipitation change for individual models and contributing to temperature variations within approximately 2°C. More discussions are available in Chapter 11 Uncertainty Quantification.

Despite these multiple sources of uncertainty, our confidence is anchored in projections that demonstrate robustness across varying time periods, scenarios, and models employed in the analysis. Greater assurance is also placed in projections that align consistently between regional and global climate models, especially when supported by theoretical understanding.

In the utilization of V3 results, opting for the mean or median of the multi-model ensemble can provide an indicative measure of change. However, for decision-making that prioritizes robustness, it is advisable to consider the complete multi-model range of the variables of interest. This comprehensive approach ensures a more nuanced and thorough understanding of the potential climate shifts in Singapore's future. Additional information on science communication can be found in Chapter 14 V3 Comms.

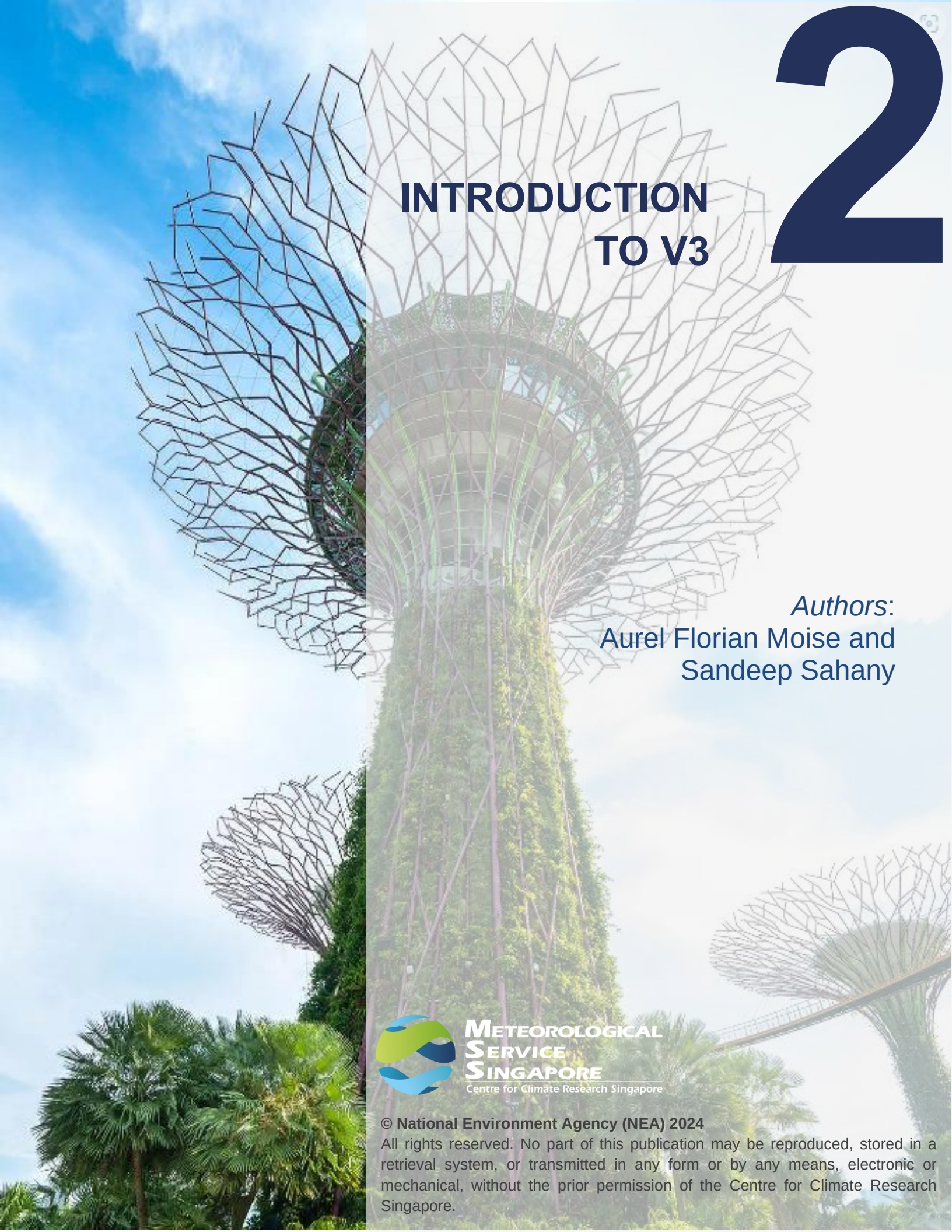

2

INTRODUCTION TO V3

Authors:
Aurel Florian Moise and
Sandeep Sahany

METEOROLOGICAL SERVICE SINGAPORE
Centre for Climate Research Singapore

2.1 Climate Change Governance in Singapore

The release of the IPCC 6th Assessment Report in 2021/22 provided further strong evidence on the state of the science around climate change, from basic science, impacts, adaptation to mitigation (IPCC 2021, 2022a, 2022b). While there is a strong focus on the global picture, many of the conclusions can be translated directly to the various regions. The United Nations Director General Antonio Guterres spoke about 'Code Red for humanity' following the release of the first AR6 report in 2021 and some examples of these conclusions also relevant for our region are:

Recent changes in the climate are widespread, rapid, and intensifying, and unprecedented in thousands of years. Unless there are immediate, rapid, and large-scale reductions in greenhouse gas emissions, limiting warming to 1.5°C will be beyond reach.

It is indisputable that human activities are causing climate change, making extreme climate events, including heat waves, heavy rainfall, and droughts, more frequent and severe.

Climate change is already affecting every region on Earth, in multiple ways. The changes we experience will increase with further warming. There's no going back from some changes in the climate system…

At the release of the second AR6 report on Impacts, Vulnerability and Adaptation in 2022, Hoesung Lee, Chair of the IPCC, concluded "*The report is a dire warning about the consequences of inaction. It shows that climate change is a grave & mounting threat to our wellbeing and to a healthy planet*."

Global warming has caused dangerous and widespread disruption in nature and climate change is affecting the lives of billions of people despite efforts to adapt (IPCC, 2022a). Also, impacts are magnified in cities where more than half of the world's population lives. Climate risks are now regarded as higher even at lower temperatures – and likely to happen sooner & with greater intensity. One of the key conclusions of the WG-II report from AR6 is: "The Science is clear. We have a rapidly narrowing window of opportunity to secure a sustainable & liveable future." (IPCC WG-II Press Release (2022): Press release | Climate Change 2022: Impacts, Adaptation and Vulnerability (ipcc.ch)).

While climate resilience development is already challenging at current global warming levels, Singapore has been committed to enhancing its resilience through multiple pathways. The Energy & Climate Policy Division (ECPD) under the Ministry of Sustainability and the Environment, Government of Singapore, oversees issues such as energy efficiency, renewable energy, climate science and adaptation. Some key aspects of Singapore's plans for climate resilience include (1) enhancement of knowledge and expertise on climate change, (2) coastal protection, (3) water resource management, and (4) drainage and flood prevention.

In addition to building climate resilience through active adaptation planning and implementation, Singapore also has strong climate change mitigation ambitions. Singapore has committed to achieve net zero emissions by 2050 by continuing to find innovative ways to accelerate the low-carbon transition for industry, economy and society through four key thrusts:

1. Catalysing business transformation;
2. Investing in low-carbon technologies;
3. Pursuing effective international cooperation; and
4. Adopting low-carbon practices

The Singapore Green Plan 2030 is a whole-of-nation movement to advance Singapore's national agenda on sustainable development. It charts ambitious and concrete targets over the next 10 years, strengthening Singapore's commitments under the UN's 2030 Sustainable Development Agenda and Paris Agreement, and positioning it to achieve its long-term net zero emissions aspiration by 2050.

Figure 2.1 shows the committees and working groups addressing Singapore's climate change related issues. The Inter-Ministerial Committee on

Climate Change (IMCCC) enhances whole – of – government coordination on climate change policies to ensure that Singapore is prepared for the impacts of climate change. Established in 2007, IMCCC is chaired by Mr Teo Chee Hean, Senior Minister and Coordinating Minister for National Security. The IMCCC is supported by an Executive Committee (Exco) comprising the permanent secretaries of the respective Ministries. The IMCCC Exco oversees the work of the Long-Term Emissions and Mitigation Working Group (LWG), Resilience Working Group (RWG), Sustainability Working Group (SWG), Green Economy Working Group (GEWG) and Communications and Engagement Working Group (CEWG).

Figure 2.1: Climate Change Governance in Singapore (from NCCS, 2023).

Singapore's National Climate Change Secretariat (NCCS) was established on 1 July 2010 under the Prime Minister's Office (PMO) to develop and implement Singapore's domestic and international policies and strategies to tackle climate change. NCCS is part of the Strategy Group, which supports the Prime Minister and his Cabinet to establish priorities and strengthen strategic alignment across the Government. The inclusion of NCCS enhances strategy-making and planning on vital issues that span multiple Government ministries and agencies.

NCCS' areas of responsibility are to:

- facilitate efforts to mitigate carbon emissions in all sectors;
- help Singapore adapt to the effects of climate change;
- harness economic and green growth opportunities arising from climate change;
- encourage public awareness and promote action on climate change;

The Resilience Working Group (RWG) studies Singapore's vulnerability to the effects of climate change and develops long-term plans that ensure the nation's resilience to future environmental changes. The Long-Term Emissions and Mitigation Working Group (LWG) develops plans to reduce Singapore's long-term emissions. LWG examines mitigation options, and identifies the capabilities, infrastructure and policies needed for long-term emissions reduction. The Sustainability Working Group (SWG) develops the national sustainability agenda to strengthen Singapore's resource resilience and addresses emerging and cross-cutting issues on sustainability. The Green Economy Working Group (GEWG) coordinates and enables the growth of Singapore's green economy, to seize new economic opportunities in sustainability and create good jobs for Singaporeans. Communications and Engagement Working Group (CEWG) establishes communications priorities, to achieve greater whole-of-government coordination in climate change communications and engagement efforts, and to build consensus on Singapore's climate change plans and targets.

The Centre for Climate Research Singapore (CCRS) was launched in 2013 as a government research center to help address some of the key questions for the Singapore Government on tropical weather and climate variability and change and their impacts to Singapore's adaptation and policy planning. In 2018, CCRS was tasked to coordinate the National Sea Level Program to address key gaps in sea- level science. At the same time, initial plans were drafted for the Third National Climate Change Study (V3). Since the delivery of the results from the Second National Climate Change Study (V2) in 2015, the Singapore government has been relying on CCRS to continue to deliver important information on future climate change topics as they are relevant for Singapore and the wider Southeast Asia (SEA) region. In July 2022, the Climate Impact Science Research (CISR) Programme was launched to better understand

the long-term impact of climate change on Singapore. The S$23.5 million CISR Programme, managed by CCRS, will focus on five key priority areas – sea level rise; water resource and flood management; biodiversity and food security; human health and energy; and cross-cutting research to bridge science-policy translation.

2.2 Introduction to the V3 study

V3 is Singapore's Third National Climate Change Study and builds on Singapore's Second National Climate Change Study (V2, Marzin et al. 2015). Although V2 was commissioned by Singapore's National Environment Agency (NEA) to the Met Office Hadley Centre in the UK, the involvement of CCRS scientists in the co-production of V2 significantly helped in taking the leap forward to V3 which is produced entirely in-house by CCRS. Various experiences ranging from stakeholder engagement, model sub-selection, conducting dynamical downscaling simulations, analysis of past, present and future climate, bias adjustment, writing of the V2 Stakeholder and Technical reports, and data dissemination, provided the necessary exposure and confidence to CCRS scientists to be able to make V3 an in-house production.

Stakeholder engagement has been an important part of the V3 production process, through two annual workshops conducted by CCRS' Climate Science Research Programme Office (CSRPO) in November 2020 and January 2022, and various ad-hoc engagements throughout the year. CCRS has also been working closely with stakeholders through working groups and task forces (e.g. with the Public Utilities Board and the Singapore Food Agency) that were established to deliver science that is readily usable by our stakeholders.

The use of SINGV-RCM (adapted version of the SINGV NWP model operationally used by CCRS/MSS) for the production of V3 has been an important outcome of the SINGV project (Huang *et al.*, 2019) named after the five-year collaborative project between the UKMO and MSS to develop a convective-scale NWP system for Singapore based on the UKV model of the UK Met Office.

At the time V3 was planned, Singapore was yet to have a supercomputer to match the computing and storage needs of V3 simulations. Based on stakeholder needs, Singapore's National Supercomputing Centre (NSCC) was in the process of upgrading their HPC ASPIRE-1 to ASPIRE-2A (A2A) which is around 10 times more powerful than its predecessor. This upgrade was able to match the needs of V3 and finally a large fraction of the downscaling was conducted on A2A, and the simulations were able to be completed for timely delivery.

V3 aimed at building the next generation of climate projections for a climate-resilient Singapore. Singapore recognises the need to meet the challenges posed by climate change with actions based on robust science. To further advance our understanding of tropical climate variability and change and its implications for Singapore and the Southeast Asia region, CCRS is carrying out V3 to produce high-resolution future climate projections under various global warming scenarios that are actionable and of use to policymakers.

The **key deliverables** of V3 include past and future high-resolution climate data over Singapore and SEA region, the V3 Stakeholder Report, this Technical Report, communication and outreach materials such as infographics and videos, the V3 Data Sharing and Visualisation Portal, and peer-reviewed scientific publications. The outputs of V3 will not only form the basis of various impact assessment and adaptation studies for various Singapore Government Stakeholder agencies, but they will also underpin key areas of research supported by the Climate Science Research Programme Office (CSRPO) at CCRS, such as sea- level change, water resources, human health, energy, biodiversity, and food security. Details on the workflow of V3 are discussed in Section 2.4.

2.3 Building on Current and Past Science Excellence

The planning and design of V3 very much leveraged from lessons learned in the past, especially the previous V2 project, delivered in

2015 (Marzin et al. 2015). V2 consisted of two phases. The objective of the first phase was to produce high -resolution climate change projections relevant to Singapore, and that of the second phase was to carry out vulnerability assessment to various sectors by using the high-resolution climate change projections from Phase one of the study. Phase one of the V2 study was commissioned by Singapore's National Environment Agency (NEA) and was undertaken by the Met Office Hadley Centre in the UK jointly with scientists from CCRS and included important contributions from the National Oceanography Centre, Liverpool (NOC), and the Australian Commonwealth Scientific and Industrial Research Organisation (CSIRO) for the sea level projections. The previous generation Global Climate Models (GCMs) used for IPCC AR5 were used for V2 (from the 5th phase of the World Climate Research Programme's (WCRP) Coupled Model Intercomparison Project, or CMIP5 GCMs), whereas V3 uses the latest and most advanced GCMs that underpin the latest IPCC AR6 reports. These new GCMs (from the 6th phase of CMIP, or CMIP6 GCMs) have been assessed to provide more accurate simulations of the global climate. Key improvements in V3 over V2 are summarized in Table 2.1 below.

Table 2.1: Key improvements in V3 over V2

	V2 (2015)	V3 (2023)
Global Model	CMIP5	CMIP6 [latest IPCC models]
Regional Model	UK Met Office HadGEM3-RA	SINGV-RCM [NEW, CCRS in-house]
Future Scenarios	RCP4.5, RCP8.5	SSP1-2.6, SSP2-4.5, SSP5-8.5 [latest IPCC AR6 and more scenarios]
Spatial Resolution	12km	8km and 2km [higher resolution]
Temporal Resolution of Rainfall	Daily	12min@8km and 10min@2km [higher resolution]
Domain Size	Partially covers SEA	8km domain covers almost entire SEA and is 3 times the V2 domain. [full SEA coverage]
Bias Adjustment	Simple Quantile Mapping	Trend-preserving Quantile Mapping used in ISIMIP3. [more sophisticated method]
Assessment of Dynamical Downscaling Uncertainty	No	Yes [added uncertainty assessment]

2.4 Stages of V3

The V3 study consisted of various stages with well-defined objectives and deliverables attached to each of them, as shown in Figure 2.2. Each of the stages and the key components of work for each of them have been described in detail in the following paragraphs.

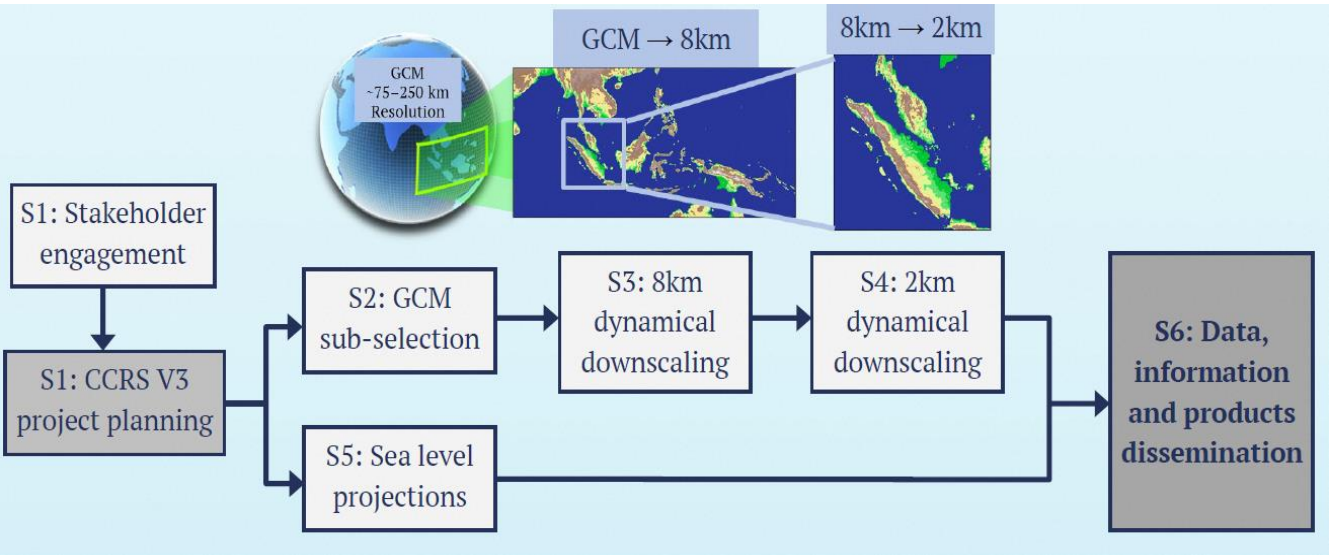

Figure 2.2: V3 Project flow chart.

The first stage of the study consisted of two parts, while one part focused on the stakeholder engagement with various Singapore Government agencies which are a part of the RWG and will be either directly or indirectly using the data and products coming out of V3, the other focused on planning the study and incorporating the stakeholder inputs into the plans. CSRPO organized the first V3 Stakeholder Engagement Workshop in November 2020, which was attended by around 100 participants from 20 Singapore Government agencies. Inputs provided by the agencies at the workshop were incorporated into the overall planning of V3. For example, some climate variables such as incoming solar radiation at the surface which were initially not a part of the V3 data sharing plan were later included based on stakeholder request.

The second stage of the study focused on sub-selecting the tentative list of CMIP6 GCMs that were to be dynamically downscaled to 8km and 2km resolutions for the historical period (1955-2014) and future (2015-2099) for the 3 global warming scenarios used in IPCC AR6, namely, SSP1-2.6 (low challenges to mitigation and adaptation), SSP2-4.5 (medium challenges to mitigation and adaptation), and SSP5-8.5 (high challenges to mitigation, low challenges to adaptation). In order to carry out sub-selection we followed standard practices suggested by the Coordinated Regional Climate Downscaling Experiment (CORDEX; e.g. Gutowski et al. 2016) of the World Climate Research Program. Thus, the sub-selected GCMs should: (1) span the range of GCM projections of temperature and precipitation over SEA, (2) perform satisfactorily in the historical climate, (3) span the range of model diversity in terms of genealogy (e.g. Knutti et al. 2013), and (4) have 6-hourly lateral boundary conditions (LBCs) available to drive the regional climate model. In addition to the aforementioned criteria, we also make use of expert judgment to discard models that are unable to simulate important aspects of regional climate over Southeast Asia (SEA). Based on the above criteria, we finalized the following CMIP6 GCMs for downscaling: **ACCESS-CM2** (Australia), **EC-Earth3** (Europe), **MIROC6** (Japan), **MPI-ESM1-2-HR** (Germany), **NorESM2-MM** (Norway), and **UKESM1-0-LL** (UK).

The third and fourth stages of the study focused on dynamically downscaling the coarse resolution GCM data (~100km grid spacing) to 8km and 2km resolutions, respectively. Generally, the latest GCMs have a resolution of 75–250 km, which means that Earth's atmosphere is divided into grid cells that are 75–250 km along each side. In each grid cell, climate information, such as temperature, humidity and topography, has only a single value. At the coarse resolution of GCMs, Singapore is not represented as being a separate island because it is smaller than the size of one

grid cell. Most climate change impacts (especially those resulting from extreme events) take place at regional and/or local scale. Due to the coarse resolution of GCMs, they cannot be used to understand details of climate processes occurring over small features (e.g. buildings, hills) at more modest regional and local scales. For scientists to understand climate change and its impacts at regional and local scales in order to inform climate change adaptation, downscaling GCMs using a higher-resolution regional climate model (RCM) to obtain more details is necessary. The dynamical downscaling design for V3 is shown in Figure 2.3 below.

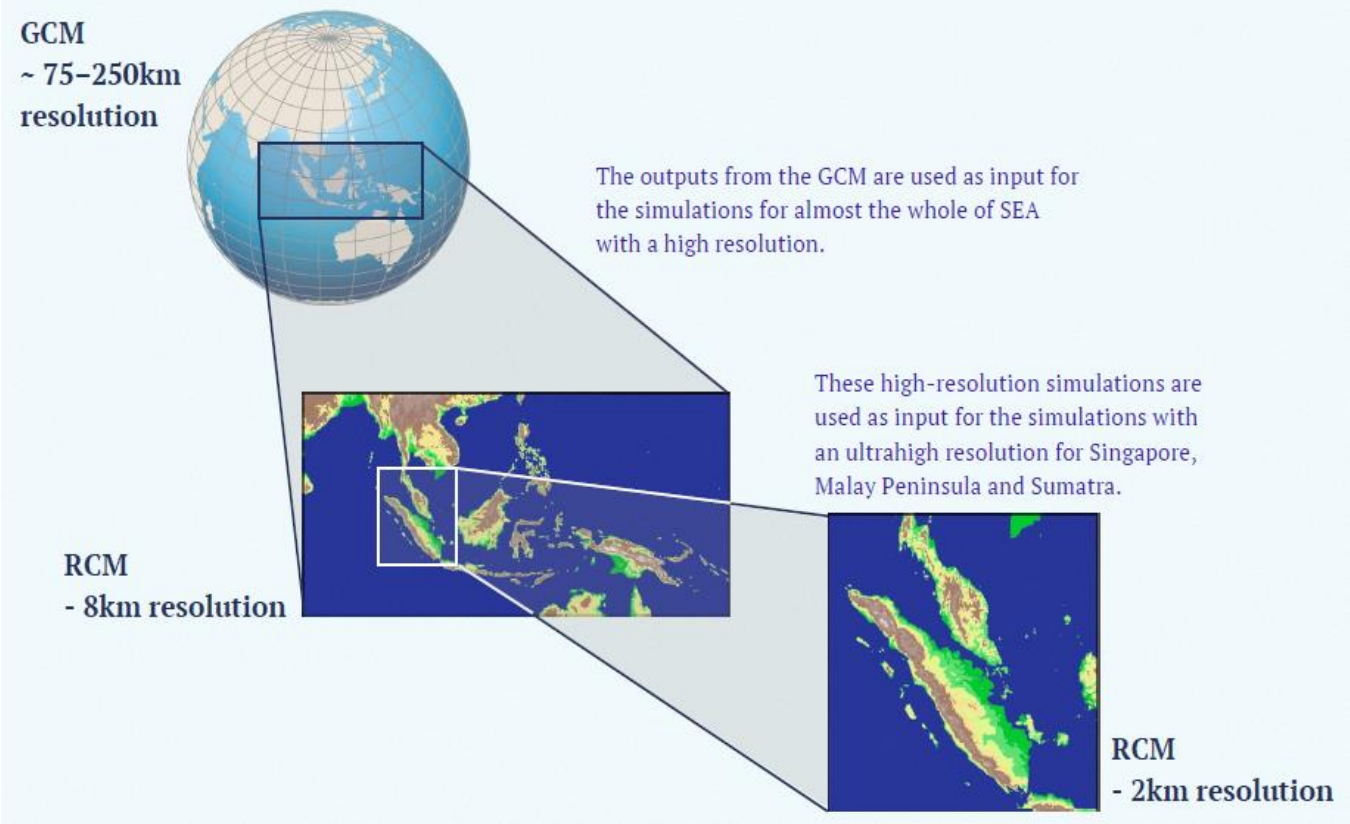

Figure 2.3: The dynamical downscaling design for V3.

The third stage of the study focused on dynamically downscaling ERA5 and the 6 sub-selected GCMs for the historical and future from their native global model resolution (in the range of 75km to 250km) to 8 km horizontal resolution over the SEA domain (shown in Figure 2.3) using the Singapore Variable Resolution - Regional Climate Model (SINGV-RCM).

SINGV-RCM is an adapted version of SINGV, which is the operational numerical weather prediction model used at CCRS and has undergone comprehensive evaluation over Singapore and SEA, and hence provides us confidence for it to be used for long-term climate change projections. For details of the model and configuration please see Chapter 6.

Major sub-components of stage three included (i) development of SINGV-RCM from SINGV which was done on the CCRS HPC system Athena, (ii) porting and testing of SINGV-RCM on the National Supercomputing Centre (NSCC) HPC system (Koppen), (iii) creation of the ancillary fields such as Land Use and Land Cover (LULC), topography, etc., (iv) downloading hundreds of Terabytes (TBs) of 6-hourly GCM forcing data from the Earth System Grid Federation (ESGF) to Koppen, (v) downloading similar big data files from the European Reanalysis Project 5 (ERA5)

from the Copernicus Data Server (vi) generating the lateral boundary conditions and the sea surface temperature, and finally (vii) running the model that also includes troubleshooting and regular housekeeping. The simulation details are shown in Table 2.2.

Table 2.2: 8 km Dynamical Downscaling Simulations

	Length of **8km** simulations/scenarios
ERA5	1 x 36 years (1979-2014)
CMIP6 GCMs for **historical**	6 x 60 years (1955-2014)
CMIP6 GCMs for **future**	6 x 85 years (2015-2099)
Number of future scenarios	3 (SSP1-2.6, SSP2-4.5, SSP5-8.5)
Total number of years	~2000

Table 2.3: 2 km Dynamical Downscaling Simulations

	Length of **2km** simulations/scenarios
ERA5	1 x 20yrs (1995-2014)
CMIP6 GCMs for **historical**	5 x 20yrs (1995-2014)
CMIP6 GCMs for **future**	5 x 40yrs (2040-2059; 2080-2099)
Number of future scenarios	3 (SSP1-2.6, SSP2-4.5, SSP5-8.5)
Total number of years	~750

The fourth stage of the study focused on further downscaling of five out of six GCMs from 8km to 2km resolution over the western Maritime Continent domain covering Singapore, Peninsular Malaysia and parts of Indonesia (shown in Figure 12.3). The simulation details are shown in Table 2.3. Although the 8 km simulations were carried out for longer time periods (60 years for the historical and 85 years for the future), the 2km simulations, being significantly more computationally expensive were run for 20-year time slices for the historical (1995-2014), mid-century (2040-2059) and end-century (2080-2099).

The fifth stage of the study focused on observed sea-level rise and sea-level projections and was carried out in parallel while the dynamical downscaling of atmospheric climate variables was ongoing. The sea-level projections for Singapore did not involve regional ocean downscaling but were mainly derived through synthesizing available sea-level projections from the Framework for Assessing Changes to Sea-level (FACTS; Kopp et al, 2023), which also served as the basis for the IPCC AR6 sea-level projections. The site-specific (at tide-gauge locations) projections from FACTS were evaluated and assessed in Singapore's context by comparing projections with historical sea-level rise estimated at Singapore's tide-gauge stations. For instance, by correcting the tide-gauge datum shift and updating the local VLM (Vertical Land Movements) at tide-gauge stations, V3 provides an updated set of relative sea-level rise projections for Singapore. The report also provides an overview of the sea-level drivers, observed sea-level rise in the Southeast Asian region over the last three decades and a detailed discussion on the local VLM in Singapore (Chapter 12).

The sixth and final stage of the study focused on data processing, analysis, report writing, manuscript writing for scientific journals, design, content creation and testing of the V3-DSVP web portal, and production of communication materials in the form of brochures and videos. Almost 10 PetaBytes (PBs) of data was processed from raw model outputs to standardized datasets that are compliant with CMIP and CORDEX standards.

Beyond undertaking the downscaling simulations, some of the key post-downscaling Milestones of the V3 Study include:

Data processing: The processing of the data was carried out using an in-house climate toolbox that was developed for this purpose. One of the

major steps in data processing was the bias adjustment of the downscaled data over Singapore, using an advanced method from the ISIMIP3. As a part of bias adjustment, an in-house daily gridded rainfall dataset over Singapore was developed from rain gauge observations by using the kriging method at 2km and 8km resolutions.

Analysis: Analysis of the results comprised of both historical evaluation and future climate change projections of dynamically downscaled data at 8 km and 2 km resolutions for key climate variables (rainfall, temperature, winds, and humidity), and climate drivers (monsoon, ENSO teleconnections, cold surges, and weather regimes). The sea level analysis presented findings on observed and projected sea-level change in Singapore and its surrounding regions.

Report writing: Two V3 reports were written - Report for Stakeholders and the Technical Report. The Stakeholder Report provides key messages of the V3 study and is designed for the Stakeholder agencies, policymakers, and the public, whereas the Technical Report spanning 14 chapters is designed to provide more technical details and would be useful for agencies interested in more in-depth information, researchers from Singapore Institutes of Higher Learning (IHLs), and regional as well as international researchers.

Journal Manuscripts: While the primary objective of V3 is to produce high-resolution climate change projections over Singapore and SEA to assist vulnerability assessment and adaptation planning, it also aims to improve our understanding of the drivers of climate variability and change over the region. New scientific insights developed from the analysis of high-resolution downscaled model outputs will be reported in peer-reviewed scientific journals as our contribution to the scientific literature on climate variability and change over the region.

V3-DSVP: In order to share data, figures, reports, and various communication materials with Stakeholder agencies, researchers and the public, we will be making all this available through a data sharing and visualization portal (DSVP). There will be an interim portal which will be used to share everything mentioned above other than data that will be launched together with the V3 public release, whereas, the final portal will be more advanced and will have the capability to host data as well as have interactive data analytics capability for advanced users that will be tentatively operational in late 2024. The design document along with all the contents of the two web portals have been developed in-house at CCRS, whereas the software development of the portal is outsourced.

Communication materials: Brochures, videos and infographics to communicate various aspects of V3 are developed by CCRS and the MSS Business and Strategy Division. Topics for the brochures and videos include: (1) introduction to V3, (2) dynamical downscaling, (3) sea level projections, (4) climate extremes, (5) using climate change projections in risk assessments, (6) probabilistic climate change projections, (7) weather and climate drivers of Singapore, and (8) application-ready datasets.

2.5 Outline of the V3 Technical Report

The V3 Technical Report is an in-depth description of all the components of the V3 project, as well as highlighting the key results from our analysis. The report consists of 14 chapters; the initial chapters will provide details on historically observed changes in Singapore's climate and the process going from global climate change analysis (as in the recent IPCC AR6 report) to a regional and then local approach applied in V3.

Following on, an evaluation and analysis of the regional and local downscaling is presented. This includes chapters on both bias correction and uncertainty assessment.

As a separate chapter, emphasizing the importance but also the fact that the methodology is different, we present the new sea level projections for Singapore based on IPCC AR6 methodology.

Finally, we give an overview of two important project efforts crucial for the success overall: first, the extensive work on HPC to undertake dynamical downscaling and second, the science communication effort to disseminate the information locally and regionally.

References

NCCS (2023) accessed National Climate Change Secretariat website at https://www.nccs.gov.sg/singapores-climate-action/mitigation-efforts/overview/ and https://www.nccs.gov.sg/who-we-are/inter-ministerial-committee-on-climate-change/

NEA (2022) https://www.nea.gov.sg/media/news/news/index/23.5-million-climate-impact-science-research-(cisr)-programme-launched-to-support-long-term-climate-change-adaptation-planning

National Climate Change Secretariat. (2023). Mitigation Efforts: Overview . Retrieved September 19, 2023, from https://www.nccs.gov.sg/singapores-climate-action/mitigation-efforts/overview/

National Climate Change Secretariat. (2023). Inter-Ministerial Committee on Climate Change (IMCCC). Retrieved September 19, 2023, from https://www.nccs.gov.sg/who-we-are/inter-ministerial-committee-on-climate-change/

Knutti, R., Masson, D., & Gettelman, A. (2013). Climate model genealogy: Generation CMIP5 and how we got there. Geophysical Research Letters, 40 (6), 1194–1199.

Gutowski Jr., W. J., Giorgi, F., Timbal, B., Frigon, A., Jacob, D., Kang, H.-S., et al. (2016). WCRP COordinated Regional Downscaling EXperiment (CORDEX): a diagnostic MIP for CMIP6. *Geoscientific Model Development*, *9*(11), 4087–4095.

Huang, X.-Y., Barker, D., Webster, S., Dipankar, A., Lock, A., Mittermaier, M., Sun, X.M., North, R., Darvell, R., Boyd, D., Lo, J., Liu, J.Y., Macpherson, B., Heng, P., Maycock, A., Pitcher, L., Tubbs, R., McMillan, M., Zhang, S.J., Hagelin, S., Porson, A., Song, G.T., Beckett, B., Cheong, W.K., Semple, A. and Gordon, C. (2019) SINGV–the convective-scale numerical weather prediction system for Singapore. ASEAN Journal on Science and Technology for Development, 36(3), 81–90.

IPCC (2021) *Climate Change 2021: The Physical Science Basis*. Contribution of Working Group I to the Sixth Assessment Report of the Intergovernmental Panel on Climate Change [Masson-Delmotte, V., P. Zhai, A. Pirani, S.L. Connors, C. Péan, S. Berger, N. Caud, Y. Chen, L. Goldfarb, M.I. Gomis, M. Huang, K. Leitzell, E. Lonnoy, J.B.R. Matthews, T.K. Maycock, T. Waterfield, O. Yelekçi, R. Yu, and B. Zhou (eds.)]. Cambridge University Press, Cambridge, United Kingdom and New York, NY, USA, 2391 pp. doi:10.1017/9781009157896.

IPCC (2022a) *Climate Change 2022: Impacts, Adaptation, and Vulnerability.* Contribution of Working Group II to the Sixth Assessment Report of the Intergovernmental Panel on Climate Change [H.-O. Pörtner, D.C. Roberts, M. Tignor, E.S. Poloczanska, K. Mintenbeck, A. Alegría, M. Craig, S. Langsdorf, S. Löschke, V. Möller, A. Okem, B. Rama (eds.)]. Cambridge University Press. Cambridge University Press, Cambridge, UK and New York, NY, USA, 3056 pp., doi:10.1017/9781009325844.

IPCC (2022b) *Climate Change 2022: Mitigation of Climate Change.* Contribution of Working Group III to the Sixth Assessment Report of the Intergovernmental Panel on Climate Change [P.R. Shukla, J. Skea, R. Slade, A. Al Khourdajie, R. van Diemen, D. McCollum, M. Pathak, S. Some, P. Vyas, R. Fradera, M. Belkacemi, A. Hasija, G. Lisboa, S. Luz, J. Malley, (eds.)]. Cambridge University Press, Cambridge, UK and New York, NY, USA. doi: 10.1017/9781009157926

Marzin, C.; Rahmat, R.; Bernie, D.; Bricheno, L.M.; Buonomo, E.; Calvert, D.; Cannaby, H.; Chan, S.; Chattopadhyay, M.; Cheong, W.-K.; et al. (2015) Climate Change Projections. In Singapore's Second National Climate Change Study—Climate Projections to 2100 Science Report; National Climate Change Secretariat: Singapore, 2015.

3 Observed Climate Change over Singapore

Authors:
Aurel Moise, Sandeep Sahany, Muhammad Eeqmal Hassim, Chen Chen, Xin Rong Chua, Venkatraman Prasanna, Gerald Lim, Pavan Harika Raavi, Jianjun Yu, Fei Luo

Meteorological Service Singapore
Centre for Climate Research Singapore

3.1 Introduction

There have been two key reports published recently providing important information on global and regional observed climate changes. First, the Sixth Assessment Report (AR6) of the Intergovernmental Panel on Climate Change (IPCC) notes that many of the changes observed in the climate are unprecedented in thousands of years and have already set in motion changes such as sea level rise that are irreversible over hundreds to thousands of years (often referred to as the locked-in climate change).

Secondly, the World Meteorological Organization (WMO) published its annual state of the global climate report based on a network of observing systems spread across the world which are maintained by various organisations, with the National Meteorological and Hydrological Services playing a key role in this effort. Some of the highlight statements from the WMO Report for the year 2022 are:

- The global mean temperature in 2022 was 1.15 [1.02–1.28] °C above the 1850–1900 average. The years 2015 to 2022 were the eight warmest in the 173-year instrumental record. The year 2022 was the fifth or sixth warmest year on record, despite ongoing La Niña conditions.

- The year 2022 marked the third consecutive year of La Niña conditions, an episode which has only occurred three times in the past 50 years.

- Despite continuing La Niña conditions, 58% of the ocean surface experienced at least one marine heatwave during 2022.

- Global mean sea level continued to rise in 2022, reaching a new record high for the satellite altimeter record (1993–2022). The rate of global mean sea level rise has doubled between the first decade of the satellite record (1993–2002, 2.27 mm per year) and the last (2013–2022, 4.62 mm per year).

Most relevant for Singapore, the Meteorological Service Singapore (MSS) publishes its Annual Climate Assessment Report (ACAR) each year on 23rd March, celebrated as the World Meteorological Day, which is an annual assessment of Singapore's climate. Some of the highlight statements from the latest ACAR (ACAR 2022) for the year 2022 are:

- 2022 was Singapore's sixth wettest year since 1980 with an average annual total rainfall of 3012 mm. This is nearly 19% higher than the long-term 1991 – 2020 average. Rainfall for most months was above average, with October 2022 recording the highest October total rainfall in the last four decades.

- Despite the high rainfall, Singapore's annual mean temperature in 2022 was the tenth highest since temperature records began in 1929, tied with five other years.

3.1.1 Climate Monitoring over Singapore

MSS has a network of meteorological observing stations, which includes manned as well as automated stations that provide real-time observations across Singapore (Figure 3.1). MSS currently operates a network of five manned observation stations, one upper air observatory and around 100 automatic weather stations. All the automatic weather stations measure rainfall, and more than one-fifth measure other meteorological variables, including temperature, relative humidity, pressure, and wind. This observation network serves as the primary source of climate data for this report.

The manned observation station at Changi is MSS's designated climate station (see Figure 3.2). The climate station, first located at Outram in 1869, has moved several times over the years due to changes in local land use before moving to its current site at Changi. The climate station serves as the reference station where its records are used for tracking the national long-term climate trends. The oldest climate station records are for monthly rainfall (starting from 1869) and temperature (starting from 1929, with a break from 1942 to 1947 due to World War II).

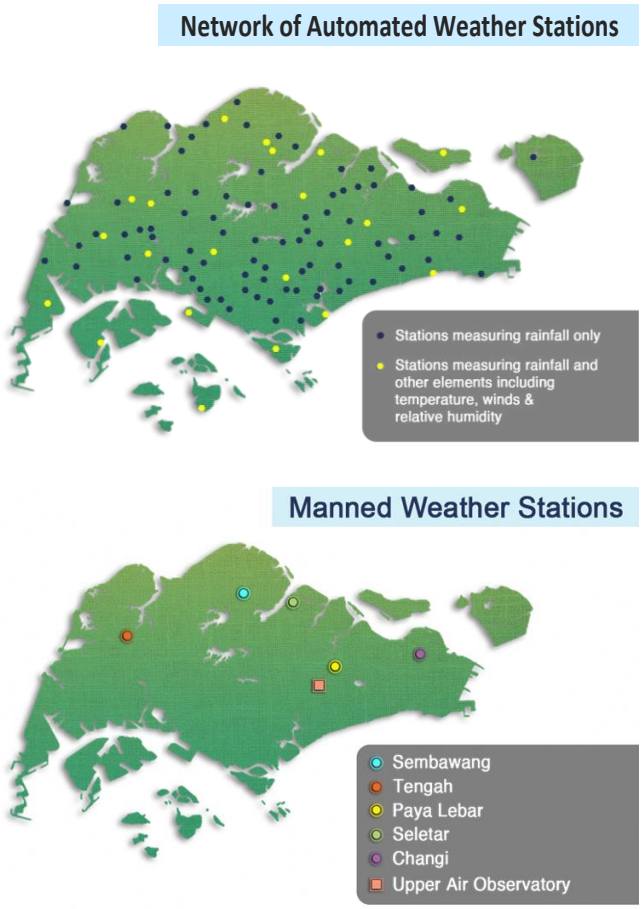

Figure 3.1: Network of automated weather stations (top), and manned weather stations (bottom).

Figure 3.2: Changi climate station.

Figure 3.3: Upper Air Observatory

The installation of the automatic weather station network since 2009 greatly expanded the coverage of weather observations across Singapore. Prior to this, there were around 40 manual rainfall stations and just a few temperature stations in Singapore. For the purpose of analysing long-term climate trends and establishing climatological averages, only stations with continuous long-term (at least 30 years) records can be used.

Singapore is located deep within the tropics, where wind and atmospheric conditions evolve rapidly. The twice-daily soundings provide the main source of complete upper-air information to support operations. In addition to operational purposes, the observation records from the station can also be useful for monitoring long-term upper air conditions in the equatorial tropics, as the records extend back many decades to the 1950s (see Figure 3.3).

MSS also operates two weather radars, an S-band radar located at Changi and a C-band radar located at Seletar airport, to monitor the development of weather systems covering a radius of up to 480 km.

In addition to the atmospheric monitoring, Singapore also monitors its sea levels using tide gauges. To the best of our current knowledge, Singapore has 19 tide gauges owned and maintained by the Maritime & Port Authority of Singapore (MPA; see Figure 3.4).

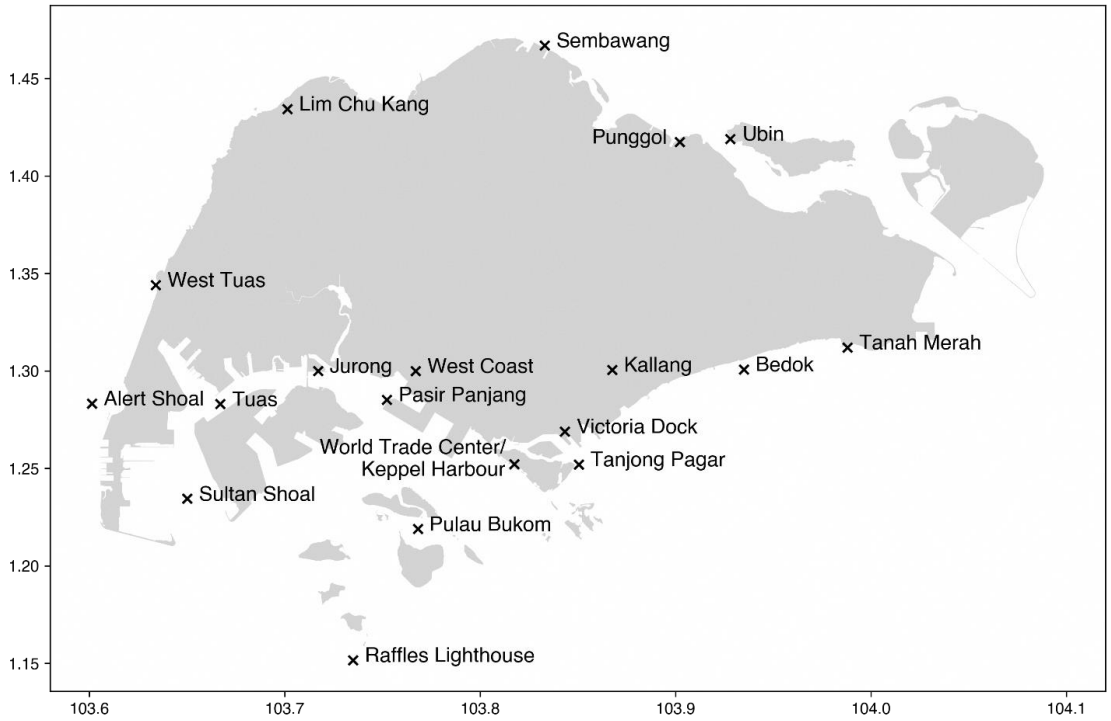

Figure 3.4: Location of the 19 tide gauges around Singapore. Tide-gauge at offshore island, Horsburgh Lighthouse, not shown here.

3.1.2 Importance of high-quality observations

High temporal and spatial resolution long-term observations which have undergone rigorous quality control are essential for monitoring and understanding the past climate, and also for validating how well the numerical models simulate the important climate variables. This in turn helps further model development to improve the accuracy of simulations and reliability of future projections.

In addition, high-quality observations play an important role in carrying out post-processing of model simulations such as bias-adjustment, whether they be short to medium-range weather forecasts, sub-seasonal to seasonal predictions or climate change projections.

3.1.3 General Climate of Singapore and their Drivers

Singapore has a tropical climate, which is warm and humid, with an abundant total annual rainfall of approximately 2490 mm (Hassim & Timbal, 2019). Generally, the eastern parts of Singapore receive less rainfall compared to other parts of the island. The climatological annual mean rainfall is shown in Figure 3.5 below. The winds are generally light but with a diurnal variation due to land and sea breezes.

The temperature variation throughout the year is relatively small compared to mid-latitude regions. The daily temperature range has a minimum usually not falling below 23–25°C during the night, and a maximum usually not rising above 31–33°C during the day.

Singapore's climate is traditionally classified into four periods according to the average prevailing wind direction:

1. Northeast Monsoon (December to early March)
2. Inter-monsoon (Late March to May)
3. Southwest Monsoon (June to September)
4. Inter-monsoon (October to November)

The northeast monsoon season has a wet phase during Dec-Jan and a dry phase during Feb-Mar, whereas there is no strong intraseasonal variation during the southwest monsoon season. The transitions between the monsoon seasons occur gradually, generally over a period of two months (the inter-monsoon periods). The winds during the inter-monsoon periods are usually light and variable in direction.

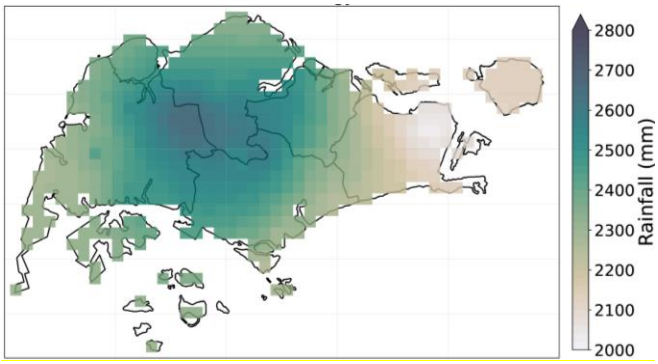

Figure 3.5: Annual rainfall for the 30-year (1991-2020) climatological period based on 28 rainfall stations across Singapore.

The major weather and climate features are influenced by climate drivers operating on different temporal and spatial scales, from the seasonal migration of the monsoon (i.e., the Intertropical Convergence Zone (ITCZ)), and other large-scale drivers such as El-Nino Southern Oscillation (ENSO), Indian Ocean Dipole (IOD), and the Madden-Julian Oscillation (MJO), to smaller scale features such as Sumatra squalls, the Borneo Vortex and remote influences from tropical cyclones (see Figure 3.6).

These features, sometimes several occurring at the same time, affect the regional pattern in rainfall, temperature, winds, ocean currents, and many other aspects of the climate and the environment in general.

Understanding the large- and small-scale features that influence climate variability across the Maritime Continent is essential in predicting Singapore's weather and climate as well as understanding how the climate may change in the future. Such knowledge helps to inform climate adaptation planning and preparedness and supports resilient development in vulnerable local communities. The provision of reliable scientific information for decision-making enables more effective adaptation planning: an essential requirement for securing sustainable development in the region.

The **El Niño – Southern Oscillation (ENSO)** is the major influence on climate variability in the western tropical Pacific and Maritime Continent. It affects the year-to-year chance of droughts, extreme rainfall and floods, tropical cyclones, extreme sea levels, and coral bleaching.

The **Intertropical Convergence Zone (ITCZ)** is a persistent east-west band of converging low-level winds, cloudiness, and rainfall stretching across the Maritime Continent into the Pacific Ocean bringing monsoonal rains. It migrates every year southward across the equator and back again, affecting most countries across the Maritime Continent including Singapore. There are interannual variations in the width and strength of the ITCZ that can have a large influence on the rainfall over the region and over Singapore. For example, one of the worst droughts over Singapore that happened in February 2014 was associated with the narrowing of the ITCZ over Singapore (McBride et al., 2015).

The **Indian Ocean Dipole (IOD):** Indian Ocean sea surface temperatures impact rainfall and temperature patterns across the Maritime Continent. Warmer than average sea surface temperatures can provide more moisture for weather systems crossing the region. Sustained changes in the difference between sea surface temperatures of the tropical western and eastern Indian Ocean are known as the Indian Ocean Dipole (IOD). The IOD has three phases: neutral, positive, and negative.

The **Madden-Julian Oscillation (MJO):** MJO can be characterised as an eastward moving "pulse" of cloud and rainfall near the equator that typically takes around 30 to 60 days to circle the globe, although the signal of the MJO in the tropical atmosphere is not always present. MJO effects are most evident over the Indian Ocean and the Maritime Continent. Besides influencing the region's wind and bringing more rain, it can also bring periods of drier conditions associated with its dry or 'suppressed' phase.

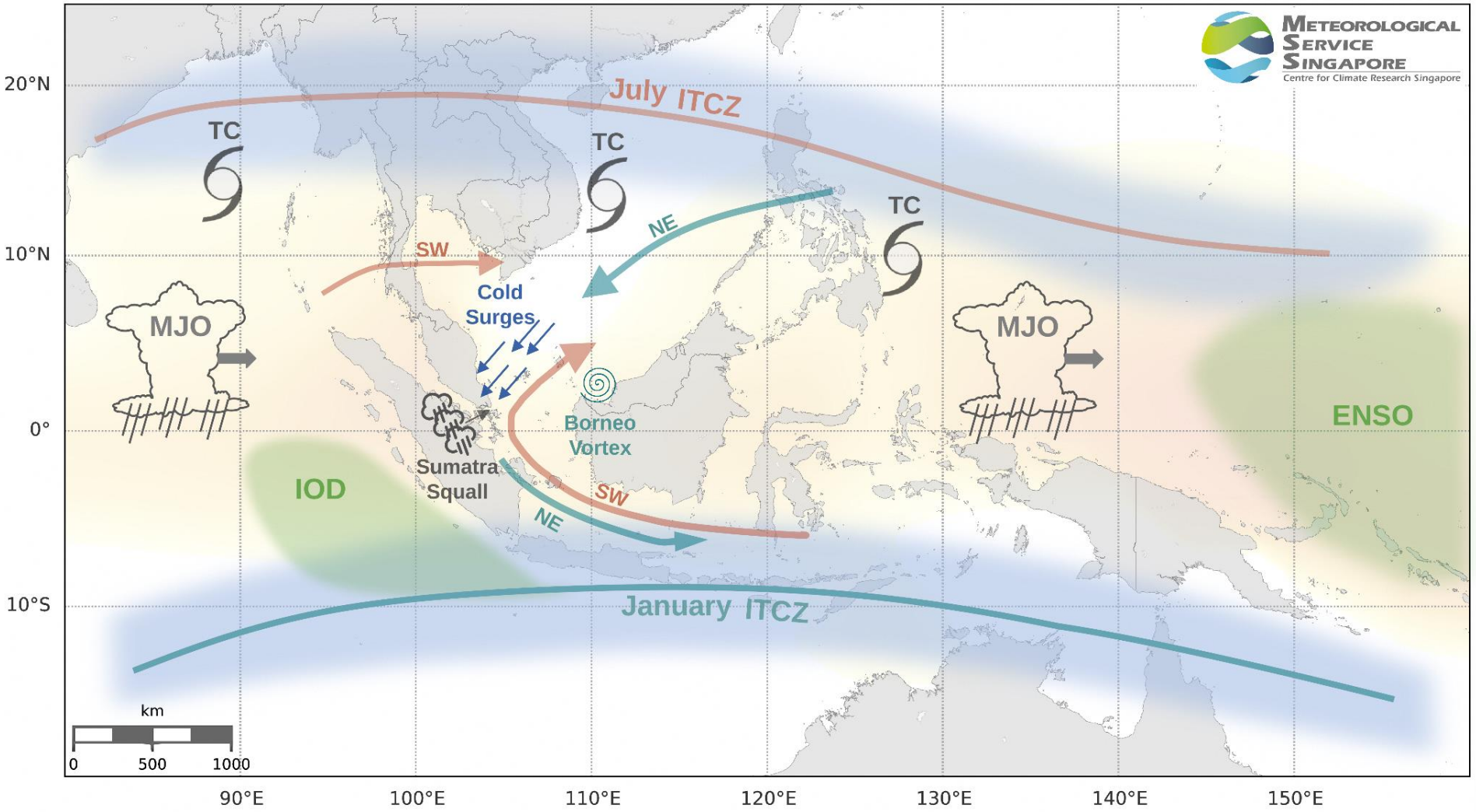

Figure 3.6: Climate drivers influencing weather and climate for the region around Singapore. Included are the average position of the Intertropical Convergence Zone (ITCZ) in blue indicating the furthest northward and southward extent of the seasonal migration of the regional monsoon system. The green and orange arrows indicate the corresponding Northeast and Southwest monsoonal flows. Against the background of warm ocean waters (soft orange colour indicating regions above 28.5°C), the El Niño–Southern Oscillation (ENSO) and Indian Ocean Dipole (IOD) impact the region's rainfall patterns on seasonal and inter-annual timescales, while the Madden-Julian Oscillation (MJO) impacts the region's rainfall at weekly to monthly timescales. At shorter timescales, Sumatra Squalls, Cold Surges and the Borneo Vortex can be sources of strong rainfall events. Further afar, tropical cyclones (TCs) can develop near the ITCZ away from the equator.

Sumatra Squall Lines: It is an organised line of thunderstorm that develops over Sumatra or the Strait of Malacca, and typically moves eastward towards Singapore under the influence of south-westerly or westerly winds. It commonly occurs during the Southwest Monsoon and Inter-monsoon periods, and usually affects Singapore overnight or in the morning, often bringing strong gusty surface winds of 40 to 80 km/h and heavy rain lasting from one to two hours.

Northeast Monsoon Surges: Monsoon surges are a key synoptic feature of the boreal winter circulation over the Maritime Continent (e.g. Chang et al., 2005) and can lead to extreme rainfall. During the period December through early March, the continental northern Asia including Siberia, experiences very low, cold temperatures. From time to time, this cold air surges southward from Central Asia to the South China Sea. This results in a sudden increase in north-easterly winds over the South China Sea, blowing toward the warm tropics. The sea warms and moistens the overlying air, and the winds converge to bring widespread rain in the tropics.

December and January are usually the wettest months of the year in Singapore. The few widespread moderate to heavy rain spells caused by surges of Northeast Monsoon winds contribute significantly to the rainfall in these months. A typical rain spell generally lasts for a few days. The cold surges can also be enhanced by the presence of a favourable phase of the MJO (e.g. Lim et al., 2017) and might also aid the MJO in its passage across the Maritime Continent (Pang et al., 2018).

Borneo Vortex: It typically appears off the north-western coast of northern Borneo. If a monsoon cold surge event coincides with a vortex, Singapore can experience enhanced rainfall as the convection strengthens over northwest Borneo and weakens north of Java. The lifetime of the vortex is typically a few days.

Tropical cyclones (TCs) usually form over large bodies of relatively warm water away from the equator. Because of the large-scale spatial extent of some TCs, they can have a remote impact on Singapore's weather. Generally, tropical cyclones occur between 5 and 30 degrees latitude (north), and do not form in the equatorial regions because the Coriolis effect is negligible near the equator. However, the rare occurrence of two colliding systems can lead to cyclone development. In December 2001, typhoon Vamei formed when strong winds from a monsoon surge interacted with an intense circulation system in the South China Sea. Typhoon Vamei came within 50 km northeast of Singapore and brought windy and wet conditions to Singapore.

3.2 Observed changes in temperature

Historical archives from the National Library of Singapore indicate that observations of monthly temperature and rainy days in Singapore were taken from as far back as 1820 during British colonial times by various individuals, the earliest of which was by Singapore's first Resident, William Farquhar. However, routine measurements for rainfall only began from 1869 when the practice was formally institutionalised by the Medical Department of the Straits Settlements, first in places such as the Convict Jail Hospital in Bras Basah, the Convict Prison in Outram and later at Kandang Kerbau Hospital (Table 3.1).

The location of the officially designated climate station has varied over time following the formation of the Malayan Meteorological Service – the predecessor to the Meteorological Service Singapore – in 1929, beginning with Mount Faber in the south of Singapore (Figure 3.7). Measurements ceased between 1941 to 1947 due to World War II; during this period, the climate station was located at the Botanic Gardens. The climate station was then located at Kallang Airport and then at Paya Lebar Airport before its current site at Changi in the east of Singapore, where it has been since July 1981.

The official climate station record for monthly mean temperature dates back to January 1929 from Mount Faber (Figure 3.8). However, monthly mean temperature observations from Changi climate station (derived from daily mean values) were only used in the official climate station

record from 1984 onwards. Prior to that, between 1981 to 1984, the monthly mean observations from Paya Lebar were still used.

As the site of the climate station has changed over time, we consider the period 1984 – present from Changi to constitute the longest and most homogeneous climate station record for monthly mean temperature. Another weather observation station that has long-term daily temperature records going back to 1972 is Tengah, situated in the west of Singapore (Fig. 3.7). The western location of Tengah and its long time series allows us to compare how temperatures across the island have evolved over time during the common overlapping 1984 – 2018 period between the two stations.

Table 3.1: Locations of the Climate Station in Singapore and their period of active service. Reproduced from www.weather.gov.sg/learn_climate. Only records from Mount Faber, Kallang, Paya Lebar and Changi constitute the official climate station record for monthly mean temperature.

	Period of Service	Location of Climate Station
1	Jan 1860 - Dec 1874	Convict Prison (Outram)
2	Jan 1875 - Dec 1928	Kandang Kerbau Hospital
3	Jan 1929 - May 1934	Mount Faber
4	Jun 1934 - Dec 1941	Kallang
5	Jan 1942 - Dec 1947	Botanical Gardens
6	Jan 1948 - Aug 1955	Kallang
7	Sep 1955 - Dec 1983	Paya Lebar
8	Jan 1984 - present	Changi

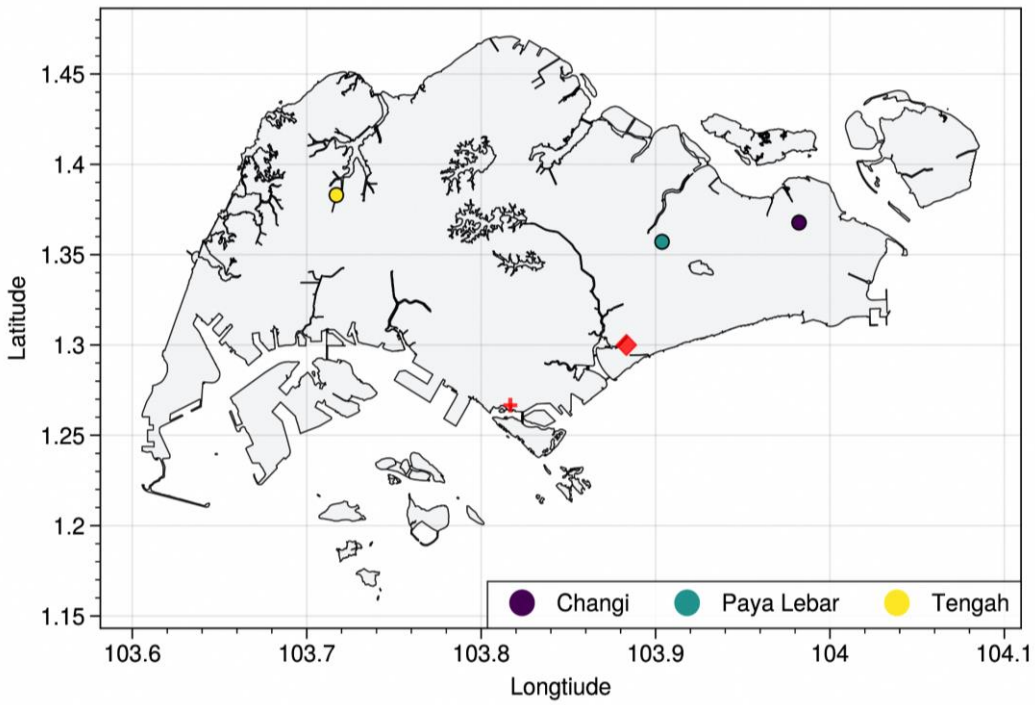

Figure 3.7: Location of Changi Climate Station and the manned stations at Tengah and Paya Lebar (previous climate station from 1955-1984) with long-term observations going back prior 1980. The location of the early climate stations of Singapore (Mt

Faber, 1929-1934) and Kallang Airport (1935-1941, 1948-1955) whose temperature observations are included in the long-term climate station record, are marked by the red cross and red diamond, respectively.

3.2.1 Mean Temperature

Over the last 39 years since 1984, the average daily mean temperature has been steadily rising at the climate station, as seen in Figure 3.8. This rise in temperature is evident even with the large year-to-year variability due to the influence of large-scale climate drivers such as the El Niño-Southern Oscillation (ENSO). El Niño events tend to increase annual mean temperatures across Singapore, while La Niña events tend to moderate them.

Over the 1984 to 2022 period, the long-term warming rate across the two stations are very comparable: the mean temperature at the climate station has increased at a rate of 0.24°C per decade, while Tengah has warmed at a slightly higher rate of 0.26°C per decade. The slightly higher rate is likely due to the rapid rise in annual mean temperature in the last decade (from 2010). Both Tengah and Changi exhibit a warming rate that is slightly higher than the global mean temperature (derived from the Berkeley Earth dataset), which shows a warming trend of 0.21°C per decade over the 1984 to 2022 period.

Singapore showed an upward trend of 0.67°C per decade in daily mean temperature during 1973-1992, with a slower rate of increase at 0.17°C per decade during 2003-2022. The corresponding values for global trends are 0.17°C and 0.22°C per decade respectively. The high value of the upward trend during 1973-1992 can be attributed to rapid urbanisation in Singapore at the time. The accompanying effect on temperature is called the Urban Heat Island (UHI) effect whereby towns and city areas experience much higher temperatures and remain warmer than their greener surroundings. The effect is most noticeable at night when temperatures in more built-up environments can be several degrees higher than less developed areas surrounded by more trees and/or water bodies (ACAR 2022).

This UHI effect is on top of long-term warming trends due to climate change.

In contrast, the global mean warming rate shows an upward trend of 0.17°C per decade and 0.22°C per decade for the corresponding periods, largely driven by the accelerated warming over the northern hemisphere high latitude regions (Arctic region amplification) in the recent decades.

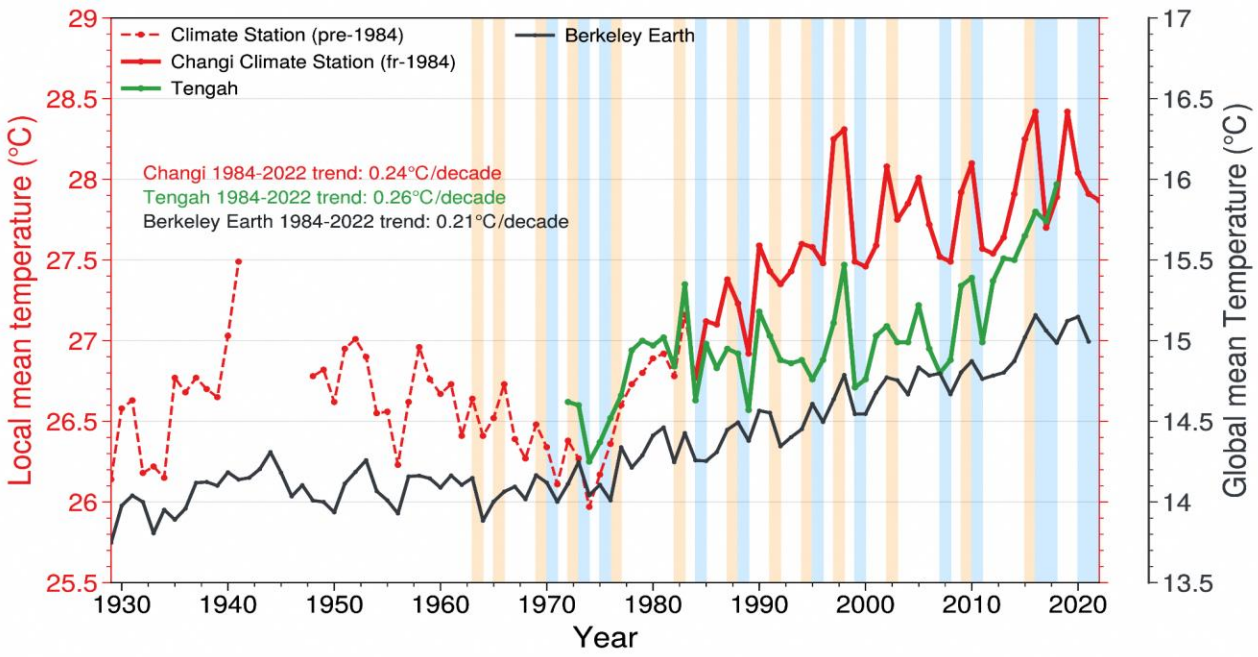

Figure 3.8: Time series of the local annual mean temperature from the climate station (dotted and solid red lines, for pre-1984 and from 1984, respectively) and Tengah (green). Also shown is the global mean temperature time series plotted on the right secondary axis for comparison. The orange and blue shades denote El Niño and La Niña years from 1980, respectively.

Table 3.2: Decade-by-decade trend analysis for the Climate Station vs. the Berkeley Earth global mean (land+ocean) dataset for 1984-2022.

	Decade-by-decade trends (°C per decade)	
	Station Data (Singapore Climate Station)	Gridded Data Berkeley Earth (land+ocean)
1984-1993	0.52	0.24
1993-2002	0.17	0.31
2003-2012	-0.23	0.07
2013-2022	0.07	0.27

3.2.2 Daily Minimum and Maximum Temperatures

Figure 3.9 compares the mean daily minimum temperature anomalies between the Tengah station, the Changi climate station and the global average air temperature over land. The Tengah station is situated close to the Tengah River, surrounded by the more forested areas of western Singapore, while the Changi station is sited near the more developed residential parts in eastern Singapore and close to the airport's runway. Over the last 50 years (1973 – 2022), the night-time minimum temperatures at Changi have warmed more rapidly (0.21°C/decade, Figure 3.9a) than the location's daytime maximum temperatures, which show no significant trend (0.06°C/decade, Figure 3.9b). In contrast, both the night-time low and daytime high temperatures at Tengah are rising almost in tandem (at 0.14°C/decade and 0.13°C/decade, respectively; both trends are statistically significant at the 5% level). In fact, the minimum temperatures at Changi are warming 1.5 times faster than those at Tengah, and comparable to the global land average (0.24°C/decade).

A consequence of Changi warming much faster during the night than it does during the day is that we see a significant reduction in its diurnal temperature range (DTR) (Figure 3.9c). In contrast, the DTR at Tengah exhibits a negligible trend since both daytime maximum and night-time minimum temperatures show similar warming rates there.

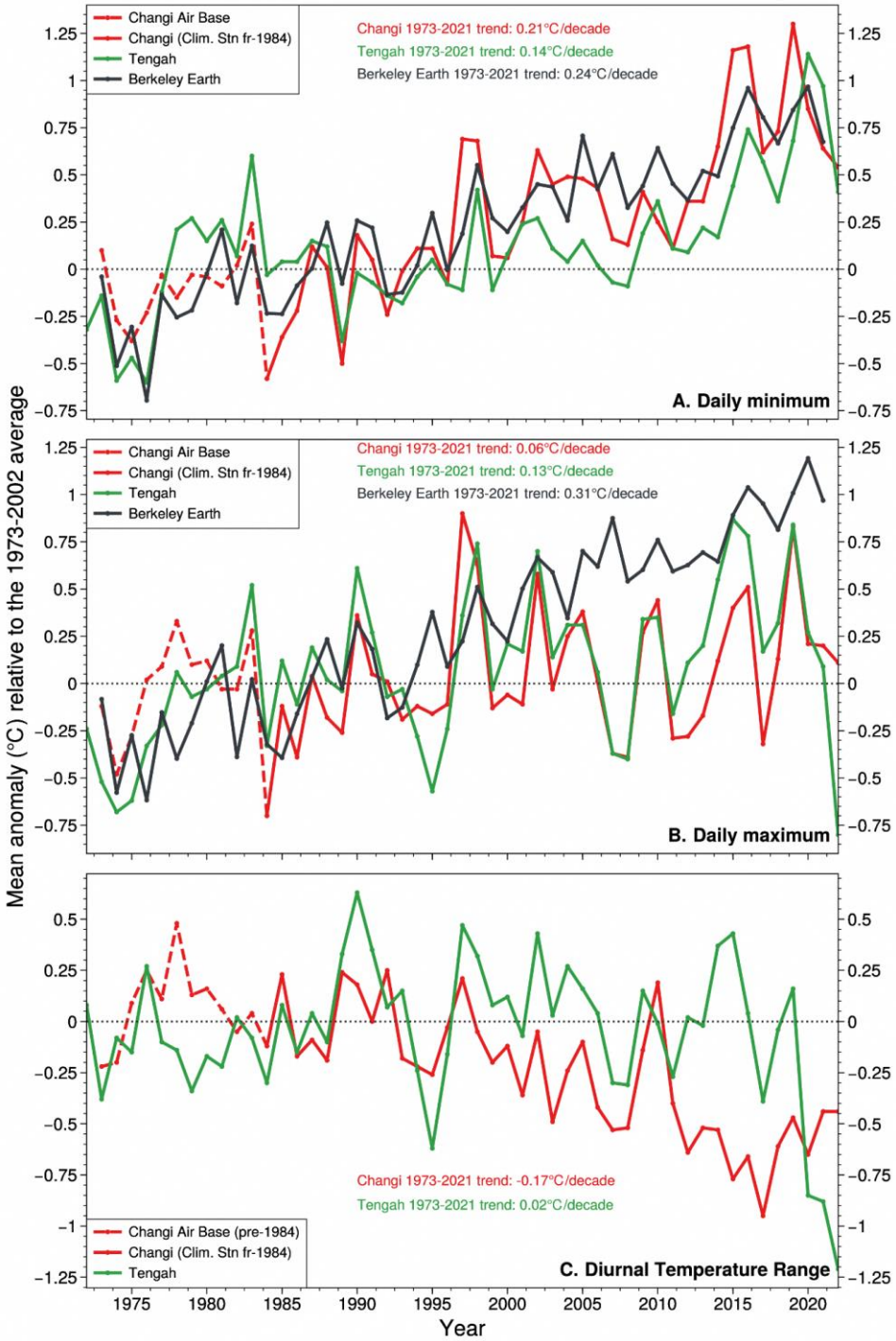

Figure 3.9: As in Fig. 2.1 but for annual average anomaly of (a) daily minimum and (b) daily maximum compared to the corresponding Berkeley Earth Surface Temperature dataset for global land only (black solid line). The diurnal temperature range is shown in (c). The anomalies are calculated relative to the 1981-2010 climatology. Also shown are respective trends (dotted lines) for the 1970-2022 period (greyed background).

3.2.3 Warm Days

Since the mid-1970s, there has been an overall increase in the number of warm days (days when the daily maximum temperature exceeds 34℃), as can be seen in Figure 3.10. An upward trend was observed in some weather stations. For instance, the number of warm days recorded at Tengah and Seletar stations increased to 1.3 and 0.8 days per year between 1972 and 2022, respectively. High temperature characteristics vary spatially across the island, with Changi station experiencing fewer warm days than the other two stations. The fewer warm days could be due to the sea breeze effect. As Changi is located near the coast, where cooler air from the sea replaces the warm air on the island, this can reduce the high afternoon temperatures and relieve the heat. However, it is worth noting that the frequency of warm days exceeding 20 days per year in Changi has increased.

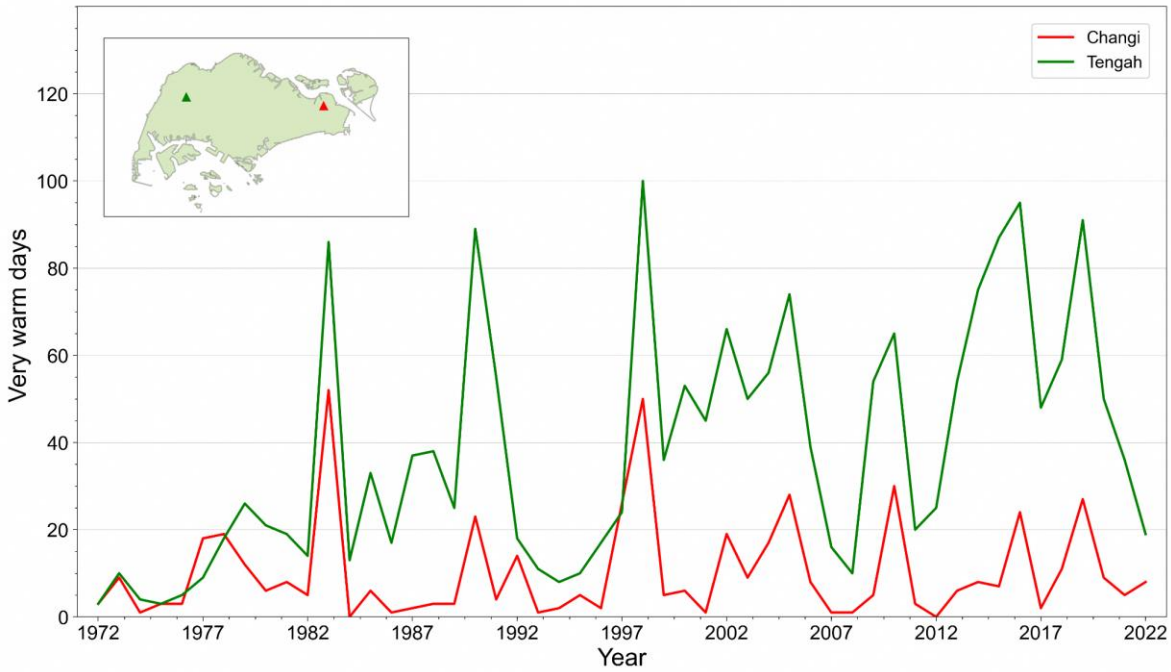

Figure 3.10: The number of warm days, counted as days with maximum daily temperature above 34℃ for Changi (red) and Tengah (green) weather stations from 1972 - 2022.

3.3 Observed change in heat stress

According to the IPCC AR6 WG-II report, heat stress is a range of conditions when the body absorbs excess heat during overexposure to high air or water temperatures or thermal radiation. Heat stress in humans is exacerbated by a detrimental combination of ambient heat, high humidity and low wind speed, causing the regulation of body temperature to fail. Although heat stress can be measured by empirical measures such as wet-bulb globe temperature (WBGT) and apparent temperature that are functions of temperature, humidity, wind and sunlight, we use the wet-bulb temperature (WBT) as a simple and powerful indicator of heat stress.

In Figure 3.11, we show the annual mean of the daily maximum WBT from Changi and Tengah weather stations for the period 1985-2020. It can be seen from the figure that there is no monotonic trend in WBT in either of the stations. There is a strong year-to-year variability associated with

ENSO. During the last decade, while Changi has shown a decreasing trend, Tengah has shown an increasing trend in WBT, which highlights the spatial differences in trends within Singapore.

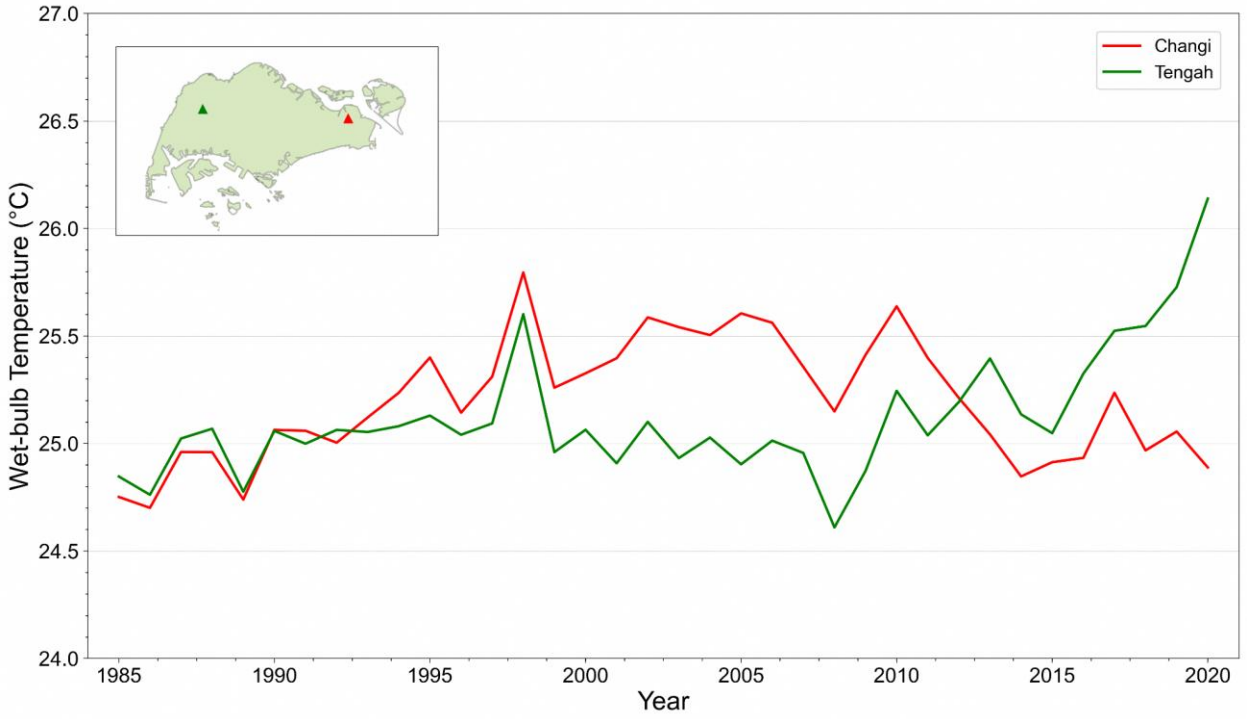

Figure 3.11: Mean wet-bulb temperature at Changi (red) and Tengah (green) weather stations from 1985-2020.

3.4 Observed change in rainfall

3.4.1 Annual Rainfall

The annual total rainfall for Singapore has a gradually increasing trend of 83 mm per decade from 1980 to 2022. However, this trend is not statistically significant (see Figure 3.12). Instead, years that experienced predominantly La Niña conditions (e.g. 2022, 2021, 2011) tend to be wetter, while years when El Niño conditions developed (e.g. 1982, 1997, 2015) tend to be drier. In addition, the first half of the 1980 – 2022 period saw more El Niño events (5 events between 1980 and 2000) compared to the second half (3 events between 2002 and 2022) and fewer La Niña events (4 events compared to 7 events). Future changes in the frequency and intensity of ENSO events will likely impact Singapore's rainfall.

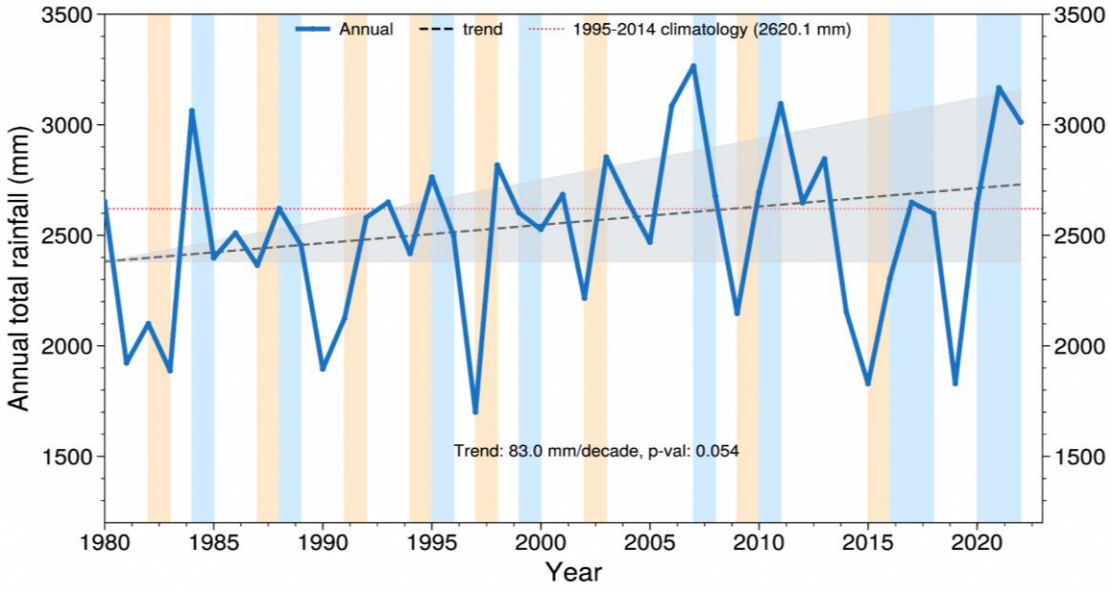

Figure 3.12: Time series of the annual total rainfall (solid blue)averaged over 32 stations with long-term records. The 1995-2014 climatology (2620.1 mm) is shown by the horizontal red dotted line. The black dashed line depicts the upward linear trend (83 mm/decade), computed using the robust non-parametric Theil-Sen slope estimator. Grey-shaded areas represent the 95% confidence interval of the estimated slope.

3.4.2 Monthly and seasonal rainfall

For monthly rainfall (Figure 3.13), statistically significant upward trends at the 5% level are seen only for June (18.4 mm/decade) and April (14.6mm/decade). A strong upward trend is also seen for November (16.8 mm/decade) but this trend is not yet significant at the 5% level.

In contrast, the month of February, the driest month of the year climatologically, is showing the strongest drying (-6.9 mm/decade), though not yet significant. Other months that show slightly negative trends are July (-3.2 mm/decade), March (-2.3 mm/decade) and May (-1.7 mm/decade).

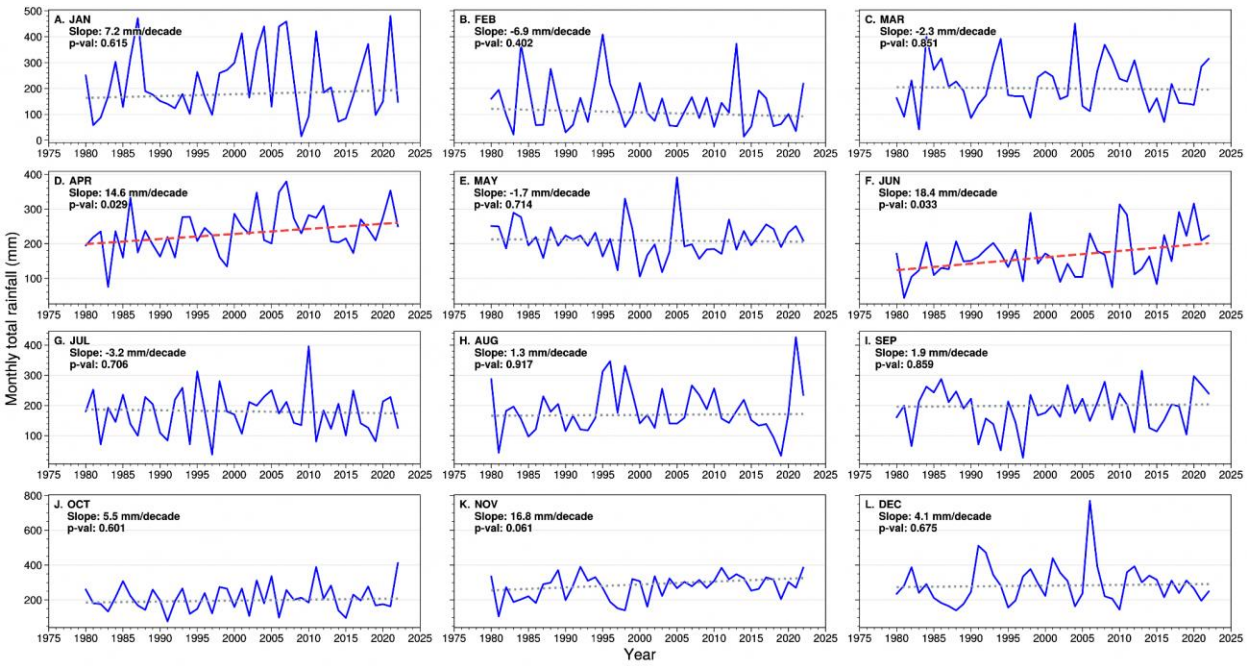

Figure 3.13: Time series of monthly total rainfall averaged from the 32-station record. The red dashed line depicts the individual slope of the trend for each month. Linear trend values, along with the respective *p*-values are shown for reference. All trends are computed using the Mann-Kendall test and the Theil-Sen slope estimator.

Among the four seasons, the second intermonsoon period (Oct-Nov) shows the highest rate of rainfall increase since 1980 at 24.6 mm/decade (95% significance level), followed by southwest monsoon season (JJAS) at 17.0 mm/decade as can be seen in Figure. 3.14. The wet phase of the northeast monsoon season (Dec-Jan) shows an increasing trend of 18.6 mm/decade (90% significance level), and the dry phase of the northeast monsoon (Feb-Mar) shows an decreasing trend at -7.8 mm/decade (90% significance level).

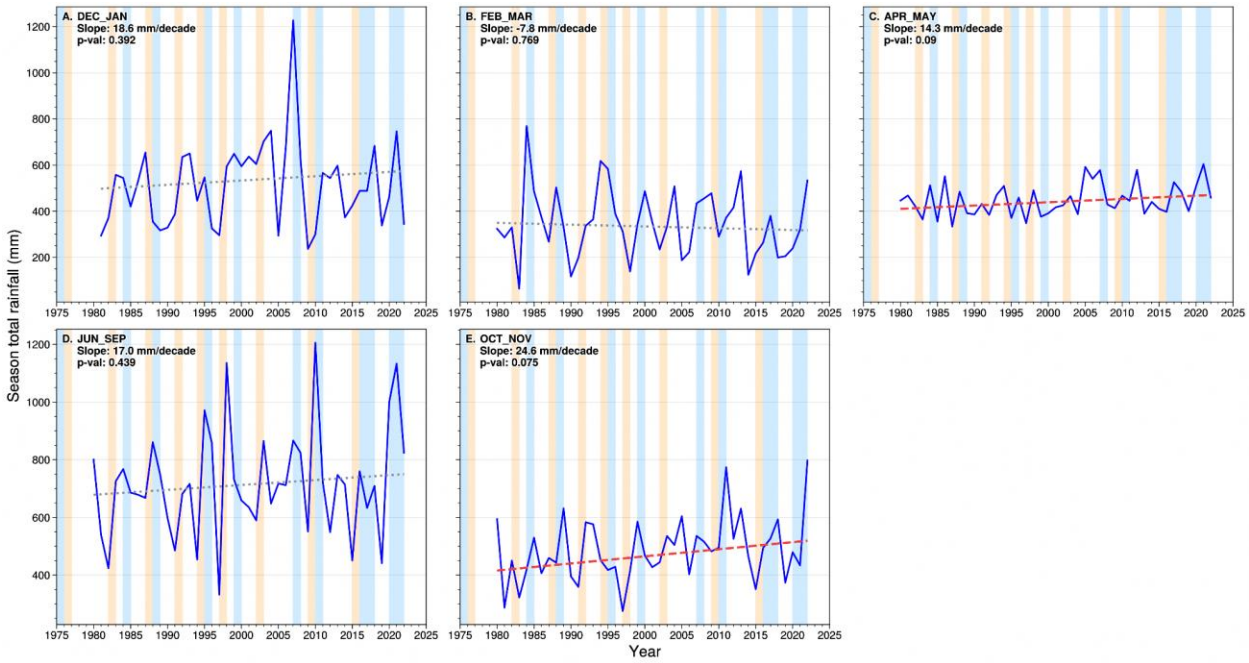

Figure 3.14: Time series of seasonal total rainfall averaged from the 32-station record. The red dashed line depicts the individual slope of the trend for each season. Linear trend values, along with the respective *p*-values are shown for reference. All trends are computed using the Mann-Kendall test and the Theil-Sen slope estimator.

3.4.3 Rainfall Extremes

Singapore's rainfall climate is largely dominated by convective rainfall. This type of rainfall typically occurs in the mid-to-late afternoon for much of the year. Severe convective storms with very high rainfall rates can often lead to flash floods since they tend to develop quickly on the order of sub-hourly to hourly time scales under very unstable atmospheric conditions with lots of moisture.

Figure 3.15 presents the annual maximum rainfall intensity at 15 min (RX15min), 30 min (RX30min) and 60 min (RX60min) durations. Overall, no trends have been detected over the last 43 years in the extreme rain rates across the three time windows, with RX15min showing a small insignificant decrease of -1.0 mm/decade and RX30min rainfall depicting only a tiny increase of 0.8 mm/decade. RX60min shows no trend at all (0 mm/decade). There is also little correlation with the ENSO phase on yearly time scales. However, RX60min exhibits variability on inter-decadal timescales as shown by the period averages, i.e. 97.3 mm between 1980 and 1994, 111.8 mm between 1995 and 2010, and 96.4 mm between 2011 and 2022. The multi-decadal variability in RX60min suggests the possible influence of long-term climate drivers in the Pacific, such as the Inter-decadal Pacific Oscillation (IPO) and warrants further investigation.

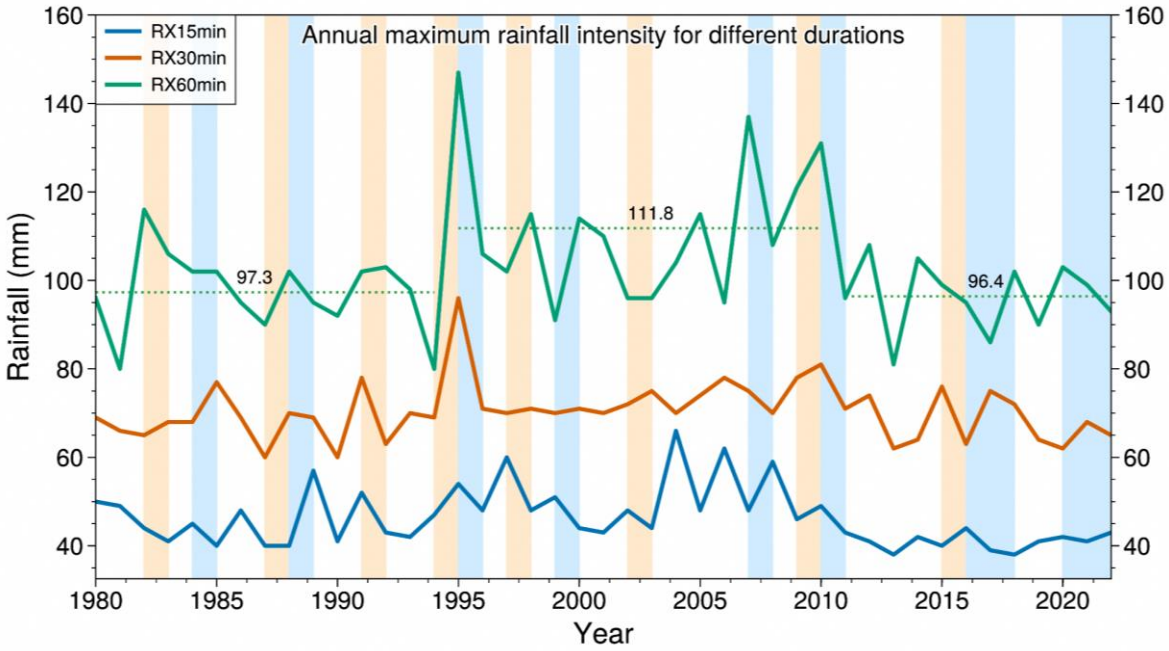

Figure 3.15: Time series of the annual maximum rainfall intensity at 15 min (RX15min, blue), 30 min (RX30min, orange) and 60 min (RX60min, green) durations, computed from a set of 23 stations with long-term observations going back to 1980. Numbers above the green dotted lines denote the RX60min averages for the corresponding periods mentioned in the text. Note that El Niño and La Niña years are highlighted by the light orange and blue vertical bars, respectively.

3.5 Observed change in relative humidity

The annual mean near-surface relative humidity (RH) from Changi and Tengah stations for 1985-2020 are shown in Figure 3.16. The figure shows that while there was no discernible trend in RH during 1985-2010, there has been a decreasing trend during the last decade. The observed decreasing trend in RH might look counter-intuitive given the increase in temperature and the expected increase in moisture along with increased temperatures due to more evaporation. Still, the fact is that while the actual moisture content of the air may be increasing, the rate of increase in temperature is higher than that of moisture thus leading to a negative change in RH.

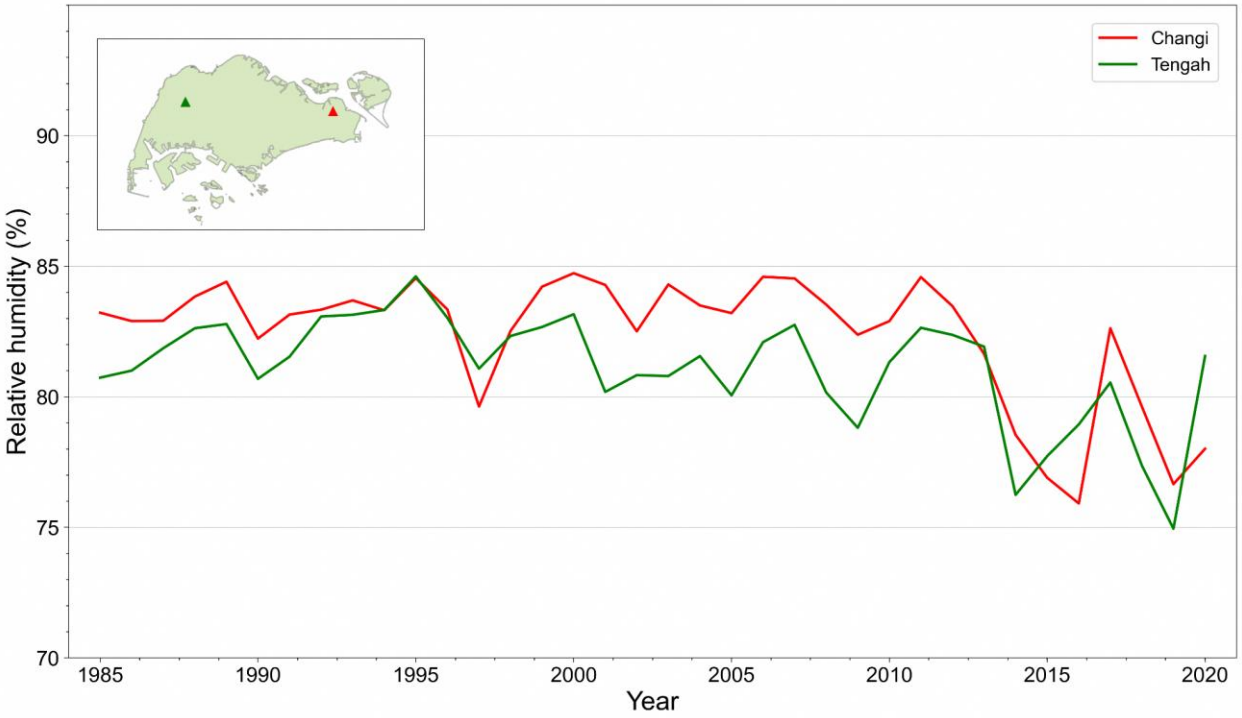

Figure 3.16: Mean relative humidity at Changi (red) and Tengah (green) weather stations from 1985-2020

3.6 Observed change in surface winds

While Singapore does experience a general shift in wind direction from the northeast to southwest monsoon, the average wind speeds are not large. Over the inter monsoon period, the winds are even lighter and variable in direction. The annual mean wind speed over the two stations (Changi and Tengah) shows inter-annual variability as well as multi-decadal variability (Fig. 3.17). However, in the last couple of decades, the time series appears to show an increasing trend, but it could also be a part of the multi-decadal variability since there was an apparent decreasing trend from around 1985 to the late 1990s and early 2000, and a reversal after that.

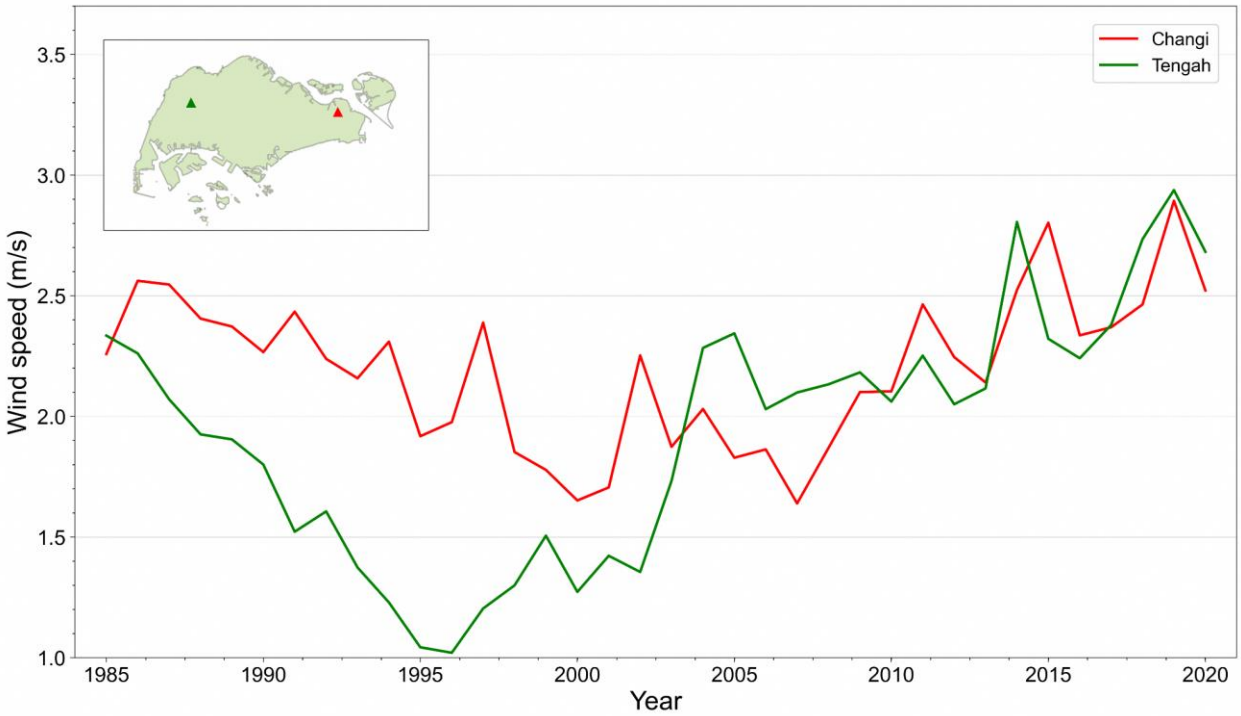

Figure 3.17: Mean wind speed at Changi (red) and Tengah (green) weather stations from 1985-2020

3.7 Observed change in northeast monsoon surges

Our work on northeast monsoon surges predominantly builds on the prior work done at CCRS (Lim et al., 2017), which focuses on the links between the northeast monsoon surge and Southeast Asia rainfall and as such is highly relevant for our region. Their study notes that monsoon surges contribute up to 40% of the total NDJF rainfall and that monsoon surges can increase rainfall to more than 50% above the mean in the checkmark-shaped region that includes Singapore, and potentially even more when combined with MJO events (as shown in their Figure 7a-c).

Little prior work has been done on quantifying changes in northeast monsoon surges over Southeast Asia. To understand observed changes, we examined studies using other definitions relevant to northeast monsoon surges. One caveat is that surges in the high latitudes may not affect our region. In the classification by Abdillah et al. (2020), only 39% of cold air outbreaks from the high latitudes impact the South China Sea. Nevertheless, as a proxy, we note that Juneng and Tanjang (2010) analysed trends in cold surge winds from 1962–2007, as measured by the DJF seasonal 950 hPa wind averaged over 110-117.5E and 12.5-15N, and found that the easterly component had strengthened significantly, but with no significant changes in the northerly component. However, this does not directly indicate the frequency of strong winds, which is used in the definition of a northeast monsoon surge over this region (e.g. Lim et al., 2017). Ting et al. 2009 conducted a study with station data from Mainland China from 1960-2008 and found a long-term decreasing trend (-0.2 times/decade) in cold surges over northeast China. There are signs that this decreasing trend extends slightly south of 30°N, but it is weak at best. Recently, using a cold surge definition using winds over the South China Sea (925 hPa meridional winds averaged over 110–117.5°E along 15°N) and sea level pressure anomalies over East Asia (15–45°N, 100–120°E), Pang et al. (2023) find an increase in surge days in 2005-2020 relative to 1989-2004.

Figure 3.18 shows the number of surge days in each season using a definition of cold surges relevant to the Maritime Continent (Table 3.3) over 64 years (NDJF seasons starting 1959-2022) using ERA5 winds and sea level pressure. We do not find any significant (e.g. 90% significance level) trend in the frequency of surge days, showing the large role of interannual variability. There is also no significant difference (e.g. 90% significance level) in the number of surge days in El Nino or La Nina years as compared to neutral years.

Table 3.3: Criteria used for defining cold surges (Lim et al., 2017).

Variable	Criteria	Domain
Mean 850 hPa wind over the domain	Calm or easterly Northerly Wind speed at least 0.75 standard deviations above the long-term NDJF mean	5-10°N, 107-115°E
Max sea level pressure over the domain	At least 1020 hPa.	18-22°N, 105-122°E

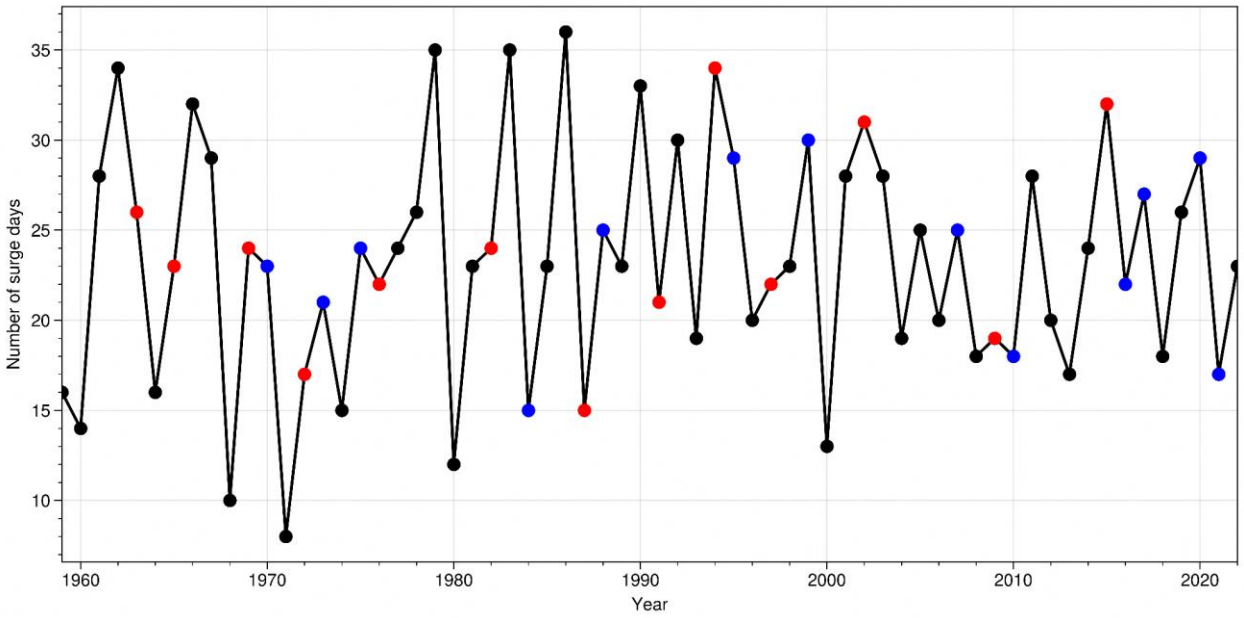

Figure 3.18: Number of surge days in each NDJF season for 1959-2022, using ERA5 winds and sea level pressure. The year shown marks the beginning of the season (e.g. 2022 for the 2022-2023 season). El Niño, ENSO-neutral, and La Nina years are indicated with the red, black and blue dots, respectively.

3.8 Observed change in sea level

In this report, all material on ocean and sea level science is covered in Chapter 12 - Past and Future Sea-level Change.

3.9 Summary

The current chapter discusses the observed climate change information across Singapore using different observational datasets such as automated weather stations, manned weather stations, and tide gauges. Singapore's climate varies across four different periods: Northeast monsoon (December to March), first intermonsoon (April to May), southwest monsoon (June to September), and second intermonsoon (October to November). Different climate drivers at various spatial and temporal scales influence the Singapore weather and climate features. These drivers include seasonal migration of the Intertropical Convergence Zone, ENSO, IOD, MJO, northeast monsoon surges, Sumatra Squalls, Borneo vortex, and remote influences from Tropical cyclones.

Since 1984, the observed daily mean temperatures show an increasing trend with a large interannual variability. At two distinct stations (Changi climate station and Tengah), the warming rate between 1984 and 2022 was 0.24°C and 0.26°C per decade, respectively (Table 3.4). In contrast to the increasing decadal rate of global temperatures, the Singapore temperatures indicate a decreasing rate from 0.52°C/decade (1984-1993) to 0.07°C/decade (2013-2022). At the two weather stations, the daily minimum temperatures show a statistically significant trend of 0.21°C per decade and 0.14°C per decade. Additionally, daily maximum temperatures are increasing at 0.06°C/decade (insignificant) and 0.13°C/decade (95% significant). There has been an increase in the frequency of extremely warm days, with a difference in the number of warm days between Singapore's coastal and inland regions of Singapore (Table 3.4). Despite the WBT's significant year-to-year variability, neither of the two weather stations exhibits a monotonic pattern in time. One station exhibits an increasing trend, while the other exhibits a declining tendency in the WBT.

Table 3.4: Trends in observed Mean and Extreme Temperatures for two Singapore stations.

Weather station	Mean temperature trend [°C/decade]	Daily maximum temperature trend [°C/decade]	Daily minimum temperature trend [°C/decade]	Warm days trend [days/year]	WBT trend
Changi (Coastal)	0.24	0.06	0.21	0.8	Decreasing
Tengah (Inland)	0.26	0.13	0.14	1.3	Increasing

The total annual rainfall over Singapore shows an increasing trend of 83 mm per decade from 1980 to 2022 (Table 3.5). The rainfall over Singapore is strongly modulated by ENSO, with La Niña years experiencing increased rainfall and El Niño years having decreased rainfall. There are also monthly and seasonal variations in total rainfalls across Singapore. The months of June and April show statistically significant increasing trends of rainfall at 18.4 mm/decade and 14.6 mm/decade, respectively; November shows an increase of 16.8 mm/decade (not significant), whereas some months (July, March, and May) show a decreasing trend (not significant). Although insignificant, the total seasonal rainfalls show an increasing trend across Singapore (Table 3.5). The SON season has the highest rate of rainfall increases since 1980 at 9.5 mm/decade, followed by MAM and JJA at 6.8 mm/decade, and the DJF shows the least amount of rainfall increases by 2.4mm/decade. Rainfall extremes measured using annual maximum intensity at 15 min, 30 min, and 60 min durations show no significant trend (Table 3.5). However, the RX60min shows strong inter-decadal variability with rainfall averages of 97.3 mm between 1980 and 1994, 111.8 mm between 1995 and 2010, and 96.4 mm between 2011 and 2022.

Table 3.5: Trends in Observed Mean annual, monthly, seasonal, and extreme Rainfall, indicating 95% (*) and 90% ($^{+}$) significance level respectively.

Mean ANNUAL rainfall trend (mm/decade)	Mean MONTHLY rainfall trend (mm/decade)	Mean SEASONAL Rainfall trend (mm/decade)	EXTREME rainfall trend (RX15min, RX30min, RX60min)

83	+4.1 (Dec) +7.2 (Jan) -6.9 (Feb) -2.3 (Mar) +14.6 (Apr)* -1.7 (May) +18.4 (June)* -3.2 (July) +1.3 (Aug) +1.9 (Sep) +5.9 (Oct) +16.8 (Nov)$^{+}$	+18.6 (DJ) -7.8 (FM)$^{+}$ +14.3 (AM) +17.0 (JJAS)$^{+}$ +24.6 (ON)*	No significant trend

The annual mean near-surface relative humidity (RH) decreases at the two weather stations across Singapore for the period 1985-2020.

The annual mean surface wind speed appears to have an increasing trend in the last couple of decades. However, it is also possible that it is just the multi-decadal variability that we see in the time series from the two stations, with decrease in the first part of the times series followed by an increase. There is no apparent trend in the number of northeast monsoon surge days that has a large interannual variability.

Overall, we observe an increase in mean surface temperatures, daily minimum temperatures, daily maximum temperatures, annual mean rainfall totals, and seasonal rainfall across Singapore. There are spatial variations in the changes of daily minimum temperatures, daily maximum temperatures, and WBT. Additionally, there is a strong relationship between ENSO and Singapore's rainfall. There is a decreasing trend of the mean surface relative humidity and no significant trend in the number of surge days.

References

ACAR (2022) - Singapore Annual Climate Assessment Report, MSS, http://www.weather.gov.sg/wp-content/uploads/2023/03/ACAR_2022.pdf)

Lim, T. S., “Cloudy with A Slight Chance of Rain: Singapore’s Meteorological Service”, National Library of Singapore, https://biblioasia.nlb.gov.sg/vol-16/issue-2/jul-sep-2020/rain, accessed 15 Feb 2023.

IPCC, 2021: Climate Change 2021: The Physical Science Basis. Contribution of Working Group I to the Sixth Assessment Report of the Intergovernmental Panel on Climate Change[Masson-Delmotte, V., P. Zhai, A. Pirani, S.L. Connors, C. Péan, S. Berger, N. Caud, Y. Chen, L. Goldfarb, M.I. Gomis, M. Huang, K. Leitzell, E. Lonnoy, J.B.R. Matthews, T.K. Maycock, T. Waterfield, O. Yelekçi, R. Yu, and B. Zhou (eds.)]. Cambridge University Press, Cambridge, United Kingdom and New York, NY, USA, In press, doi:10.1017/9781009157896.

McBride, J. L., Sahany, S., Hassim, M. E. E., Nguyen, C. M., Lim, S.-Y., Rahmat, R., & Cheong, W.-K. (2015). 25. The 2014 Record Dry Spell at Singapore: An Intertropical Convergence Zone (ITCZ) Drought. *Bulletin of the American Meteorological Society*, *96*(12), S126–S130.

From Global to Regional Projections – Insights from CMIP6

4

Authors:
Aurel Florian Moise, Sandeep Sahany, Muhammad Eeqmal Hassim, Chen Chen, Xin Rong Chua, Venkatraman Prasanna, Gerald Lim, Pavan Harika Raavi, Fei Luo

METEOROLOGICAL SERVICE SINGAPORE
Centre for Climate Research Singapore

4.1 Introduction

Climate change is an existential threat to humans and other beings on Earth. Hence it needs to be strategically understood and responded to in order to effectively manage the various risks associated with it. There is increasing evidence of the risks associated with climate change, and countries globally, especially small island nations like Singapore, need reliable and actionable climate change information to be prepared well in advance to adapt to the multi-faceted risks due to climate change.

Every ~7 years, the Intergovernmental Panel on Climate Change (IPCC) publishes Assessment Reports (ARs) that provide information about the state of scientific, technical and socio-economic knowledge on climate change, its impacts and future risks, and options for reducing the rate at which climate change is taking place. The IPCC, in its latest and sixth assessment cycle, produced the Working Group-I (WG-I) report on the Physical Science Basis (released on 09 August 2021), the WG-II report on Impacts, Adaptation and Vulnerability (released on 28 February, 2022), the WG-III report on Mitigation of Climate Change (released on 4 April, 2022), and finally the Synthesis Report (released on 20 March, 2023). The IPCC also produces Special Reports intermittently. Also, for the first time, as a part of the sixth assessment cycle, IPCC came up with the Climate Change Atlas which provides climate change information regionally. Although these reports are very useful to be informed on the global and large-scale climate change, since they are produced based on the literature that primarily comes from the climate change projections that comes from global climate models, they lack enough granularity to assess climate change at regional/local level and use the information for adaptation planning. Hence, as a follow up on Singapore's Second National Climate Change Study (V2), Singapore's Third National Climate Change Study (V3) aims to provide high resolution climate change projections for Singapore and the larger SEA region, by dynamically downscaling the coarse resolution global model data, that can be readily used for adaptation planning and thus help safeguard Singapore from the adverse effects of climate change.

The Third National Climate Change Study (V3) was commissioned by the National Environment Agency (NEA) under the Resilience Working Group (RWG) that studies Singapore's vulnerability to the effects of climate change and develops long-term plans that ensure the nation's resilience to future environmental changes. The RWG, is one out of the 5 WGs, namely, the Long-Term Emissions and Mitigation Working Group (LWG), Resilience Working Group, Sustainability Working Group (SWG), Green Economy Working Group (GEWG) and Communications and Engagement Working Group (CEWG), overseen by the Executive Committee (Exco) of the Inter-Ministerial Committee on Climate Change (IMCCC). The scientific work on producing the high-resolution downscaled climate projections was undertaken by the Meteorological Service Singapore's Centre for Climate Research Singapore (CCRS).

4.2 Key differences between CMIP5 and CMIP6

Climate models are considered as key tools for scientists to understand the past and present climate, predict the weather and climate on timescales from hours through years, and project climate change for decades and centuries under various global warming scenarios developed by the socio-economic scientists. These models simulate the physics, chemistry and biology of the climate system, owing to their numerical and scientific complexity, require the most advanced supercomputers to carry out long-term simulations.

The development of climate models has been a work-in-progress for many decades now, with increased spatial resolution, more advanced physics, and more advanced numerical methods to optimally utilise the advances in supercomputers. With numerous institutions developing and running climate models, the opportunity arose to coordinate globally standardised experiments using these models in order to find answers to specific science questions, especially on future climate change. This is where the Coupled Model Intercomparison Project (CMIP; https://www.wcrp-climate.org/

wgcm-cmip) comes in. CMIP is a framework for climate model experiments, allowing scientists to analyse, validate and improve GCMs in a systematic way. The “coupled” term in the name means that all the climate models in the project are atmosphere-land-ocean-sea ice components coupled GCMs. The word “intercomparison” is also important, as these coupled models are run in the same way as prescribed in the CMIP protocols so that the differences in model simulations can be directly attributed to the differences in the models and not to the differences in the way they are run (https://www.carbonbrief.org/qa -how- do -climate-models-work/#cmip).

CMIP started in 1995 and has been through several cycles to date. It comes under the purview of the Working Group on Coupled Modelling committee, which is part of the World Climate Research Programme (WCRP) based at the World Meteorological Organization (WMO) in Geneva. Literature produced in the form of peer-reviewed publications using the model simulations of CMIP has formed the basis for the IPCC assessment reports since the last couple of decades. The latest CMIP cycle that concluded around 2019 is called CMIP6 and provided most of the simulations that underpin the climate science assessed in the latest IPCC AR6 reports.

According to Eyring et al. (2016), with the Grand Science Challenges of the World Climate Research Programme (WCRP) as its scientific backdrop, CMIP6 aims to contribute to addressing three broad important science questions:

1. How does the Earth system respond to forcing?
2. What are the origins and consequences of systematic model biases?
3. How can we assess future climate changes given internal climate variability, predictability, and uncertainties in scenarios?

In the following subsections we discuss in more detail the three key differences between the CMIP5 and CMIP6 models relating to the equilibrium climate sensitivity in the two sets of models, shared socioeconomic pathways (future forcing scenarios used in the CMIP6 Scenario Model Intercomparison Project [ScenarioMIP]) and the key differences in the modelling systems used for simulations in the two generations of CMIP.

4.2.1 Equilibrium Climate Sensitivity (ECS)

The Equilibrium Climate Sensitivity (ECS) is defined as the global- and annual-mean near-surface air temperature rise that is expected to occur eventually, once all the excess heat trapped (top-of-atmosphere radiative imbalance) by the doubling of CO2 concentration relative to pre-industrial levels has been distributed evenly down into the deep ocean (i.e. when both the atmosphere and ocean have reached equilibrium with one another - a coupled equilibrium state). Many CMIP6 models exhibit an ECS of 5°C or higher (Zelinka et al., 2020), much higher than the upper value of the CMIP5 range of 4.5°C. Historically, the ECS range reported in CMIP has not shown much variation. The IPCC First Assessment Report (FAR) in 1990 estimated an ECS of 1.5 – 4.5°C, and the Second and Third Assessment Reports in 1996 and 2001 both were consistent with the ECS range reported in FAR. In AR4 the lower bond increased to 2.0°C from the earlier 1.5°C, but in AR5 this reverted back to the original range. All of these IPCC reports have been largely consistent with the 1979 US National Academies of Sciences Charney Report - the first comprehensive global assessment of climate change — which estimated ECS at the range of 1.5 – 4.5°C.

Given the ECS values have been increasing in many of the CMIP6 GCMs, in the Sixth Assessment Report (AR6), the IPCC narrowed down the Likely Range for ECS based on different approaches and considered evidence from multiple independent sources such as instrumental records, paleoclimate proxies, physical principles and also climate models (Sherwood et al., 2020).

Based on the analysis of Sherwood et al. (2020), the IPCC adopted the approach of employing an emulator for constraining temperature and all parameters scaling with temperature. Therefore, the IPCC reported uncertainty envelope has been significantly reduced (see also Chapter 11). This

is one of the key achievements in AR6 which has not been widely appreciated, but the efforts on narrowing the uncertainty of the range of model response to standard CO2 doubling has been long-standing and only in AR6 we see a significant narrowing.

The Likely Range now ranges between 2.5 - 4.0°C, down from what was reported in AR5. The IPCC also narrowed the Very Likely Range of ECS to be between 2.0 to 5.0°C, down from 1.0 to 6.0°C (Table 4.1).

Table 4.1: The Equilibrium Climate Sensitivity (ECS) ranges, as assessed by the IPCC in AR6, compared with the corresponding ranges reported in AR5

IPCC ECS Assessment	**AR6**	AR5
Likely Range	**2.5 to 4.0 K**	1.5 to 4.5 K
Very Likely Range	**2.0 to 5.0 K**	1.0 to 6.0 K

4.2.2 Shared Socioeconomic Pathways (SSPs)

A major difference between CMIP5 and CMIP6 is the future global warming scenarios used for climate change projections. The CMIP5 used four representative concentration pathways (RCPs), namely, RCPs 2.6, 4.5, 6.0, and 8.5, defined according to the radiative forcing levels reached by 2100 but did not include any socioeconomic storyline to go alongside them.

However, CMIP6 uses scenarios rooted in the socioeconomic trajectories that lead to corresponding radiative forcing levels, termed as Shared Socioeconomic Pathways (SSPs) (O'Neill et al., 2016). The four Tier-I (key scenarios to be used in various MIPs endorsed by CMIP6) scenarios include SSP1-2.6, SSP2-4.5, SSP3-7.0, and SSP5-8.5 (see Section 4.3 for more details). These SSPs were created, with varying assumptions about human developments including: population, urbanization, economic growth, technological developments, greenhouse gas and aerosol emissions, energy supply and demand, land-use changes, etc. The SSPs represent alternative storylines about how the world might develop over the coming century according to different climate policies, mitigation or adaptation responses.

There is a mapping between the SSPs and the corresponding RCPs used in CMIP5. The SSPs are mapped with the corresponding radiative forcing they are compatible with. For example, the SSP1 socioeconomic storyline cannot lead to 8.5W/m2 of radiative forcing in 2100, whereas SSP5 can. Hence SSP5-8.5 is a feasible scenario while SSP1-8.5 is not.

4.2.3 Models

The CMIP6 model archive consists of models at higher spatial resolution, more advanced physical parameterizations, and more earth system models with carbon cycle and biogeochemistry. The number of modelling groups participating in CMIP6 has also significantly gone up (49) as compared to 28 in CMIP5. This resulted in many separate models (>100) with different modelling centers contributing with more than one global climate model. In CMIP5 this number was less than half. Note that not all the different models contribute to all the various experiments, e.g. for the ScenarioMIP we saw only 49 models. This is because CMIP6 is made up of 20+ MIPs (Eyring et al., 2016), all addressing different research questions.

While many of the modelling centres have also increased the spatial resolution of their models in CMIP6 as compared to CMIP5, a few still have kept it the same. For example, for the scenario experiments exploring the evolution of future climate in response to changing greenhouse gas (GHG) emissions, the French model IPSL-CM5-LR (used in CMIP5) had a resolution of 1.9° latitude x 3.75° longitude, whereas the latest

version of this model (IPSL-CM6A-LR) used in CMIP6 has a resolution of 1.25° latitude x 2.5° longitude. On the other hand, CanESM2 (CMIP5) and CanESM5 (CMIP6) from the Canadian Centre for Climate Modelling and Analysis (CCCma) both have the same spatial resolution of 2.8° latitude x 2.8° longitude. Please see more model information in Table 5.1, and discussions on model independence in Chapter 5 section 5.5 (Table 5.3).

4.3 Future Climate Scenarios

According to Eyring et al. (2016), a set of common experiments within the CMIP6 called DECK (Diagnostic, Evaluation and Characterization of Klima) and the CMIP historical simulations (1850–near present) will maintain continuity and help document basic characteristics of models across different phases of CMIP. This was a key element of the CMIP6 design.

DECK: The DECK comprises four baseline experiments: (a) a historical Atmospheric Model Intercomparison Project (AMIP) simulation, (b) a pre-industrial control simulation (piControl), (c) a simulation forced by an abrupt quadrupling of CO2 (abrupt-4×CO2) and (d) a simulation forced by a 1 % yr−1 CO2 increase (1pctCO2). In addition to the DECK and historical simulations, there are 21 model intercomparison projects (MIPs) endorsed by CMIP6. ScenarioMIP is one of the key MIPs and the one that produces the simulations by forcing the GCMs with various future scenarios. Note that the AMIP experiments are atmosphere-only, coupled to land (but not ocean or sea ice) and that the latter are provided as boundary conditions.

Shared Socioeconomic Pathways (SSPs): The AR6 Report assesses the climate response to five global warming scenarios that cover the range of possible future development of climate change drivers found in the literature. The underlying model simulations come from ScenarioMIP mentioned above. The scenarios in the model simulations start in 2015 and are as follows:

(1) SSP1-1.9 - very low GHG emissions and CO2 emissions declining to net zero around or after 2050, followed by varying levels of net negative CO2 emissions,

(2) SSP1-2.6: low GHG emissions and CO2 emissions declining to net zero around or after 2050, followed by varying levels of net negative CO2 emissions,

(3) SSP2-4.5: intermediate GHG emissions and CO2 emissions remaining around current levels until the middle of the century,

(4) SSP3-7.0: high GHG emissions and CO2 emissions that roughly double from current levels by 2100, and

(5) SSP5-8.5: very high GHG emissions and CO2 emissions that roughly double from current levels by 2050, as illustrated in Figure 4.1. Emissions vary between scenarios depending on socio-economic assumptions, levels of climate change mitigation and air pollution controls.

Compared to CMIP5, the concept of SSPs expands on the framework of RCPs (Representative Concentration Pathways) by including various levels of socio-economic pathways (O'Neill et al., 2016)
.

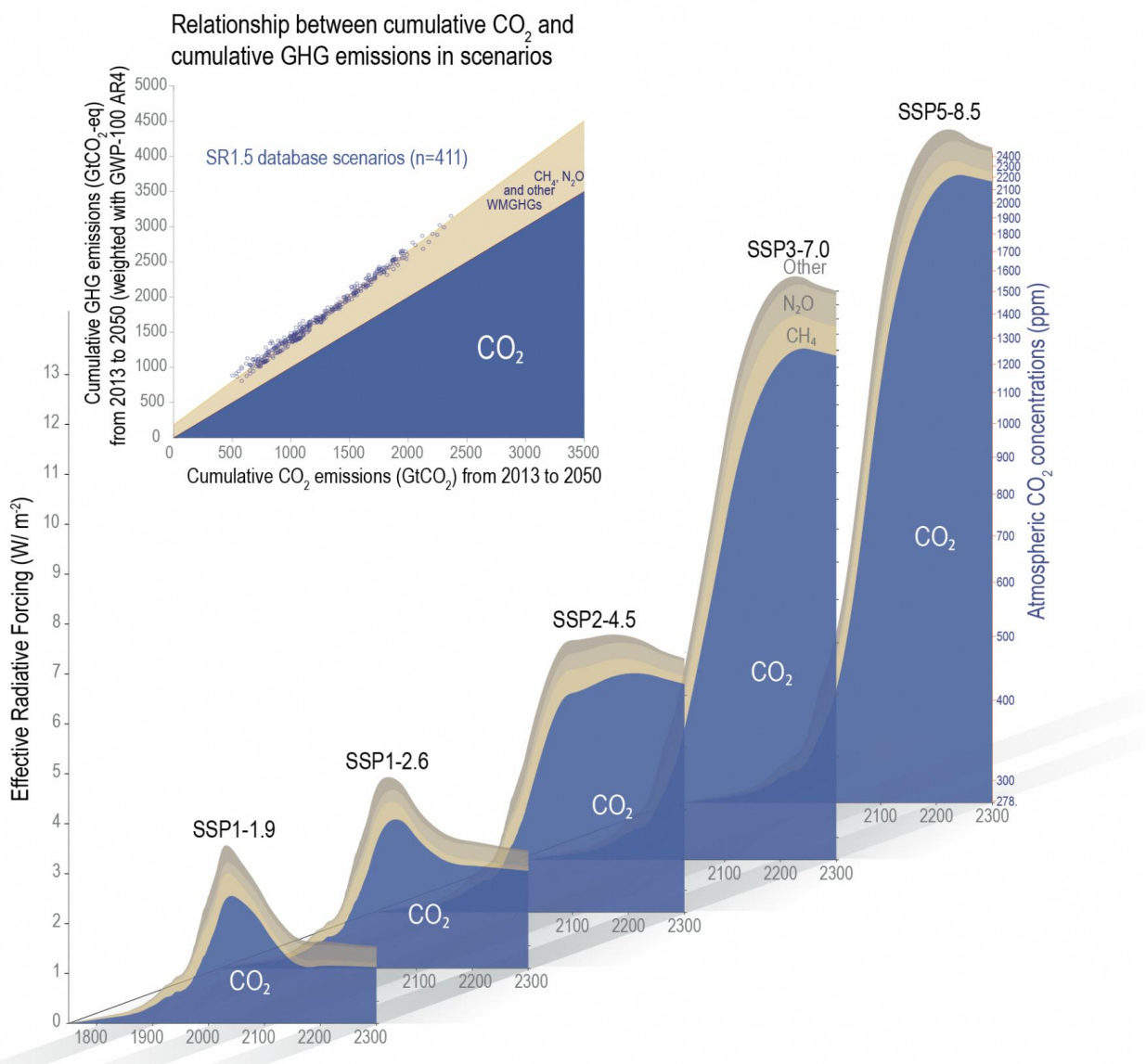

Figure 4.1: The role of CO_2 in driving future climate change in comparison to other greenhouse gases (GHGs). The GHGs included here are CH_4, N_2O, and 40 other long-lived, well-mixed GHGs. The blue shaded area indicates the approximate forcing exerted by CO_2 in Shared Socio-economic Pathways (SSP) scenarios, ranging from very low SSP1-1.9 to very high SSP5-8.5 (Chapter 7). The CO_2 concentrations under the SSP1-1.9 scenarios reach approximately 350 ppm after 2150, while those of SSP5-8.5 exceed 2000 ppm CO_2 in the longer term (up to year 2300). Similar to the dominant radiative forcing share at each point in time (lower area plots), cumulative GWP-100-weighted GHG emissions happen to be closely correlated with cumulative CO_2 emissions, allowing policymakers to make use of the carbon budget concept in a policy context with multi-gas GHG baskets as it exhibits relatively low variation across scenarios with similar cumulative emissions until 2050 (inset panel). (Figure 1.29 in IPCC, 2021: Chapter 1).

4.4 GCM-based global climate projections

In this section, we present the global climate projections reported in the IPCC AR6. Specifically, we present projected changes in global mean near-surface air temperature, rainfall, monsoon, ENSO, IOD, and MJO.

4.4.1 Temperature

The recent AR6 report states that the near-term (2021-2040) mean global surface air temperature

(GSAT) is extremely likely to increase by 0.4°C to 1.0°C relative to 1995 - 2014 with less dependence on the SSP scenario. However, the AR6 temperature projections using CMIP6 models predict an increase of 0.1°C to 0.2°C over the AR5 projections. In the near-term, the likelihood that the average GSAT would rise by 1.5°C relative to the 1850-1900 is higher in CMIP6 models under different scenarios due to improved methodology and continued global surface warming. The regional variations in surface temperatures indicate significant warming at higher latitudes, particularly during the Arctic's boreal winter. The highest rises in seasonal mean surface temperature under the SSP1-2.6 and SSP3-7.0 scenarios occur over land rather than oceans. In both scenarios, it is projected that seasonal mean surface temperatures of the Northern Hemisphere will increase by 1.0°C over the land regions.

The multi-model mean GSAT change (relative to 1850-1900; pre-industrial [PI]) from the CMIP6 GCMs with a higher ECS (>4°C) and those with medium ECS (2.5 °C <=T<=4°C) are shown in Figure 4.2. ECS values between 2.5 °C to 4°C are considered to be within the likely range as assessed by IPCC in AR6. Also shown are the observed anomalies from the same baseline using the Berkeley Earth dataset for the period 1850-2021. The historical anomalies are further merged with the projected change in GSAT for the high- and low-ECS models under the SSP5-8.5 scenario from 2015 to 2100.

The observed PI mean GSAT is found to be 13.8 °C. Both the high-ECS models and the medium-ECS models are found to underestimate the observed value (13.1°C in high-ECS models and 13.6°C in medium-ECS models). Notably, the high-ECS models simulate a cooler PI period as compared to the medium-ECS ones.

The observed anomalies for the period 1995-2014 (IPCC AR6 historical baseline period) from the PI were found to be 0.9°C. The corresponding anomalies for the high-ECS models during the same period were found to be the same as observed, and that for the medium-ECS models were lower than observed (0.7°C). Thus, even in the historical period the high-ECS models were warming at a higher rate.

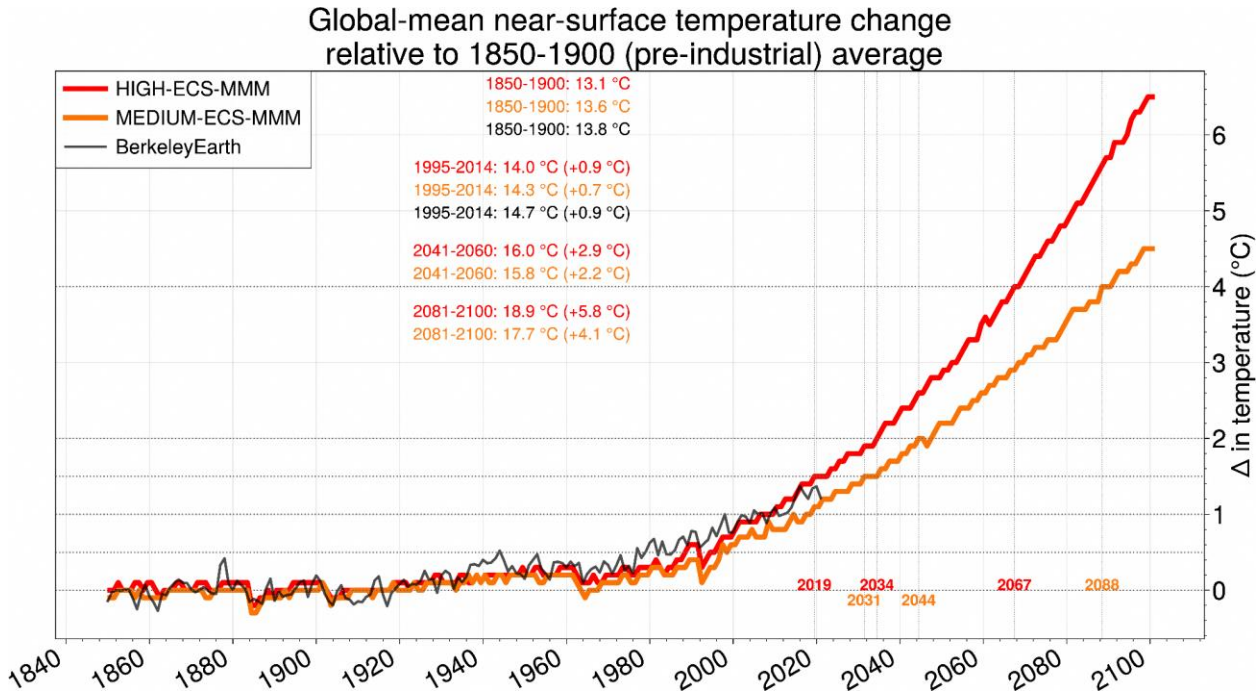

Figure 4.2: Time series of the multi-model mean (MMM) global average temperature anomaly from the HIGH-ECS (red line) and MEDIUM-ECS (orange line) model sets, respectively. Anomalies are relative to the 1850-1900 (pre-industrial) average. The observational time series is given by the Berkeley-Earth surface air temperature dataset (black line). The corresponding MMM

global average temperature for each dataset for the pre-industrial world (1850-1900), recent historical (1995-2014), mid-century (2041-2060) and end-century (2081-2100) periods are shown. Changes in the MMM global average temperature relative to the pre-industrial world in each dataset are shown in brackets. Coloured year values denote the first year in which the 1.5℃ and 2℃ global mean anomaly threshold is crossed in the HIGH- and MEDIUM-ECS models.

The projected mid-century (2041-2060) change for the high-ECS models was found to be 2.9°C and that for the medium-ECS models was found to be 2.2°C. By the end-century (2081-2100), the high-ECS models had warmed at an even faster rate and the multi-model mean projected change was found to be 5.8°C as compared to the corresponding change of 4.1°C projected by the medium-ECS models. Thus, the gap in the projected GSAT change between the high- and medium-ECS models kept increasing throughout the 21st century. The figure also shows that while the medium-ECS models will breach the 1.5°C global warming level (from PI) around 2031, the 2°C level around 2044, and the 4ºC level around 2088, the high-ECS models will reach the corresponding levels around 2019, 2034, and 2067, respectively. Note that the years mentioned above are based on annual mean values and not 20-year means and hence represent the first year when the corresponding warming level is reached.

4.4.2 Rainfall

According to the AR6 report, as the GSAT is projected to increase, there is an increased global land precipitation in the 21st century. At the end of the century (2081-2100), under the low emission scenario, the precipitation is projected to change by -0.2% to +4.7% and in the high emission scenario, the change is 0.9-12.9% relative to 1995-2014. More precipitation occurs at higher latitudes over oceans, wet tropical regions, and less over dry subtropics.

There are regional uncertainties and seasonal differences in the precipitation changes in the future warmer climate due to multiple reasons. Precipitation variations in the tropical oceans are mostly influenced by the changes in SST patterns, but in the subtropics, they are primarily influenced by the quick response to CO2 forcing (He & Soden, 2017). Natural and man-made aerosols have an impact on regional precipitation patterns in addition to their response to CO2 forcing (Shawki et al., 2018; Liu et al., 2018). The uncertainty in the precipitation estimates is attributed to model uncertainty, internal variability, and uncertainties in natural and anthropogenic aerosol emissions.

4.4.3 Monsoon

In CMIP6 models, under all future warming scenarios, the monsoon precipitation index, the area-weighted precipitation rate over the global monsoon land regions, is expected to rise due to increased moisture content (Chen et al., 2020). The CMIP6 projections indicate an increase in the global land monsoon precipitation by 1.3 -2.4 % per ºC of GSAT increase under different scenarios. In four of the five SSP scenarios, there is a tendency for the northern hemisphere summer monsoon circulation index (i.e., the vertical shear of zonal winds between 200 and 850 hPa averaged in an area 0-20N; 120W-120E) to decrease, potentially counteracting an increase in monsoon precipitation. Because of internal variability, including Atlantic Multi-decadal Variability (AMV) and Pacific Decadal Variability (PDV), the expected changes in the monsoon circulation are mainly uncertain.

The mid-century and end century projections indicate an asymmetry in monsoon rainfall with increased rainfall in the Northern Hemisphere than Southern Hemisphere, and an East-West asymmetry with enhanced Asian-African monsoon and weakened North American monsoon (Pascale et al., 2021; Wang et al., 2021). Overall, the global land monsoon precipitation is projected to increase despite reduced circulation under different scenarios in mid-century and end century. The combined contributions of model uncertainty and internal variability will have an impact on the projected changes in global monsoon precipitation and circulation.

4.4.4 ENSO

ENSO impacts precipitation variabilities worldwide (Ropelewski and Halpert 1987; Hendon

2003). Across the Indo-Pacific Ocean, ENSO induces a zonal dipole pattern of precipitation variability, i.e., positive variability in the tropical Pacific (TP) and “horseshoe” shaped negative variability towards the Maritime Continent (MC) (Langenbrunner and Neelin 2013). That is, TP becomes wetter than normal while MC becomes drier. Physically, ENSO-rainfall teleconnection over the MC is part of the ENSO-induced circulation responses over the tropics (Wang et al. 2003; Lau and Nath 2003; Stuecker et al. 2015). In boreal summer, when El Niño develops, a sequence of evolution begins with the eastward shifting of Walker Circulation due to the anomalous warming in the eastern Pacific. The shift suppresses convection over the MC (also weakens Asian–Australian Monsoon) and enhances convection in the Central Pacific.

Under warming, ENSO responses are uncertain across various emission scenarios and idealized simulations (Chen et al. 2017; Callahan et al. 2021; Cai et al. 2021; Brown et al. 2020). Tropical surface temperature variability changes are complex given oceanic and atmospheric processes, and the net effect of diverging feedbacks could potentially give less robust changes to the surface temperature variability and a low model agreement. On the contrary, the ENSO-induced precipitation variability over the TP strengthens robustly. It involves mean state changes beyond the bonds by ENSO itself, e.g. the tropical rainfall variability is strongly related to mean atmospheric changes associated with Clausius–Clapeyron relationship (Hu et al. 2021).

CMIP3 and CMIP5 models robustly projected that over the central-eastern Pacific the ENSO-induced rainfall variability strengthens (Bonfils et al. 2015; Perry et al. 2017; Yeh et al. 2018; Power et al. 2013; Kug et al. 2010; Chung and Power 2014; Chung et al. 2014; Chung and Power 2016, 2015). Besides the intensification, CMIP3 and CMIP5 models robustly project that, over the TP, ENSO-induced rainfall variability shifts eastward under warming (Yeh et al. 2018; Taschetto et al. 2020; Yan et al. 2020; Coelho and Goddard 2009; Huang and Xie 2015; Bayr et al. 2014; Kug et al. 2010; Power et al. 2013).

4.4.5 IOD

The mean climate state projections of the tropical Indian Ocean sea surface temperatures resemble the positive phase of the IOD mode with rapid warming in the west compared to the east. With no discernible change in frequency, these mean state modifications result in decreased amplitude differences between positive and negative IOD events. (Cai et al., 2013). However, these projected mean state changes might be due to biases of the model simulated current climate (Li et.al., 2016). Cai et al., (2021) showed an increased frequency of strong positive IOD events and a reduced frequency of moderate positive IOD events using the CMIP5 RCP8.5 and CMIP6 SSP5-8.5 simulations. These IOD projections indeed may depend on the realistic simulations of the background mean state changes of the Indian Ocean (Li et al., 2016). Hence, the future projections of IOD changes in the mid-term and long term remain uncertain due to lack of robust evidence and its reliance on the model's mean state biases.

4.4.6 MJO

According to sensitivity studies, MJO precipitation is expected to rise in magnitude with up to 14% per degree increases in warming (Adames et al., 2017; Wolding et al., 2017). In comparison to the CMIP3 or CMIP5 models, the CMIP6 models are significantly better at simulating the MJO. Reduced dry moisture bias in mean states results in improved and eastward propagation of the MJO over the MC (Ahn et al., 2020). Additionally, the amplitudes of MJO precipitation and zonal winds can now be reliably simulated in CMIP6 models (Orbe et al., 2020), and the model spread of the MJO characteristics has decreased (Chen et al., 2022). A multi-model mean of CMIP6 models shows a 17% increase in amplitude of precipitation, a 9% increase in MJO propagation speed, a 2-day reduction in MJO period, and a 5-degree eastward extension (Wang et al., 2023). The MJO is projected to become more intense under a warmer environment in the future, along with an increase in the associated precipitation amplitude.

4.5 GCM-based regional climate projections

In this section, we present the regional climate projections over the Southeast Asia/Maritime Continent region from our in-house analysis and relevant literature from the IPCC AR6 regional fact sheet for Asia. These regional climate projections are constructed based on the global climate models. Specifically, we present a summary of key climate change information over SEA from the IPCC AR6 regional fact sheet for Asia, projected changes in precipitation, projected changes in temperature, projected changes in ENSO teleconnections, and finally, projected changes in northeast monsoon surges.

Although one may still be able to derive some useful high-level information (for example, related to large-scale climate drivers such as ENSO) on regional climate change from GCM data, it is to be noted that the GCMs, due to their coarse spatial resolution, and also the complex topography and coastlines of the Maritime Continent are unable to accurately represent small islands such as Singapore in the model. For example, while one GCM may "see" Singapore as a part of peninsular Malaysia, another GCM may "see" it as an ocean point. This is precisely the reason why high-resolution regional climate change projections such as V3 need to be carried out, so that the finer spatial scale information can be produced, both for more reliable physical climate change assessment and for conducting downstream high-resolution impact studies.

4.5.1 Summary of SEA Projections from the IPCC AR6 Climate Atlas

As one of the outreach products, the IPCC AR6 constructed regional fact sheets by dividing the world into 11 regions and collating key climate change messages for each of these regions. These regions are further divided into subregions. The fact sheets constitute an entry point for regionalized information in the Chapters, the Technical Summary and the Interactive Atlas. The Asian region and its various subregions are shown in Figure 4.3. The Southeast Asian subregion is marked as "SEA" in the figure.

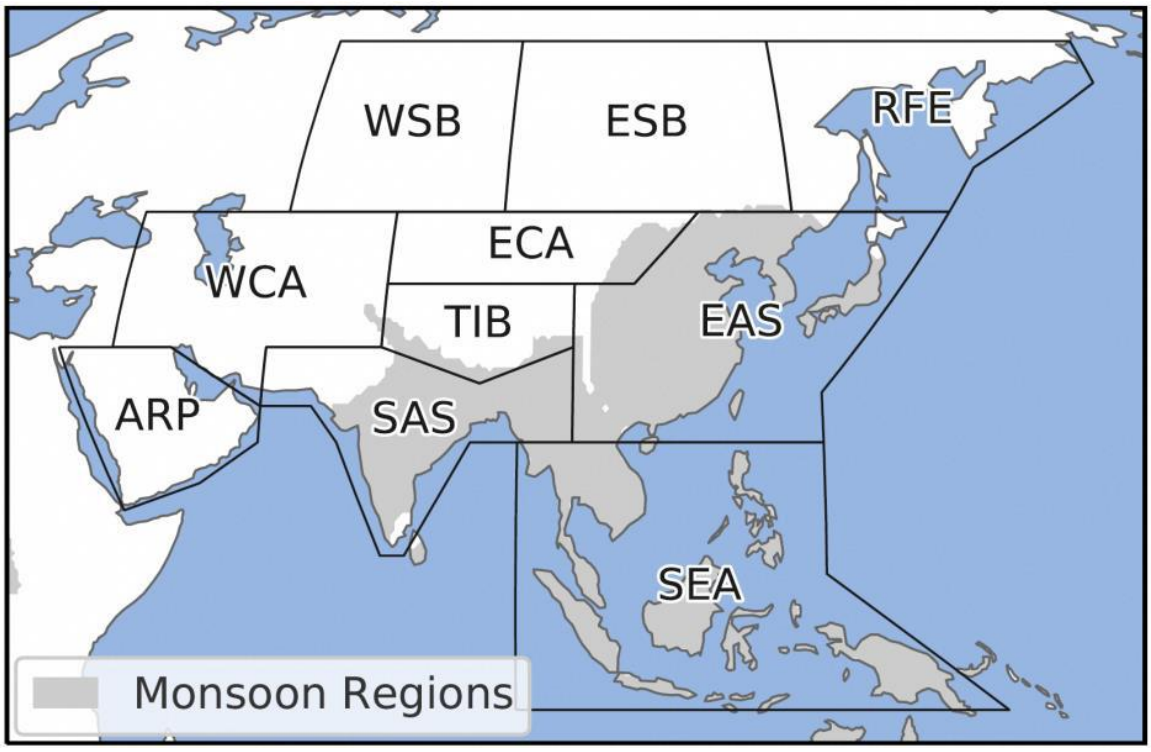

Figure 4.3: The various subregions of Asia for which climate change information has been provided in the regional factsheet. Also shown in grey are the monsoon regions. (Map from the Regional fact sheet for Asia, IPCC).

Key messages for the SEA subregion are presented below, along with the associated confidence levels (where available) assessed by the IPCC:

1. Future warming over SEA will be slightly less than the global average (high confidence).
2. Rainfall will increase in the northern parts of mainland SEA and decrease in the Maritime Continent in some seasons (medium confidence).
3. In the near-term, South and Southeast Asian monsoon and East Asian summer monsoon precipitation changes will be dominated by the effects of internal variability (medium confidence).
4. Compound impacts of climate change, land subsidence, and local human activities will lead to higher flood levels and prolonged inundation in the Mekong Delta (high confidence).

4.5.2 Precipitation Changes over SEA from CMIP6 GCMs

The mean multi-model changes in the annual mean and seasonally-averaged rainfall for the end-century 2081-2100 period are shown in Figure 4.4 for all available CMIP6 models. Also shown are the mean changes found in the subset of models with high ECS (ECS > 4 K) and those with medium climate sensitivity (2.5 ≤ ECS ≤ 4 K).

On the annual time scale, precipitation is likely to increase overall land areas. The biggest changes are projected over the northern (mainland) SEA region and over Borneo and New Guinea. In contrast, decreases are seen over large portions of water. Also note that Singapore lies in between wider areas of projected rainfall increase and projected rainfall decrease in most of the season, making rainfall projections for Singapore particularly challenging. The magnitude of projected changes in mean annual rainfall appears largely similar between high and medium ECS models, except in the easternmost portion of the domain (equatorial western Pacific), where the high ECS models show a larger magnitude.

A different story emerges between the two subsets of high ECS and medium ECS models. For seasons other than the northern hemisphere winter (DJF), the spatial pattern of changes is largely coherent between the high and medium ECS models. However, the high ECS models (Figure 4.4 e,h,k,n) project much stronger changes in mean seasonal rainfall over many land and water areas than the medium ECS models (Figure 4.4 f,i,l,o). This suggests that the regional precipitation response tends to scale with the level of warming. Most notable are the strong drying signals projected for vast areas north (south) of the equator in MAM (JJA).

The spatial pattern of these signals largely resembles the historically known mean response to El Niño events. They are, therefore, most likely associated with the projected emergence of more El Niño-like conditions in the future (e.g. Cai et al., 2014, 2021) and the enhanced and eastward shift of the ENSO-rainfall teleconnection over the region (Chen et al. 2023; see also Sec 4.5.4). Interestingly, the full ensemble signals for MAM, JJA and SON in Figure 4.4 g, j, m, appear to be mainly driven by changes projected by the high ECS models.

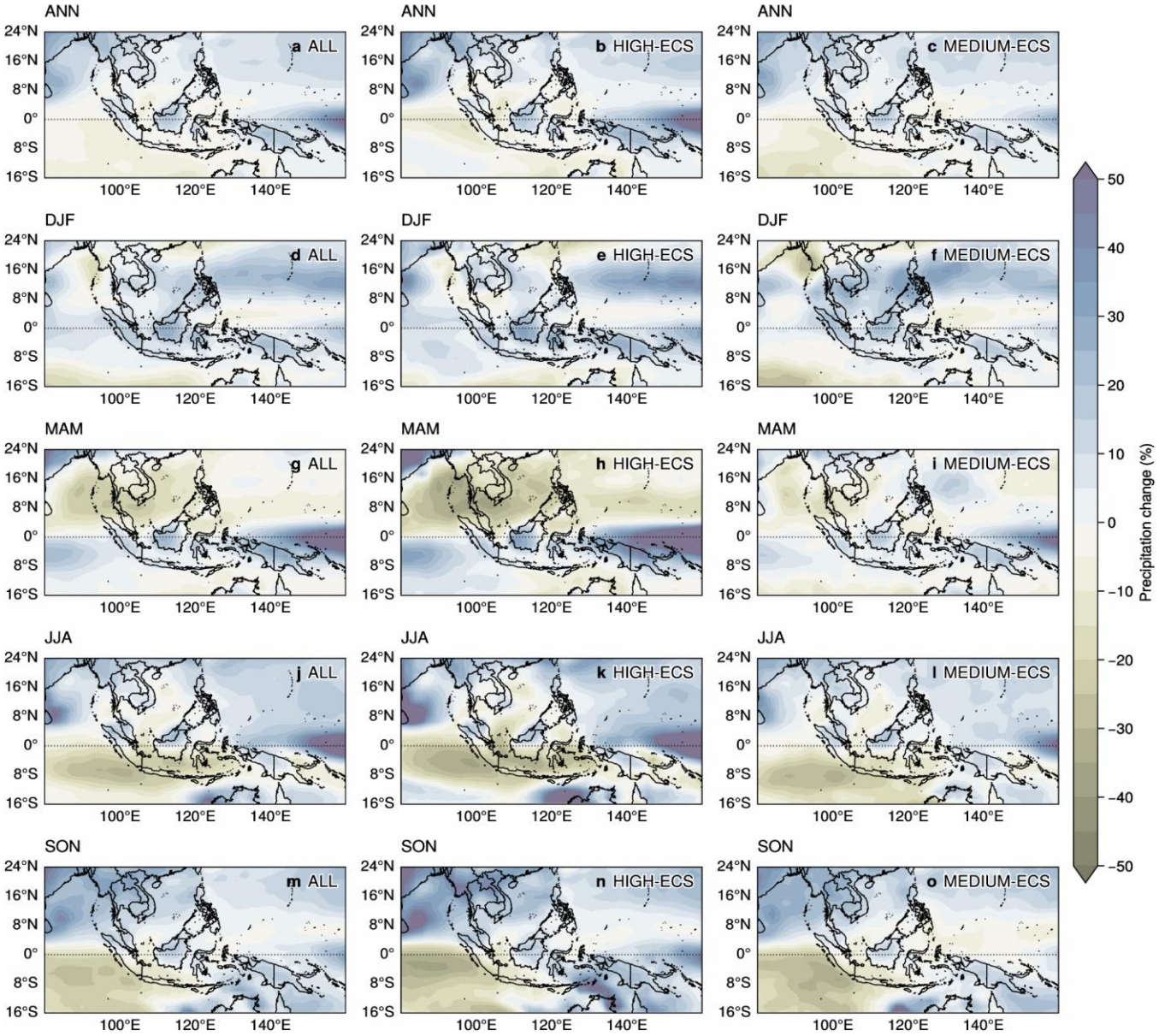

Figure 4.4: Mean multi-model changes in precipitation (in %) for end-century (2081-2100) under the SSP5-8.5 scenario for CMIP6 GCMs that have both future and historical periods available. Each column shows the set of ALL CMIP6 (n=36), HIGH-ECS (n=13) and MEDIUM-ECS (n=13) models, respectively, and each row shows the season. (a-c) Annual (ANN) changes. (d-f) December-February (DJF) changes. (g-i) March-May (MAM) changes. (j-l) June-August (JJA) changes. (m-o) September-November (SON) changes.

4.5.3 Temperature Changes over SEA from CMIP6 GCMs

Changes in daily mean temperature across the SEA domain are shown in Figure 4.5. As expected, the high ECS models project much higher daily mean temperature changes over both land and sea and also stronger land-sea contrasts on the annual and seasonal time scales (Fig. 4.5 b, e, h, k, n). Changes in excess of 5°C are even projected in the hotter summer periods of the year in MAM and JJA, particularly in the interior northern portions of mainland SEA. Differences in the projected temperature changes between the high and medium ECS models amount to at least 1°C over sea and up to around 2°C over land. Furthermore, similar magnitudes of temperature change are projected regardless of season within

each group of models, suggesting that global warming affects all seasons equally.

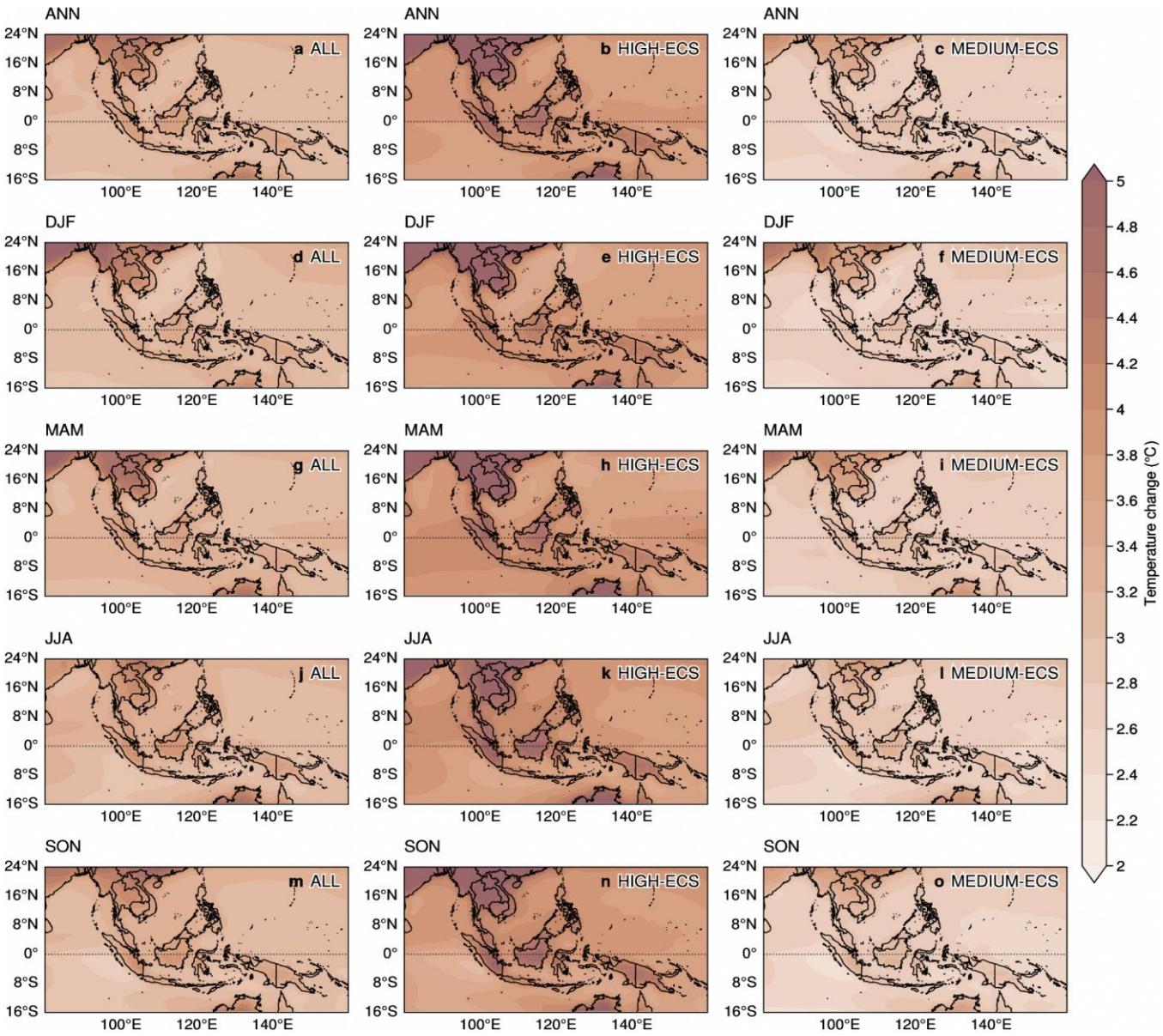

Figure 4.5: As in Fig. 4.4 but for mean multi-model changes in daily average temperature (in °C).

4.5.4 ENSO teleconnection changes under warming

The Maritime Continent (MC), located in the heart of the Indo-Pacific warm pool, plays an important role in the global climate. However, the future MC climate is largely unknown, in particular the ENSO-rainfall teleconnection (Fig. 4.6 & Fig. 4.9). ENSO induces a zonal dipole pattern of rainfall variability across the Indo-Pacific Ocean, i.e., positive variability in the Tropical Pacific and negative variability towards the MC. Here, new CMIP6 models robustly project that, for both land and sea rainfall, the negative ENSO teleconnection over the MC (drier/wetter during El Niño/La Niña) could intensify significantly under the SSP585 warming scenarios (Fig. 4.7). Strengthened teleconnection may cause

enhanced droughts and flooding, leading to agricultural impacts and altering rainfall predictability over the region. Models also project that the Indo-Pacific rainfall center and the zero-crossing of dipole-like rainfall variability both shift eastward, which adjustments are more notable during boreal summer than winter (Fig. 4.8). All these projections are robustly supported by the model agreement and scale up with the warming trend.

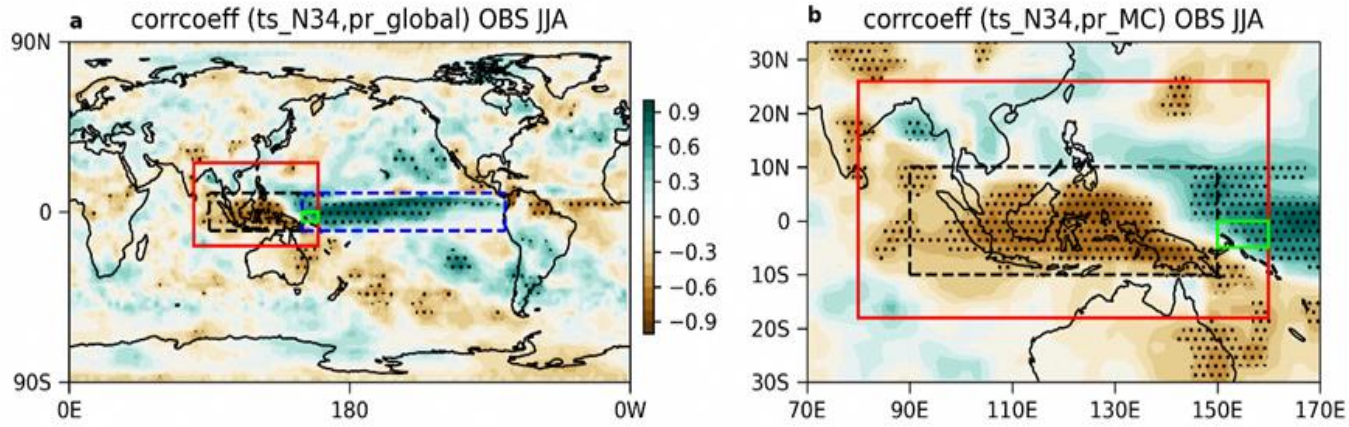

Figure 4.6: Observed ENSO-rainfall teleconnection. a. Observed global ENSO-precipitation correlation coefficient during boreal summer (JJA). Here the correlation coefficient is calculated between the anomalous precipitation (pr) and Niño3.4 sea surface temperature (ts). Stipping area indicates significant correlation with p-value<0.01. Defined domains of Maritime Continent (MC) (red box), Central Maritime Continent (CMC) (black dashed box), Eastern Maritime Continent (EMC) (green box), and tropical Pacific (TP)(blue dashed box) are shown. b. similar to a, but focusing on the MC.

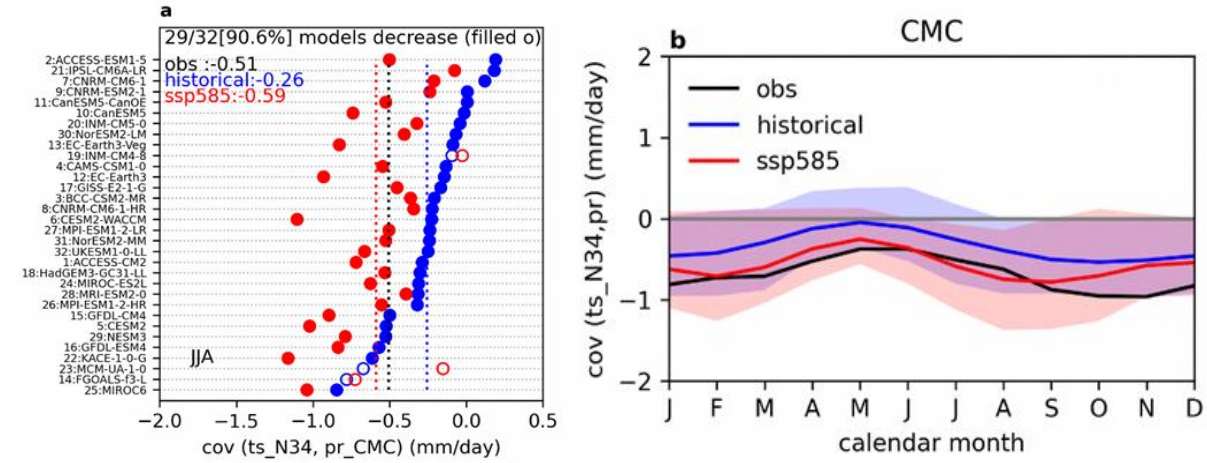

Figure 4.7: Summer (JJA) ENSO-rainfall teleconnection in the CMC is enhanced under warming. a. ENSO-precipitation covariance for the CMC domain across 32 CMIP6 models. The observation (black line), the model mean for the historical period (blue line), and the model mean for the future SSP585 scenario (red line) are shown. Model results are ranked by their values in the historical period. Model agreement on the future change is shown on the top. b. 12-month ENSO-precipitation covariance across the CMC. Observations (GPCP, black curve), the multi-model mean of 32 CMIP6 models for the historical period (blue curve), and the multi-model mean for the SSP585 scenario (red curve) are shown. The shades indicate the 95% model range.

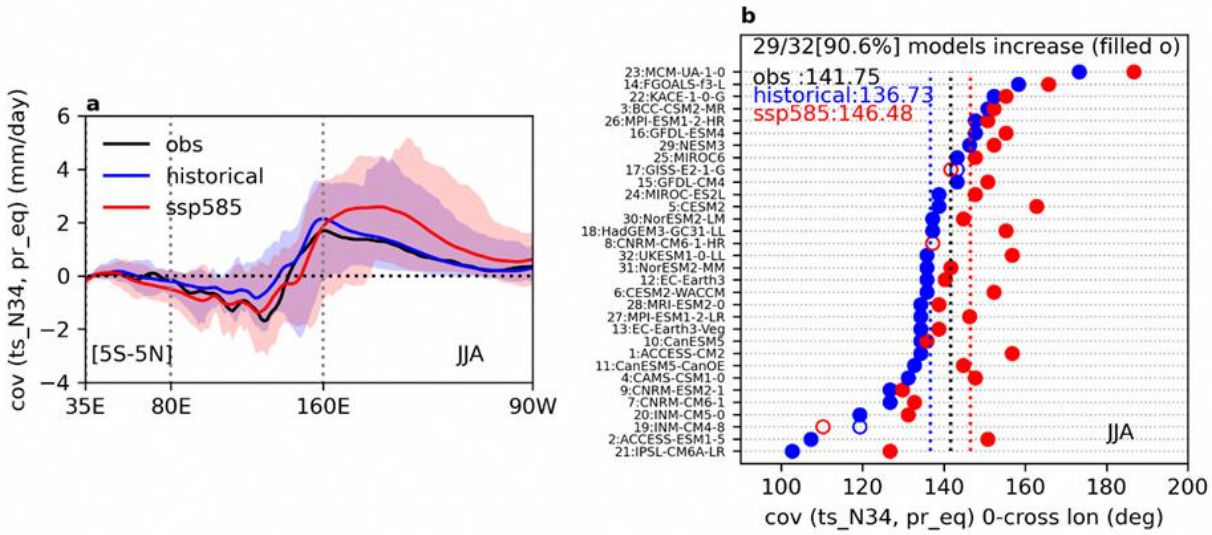

Figure 4.8: Summer (JJA) zonal dipole-like ENSO-rainfall teleconnection shifts eastward under warming. a. Equatorial precipitation [5S-5N averaged] covariance with Niño3.4 sea surface temperature. Observations (GPCP, black curve), the multi-model mean of 32 CMIP6 models for the historical period (blue curve), and the multi-model mean for the SSP585 scenario (red curve) are shown. The shades indicate the 95% model range. b. Zero-crossing longitude of the precipitation covariance across 32 CMIP6 models. The observation (black line), the model mean for the historical period (blue line), and the model mean for the future SSP585 scenario (red line) are shown. Model results are ordered by their values in the historical period. Model agreement on the future change is shown on the top.

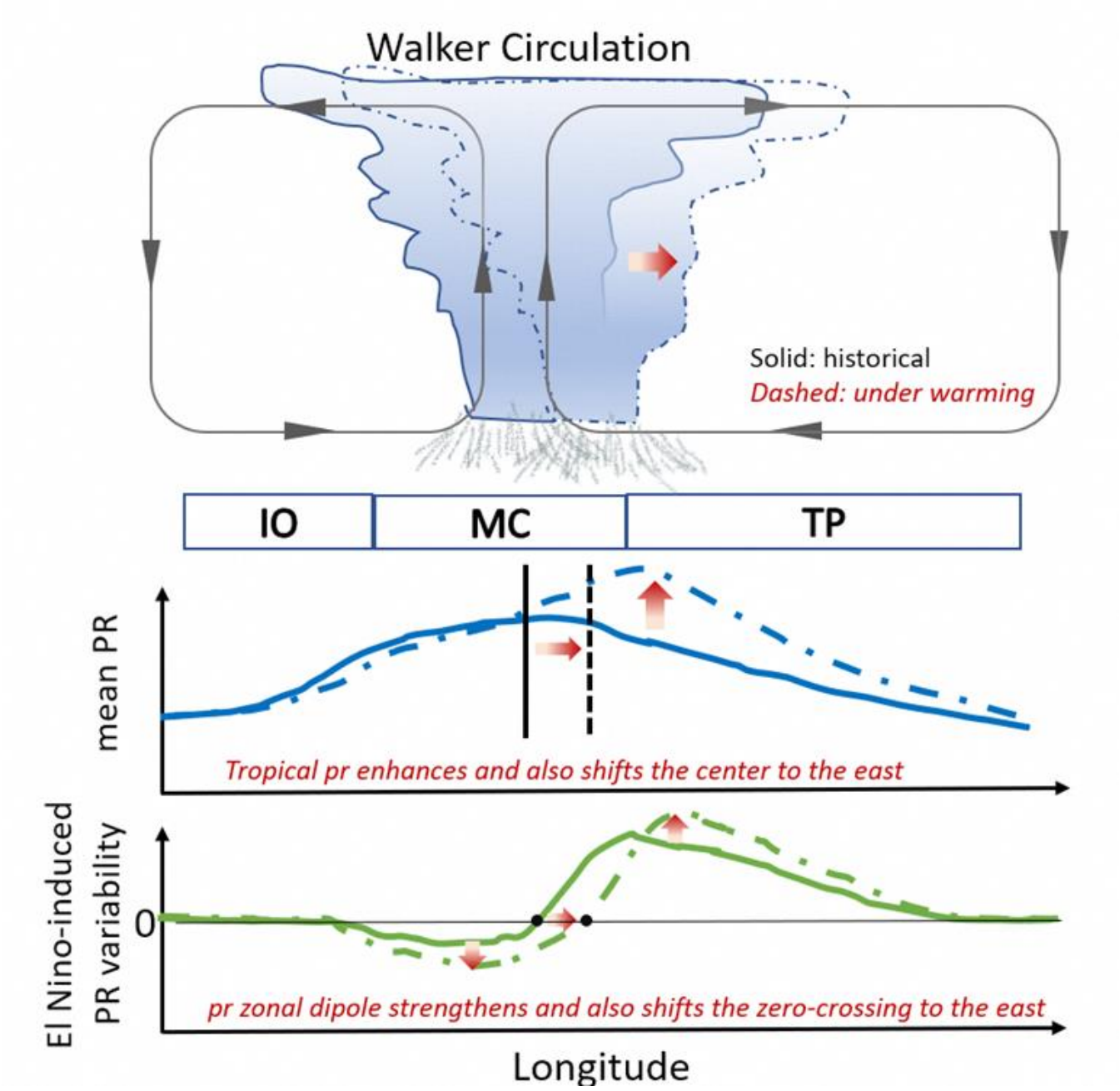

Figure 4.9: Schematic diagram showing the physical relationship between future changes in rainfall and ENSO-rainfall teleconnection. Across the longitude, the left is the Indian Ocean (IO), the middle is the Maritime Continent (MC), and the right is the Tropical Pacific (TP). Under warming, the deep convection center above the warm pool and the Walker Circulation shifts eastward. The first row shows that tropical precipitation enhances but also shifts the center to the east. The second row shows that ENSO-induced precipitation variability displays a zonal dipole structure (positive in the TP and negative in the MC), and this dipole strengthens under warming and shifts the zero-crossing longitude to the east.

4.5.5 Northeast Monsoon Surge changes under warming

Figure 4.10 shows the projected changes in rainfall and 850 hPa winds composited over northeast monsoon surge days using 6 GCMs. The definition of surge days follows in Chapter 3.7, where the mean and standard deviation are calculated separately for historical and SSP5-8.5. Rainfall increases are projected around Borneo,

Sulawesi, south Sumatra, New Guinea, and east of the Philippines, and drying around the Maluku Islands). The increase in surge rainfall over Borneo and New Guinea, together with the increase of DJF and SON rainfall over these two regions (Figure 4.4), suggests the surges could be related to changes in rainfall over those time periods. As for winds, the projected changes include easterlies over Indochina and west of Sumatra, as well as westerlies north of New Guinea. There is also an increase in surge frequency from 18% to 19%.

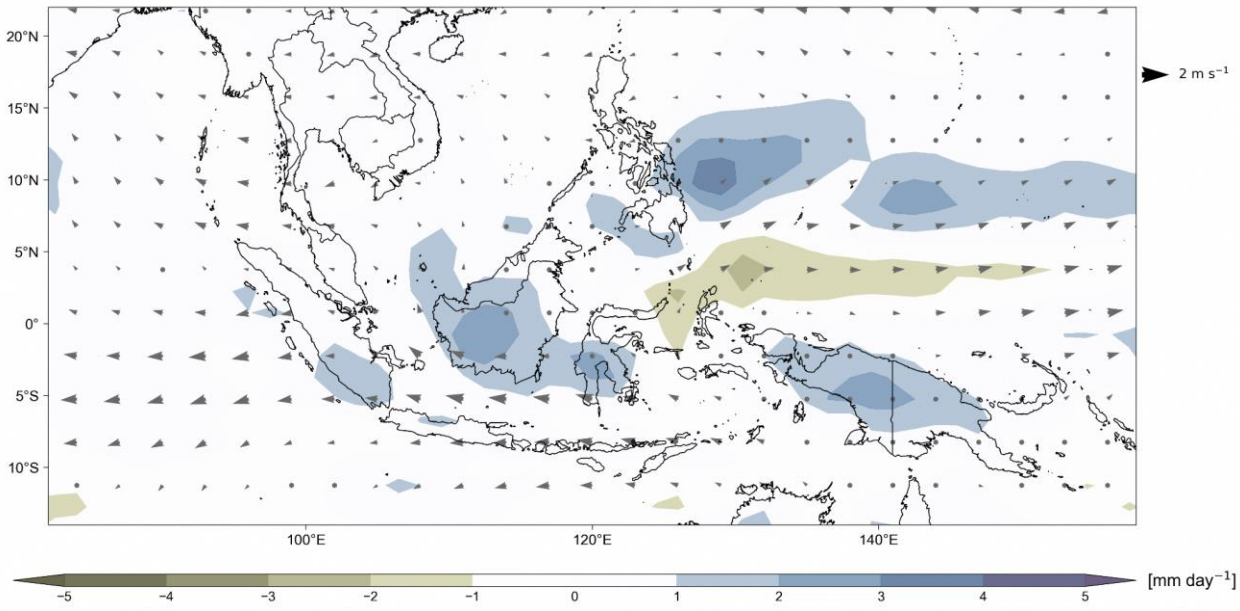

Figure 4.10: shows the change in 850 hPa wind direction (arrows) and rainfall (shaded) composited over surge days from 2080-2099 in SSP5-8.5 with respect to 1995-2014 in 6 GCMs, regridded to 1.5 x1.5 (those used for downscaling).

The results indicate that Singapore might experience more surge events, but that the magnitude of rainfall from these events as a whole might not change much. One caveat is that we have not examined how changes in the strongest monsoon surge events might change with warming, which has implications for the precipitation extremes experienced over Singapore (see Chapter 10.3 for further discussion).

4.6 Summary

The current chapter focuses on using Global and regional climate projections from the CMIP6 models (used in IPCC AR6) to comprehend information about climate change at global and regional scales. Here, we describe the projected changes in some important climate variables (i.e. temperature and rainfall), associated climate drivers (monsoon, ENSO, IOD, MJO), and regional teleconnections mainly influencing the Southeast Asian climate.

The CMIP6 models have higher spatial resolution, improved model physics (parameterization schemes), and more earth system models with carbon cycle and biogeochemistry compared to the CMIP5 models. The equilibrium climate sensitivity (ECS) values in many of the CMIP6 models are projected to be higher than the CMIP5 models. The CMIP6 models, compared to earlier CMIP5 models, also have a socioeconomic storyline (SSP1-2.6, SSP2-4.5, SSP3-7.0, and SSP5-8.5) along with radiative forcing levels (CMIP5 models; Representative Concentration Pathways (RCP) 2.6, 4.5, 6.0 & 8.5) for the future warming scenarios. Therefore, one may expect higher confidence in the future projections of different climate variables and processes using

the CMIP6 models compared to earlier CMIP5 models.

The global mean surface air temperature is projected to increase by 0.4 to 1.0^{o}C relative to 1995 - 2014 across most of the scenarios in the near term (2021-2040). Also, the land surface temperatures are expected to rise at least 1.0^{o}C higher than the oceans during the same period. The near-term land precipitation is expected to increase under both low emission (-0.2 to 4.7%) and high emission (0.9 to 12.9%) scenarios with certain regional uncertainties due to internal variability, model uncertainty, and uncertainties in aerosol emissions.

Under different warming scenarios, the global monsoon precipitation is expected to increase despite reduced circulation strength both in the mid and end century. The ENSO response due to warming is uncertain across different scenarios but has a strong signal of ENSO-induced precipitation variability over the tropical Pacific. Although the frequency of strong positive IOD is projected to increase, the IOD response is uncertain due to the lack of strong evidence and dependency on mean state biases of the model. In a future warmer climate, the MJO is projected to become more intense with an increased magnitude of associated precipitation.

The regional projections over the SEA region show that mean surface temperature increases across the SEA are slightly less than the global. The daily mean surface temperatures are expected to increase over land and oceans with stronger land-sea contrast in high ECS models at annual and seasonal time scales. The temperatures are expected to rise up to 5^{o}C during hot summer periods in MAM and JJA seasons over northern parts of SEA. The mean annual rainfall projections show increased values over most of the land regions of SEA, with higher increases over the northern SEA, Borneo, and New Guinea. The regional precipitation response across different seasons tends to scale with the level of warming, i.e. the high ECS models have stronger regional rainfall changes compared to the medium ECS models. In CMIP6 models, under the higher warming scenario (SSP5-8.5), there is a strong ENSO-rainfall signal over the MC with strong drier conditions during El Niño and strong wetter conditions during La Niña.

There is an increased frequency of Northeast monsoon surges to 19% (from the current 18%) with increased rainfall over Borneo, Sulawesi, south Sumatra, New Guinea, and east of the Philippines, and reduced rainfall around the Maluku islands. Due to the combined effects of climate change, land subsidence, and regional human activity, there is a higher degree of confidence in the increasing floods and prolonged inundation across the Mekong Delta region.

Overall, the CMIP6 future projections indicate increased global and regional surface air temperatures, enhanced global precipitation (regional differences; wet gets wetter, dry gets drier), increased monsoon land precipitation, and enhanced ENSO-rainfall teleconnections. In addition to the mean changes, extremes in temperature and rainfall are projected to increase, especially under SSP5-8.5 over many parts of the globe, including SEA.

References

Adames, Á.F., Kim, D., Sobel, A.H., Del Genio, A. and Wu, J., 2017. Characterization of moist processes associated with changes in the propagation of the MJO with increasing CO2. Journal of advances in modeling earth systems, 9(8), pp.2946-2967.

Ahn, M.S., Kim, D., Kang, D., Lee, J., Sperber, K.R., Gleckler, P.J., Jiang, X., Ham, Y.G. and Kim, H., 2020. MJO propagation across the Maritime Continent: Are CMIP6 models better than CMIP5 models? Geophysical Research Letters, 47(11), p.e2020GL087250.

Arnold, N.P. and Randall, D.A., 2015. Global-scale convective aggregation: Implications for the Madden-Julian Oscillation. Journal of Advances in Modeling Earth Systems, 7(4), pp.1499-1518.

Bayr, T., D. Dommenget, T. Martin, and S. B. Power, 2014: The eastward shift of the Walker Circulation in response to global warming and its relationship to ENSO variability. Clim. Dyn., 43, 2747–2763, https://doi.org/10.1007/s00382-014-2091-y.

Bonfils, C. J. W., B. D. Santer, T. J. Phillips, K. Marvel, L. Ruby Leung, C. Doutriaux, and A. Capotondi, 2015: Relative contributions of mean-state shifts and ENSO-driven variability to precipitation changes in a warming climate. J. Clim., 28, 9997–10013, https://doi.org/10.1175/JCLI-D-15-0341.1.

Brown, J., and Coauthors, 2020: Comparison of past and future simulations of ENSO in CMIP5/PMIP3 and CMIP6/PMIP4 models. Clim. Past Discuss., 1–44, https://doi.org/10.5194/cp-2019-155.

Chen, C., M. A. Cane, A. T. Wittenberg, and D. Chen, 2017: ENSO in the CMIP5 Simulations: Life Cycles, Diversity, and Responses to Climate Change. J. Clim., 30, 775–801, https://doi.org/10.1175/JCLI-D-15-0901.1.

Chen, G., Ling, J., Zhang, R., Xiao, Z. and Li, C., 2022. The MJO from CMIP5 to CMIP6: Perspectives from tracking MJO precipitation. Geophysical Research Letters, 49(1), p.e2021GL095241.

Callahan, C. W., C. Chen, M. Rugenstein, J. Bloch-Johnson, S. Yang, and E. J. Moyer, 2021: Robust decrease in El Niño/Southern Oscillation amplitude under long-term warming. Nat. Clim. Chang., 11, 752–757, https://doi.org/10.1038/s41558-021-01099-2.

Cai, W., Zheng, X.T., Weller, E., Collins, M., Cowan, T., Lengaigne, M., Yu, W. and Yamagata, T., 2013. Projected response of the Indian Ocean Dipole to greenhouse warming. Nature geoscience, 6(12), pp.999-1007.

Cai, W., Santoso, A., Wang, G., Weller, E., Wu, L., Ashok, K., Masumoto, Y. and Yamagata, T., 2014. Increased frequency of extreme Indian Ocean Dipole events due to greenhouse warming. Nature, 510(7504), pp.254-258.

Cai, W., Yang, K., Wu, L., Huang, G., Santoso, A., Ng, B., Wang, G. and Yamagata, T., 2021. Opposite response of strong and moderate positive Indian Ocean Dipole to global warming. Nature Climate Change, 11(1), pp.27-32.

Cai, W., and Coauthors, 2021: Changing El Niño–Southern Oscillation in a warming climate. Nat. Rev. Earth Environ., 2, 628–644, https://doi.org/10.1038/s43017-021-00199-z.

Chu, J.E., Ha, K.J., Lee, J.Y., Wang, B., Kim, B.H. and Chung, C.E., 2014. Future change of the Indian Ocean basin-wide and dipole modes in the CMIP5. Climate dynamics, 43, pp.535-551.

Chung, C. T. Y., and S. B. Power, 2014: Precipitation response to La Niña and global warming in the Indo-Pacific. Clim. Dyn., 43, 3293–3307, https://doi.org/10.1007/s00382-014-2105-9.

Chung, C. T. Y., S. B. Power, J. M. Arblaster, H. A. Rashid, and G. L. Roff, 2014: Nonlinear precipitation response to El Niño and global warming in the Indo-Pacific. Clim. Dyn., 42, 1837–1856, https://doi.org/10.1007/s00382-013-1892-8.

Chung, C. T. Y., and S. B. Power, 2015: Modelled rainfall response to strong El Niño sea surface temperature anomalies in the tropical pacific. J. Clim., 28, 3133–3151, https://doi.org/10.1175/JCLI-D-14-00610.1.

Chung, C. T. Y., and S. B. Power, 2016: Modelled impact of global warming on ENSO-driven precipitation changes in the tropical Pacific. Clim. Dyn., 47, 1303–1323, https://doi.org/10.1007/s00382-015-2902-9.

Coelho, C. A. S., and L. Goddard, 2009: El Niño-induced tropical droughts in climate change projections. J. Clim., 22, 6456–6476, https://doi.org/10.1175/2009JCLI3185.1.

Hendon, H. H., 2003: Indonesian Rainfall Variability: Impacts of ENSO and Local Air–Sea Interaction. J. Clim., 16, 1775–1790.

Hu, K., G. Huang, P. Huang, Y. Kosaka, and S.-P. Xie, 2021: Intensification of El Niño-induced atmospheric

anomalies under greenhouse warming. Nat. Geosci., https://doi.org/10.1038/s41561-021-00730-3.

Huang, P., and S.-P. Xie, 2015: Mechanisms of change in ENSO-induced tropical Pacific rainfall variability in a warming climate. Nat. Geosci., 1–13, https://doi.org/10.1038/ngeo2571.

Kikuchi, K., Wang, B. and Kajikawa, Y., 2012. Bimodal representation of the tropical intraseasonal oscillation. Climate Dynamics, 38, pp.1989-2000.

Kim, H., Vitart, F. and Waliser, D.E., 2018. Prediction of the Madden–Julian oscillation: A review. Journal of Climate, 31(23), pp.9425-9443.

Langenbrunner, B., and J. D. Neelin, 2013: Analyzing ENSO Teleconnections in CMIP Models as a Measure of Model Fidelity in Simulating Precipitation. J. Clim., 26, 4431–4446, https://doi.org/10.1175/JCLI-D-12-00542.1.

Lau, N. C., and M. J. Nath, 2003: Atmosphere-ocean variations in the Indo-Pacific sector during ENSO episodes. J. Clim., 16, 3–20.

Lee, J.Y., Wang, B., Wheeler, M.C., Fu, X., Waliser, D.E. and Kang, I.S., 2013. Real-time multivariate indices for the boreal summer intraseasonal oscillation over the Asian summer monsoon region. Climate Dynamics, 40, pp.493-509.

Li, G., Xie, S.P. and Du, Y., 2016. A robust but spurious pattern of climate change in model projections over the tropical Indian Ocean. Journal of Climate, 29(15), pp.5589-5608.

Kug, J. S., S. Il An, Y. G. Ham, and I. S. Kang, 2010: Changes in El Niño and La Niña teleconnections over North Pacific-America in the global warming simulations. Theor. Appl. Climatol., 100, 275–282, https://doi.org/10.1007/s00704-009-0183-0.

Madden, R.A., 1986. Seasonal variations of the 40-50 day oscillation in the tropics. Journal of Atmospheric Sciences, 43(24), pp.3138-3158.

Madden, R.A. and Julian, P.R., 1994. Observations of the 40–50-day tropical oscillation—A review. Monthly weather review, 122(5), pp.814-837.

Maloney, E.D., Adames, Á.F. and Bui, H.X., 2019. Madden–Julian oscillation changes under anthropogenic warming. Nature Climate Change, 9(1), pp.26-33.

Power, S., F. Delage, C. Chung, G. Kociuba, and K. Keay, 2013: Robust twenty-first-century projections of El Niño and related precipitation variability. Nature, 502, 541–545, https://doi.org/10.1038/nature12580.

Ropelewski, C. F., and M. S. Halpert, 1987: Global and Regional Scale Precipitation Patterns Associated with the El Niño/Southern Oscillation. Mon. Weather Rev., 115, 1606–1626, https://doi.org/10.1175/1520-0493(1987)115<1606:GARSPP>2.0.CO;2.

Roxy, M.K., Dasgupta, P., McPhaden, M.J., Suematsu, T., Zhang, C. and Kim, D., 2019. Twofold expansion of the Indo-Pacific warm pool warps the MJO life cycle. Nature, 575(7784), pp.647-651.

O'Neill, B. C., Tebaldi, C., van Vuuren, D. P., Eyring, V., Friedlingstein, P., Hurtt, G., et al. (2016). The Scenario Model Intercomparison Project (ScenarioMIP) for CMIP6. Geoscientific Model Development, 9(9), 3461–3482. https://doi.org/10.5194/gmd-9-3461-2016

Perry, S. J., S. McGregor, A. Sen Gupta, and M. H. England, 2017: Future Changes to El Niño–Southern Oscillation Temperature and Precipitation Teleconnections. Geophys. Res. Lett., 44, 10,608-10,616, https://doi.org/10.1002/2017GL074509.

Pillai, P.A., Nair, R.C. and Vidhya, C.V., 2019. Recent changes in the prominent modes of Indian Ocean dipole in response to the tropical Pacific Ocean SST patterns. Theoretical and Applied Climatology, 138, pp.941-951.

Saji, N.H., Goswami, B.N., Vinayachandran, P.N. and Yamagata, T., 1999. A dipole mode in the tropical Indian Ocean. Nature, 401(6751), pp.360-363.

Saji, N.H. and Yamagata, T., 2003. Structure of SST and surface wind variability during Indian Ocean dipole mode events: COADS observations. Journal of Climate, 16(16), pp.2735-2751.

Schott, F.A., Xie, S.P. and McCreary Jr, J.P., 2009. Indian Ocean circulation and climate variability. Reviews of Geophysics, 47(1).

S. C. Sherwood, M. J. Webb, J. D. Annan, K. C. Armour, P. M. Forster, J. C. Hargreaves, G. Hegerl, S. A. Klein, K. D. Marvel, E. J. Rohling, M. Watanabe, T. Andrews, P. Braconnot, C. S. Bretherton, G. L. Foster, Z. Hausfather, A. S. von der Heydt, R. Knutti, T. Mauritsen, J. R. Norris, C. Proistosescu, M. Rugenstein, G. A. Schmidt, K. B. Tokarska, M. D. Zelinka, 2020. An Assessment of Earth's Climate Sensitivity Using Multiple Lines of Evidence. Reviews of Geophysics, DOI:10.1029/2019RG000678.

Stuecker, M.F., Timmermann, A., Jin, F.F., Chikamoto, Y., Zhang, W., Wittenberg, A.T., Widiasih, E. and Zhao, S., 2017. Revisiting ENSO/Indian Ocean dipole phase relationships. Geophysical Research Letters, 44(5), pp.2481-2492.

Stuecker, M. F., F. F. Jin, A. Timmermann, and S. Mcgregor, 2015: Combination mode dynamics of the anomalous northwest pacific anticyclone. J. Clim., 28, 1093–1111, https://doi.org/10.1175/JCLI-D-14-00225.1.

Taschetto, A. S., C. C. Ummenhofer, M. F. Stuecker, D. Dommenget, K. Ashok, R. R. Rodrigues, and S. Yeh, 2020: ENSO Atmospheric Teleconnections. 309–335.

Wang, B., R. Wu, and T. Li, 2003: Atmosphere-warm ocean interaction and its impacts on Asian-Australian monsoon variation. J. Clim., 16, 1195–1211, https://doi.org/10.1175/1520-0442(2003)16<1195:AOIAII>2.0.CO;2.

Wang, J., DeFlorio, M.J., Kim, H., Guirguis, K. and Gershunov, A., 2023. CMIP6 projections of future MJO changes under steepened moisture gradient conditions over the Indo-Pacific warm pool. Authorea Preprints.

Wheeler, M.C., Kim, H.J., Lee, J.Y. and Gottschalck, J.C., 2017. Real-time forecasting of modes of tropical intraseasonal variability: The Madden-Julian and boreal summer intraseasonal oscillations. In The Global Monsoon System: Research and Forecast (pp. 131-138).

Wolding, B.O., Maloney, E.D., Henderson, S. and Branson, M., 2017. Climate change and the Madden-Julian Oscillation: A vertically resolved weak temperature gradient analysis. Journal of Advances in Modeling Earth Systems, 9(1), pp.307-331.

Yan, Z., B. Wu, T. Li, M. Collins, R. Clark, T. Zhou, J. Murphy, and G. Tan, 2020: Eastward shift and extension of ENSO-induced tropical precipitation anomalies under global warming. 1–11.

Yeh, S. W., and Coauthors, 2018: ENSO Atmospheric Teleconnections and Their Response to Greenhouse Gas Forcing. Rev. Geophys., 56, 185–206, https://doi.org/10.1002/2017RG000568.

Zelinka, M. D., Myers, T. A., McCoy, D. T., Po-Chedley, S., Caldwell, P. M., Ceppi, P., et al. (2020). Causes of Higher Climate Sensitivity in CMIP6 Models. Geophysical Research Letters, 47(1), e2019GL085782. https://doi.org/10.1029/2019GL085782

Zhang, C., 2005. Madden-julian oscillation. Reviews of Geophysics, 43(2).

Eyring, V., Bony, S., Meehl, G. A., Senior, C. A., Stevens, B., Stouffer, R. J., & Taylor, K. E. (2016). Overview of the Coupled Model Intercomparison Project Phase 6 (CMIP6) experimental design and organization. Geoscientific Model Development, 9(5), 1937–1958. https://doi.org/10.5194/gmd-9-1937-2016.

Evaluation and Sub-selection of CMIP6 GCMs over Southeast Asia for Dynamical Downscaling

5

Authors:
Aurel Florian Moise, Sandeep Sahany, Muhammad Eeqmal Hassim, Chen Chen, Xin Rong Chua, Venkatraman Prasanna, Gerald Lim, Pavan Harika Raavi, Fei Luo

Meteorological Service Singapore
Centre for Climate Research Singapore

5.1 Introduction

The Southeast Asia (SEA) region is home to ca. 8.5% of the global population and is highly vulnerable to climate change both due to the projected increase in natural hazards and the limited adaptive capacity of many of the SEA countries. The weather and climate over SEA are influenced by many local, regional, and large-scale processes. Some of the important large scale processes include the Asian-Australian monsoon system, the Madden Julian Oscillation (MJO), El-Nino Southern Oscillation (ENSO), Indian Ocean Dipole (IOD), etc. Even within this region there is a large variation in the climatic conditions both in terms of mean and variability.

In line with the previous generations of the Coupled Model Intercomparison Projects (CMIPs), the CMIP6 (Eyring et al, 2016) provides us with a coordinated set of climate model simulations from climate modelling centres around the world. Although global models have been known to perform well in providing large scale climate information, such as global mean temperature and rainfall, the regional and local climatic features are more prone to biases.

According to the Sixth Assessment Report (AR6) by the Intergovernmental Panel on Climate Change (IPCC) the CMIP6 multi-model mean is cooler over the period 1980-2000 than both observations and CMIP5 (Bock et al., 2020; Flynn and Mauritsen, 2020), and that these biases of several tenths of a degree in some CMIP6 models could be due to an overestimate in aerosol radiative forcing during the period (Andrews et al., 2020; Dittus et al., 2020; Flynn and Mauritsen, 2020).

There have also been studies on regional climate using the CMIP6 models. For example, Khadka et al. (2021) used model data from CMIP5 and CMIP6 to evaluate summer rainfall in Southeast Asia. They found CMIP6 models to be superior to CMIP5 ones in simulating rainfall and large-scale circulation, and attributed it to CMIP6 models' higher spatial resolutions, increased number of vertical levels, and improved atmospheric and land surface parameterizations. They also reported that CMIP6 models are better at representing the annual cycle of rainfall but many still show dry biases like their predecessors. Many of the climate models from both CMIPs were reported to show a shorter rainy season due to late onset and early retreat. In another relevant study Ge et al. (2021) used outputs from 15 CMIP6 GCMs to estimate projected changes in precipitation extremes for SEA at the end of the 21st century and reported that the projected precipitation extremes increase significantly over the Indochina Peninsula and the Maritime Continent.

The IPCC AR6 further reports with medium confidence that CMIP5 and CMIP6 models continue to overestimate observed warming in the upper tropical troposphere over the 1979-2014 period by at least 0.1°C per decade, partly because of an overestimation of the tropical SST trends during this period.

Kim et al. (2020) evaluated CMIP6 models for their performance in simulating the climate extreme indices defined by the Expert Team on Climate Change Detection and Indices (ETCCDI) and reported that the CMIP6 models generally capture the observed global and regional patterns of temperature extremes with limited improvements compared to the CMIP5 models. They also reported that the CMIP6 model skills for the precipitation intensity and frequency indices are broadly comparable to those of CMIP5 models, but with an improvement in precipitation intensity amplitudes.

Fiedler et al. (2020) evaluated the simulation of MJO in CMIP6 models by calculating the ratio of the eastward-propagating spectral power of tropical precipitation to that of its westward-propagating counterpart summed up over the MJO characteristic wavenumbers one to three and periods of 20–100 days for the November to April season between 10oS and 10oN (a quantity often used as a measure for the MJO). It was found that while for observations this ratio was found to be in the range of 3.2 to 3.4 for CMIP6 multi model mean it was found to be around 2.2. While this is better than that in CMIP6, there is scope for further improvement in future CMIPs. In the same paper they also evaluated ENSO-rainfall teleconnections in the CMIP6 models by using the method from Power et al. (2013) by computing the empirical orthogonal function (EOF) of SST

means for June–December within 15oS–15oN, 140oE–100oW, based on detrended and filtered SST time series, and found that there are two clear regions with systematic biases in precipitation associated with El Niño events, (i) too-strong positive anomaly around the Maritime Continent indicating a westward displaced precipitation maximum during El Niño events, and (ii) too pronounced double ITCZ.

The IPCC AR6 Atlas provides only the large-scale information, and higher resolution information still needs to be generated by means of downscaling. Most of the CMIP6 models that have contributed to the WG-I report do not have Singapore as an island due to coarse resolution, and either represent it as a part of the Malay peninsula or show it as an ocean point. In order to make physical climate change projections on regional scales and also for making the global model data usable by the vulnerability and impacts assessment community, the coarse resolution global model data needs to be downscaled to higher resolutions. As was the case with CMIP5, CMIP6 also provides 6-hourly fields of model variables that can be further used to carry out dynamical downscaling to generate more reliable high resolution climate change projections at a regional level. It is imperative to thoroughly evaluate the historical simulations against observations and reanalysis to have confidence in the future large-scale climate change projections, and also for sub-selection of the models for downscaling.

Dynamically downscaled projections are produced in a coordinated way under the Coordinated Regional Climate Downscaling Experiment (CORDEX), a programme under the auspices of the World Climate Research Programme (Giorgi et al., 2009). During the last few years, a set of downscaled RCMs projections for the Southeast Asia domain has become available under the Coordinated Regional Climate Downscaling Experiment – Southeast Asia (CORDEX-SEA) (Juneng et al., 2016; Ngo-Duc et al., 2017; Supari et al., 2020; Tangang et al., 2018, 2020), and is used by SEA countries for their national climate change assessments and adaptation planning.

As a part of the Third National Climate Change Study for Singapore (V3) the Centre for Climate Research Singapore (CCRS) has dynamically downscaled 6 CMIP6 GCMs over Southeast Asia to 8 km resolution, and 5 of them were further downscaled over the western Maritime Continent to 2 km resolution for the historical period (1955-2014) and future (2015-2100) for 3 Shared Socioeconomic Pathways (SSPs) used in the IPCC AR6, namely, SSP1-2.6, SSP2-4.5 and SSP5-8.5. The dynamical downscaling domain is discussed in Chapter 2, and SINGV-RCM is discussed in Chapter 6 of this report.

There is no universally accepted methodology on how to select a subset of GCMs for downscaling, but in order to be consistent with the practice of the dynamical downscaling community, we follow a methodology in-line with the CORDEX experiment design protocol standard described in Section 5.2.4. The data and methods used in this work are described in Section 5.2. The evaluation of CMIP6 GCMs and the process of sub-selection is presented in Section 5.3, followed by discussion and conclusions presented in Section 5.4.

5.2 Data and Methods

In this section we present the various datasets used (observations, reanalysis and CMIP6 model outputs), the different metrics used for evaluation (root mean squared error, pattern correlation coefficient, etc.), the sub-setting criteria used, and the domain of evaluation such that it is relevant for our purpose of dynamical downscaling.

5.2.1 CMIP6 Model Data

Model outputs from historical simulations of 49 CMIP6 GCMs were used in our analysis. For some of the variables data from all 49 GCMs were not available so we used whatever was available during the time of analysis. Information on the GCMs, including their name, modelling centre, nominal grid resolution and ensemble member used in analysis have been presented in Table 5.1. The variables include 2m air temperature, surface temperature, rainfall, 2m specific humidity, winds and mean sea level pressure. We have used the period 1995-2014 for most of the evaluations.

Table 5.1: List of CMIP6 GCMs, modelling centre, nominal grid resolution and ensemble member. The dark green colour highlights models which had 6-hourly data available at the time of the downscaling.

Sl. No.	Model Name	Institution	Country	Nominal Resolution	Ensemble member
1	ACCESS-CM2	CSIRO-ARCCSS-BoM	Australia	250 km	/r4i1p1f1
2	ACCESS-ESM1-5	CSIRO	Australia	250 km	r1i1p1f1
3	AWI-CM-1-1-MR	AWI	Germany	100 km	r1i1p1f1
4	BCC-CSM2-MR	BCC	China	100 km	r1i1p1f1
5	BCC-ESM1	BCC	China	250 km	r1i1p1f1
6	CAMS-CSM1-0	CAMS	USA	100 km	r1i1p1f1
7	CESM2	NCAR	USA	100 km	r1i1p1f1
8	CESM2-FV2	NCAR	USA	250 km	r1i1p1f1
9	CESM2-WACCM	NCAR	USA	100 km	r1i1p1f1
10	CESM2-WACCM-FV2	NCAR	USA	100 km	r1i1p1f1
11	CIESM	THU	China	100 km	r1i1p1f1
12	CNRM-CM6-1	CNRM-CERFACS	France	250 km	r1i1p1f2
13	CNRM-CM6-1-HR	CNRM-CERFACS	France	50 km	r1i1p1f2
14	CNRM-ESM2-1	CNRM-CERFACS	France	250 km	r1i1p1f2
15	CanESM5	CCCma	Canada	500 km	r1i1p1f1
16	CanESM5-CanOE	CCCma	Canada	500 km	r1i1p2f1
17	E3SM-1-0	DOE E3SM-Project	USA	100 km	r1i1p1f1
18	E3SM-1-1	DOE E3SM-Project	USA	100 km	r1i1p1f1
19	E3SM-1-1-ECA	DOE E3SM-Project	USA	100 km	r1i1p1f1
20	EC-Earth3	EC-Earth-Consortium	Europe	100 km	r1i1p1f1
21	EC-Earth3-Veg	EC-Earth-Consortium	Europe	100 km	r1i1p1f1
22	FGOALS-f3-L	CAS	China	100 km	r1i1p1f1
23	FGOALS-g3	CAS	China	250 km	r1i1p1f1
24	FIO-ESM-2-0	FIO-QLNM	China	100 km	r1i1p1f1
25	GFDL-CM4	NOAA-GFDL	USA	100 km	r1i1p1f1
26	GFDL-ESM4	NOAA-GFDL	USA	100 km	r1i1p1f1
27	GISS-E2-1-G	NASA-GISS	USA	250 km	r1i1p1f1
28	GISS-E2-1-G-CC	NASA-GISS	USA	250 km	r1i1p1f1
29	GISS-E2-1-H	NASA-GISS	USA	250 km	r1i1p1f1
30	HadGEM3-GC31-LL	MOHC	UK	250 km	r1i1p1f3
31	HadGEM3-GC31-MM	MOHC	UK	100 km	r1i1p1f3
32	INM-CM4-8	INM	Russia	100 km	r1i1p1f1
33	INM-CM5-0	INM	Russia	100 km	r1i1p1f1
34	IPSL-CM6A-LR	IPSL	France	250 km	r1i1p1f1
35	KACE-1-0-G	NIMS-KMA	South Korea	250 km	r1i1p1f1
36	MCM-UA-1-0	UA	USA	250 km	r1i1p1f1
37	MIROC-ES2L	MIROC	Japan	500 km	r1i1p1f2
38	MIROC6	MIROC	Japan	250 km	r1i1p1f1
39	MPI-ESM-1-2-HAM	HAMMOZ-Consortium	Germany	250 km	r1i1p1f1
40	MPI-ESM1-2-HR	MPI-M	Germany	100 km	r1i1p1f1
41	MPI-ESM1-2-LR	MPI-M	Germany	250 km	r1i1p1f1
42	MRI-ESM2-0	MRI	Japan	100 km	r1i1p1f1
43	NESM3	NUIST	China	250 km	r1i1p1f1
44	NorCPM1	NCC	Norway	250 km	r1i1p1f1
45	NorESM2-LM	NCC	Norway	250 km	r1i1p1f1
46	NorESM2-MM	NCC	Norway	100 km	r1i1p1f1
47	SAM0-UNICON	SNU	South Korea	100 km	r1i1p1f1
48	TaiESM1	AS-RCEC	Taiwan	100 km	r1i1p1f1
49	UKESM1-0-LL	MOHC	UK	250 km	r1i1p1f2

5.2.2 Observations and Reanalysis

Multiple observational and reanalysis datasets have been used for evaluation. See Table 5.2 for details. We have used ensemble means of observations/reanalysis where feasible as our baseline to compute model biases, to address observational/reanalysis uncertainty.

Table 5.2: List of gridded observational (blue) and reanalysis data sets (green) used for evaluation in this chapter (all the data was regridded to 1.5°x1.5°, monthly, below shows the original grids), their climate fields used, and reference. The abbreviation pr refers to precipitation; TAS: surface air temperature; PSL: mean sea level pressure; SST: sea surface temperature; HUSS: specific humidity.

NAME	FIELDS (resol./freq.)	REFERENCES
HadISST v1	SST (1°x1°, monthly)	Rayner et al. 2003
COBE v2	SST (1°x1°, monthly)	Hirahara et al. 2014
OISST v2	SST (0.25°x0.25°, monthly)	Reynolds et al. 2007
ERSST v5	SST (2°x2°, monthly)	Huang et al. 2017
HURRELL	SST (1°x1°, monthly)	Hurrell et al. 2008
HadCRUT4	TAS (5°x5°, monthly)	Morice et al. 2012
BEST	TAS (1°x1°, monthly)	Rohde and Hausfather, 2020
FROGs	PR (1°x1°, daily)	Roca et al. 2019
IMERG V06	PR (0.1°x0.1°, 30 mins)	Huffman et al., 2019
GSMAP	PR (0.1°x0.1°, hourly)	Okamoto et al. 2005
TRMM 3B42	PR (0.25°x0.25°, 3 hours)	Huffman et al., 2007
PERSIANN_CDR	PR (0.25°x0.25°, sub-daily)	Ashouri et al., 2015
CMORPH_v1	PR (0.25°x0.25°, 3 hours)	Xie et al., 2017
GPCP	PR (1°x1°, daily)	Adler et al. 2003
ERA5 reanalysis	SST, TAS, HUSS, PSL, WINDS (0.25°x0.25°, hourly)	Hersbach et al. 2020
MERRA2 reanalysis	SST, TAS, HUSS, PSL, WINDS (0.5° x 0.625°, daily)	Gelaro et al. 2017
JRA55 reanalysis	SST, TAS, HUSS, PSL, WINDS (0.56°x0.56°, sub-daily, monthly)	Kobayashi et al. 2015

5.2.3 Metrics

Various statistical measures such as pattern correlation coefficient (PCC), mean absolute error (MSE), and root mean square error (RMSE) have been used to assess the performance of the models against observations and reanalysis. In addition, advanced metrics such as the Taylor diagram have also been used to assess the performance of the models.

5.2.4 Sub-setting of CMIP6 GCMs

In order to carry out sub-selection we follow standard practices suggested by the coordinated regional climate downscaling experiment (CORDEX; e.g. Gutowski et al. 2016). Thus, the sub-selected GCMs should: (1) span the range of GCM projections of temperature and precipitation over SEA, (2) perform satisfactorily in the historical climate, (3) span the range of model diversity in terms of genealogy (e.g., Knutti et al. 2013), and (4) have 6-hourly lateral boundary conditions (LBCs) available to drive the regional climate model. In addition to the aforementioned criteria, we also make use of expert judgement to discard models that are unable to simulate important aspects of regional climate over SEA.

5.2.5 Domain

Our domain of analysis focuses mostly on SEA, but for some of the tropical processes of interest included in tier-II of the analysis we have used larger domains. For example, for ENSO and cold-tongue bias analysis we have used the entire tropical Pacific domain. Figure 5.1 shows the 8 km and 2 km downscaling domains used in the V3 study. The D1 domain (8 km resolution) covers almost the whole of SEA and is slightly larger than

the CORDEX-SEA domain, whereas, the D2 domain (2 km resolution) covers Singapore and the western Maritime Continent. We use a one-way offline nesting, and the lateral boundary conditions for the 2 km model come from the 8 km downscaled data. Since the lateral and lower boundary conditions to drive the 8 km downscaling are obtained directly from the CMIP6 GCMs, our evaluation primarily focuses on the 8 km domain.

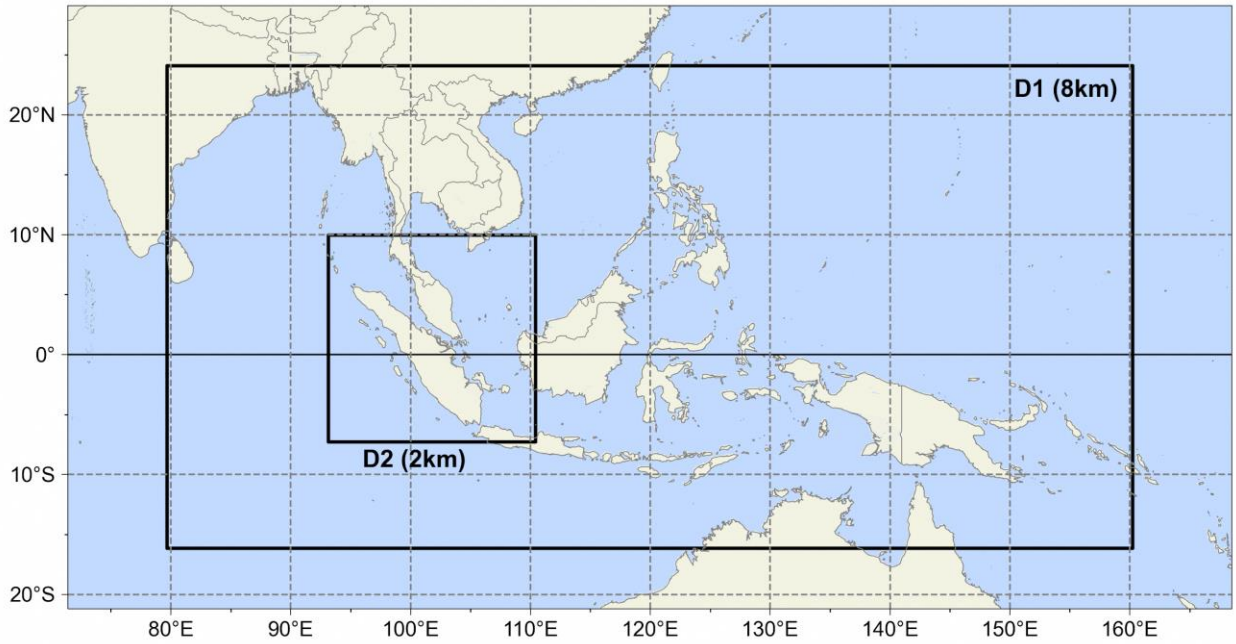

Figure 5.1: Dynamical downscaling domains for Singapore's Third National Climate Change Study at 8 km and 2 km resolutions.

5.3 Evaluation of Key Climate Variables

In this section we present the evaluation of key climate variables, namely, temperature, rainfall, winds, humidity and mean sea level pressure from the CMIP6 GCMs with an objective to identify the GCMs that show consistently poor performance and hence may not be considered fit for downscaling. The resolution used for multi-model mean for the GCMs is 1.5º, although not the lowest model resolution, it is the resolution fits for majority of the models. Thus, all the variables are conservatively re-gridded to 1.5º. The observational datasets are mostly 1º degree then all re-gridded to 1.5º to be able to compare to the model outputs.

5.3.1 Temperature

Figure 5.2 shows the climatological annual mean surface air temperature (tas) in observations (and reanalysis) and CMIP6 GCMs. Overall, the models perform well on annual timescales with low biases (white colour; biases in the range of +/- 0.5C) over almost half of the domain. For example, the biases are quite low over the tropical Indian Ocean. However, there are some notable biases which can be seen from Figs. 5.2e and f. Figure 5.2e shows (i) large positive biases over the Southern Ocean and east Pacific, (ii) negative biases over western and central tropical Pacific, (iii) negative bias over North Atlantic, and (iv) negative bias over Indochina. Figure 5.2f shows that the bias over large parts of the Maritime Continent is within +/- 0.5C, with exceptions such as Indochina and tropical western Pacific which show negative biases.

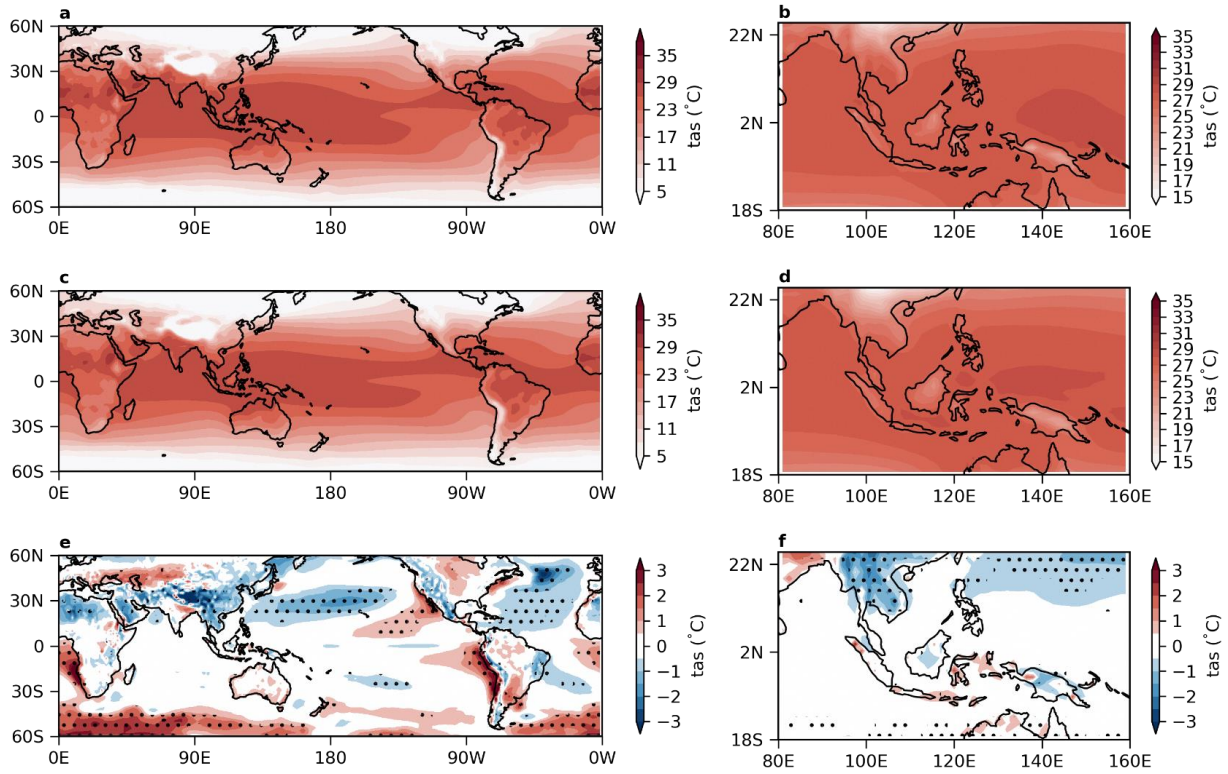

Figure 5.2: 1995-2014 mean surface air temperature (tas) in observation (a,b) and models (c,d). a. mean of five observational and reanalysis datasets (BEST, ERA5, HADCRUT4, JRA55, and MERRA2) for the 60N-60S domain. b. similar to a, but for the SEA domain. c. multimodel mean of tas from 47 CMIP6 models for the 60N-60S domain. d. similar to c, but for the SEA domain. e. model bias (multimodel mean from 47 models minus the observational mean). Hatched areas indicate the agreement by 70% of models on the sign of bias. f. similar to e, but for the SEA domain.

Figure 5.3 shows the distribution of model simulated tas values along with their RMSE and PCC for the global and SEA domains and for the annual mean and all seasons. Figure 5.3a, b show that the median of the multimodal ensemble lies within the spread of the reanalysis for annual mean as well as for each season over both global and SEA domains. The 25-75 percentile range of tas in models spans the reanalysis uncertainty range for all seasons and both domains. Figure 5.3c, d show that the median RMSE values are highest in DJF over both domains as compared to annual mean and other seasons. Given that the mean tas for DJF is already lower as compared to other seasons, higher RMSE values would mean even higher percentage errors. Figure 5.3e, f shows that the median PCC values are much higher over the global domain (~0.99), whereas it is somewhat lower over the SEA domain. Notably, the DJF PCC values are higher, especially over SEA.

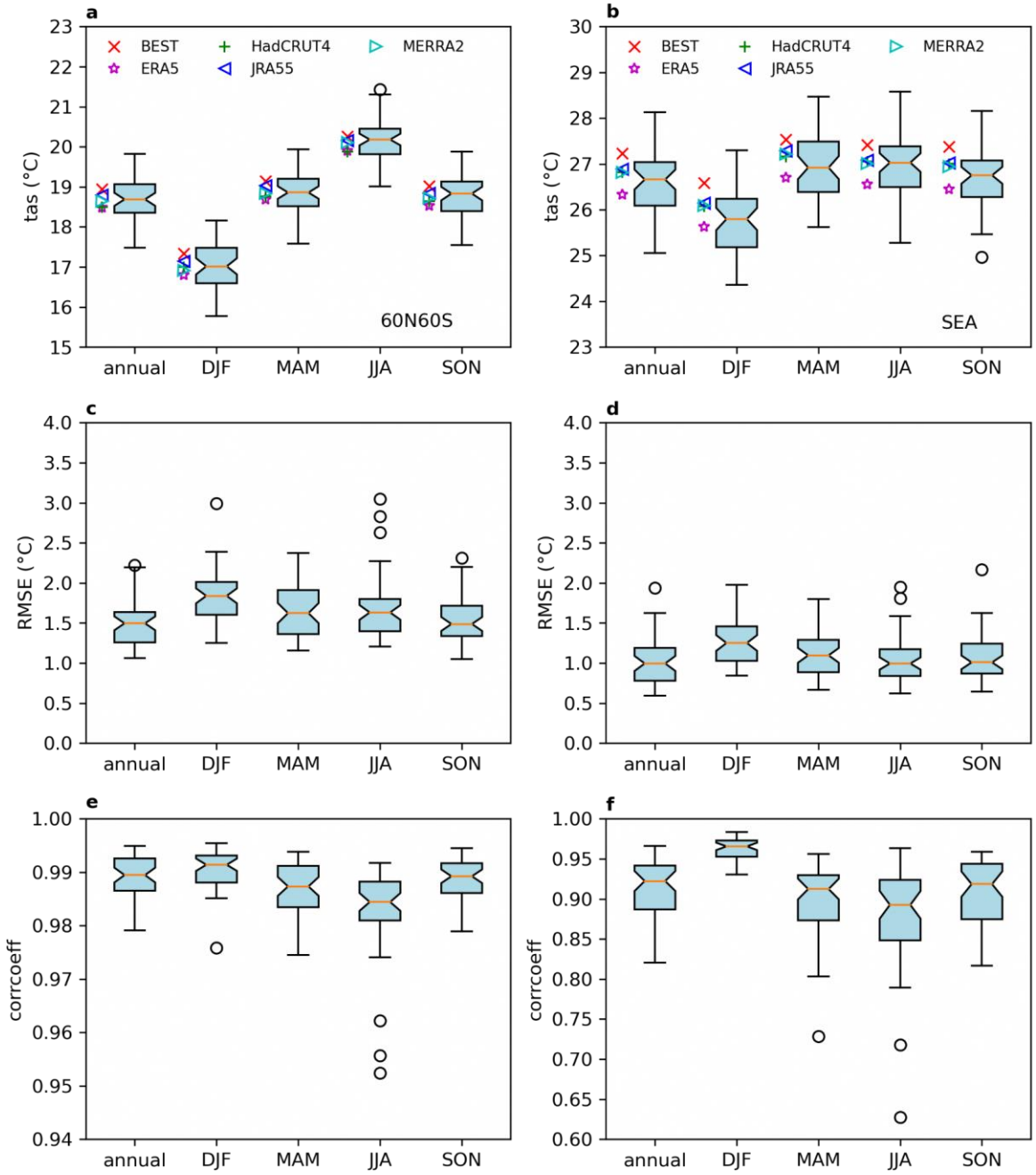

Figure 5.3: 1995-2014 mean tas averaged over the 60N-60S domain (a) and the SEA (b) in five observational and reanalysis datasets and 47 CMIP6 models. c. RMSE of models for the annual and seasonal tas in the 60N60S. d. similar to c, but for the SEA. e. PCC of models for the annual and seasonal tas in the 60N60S. f. similar to e, but for the SEA. The orange lines represent the median. The lower hinge is the Q1 quartile (25th), and the upper hinge is the Q3 quartile (75th). The upper and lower bars are based on 1.5 times the interquartile range (IQR) value. The outliers are shown in the open circles.

Figure 5.4 shows the performance of the individual CMIP6 GCMs for the global (60oS to 60oN) and SEA domains assessed from their RMSE and PCC values. For the global domain, we find that the annual mean RMSE mostly lies between the range of 1oC to 2oC, with around 5 models exceeding 2oC. The seasonal means also show a similar behaviour. It is to be noted that we

exclude the poles because we noted much larger biases over the polar region that may not be directly relevant to our purpose of sub-selection and at the same time masks the performance of the GCMs in the mid- and low-latitudes because of their lower values as compared to the higher latitudes. RMSE over SEA domain (Fig. 5.4b) mostly lies between around 0.7oC to 2oC, which was counter-intuitive since we were expecting regional biases to be larger than the global biases, but the regional biases over different regions can be higher or lower than the global mean, and it was good to see that the CMIP6 models have lower biases over our domain of interest. It is to be noted that many of the models show higher biases in DJF compared to other seasons and annual mean. The bottom five models based on annual mean RMSE are NorCPM1, BCC-ESM1, CNRM-CM6-1, BCC-CSM2-MR, and CNRM-CM6-1-HR.

The PCCs are shown in Figure 5.4c, d, for the global and SEA domains, respectively. The PCCs are generally quite high over the global domain with values greater than around 0.94 for the annual mean as well as all seasons. However, the PCCs over the SEA domain, in general, seem to be lower than the global, with values as low as around 0.65 for the JJA season. In general, DJF seems to have the highest PCCs, whereas JJA seems to have the lowest PCCs. Note that while the PCCs are generally higher in DJF, the RMSEs are also higher, as seen above. The bottom five models based on annual mean PCCs over the SEA domain are INM-CM4-8, NorCPM1, MCM-UA-1-0, GISS-E2-1-H, and MIROC-ES2L.

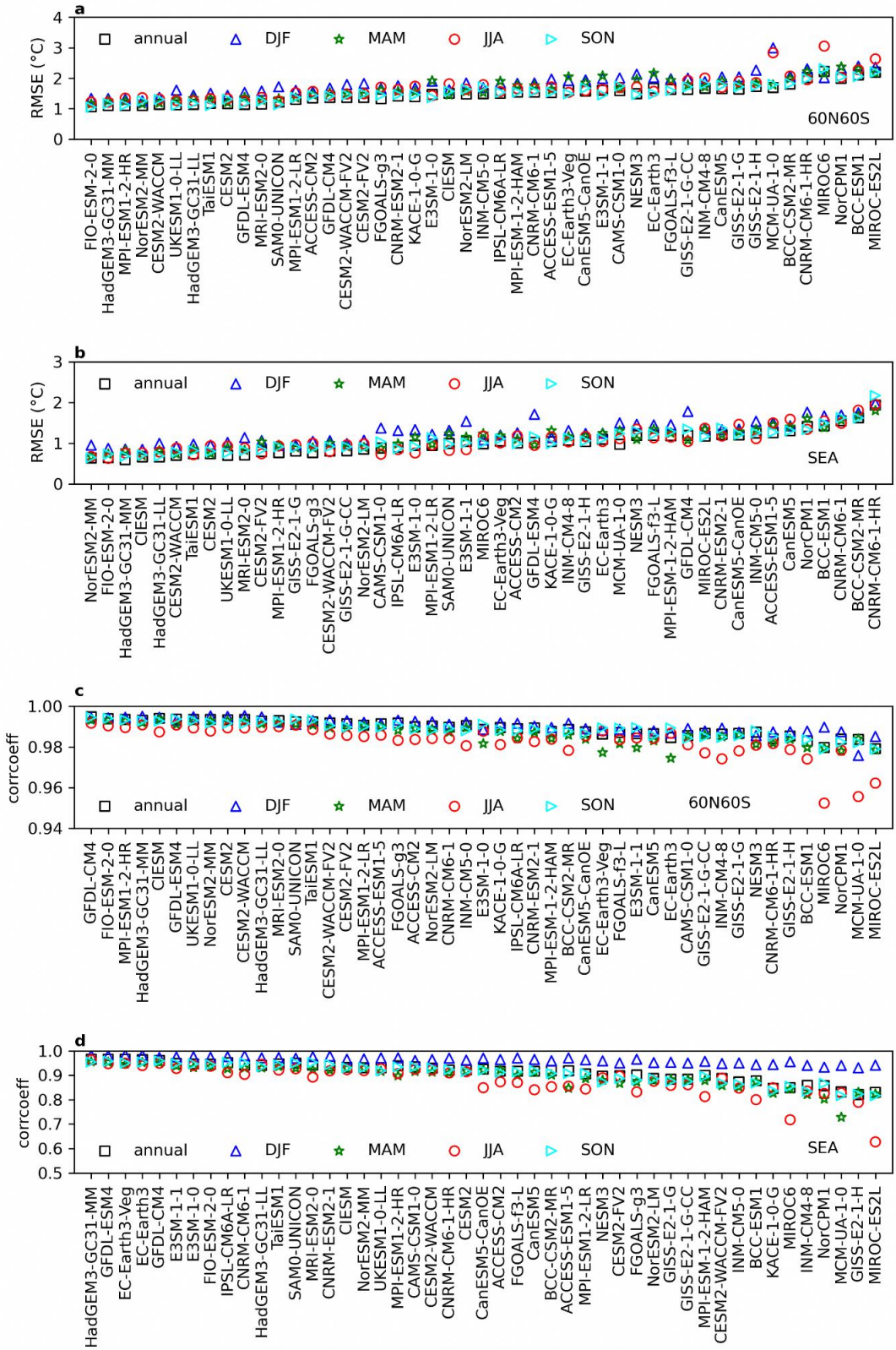

Figure 5.4: Performance of CMIP6 models as to RMSE for the annual and seasonal tas over the 60N60S (a) and SEA (b). Performance of CMIP6 models as to PCC for tas over the 60N60S (c) and SEA (d).

5.3.2 Rainfall

Similar analysis as presented above for near-surface air temperature is then carried out for rainfall and presented in Figures 5.5 to 5.7. Figure 5.5 shows the annual mean precipitation for the global and SEA domains and the corresponding biases based on multi-model means. From Figures 5.5a and 5.5c it can be seen that overall the CMIP6 GCMs perform well in simulating the large scale pattern and magnitude of rainfall, although there are some biases that can be more clearly seen in panels e and f of the figure. For example, even from the absolute values we can see the well-known double ITCZ bias over the tropical Pacific which has been present in previous generations of CMIP. From Figure 5.5e it can be seen that there are robust biases (based on 70% model agreement) over the tropical Pacific, tropical Atlantic, and western equatorial Indian ocean. Zooming into the SEA domain, we find positive biases over the South China Sea and over east of Borneo. In contrast, we see a large negative bias over the northern Bay of Bengal. Similar to the annual mean rainfall in Figure 5.5, JJA season rainfall in FigureA5.1 and the DJF season rainfall in Figure A5.2 also show consistent understanding of the evaluations.

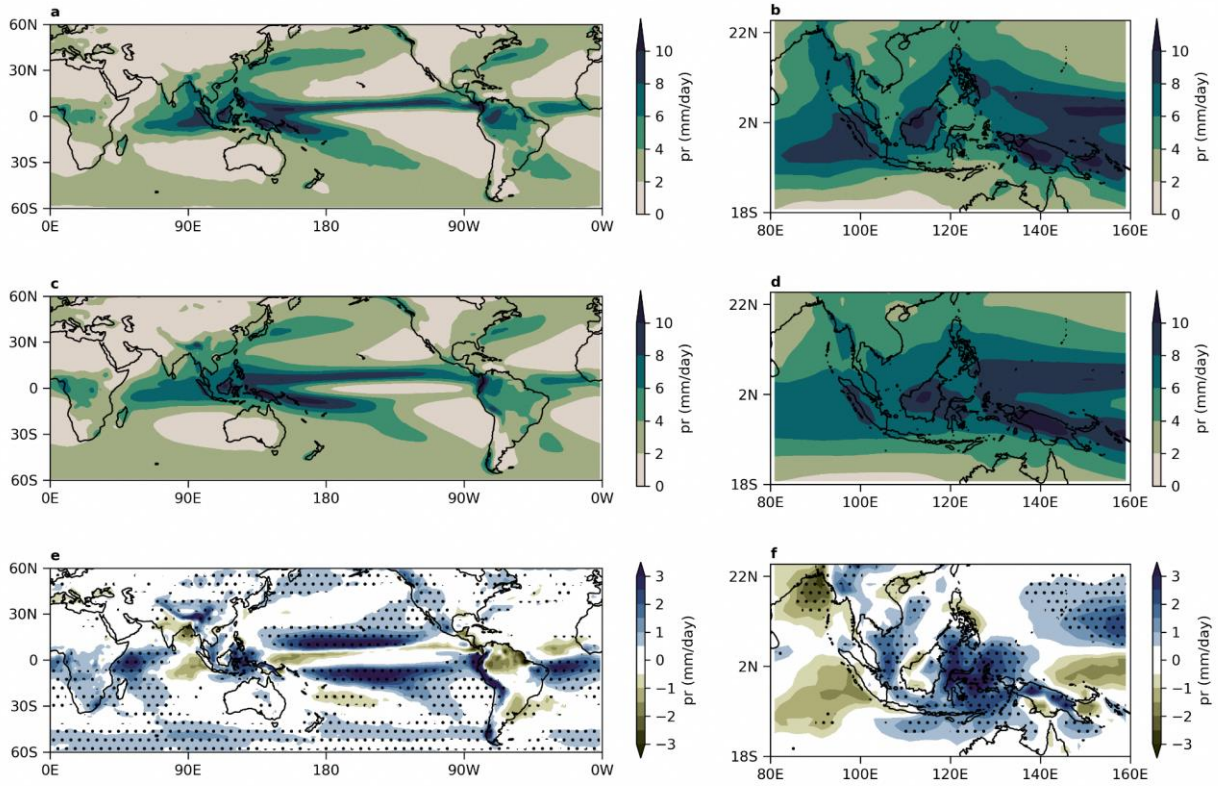

Figure 5.5: 1995-2014 mean precipitation (pr) in observation (a, b) and models (c, d). a. FROGS datasets for the 60N-60S domain. b. similar to a, but for the SEA domain. c. multi-model mean of pr from 48 CMIP6 models for the 60N-60S domain. d. similar to c, but for the SEA domain. e. model bias (e.g., multi-model mean from 48 models minus the observational mean). Stippled areas indicate the agreement by 70% of models. f. similar to e, but for the SEA domain.

Figure 5.6 shows the inter-model spread of the absolute values of precipitation, RMSE, and PCC over the global and SEA domains. From Figure 5.6a we see that the observed mean for the global domain is around 2.8mm/day, for annual as well as for various seasons with small seasonal variations. The CMIP6 GCMs, overall, overestimate the rainfall on seasonal as well as annual timescale scales with the median of the inter-model spread showing a value of around 3.2 mm/day (an overestimate of around 14%). Notably, because of the overall overestimation in

the GCMs the one that is closest to observations is considered an outlier in the distribution. As expected, the observed annual and seasonal means are higher over the SEA domain with higher seasonal variations (JJA being the highest and MAM being the lowest). The CMIP6 GCMs are found to perform quite well over SEA with the median value of the multi-model distribution overestimating the observed values by up to 5% on annual as well as seasonal timescales.

From Figure 5.6c we find that the annual mean RMSE over the global domain is lower than the seasonal (as expected), and the values for MAM and JJA are slightly higher than other seasons. The RMSE values are relatively higher over the SEA domain on annual and seasonal timescales, with JJA showing the highest value and MAM showing the lowest, noting that these are also the wettest and driest seasons over the SEA domain, respectively (Figure 5.6d). For the global domain, the PCC values are generally high (0.8 to 0.9) for annual and all seasons except MAM (around 0.75), as seen from Figure 5e. Whereas, for the SEA domain, they are slightly lower (0.7 to 0.8), with DJF showing a somewhat higher PCC of around 0.83.

Figure 5.7 shows the annual and seasonal RMSE and PCC for the global and SEA domains for the individual models, with the best to worst shown from left to right, based on the annual values. For the global domain, the RMSE values are found to be higher in the JJA and MAM seasons, while for the SEA domain they are highest in JJA (Figure 5.7a, b). The bottom 5 models based on SEA annual performance using RMSE are MPI-ESM-1-2-HAM, INM-CM4-8, MCM-UA-1-0, FGOALS-g3, and IPSL-CM6A-LR.

For the global domain, MAM is found to have the lowest PCC, whereas, for the SEA domain the PCC values are higher during DJF and lower during JJA (Figure 5.7c, d). Overall, as expected, the PCC values are lower than global both on annual and seasonal timescales. The bottom 5 models based on annual rainfall PCC over the SEA domain are MPI-ESM-1-2-HAM, INM-CM5-0, MCM-UA-1-0, IPSL-CM6A-LR, and INM-CM4-8.

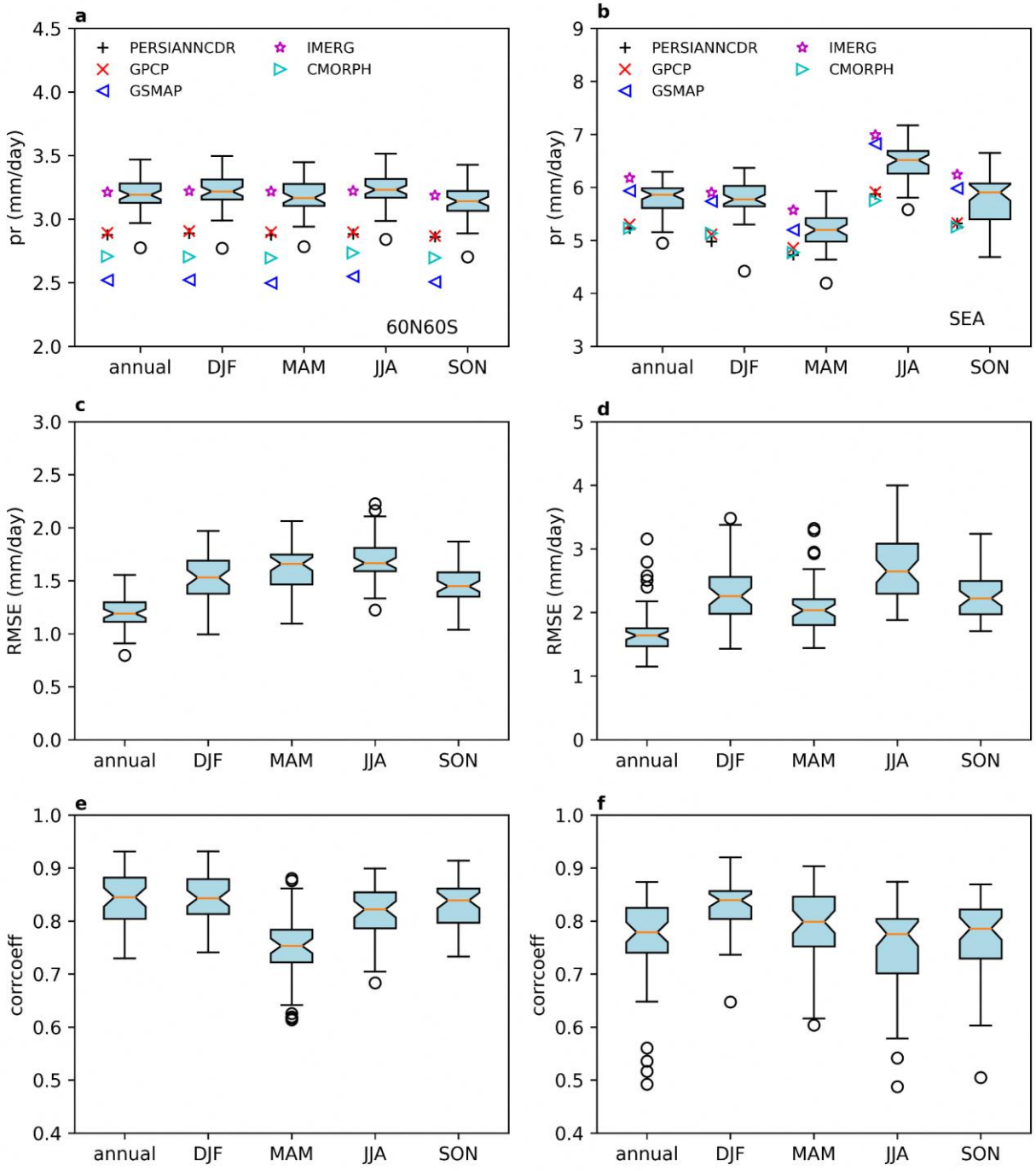

Figure 5.6: 1995-2014 mean pr averaged over the 60N-60S domain (a) and the SEA (b) in FROGS observational datasets (including PERSIANN-CDR, IMERG, GPCP, CMORPH, GSMAP) and 48 CMIP6 models. c. RMSE of models for the annual and seasonal pr in the 60N60S. d. similar to c, but for the SEA. e. PCC of models for the annual and seasonal pr in the 60N60S. f. similar to e, but for the SEA.

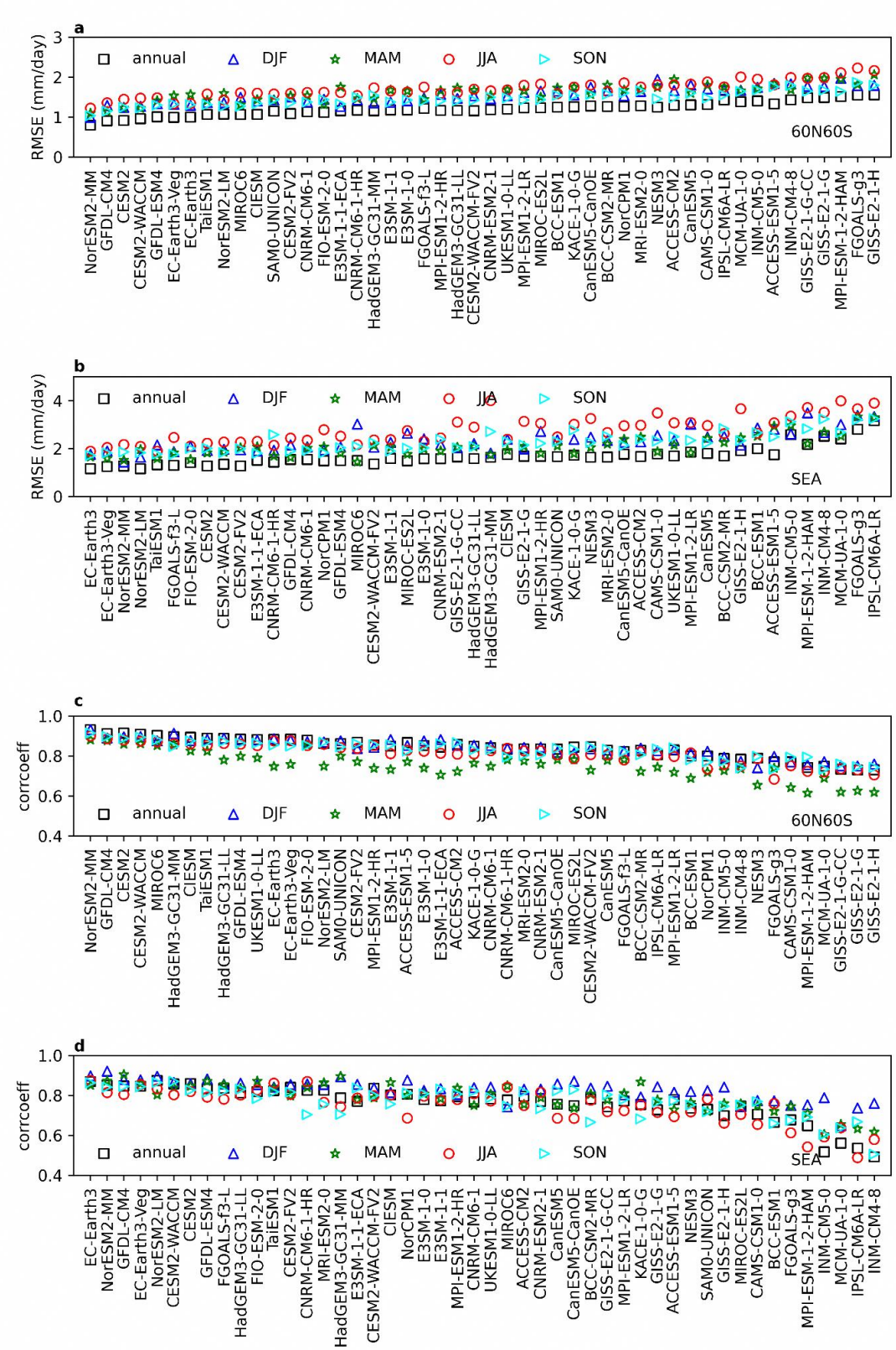

Figure 5.7: Performance of CMIP6 models as to RMSE for the annual and seasonal pr over the 60N60S (a) and SEA (b). Performance of CMIP6 models as to PCC for pr over the 60N60S (c) and SEA (d).

5.3.3 Mean Sea Level Pressure

In Figure 5.8 we compare the psl from 48 CMIP6 models to the ensemble-mean reanalysis (JRA-55, ERA5 and MERRA2) for the global and SEA domains.

The subtropical oceanic highs in reanalysis (Figure 5.8a) are well captured by the models (Figure 5.8c), as is the relatively low psl over SEA. Figures 5.8b, d show that the southwest to northeast spatial gradient in psl is also simulated in models. The sign of the bias is not systematic across models, and is generally higher outside SEA, with some of the highest values collocated with mountain ranges (e.g. Himalayas, Rockies, Andes). Over SEA, there is a high over Indochina and low around east Java and Sulawesi, alongside a corresponding low/high bias in tas. Nevertheless, biases in psl are relatively small over much of SEA.

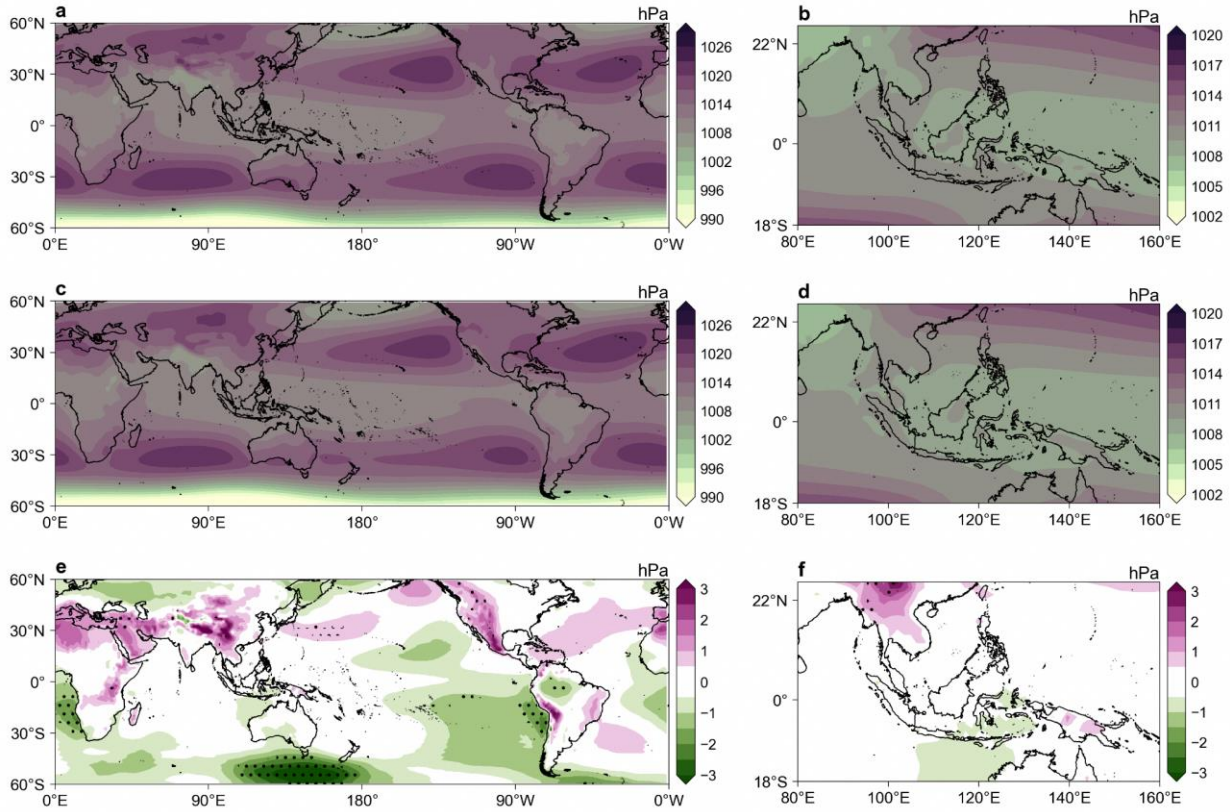

Figure 5.8: 1995-2014 mean sea level pressure (slp) in observation (a, b) and models (c, d). a. Mean of JRA-55, ERA5 and MERRA2 for the 60N-60S domain. b. Similar to a, but for the SEA domain. c. Multimodel mean of slp from 48 CMIP6 models for the 60N-60S domain. d. Similar to c, but for the SEA domain. e. Model bias (multimodal mean from 48 models minus the observational mean). Stippled areas indicate the agreement by 70% of models on the sign of bias. f. Similar to e, but for the SEA domain.

5.3.4 Humidity

Figure 5.9 shows the annual mean specific humidity (huss) from the ensemble mean reanalysis (JRA-55, ERA5 and MERRA2) for the global and SEA domains, the same from the CMIP6 multi-model means, and the corresponding biases. Overall, the large-scale pattern in huss is simulated well in CMIP6 GCMs, although there are regional biases which can be seen in Figure 5.9e, f. Over the global domain there is large negative bias over the Indian region, South America, and western and central North Pacific, whereas, there is positive bias over tropical eastern Pacific, east Atlantic near the west coast of Africa, and the southern oceans. Over the

SEA domain the biases are generally low, except for the dry bias over Indo-China, and southern equatorial Indian Ocean. Since the humidity field over the SEA domain is generally well simulated, we don't show the inter-model spread in RMSE and PCC, and the rankings of the individual models for this variable.

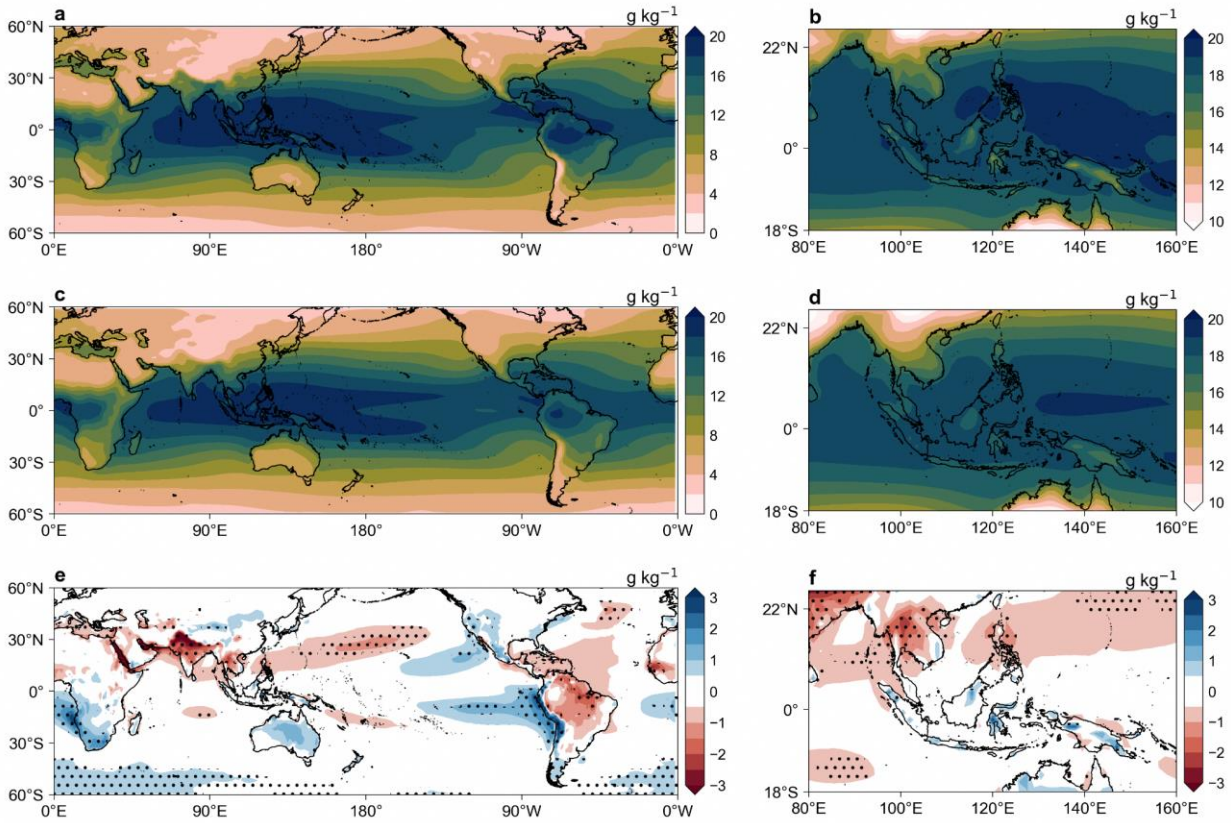

Figure 5.9: 1995-2014 annual mean specific humidity (huss) in reanalysis (a, b) and models (c, d). a. Mean of JRA-55, ERA5 and MERRA2 for the 60N-60S domain. b. Similar to a, but for the SEA domain. c. Multimodel mean of huss from 48 CMIP6 models for the 60N-60S domain. d. Similar to c, but for the SEA domain. e. Model bias (multimodal mean from 48 models minus the observational mean). Stippled areas indicate the agreement by 70% of models on the sign of bias. f. Similar to e, but for the SEA domain.

5.3.5 Winds

Next, we evaluate the 850hPa annual mean and seasonal winds over the global and SEA domains to check if there are any CMIP6 GCMs with unrealistic wind patterns, especially in regard to the monsoonal wind flow patterns.

The results of Tangang et al., (2019) indicate anomalously strong easterlies over Papua in JJA, as well as anomalous westerlies around the tip of Sumatra that extend to the Malay Peninsula. McSweeney et al., (2015) examined 39 CMIP5 GCMs and noted that models were generally able to simulate the Somali jet in terms of having the highest wind speeds near the core, as well as a predominantly westerly flow over India that turns south-westerly over the Bay of Bengal, then westerly over Indochina and turning southerly west of the Philippines.

A small number of models exhibited an unrealistic feature of the winds turning southerly west of continental Southeast Asia. Some models were also noted for a monsoon flow that was too weak (e.g. in the region of the Somali jet).

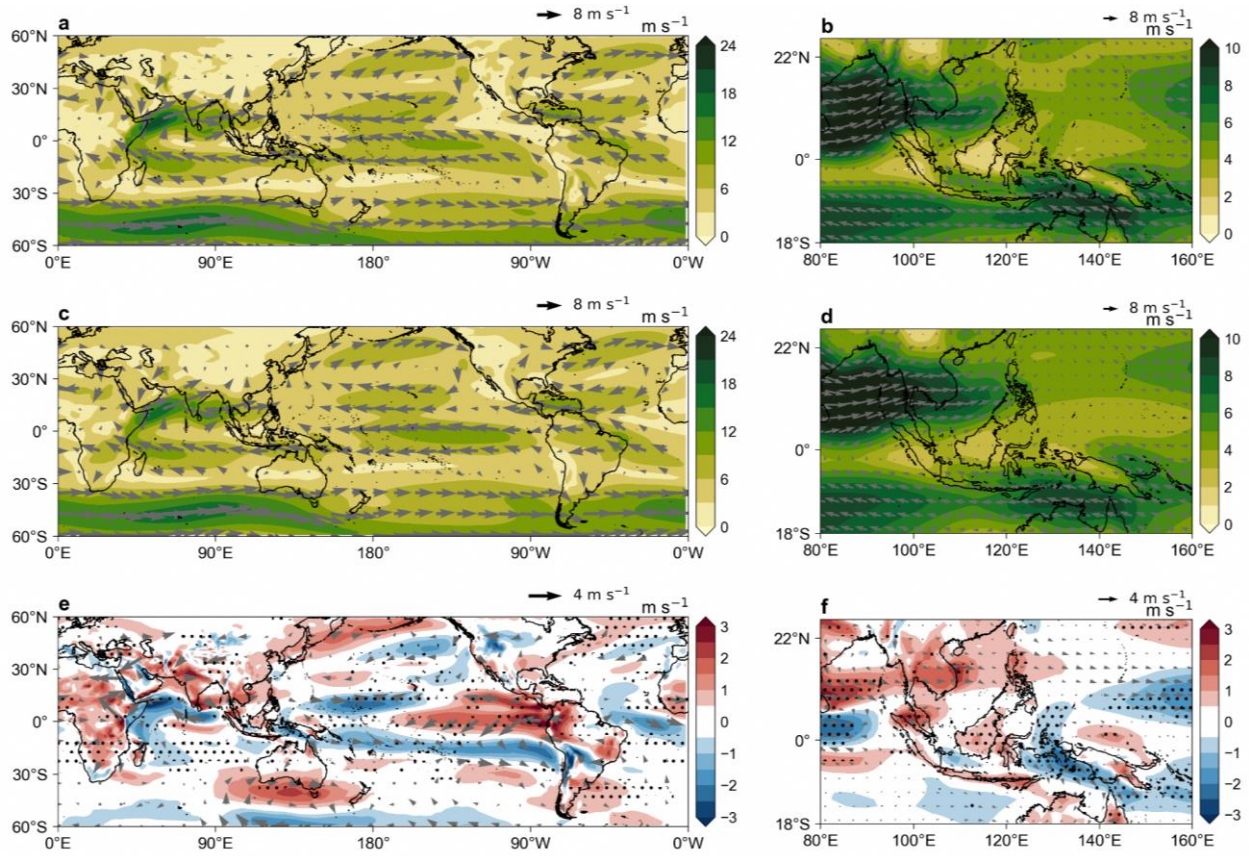

Figure 5.10: 1995-2014 annual mean 850hPa JJA winds in reanalysis (a, b) and models (c, d). a. Mean of JRA-55, ERA5 and MERRA2 for the 60N-60S domain. b. Similar to a, but for the SEA domain. c. Multimodel mean winds from 49 CMIP6 models for the 60N-60S domain. d. Similar to c, but for the SEA domain. e. Model bias (multimodel mean from 49 models minus the observational mean). Stippled areas indicate the agreement by 70% of models on the sign of bias. f. Similar to e, but for the SEA domain.

These observational features can be seen in Figure 5.10a, b. Figure 5.10c, d is broadly consistent with the notion that models are generally able to simulate the South-westerly monsoon. Models exhibit a diversity of responses with regard to the strength of the Somali Jet, being slightly weaker on average (Figure 5.10e). Here a positive bias in speed is shown to the north over the Arabian Sea and northern India.

Such characteristic anticyclonic bias is linked to the tendency for the westerly flow to extend too strongly over Southeast Asia into the South China Sea associated with an eastward shift and weakening of the Western North Pacific Subtropical High (WNPSH).

Over the East of India, there is a robust northward shift of wind speeds near Sri Lanka upstream of a robust increase in winds over the Malay Peninsula and Borneo and decrease in winds closer to New Guinea. Figure f indicates that the anomalously strong westerlies near the tip of Sumatra seen in the CMIP5 multi-model mean remains a common issue in CMIP6 GCMs. The representation of the monsoon in the individual models (not shown) is generally realistic.

A key feature of DJF circulation over the Maritime Continent is the turning of the northeasterly winds over the South China sea towards the Malay Peninsula, and its subsequent convergence with westerlies from the Indian ocean (McSweeney et al., 2015). This is generally captured by the multi-model mean (Figure 5.11a, d).

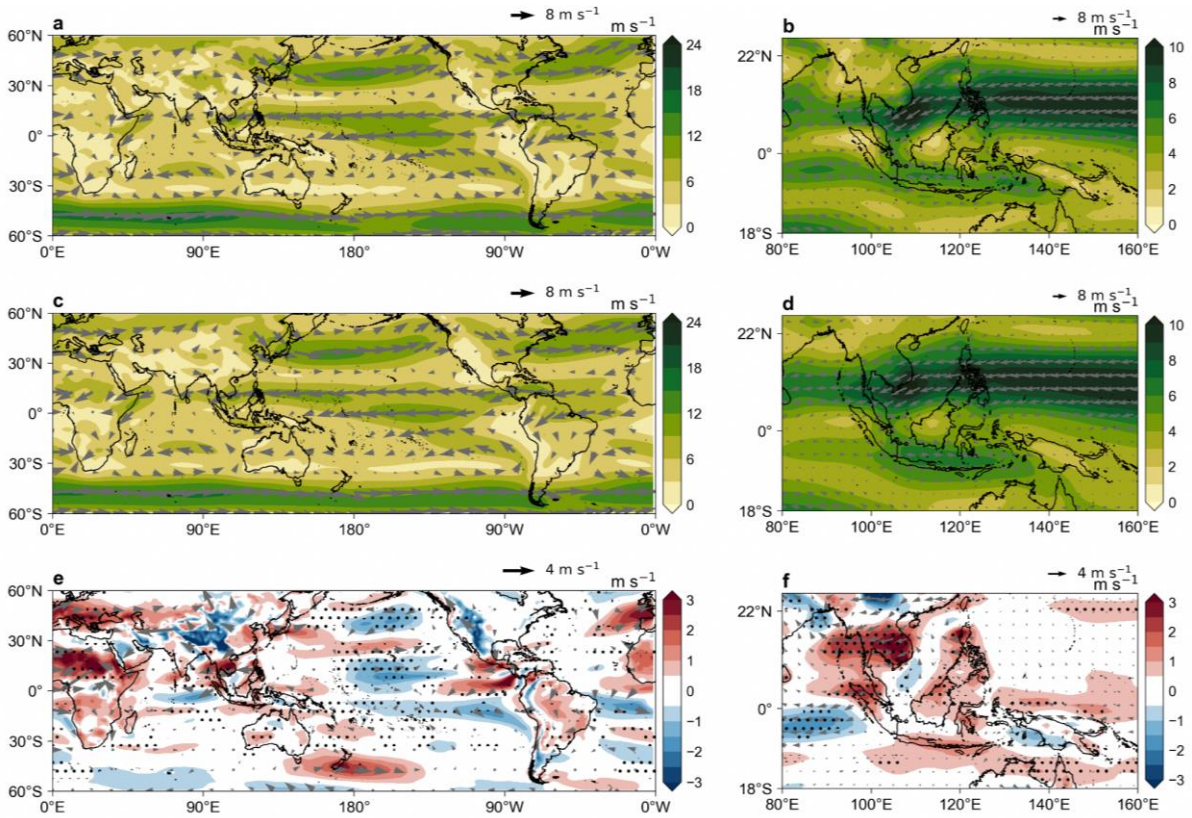

Figure 5.11: As in Fig. 5.10, but for DJF.

In their analysis of the ensemble mean of 11 CMIP5 GCMs, Tangang et al. (2019) noted an easterly component of wind that was too strong over Indochina in DJF, and anomalously strong easterlies over Papua. As for individual models, McSweeney et al., (2015) presented results from 38 CMIP5 GCMs and noted that some models had an anomalously strong easterly component, such that the flow was directed towards Vietnam rather than the Malay Peninsula.

Anomalously strong easterlies remain a robust bias in CMIP6 models (Figure 5.11d, f), together with anomalously strong outflows over the Indian Ocean (net reduction in wind speed).

Figure 5.12a, b shows the range of model ws850 values along with that from the reanalyses. Overall, we find that the models simulate ws850 satisfactorily. The median ws850 values are lower in SEA as compared to GLOB. However, in some cases, the RMSE of ws850 in SEA can exceed that of GLOB (Figure 5.12c, d). Pattern correlation of ws850 is generally quite high for GLOB but falls over SEA (below 0.6 in one case), as can be seen in Figure 5.12e, f.

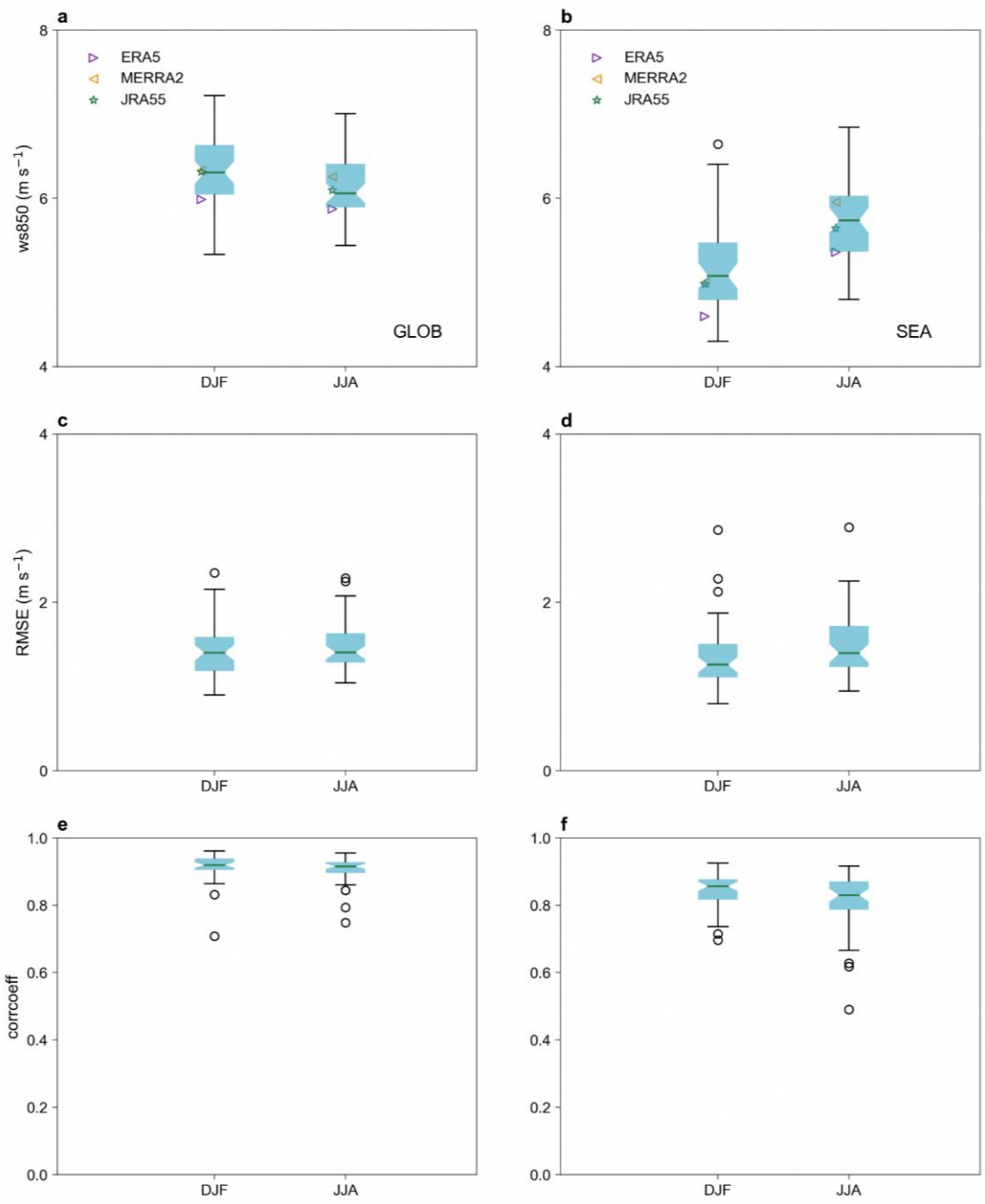

Figure 5.12: (a) Boxplot of wind speed at 850 hPa (ws850) over GLOB in CMIP6 models for DJF and JJA. Values for three reanalyses are shown with symbols. (c) Boxplots of RMSE of ws850 against values computed with the ensemble mean of the three reanalyses. (e) As in (c), but for pattern correlation. (b, d, f) as in (a, c, e), but over SEA.

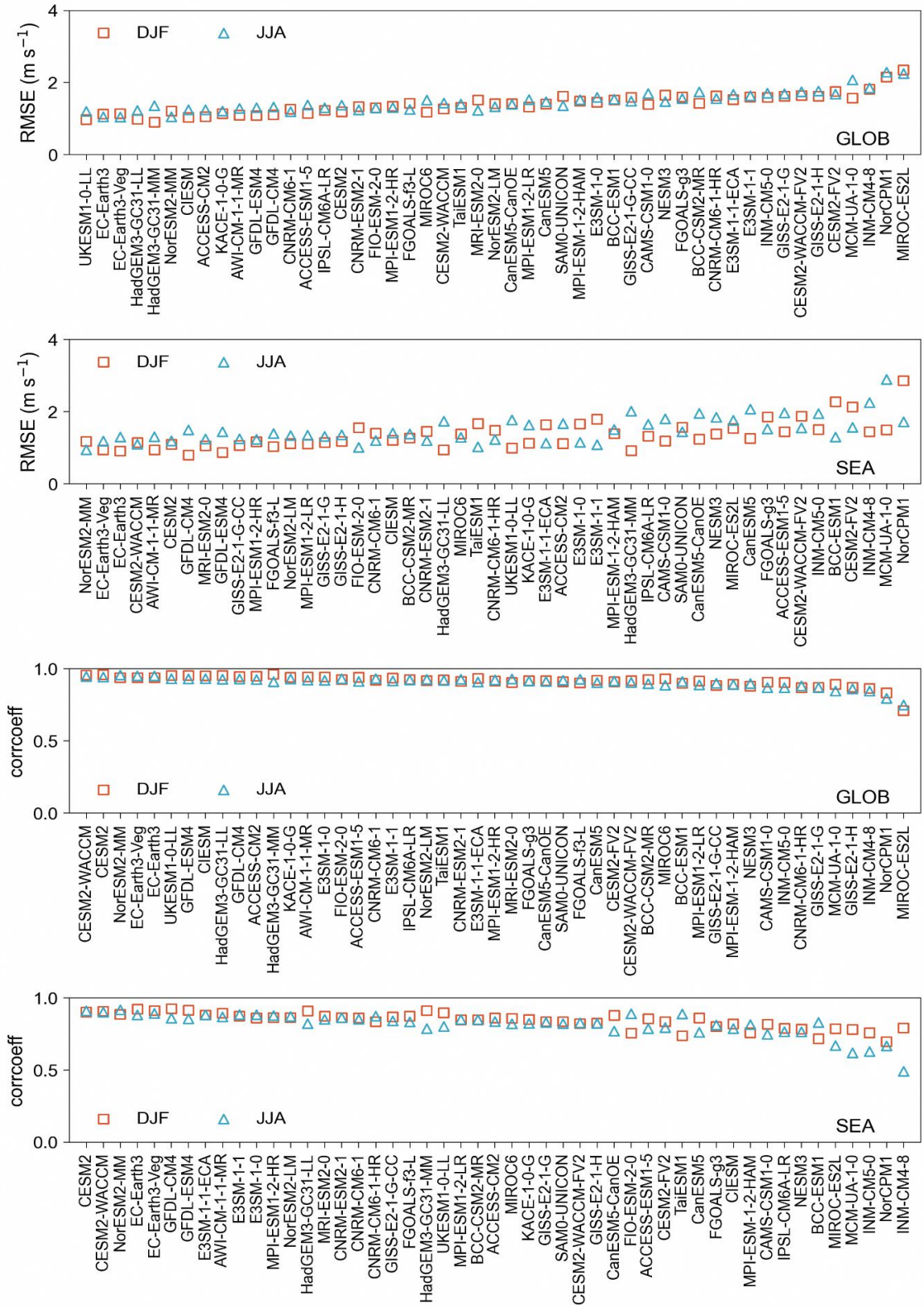

Figure 5.13: Model performance (better to worse) in ws850 as measured by RMSE over (a) GLOB and (b) SEA. (c-d). As in (a-b), but for pattern correlation.

Model simulations of ws850 are generally better over GLOB as compared to over SEA. Some notable outliers over SEA are NorCPM1, which has anomalously strong winds over Indochina and its nearby latitudinal region in DJF, and the INM models (INM-CM4-8 and INM-CM5-0), where the south-westerly monsoonal flow in JJA is weaker and/or angled too far north (above the South China Sea). Based on RMSE over the SEA domain for the 2 seasons, the bottom 5 models are BCC-ESM1, CESM2-FV2, INM-CM4-8, MCM-UA-1-0, and NorCPM1. Based on PCC the bottom 5 models are MIROC-ES2L, MCM-UA-1-0, INM-CM5-0, NorCPM1, and INM-CM4-8.

In summary, we find that, many of the CMIP6 GCMs are able to simulate the large-scale patterns of rainfall, temperature, winds, humidity and psl over the global and SEA domains, on annual and seasonal timescales. However, there are some biases in each of these variables that are regionally and seasonally dependent. Although many models are found to perform quite well, some are found to perform unsatisfactorily to an extent that we don't have enough confidence in them to consider for our dynamical downscaling. Some of the models that we have identified to discard are: INM-CM4-8, INM-CM5-0, NorCPM1, MCM-UA-1-0, and MIROC-ES2L.

5.4 Evaluation of Key Climate Processes

In this section we present the evaluation of key climate processes that are important drivers of weather and climate over Maritime Continent region, namely, monsoon, ENSO, IOD, equatorial Pacific cold tongue, northeast monsoon surge, and MJO from the CMIP6 GCMs with the same objective as the in section above, i.e. to identify the GCMs that show consistently poor performance and hence may not be considered fit for downscaling.

5.4.1 Monsoon

Monsoon rainfall, associated with changes in wind circulation and the north-south movement of the ITCZ dominates the seasonal variations of rainfall in the tropics. The easterlies in the southern hemisphere and westerlies in the northern hemisphere, along with the cross-equatorial flow over the western equatorial Indian ocean are notable features of the boreal summer monsoon (Figure 5.10a). Similarly, the corresponding wind circulation features can be seen from Figure 5.11a that are associated with the boreal winter monsoons. Monsoons have a key role in shaping the weather and climate of the MC domain. The MC domain is affected by the boreal summer monsoon (JJA; southwest monsoon) as well as the boreal winter monsoon (DJF; northeast monsoon).

Seasonal migration of ITCZ leads to climatological rainfall peaks during the monsoon season in Northern and Southern hemispheres. Figure 5.14 (top left) shows the observed migration of monsoon rainfall for the 1995-2014 period with NH peaks during JJAS and SH peaks in DJFM. Note the more persistent wet all year around in the equatorial (+/- 5 degrees) region. Also, the NH monsoon extends further north compared to the SH monsoon extension southward.

CMIP6 models on average simulate the seasonal migration of the ITCZ, but individual models can show significant systematic errors, such as shifting the monsoonal peaks in time (lagged) or in space (not reaching as far north/south). Many models are too intense (both in boreal and austral summer) plus there are shifts in peaks, but not necessarily in equatorial tropics.

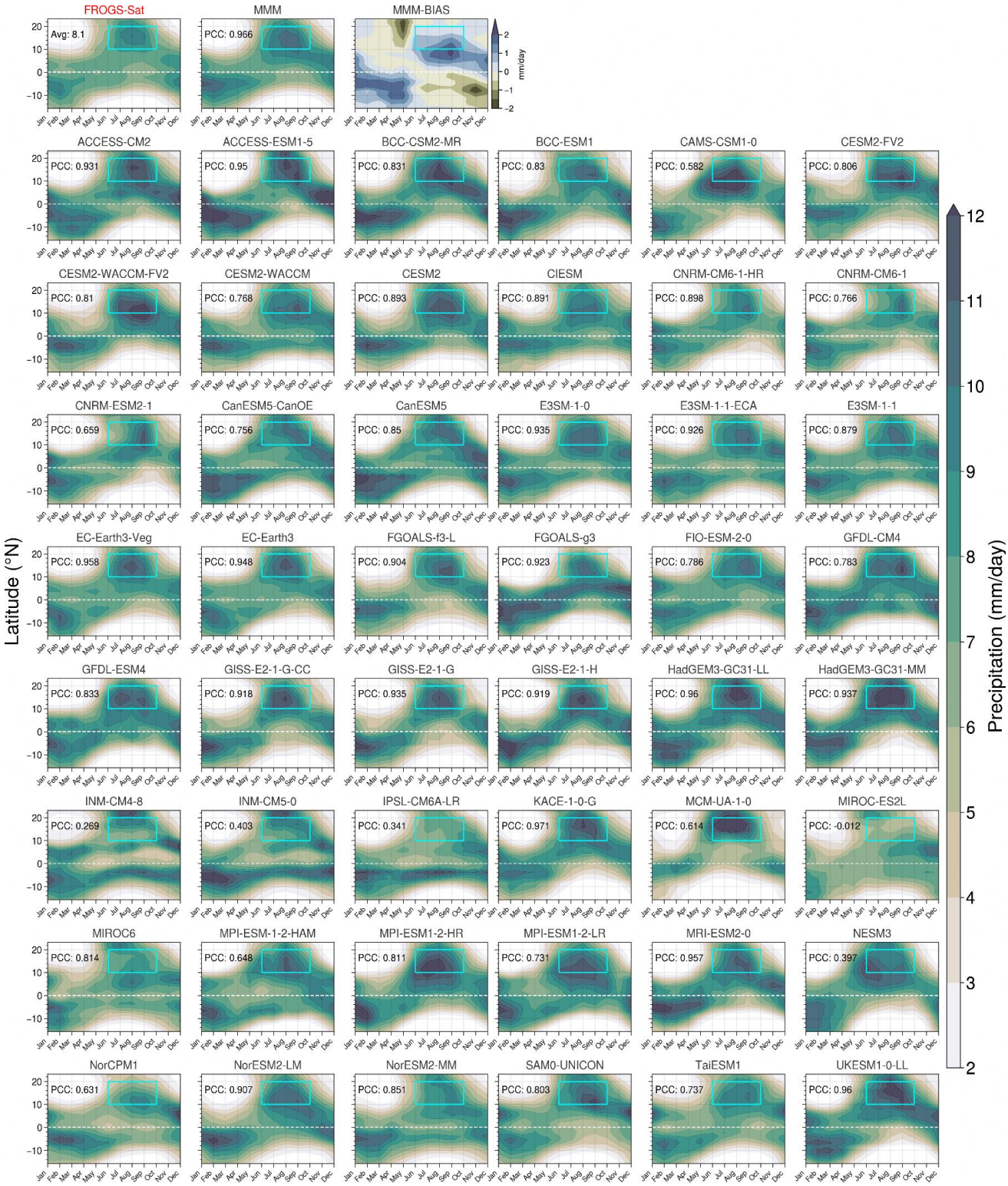

Figure 5.14: The time-latitudinal progression of zonally-averaged (80-160E) climatological monthly precipitation (i.e. passage of the ITCZ-monsoon rain belt) for the period 1995-2014. (Top row) Multi-satellite-mean observations from the FROGS database (FROGS-Sat), the multi-model mean (MMM) and the bias in the MMM (MMM-Bias). The 48 CMIP6 models are individually shown in subsequent rows. Also shown is the pattern correlation coefficient (PCC) value between each model and FROGS computed over the cyan box (June-October, 10-20N, representing the boreal summer monsoon season). The area average represented by the cyan box is shown for FROGs (8.1 mm/day).

Figure 5.15 shows the ranked pattern correlation values comparing zonally-averaged climatological monthly rainfall from each CMIP6 GCM with satellite observations for the June to October period across 10-20N. It can be seen from the figure that many of the CMIP6 GCMs perform quite well in simulating monsoons with around 18 of them having PCC of more than 0.9. Based on the monsoon PCC shown here the bottom 5 models are MIROC-ES2L, INM-CM4-8, IPSL-CM6A-LR, NESM3, and INM-CM5-0.

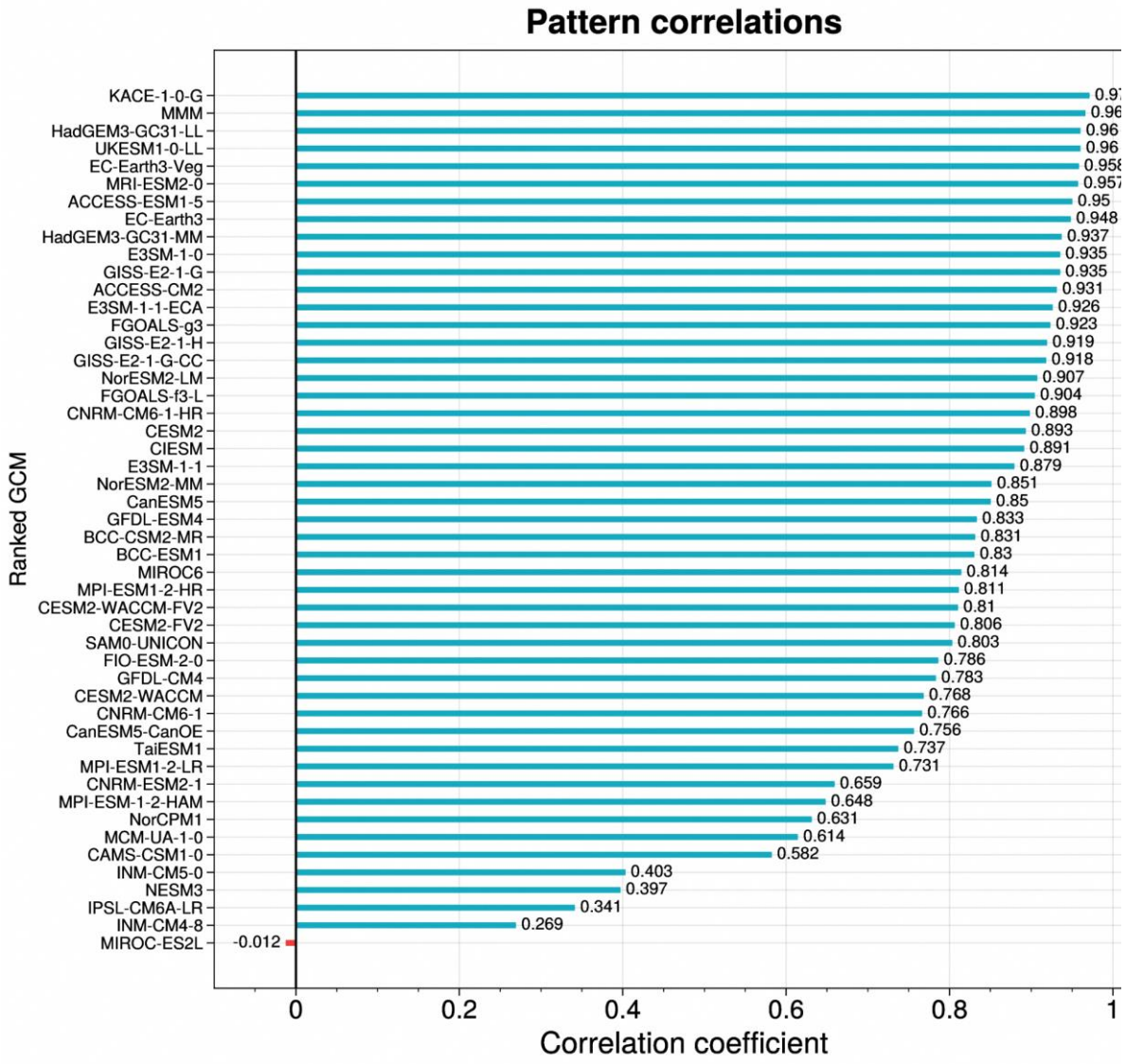

Figure 5.15: Ranked pattern correlation values comparing zonally-averaged climatological monthly rainfall from each model with satellite observations for the boreal summer monsoon period (June to October) across 10-20N.

In Figure 5.16 we show the normalised model bias in area average rainfall during the Jun-Oct period relative to satellite observations. We can see from the figure that 38/48 models show wet bias, with a considerable spread that varies in the range 2-36%. Overall, the multi-model mean (MMM) shows 9% wet bias, and shows really good pattern correlation (0.966; Figure 5.15). This is consistent with other studies (e.g., Martin et al. 2021) that show models tend to underestimate rainfall over the Indonesian island region in JJA and overestimate it over the region of the South China Sea and western Pacific (this is particularly prevalent in the HadGEM3 family of models).

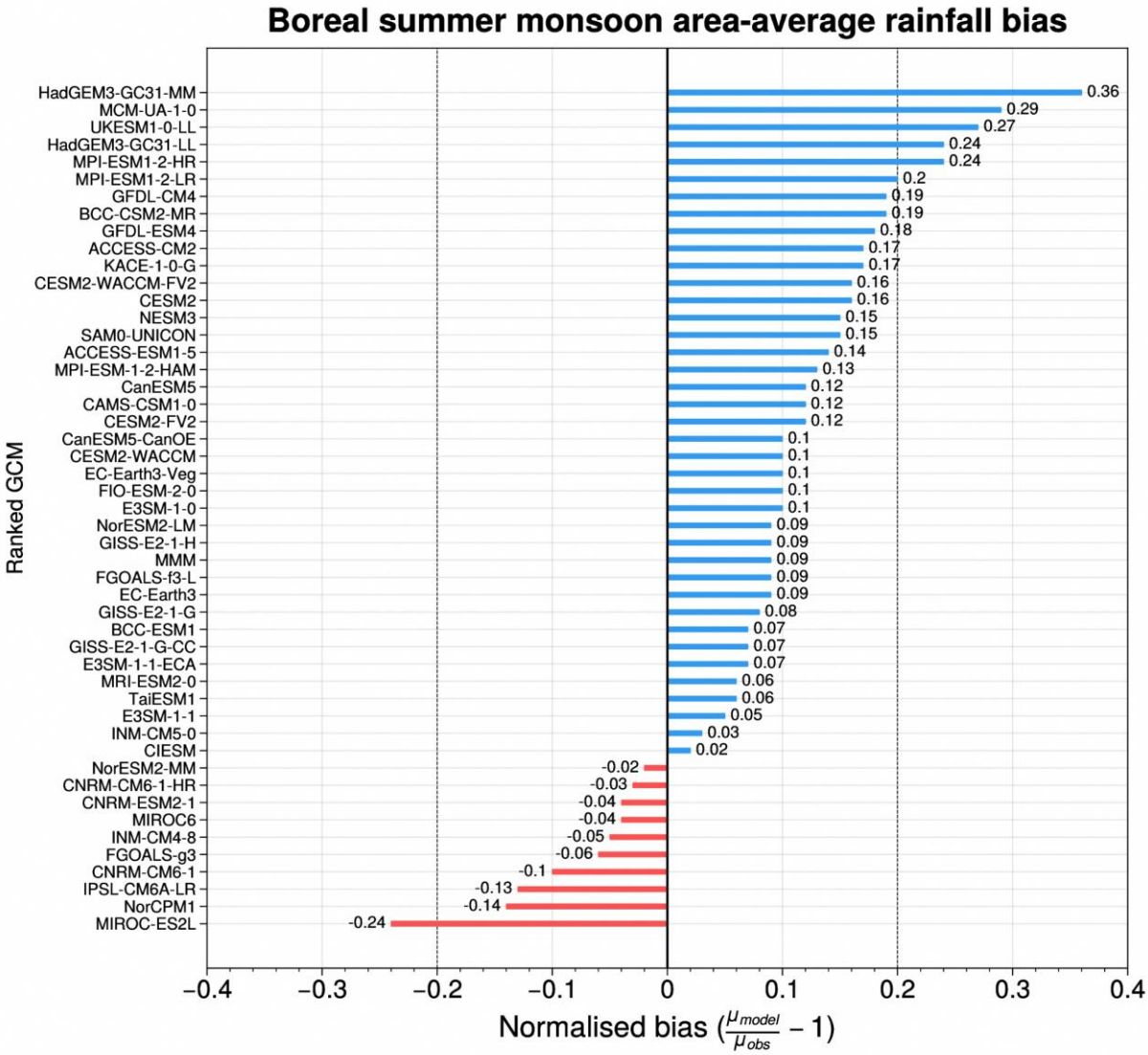

Figure 5.16: Normalised model bias in areal average rainfall during the boreal summer monsoon period (Jun-Oct) relative to satellite observations across 10-20N.

Unlike the off-equatorial tropics, the ITCZ crosses the equatorial zone both during the northward and southward movement, hence providing a somewhat different flavour to the monsoons. In Figure 5.17 we show the climatological (1995-2014) annual cycle of rainfall area-averaged over the equatorial region 80–160E, -2.25–2.25N from observations and from CMIP6. For the CMIP6 GCMs we show the multimodel mean (MMM), multimodel maximum (MMX) and multimodel minimum (MMN). Although there is a large diversity in the models as can be seen from the difference between the MMX and MMN, overall, the MMM resembles the both satellite rainfall (FROGS) over the region and the station-based rainfall annual cycle quite well. This is further confirmed from the DJF spatial pattern of rainfall from FROGS and MMM.

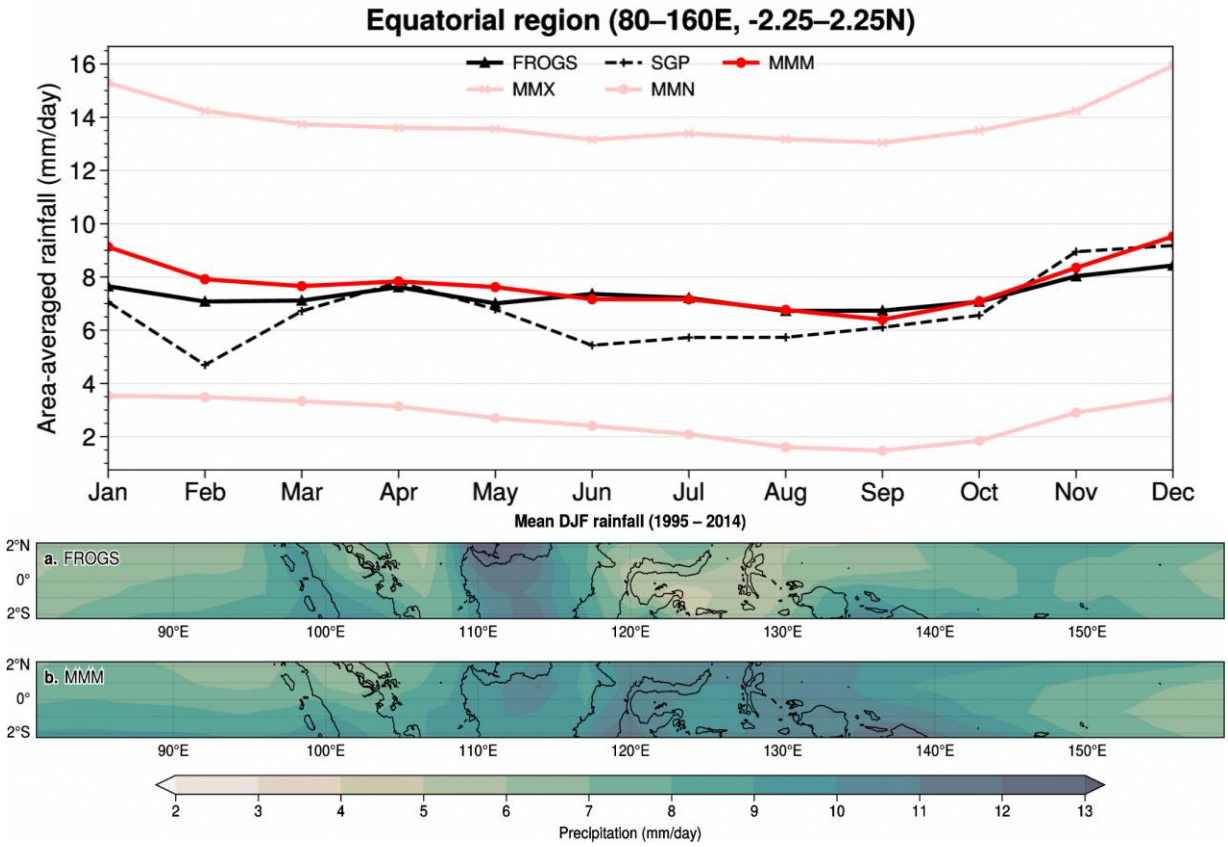

Figure 5.17: (Top panel) Climatological (1995-2014) annual cycle of rainfall area-averaged over the equatorial region 80–160E, -2.25–2.25N in the FROGS multi-satellite and CMIP6 multimodel mean (MMM), multimodel maximum (MMX) and multimodel minimum (MMN). The climatological annual cycle over Singapore (28-station average) is shown for comparison. The bottom panel shows the DJF rainfall from FROGS and MMM.

Monsoons are traditionally associated with a reversal of low-level winds, turning from easterlies to monsoon westerlies upon the arrival of the first strong monsoon surge. Figure 5.18 shows this for regions north and south of the equator indicating the climatological monsoon onset to be in May for the northern hemisphere and December for the southern hemisphere monsoon periods. Looking at the equator, the passing over of the ITCZ twice a year creates a different situation with winds being (a) generally weak throughout the year and (b) only weak wind reversals with mostly climatological weak westerlies for most months. The multi-model mean from the CMIP6 GCMs performs quite well in simulating the overall annual cycle and the May and December monsoon onsets in the northern and southern hemispheres, respectively.

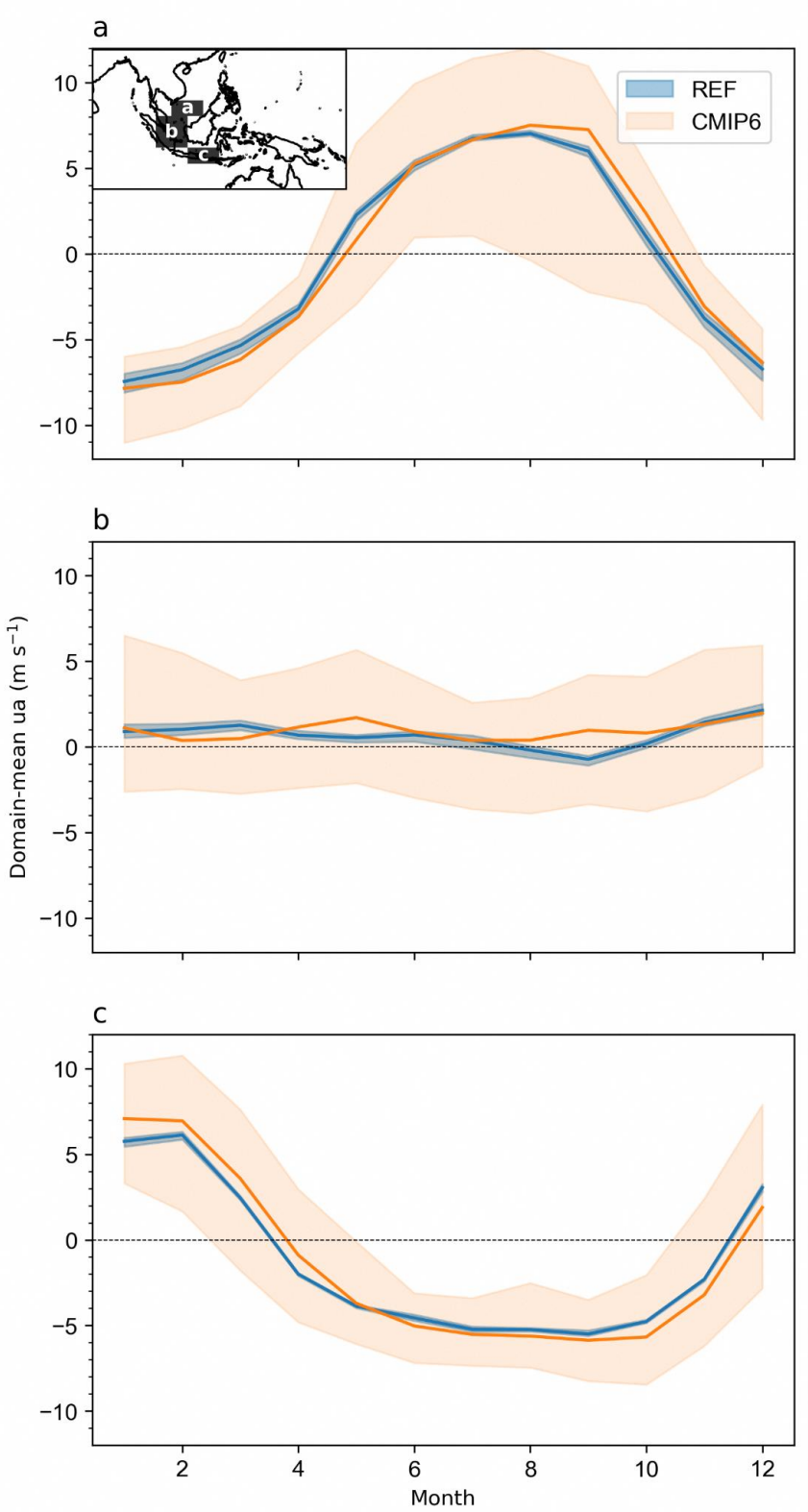

Figure 5.18: Domain mean of climatological (1995-2014) zonal wind at 850 hPa over (a) 110E to 115E, 5N to 10N (b) 100E to 110E, 5S to 5N, (c) 110E to 120E, 10S to 5S. The three domains are shown in the inset in (a). The shading shows the full range of the reference reanalysis datasets (ERA5, JRA55, MERRA2) as well as 49 CMIP6 models.

5.4.2 ENSO

ENSO is associated with the equatorial Pacific Ocean variability influencing atmospheric processes remotely and thereby one of the most important climate drivers that influences year to year variability of temperature and rainfall across the Maritime Continent (Juneng and Tangang 2005). Across the Indo-Pacific Ocean, ENSO induces a zonal dipole pattern of precipitation variability, i.e., positive variability in the Tropical Pacific (TP) and "horseshoe" shaped negative variability towards the MC (Langenbrunner and Neelin 2013). That is, TP becomes wetter than normal while MC becomes drier. Physically, ENSO-rainfall teleconnection over the MC is part of the ENSO-induced circulation responses over the tropics (Wang et al. 2003; Lau and Nath 2003; Stuecker et al. 2015).

In boreal summer when El Niño develops, a sequence of evolution begins with the eastward shifting of Walker Circulation due to the anomalous warming in eastern Pacific. The shift suppresses convection over the MC (also weakens Asian–Australian Monsoon) and enhances convection in the Central Pacific. Also note that the ENSO evolution during summer depends on what has happened in the previous boreal winter.

Here we investigate GCM's performance on ENSO, and we mainly focus on the climatology of ENSO amplitude, frequency, and its teleconnection. ENSO also varies from decade to decade, not only in amplitude and frequency (Wittenberg 2009) but also in its diversity and asymmetry characteristics (Chen et al. 2017). To provide a more reliable evaluation for ENSO interannual variability, we choose a longer 30-year period (1985-2014) as the study period instead of using 1995-2014 (20-year chosen by IPCC AR6).

ENSO Amplitude

Here as part of the evaluation for regional downscaling, we briefly investigate whether CMIP6 models can simulate reasonable realistic amplitude for ENSO. ENSO amplitude is normally represented using the DJF season standard deviation of the Nino3.4 index. This amplitude varies largely across different ENSO events (e.g., weak, moderate, and extreme events) as part of the natural variability of the ocean state. Additionally, simulations of these events show variations across these climate models (e.g, Chen et al. 2017) which originate from model-internal sources. Future projection for ENSO amplitude is also very uncertain (e.g., Beobide-Arsuaga et al. 2021) because of the difficulties in estimating how the natural variability might change as well as the remote teleconnections associated with ENSO.

As can be seen from Figure 5.19, ENSO amplitude average from observation and reanalysis is 1.13°C. Model mean ENSO amplitude is 1.19°C, which is very close to the observation. We do notice a large spread across individual models, from very low (around 0.5°C) or very high (over 2°C) ENSO amplitude. Based on ENSO amplitude the bottom 6 models are INM-CM4-8, CNRM-CM6-1-HR, INM-CM5-0, CESM2-FV2, MIROC-ES2L, and NorESM2-MM.

ENSO Frequency

ENSO generally occurs every 2 to 7 years (Cane and Zebiak, 1985). Studies suggested that extreme El Niño and La Niña events in CMIP5 models will occur more frequently in a changing climate (Cai et al. 2014, 2015). However, as to frequency of all ENSO events, many studies concluded that ENSO frequency changes are strongly model-dependent, and the model consensus is not robust on how ENSO frequency will change in a changing climate (Guilyardi (2006), Callahan et al. (2021)).

Given that ENSO tends to peak during boreal winter (DJF season), here we use the index Y=DJF season averaged Niño3.4 anomaly, and we define a threshold TH=0.6 X standard deviation of Y. Thus a given year is considered to be in an El Niño state when Y>TH. The year in a La Niña state is when Y<-TH. The year in the neutral state is when -TH<=Y<=TH. Note that we classify individual years instead of months. Also note that we do not use a fixed threshold rather a model-dependent threshold. For HadISST, the threshold is 0.68°C, ERA5's threshold is 0.74°C, and MERRA2's threshold is 0.68°C.

We define the frequency of El Niño years (FEN) as the number of El Niño years divided by the total number of years. We also define the frequency of La Niña years (FLN) and the frequency of neutral

years (FNEU) in a similar way, and FEN+FLN+FNEU=1. It is known that El Niño occurs every 2 to 7 years, such that 0.14<FEN<0.5. As can be seen from Figure 5.20, from observations and reanalysis, for El Niño, observation mean frequency is 0.3. For models, multi-model mean for El Niño FEN_model=0.29, which is very close to the observation and reanalysis. Models have a spread as to the frequency, from 0.15 to 0.4. Based on the ENSO frequency the bottom few models are KACE-1-0-G, CanESM5, IPSL-CM6A-LR, CESM2-WACCM-FV2, FGOALS-g3, and GISS-E2-1-G-CC.

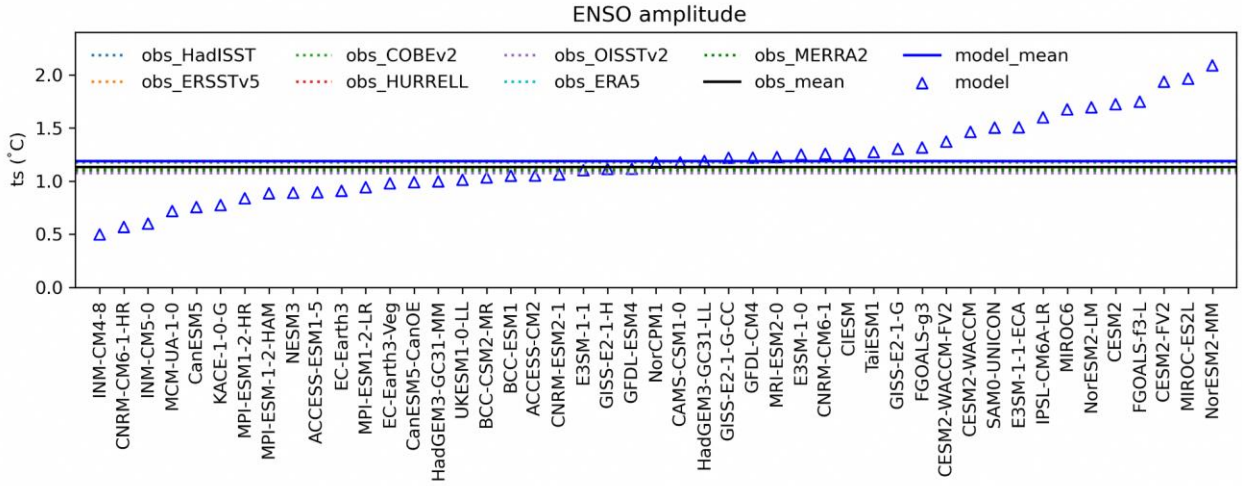

Figure 5.19: ENSO amplitude defined as standard deviation of Nino3.4 index (1985-2014 DJF mean).

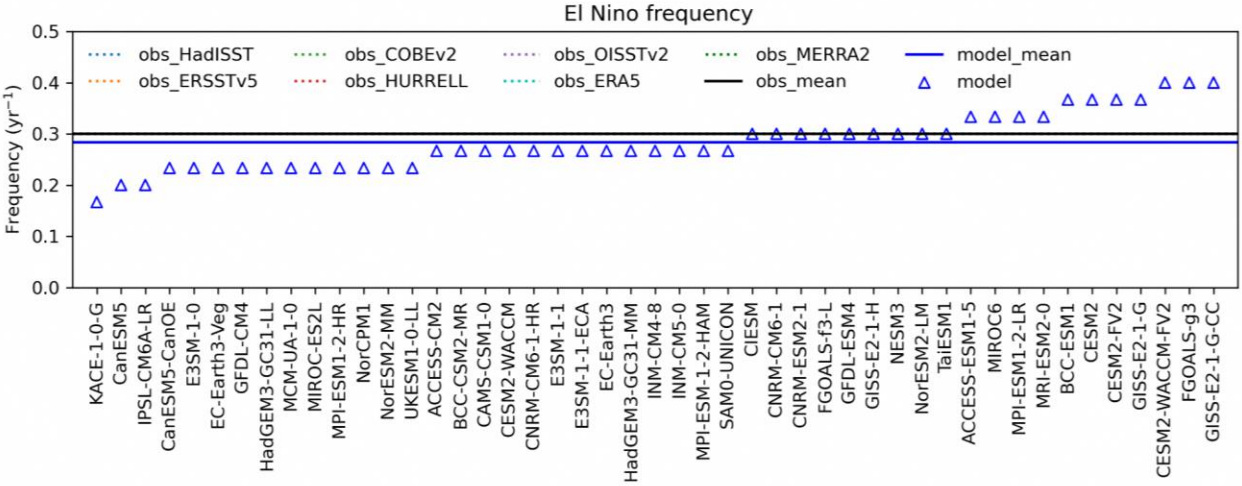

Figure 5.20: The frequency of El Niño for 47 CMIP6 GCMs and from observations and reanalysis from 1985 to 2014. Also shown are the ensemble mean for models and for observations and reanalysis.

ENSO Teleconnection

ENSO has impacts on worldwide precipitation variabilities (Ropelewski and Halpert 1987). Across the Indo-Pacific Ocean, a zonal dipole pattern of precipitation variability occurs during El Niño, i.e., positive variability in the Tropical Pacific (TP) and “horseshoe” shaped negative variability towards the Maritime Continent (MC) (Langenbrunner and Neelin 2013). That is, TP

becomes wetter than normal while MC becomes drier. In boreal summer when El Niño develops, a sequence of evolution begins with the eastward shifting of Walker Circulation due to the anomalous warming in eastern Pacific. The shift suppresses convection over the MC (also weakens Asian–Australian Monsoon) and enhances convection in the Central Pacific (Wang et al. 2003; Lau and Nath 2003; Stuecker et al. 2015).

As to the model performance on the ENSO teleconnection over the MC and Western Pacific, both CMIP5 and CMIP6 models tend to underestimate the negative rainfall teleconnection over the Central Maritime Continent but overestimate the positive ENSO rainfall teleconnection in the western Pacific and Eastern Maritime Continent (Jiang et al. 2022). Here, as part of the model evaluation for regional downscaling, we evaluate the performance of ENSO-rainfall teleconnection over the Tropical Pacific and the Maritime Continent in CMIP6 models and show it in Figure 5.21. We define the domain averaged rainfall and calculate the lag-0 correlation and covariance between the rainfall and the Niño3.4 TS anomaly (divided by one standard deviation of SST to only retain the pr unit of mm/day). We use the HadISST ts and GPCP rainfall as the observation benchmark.

We find that models perform well for the TP region. However, models overestimate the rainfall variability over the eastern MC but underestimate the El Niño-induced rainfall variability over the central MC. It is due to the westward extension of the cold tongue bias that pushes the surface temperature and rainfall variability from the western Pacific to the MC. For the CMC during the JJA season, observed rainfall variability is -0.51 mm/day, and model variability is -0.26 mm/day (0.25 mm/day weaker than the observation). During the DJF season, observed rainfall variability is -0.81 mm/day, and model variability is -0.46 mm/day (0.35 mm/day weaker than the observation).

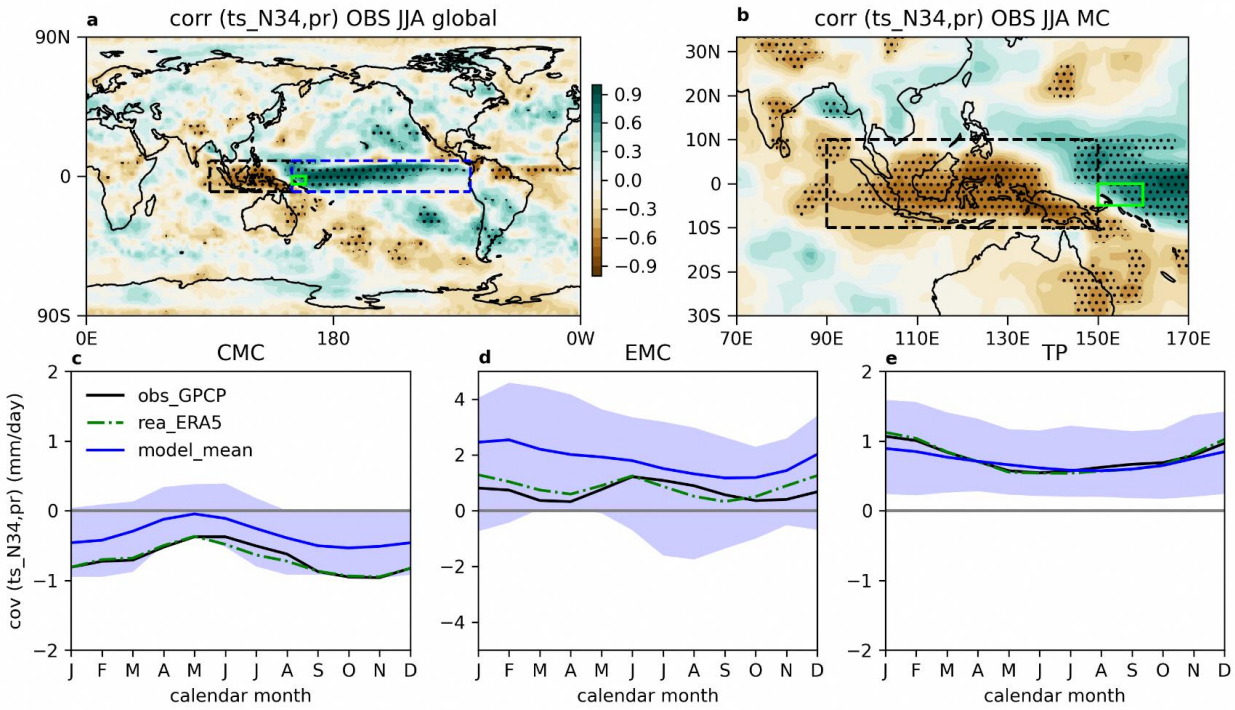

Figure 5.21: ENSO-rainfall teleconnection in the observation and CMIP6 models. a. Observed global ENSO-precipitation correlation coefficient during boreal summer (JJA). Here the correlation coefficient is calculated between the anomalous precipitation (pr) and Niño3.4 sea surface temperature (TS). Stippled area indicates significant correlation with p-value<0.01. Defined domains of Central Maritime Continent (CMC) (black dashed box), Eastern Maritime Continent (EMC) (green box), and tropical Pacific (TP)(blue dashed box) are shown. b. similar to a, but focusing on the MC. c-e shows the model performance as to the ENSO-rainfall teleconnection. c. 12-month covariance between the Niño3.4 TS and the CMC domain-averaged

precipitation. Observations (GPCP, black curve), reanalysis (ERA5, green dashed curve), and the multi-model mean of 32 CMIP6 models for the historical period (blue curve) are shown. The shade covers the 95% model range. d. similar to c but showing the EMC domain. e. similar to c but showing the TP domain.

5.4.3 IOD

The Maritime Continent is in between the Indian Ocean and Pacific Ocean and is affected by the ocean state in both. Hence, we also evaluate model performance over the Indian Ocean. We define the IODe index =ts averaged over the eastern IO [90E-110E, 10S-0S]. IODw index= ts averaged over the western IO [50E-70E, 10S-10N]. Then we define the IODemw index=IODe minus IODw, which indicates the zonal ts gradient.

We analyzed the amplitude of IOD, defined as one standard deviation of the monthly ts anomaly in IODemw. Observed IOD amplitude is 0.4°C, model mean IOD amplitude is 0.52°C (0.12°C stronger). Here models tend to have slightly stronger variability than the observation (Figure 5.22). Based on IOD amplitude the bottom few models are the 2 INM models, TAIESM-1, SAM0-UNICON, and CESM-FV2.

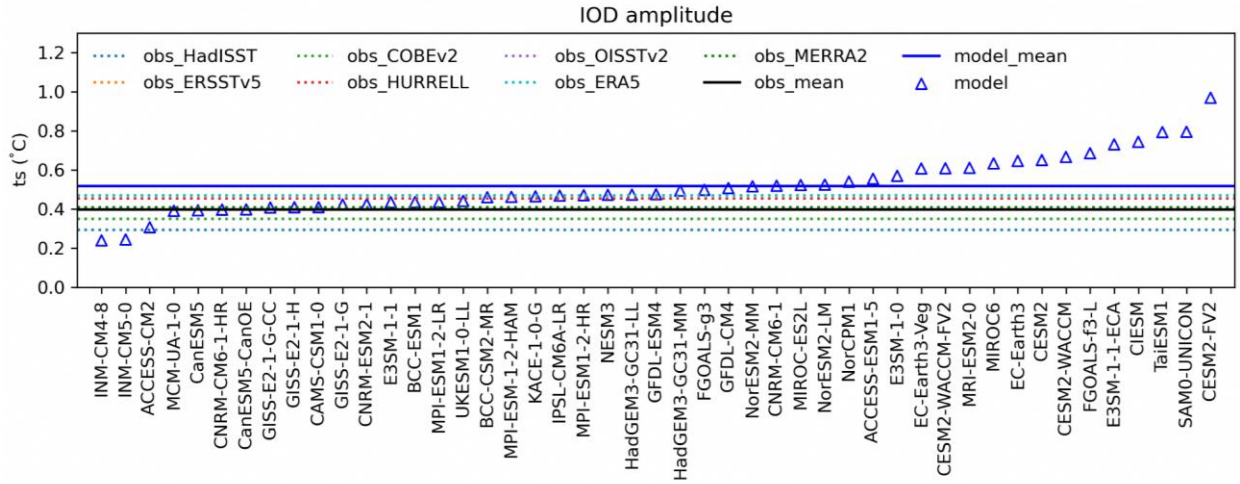

Figure 5.22: IOD amplitude in observations (mean in black line) and models (mean in black line). IOD amplitude is calculated using one standard deviation of the IODemw index (annual mean, 1985-2014).

5.4.4 Equatorial Pacific Cold Tongue

Here we define an index to measure the overall equatorial Pacific ts. TPI =whole equatorial Pacific averaged over [150E-280E 5N-5S]. Within the TP, the warm pool is on the western side, and the cold tongue is on the eastern side. Here we define the CTI index = averaged ts over the cold tongue region [180°E-270°E,5°N-5°S]. The zonal ts gradient is also an important dynamical feature to simulate. Here we define a CTGI=cold tongue gradient index =CTI-TPI, annual mean from 1985 to 2014. CTGI tells the cold tongue ts relative to the whole equatorial Pacific. annual mean observation CTGI is -0.54°C. Model mean CTGI is -0.62°C (-0.08°C slightly stronger cold tongue relative to the whole TP, also indicating a stronger zonal ts difference) (Figure 5.23). This stronger cold tongue in models is associated with a stronger zonal wind and westward extension of the cold tongue into the warm pool. Based on the equatorial Pacific cold tongue bias, the bottom few models are MPI-ESM1-2-HR, NorESM2-LM, GISS-E2-1-G, and GISS-E2-1-G-CC.

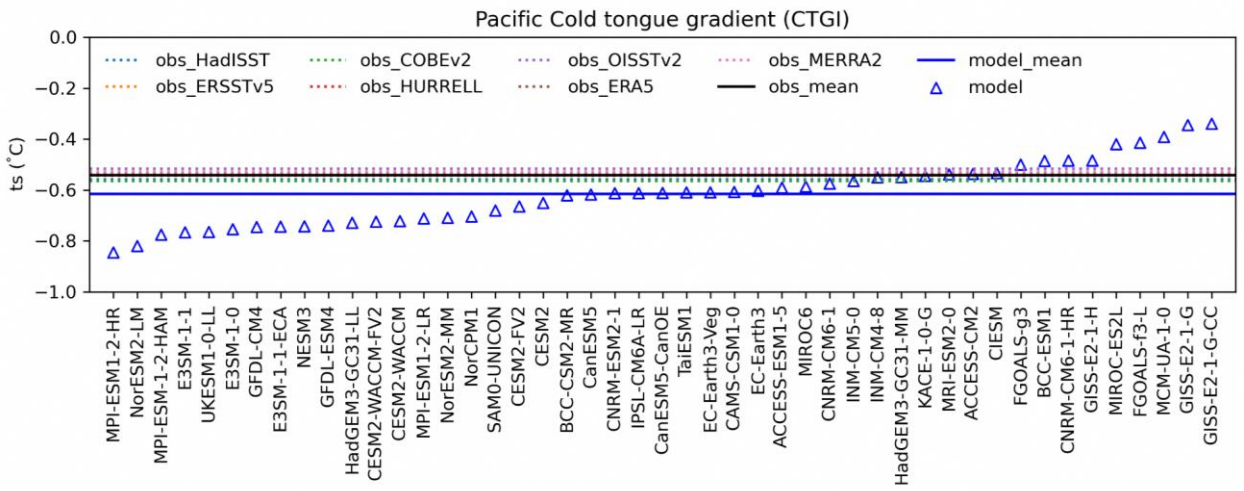

Figure 5.23: Pacific cold tongue gradient index (CTGI) in observation and models (1985-2014). The negative value indicates the eastern cold tongue area is cooler than the western warm pool.

5.4.5 Northeast Monsoon Surge

Northeast monsoon surges are a key synoptic feature of the boreal winter circulation over the Maritime Continent (e.g. Chang et al., 2005) and can lead to extreme rainfall. These surges can also be enhanced by the presence of a favourable phase of the MJO (e.g. Lim et al., 2017) and might also aid the MJO in its passage across the Maritime Continent (Pang et al., 2018). Given the importance of boreal winter monsoon cold surges to the weather and climate of SEA, the performance of CMIP6 models in simulating cold surges is quite relevant to the evaluation and subsequent sub-selection for dynamical downscaling.

Most of the existing literature on boreal winter cold surges over the Maritime Continent have focused on their observed characteristics, with relatively little mentioned on their simulation in models. An earlier analysis of CMIP5 models (McSweeney et al., Appendix 3 of V2) reported that the easterly component of surge winds were too strong in some models relative to the northerly component, with the flow directed towards Vietnam rather than southwards, while a more recent study by Xavier et al (2020) found that the UKMO Global Atmosphere 7.0 (GA7.0) and Global Coupled 3.0 (GC3.0) configurations of the Unified Model yield a dry bias in the simulation of surge rainfall.

In Figure 5.24 we present the evaluation of cold surge simulations in CMIP6 models, defined in Chapter 3.7. Based on reanalysis data, one can see from Figure 5.24a that the north-easterly winds over the South China Sea turn north-westerly after crossing the equator, together with high rainfall, especially over Philippines and Borneo. Figure 5.24b shows that the models are able to capture the general flow of the surge winds, including the turning at the equator. The easterly bias flagged in (McSweeney et al., Appendix 3 of V2) is not immediately obvious in the individual models (figure not shown), with the caveat that their analysis was performed using a fixed wind speed threshold, whereas this analysis uses a threshold that is tied to the mean and standard deviation of each model.

Models generally have a wet bias over Sulawesi and a dry bias over the Philippines (Figure 5.24c), possibly related to the model resolution of the topography of the Philippines. Models generally underestimate the rainfall over the Indian Ocean, with the multi-model anomalous winds directed over the Indian subcontinent. Over the Western Maritime Continent, rainfall bias can be either positive or negative. Models generally underestimate the percentage of surge days in NDJF (19% in REF), with 32 out of 36 models used for this analysis, exhibiting frequencies from 15 to 19%, and four models below 15%: AWI-ESM-1-1-LR (14%), FGOALS-f3-L (14%), KACE-1-0-G (12%) and TaiESM1 (8%).

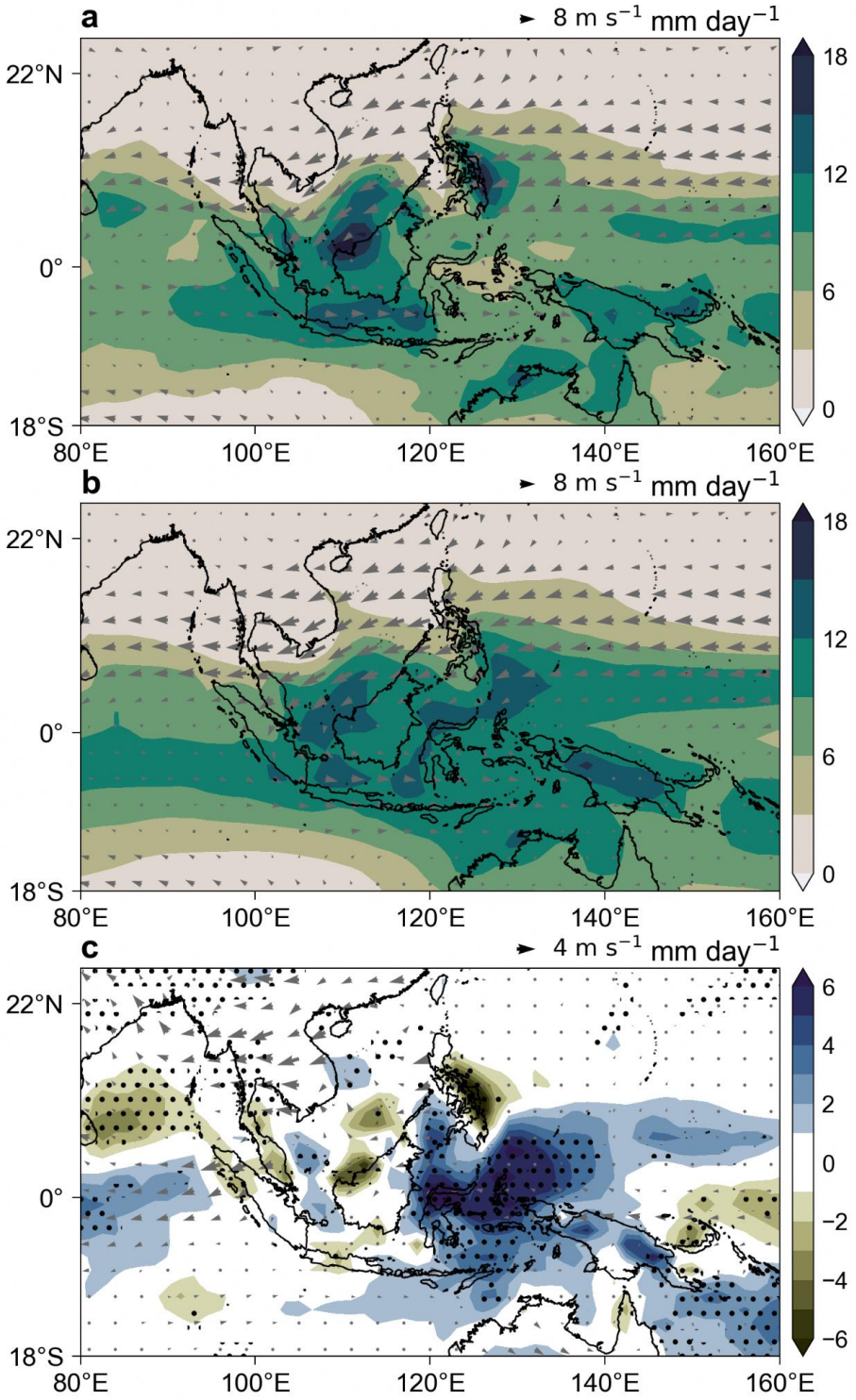

Figure 5.24: (a) Precipitation and 850 hPa winds composited over surge days in REF (winds and PSL are derived from the ensemble mean of ERA5, MERRA2, and JRA55, precipitation the ensemble mean of 5 datasets from FROGs: CMORPH, GSMAP, IMERG, PERSIANN-CDR, and TRMM 3B42). (b) As in (a), but for 36 CMIP6 models. (c) Model bias in surge precipitation and winds (i.e. (b) - (a)).

5.4.6 MJO

The Madden-Julian Oscillation (MJO; Madden & Julian, 1971, 1972), characterized by an eastward-propagating large-scale band of convection from the Indian Ocean to the central Pacific, is one of the important climate drivers affecting global weather and climate, and especially the Maritime continent region (e.g., Lim et al. 2017). However, representing the MJO in climate models has been a challenge. In a recent study, Chen et al. (2021) evaluated the simulation of MJO in CMIP5 and CMIP6 models and reported that the MJO characteristics are better reproduced in CMIP6 with a corresponding decrease in inter-model spread in biases. However, there still are existing biases in CMIP6 models, such as, underestimation of frequency of initiation, underestimation of amplitude, and overestimation of the MC barrier effect on MJO propagation speeds. From CMIP5 to CMIP6, while some models have improved skills, some others have degraded. Le et al., (2021) reported that the MJO-related precipitation over the MC is still underestimated in CMIP6 models.

While various metrics have been used in the literature to evaluate the performance skill in models, one of the widely used metrics used for evaluation is the Eastward/Westward power ratio (E/W ratio hereafter). This metric indicates the robustness of eastward propagating feature of the MJO (Zhang and Hendon 1997), and has been widely used in observational (e.g., Zhang and Hendon 1997; Hendon et al. 1999) and modelling studies (e.g., Lin et al. 2006; Kim et al. 2009). In Figure 22 we show the E/W ratio for the months November-April over the period 1995-2014 using precipitation from GPCP v1.3 as the baseline and compare the same with CMIP6 models.

While the observed ratio is around 2.8, in models it can vary from less than 1 (westward propagating) to more than 5 (strongly eastward propagating). From this figure, some CMIP6 models, namely, CanESM5, INM-CM4-8, and INM-CM5-0 can clearly be discarded as they show a westward propagating MJO. Most of the models show an E/W ratio lower than observed, and hence a slower eastward propagation, maybe due to stronger barrier effect of the MC.

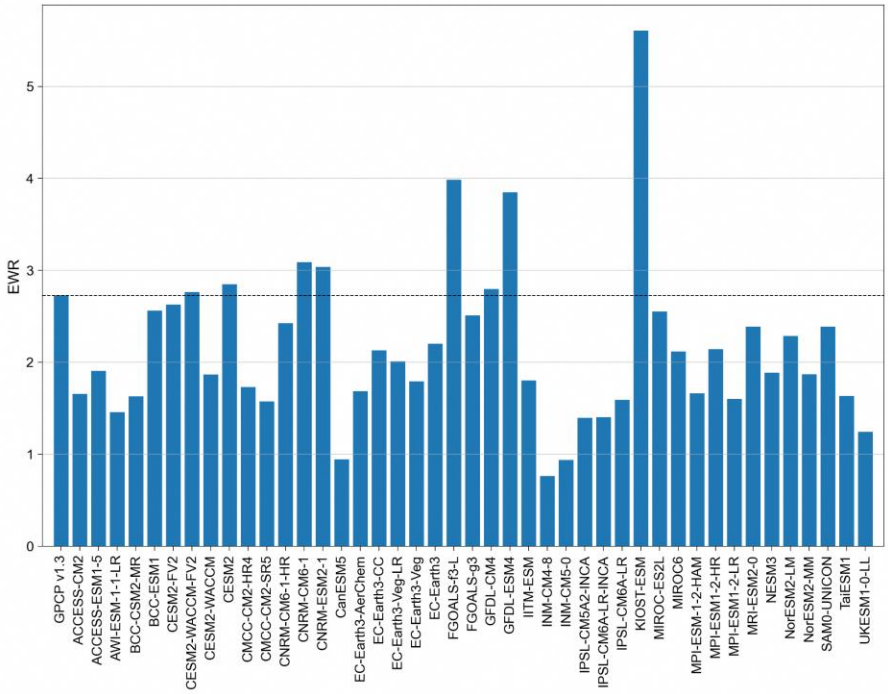

Figure 5.25: East-West power ratio of CMIP6 GCMs for November-April from 1995 to 2014 compared to GPCP v1.3.

5.5 Model Independence

Following Brunner et al (2020), Table 5.3 shows the CMIP model families built on similar internal schemes for atmosphere, ocean, etc. It has been shown in some past studies that the CMIP model archive is not an archive of completely independent models. This raises the question about independent realisations of future climates and in general the understanding is that the CMIP ensemble is a somewhat 'degenerated' ensemble of future states.

Table 5.3: CMIP6 model families based on the genealogy reported in Brunner et al. (2020) using 33 models. The genealogy is computed based on the global mean surface-air temperature and mean sea level pressure. Models in bold were selected for downscaling.

Model Family	Models belonging to specific family	Common family feature
1	CanESM5-CanOE, CanESM5	Built within ONE modelling centre on similar schemes
2	CESM2-WACCM, CESM2, **NorESM2-MM**, FIO-ESM-2-0	Built on NCAR's atmosphere model
3	CNRM-ESM2-1, CNRM-CM6-1, CNRM-CM6-1-HR	Built within ONE modelling centre on similar schemes
4	EC-Earth3-Veg, **EC-Earth3**	Built within ONE modelling centre on similar schemes
5	FGOALS-f3-L, FGOALS-g3	Built within ONE modelling centre on similar schemes
6	INM-CM5-0, INM-CM4-8	Built within ONE modelling centre on similar schemes
7	MIROC-ES2L, **MIROC6**	Built within ONE modelling centre on similar schemes
8	MPI-ESM1-2-LR, **MPI-ESM1-2-HR**, AWI-CM1-1-MR, NESM3	All using ECHAM-like atmosphere model
9	**UKESM1-0-LL**, HadGEM3-GC31-LL, **ACCESS-CM2**, KACE-1-0-G, ACCESS-ESM1-5	All using the UM as a core atmospheric model system
NA	GFDL-CM4, GFDL-ESM4, MRI-ESM2-0, CAMS-CSM1-0, GISS-E2-1-G, BCC-CSM2-MR, IPSL-CM6A-LR, MCM-UA-1-0	More distant association with some of the other families

In order to provide a downscaling ensemble from as independent as possible GCMs, we have identified a number of models which are possible choices, and together with other sub-selection metrics might help identify the most suitable set of independent models to use for downscaling.

5.6 Range of Future Projections and ECS

As discussed in Chapter 4 (subsection 4.2.1), the Equilibrium Climate Sensitivity (ECS) is defined as the global- and annual-mean near-surface air temperature rise that is expected to occur eventually, once all the excess heat trapped (top-of-atmosphere radiative imbalance) by the doubling of CO2 has been distributed evenly down into the deep ocean (i.e. when both the atmosphere and ocean have reached equilibrium with one another - a coupled equilibrium state).

Many CMIP6 models exhibit an ECS of 5°C or higher (Zelinka et al., 2020), much higher than the upper value of the CMIP5 range of 4.5°C. Based on the analysis of Sherwood et al. (2020), the Likely Range now range in ECS was constrained to lie in the range 2.5 - 4.0°C, down from what was reported in AR5. The IPCC also narrowed the Very Likely Range of ECS to be between 2.0 to 5.0°C, down from 1.0 to 6.0°C. The likely and very likely range of ECS in AR5 and AR6 are shown in Figure 5.26 for reference.

Figure 5.27 shows the ECS from the various available CMIP6 GCMs. The wide range of ECS can be seen from the figure with models like those from the INM showing values of less than 2oC,

whereas, there are models like CanESM5, CIESM, and HadGEM3-GC3-1-LL that have ECS values greater than 5.5oC. Ideally, we would like to span the range of ECS, while keeping other sub-selection dimensions under consideration, and also the AR6 constrained range.

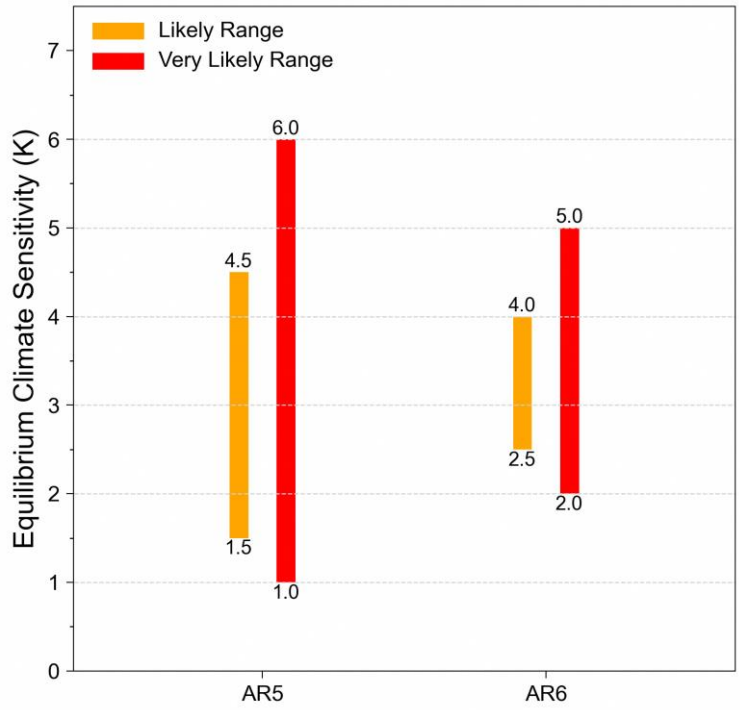

Figure 5.26: Likely and very likely range of ECS in AR5 and AR6

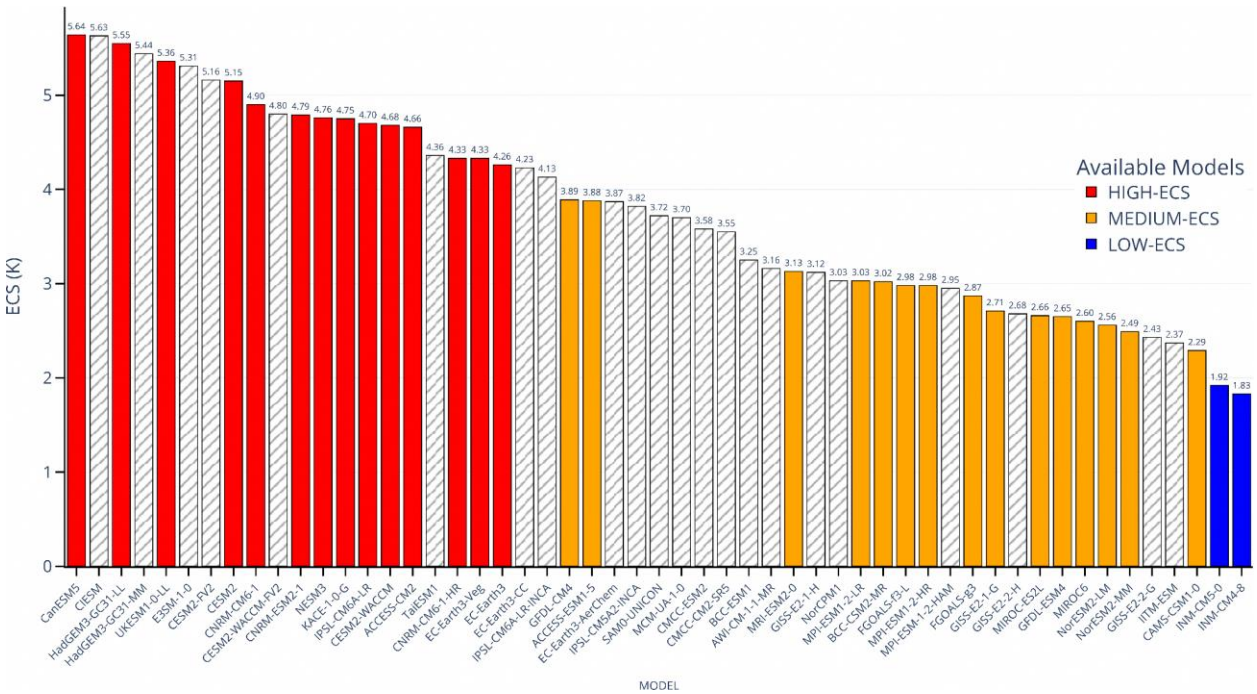

Figure 5.27: Equilibrium climate sensitivity of CMIP6 GCMs ranked high to low from left to right. The gray bars indicate models that we do not have full variable lists to analyze at the time of the V3 study.

5.7 Data Availability

For the purpose of our dynamical downscaling, we need 6-hourly profiles of temperature, zonal and meridional winds, and specific humidity (for initial conditions and lateral boundary conditions), surface pressure (for initial conditions), and 6-hourly sea surface temperatures (for initial condition and lower boundary condition). We also required that model outputs were available at 20 levels and up to at least a pressure level of 5 hPa. Where available we used the skin temperature (ts), else, a combination of surface air temperature (tas) and surface ocean temperature (tos).

An important difference in the CMIP6 archive as compared to CMIP5 is that the sub-daily data is not a part of the core delivery of the DECK experiment as well as scenario-MIP. Hence, a lot of modelling groups chose not to save and upload sub-daily data to the Earth System Grid Federation (ESGF). Since we need sub-daily data for our dynamical downscaling, this criteria plays a crucial role for our sub-selection exercise. We also would like to flag this as a possible significant constraint for CORDEX dynamical downscaling experiments.

At the time when we started the downscaling of CMIP6 GCMs in late 2020, very few GCMs had all the driving variables to run our downscaling simulations. In Table 5.1 we have highlighted the list of GCMs with availability of 6-hourly forcing fields.

As an example of how data availability drives opportunities, we did consider using data from GFDL-CM4, CNRM-CM6-1-HR and HadGEM2-MM models, but couldn't access their data on the ESGF. Upon separate conversations with the modelling groups, we were also told that not all scenarios were simulated by these models.

Based on our dynamical downscaling requirement of 6-hourly data for historical (1955-2014), and 3 SSPs (SSP1-2.6, SSP2-4.5, and SSP5-8.5) for the required variables (hus, ps, ta, tos, ua, va) and pressure level data for at least 5hPa, the latest availability as of June 2023 is shown in Table 5.1. The table shows all models running ScenarioMIP and the ones highlighted are the ones having 6-hourly data for the required variables. As can be seen from the table, only 10 models have all 4 experiments covered. GCM data needs for V3 dynamical downscaling may not be very different from that of the CORDEX community, and the availability of downscaling data from only a very few models shows that this could be a major constraint for the CORDEX community as well. It is to be noted that in CMIP5 there were many more GCMs with 6-hourly data needed for dynamical downscaling.

5.8 Future climate change spread

One additional dimension for sub-selection is to ensure that the smaller ensemble of GCMs still cover as much as possible the projected range of future climate change, especially for temperature and rainfall. Figure 5.28 shows the end-century change in rainfall and temperature over SEA from 34 CMIP6 GCMs under SSP5-8.5.

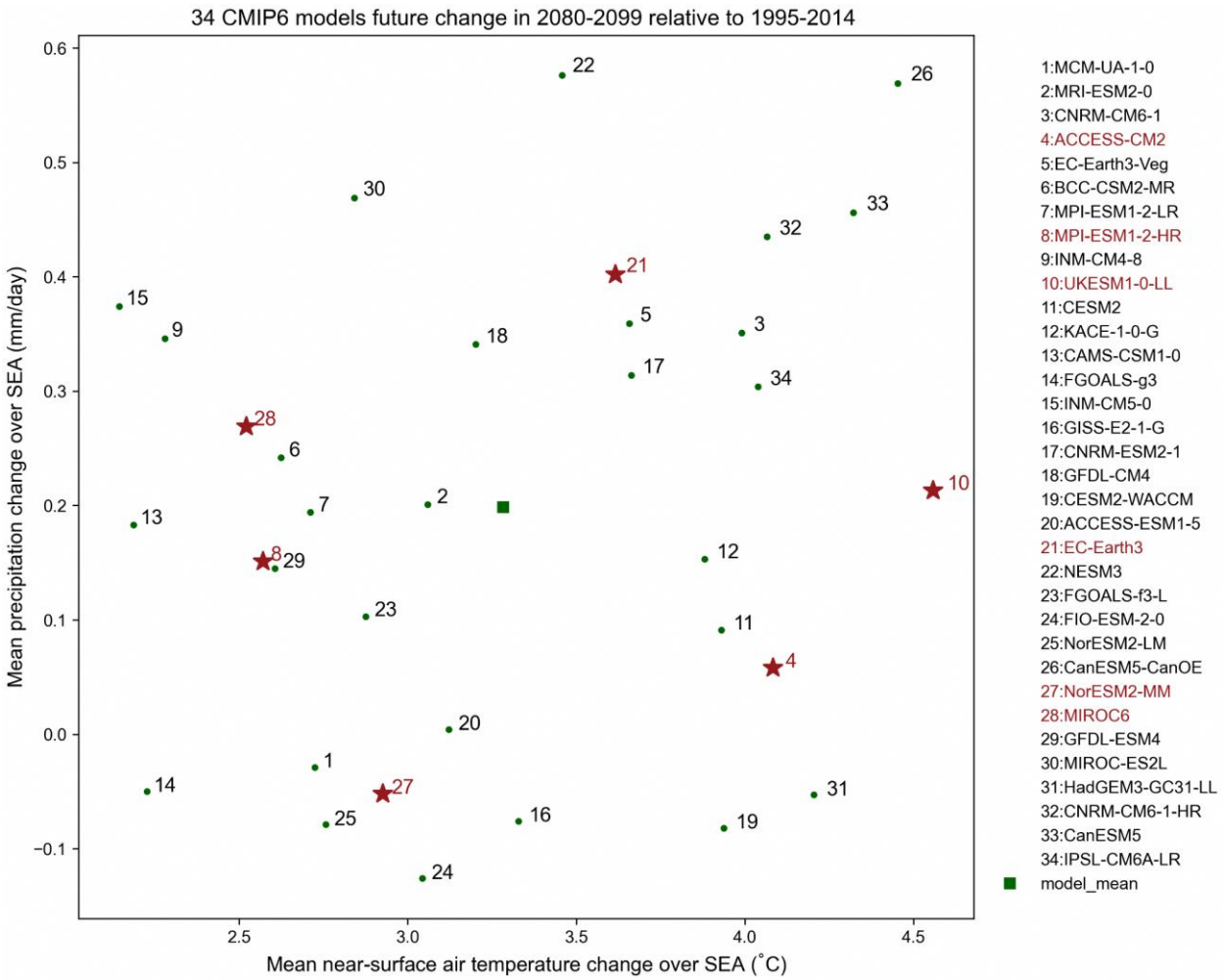

Figure 5.28: End-century (2080-2099) change (relative to 1995-2014) in rainfall and temperature over SEA from 34 CMIP6 GCMs under SSP5-8.5 (red stars denote the chosen models in our study).

5.9 Model Sub-selection

Considering all the information from the previous sections, we selected initially 8 models for further consideration based on 5.3-5.8. For our sub-selection process, we did not use any combined ranking system across all skills, rather, we mainly excluded very deficient looking models along the Tier-1 (climate variables) and Tier-2 (climate processes) skill metrics.

Combined with desired spread in ECS, independence and spread of future climates, we landed on a set of 8 models. The final list of sub-selected models are shown in Table 5.4 with the ones that made it to the final list of models that made available all the forcing data we need for downscaling highlighted in dark grey.

While we were sub-selecting the CMIP6 GCMs the various modelling groups were still in the process of uploading data to the ESGF, so we included some of the models that also had partial data and were expected to upload all of it in time. Finally, because of data availability, 3 (CNRM-CM6-1, GFDL-CM4, and HadGEM3-GC31-LL) out of the 8 models could not be used. Since we had planned to downscale at least 6 GCMs, we replaced HadGEM3-GC31-LL with a similar performing model (UKESM1-0-LL) from the same family.

Table 5.4: List of sub-selected CMIP6 GCMs for V3 Dynamical Downscaling

Sub-selected Model	ECS	Family	End-century change over SEA under SSP5-8.5 scenario	
			Precipitation (mm/day)	Temperature (°C)
ACCESS-CM2	4.66	9	0.06	4.08
CNRM-CM6-1	4.90	3	0.35	3.99
EC-EARTH3	4.26	4	0.40	3.62
GFDL-CM4	3.89	Independent	0.34	3.20
HadGEM3-GC31-LL	5.44	9	-0.05	4.21
MIROC6	2.60	7	0.27	2.52
MPI-ESM1-2-HR	2.98	8	0.15	2.57
NorESM2-MM	2.49	2	-0.05	2.93

While we were sub-selecting the CMIP6 GCMs the various modelling groups were still in the process of uploading data to the ESGF, so we included some of the models that also had partial data and were expected to upload all of it in time. Finally, because of data availability, 3 (CNRM-CM6-1, GFDL-CM4, and HadGEM3-GC31-LL) out of the 8 models could not be used. Since we had planned to downscale at least 6 GCMs, we replaced HadGEM3-GC31-LL with a similar performing model (UKESM1-0-LL) from the same family.

5.10 Summary and Discussion

For the purpose of regional climate change projections it is desirable to cover as much as possible various sources of uncertainty in order to design adaptation options that cover a wider range of climate change risks. In regard to regional climate change projections, a large amount of uncertainty often comes from the choice of scenario. It is advisable to either choose a low/high (as was done in V2) or a low/medium/high set of scenarios. In our case we chose a low/medium/high set of scenarios, namely, SSP1-2.6, SSP2-4.5, and SSP5-8.5 (O'Neill et al. 2016). The SSP1-2.6 scenario approximately corresponds to the previous scenario generation Representative Concentration Pathway (RCP) 2.6, and was chosen as the low scenario for our study as it was designed to have a likely warming within the Paris Agreement target of below 2C warming level. SSP2-4.5, corresponds to RCP4.5, and was chosen as the medium scenario as it was designed as a middle-of-the-road scenario between the low and high ones. Regarding the high scenario, we had the choice of SSP3-7.0 vs SSP5-8.5, and we chose the latter because it corresponds to RCP8.5 that was used in V2, and is also likely to cover the upper end of the scenario uncertainty spectrum. Notably, as per the CORDEX experiment design for dynamical downscaling of CMIP6, SSP3-7.0 and SSP1-2.6 scenarios were chosen to be downscaled first, followed by additional downscaling using the SSP2-4.5 scenario and/or the SSP5-8.5 scenario based on the availability of computational resources.

A similar dynamical downscaling exercise is underway by the CORDEX-SEA community to produce high resolution climate change projections over SEA. There are several similarities and differences between the 2 efforts which make them highly complementary. Similarities include the choice of GCMs to be downscaled, large overlap in the downscaling domain and a common future scenario (SSP1-2.6). Differences include: (1) horizontal resolution (our downscaling is conducted at 8 km for SEA and 2km for WMC), whereas, most of the CORDEX-SEA downscaling will be carried out at 25 km horizontal resolution, (2) the N-S extent of our domains are very similar but our E-W extent is larger by around 20 degrees, (3) we use SSP5-8.5 as the high scenario, whereas CORDEX-SEA

uses SSP3-7.0, and (4) we use SINGV-RCM (Prasanna et al. 2023; submitted) and WRF (for a subset of the runs carried out using SINGV-RCM in order to assess downscaling uncertainty) as the downscaling model, whereas, CORDEX-SEA uses RegCM and WRF.

It is to be noted that while our intention was to sample as many family of models as feasible based on existing literature on model genealogy, we decided to have 2 models from one family (ACCESS-CM2 and UKESM1-0-LL) for 2 reasons: (1) the 2 models satisfied all our other criteria for model sub-selection, and (2) to analyse how similar or different can be the regional projections from 2 models of the same family, although they have different ocean models.

It is also to be noted that one of our final models that was used for downscaling (UKESM1-0-LL) has an ECS of 5.36oC which is beyond the very likely range of IPCC AR6 (2oC-5oC). Since we think it is important to span the range of ECS, provided the other sub-selection criteria are met, and the model being a credible GCM from the UKMO, we decided to go ahead with it.

In summary, we evaluated 49 CMIP6 GCMs for key climate variables and processes and using multiple dimensions of sub-selection we finally sub-selected 6 GCMs for dynamical downscaling over the 8 km SEA domain to produce the Third National Climate Change projections for Singapore.

References

Adler, R. F., G. J. Huffman, A. Chang, R. Ferraro, P. Xie, J. Janowiak, B. Rudolf, U. Schneider, S. Curtis, D. Bolvin, A. Gruber, J. Susskind, P. Arkin, and E. Nelkin, (2003) The version 2 Global Precipitation Climatology Project (GPCP) monthly precipitation analysis (1979-present). J. Hydrometeor, 4(6), 1147-1167.

Ashouri, H., Hsu, K.-L., Sorooshian, S., Braithwaite, D. K., Knapp, K. R., Cecil, L. D., et al. (2015). PERSIANN-CDR: Daily Precipitation Climate Data Record from Multisatellite Observations for Hydrological and Climate Studies. Bulletin of the American Meteorological Society, 96(1), 69–83. https://doi.org/10.1175/BAMS-D-13-00068.1

Bock, L., Lauer, A., Schlund, M., Barreiro, M., Bellouin, N., Jones, C., et al. (2020). Quantifying Progress Across Different CMIP Phases With the ESMValTool. Journal of Geophysical Research: Atmospheres, 125(21), e2019JD032321.

CORDEX (2021) (https://cordex.org/wp-content/uploads/2021/05/CORDEX-CMIP6_exp_ design _RCM.pdf; last accessed 09 Feb 2023)

Eyring, V., Bony, S., Meehl, G. A., Senior, C. A., Stevens, B., Stouffer, R. J., & Taylor, K. E. (2016). Overview of the Coupled Model Intercomparison Project Phase 6 (CMIP6) experimental design and organization. Geoscientific Model Development, 9(5), 1937–1958.

Fiedler, S., and Coauthors (2020) Simulated Tropical Precipitation Assessed across Three Major Phases of the Coupled Model Intercomparison Project (CMIP). Mon. Wea. Rev., 148, 3653–3680, https://doi.org/10.1175/MWR-D-19-0404.1.

Flynn, C. M., & Mauritsen, T. (2020). On the climate sensitivity and historical warming evolution in recent coupled model ensembles. Atmospheric Chemistry and Physics, 20(13), 7829–7842.

Gelaro, R., and Coauthors (2017) The Modern-Era Retrospective Analysis for Research and Applications, Version 2 (MERRA-2). J. Climate, 30, 5419–5454, https://doi.org/10.1175/JCLI-D-16-0758.1.

Hersbach, H, Bell, B, Berrisford, P, et al. (2020) The ERA5 global reanalysis. Q J R Meteorol Soc.; 146: 1999– 2049. https://doi.org/10.1002/qj.3803.

Hirahara, S., Ishii, M., and Y. Fukuda (2014) Centennial-scale sea surface temperature analysis and its uncertainty. J of Climate, 27, 57-75.

Huang, B., Peter W. Thorne, et. al. (2017) Extended Reconstructed Sea Surface Temperature version 5 (ERSSTv5), Upgrades, validations, and intercomparisons. J. Climate, doi: 10.1175/JCLI-D-16-0836.1

Huffman, G.J.; Bolvin, D.T.; Braithwaite, D.; Hsu, K.; Joyce, R.; Kidd, C.; Nelkin, E.J.; Sorooshian, S.; Tan, J.; Xie, P. (2019) NASA Global Precipitation Measurement (GPM) Integrated Multi-satellitE Retrievals for GPM (IMERG). In Algorithm Theoretical Basis Document (ATBD) Version 06; NASA/GSFC: Greenbelt, MD, USA.

Huffman, George J., Bolvin, David T., Nelkin, Eric J., Wolff, David B., Adler, Robert F., Gu, Guojun, Hong, Yang, Bowman, Kenneth P., Stocker, Erich F. (2007) The TRMM Multisatellite Precipitation Analysis (TMPA): Quasi-Global, Multiyear, Combined-Sensor Precipitation Estimates at Fine Scales. Journal of Hydrometeorology. Vol. 8, No. 1, pp. 38-55. DOI: 10.1175/JHM560.1 ISSN: 1525-755X, 1525-7541

Hurrell, J. W., J. J. Hack, D. Shea, J. M. Caron, and J. Rosinski (2008) A New Sea Surface Temperature and Sea Ice Boundary Dataset for the Community Atmosphere Model. Journal of Climate, 21, 5145–5153, https://doi.org/10.1175/2008jcli2292.1.

K. Okamoto, T. Iguchi, N. Takahashi, K. Iwanami and T. Ushio (2005) The global satellite mapping of precipitation (GSMaP) project, 25th IGARSS Proceedings, pp. 3414-3416.

Knutti, R., Masson, D., & Gettelman, A. (2013). Climate model genealogy: Generation CMIP5 and how we got there. Geophysical Research Letters, 40(6), 1194–1199. https://doi.org/10.1002/grl.50256

Kubota T et al. (2007) Global pecipitation map using satellite-borne microwave radiometers by the GSMaP project: production and validation IEEE Trans. Geosci. Remote 45 2259–75

Martin, G. M., Levine, R. C., Rodriguez, J. M., and Vellinga, M. (2021) Understanding the development of systematic errors in the Asian summer monsoon, Geosci. Model Dev., 14, 1007–1035, https://doi.org/10.5194/gmd-14-1007-2021.

McSweeney, C., Rahmat, R., Redmond, G., Marzin, C., Murphy, J., Jones, R., et al. (2015) Sub-selection of CMIP5 GCMs for downscaling over Singapore (Vol. 2).

Morice, C. P., J. J. Kennedy, N. A. Rayner, and P. D. Jones (2012) Quantifying uncertainties in global and regional temperature change using an ensemble of observational estimates: The HadCRUT4 dataset, J.

Geophys. Res., 117, D08101, doi:10.1029/2011JD017187.

Nguyen, P., E.J. Shearer, H. Tran, M. Ombadi, N. Hayatbini, T. Palacios, P. Huynh, G. Updegraff, K. Hsu, B. Kuligowski, W.S. Logan, and S. Sorooshian (2019) The CHRS Data Portal, an easily accessible public repository for PERSIANN global satellite precipitation data, Nature Scientific Data, Vol. 6, Article 180296. doi: https://doi.org/10.1038/sdata.2018.296

Power, S., F. Delage, C. Chung, G. Kociuba, and K. Keay (2013) Robust twenty-first-century projections of El Niño and related precipitation variability. Nature, 502, 541–545, https://doi.org/10.1038/nature12580.

Rayner, N. A., Parker, D. E., Horton, E. B., Folland, C. K., Alexander, L. V., Rowell, D. P., Kent, E. C., and Kaplan, A. (2003) Global analyses of sea surface temperature, sea ice, and night marine air temperature since the late nineteenth century, J. Geophys. Res., 108, 4407, doi:10.1029/2002JD002670, D14.

Reynolds, Richard W., Thomas M. Smith, Chunying Liu, Dudley B. Chelton, Kenneth S. Casey, Michael G. Schlax (2007) Daily High-Resolution-Blended Analyses for Sea Surface Temperature. J. Climate, 20, 5473-5496.

Roca, R., Alexander, L. V., Potter, G., Bador, M., Jucá, R., Contractor, S., et al. (2019) FROGS: a daily 1° × 1° gridded precipitation database of rain gauge, satellite and reanalysis products. Earth System Science Data, 11(3), 1017–1035. https://doi.org/10.5194/essd-11-1017-2019.

Rohde, R. A. and Hausfather, Z.: (2020) The Berkeley Earth Land/Ocean Temperature Record, Earth Syst. Sci. Data, 12, 3469–3479, https://doi.org/10.5194/essd-12-3469-2020.

Sadeghi, M., Nguyen, P., Naeini, M. R., Hsu, K., Braithwaite, D., & Sorooshian, S. (2021) PERSIANN-CCS-CDR, a 3-hourly 0.04° global precipitation climate data record for heavy precipitation studies. Scientific Data, 8(1), 157. https://doi.org/10.1038/s41597-021-00940-9.

Shinya KOBAYASHI, Yukinari OTA, Yayoi HARADA, Ayataka EBITA, Masami MORIYA, Hirokatsu ONODA, Kazutoshi ONOGI, Hirotaka KAMAHORI, Chiaki KOBAYASHI, Hirokazu ENDO, Kengo MIYAOKA, Kiyotoshi TAKAHASHI (2015) The JRA-55 Reanalysis: General Specifications and Basic Characteristics, Journal of the Meteorological Society of Japan. Ser. II, Volume 93, Issue 1, Pages 5-48, Released on J-STAGE March 18, 2015, Online ISSN 2186-9057, Print ISSN 0026-1165, https://doi.org/10.2151/jmsj.2015-001

Xie P., Joyce R., Wu S., Yoo S.-H., Yarosh Y., Sun F. and Lin R. (2017) Reprocessed, bias-corrected CMORPH global high-resolution precipitation estimates from 1998 J. Hydrometeorol. 18 1617–41.

Appendix

A5.1 Evaluations for seasonal rainfall

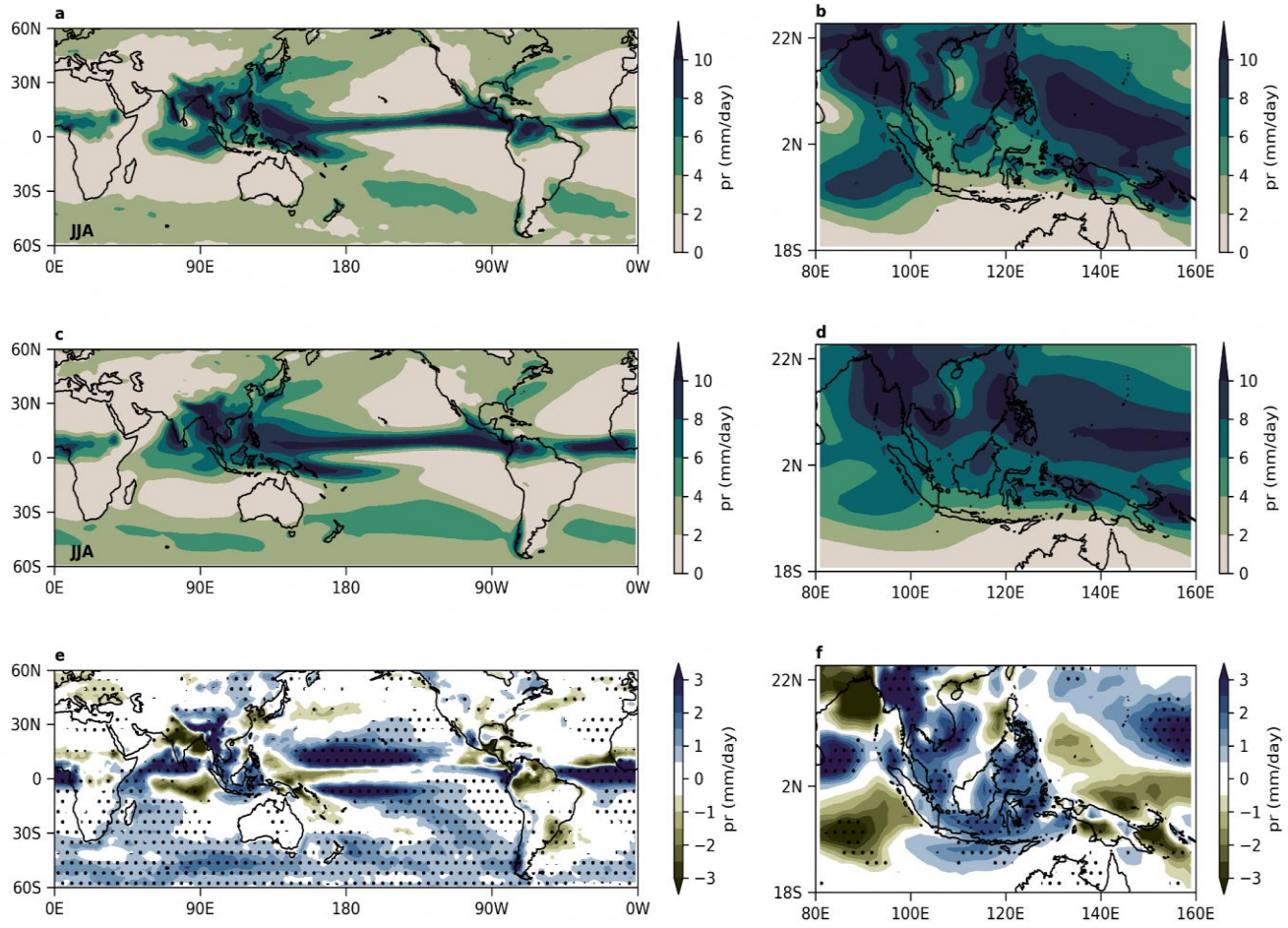

Figure A5.1: 1995-2014 JJA season mean precipitation (pr) in observation (a,b) and models (c,d). a. FROGS datasets for the 60N-60S domain. b. similar to a, but for the SEA domain. c. multi-model mean of pr from 48 CMIP6 models for the 60N-60S domain. d. similar to c, but for the SEA domain. e. model bias (e.g., multi-model mean from 48 models minus the observational mean). Stippled areas indicate the agreement by 70% of models. f. similar to e, but for the SEA domain.

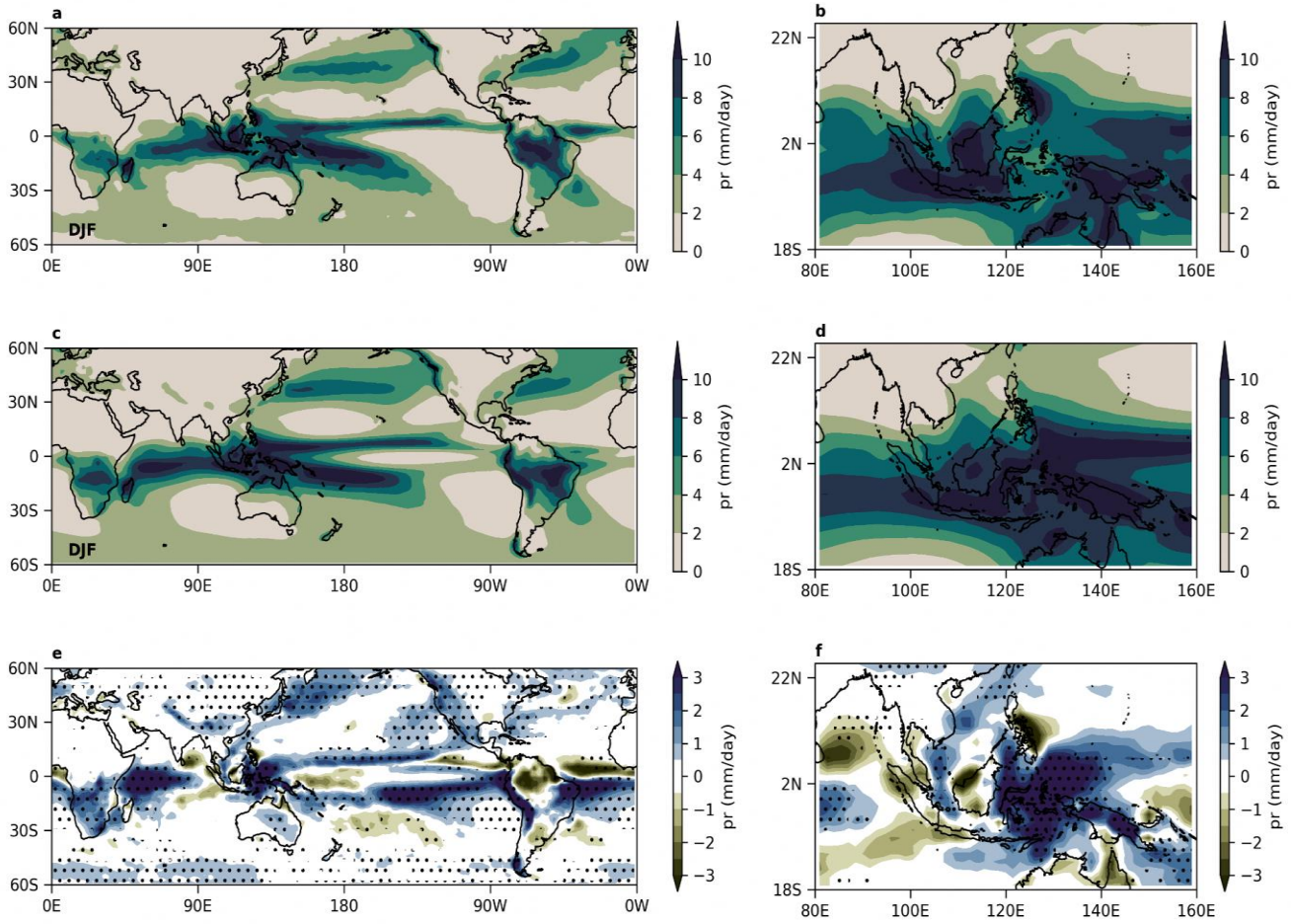

Figure A5.2: 1995-2014 DJF season mean precipitation (pr) in observation (a,b) and models (c,d). a. FROGS datasets for the 60N-60S domain. b. similar to a, but for the SEA domain. c. multi-model mean of pr from 48 CMIP6 models for the 60N-60S domain. d. similar to c, but for the SEA domain. e. model bias (e.g., multi-model mean from 48 models minus the observational mean). Stippled areas indicate the agreement by 70% of models. f. similar to e, but for the SEA domain.

6

Singapore's Regional Climate Model SINGV-RCM

Authors:
Venkatraman Prasanna, Aurel Florian Moise, Sandeep Sahany, Muhammad Eeqmal Hassim, Chen Chen, Xin Rong Chua, Gerald Lim, Pavan Harika Raavi, Fei Luo

Meteorological Service Singapore
Centre for Climate Research Singapore

6.1 Introduction

With the advancements in supercomputing over the recent decade, GCMs are now capable of global climate simulations of order of few hundred years at a grid resolution of 50-100 km (Eyring et al. 2016; Haarsma et al. 2016), which can be further downscaled using a regional climate model to a 10-20 km grid resolution to capture regional scales in detail (Zhao et al. 2021; Gianotti et al. 2012; Qian 2008).

While a grid resolution of 10-20 km is found to perform reasonably well in the extra tropical regions (Ban et al. 2014), it is difficult to justify if such a coarse grid resolution, where one needs convective parameterisation, will perform equally well in a tropical region like Singapore where the processes (e.g., localized thunderstorms) that characterise the local climate are small- scale (Ngo-Duc et a.l. 2017; Nguyen et al. 2022; Hariadi et al. 2022).

Based on our own experience in weather modelling and the results from existing literature (Marsham et al. 2013; Birch et al. 2014; Prein et al. 2015; Huang et al. 2019; Dipankar et al. 2020; Li et al. 2020a, 2020b; Dipankar et al. 2021; Lee et al. 2021), we believe that a convection-permitting grid resolution, although considerably computationally expensive, is better suited to study the climate change impact on the city state Singapore. Our aim of this study is to document the development of a reliable and high-grid resolution climate modelling system over the Maritime continent for downscaling CMIP6 models for Singapore's Third National Climate Change Projections (V3) studies.

To customize and improve the model for the tropical region, particularly around Singapore, in partnership with the UK Met Office, CCRS-Singapore developed a numerical weather prediction model called SINGV (Huang et al. 2019), which is now run operationally by the Meteorological Service Singapore (MSS) for daily weather predictions. SINGV benefits from daily scrutiny by forecasters and its performance is assessed using a wide range of objective evaluation metrics. This is a very strong basis to establish Singapore variable grid resolution model (SINGV) as the regional climate model (RCM) of choice to complete the third National Climate Change projections (V3).

High spatial resolution (~ 2-8 km) climate information is of much relevance to Singapore due to the size of the city-state. Due to the coarse grid resolutions of the GCMs (~ 50-100 km), it is necessary to downscale the climate information from GCMs, to improve the understanding of climate processes at small-scales that can be resolved by RCMs unlike GCMs. Therefore, simulating sufficiently very high resolution atmospheric variables (at km-scale) around the Singapore – Malay Peninsula region (SG-domain) and a larger domain covering the entire Maritime Continent (MC-domain) at 2km and 8km grid resolutions, respectively using ERA5 fields as a driving model, serves as a benchmark for SINGV-RCM simulations over the region to conduct Singapore's Third National Climate Change Projections (V3).

Earlier Studies done by Kendon et al. (2012, 2014) showed, that the United Kingdom Met Office (UKMO) RCM simulated rainfall characteristics are better than using coarse-grid resolution simulations from other models or using the same model at a high resolution of 1.5 km, produced a much better results, a testimony to model skills when moving from RCM to convection enabling resolutions in UKMO model, which gives confidence to us that the SINGV-RCM shares the same infrastructure of UKMO model and better tuned to the Singapore region and tropics in general.

In this study detailed analyses are done to investigate the SINGV-RCM model performance to reproduce the observed climate at all spatial and timescales. Model is tested with best possible dynamics and physics to fairly reproduce the observed diurnal cycle, observed spatial climatology and observed distribution of heavy rainfall and also tested for the evolution of the peak diurnal timing and intensity of rainfall.

The contents of the manuscript are as follows, the description of data and modelling framework are dealt in section 2, section 3 examines the results and finally the summary and discussions are in section 4 respectively.

6.2 SINGV Model setup

In this section we present the details of the model set up of SINGV. Specifically, we present details on the modelling framework used, dynamics, physics and model versions used, the model nesting suite, observational data used for

validation, and the reanalysis datasets used as forcing fields.

6.2.1 Modelling framework

The modelling experiments are conducted to explore SINGV's potential as a Regional Climate Model (RCM) for the MC domain; previously several studies were conducted with the SINGV-NWP system and found to have high skills in predicting the convection realistically over the Singapore region. (Huang et al. 2019; Dipankar et al. 2020; Doan et al. 2021). Results presented in this study are for two versions of SINGV namely, version v5.0 and the earlier version v4.1. SINGV v5.0 is based on the dynamical core of Unified Model (UM) version 11.1, and the Physics basis from the tropical version of the UM known as RA1T (Regional Atmosphere 1 – Tropical) (Bush et al. 2019). SINGV v5.0 is the version of the RCM proposed for the delivery of V3 study (Timbal et al. 2019).

UK Met Office's unified model (UM), a seamless modelling system in which largely the same model is used to simulate the atmosphere at all scales, from the large-scale global circulation to finer-scale grid resolution regional weather. This seamless system provides a consistent modelling approach and has significant advantages for nested modelling approach, in which high-grid resolution models are embedded within the coarser grid resolution models (Golding et al. 2014; Boutle et al. 2016; Bush et al. 2019), by enhancing the horizontal grid resolution a more detailed atmospheric simulations can be obtained (Golding et al. 2014; Boutle et al. 2016; Bush et al. 2019). The current modelling system which is, Singapore regional climate model (SINGV-RCM) to be used for the third National Climate Change projection studies (V3) is based on the UM modelling system.

The nesting suite infrastructure of SINGV-RCM will be able to provide high-grid resolution precipitation simulation along with other atmospheric variables. ERA5 reanalysis output is used for initial condition (IC), lateral boundary conditions (LBC) and surface boundary (SST) to drive the SINGV Model in a nesting suite setup to achieve 8km and 2km grid resolutions. Additional experiments are also conducted at 9km, 4.5km and 1.5km grid resolutions with an earlier version of SINGV-RCM (v4.1) and the results are then validated against the Satellite based observation to quantify the accuracy of the SINGV-RCM model's skill in simulating the precipitation over the vicinity of SINGV-domain (SG-domain) and the entire Maritime Continent (MC-domain). The new version of SINGV (v5.0) and the previous version of SINGV (v4.1) differ majorly only in the surface ancillaries and a few minor changes in terms of physics and dynamics. These minor changes in Physics won't change the simulation results significantly.

The dynamical core for the SINGV model used in this study is from the Met Office Unified model [UM v11.1 & v10.6] for the Singapore versions [SINGV v5.0 & v4.1] configured as a suite of models nested to one another and decreasing in domain size while increasing in model grid resolution. The current configuration of the suite ranges from 8km to 2km as one set with SINGV v5.0 and 9km to 4.5km and finally to 1.5km grid sizes as another set with SINGV v4.1, the lateral boundary conditions (LBCs) are from the ~31 km ERA5 reanalysis model data and are used to drive the next higher grid resolution nested model. Use of the same model for the nested suite means that treatment of the dynamics and the parameterised and resolved physics processes are consistent.

The downscaling is performed using ERA5 initial condition (IC), lateral boundary conditions (LBC) and surface boundary (SST) at different horizontal grid resolutions nested to one another as shown by the schematic diagram (Figure 6.1). The current version of SINGV-RCM (v5.0) tested for V3 domains are shown in solid boxes 8 km (D1) and 2 km (D2) and a slightly earlier version of SINGV-RCM (v4.1), which was tested for different set of domains, are shown in red dashed boxes, 9 km and 4.5 km (D3), 1.5 km (D4) and a common domain for comparison of all results are shown by dotted and dashed box for MC and SG domains.

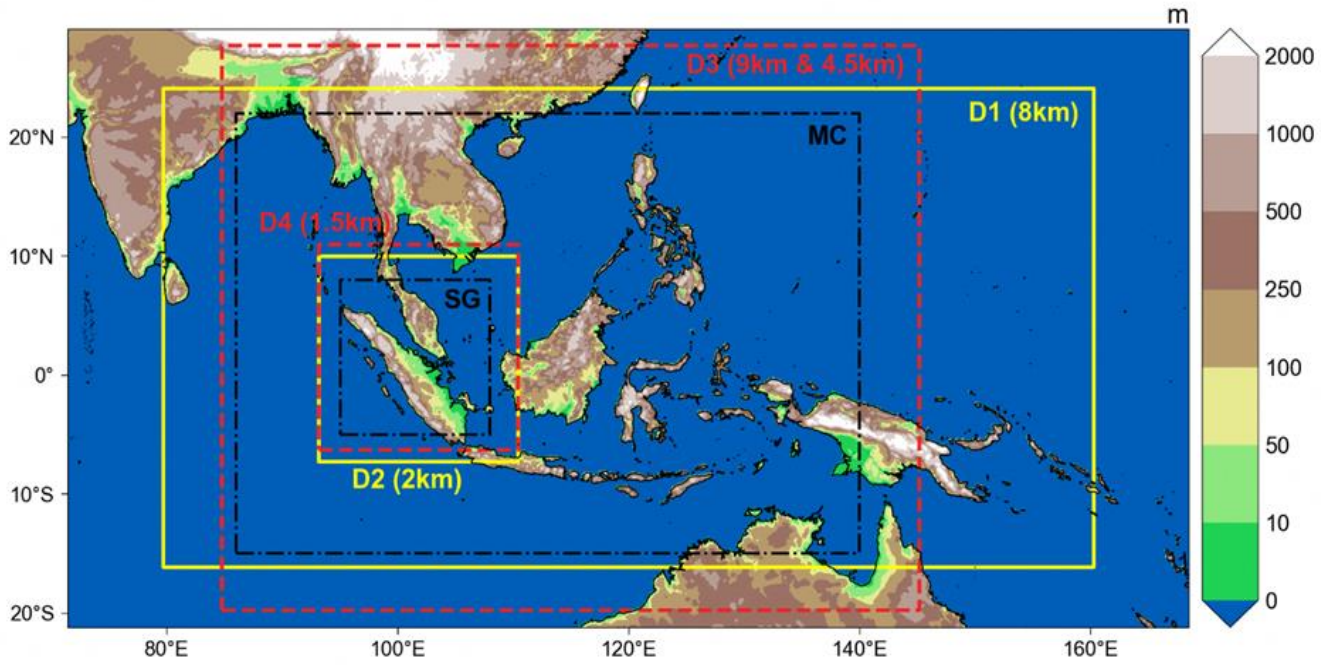

Figure 6.1: Downscaling domains tested for V3 study. D1 (16.16 S – 24.08 N; 79.68 E – 160.248 E) is the 8 km domain, and D2 (7.29 S – 9.972 N; 93.16 E – 110.422 E) is the 2 km domain (in solid line). D3 (16.16 S – 24.08 N; 79.68 E – 160.248 E) is the 9 km and 4.5 km domains and D4 (7.29 S – 9.972 N; 93.16 E – 110.422 E) is the 1.5 km domain (in dashed lines). Box for MC domain (-15-22N; 86-140E) and SG domain (-5-8N; 95-108E) selected for comparison of results for respective domains (in dotted & dashed line).

6.2.2. Dynamics, Physics and model versions used in SINGV-RCM

The SINGV-regional climate model (SINGV-RCM) consists of key components of dynamics and physics, which are explained briefly in this section.

The set of basic equations representing the model dynamics are non-hydrostatic finite difference models with full equations. The prognostic variables are horizontal and vertical wind components, potential temperature, pressure, density, specific humidity, cloud liquid water content etc. The integration domain is the entire Maritime continent (@8km grid resolution) and Singapore domain (@2km grid resolution) forced by the 8km domain output. The horizontal grid consists of a spherical latitude-longitude grid with Arakawa C-grid staggering of variables. The vertical grid consists of 80 levels extending from surface to 38.5km at the top, the levels are height-based hybrid-η vertical coordinate with Charney and Phillips (1953) grid staggering of variables. Semi-lagrangian is used to treat the advection term and semi-implicit method for time integration. The model time steps are roughly 240 seconds (4mins) for 8km and 120 seconds (2mins) for 2km. Additional configurations are Maritime continent (@9km and @4.5km grid resolutions with model time steps 4mins & 3mins) and Singapore domain (@1.5 km grid resolution @1min model time step).

Some details of Physics options used in the model are given below.

1. The cloud scheme is the Prognostic cloud fraction and condensate cloud scheme (PC2 scheme) of Wilson et al. (2008a, b). Precipitation is treated by Wilson and Ballard (1999) single-moment bulk microphysics scheme, coupled with the PC2 cloud scheme.
2. Radiation in the model is treated by Edwards and Slingo (1996) radiation scheme with non-spherical ice spectral files with 6 absorption bands in the SW (shortwave) and 9 bands in the LW (Longwave).
3. The Boundary Layer scheme includes a blending of 1D boundary-layer scheme for vertical mixing by Lock et al. (2000, 2001) and 2D scheme following Smagorinsky (1963). The Gravity wave drag is treated by Orographic scheme including a flow blocking scheme, which represents the effects of sub-grid scale orography and the non-orographic spectral scheme is also included which represents the effect of gravity waves in the

stratosphere and mesosphere. Land surface scheme used in the model is the Joint UK Land Environment Simulator (JULES) (Best et al. 2011) 4-layer soil model using Genuchten (1980) soil hydrology.

Table 6.1 shows the details of the two different configurations with respect to model dynamics, physics and the actual model setup.

Table 6.1: Model parameters and setup for two versions of SINGV-RCM

Model	**SINGV-RCM (v5.0) current version used for V3 study**	**SINGV-RCM (v4.1) previous version tested for V3 study**
Dynamics/ Physics	(UM - Version 11.1) - End-Game Dynamical core with Physics package: RA1T	(UM - Version 10.6) - End-Game Dynamical core with Physics package: RA
Horizontal grid resolution	SINGV-RCM: 8.0km Grids: 1120 x 560 and 2.0 km Grids: 960 x 960.	SINGV-RCM: 9.0km Grids: 642 x 546, 4.5km Grids: 1304x1112 and 1.5km Grids: 1092 x 1026.
Time steps	8km: 240 seconds (4minutes); 2km: 120 seconds (2minutes).	9km: 240 seconds (4minutes); 4.5km: 180 seconds (3minutes); 1.5km: 60 seconds (1minute).
Surface ancillary files	Tested for both CCI and IGBP Land-surface ancillaries. CCI (Climate Change Initiative) from the European Space agency uses latest satellite data for preparing the latest ancillary files.	Only IGBP Land-surface ancillaries. IGBP (international Geosphere-Biosphere Program) program produced the ancillary dataset, which is based on an old global dataset and
Surface B. C.	Sea Surface Temperature (SST) from ERA5 reanalysis interpolated to 8.0km and 2.0km grid resolutions of SINGV-RCM.	Sea Surface Temperature (SST) from ERA5 reanalysis interpolated to 9.0km, 4.5km and 1.5km grid resolutions of SINGV-RCM.
Driving model	Global Driving Model: ERA5 (~31km) and ERA-Interim (~75km)	
SST update Frequency	Updated 8 times daily @ 3-hourly frequency- (00, 03, 06, 09, 12, 15, 18, 21 UTC)	
Initial condition (I.C)	ERA5-IC: Jan1, 2001	
Boundary condition (LBC)	Global model: ERA5 – LBC @3hr interval (~31 km grid resolution)	
Vertical grid resolution	L80: 80 levels (surface to ~38.5 km height)	
Simulation & Analysis period	Simulation for periods: Jan1, 2001 to Jan31, 2001 (31 days) and analysis period: Jan2, 2001 to Jan 30, 2001 (29days).	
Radiation Process	Edwards-Slingo general 2-stream scheme (Edwards and Slingo 1996)	
Surface soil Process	Joint UK Land Environment Simulator (JULES) (Best et al. 2011): 4-layer soil model using Genuchten (1980) soil hydrology	
PBL Process	A 2D and 1D vertical blended scheme. 1D boundary-layer scheme for vertical mixing Lock et al. (2000, 2001) and 2D Smagorinsky scheme (Smagorinsky 1963)	
Microphysics	Mixed-phase precipitation (Wilson and Ballard 1999)	
Gravity Wave Drag	Gravity Wave drag due to orography	

The model setup is similar to the SINGV-NWP setup, except that it is a free run with the regular update of sea surface temperature at 3 hourly intervals. These similar SINGV-NWP configurations were also used in other applications like urban studies (Simon et al.

2020; Doan et al. 2021), and it was demonstrated that the model configuration is evaluated well over this region.

Before running the UM model on climate mode for multiple domains with incremental spatial-grid resolutions, the ancillary files are prepared using the rose suite, central ancillary program (CAP) and Ancillary tool software (ANTS). The hierarchy of ancillary datasets are given by, 1) Land-Sea Mask, 2) Model orography, 3) Soil parameters, 4) Vegetation, surface type and Leaf Area Index, 5) Soil moisture and snow climatology, 6) Aerosol climatology, 7) SST and Sea Ice climatology.

The ancillary data provides the external driving conditions for the model. Ancillary files hold data relating to model orography, soil and vegetation types, climatologies for sea surface temperature and sea ice amongst others. The CAP or ANTS creates the ancillary files by reading post-processed source data and writing them in UM fields-file format.

6.2.3 SINGV model nesting suite's experimental setup

The UM model is set to run on a multiple one-way nesting mode. The set-up of both experiments (SINGV5.0 and SINGV4.1) are broadly similar except for horizontal grid resolutions. The increased grid resolution improves the model results considerably (Stein et al. 2014, 2015; Clark et al. 2016). The time step of each nesting domain must be reduced by a similar magnitude to the reduction in grid-length, to ensure a similar level of stability and accuracy of the model dynamics.

The vertical grid spacing of the nesting suite is kept at 80 levels as used in the operational model. The model turbulence parameterisation is not changed but kept as it is (as used in the operational model), which includes a blending of 1D boundary-layer scheme for vertical mixing (Lock et al. 2000, 2001) and 3D Smagorinsky scheme (Smagorinsky 1963; Boutle et al. 2010). Both versions of SINGV-RCMs (SINGV4.1 and SINGV5.0) uses PC2 schemes. The critical relative humidity, a parameter used in the cloud scheme that represents the relative humidity at which clouds will start to form, varies from 0.96 to 0.81 up to 14 levels from the surface and at 0.8 (constant) above this level (total 80 levels) in this study.

The domain is centred over Singapore (centre grid of latitude and longitude: 0.0N; 112.0E). The simulations were done for a month-long period (Jan1-Jan 31, 2001) and are compared with the observational dataset. The model versions used for these experiments (SINGV4.1 and SINGV5.0) are based on the Unified model (Vn. 10.6 and Vn. 11.1) respectively.

6.2.4 Observational data for validation

The Integrated Multi-satellitE Retrievals for GPM (IMERG) algorithm combines information from the GPM satellite constellation to estimate precipitation over the majority of the Earth's surface (Huffman et al. 2020). In the latest Version 06 release of GPM-IMERG the algorithm fuses the early precipitation estimates collected during the operation of the TRMM satellite (2000 - 2015) with more recent precipitation estimates collected during operation of the GPM satellite (2014 - present). GPM-IMERG data are available from 2001 to present. These data are available on a 0.1° spatial grid between the coordinates 60°S to 60°N and 0° to 360° E-W. The half-hourly data are processed to obtain hourly, daily and monthly value, when necessary, over the study period.

6.2.5 Reanalysis data as forcing fields

ERA5 is a global atmospheric reanalysis from 1979 produced by the European Centre for Medium range Weather Forecasting (ECMWF), UK. Six hourly surface and vertical pressure fields for important meteorological variables at a grid resolution of 0.25° were downloaded from the data website and used as a forcing field for SINGV-RCM model simulations for the 8km-Maritime continent domain. Hersbach et al. (2019, 2020) have documented the ERA5 reanalysis product in detail.

6.3 From SINGV-NWP to SINGV-RCM

Here we discuss the evolution of SINGV-RCM from SINGV-NWP and the modifications/changes made to the model with the previous version of the model. We also discuss the result obtained from the sensitivity experiments done with the improved version compared to the previous version. The SINGV-

NWP model has been adapted to perform as SINGV-RCM for V3 studies. The adopted SINGV-RCM model is used for dynamical downscaling over the Maritime Continent (MC) and Singapore (SG) domains with the nesting suite to achieve an inner nest of higher grid resolution (to the order of a few kms). The details of the experimental setup using initial (IC) and boundary conditions (LBC) from ERA5 (~30km) to the MC domain (9km, 8km, 4.5km) and the SG-domain (2 km, 1.5km) is shown in Table 6.1. Multiple nests are used in the SINGV-RCM to achieve high-grid resolution climate simulation (downscaling of atmospheric variables), in which the 30km ERA5 is progressively nested in increasing grid resolutions over the maritime continent domain at 9km, 8km, 4.5km and finally to 2km and 1.5km over SG domain. As part of sensitivity studies, we conducted several experiments to assess model performance with respect to the model changes. Some of them, which we believe are important, are listed below.

6.3.1 Implementation of prescribed Diurnal cycle of SST

SST fields are interpolated from the ERA5 data (~30km grid resolution) to the SINGV-RCM grid resolutions (9km, 8km, 4.5km, 2km and 1.5km) and updated every 3 hours. The ancillary files like SST and Sea ice are created using the X-ancils application and are then linked in the namelist file of the RA1T science configuration file. The 3 days of 3 hourly input SST from the driving model and the corresponding hourly output from the SINGV-RCM are shown in Figure 6.2. Earlier TRMM based precipitation studies have brought out the importance of observed diurnal variability of precipitation over maritime continent a few to mention (Mori et al., 2004; Ichikawa and Yasunari, 2006) and role of diurnal cycle of SST becomes more important over the maritime continent, as the diurnal changes in SSTs and the interaction of land-Sea breezes with the topographic changes to contribute to the diurnal precipitation changes. Recently, Dipankar et al. (2019) using data from the pilot field campaign of Years of the Maritime Continent (pre-YMC) Yoneyama and Zhang (2020) are used to understand the model biases, their results also support the earlier findings that the convection over coastal land and sea is strongly coupled. They also found that EC-SST fields when corrected for bias up to 2-degree K, found that the simulation improved in the representation of diurnal convective activity and comparable to the Ocean point observation (where MIRAI ship was stationed) about 55km away from the coastal station Bengkulu. This result strongly suggests the high temporal frequency of SST update can help the model to capture the diurnal variability of convection over the Maritime Continent. Therefore using 3-hourly input SSTs can improve the diurnal variability of precipitation over the Maritime continent.

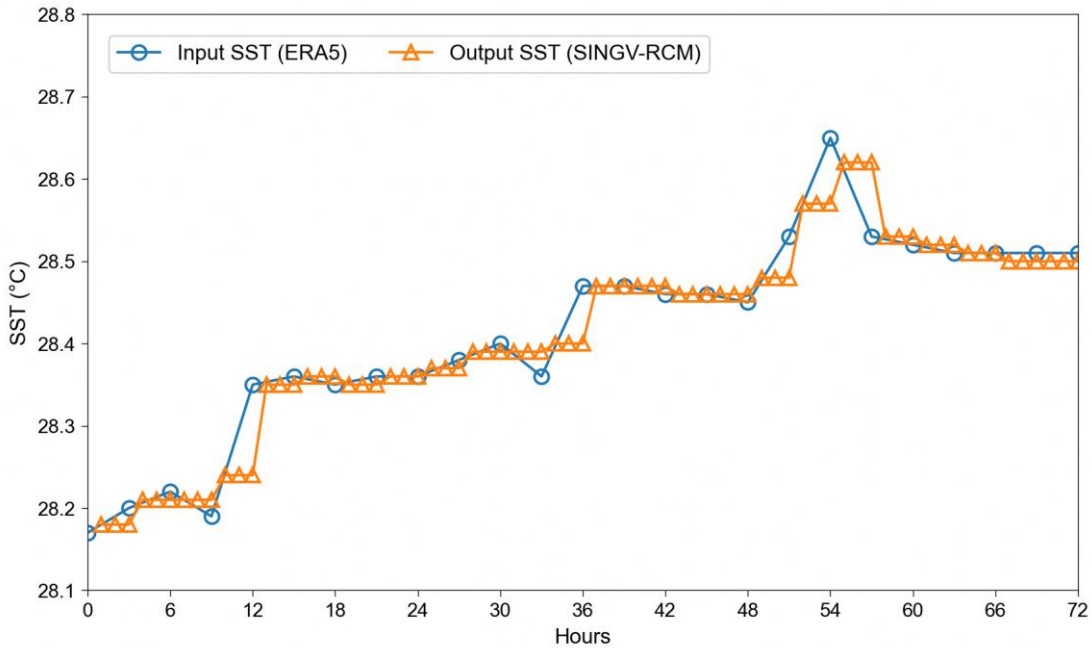

Figure 6.2: Domain averaged input SST profiles from ERA5 driving model (~30km) at 3hr frequency and output SST profiles from SINGV-RCM (~8 km) at 1hr frequency for 3 consecutive days are shown here. Units in degree C.

6.3.2 Changes to the land—surface representation

We modified the IGBP land use data (vegetation) to CCI land use data (vegetation fraction) (Figure 6.3a, b).

We also modified the Land Use and Land cover Change (LULC) non-vegetation fraction ancillary along with vegetation fraction ancillary to the latest European Space Agency (ESA) based Climate change Initiative (CCI) data, it is a global LULC climatology data computed at 300m grid resolution from 1992 to 2020, compared to the previously used data of International Geosphere Biosphere Program created (IGBP) LULC data a coarse-grid resolution of 1km. More realistic Urban Land fraction for Kuala Lumpur and Singapore is evident from the CCI data as shown in Figure 6.4 (a, d) compared to IGBP data Figure 6.4 (b, e) and are compared with satellite images for Kuala Lumpur figure 6.4 (c) and Singapore figure 6.4 (f).

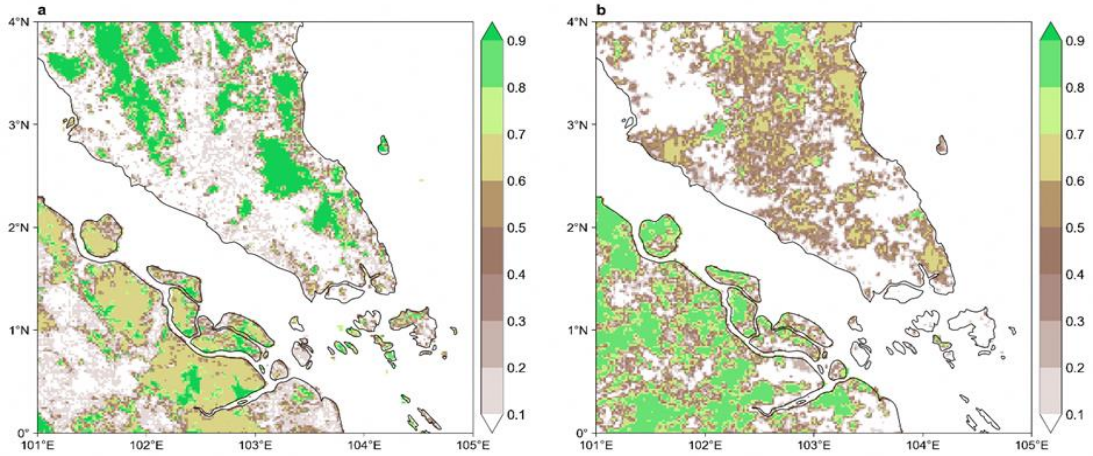

Figure 6.3: Broad Leaf fraction comparison. a) CCI data, b) IGBP data. Units in fractions.

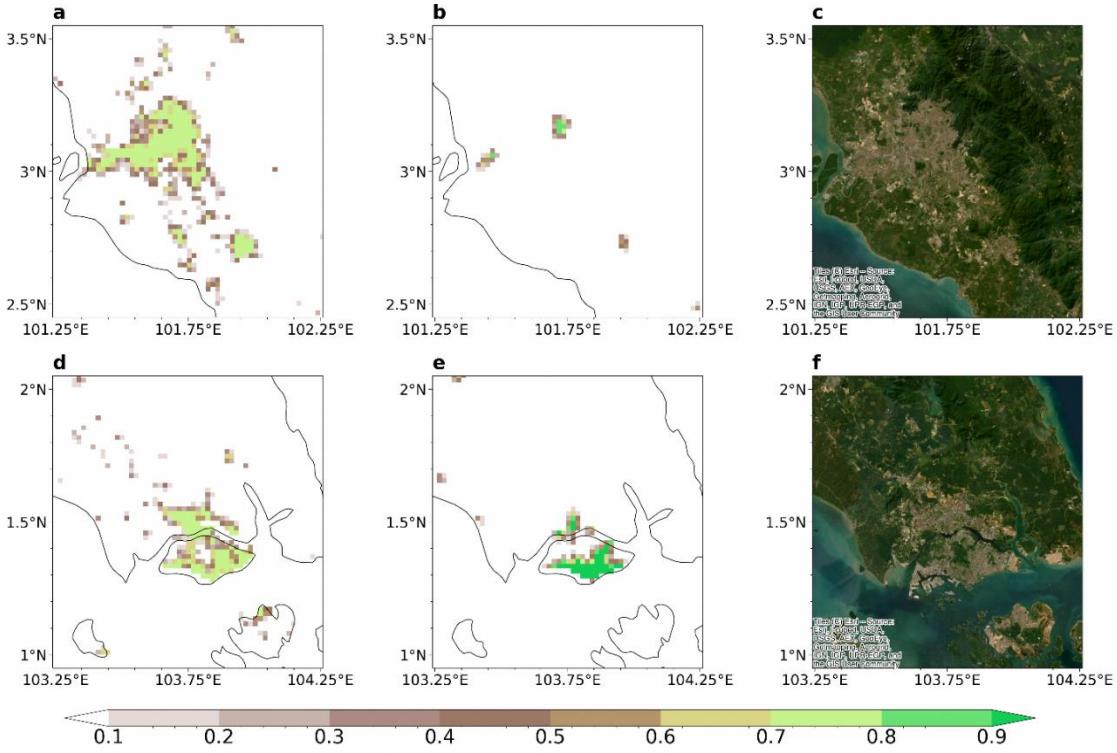

Figure 6.4: Urban Land fraction comparison. a) CCI data for Kuala Lumpur, b) IGBP data for Kuala Lumpur, c) Satellite image for Kuala Lumpur, d) CCI data for Singapore, e) IGBP data for Singapore, f) Satellite image for Singapore. Units in fractions.

CCI data corrects the land use and land cover fraction in IGBP, as it is the latest improved version of land use and land cover fraction data available on a continental scale. We notice less broad leaf fraction in the CCI data over our region compared to IGBP; IGBP shows more vegetation fraction over Indonesia and less over Malaysia, while CCI is vice versa Figure 6.3 (a, b). But in the urban tile, CCI data has captured the urban extent of Kuala Lumpur much better than the IGBP data compared to satellite map as shown in Figure 6.4 (a, b, c) and the urban extent of Singapore and Johor Bahru much better than the IGBP data compared to satellite map as shown in Figure 6.4 (d, e, f). Overall, the CCI data is a more improved data compared to IGBP. Considerable differences are noted in the representation of vegetation fraction as well as in the urban tile in these two datasets, CCI-data has shown improved representation of urban extent.

We studied the impact of vegetation + non vegetation fraction ancillary changes in the model simulations and noted only marginal improvements in the model precipitation simulation (Figure 6.6a) due to the length of the simulation being a short run (one month long); while a long-term simulation for over 30-year period might have a significant change from modifying the IGBP land use data (vegetation + non vegetation fraction) to CCI land use data (vegetation + non vegetation fraction) (Figure 6.3a, b, Figure 6.4a, b and Figure 6.4d, e).

The orography of the 2km model clearly brings out the finer details of the orographic height compared to the 8km smoothed orography over the region as shown in Figure 6.5 (a, b). Precipitation is less intense with smoothed orography; the impact of high-resolution orography is visible in the vicinity of areas with high orography (Figure 6.6b). Rainfall intensity is increased in the run with better resolved orography (Figure 6.6b) which is in accord with the earlier findings (Sethunadh et al. 2019).

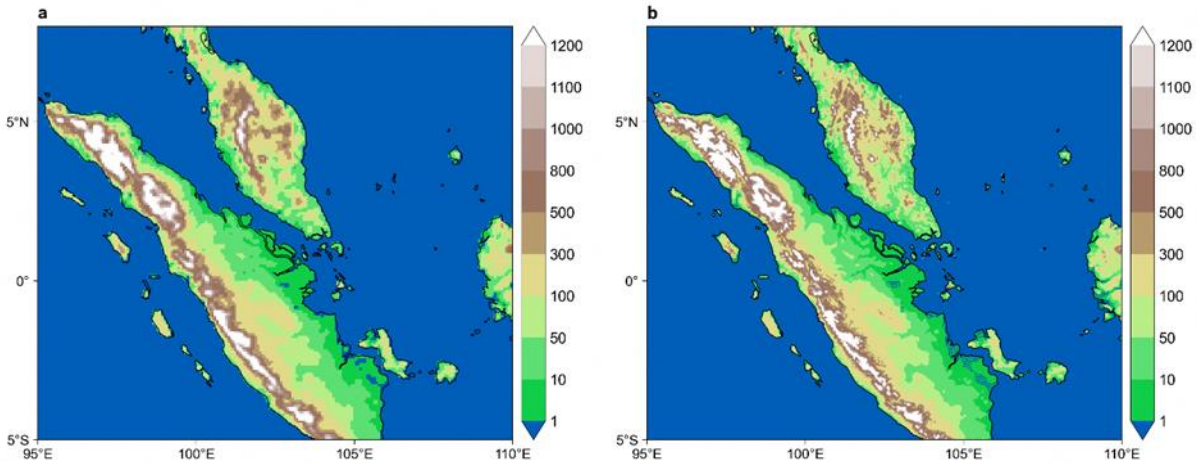

Figure 6.5: Coarse grid resolution (8 km) vs. fine grid resolution (2 km) orography. Units in m.

The orography over the Singapore domain (SG) tested with an 8km smoothed orography and a fine grid resolution of 2km orography and found only marginal improvements in the model precipitation simulation over the Indonesian and Malaysian regions due to the length of the simulation being only one month long (Figure 6.6 b). Previous studies have also noted the importance of the interaction between landmasses, low-level flow, with orography, to capture the diurnal cycle and the development of heavy rainfall events over peninsular Malaysia and Sumatra Island (Nor et al. 2020).

Tan et al. (2020) explored the role of topography on a Madden–Julian Oscillation (MJO) event in the Maritime Continent (MC) using a regional model and found that low-resolution simulations with its inadequate representation of topography combined with the deficiency from cumulus parameterisation have difficulty in simulating MJO across the MC and suggested that the improvement in the simulated MJO in the high horizontal-resolution compared to the low horizontal-resolution model may come, not only from the absence of cumulus parameterisation, but also from the better representation of topography in higher resolution simulation.

6.3.3 Updating Model forcing fields (ERA5 vs ERA-I)

We also looked at the SINGV-RCM precipitation biases (Figure 6.6c), if any systematic difference in precipitation bias arise in the ERA5 newer reanalysis (~30km) driving fields versus the older version of reanalysis ERA-Interim (~75km) driving fields, no systematic differences are evident as we can only observe noisy pattern emerge from the differences between ERA5 and ERAI forced runs (Fig. 6.6c).

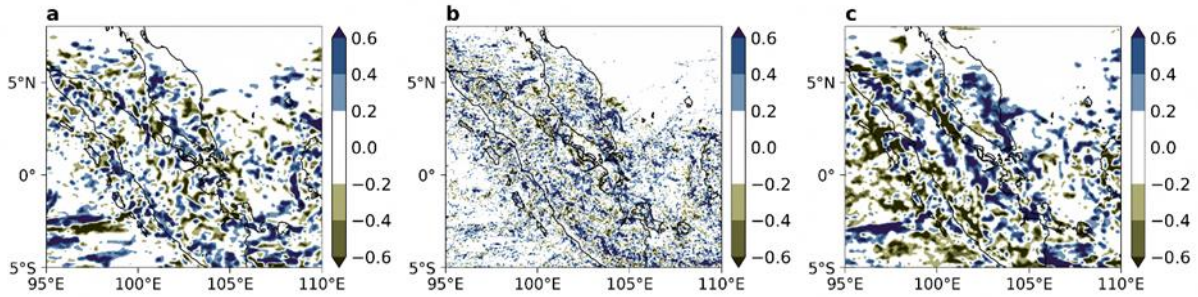

Figure 6.6: (a) Impact on Precipitation difference (CCI – IGBP ancillaries), (b) Impact on Precipitation difference (2 km Orography – smoothed 8 km orography), (c) Impact on Precipitation difference (ERA5 – ERA-Int.) Units in mm/hr.

6.3.4 Changes to the vertical resolution of the forcing field data

Most of the CMIP6 model data are coarsely resolved in the vertical as compared to SINGV-RCM that uses 80 levels up to z = 38.5 km. Vertical interpolation of driving data to higher resolution are known to produce model biases. To get an understanding of expected model bias in the future climate projections due to the loss of vertical resolution in the driving data, we compared the simulations driven using ERA5 data with full (137) vertical levels and the simulation with only 37 levels in the vertical against the ERA5 reanalysis. Focus is given to the vertical velocities considering its role driving convection in the region. From the test results, very small differences on large domain (MC) were noted (Figure 6.7a), but more sizeable in the small domain (SG) is evident (Figure 6.7b) between the runs. We also noted that the ERA5 vertical velocities (omega) are much stronger compared to the downscaled ones, this is largely due to reduced convection in SINGV-RCM (Figure 6.7 a, b). The lower boundary condition in ERA5 (i.e. SSTs) also showed colder SST bias with respect to O-I SST (figure not shown) adjacent to the Singapore and Malaysian archipelago compared to the entire Maritime continent domain. Also, studies done by Yang et al (2021) have shown that ERA5 SST product has a colder bias over the maritime continent when compared to the ensemble median of SST products for the period of 1982–2002.

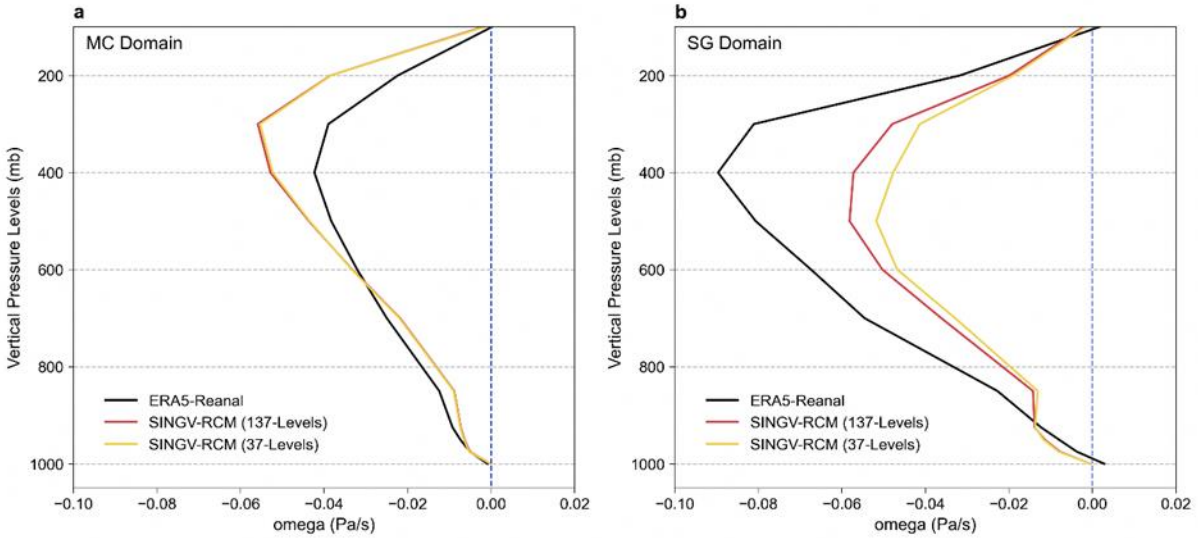

Figure 6.7: Impact of vertical levels in the forcing fields (ERA5-Reanalysis: ~30km, SINGV-RCM: 9 km). SINGV-RCM forced with ERA5-137 levels; vs ERA5-37 levels. a) MC domain b) SG domain. Units in Pa/Sec.

Though the ratio of MC land points to total grids points is 18% compared to the ratio of SG land points to the total grids at 27% (Slightly higher compared to MC domain), one of the reasons for less convection in the SINGV-RCM over the SG domain may be attributed to the colder SSTs seen around the SG domain in the ERA5 driving model, as evidenced by dry precipitation bias prevailing over the SG domain (look at Figure 6.10 a-d and 6.11. a-d, precipitation biases for different grid resolutions) in SINGV-RCM.

6.3.5 Sensitivity to Model grid resolutions

We tested the SINGV-RCM with different model grid resolutions and domain sizes with the MC domain having grid resolutions like only 9km, 8km, 4.5km and the SG-domain having additional grid resolutions like 2 km, 1.5km respectively. Figure 8 shows the area averaged diurnal precipitation cycle over the common and overlapping grid resolutions for MC and SG domains area bound by the dashed and dotted boxes shown in Figure 6.1.

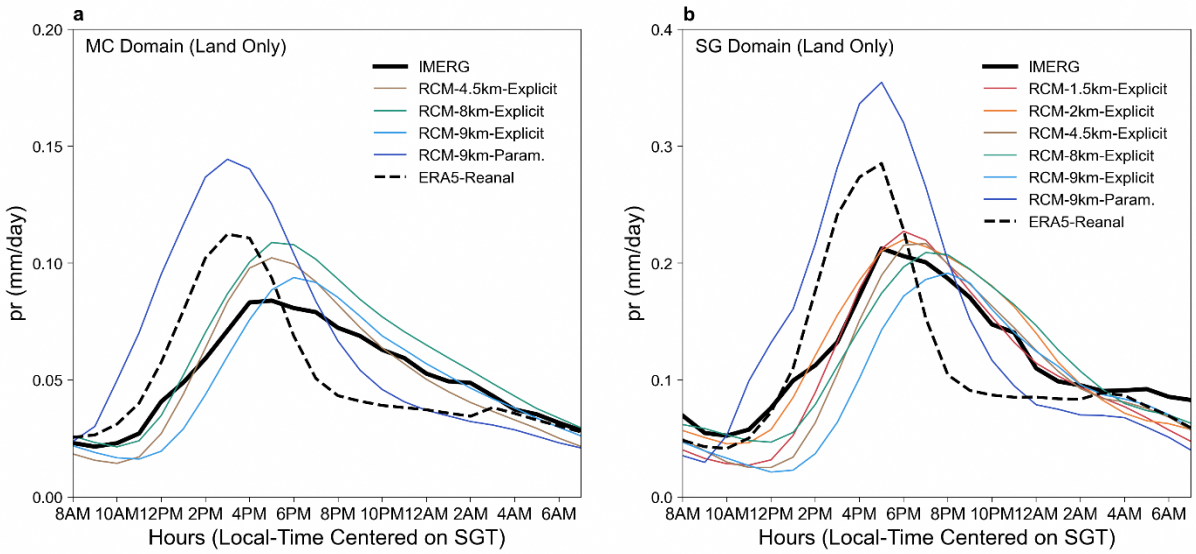

Figure 6.8: Diurnal cycle of Precipitation area averaged over MC and SG domains. The MC-domain (9 km, 8 km, 4.5 km) and the SG-domain (9 km, 8 km, 4.5 km, 2 km, 1.5 km). Units in mm/hr.

We notice from the Figure 6.8a that SINGV-RCM with explicit representation of convection is able to capture the diurnal cycle of precipitation close to observation (IMERG). While the ERA5 driving model and 9km parameterised runs show earlier diurnal peak than the observed. The results are quite similar for SG domain as well (Figure 6.8b).

High grid resolution runs of 2km and 1.5km have a better diurnal peak timing as well as intensity compared to coarse grid resolution simulations of 9km, 8km and 4.5km, this may be due to the fact that, it takes longer for the system to work up enough energy to lift a larger grid box when having to convect on that grid scale.

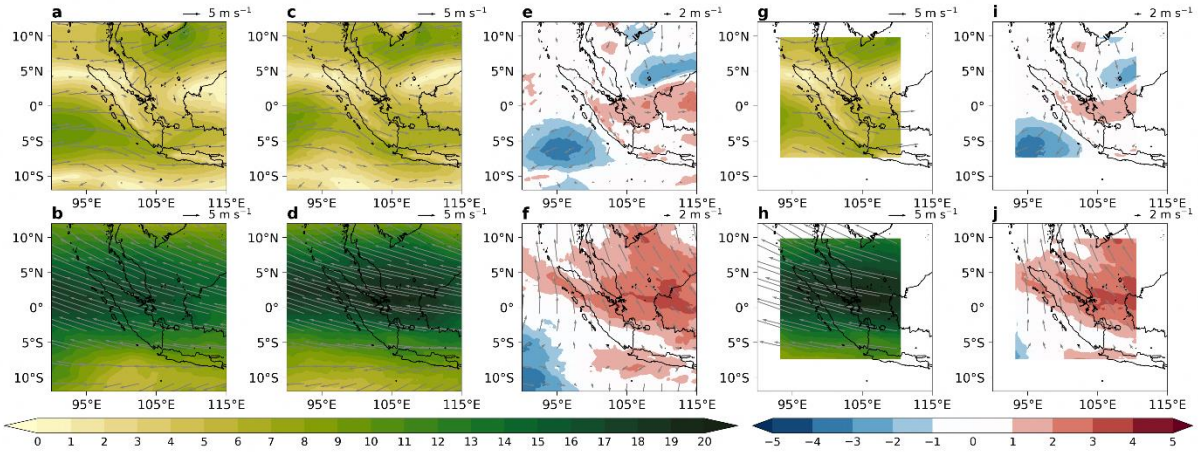

Figure 6.9: Mean simulated Circulation (850hPa and 200hPa) and bias w.r.to ERA5 for SINGV-5.0 version for 8 km & 2km resolutions. Mean circulation (a. ERA5-850hPa winds, b. ERA5-200hPa winds c. 8km-850hPa winds, d. 8km-200hPa winds, g. 2km-850hPa winds, h. 2km-200hPa winds) and bias in the circulation (e. 8km-ERA5 for 850hPa, f. 8km-ERA5 for 200hPa, i. 2km-ERA5 for 850hPa, j. 2km-ERA5 for 200hPa). Units in m/s.

From Figure 6.8, we found that the precipitation features for different resolutions look quite consistent. Meanwhile, we wanted to examine how the circulation features (Two upper levels: 850 hPa and 200 hPa) are simulated after downscaling to 8 km from the driving model (ERA5) and then from 8 km to 2 km resolution. Therefore, we plotted the mean circulation feature changes over the MC domain from 8 km and 2 km simulation with ERA5. We notice from the Figure 6.9 (ERA5, SINGV-RCM and differences at 2 different levels: 850hPa and 200hPa) that SINGV-RCM exhibit negative bias in the 850hPa to the East of Malaysian peninsula and positive bias over regions close to south of Indonesia and Borneo (Figure 6.9e [8km] and Figure 6.9i [2km]). While the SINGV-RCM exhibits positive bias in the 200hPa over the entire region covering more than 50% western maritime continent (Figure 6.9f [8km] and Figure 6.9j [2km]). But nevertheless, the large-scale pattern for 850hPa and 200hPa wind circulation after downscaling from ERA5 to 8km and to 2km looks quite similar to the driving model ERA5 (Figure 6.9 a-d and g, h).

6.4 Evaluation of SINGV-RCM over Southeast Asia

The SINGV-RCM model's ability in simulating the climate realistically arises from the model itself: e.g., dynamical core or physical parameterisations and the skill of the driving model in the region through Lateral Boundary Condition (LBC) and surface condition (SST). Therefore, evaluation of the model simulations of SINGV-RCM shall include diurnal cycles of rainfall, the Probability Distribution Functions (PDFs) of model simulated rainfall with focus on extremes, spatial model biases of mean rainfall and to evaluate the models' performance over two domains, Maritime Continent (MC) domain and Singapore (SG) domain and for different grid resolutions.

6.4.1 Mean precipitation

In terms of the mean precipitation biases, we notice dry bias close to Singapore is large in the parameterised run (Figure 6.10a) compared to the explicit run (Figure 6.10b). For the other explicit runs like 4.5km (Figure 6.10c) and 8km (Figure 6.10d) over the MC domain, the biases are quite similar and the dry bias decreases from coarse grid resolution to high grid resolution around the Singapore-Malaysia region.

The mean precipitation averaged over the MC-domain for GPM-IMERG Precipitation is 0.29 mm/hr. The Mean, Bias, PCC and RMSE with respect to IMERG for each simulation is shown at the top of each figure panel (Figure 6.10a-d). Generally, the Bias value decreases and pattern correlation coefficient (PCC) increases, when moving from Parameterisation to Explicit convection and to higher grid resolution (9km-Param. 9km-explicit and 4.5km-explicit) in SINGV-RCM (Figure 6.10a-c). The Bias becomes slightly positive for the 8km simulation over the MC domain with highest PCC over the MC domain (Figure 6.10d)

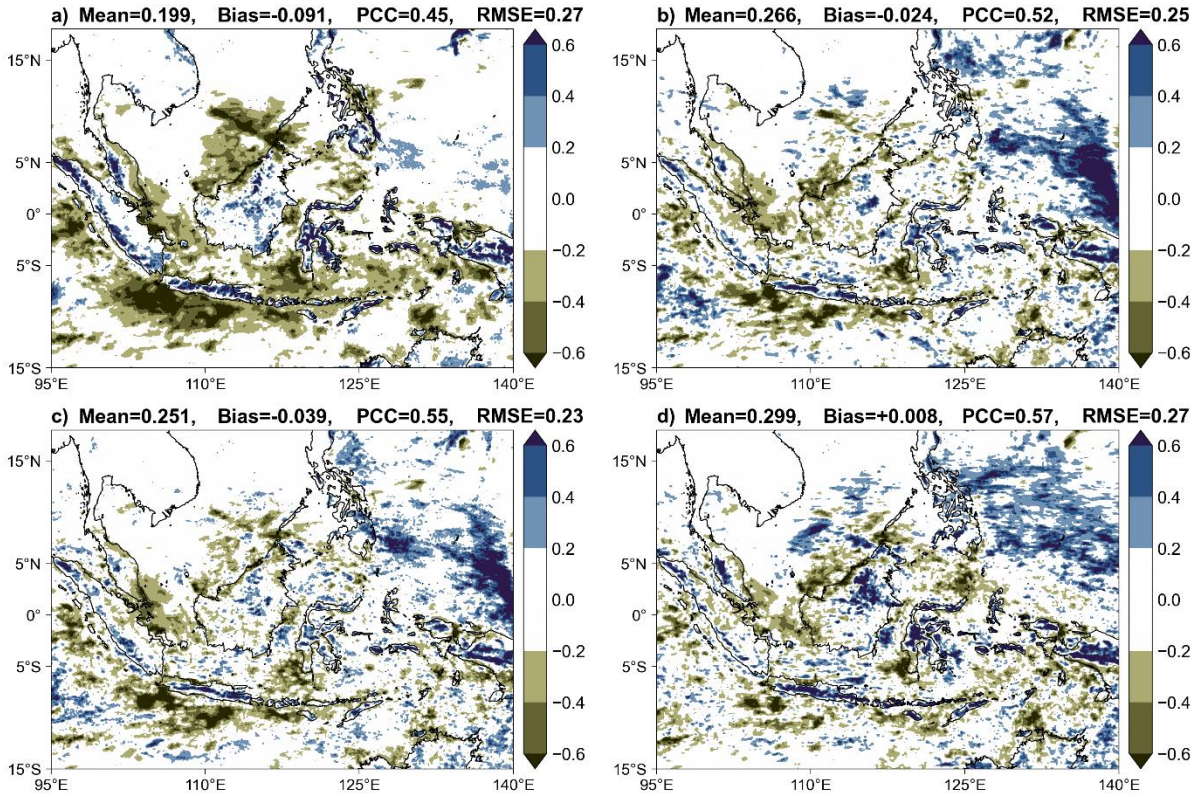

Figure 6.10: Mean simulated Precipitation bias w.r.to GPM-IMERG for SINGV-4.1 version for 9 km (a. Parameterised, b. Explicit), c. 4.5 km (Explicit) and for SINGV-5.0 version d. 8 km (Explicit) simulations over the MC-domain downscaled from ERA5 driving model. Units in mm/hr. GPM-IMERG Precipitation mean for the domain is 0.29 mm/hr.

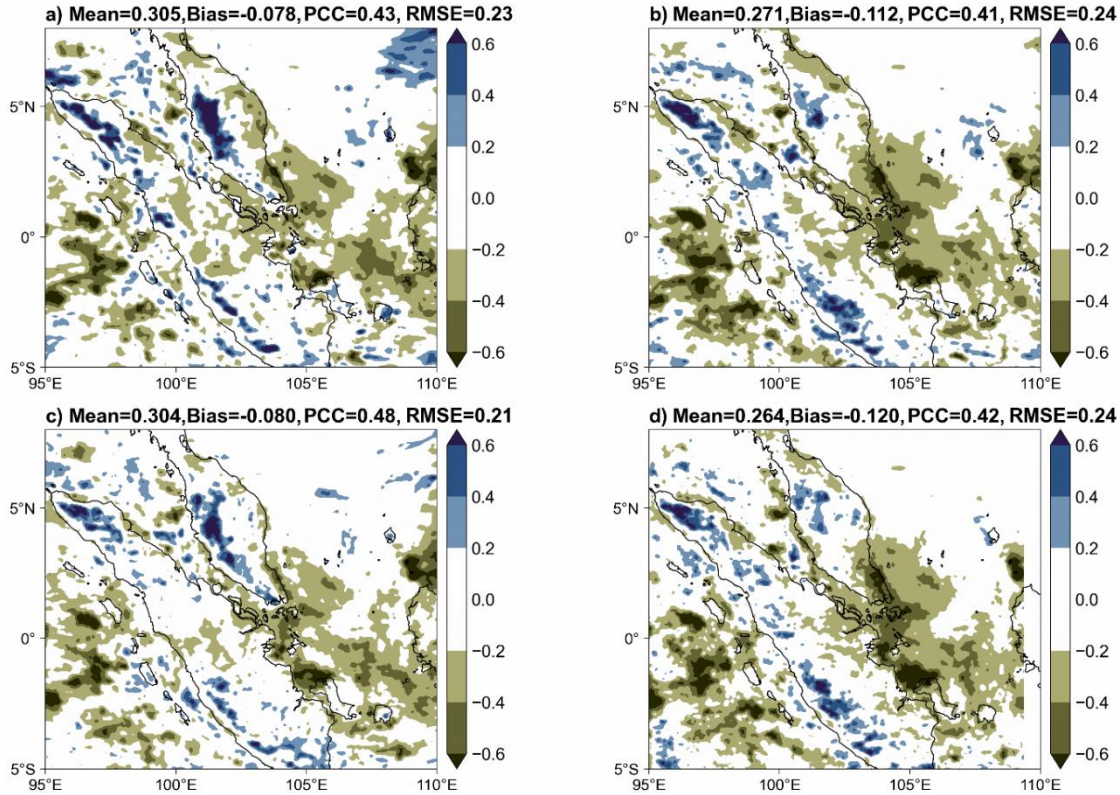

Figure 6.11: Mean simulated Precipitation bias w.r.to GPM-IMERG for SINGV-5.0 version (a) 8 km, (c) 2 km and for SINGV-4.1 version (b) 4.5 km (d) 1.5 km simulations over the SG-domain downscaled from ERA5, 8 km-Explicit, 9 km-Explicit and 4.5 km-Explicit SINGV-RCM simulations, respectively. Units in mm/hr. GPM-IMERG Precipitation mean for the domain is 0.385 mm/hr.

Even the high-grid resolution simulations like 2 km (Figure 6.11c) and 1.5 km (Figure 6.11d) for the smaller domain around Singapore (SG) domain downscaled from 8 km (Figure 6.11a) and 4.5 km (Figure 6.11b) larger MC domain show dry bias close to Singapore (SG) domain. The new version SINGV5.0 has less dry bias around SG domain compared to the older version SINGV4.1, which supports the use of newer version of SINGV-RCM for the V3 study.

The mean precipitation averaged over the SG-domain for GPM-IMERG Precipitation is 0.385mm/hr. The Mean, Bias, PCC and RMSE with respect to IMERG for each simulation is shown at the top of each figure panel (Figure 6.11a-d). Generally, the Bias value does not change much, and pattern correlation coefficient (PCC) increases slightly, when moving from lower grid resolution to higher grid resolution (4.5km-explicit and 1.5km-explicit) in SINGV-RCM (Figure 6.11b and Figure 6.11d) and also for the 8km and 2km simulation over the SG domain (Figure 6.11a and Figure 6.11c)

The biases in simulations using 4.5 km grid resolution SINGV4.1 (Figure 6.10c) and 8 km SINGV 5.0 (Figure 6.10d) are relatively similar compared to that in the parameterised simulation (Figure 6.10a) suggesting that mean features of the rainfall can be captured relatively well even at 8 km grid resolution with explicit treatment of convection, which is computationally less demanding than the 4.5 km resolution, suggesting that there is no major detriment to the rainfall simulation when allowing explicit treatment of convection even at 8km grid resolution.

6.4.2 Diurnal representation of Precipitation

In this section the area-averaged mean diurnal cycle over land-only grid points of area bound by MC and SG domains are discussed in detail. We notice (see Figure 6.12a) a clear advantage of using 8km explicit representation of convection over the Maritime continent (MC) domain in comparison to ERA5 reanalysis, which uses convection parameterisation at 30 km grid resolution".

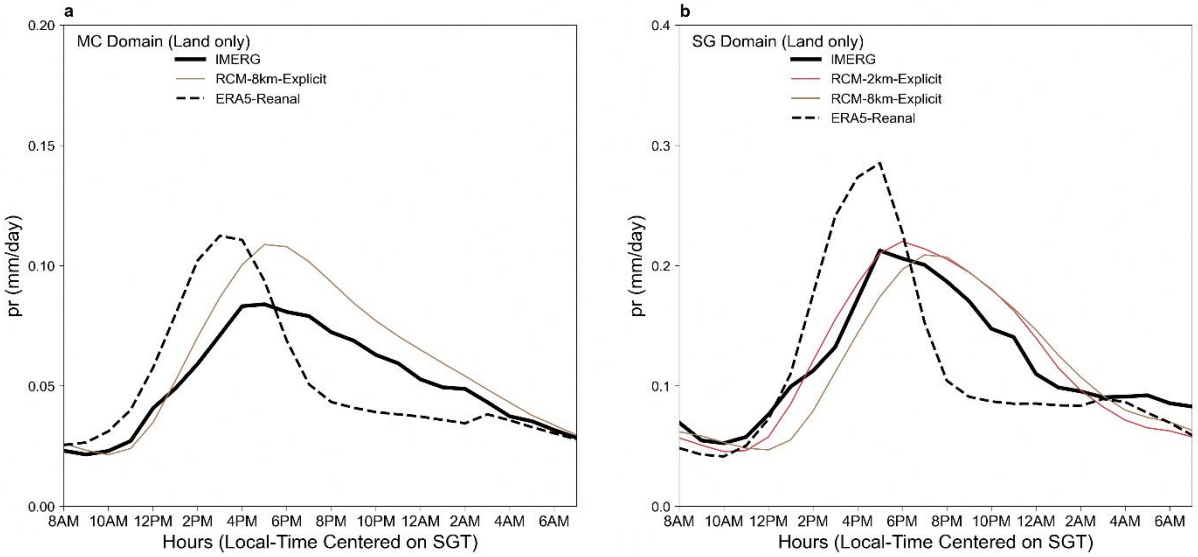

Figure 6.12: Diurnal cycle of Precipitation area averaged over land-only grids for MC and SG domains. Units in mm/hr.

It is noted that that the diurnal peak of precipitation in the ERA5 driving model is at least couple hours earlier than the observed GPM-IMERG over the area averaged over the entire land-points of MC domain, though the precipitation intensity in the SINGV-RCM is higher than the observed, the peak diurnal timing is well captured by the model over the MC domain. Similarly, from Figure 6.12b, we notice that the diurnal precipitation in ERA5 starts vigorously at least a couple hours earlier when compared GPM-IMERG. Even the rainfall intensity in ERA5 is substantially high. In SINGV-RCM, on the other hand, both precipitation intensity and phase are closer to the observation. As expected, this

correspondence with observation is better captured at 2 km grid resolution.

Figure 6.13 shows the spatial variation in the timing of the diurnal rainfall peak over SG domain compared to GPM-IMERG data at each grid point. Figure 6.13a shows the time of diurnal peak for each grid from GPM-IMERG for the analysis period, Jan 2001, Figure 6.13b is for the ERA5 reanalysis, we can notice that the diurnal timing over both land and Ocean grids points from the ERA5 reanalysis does not match with the observed IMERG. But there is a marginal improvement in the SINGV-RCM parameterised run at 9km (Figure 6.13c) compared to the driving model ERA5 reanalysis. While the explicit representation of convection run of SINGV-RCM at 9km (Figure 6.13d) is closer to the observed GPM-IMERG Peak timing of diurnal precipitation (Figure 6.13a).

We can also notice gradual improvement in the diurnal peak precipitation timing as we go from coarse-grid resolution to high-grid resolution simulations of SINGV-RCM 8km-explicit (Figure 6.13e), 4.5km-explicit (Figure 6.13f), 2km-explicit (Figure 6.13g) and 1.5km-explicit (Figure 6.13h). It is clear from these experiments that the explicit representation of convection combined with improved grid resolution corrects the diurnal cycle of precipitation over the Singapore domain.

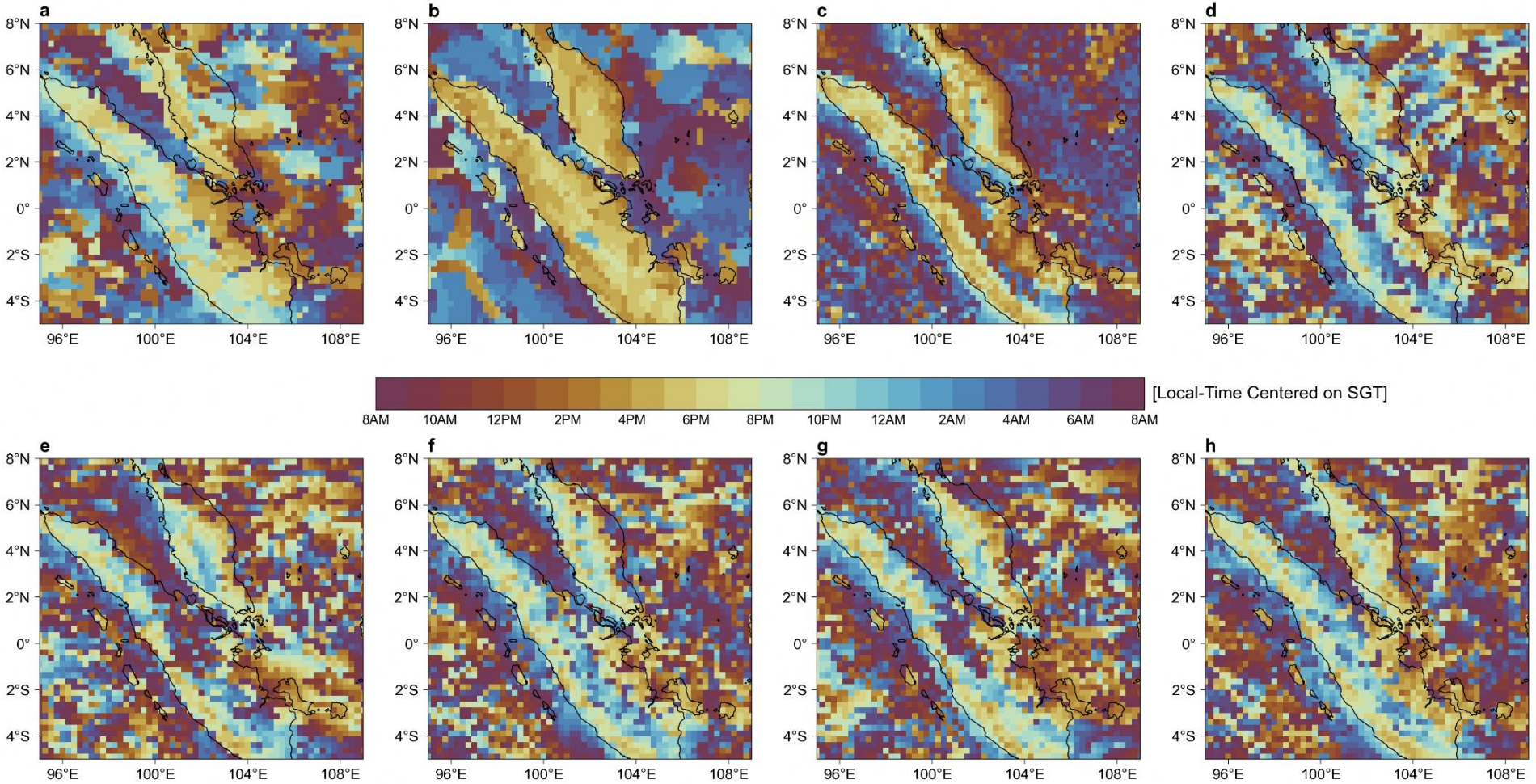

Figure 6.13: Spatial map of Peak Diurnal timing of Precipitation. a) IMERG, b) ERA5-Reanal., c) 9 km-Parameterised, d) 9 km-Explicit, e) 8 km-Explicit, f) 4.5 km-Explicit, g) 2 km-Explicit and h) 1.5 km-Explicit. Units in hour (UTC).

6.4.3 Representation of precipitation extremes

In this section the distribution of 95-percentile extremes at each grid point in the SINGV-RCM simulations for different model grid resolutions.

Figure 6.14a shows the 95-percentile extreme threshold value at each grid point from the observed GPM-IMERG data. Figure 6.14b to 6.14h show the 95-percentile extreme bias value at each grid point with respect to observed GPM-IMERG data. Figure 6.14b shows the bias for ERA5 reanalysis, dry bias is evident at every grid point, which means the driving model ERA5 is not able to get extreme rainfall above the 95 percentile threshold over the Singapore domain, but the SINGV-RCM parameterised run at 9km shows some improvement over a fewer grids (Figure 6.14c), while the SINGV-RCM 9km-explicit run shows positive bias over the majority of grid-points (Figure 6.14d). The positive bias in the 95-percentile extreme rainfall either intensifies or reduces from coarse-grid resolution to higher-grid resolution thereby becoming closer to the observation; SINGV-RCM 8km-explicit (Figure 6.14e), 4.5km-explicit (Figure 6.14f), 2km-explicit (Figure 6.14g) and 1.5km-explicit (Figure 6.14h), which is an added value of downscaling to very-high grid resolution over the Singapore domain. We have regridded the data to the lower resolution (25km), before calculating and differencing the percentiles.

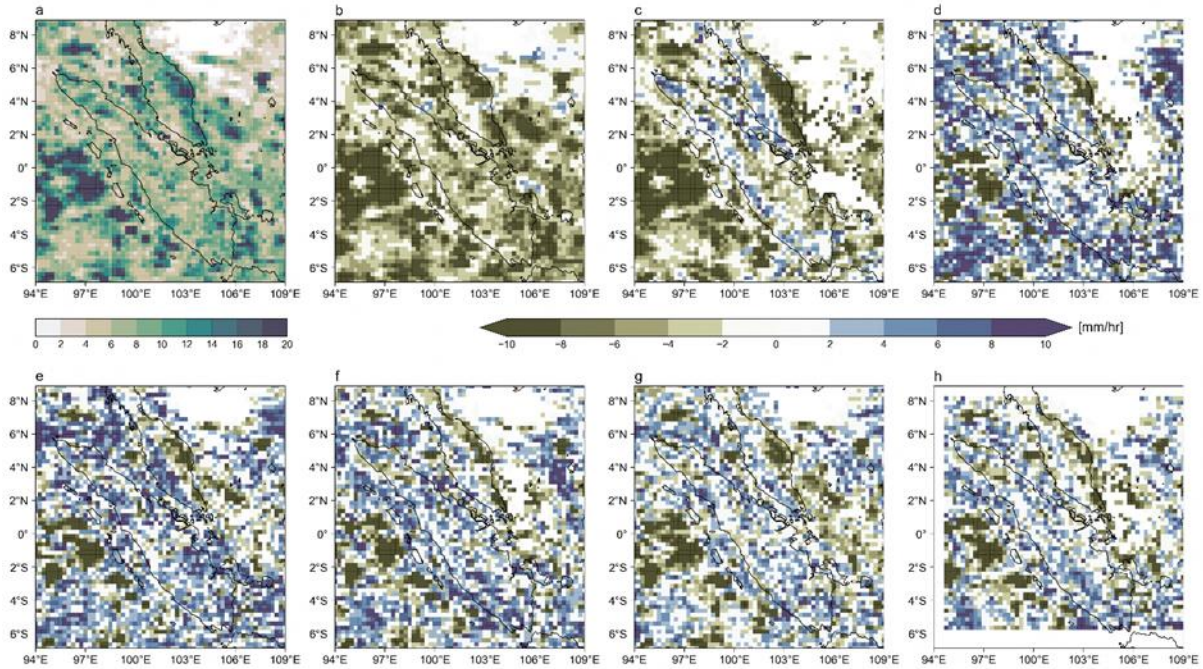

Figure 6.14: Extreme Precipitation a) 95-percentile threshold value for GPM-IMERG and rest are precipitation bias w.r.to IMERG. b) ERA5-Reanal, c) 9 km-Parameterised, d) 9 km-Explicit, e) 8 km-Explicit, f) 4.5 km-Explicit, g) 2 km-Explicit and h) 1.5 km-Explicit. Units in mm/hr.

6.4.4 Frequency Distribution of Precipitation in SINGV-RCM

The frequency distribution of rainfall between the GPM-IMERG observation and the SINGV-RCM simulations over the SG-domain for the entire period is shown in Figure 6.15. The results reveal that SINGV-RCM parameterised convection, though estimates better the light rainfall compared to the GPM-IMERG in the range of 0–1 mm/hr., but underestimates moderate and moderately high rainfalls, in the ranges 5-10 and 10–25 mm/hr., respectively. It is encouraging to see that the SINGV-RCM is close to the GPM-IMERG observation in estimating the 5-10 and 10-25 mm/hr ranges in all explicit-run grid resolutions. Heavy rainfalls in the range of 25-100 mm/hr; model is always lower than GPM-IMERG and no precipitation in the ranges above 100mm/hr. The explicit representation of convection in the model configuration simulates moderate rain rates better than the light rainfall rates, irrespective of model grid resolution and the parameterised convection simulation tend to predict better the light rainfall rates at the expense of heavy rainfall events (under-predicts above 5mm/hr).

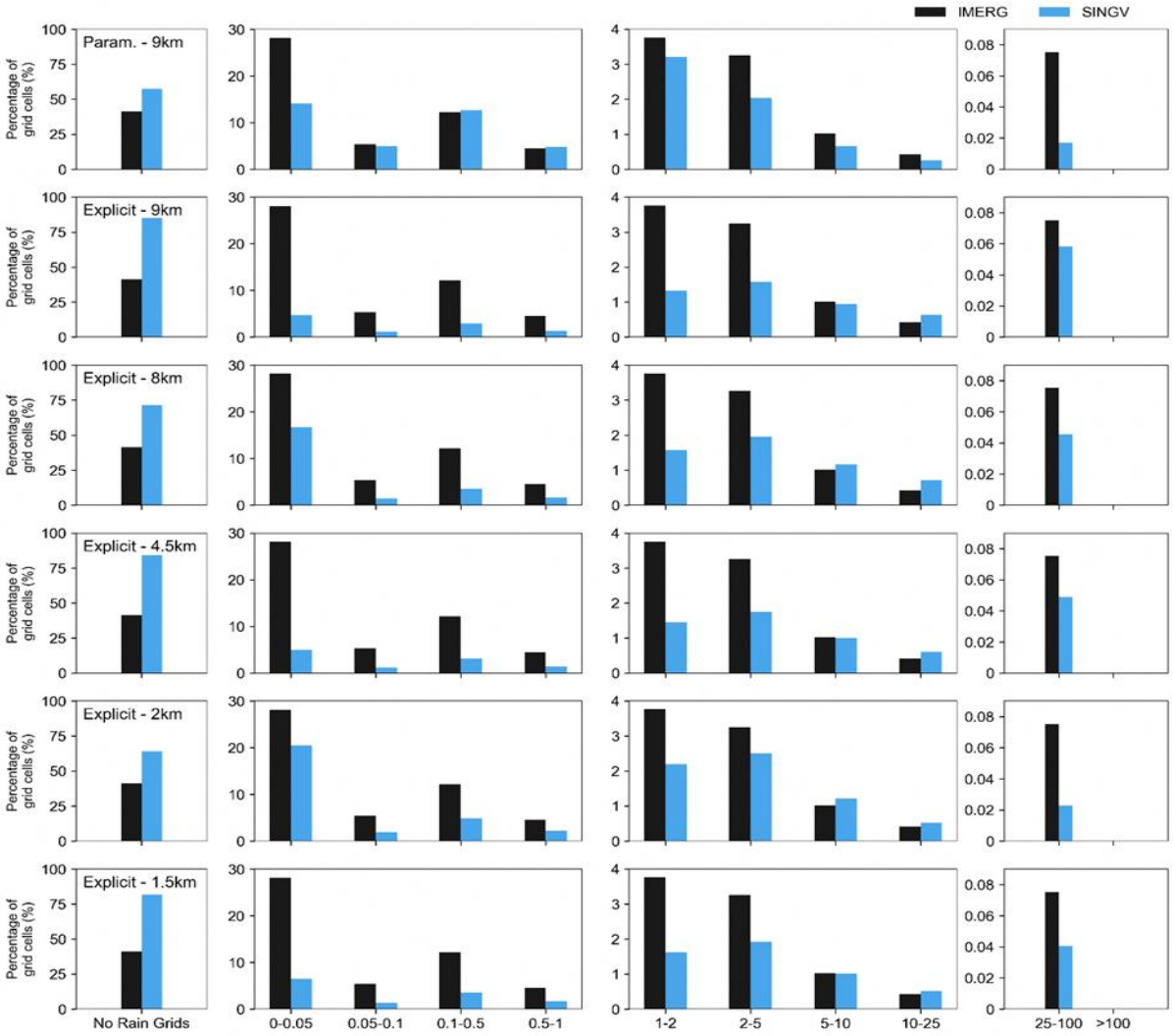

Figure 6.15: Distribution of rain rate over the grids with the older (SINGV-4.1) as well as newer (SINGV-5.0) version of SINGV-RCM with Parameterised vs explicit representation of convection at 9 km and high-grid resolution grids at 8 km, 4.5 km, 2 km and 1.5 km. Units in mm/hr.

6.4.5 Parameterised vs explicit representation of Convection

We performed simulations of both explicit and parameterised representation of convection at 9km grid resolution and we found that the explicit run is able to capture the peak diurnal timing better than the parameterised one in the area averaged profile (Figure 6.8 a, b) and in the spatial diurnal timing map (Figure 6.13c, d) compared to GPM-IMERG (Figure 6.13a). In the mean precipitation bias as well, we see the dry bias close to Singapore is large in the parameterised run (Figure 6.10a) compared to the explicit run (Figure 6.10b). For the extreme precipitation (95 percentile threshold), the parameterised-9km run 95 percentile precipitation bias (Figure 6.14c) shows large dry bias, while the explicit-9km run for 95 percentile precipitation bias (Figure 6.14d) shows reduced dry bias near the Singapore domain. We also found the parameterised one has too much light rain and less moderate and intense rainfall from the distribution analysis (Figure 6.15) compared to the other explicit grid resolutions.

6.5 Summary

We have modified the SINGV NWP model to SINGV-RCM that is fit for purpose to carry out long term climate simulations. In the process we tested SINGV-RCM with different grid resolutions 9km, 8km, 4.5km for MC domain and 2km and 1.5km over the SINGV domain and found the results are robust for both domains in

terms of capturing mean and diurnal cycle of precipitation with both earlier and newer version of SINGV-RCM. Multiple experiments performed with SINGV as an RCM proves the suitability of SINGV-RCM for the V3 study as SINGV as benefitted from the development of different SINGV versions developed over the Singapore region (Regional Tropical atmosphere version).

SINGV-RCM at different grid resolutions with explicit representation of convection performed better than the convection parameterised version at 9km grid resolution. We noted the biggest step change in performance when explicit convection is used even at coarse grid resolution. The SINGV-RCM with explicit convection has shown better diurnal cycle timing and intensity compared to the convection parameterised version with respect to GPM-IMERG precipitation data. This result of daily timing of maximum precipitation is better captured when the convection is explicit strongly suggests that even at a very coarse grid resolution of 9km or 8km, the model is already "convection-enabling" and is performing better without the convection parameterisation (Birch et al. 2016) . Furthermore, this result is consistent with other studies for Western Africa using the UM model with a 4.5km horizontal grid resolution (e.g., Berthou et al. 2019) and for the Western maritime Continent using the WRF model (Argueso et al. 2020).

We also noted better distribution of rainfall intensities (less light rain, more heavy rain). 2 km is not statistically different to 8 km-explicit over a large domain (little sensitivity to grid resolution). To balance between very high computation cost and longer/more simulations to capture uncertainty range, we may still need 2 km time slice simulations over the smaller Singapore domain in the future projection simulations for specific agency applications.

Following are some of the key summary points from this study:

1) As part of development of SINGV-RCM, we ingested the SST at a 3-hour cycle to represent the Diurnal cycle of SST over the region.

2) We modified IGBP-LULC to high-grid resolution CCI-LULC for ancillary preparation.

3) Also, we found improvements in precipitation simulation with grid resolution increase and a better representation of Orography over the region with increased grid resolution of the model.

4) We also conducted test runs with Convection parameterisation adopted from GA7 physics and explicit experiments at 9km and found that the explicit run captured the diurnal timing better than the parameterised one, which encouraged us to push the explicit representation of convection to 8km or 9km grid resolution considering the merits of reduced computational requirements.

5) We also performed high-grid resolution simulations of 2km and 1.5km for a smaller domain and found to be consistent with the larger domain simulations, we could notice added value in terms of precipitation simulation with respect to GPM-IMERG observations, which also finds usefulness in other downstream application studies.

6) We found the explicit versions of the SINGV-RCM simulations are able to capture the higher threshold precipitation rates compared to lower precipitation range bins as evidenced from the precipitation distribution analysis.

7) We have clearly shown that the added value of downscaling from the driving model (ERA-5) to 8km and 2km, will augur best possible downscaling setup for simulation with CMIP6 models for V3 studies, which goes into various climate change applications over the Singapore region.

Key findings from this study are:

- Explicit convection setting is better than parameterised due to the fact that the improvement is notable when moving from parameterised to explicit convection in the timing of the diurnal cycle, which has the potential to improve other aspects of the simulation through feedbacks on the radiative fluxes and circulation (Birch et al 2016)
- the gain by switching convection off is more than increasing resolution from 8km to 4.5km
- simulations at 2 km adds value over 8km.

References

Argüeso D, Romero R, Homar V (2020) Precipitation Features of the Maritime Continent in Parameterised and Explicit Convection Models. J Clim 33:2449–2466. https://doi.org/10.1175/JCLI-D-19-0416.1

Ban N, Schmidli J, Schär C (2014) Evaluation of the convection-resolving regional climate modeling approach in decade-long simulations. Journal of Geophysical Research: Atmospheres 119:7889–7907. https://doi.org/10.1002/2014JD021478

Berthou S, Rowell DP, Kendon EJ, et al (2019) Improved climatological precipitation characteristics over West Africa at convection-permitting scales. Clim Dyn 53:1991–2011. https://doi.org/10.1007/s00382-019-04759-4

Best MJ, et al (2011) The Joint UK Land Environment Simulator (JULES), model description. Part I: Energy and water fluxes. Geosci Model Dev 4:677–699

Birch CE, Parker DJ, Marsham JH, et al (2014) A seamless assessment of the role of convection in the water cycle of the West African Monsoon. Journal of Geophysical Research: Atmospheres 119:2890–2912. https://doi.org/10.1002/2013JD020887

Birch CE, Roberts MJ, Garcia-Carreras L, et al (2015) Sea-Breeze Dynamics and Convection Initiation: The Influence of Convective Parameterisation in Weather and Climate Model Biases. J Clim 28:8093–8108. https://doi.org/10.1175/JCLI-D-14-00850.1

Birch CE, S. Webster S, Peatman SC, et al (2016) Scale Interactions between the MJO and the Western Maritime Continent. J Clim 29:2471–2492. https://doi.org/10.1175/JCLI-D-15-0557.1

Boutle IA, Beare RJ, Belcher SE, et al (2010) The Moist Boundary Layer under a Mid-latitude Weather System. Boundary Layer Meteorol 134:367–386. https://doi.org/10.1007/s10546-009-9452-9

Boutle IA, Eyre JEJ, Lock AP (2014) Seamless Stratocumulus Simulation across the Turbulent Gray Zone. Mon Weather Rev 142:1655–1668. https://doi.org/10.1175/MWR-D-13-00229.1

Boutle IA, Finnenkoetter A, Lock AP, Wells H (2016) The London Model: forecasting fog at 333 m resolution. Quarterly Journal of the Royal Meteorological Society 142:360–371. https://doi.org/10.1002/qj.2656

Bush M, Allen T, Caroline Bain, Boutle I, Edwards J, Finnenkoetter A, Franklin C, Hanley K, Lean H, Lock A, Manners J, Mittermaier M, Morcrette C, North R, Petch J, Short C, Vosper S, Walters D, Webster S, Weeks M, Wilkinson J, Wood N, Zerroukat M (2019) The first Met Office Unified Model/JULES Regional Atmosphere and Land configuration, RAL1. Geosci Model Dev. https://doi.org/10.5194/gmd-2019-130.

Charney JG, and Phillips NA (1953) Numerical integration of the quasi-geostrophic equations for barotropic and simple baroclinic flows. J Meteor, 10:71–99

Dipankar A, Webster S, Huang X-Y, Doan VQ (2019) Understanding Biases in Simulating the Diurnal Cycle of Convection over the Western Coast of Sumatra: Comparison with Pre-YMC Observation Campaign. Mon Weather Rev 147:1615–1631. https://doi.org/10.1175/MWR-D-18-0432.1

Dipankar A, Webster S, Sun X, et al (2020) SINGV: A convective-scale weather forecast model for Singapore. Quarterly Journal of the Royal Meteorological Society 146:4131–4146. https://doi.org/10.1002/qj.3895

Doan Q, Dipankar A, Simón-Moral A, et al (2021) Urban-induced modifications to the diurnal cycle of rainfall over a tropical city. Quarterly Journal of the Royal Meteorological Society 147:1189–1201. https://doi.org/10.1002/qj.3966

Edwards JM, Slingo A (1996) Studies with a flexible new radiation code. I: Choosing a configuration for a large-scale model. Quarterly Journal of the Royal Meteorological Society 122:689–719. https://doi.org/10.1002/qj.49712253107

Eyring V, Bony S, Meehl GA, et al (2016) Overview of the Coupled Model Intercomparison Project Phase 6 (CMIP6) experimental design and organization. Geosci Model Dev 9:1937–1958. https://doi.org/10.5194/gmd-9-1937-2016

Gianotti RL, Zhang D, Eltahir EAB (2012) Assessment of the Regional Climate Model Version 3 over the Maritime Continent Using Different Cumulus Parameterisation and Land Surface Schemes. J Clim 25:638–656. https://doi.org/10.1175/JCLI-D-11-00025.1

Golding BW, Ballard SP, Mylne K, et al (2014) Forecasting Capabilities for the London 2012 Olympics. Bull Am Meteorol Soc 95:883–896. https://doi.org/10.1175/BAMS-D-13-00102.1

Haarsma RJ, Roberts MJ, Vidale PL, et al (2016) High Resolution Model Intercomparison Project (HighResMIP v1.0) for CMIP6. Geosci Model Dev 9:4185–4208. https://doi.org/10.5194/gmd-9-4185-2016

Hariadi MH, van der Schrier G, Steeneveld G, et al (2022) Evaluation of extreme precipitation over Southeast Asia in the Coupled Model Intercomparison Project Phase 5 regional climate model results and HighResMIP global climate models. International Journal of Climatology. https://doi.org/10.1002/joc.7938

Hersbach H, Bell B, Berrisford P, et al (2019) Global reanalysis: goodbye ERA-Interim, hello ERA5. ECMWF Newsletter 159:17–24

Hersbach H, Bell B, Berrisford P, et al (2020) The ERA5 global reanalysis. Quarterly Journal of the Royal Meteorological Society 146:1999–2049. https://doi.org/10.1002/qj.3803

Huang XY, Barker D, Webster S, Dipankar A, Lock A, et al (2019) SINGV–the convective-scale numerical weather prediction system for Singapore. ASEAN Journal on Science and Technology for Development 36(3):81–90

Huffman GJ, Bolvin DT, Nelkin EJ, Tan J (2020) Integrated Multi-satellitE Retrievals for GPM (IMERG). Technical Documentation

Ichikawa H and Yasunari T (2006) Time–Space Characteristics of Diurnal Rainfall over Borneo and Surrounding Oceans as Observed by TRMM-PR. J Clim 19:1238–1260

Kendon EJ, Roberts NM, Fowler HJ, et al (2014) Heavier summer downpours with climate change revealed by weather forecast resolution model. Nat Clim Chang 4:570–576. https://doi.org/10.1038/nclimate2258

Kendon EJ, Roberts NM, Senior CA, Roberts MJ (2012) Realism of Rainfall in a Very High-Resolution Regional Climate Model. J Clim 25:5791–5806. https://doi.org/10.1175/JCLI-D-11-00562.1

Lee JCK, Dipankar A, Huang XY (2021) On the Sensitivity of the Simulated Diurnal Cycle of Precipitation to 3-Hourly Radiosonde Assimilation: A Case Study over the Western Maritime Continent. . Mon Weather Rev 149:3449–3468

Li P, Furtado K, Zhou T, et al (2020a) Convection-permitting modelling improves simulated precipitation over the central and eastern Tibetan Plateau. Quarterly Journal of the Royal Meteorological Society, 147, 1–362. https://doi.org/10.1002/qj.3921

Li P, Furtado K, Zhou T, et al (2020b) The diurnal cycle of East Asian summer monsoon precipitation simulated by the Met Office Unified Model at convection-permitting scales. Clim Dyn 55:131–151. https://doi.org/10.1007/s00382-018-4368-z

Lock AP (2001) The numerical representation of entrainment in parameterisations of boundary layer turbulent mixing. Mon Wea Rev 129:1148–1163

Lock AP, Brown AR, Bush MR, Martin M, and Smith RNB (2000) A new boundary layer mixing scheme. Part I: scheme description and single-column model tests. Mon Wea Rev 128:3187–3199. https://doi.org/10.1175/1520-0493.

Lu J, Li T, Wang L (2021) Precipitation Diurnal Cycle over the Maritime Continent Modulated by the Climatological Annual Cycle. J Clim 34:1387–1402. https://doi.org/10.1175/JCLI-D-20-0130.1

Marsham JH, Dixon NS, Garcia-Carreras L, et al (2013) The role of moist convection in the West African monsoon system: Insights from continental-scale convection-permitting simulations. Geophys Res Lett 40:1843–1849. https://doi.org/10.1002/grl.50347

Mohd Nor MFF, Holloway CE, Inness PM (2020) The Role of Local Orography on the Development of a Severe Rainfall Event over Western Peninsular Malaysia: A Case Study. Mon Weather Rev 148:2191–2209. https://doi.org/10.1175/MWR-D-18-0413.1

Mori S, and Coauthors (2004) Diurnal land–sea rainfall peak migration over Sumatra Island, Indonesian Maritime Continent, observed by

TRMM satellite and intensive rawinsonde soundings. . Mon Wea Rev 132:2021–2039

Ngo-Duc T, Tangang FT, Santisirisomboon J, et al (2017) Performance evaluation of RegCM4 in simulating extreme rainfall and temperature indices over the CORDEX-Southeast Asia region. International Journal of Climatology 37:1634–1647. https://doi.org/10.1002/joc.4803

Nguyen PL, Bador M, Alexander LV, Lane TP and Ngo-Duc T (2022) More intense daily precipitation in cordex-sea regional climate models than their forcing global climate models over south East Asia. . International Journal of Climatology 42:6537–6561

Peatman SC, Matthews AJ, Stevens DP (2014) Propagation of the Madden-Julian Oscillation through the Maritime Continent and scale interaction with the diurnal cycle of precipitation. Quarterly Journal of the Royal Meteorological Society 140:814–825. https://doi.org/10.1002/qj.2161

Peatman SC, Matthews AJ, Stevens DP (2015) Propagation of the Madden–Julian Oscillation and scale interaction with the diurnal cycle in a high-resolution GCM. Clim Dyn 45:2901–2918. https://doi.org/10.1007/s00382-015-2513-5

Peatman SC, Schwendike J, Birch CE, Marsham JH, Matthews AJ and Yan G-Y (2021) A local-to-large scale view of Maritime Continent rainfall: control by ENSO, MJO, and equatorial waves. . Journal of Climate 34 (22):8933–8953

Prein AF, Langhans W, Fosser G, et al (2015) A review on regional convection-permitting climate modeling: Demonstrations, prospects, and challenges. Reviews of Geophysics 53:323–361. https://doi.org/10.1002/2014RG000475

Qian JH (2008) Why Precipitation Is Mostly Concentrated over Islands in the Maritime Continent. Journal of Atmospheric Sciences 65:1428–1441

Sethunadh J, Jayakumar A, Mohandas S, et al (2019) Impact of Cartosat-1 orography on weather prediction in a high-resolution NCMRWF unified model. Journal of Earth System Science 128:110. https://doi.org/10.1007/s12040-019-1133-6

Silva NA, Webber BGM, Matthews AJ, et al (2021) Validation of GPM IMERG Extreme Precipitation in the Maritime Continent by Station and Radar Data. Earth and Space Science 8: https://doi.org/10.1029/2021EA001738

Simón-Moral A, Dipankar A, Roth M, et al (2020) Application of MORUSES single-layer urban canopy model in a tropical city: Results from Singapore. Quarterly Journal of the Royal Meteorological Society 146:576–597. https://doi.org/10.1002/qj.3694

Smagorinsky J (1963) General circulation experiments with the primitive equations. Part 1: The basic experiment. . Mon Wea Rev 91:99–164

Tan H, Ray P, Barrett BS, Tewari M, Moncrief MW (2020) Role of topography on the MJO in the maritime continent: a numerical case study. Climate Dynamics 55:295–314

Timbal B, Prasanna V, Hassim ME (2019) SINGV as a regional climate model to deliver Singapore's 3rd national climate change study. MSS Research Letters

Van Genuchten VMT (1980) A closed-form equation for predicting the hydraulic conductivity of unsaturated soils. . Soil Sci Soc Am J 44:892–898

Wilson DR, Ballard SP (1999) A microphysically based precipitation scheme for the UK meteorological office unified model. Quarterly Journal of the Royal Meteorological Society 125:1607–1636. https://doi.org/10.1002/qj.49712555707

Wilson DR, Bushell AC, Kerr-Munslow AM, et al (2008a) PC2: A prognostic cloud fraction and condensation scheme. I: Scheme description. Quarterly Journal of the Royal Meteorological Society 134:2093–2107. https://doi.org/10.1002/qj.333

Wilson DR, Bushell Andrew C, Kerr-Munslow AM, et al (2008b) PC2: A prognostic cloud fraction and condensation scheme. II: Climate model simulations. Quarterly Journal of the Royal Meteorological Society 134:2109–2125. https://doi.org/10.1002/qj.332

Yang C, Leonelli FE, Marullo S, Vincenzo A, Helen B, Bruno BN, Toshio MC, Vincenzo DT, Simon G, Boyin H, Christopher JM, Toshiyuki S, Rosalia S, Jorge V-C, Huai-Min Z, and Andrea P (2021) Sea Surface Temperature Intercomparison in the Framework of the Copernicus Climate Change Service (C3S). J

Clim 34(13): 5257–5283. DOI: https://doi.org/10.1175/JCLI-D-20-0793.1

Yoneyama K, Zhang C (2020) Years of the Maritime Continent. Geophys Res Lett 47: https://doi.org/10.1029/2020GL087182

Zhao Y, Zhou T, Li P, et al (2021) Added Value of a Convection Permitting Model in Simulating Atmospheric Water Cycle Over the Asian Water Tower. Journal of Geophysical Research: Atmospheres 126:. https://doi.org/10.1029/2021JD034788

7

Evaluation of Dynamically Downscaled Simulations

Authors:
Venkatraman Prasanna, Aurel Florian Moise, Sandeep Sahany, Muhammad Eeqmal Hassim, Chen Chen, Xin Rong Chua, Gerald Lim, Shipra Jain, Jianjun Yu, Pavan Harika Raavi, Fei Luo

METEOROLOGICAL SERVICE SINGAPORE
Centre for Climate Research Singapore

7.1 Introduction

This chapter presents the evaluation of the 8km and 2km dynamically downscaled historical simulations against observations (both in-situ and remotely sensed) and reanalysis (gridded proxy for observations) data. Six CMIP6 GCMs have been dynamically downscaled to 8 km resolution for the historical period (1955-2014), and five out of the six 8km downscaled simulations have been further downscaled to 2 km resolution for the period 1995-2014. For details on the downscaled simulations please refer to Chapter 6.

As a part of the evaluation of the dynamically downscaled historical simulations we present the assessment of:

(1) Large-scale consistency between the driving GCM and the resulting downscaled simulations - as a result of dynamical downscaling, although we expect the downscaled simulations to capture the finer spatial scale features of rainfall, temperature, etc. due to improved representation of coastlines, mountains and land-use-land-cover we also expect the simulations to have large-scale consistency with the driving GCM.

(2) Regional (Southeast Asia and Western Maritime Continent) and local (Singapore) climatology (rainfall, temperature, humidity and winds) – it is important to know which aspects of the regional and local climatology are captured well in the downscaled simulations and which aspects are not in order to use the future projections in a more informed manner both for physical climate change assessment and climate impacts modeling.

(3) Key regional climate drivers (northeast monsoon surges and ENSO teleconnections) – evaluation of the underlying regional climate drivers helps us understand the reasons behind projected changes in climate variables (rainfall, temperature, humidity and winds).

In addition to the above mentioned aspects of evaluation, we have also analyzed and presented in this chapter the added value of downscaling (reduction in biases as compared to the coarse resolution driving GCM). While the key results from the evaluation of downscaled simulations have been presented in this chapter, more details can be found in the Appendix.

7.2 Data and Methodology

Various observational and reanalysis datasets have been used for evaluating the V3 downscaled model simulations at 8km and 2km resolutions. Even for a single variable we use multiple observational and reanalysis datasets to evaluate the downscaled simulations to account for uncertainties amongst datasets and to make a fair comparison.

We have used both gridded datasets based on in-situ and remotely sensed data and station observations from Singapore to validate the downscaled simulations. We utilize the latest iteration of the PERSIANN CCS CDR precipitation datasets for monthly precipitation analysis, benefiting from its superior spatio-temporal resolution. In the case of diurnal precipitation analysis, we rely on the IMERG dataset due to its exceptional temporal resolution. The gridded and station datasets used for evaluation have been shown in Table 7.1 and briefly described in the subsections below.

Table 7.1: Details of observational and reanalysis data products used for evaluation in this chapter, their climate fields used, and reference. The abbreviation pr refers to precipitation; TAS: surface air temperature; PSL: mean sea level pressure; SST: sea surface temperature; HUSS: specific humidity

NAME	FIELDS (resol./freq.)	REFERENCES
HadCRUT4	TAS (5°x5°, monthly)	Morice et al. 2012
BEST	TAS (1°x1°, monthly)	Rohde and Hausfather, 2020
FROGs	PR (1°x1°, daily)	Roca et al. 2019
IMERG V06	PR (0.1°x0.1°, 30 mins)	Huffman et al., 2019
TRMM 3B42	PR (0.25°x0.25°, 3 hours)	Huffman et al., 2007
PERSIANN_CDR	PR (0.25°x0.25°, sub-daily)	Ashouri et al., 2015
CMORPH_v1	PR (0.25°x0.25°, 3 hours)	Xie et al., 2017
ERA5 reanalysis	SST, TAS, HUSS, PSL, WINDS (0.25°x0.25°, hourly)	Hersbach et al. 2020
MERRA2 reanalysis	SST, TAS, HUSS, PSL, WINDS (0.5° x 0.625°, daily)	Gelaro et al. 2017
JRA55 reanalysis	SST, TAS, HUSS, PSL, WINDS (0.56°x0.56°, sub-daily, monthly)	Kobayashi et al. 2015

7.3 Assessment of large-scale consistency between GCM and RCM

We assess large-scale consistency between the driving model (either ERA5 data or CMIP6 GCMs data for the 8 km downscaling, and 8 km data for the 2 km downscaling) and the downscaler to assess the degree of deviations in the domain mean (SEA domain for 8 km, and WMC domain for 2 km) fields (precipitation, temperature and relative humidity).

Figure 7.1 shows the annual mean time series of precipitation and temperature across Southeast Asia in driving CMIP6 GCM models, and the 8 km downscaled SINGV RCM simulations during historical and SSP5-8.5 scenarios. When compared to the ERA5 during the historical period, the downscaled RCM simulations overestimate the mean precipitation and temperature. The downscaled ACCESS-CM2 simulations captures the interannual variability of the mean precipitation but overestimates the magnitude compared to the driving GCM (ACCESS-CM2). Whereas the time series of mean temperatures in the downscaled simulations closely matches with the driving model (ACCESS-CM2). The EC-EARTH3, downscaled simulations can capture the interannual variations of the mean precipitation and mean temperatures but overestimates the magnitude of precipitation and temperature, respectively. The MIROC6 model downscaled simulations can capture the interannual variations with an over estimation of the mean precipitation magnitude. Whereas the mean temperature variations and magnitude matches the driving model (MIROC6).

Similar to the MIROC6 and ACCESS-CM2 models, the downscaled simulations of MPI-ESM1-2HR and UKEESM1-0-LL models can capture interannual variability of mean precipitation with a slight overestimation of its magnitude. In contrast, the mean temperature variations and magnitude in downscaled simulation matches with the respective driving models. The NorESM2-MM downscaled simulations also capture interannual variability in the mean precipitation but largely overestimates the magnitude of the mean precipitation by about 30%. The interannual temperature variations of downscaled NorESM2-MM model matches with the driving model with an overestimation of the magnitude.

The downscaled simulations from SINGV are broadly consistent with the driving GCMs. The 8 km downscaled models' climate may have a greater potential for strong convection, which would increase the rate of precipitation compared to the driving GCM models. Most of the downscaled simulations can capture the interannual variability of temperature and precipitation but show a systematic wet bias.

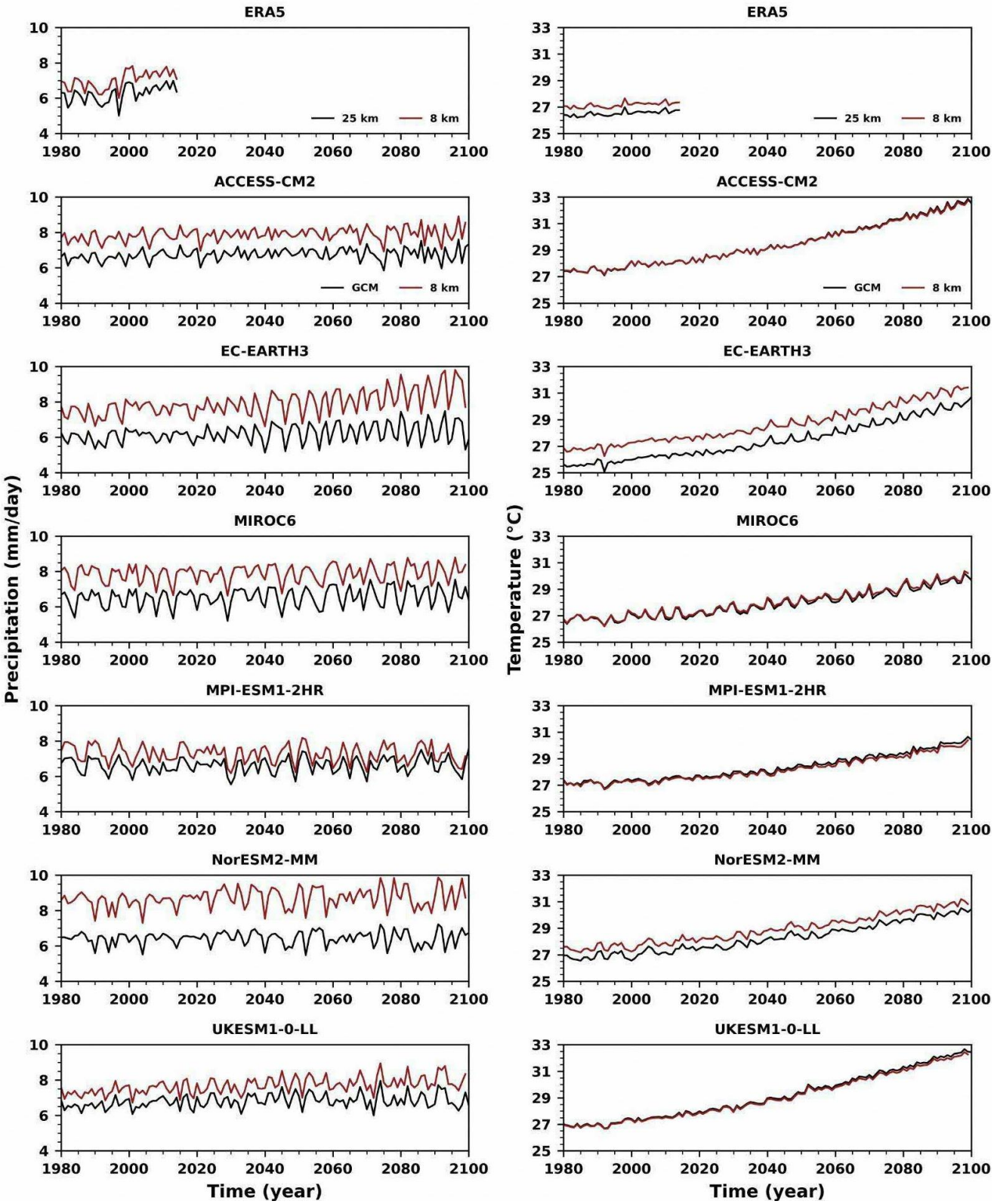

Figure 7.1: Annual mean time series of precipitation (left column) and near-surface air temperature (right column) from driving CMIP6 GCMs (150km; black) and V3 downscaled simulations (8km; red) for historical (1980-2014) and SSP5-8.5 scenario (2015-2099) for SEA region. First row shows the ERA5 reanalysis at its original resolution (25km) and from its corresponding V3 downscaled simulation (8km).

Figure 7.2 shows the annual mean time series of precipitation and temperature across Western Maritime Continent (WMC) from 8 km and 2 km downscaled SINGV simulations during historical and SSP5-8.5 scenarios. During the historical period (1995-2014) using ERA5 data, the interannual variations and magnitude of annual mean precipitation and temperatures from the 8 km simulations closely matches with the 2 km SINGV simulations. The 2 km downscaled time series of temperature and precipitation of ACCESS-CM2, MPI-ESM1-2HR and UKESM1-0-LL models closely aligns (matches the interannual variability and magnitude) with the 8 km downscaled simulations. The 2 km downscaled simulations of NorESM2-MM and EC-EARTH3 models captures the interannual variability of temperature and precipitation similar to that of the 8 km downscaled simulations but overestimates the magnitude of the precipitation slightly higher in the NorESM2-MM.

Overall, the 8 km SINGV downscaled large-scale mean climate of different driving GCM models matches with the 2 km SINGV downscaled fields across the WMC region both in historical and SSP8.5 scenarios. We might notice some spatial (local) changes between the 2 km and 8 km downscaled simulated fields compared to the domain averaged quantities due to better representation of the topographic features in 2 km resolution.

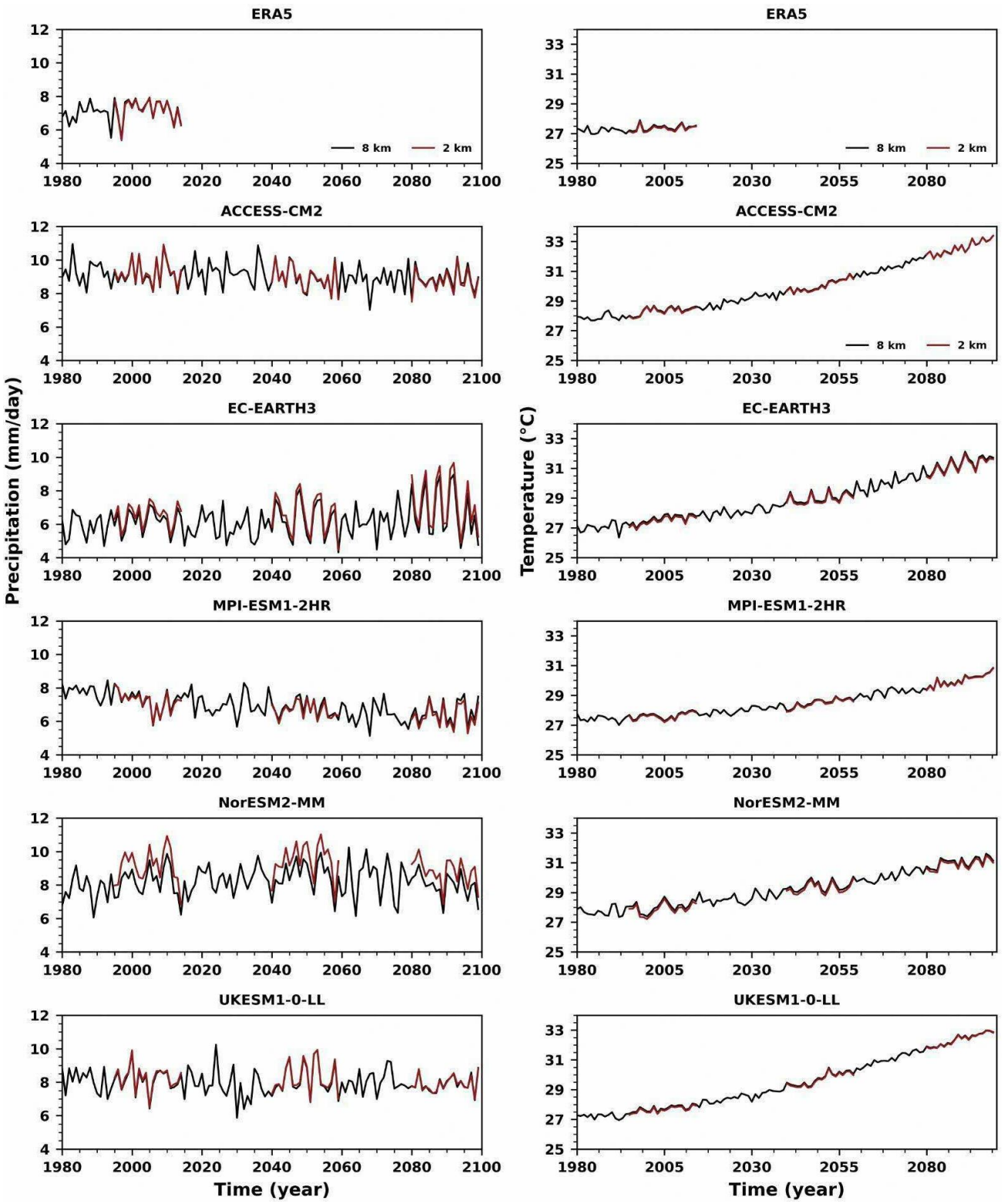

Figure 7.2: Annual mean time series of precipitation (left column) and near-surface air temperature (right column) from V3 downscaled simulations (8 km in blue and 2km in red) for historical (1995-2014) and SSP5-8.5 scenario (2040-2059 and 2080-2099) for WMC region. In the first row, the ERA5 downscaled simulations are shown at 8km and 2km resolutions for precipitation (left) and temperature (right).

7.4 Evaluation of Regional-scale climatology

This section will provide an analysis of mean and extreme rainfall and temperature as well as relative humidity and surface winds simulated by SINGV-RCM.

7.4.1 Mean Rainfall

Figure 7.3a shows that the region generally receives rainfall throughout the domain. Figure 7.3b and d show that relative to PCCSCDR (Sadeghi et al., 2021), SINGV-ERA5 enhances precipitation over areas with significant topography, such as the Sumatran Mountain range, Peninsular Malaysia, Borneo, Sulawesi, New Guinea, and Vietnam. Concurrently, there is a reduction of rainfall over land areas near these regions of high topography, such as east Sumatra and west Borneo. Near the east and west boundaries, there is an enhancement of rainfall over the wetter regions in climatology.

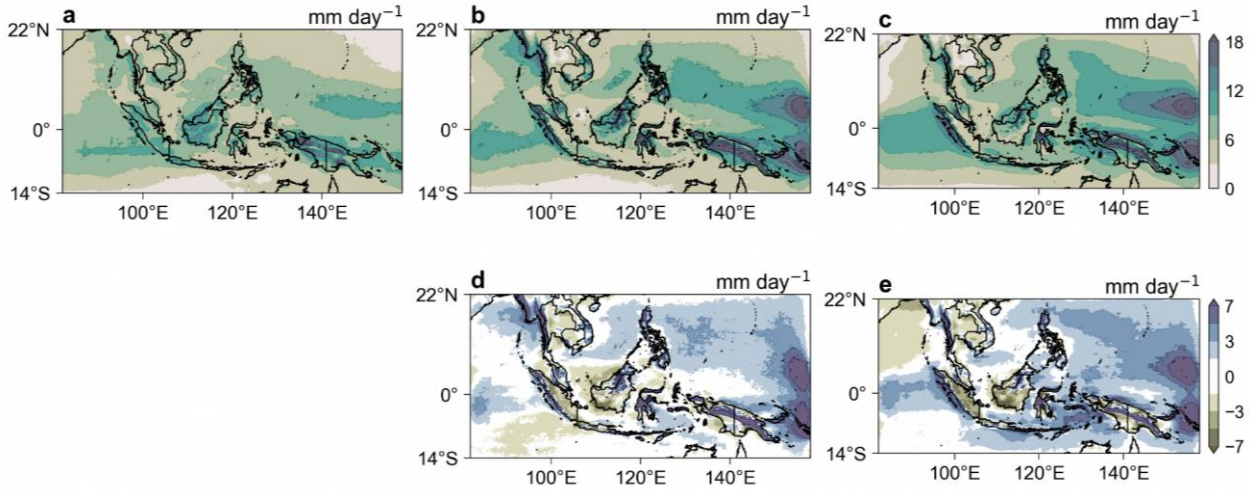

Figure 7.3: Annual mean precipitation (shaded) in (a) PCCSCDR, (b) ERA5 downscaled by SINGV (SINGV-ERA5) (c) Multimodel mean of downscaled GCM simulations with SINGV (SINGV-MMM). (d) shows the bias in SINGV-ERA5 (i.e. b -a), while (e) shows the bias in SINGV-MMM (i.e. c-a).

In DJF, the rainband shifts south of the equator, with Java, Borneo and New Guinea receiving more rainfall and Indochina being relatively dry (Figure 7.4a). Similar to the annual mean, there is an enhancement of precipitation over areas with significant topography and a reduction of precipitation in nearby areas in the downscaled simulation (Fig. 7.4b, d). There is also increased rainfall at the boundaries. SINGV-MMM shares qualitative features with SINGV-ERA5. Relative to SINGV-ERA5, SINGV-MMM simulates less rainfall west of Thailand and east of the Philippines, and increased rainfall over the Java sea (Fig. 7.4d, e). A comparison of land rainfall simulated by downscaled CORDEX models against GPCC by Tangang et al 2020 (see their Fig. 5) also shows a similar moistening in high topography regions, with drying seen parts of the east coast of Peninsular Malaysia and Sumatra and western parts of Borneo.

The rain band moves north of the equator in this JJA season, with a notable rainfall peak falling on the west coast of Indochina and the Philippines (Figure 7.5a). The enhanced rainfall over regions with high topography described in the annual mean can be seen in JJA as well (Figure 7.5b, d), such as over the west coast of Thailand and along Borneo, Sulawesi and New Guinea. In SINGV-MMM (relative to PCCSCDR) (Figure 7.5c, e) there is an enhancement of rainfall east of the Philippines and around Java, and reduced precipitation west of Myanmar. The increased rainfall on the west edge of Indochina is seen in downscaled CORDEX models relative to GPCC (Tangang et al 2020).

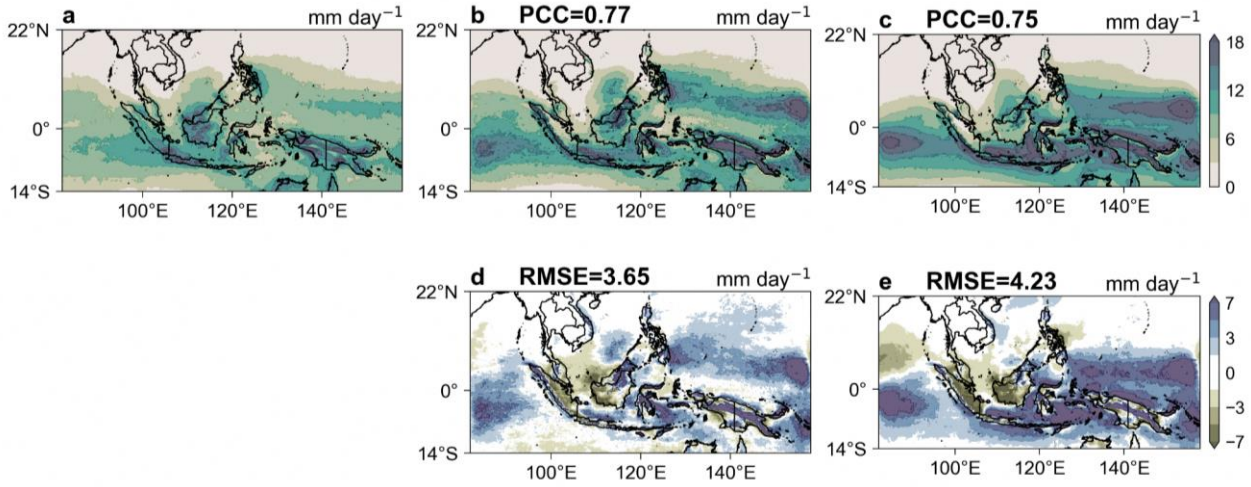

Figure 7.4: DJF mean precipitation (shaded) in (a) PCCSCDR, (b) ERA5 downscaled by SINGV (SINGV-ERA5) (c) Multimodel mean of downscaled GCM simulations with SINGV (SINGV-MMM). (d) shows the bias in SINGV-ERA5 (i.e. b -a), while (e) shows the bias in SINGV-MMM (i.e. c-a).

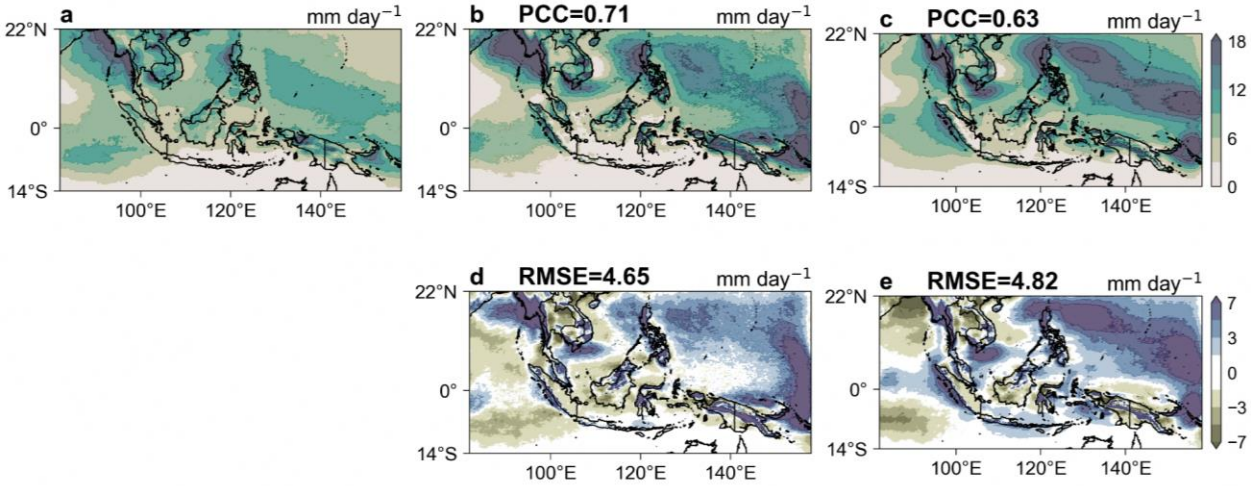

Figure 7.5: JJA mean precipitation (shaded) in (a) PCCSCDR, (b) ERA5 downscaled by SINGV (SINGV-ERA5) (c) Multimodel mean of downscaled GCM simulations with SINGV (SINGV-MMM). (d) shows the bias in SINGV-ERA5 (i.e. b -a), while (e) shows the bias in SINGV-MMM (i.e. c-a).

Annual cycle:

The annual cycle of rainfall over the Southeast Asia and Western Maritime Continent regions varies on monthly scale due to different large-scale drivers (ENSO, IOD, MJO), local drivers (sumatra squalls, northeast monsoon surges, Borneo vortex) and seasonal transition of the ITCZ. Here, we use the observational data from Precipitation Estimation from Remotely Sensed Information using Artificial Neural Networks (PERISANN), and model data from 2 km and 8 km downscaled simulations using ERA5 data. Figure 7.6 shows the area averaged precipitation annual cycle over the Southeast Asia (8 km; blue line) and Western Maritime Continent (8 km & 2 km; orange line) using SINGV RCM downscaled simulations and PERISANN (black line) over land & ocean, land only and ocean only regions (shading denotes the spread between models).

Over the SEA (Land & Ocean), and SEA (Ocean) domains, the 8 km simulation is able to capture the observed (PERISANN) annual cycle with peak precipitation during July. The SEA land precipitation annual cycle in 8 km downscaled simulation shows peak precipitation in July which is not observed in PERSIANN (peak during May). Overall, the land only precipitation annual cycle over the SEA is not captured well in the 8 km downscaled SINGV simulations.

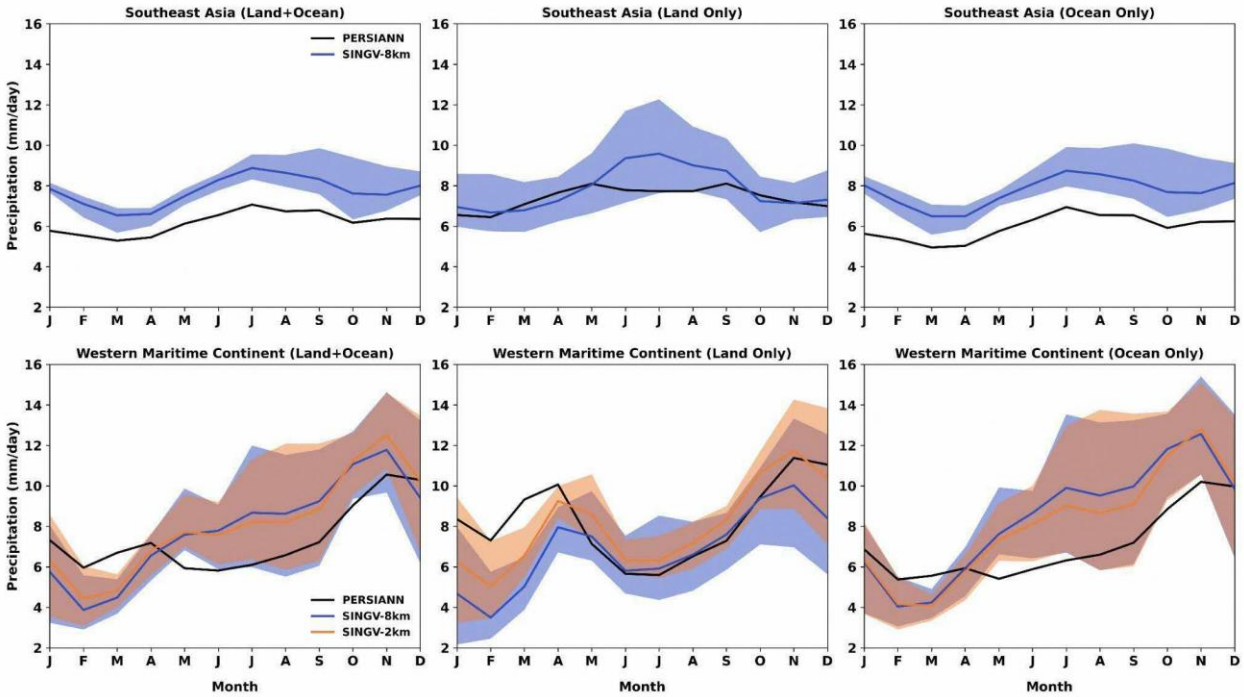

Figure 7.6: Annual cycle of precipitation (mm/day) from downscaled simulations for the historical period (1995-2014) for Southeast Asia (8km) and WMC (8km and 2km) for land + ocean, land only and ocean only. For observations, multiple datasets were used and are shown in black. The climatological period for observations varies as in Table 1.

In the WMC (land & Ocean) domain, the precipitation annual cycle in observations varied with both the 2 km and 8 km downscaled simulations during May and June. The downscaled simulations overestimates the observed precipitation magnitude in the months May to November and underestimates it in the months of January to April. In addition, there is a large intermodal difference during the southwest monsoon season i.e. July to September.

In the WMC (land only) domain, the annual cycle of precipitation is captured reasonably well by 2 km and 8 km downscaled simulations but underestimates the magnitude (greatly by 8 km simulation) compared to observations during January to April. The precipitation is overestimated in 2 km downscaled simulations from May to November compared to observations and 8 km simulations.

In WMC (ocean only), the observed annual precipitation cycle is not captured well by the 2 km and 8 km downscaled simulations during April and May. The precipitation from April to November is overestimated in both the 2 km and 8 km downscaled simulations. Also, there is a large intermodal difference during the southwest monsoon season (JJAS).

Overall, the mean precipitation annual cycle over the SEA region (Land & Ocean, Ocean) from 8 km and 2 km downscaled simulations is comparable to the observed annual cycle (PERISANN) with a difference in magnitude. The Land-only precipitation annual cycle over SEA is not captured well by the downscaled simulations. The WMC region's annual precipitation cycle using the 8 km and 2 km downscaled simulations (large intermodal spread during the southwest monsoon season) vary compared to the observed annual

cycle over Land & Ocean and Ocean only domains. The WMC region's observed land only precipitation annual cycle is captured by 2 km and 8 km downscaled simulations with a difference in magnitude.

Diurnal Cycle

The diurnal cycle of rainfall is an important component of rainfall variability in the Maritime Continent. We use hourly data from observations (IMERG) and model data from 8 km and 2 km simulations for evaluating the diurnal cycle of rainfall. Figure 7.7 shows the area averaged diurnal precipitation cycle over the 2 km WMC dynamical downscaling domain, for two seasons JJAS(a) and NDJF(b). We see from Figure 7.7a that SINGV-RCM 8 km and 2 km with explicit representation of convection is able to capture the diurnal timing of precipitation over land grid points, and the timing matches well with observation (IMERG) but the magnitude does not, and this is worse in the 2km model, for JJAS season.

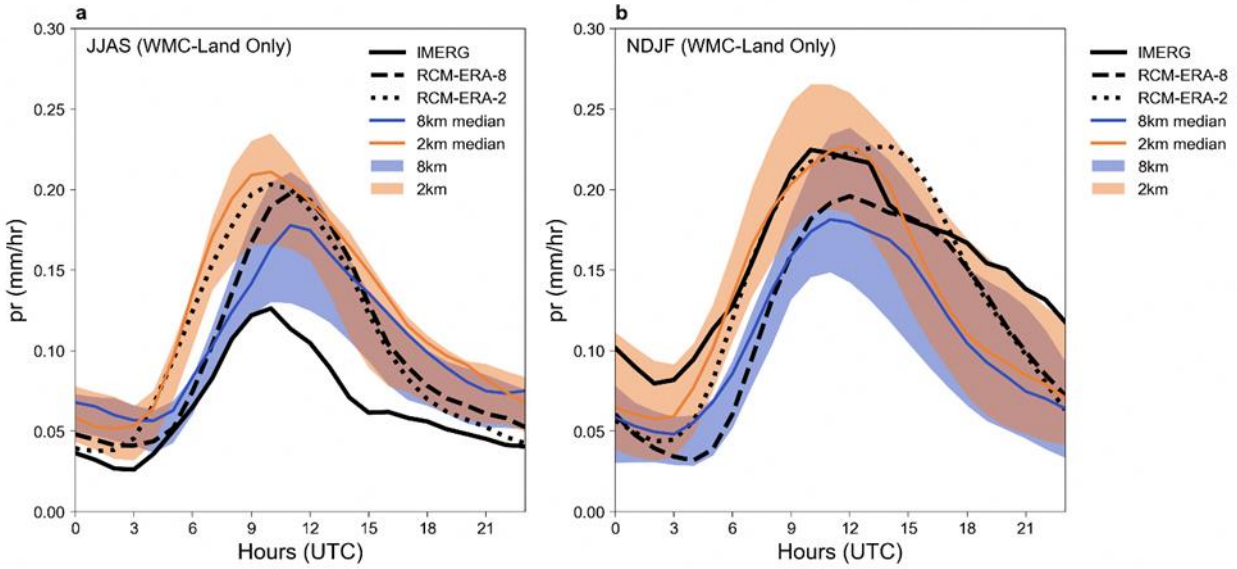

Figure 7.7: Diurnal cycle of Precipitation area averaged over WMC domain for JJAS and NDJF. a) Ensemble median and spread for SINGV-2km and SINGV-8km compared to IMERG-obs (JJAS), b) Ensemble median and spread for SINGV-2km and SINGV-8km compared to IMERG-obs (NDJF). Units in mm/hr. Note that Singapore is 8 hours ahead of UTC. The precipitation peak is around the late afternoon of Singapore local time.

Blue line for 8 km model runs and Orange line for 2 km (shades denote the spread among the models), however the downscaling to 8 km and 2 km improves the diurnal timing, we do see the added value from 8 km to 2 km, though we see improvement in the timing compared to GCM (which is not shown here), we do see the intensity is more in 8 km compared to IMERG and even more intense when we drive 2 km by 8 km output for JJAS.

The results are quite similar for NDJF as well (Figure 7.7b). High resolution runs of 2 km have a better diurnal peak timing (improvement) compared to 8 km run, while the intensity (Land grid points only) is over predicted by SINGV-RCM for JJAS season (Figure 7.7 a). Whereas the SINGV-RCM at 8 km resolution is under predicted for NDJF season compared to observation (Figure 7.7 b), while the 2km resolution corrects it (improvement). Figure 7.8 shows the spatial variation in the timing of the diurnal rainfall peak over the WMC domain compared to GPM-IMERG data at each grid point.

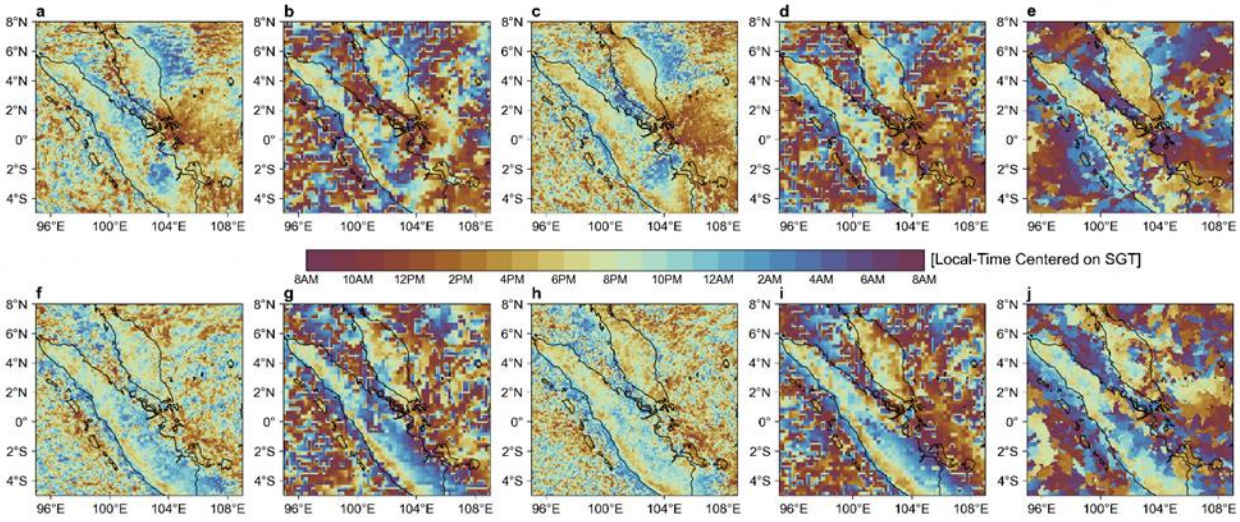

Figure 7.8: Spatial map of Peak Diurnal timing of Precipitation for JJAS and NDJF. a) Ensemble mean of SINGV-8km (JJAS), b) SINGV-8km-ERA (JJAS) c) Ensemble mean of SINGV-2km (JJAS), d) SINGV-2km-ERA (JJAS), e) IMERG-obs (JJAS). f) Ensemble mean of SINGV-8km (NDJF), g) SINGV-8km-ERA (JJAS), h) Ensemble mean of SINGV-2km (NDJF), i) SINGV-2km-ERA (JJAS), j) IMERG-obs (NDJF). Units in hour (SGT).

The spatial variation in timing of the peak rainfall for this region: earlier times over land seem largely tied to the higher orography while over much of the lower orography the peak occurs overnight/early morning (Based on Singapore local time), hence the second peak in Fig. 7.7b. There is also a later peak along the Sumatran coast and an earlier peak over and beyond the islands off the coast. The models do seem to capture this spatial variation.

7.4.2 Rainfall Extremes

Here we used the annual maximum 1-day precipitation (RX1day) to evaluate RCM's fidelity simulating the rainfall extremes. Based on the evaluation (Figure 7.9), it is observed that both SINGV-ERA5 and SINGV-MMM models tend to overestimate RX1day across the Southeast Asia (SEA) domain. This overestimation is consistent with the overestimation of the annual mean rainfall in these models.

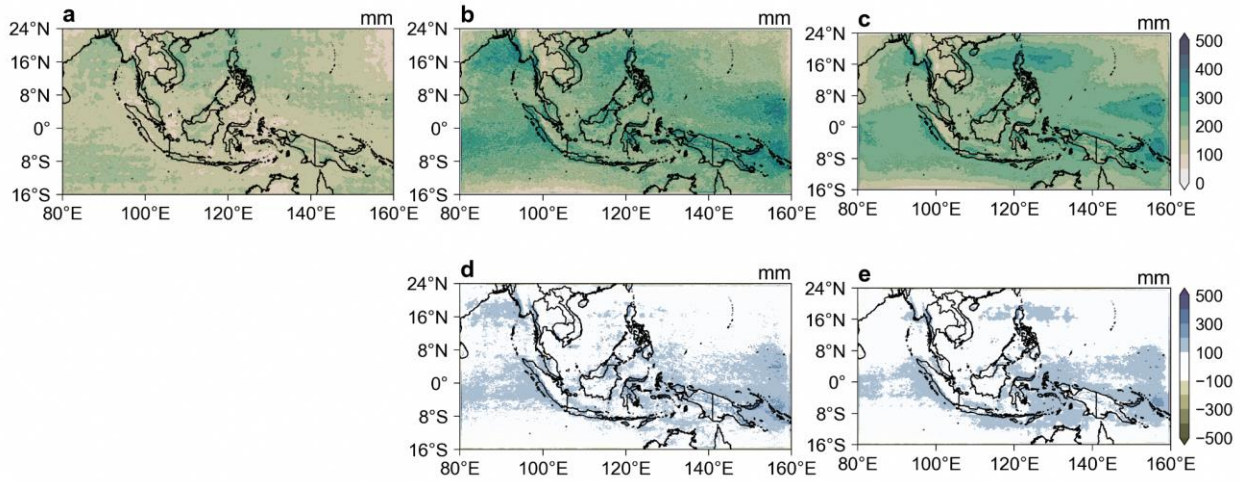

Figure 7.9: Annual RX1day in (a) PCCSCDR, (b) ERA5 downscaled by SINGV (SINGV-ERA5) (c) Multimodel mean of downscaled GCM simulations with SINGV (SINGV-MMM). (d) shows the bias in SINGV-ERA5 (i.e. b -a), while (e) shows the bias in SINGV-MMM (i.e. c-a).

It suggests that there might be a common bias in the representation of precipitation processes in these models, leading to an overestimation of both mean rainfall and extreme precipitation events. Specifically, the overestimation of RX1day is more prominent in the equatorial SEA region, while the biases in the extratropical region are relatively smaller. This spatial pattern of biases suggests that there may be certain factors or processes specific to the equatorial region that contribute to the overestimation of extreme rainfall events. These results can help identify areas where improvements are needed in the representation of precipitation processes in the RCMs, particularly in capturing the characteristics of extreme rainfall events in the equatorial SEA region.

7.4.3 Mean Temperature

Figure 7.10 shows the annual cycle of mean temperature over the SEA and WMC regions from HadCRUT observations (black line), 8 km (blue line), and 2 km (orange line) downscaled simulations for the historical period. The annual cycle of temperature in the SEA and WMC regions vary across months over land & ocean, land only, and ocean-only domains.

Over the SEA (Land & Ocean) domain, the annual cycle has a bimodal distribution with peak temperatures in May and October. The 8 km downscaled simulations are able to capture the observed annual cycle with a slight underestimation of temperatures during Jan-Apr, and Sep-Dec.

Over the SEA (land only) domain, the observed annual cycle has bimodal distribution with peak temperatures during May and October. The 8 km downscaled simulations can capture one of the peaks during May but cannot capture the other one. The temperatures are significantly underestimated by about 2oC over SEA land in the downscaled simulations. The cold biases are observed in 8km-downscaled simulations similar to the cold biases in the GCMs over the Indochina region (section 5.3.1 Figure 5.2). Over SEA (ocean only), the observed annual cycle of temperature is captured well by the 8 km downscaled simulations.

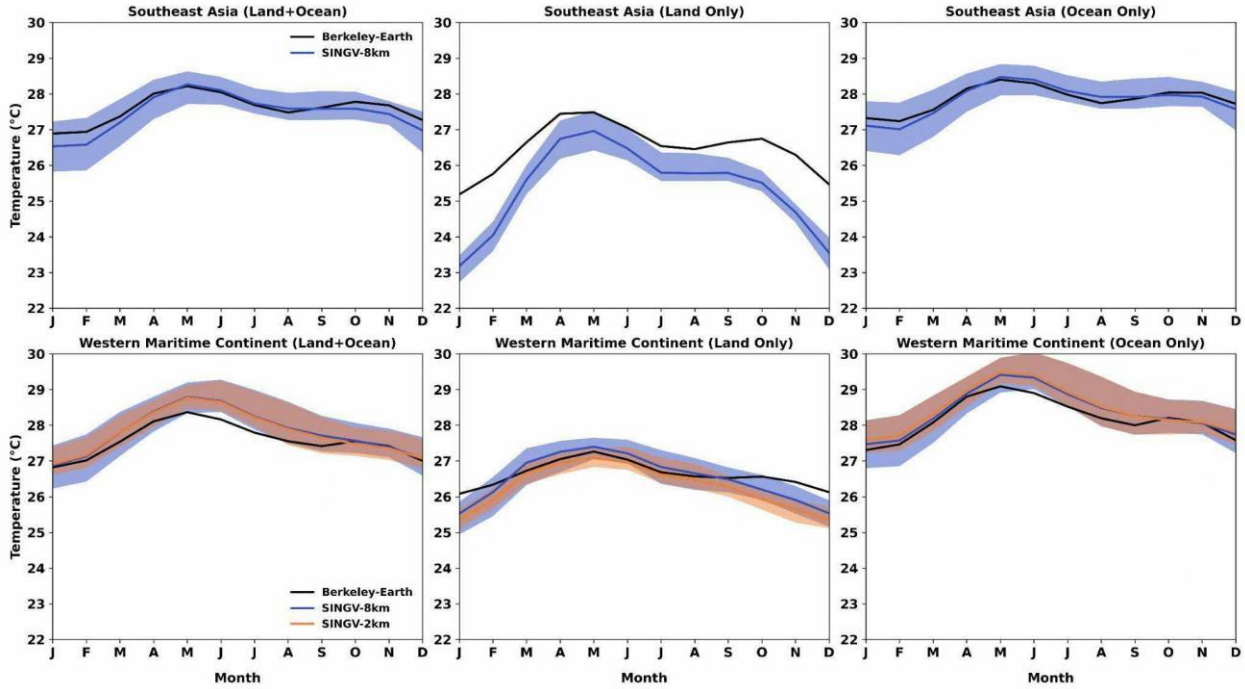

Figure 7.10: Annual cycle of temperature (deg C) from downscaled simulations for the historical period (1995-2014) for Southeast Asia (8km) and WMC (2km) for land+ocean, land only, and ocean only. For observations, HadCRUT is used for 1995-2014.

The observed mean annual cycle of temperature over the WMC region (Land & Ocean) has bimodal distribution with peak temperatures during May and October. The 8 km and 2 km downscaled simulations are able to capture the annual cycle but slightly overestimate the magnitude.

Over the WMC (Land only) domain, both the 8 km and 2 km simulations are able to capture the observed annual cycle with a slight underestimation of the magnitude. The WMC (ocean only) observed temperatures show bimodal distribution with peaks during May and October. Both the 8 km and 2 km downscaled simulations are able to capture the annual cycle but slightly overestimate the magnitude.

The historical annual temperature cycle over the SEA and WMC regions is captured reasonably well by 2 km and 8 km downscaled simulations. The 8 km downscaled simulations significantly underestimate the temperatures over the SEA (Land only) domain.

7.4.4 Temperature Extremes

The extreme temperatures are measured using the annual (or monthly) maximum of daily maximum surface temperatures (TXx). Figure 7.11 shows the TXx over the SEA land regions in ERA5 land (a), ERA5 downscaled SINGV (b), and Multimodel mean of the downscaled GCM simulations (c). As seen in the Fig. 7.11(d, e), both the ERA5 downscaled simulations and multimodel mean of downscaled simulations overestimate the TXx temperatures across most of the SEA nations (underestimate over New Guinea) with a higher magnitude of differences in GCM downscaled simulations (7.11d). Overall, the SINGV downscaled model simulations can capture the spatial pattern of historical extreme temperatures over the SEA nations with a difference in the magnitude of temperatures.

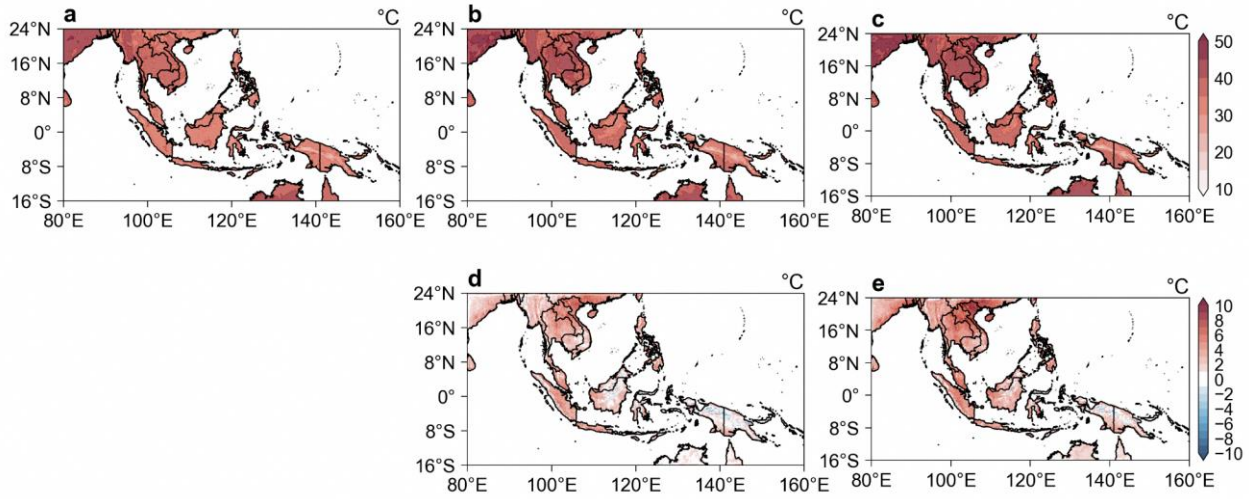

Figure 7.11: Annual TXx in (a) ERA5 Land (b) ERA5 downscaled by SINGV (SINGV-ERA5) (c) Multimodel mean of downscaled GCM simulations with SINGV (SINGV-MMM). (d) shows the bias in SINGV-ERA5 (i.e. b -a), while (e) shows the bias in SINGV-MMM (i.e. c-a).

7.4.5 Relative Humidity

Humidity is a measure of the water vapor concentration in air. Relative humidity is expressed as a percentage, which measures the amount of water vapor in the air relative to the maximum amount the air can hold at a given temperature and pressure. Figure 7.12 shows the annual cycle of Relative humidity (RH) across the SEA and WMC regions from observations (ERA5), and downscaled simulations (2 km and 8 km) during the historical period.

Over the SEA (Land & ocean) domain, the 8 km downscaled simulations of different driving GCM models can capture the observed annual variations of RH (maximum values during the southwest monsoon season) but underestimate RH magnitude. The SEA (land only), the 8 km downscaled simulations can capture the observed

annual cycle but significantly underestimate RH magnitude by about 4% compared to ERA5. The SEA (ocean only), 8 km downscaled annual cycle matches the observed annual cycle with an underestimation of the magnitude.

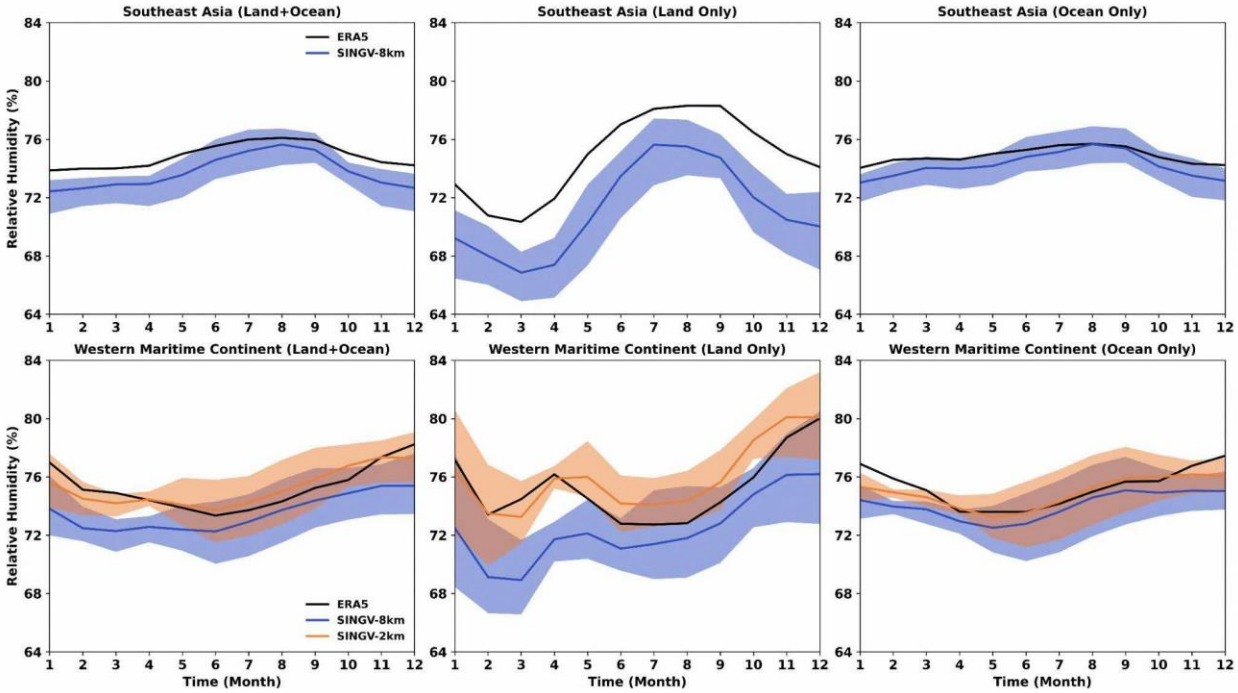

Figure 7.12: Annual cycle of relative humidity from downscaled simulations for the historical period (1995-2014) for Southeast Asia (8km) and WMC (8km + 2km) for land+ocean, land only, and ocean only. For observations, ERA5 data is used for 1995-2014.

Over the WMC (Land & Ocean), the 2 km downscaled model simulations match better with the RH in ERA5 compared to the 8 km downscaled simulations. For the historical RH annual cycle, the 2 km downscaled simulations also capture it but slightly underestimate during January to April and overestimate during April to November.

The WMC (Land only) 8 km and 2 km downscaled simulations can capture the historical RH annual cycle. The 8 km downscaled simulations significantly underestimate the magnitude and 2 km simulations slightly overestimate. The WMC (Ocean only) downscaled simulations (2 km and 8 km) can capture the annual cycle but slightly underestimate compared to the ERA5. Overall, the annual cycle of RH is captured in 2 km and 8 km downscaled SINGV simulations but underestimate the RH magnitude (largely by 8 km downscaled simulations).

7.4.6 Winds

Ali et al (2022) evaluated five CORDEX-SEA simulations of downscaled wind speed and concluded that all models were able to reproduce the spatial pattern of wind speed well, but only described three models as being able to correctly reproduce the wind direction. In a comparison of a 14-member ensemble simulation, Tangang et al (2020) noted that the patterns of bias in the RCM were generally similar to those of the parent GCM, although the RCM could make modification in some cases, such as strong southerlies in the eastern Indian Ocean and west of Sumatra. Their results also indicate a general strengthening of the bias in the downscaled simulations of the westerlies over Indochina in JJA. As for DJF, the largest biases in the multi-model mean were easterly over Indochina and westerly over much of Java.

In JJA (Figure 7.13), the southwesterly flow is strongest over the Indian ocean. Downscaling in SINGV-ERA5 enhances the westerly flow from the Andaman Sea to the Philippines relative to ERA5.

This strengthening of the monsoonal flow is enhanced for SINGV-MMM, similar to the multimodel mean JJA results of Tangang et al (2020) and the westerly bias of the 6 CMIP6 models over part of Indochina (Figure 7A.1). In contrast, the southwesterly flow for SINGV-NorESM2-MM is displaced southwards towards Sumatra, while that of MIROC6 is weaker than ERA5 (not shown). Martin et al. (2021) have noted a similar westerly bias over Indochina in the GC2 configuration of the Unified Model (UM), on which SINGV-RCM is based. Their result, combined with the occurrence of this bias even when forced with ERA5 at the boundaries (panel d), suggests that the bias is inherent in the UM. In addition, because SINGV-RCM is run with explicit convection, the development of this bias is not solely linked to the convection scheme employed by the UM.

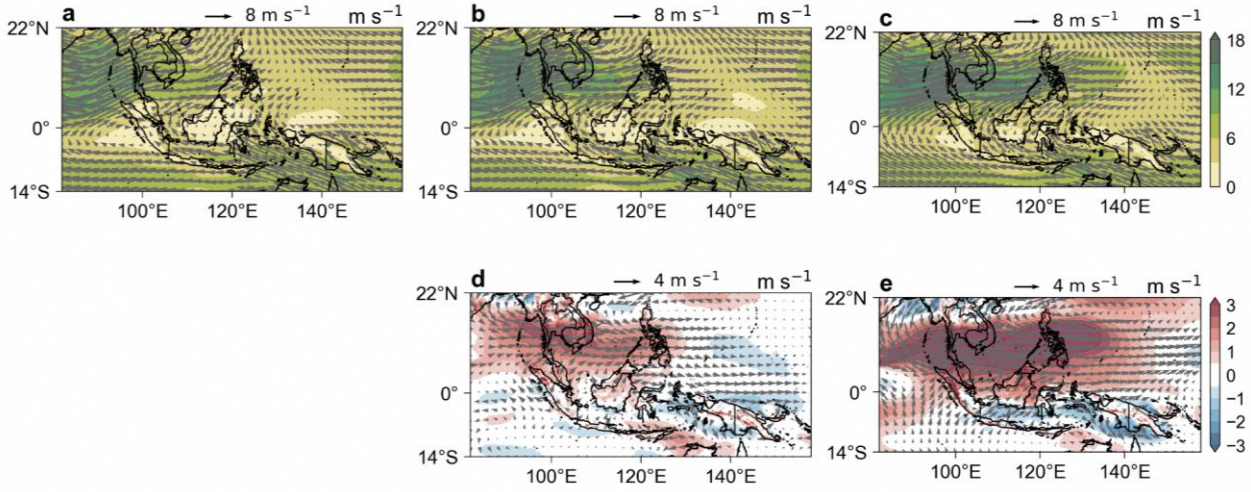

Figure 7.13: Mean JJA 850 hPa winds (quivers) and wind speed (shaded) in (a) ERA5, (b) ERA5 downscaled by SINGV (SINGV-ERA5) (c) Multimodel mean of downscaled GCM simulations with SINGV (SINGV-MMM). (d) shows the bias in SINGV-ERA5 (i.e. b -a), while (e) shows the bias in SINGV-MMM (i.e. c-a).

In DJF (Figure 7.14), the northeasterly flow reaches a peak in wind speed off the south coast of Vietnam, and turns southeasterly after crossing the equator. Downscaling in SINGV-ERA5 creates a cyclonic anomaly centered on south Vietnam, as well as enhancing the westerlies off the east coast of Borneo towards the Celebes Sea. Except for SINGV-ACCESS-CM2 (not shown), this feature is not particularly apparent in the downscaled GCMs and SINGV-MMM. Instead, the flow in SINGV-MMM is more northerly over the South China Sea along the east coast of the Malay Peninsula and towards Singapore. The downscaled simulations show small or northeasterly bias over Indochina, and a spread of wind bias over Java (not shown), which differ from the CMIP5 CORDEX-SEA downscaling findings of Tangang et al (2020) described above. A northeasterly bias in parts of Indochina can be seen in the multimodel mean of the 6 GCMs used for downscaling (Figure 7A.2).

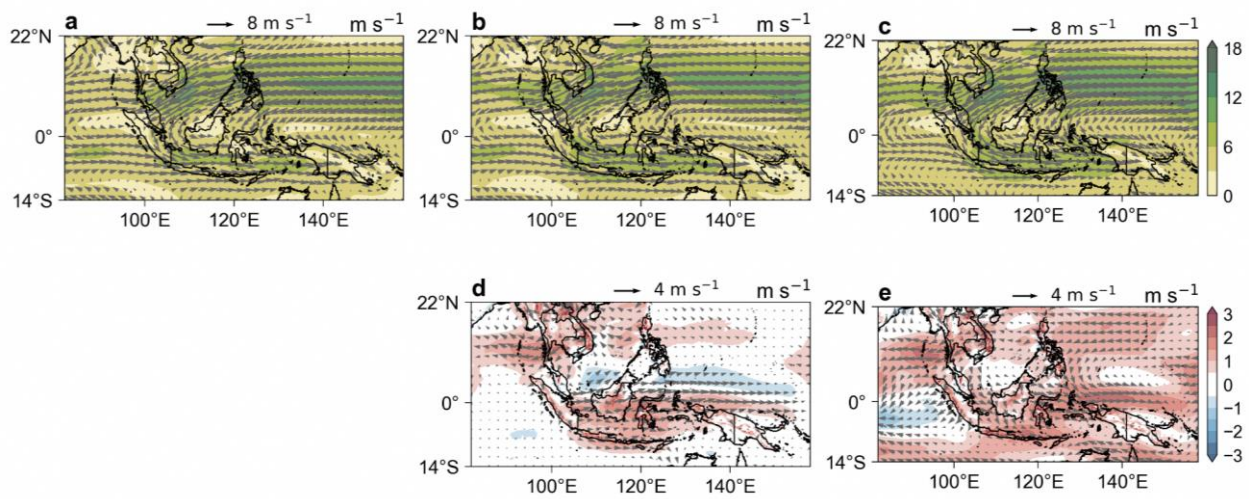

Figure 7.14: Mean DJF 850 hPa winds (quivers) and wind speed (shaded) in (a) ERA5, (b) ERA5 downscaled by SINGV (SINGV-ERA5) (c) Multimodel mean of downscaled GCM simulations with SINGV (SINGV-MMM). (d) shows the bias in SINGV-ERA5 (i.e. b -a), while (e) shows the bias in SINGV-MMM (i.e. c-a).

7.5 Evaluation of regional climate drivers

The biases in the simulation of climate variables are associated with simulation biases of the key climate drivers. In this subchapter we show the biases in the simulation of three important climate drivers - northeast monsoon surges, ENSO teleconnections, and weather regimes.

7.5.1 Monsoon

Monsoons have a key role in shaping the weather and climate of the MC domain. The MC domain is affected by the boreal summer (JJA) monsoon as well as the boreal winter (DJF) monsoon. Seasonal migration of ITCZ leads to climatological rainfall peaks during the monsoon season in Northern and Southern hemispheres.

Figure 7.15 (top left panel) shows the observed (based on PERSIANN-CCS data) migration of monsoon rainfall for the 1995-2014 period with northern hemisphere (NH) peaks during JJAS and southern hemisphere (SH) peaks in DJFM. Note the more persistent wet all year around in the equatorial region. Also, there is north-south asymmetry across the equator, with the NH monsoon extends further north compared to the SH monsoon extension southward.

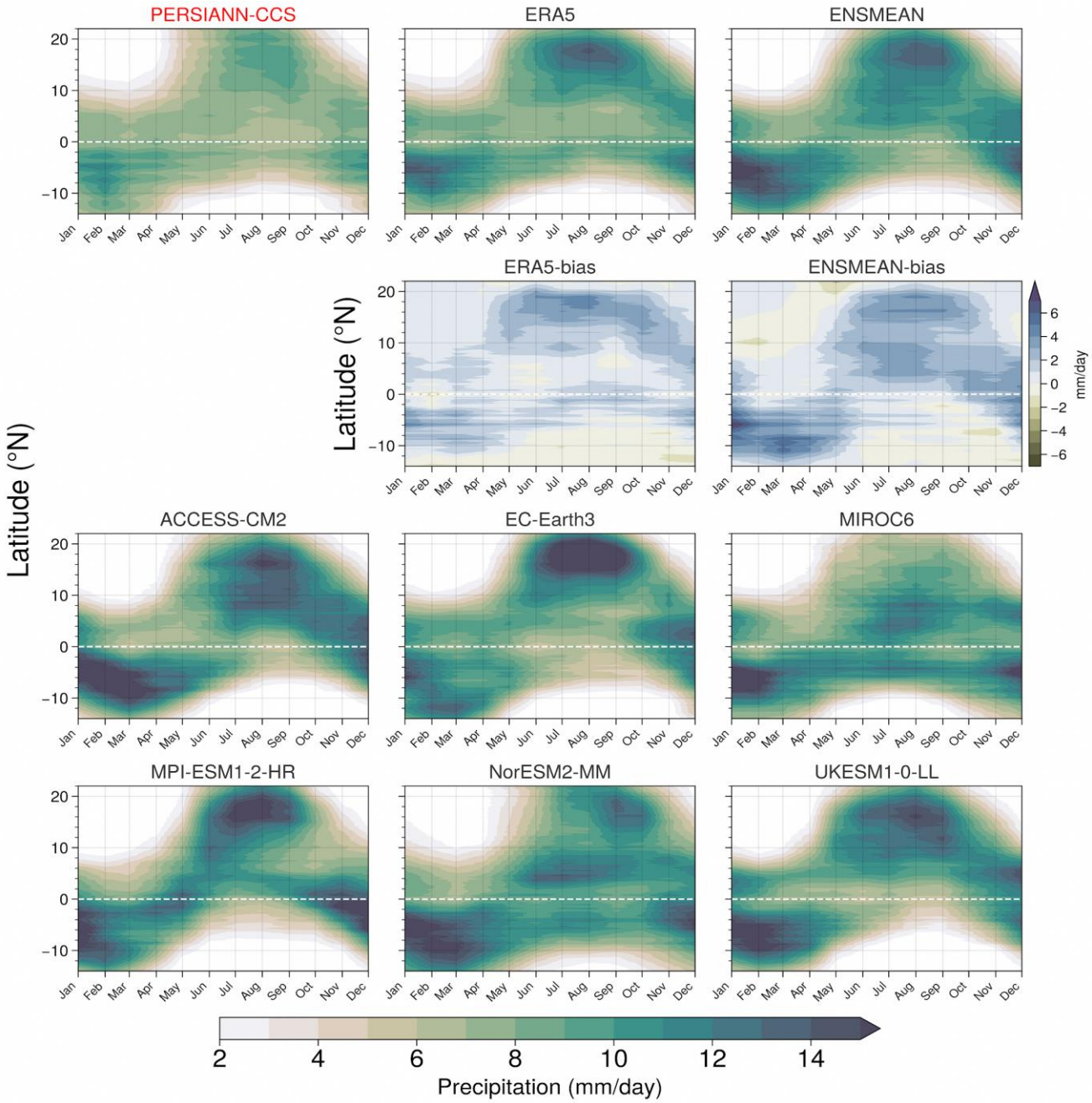

Figure 7.15: The time-latitudinal progression of zonally-averaged (80-160E) climatological monthly precipitation (i.e. passage of the ITCZ-monsoon rain belt) for the period 1995-2014 in high-resolution satellite observations (PERSIANN-CCS; regridded to 8-km) and in SINGV-RCM 8-km downscaled simulations of ERA5 and the six sub-selected GCMs (ACCESS-CM2, EC-Earth3, MIROC6, MPI-ESM1-2-HR, NorESM2-MM and UKESM1-0-LL). The multi-model ensemble mean (ENSMEAN) of the six downscaled GCMs is shown in the top right panel. Biases in the SINGV-ERA5 and ENSMEAN progression of the ITCZ rain belt are shown in the second row.

Compared to the observation reference, SINGV-ERA5 (Figure 7.15 middle panel in the 1st and 2nd rows) shows that overestimated rainfall in the NH (~15N) during the summer monsoon season (JJAS) and also overestimated rainfall in the SH (~8S) during the winter monsoon season. Multimodel mean of SINGV-RCM (SINGV-MMM) shows similar biases of overestimated monsoon rainfall as the SINGV-ERA5. Within the equatorial region, SINGV-RCMs tend to show a larger bias

compared to the SINGV-ERA5. Six RCMs overall show reasonably realistic monsoon rainfall across the year, but we do observe model diversity (Figure 7.15 lower panels), e.g., EC-Earth3 appears to have a much stronger summer monsoon rainfall while MIROC6 has weaker summer rainfall compared to other models.

Similar to significant positive bias of precipitation in a latitude band of 10-20N observed in GCM-MMM (Fig.5.14), the downscaled simulations of SINGV-RCM (8km) also show significant positive precipitation bias around the similar latitudinal band (Fig. 7.15)

7.5.2 Northeast Monsoon surge

Figure 7.16 shows the spatial pattern of mean rainfall and 850hPa winds composited over surge days (as defined in Chapter 7) for the period 1995-2014 from observations/reanalysis and downscaled 8 km simulations. Also shown are the corresponding biases. The reference (Fig. 7.16a) shows northeasterly winds over the South China Sea characteristic of surge days. After crossing the equator, the winds turn northwesterly. In the process, these winds bring heavy rainfall to the Maritime Continent, especially over the Philippines and Borneo.

Figures 7.16b and d show that SINGV-ERA5 is able to capture the wind features, with increased precipitation over the Java Sea, Sulawesi, and New Guinea, as well as the Indian ocean, and an eastward shift of the precipitation peak over Borneo. There are anomalous winds directed eastward from Borneo, as well as anticyclonic winds around Myanmar.

In SINGV-MMM (Figures. 7.16c and e; computed from the multi-model mean of the 6 downscaled 8 km simulations), there is a southward shift of precipitation, with strong precipitation over the Indian ocean and east of Borneo. Similar to GCM bias (Fig. 5.24c) we observe dry bias over Philippines and wet bias over Sulawesi in the downscaled SINGV-MMM (Fig.7.16e).

The surge frequency of the reference (not shown) is 19% which matches that of SINGV-ERA5 (19%). Other than MIROC6 (12%), the downscaled models have surge frequencies ranging from 15% in ACCESS-CM2 to 20% in UKESM1-0-LL, with a multi-model mean of 17%. This is consistent with the driving GCMs, where GCMs generally had lower surge frequencies as compared to reanalysis.

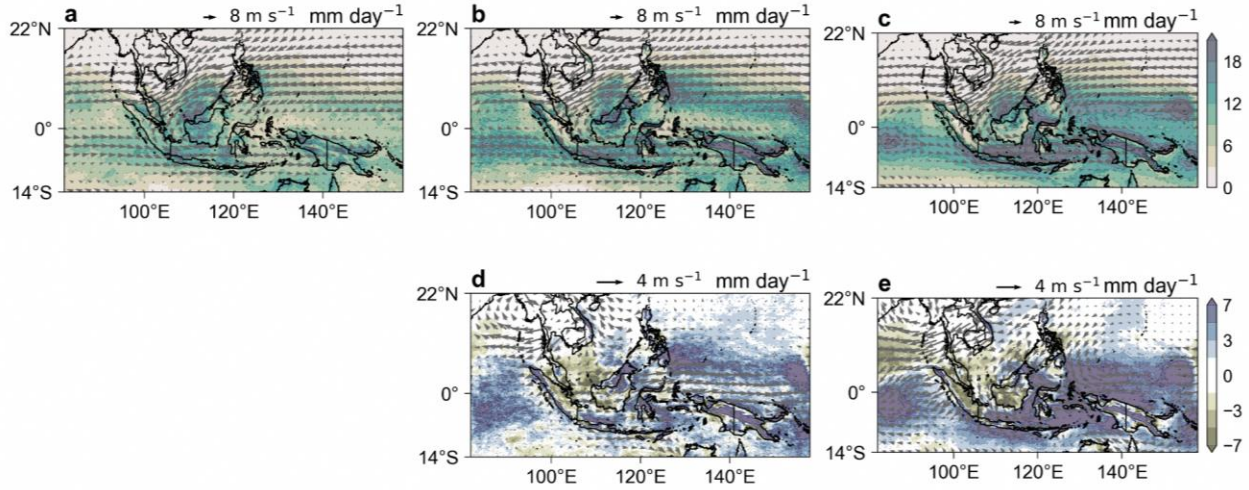

Figure 7.16: Mean 850 hPa winds (quivers) and rainfall (shaded) composited over surge-days in (a) REF (surge days and surge winds derived with ERA5 winds and sea level pressure, and using PERSIANN-CCS-CDR rainfall), (b) ERA5 downscaled by SINGV (SINGV-ERA5) (c) Multimodel mean of downscaled GCM simulations with SINGV (SINGV-MMM). (d) shows the bias in SINGV-ERA5 (i.e. b -a), while (e) shows the bias in SINGV-MMM (i.e. c-a). The reference and model datasets have different resolutions, so we use the lower of the two resolutions. For surge days and wind composites, this is 25km following the resolution of ERA5. For rainfall, values are computed at 8km resolution (following that of SINGV-RCM).

7.5.3 ENSO Teleconnections

Evaluation of the simulation of ENSO-rainfall teleconnection is proposed as one of the metrics to test the fidelity of RCMs (Torres-Alavez et al. 2021). The main goals of this evaluation are to assess: 1. whether RCMs and driving GCMs reproduce the observed large scale ENSO teleconnection patterns; 2. whether the ENSO signal propagates correctly from the driving GCMs to the RCMs; 3. whether the higher resolution of RCMs can improve the ENSO teleconnection in certain parts of the domain.

Here we analyze ENSO teleconnection over the Maritime Continent in the historical period (1995-2014) in all seasons. The observation reference is calculated using 8 km resolution PERSIANN-CCS-CDR monthly rainfall and HadISST Nino3.4 index. For the JJA season, the observed teleconnection shows negative rainfall variability induced by El Nino near the central/western MC while positive rainfall variability near the western Pacific and Northern MC (Figure 7.17a). We calculate ENSO-rainfall teleconnection in the RCM using RCM rainfall and Nino3.4 index from the corresponding driving GCM. The comparison shows that RCMs are able to reproduce consistent spatial patterns as the corresponding driving GCMs (Figure 7.17).

We further calculate two measures to compare teleconnection in RCMs and GCMs to the observation: 1. RMSE between spatial patterns of the teleconnection, 2. Correlation coefficient (corrcoeff) between spatial patterns. The results show that RCMs have similar RMSE as their corresponding driving GCMs (Figure 7.18).

RCMs have slightly lower spatial agreement with the observation compared to the driving GCMs (Figure 7.19). Across the season, RCMs have lower RMSE but similar corrcoeff to GCMs in MJJ and higher RMSE, lower corrcoeff for most of the rest of the year. The corrcoeff in RCMs is generally lower in April-July than in the other months. Note that it is difficult to identify the origins of detailed differences between GCMs and RCMs given multiple possible causes, such as spatial resolution, different physics schemes, etc.

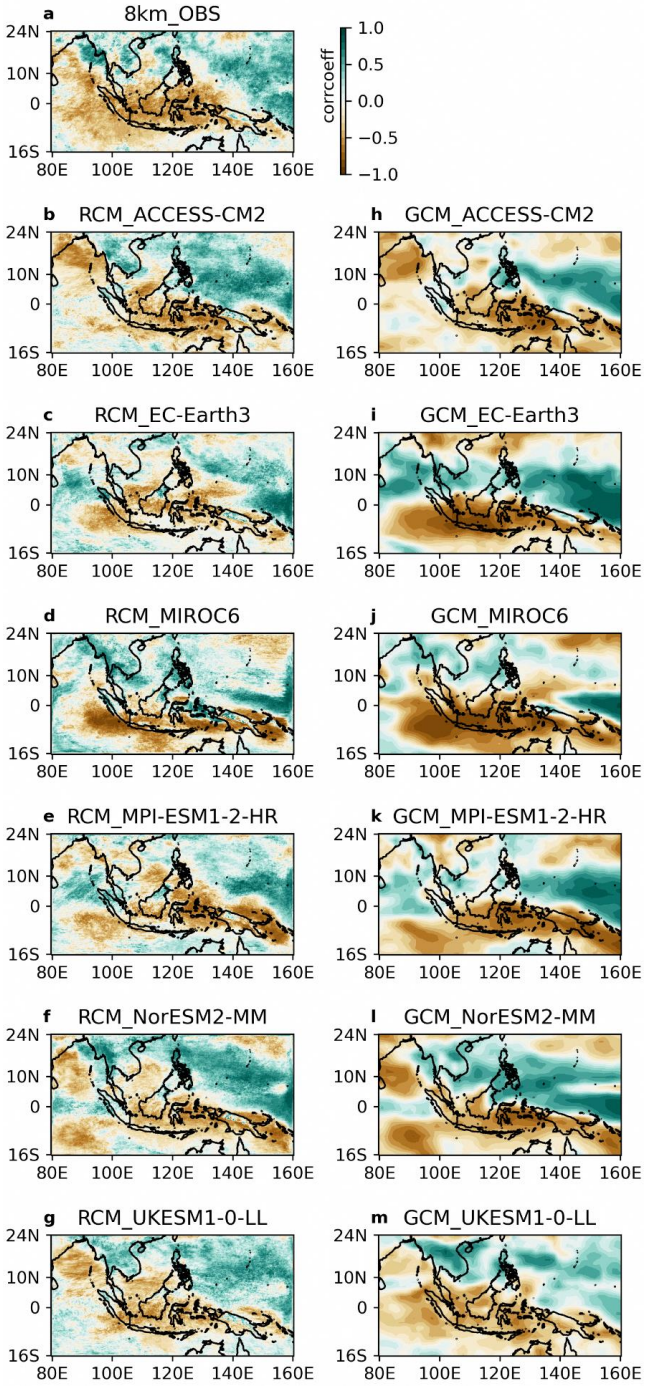

Figure 7.17: JJA ENSO-rainfall teleconnection over the Maritime Continent using correlation [corr (N34, pr)]. a. 8km resolution observation using TS_HadISST and PR_PCCSCDR. b-g. 8km resolution RCMs. h-m. GCMs remapped to 8km to facilitate the visual inspection.

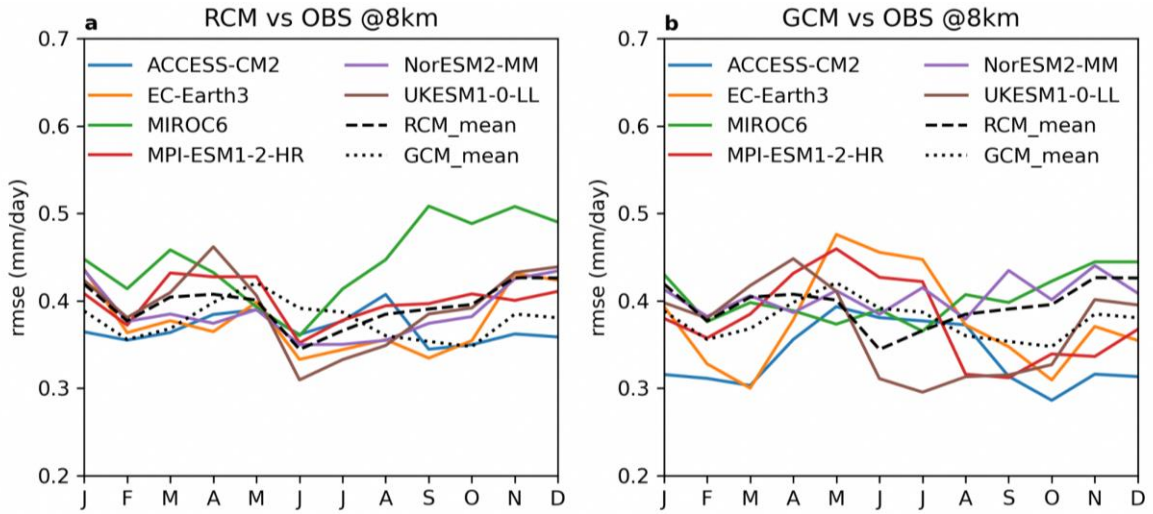

Figure 7.18: RMSE between the 8km observation and RCMs (a) or GCMs (b) over the MC region as to the ENSO teleconnection in the JJA season of the historical period (1995-2014).

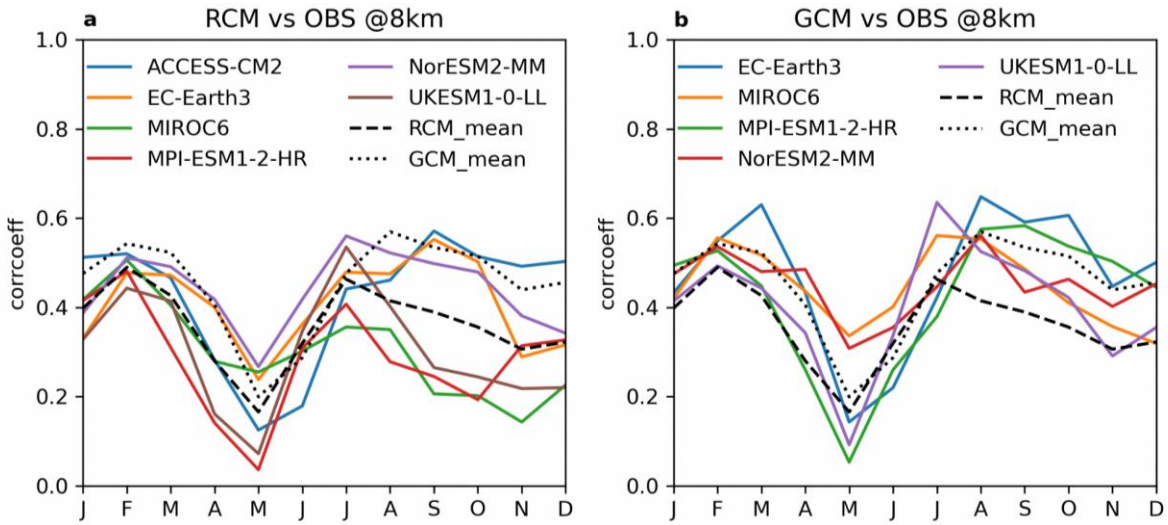

Figure 7.19: Correlation coefficient between the 8km observation and RCMs (a) or GCMs (b) over the MC region as to the ENSO teleconnection in the JJA season of the historical period (1995-2014).

7.6 Evaluation of local-scale climatology over Singapore

Assessment of regional scale climatology was presented in subchapter 7.4 above, which looked at the evaluation of key climate variables over the Maritime Continent in the 8 km downscaled simulations. In this subchapter we focus on the evaluation of 2 km downscaled simulations over Singapore. We have also carried out evaluation of the 8 km simulations over Singapore, but since the 2 km simulations are the primary dataset for the climate change projections over Singapore presented in Chapter 10, we present the evaluation of the 2 km historical simulations in this chapter.

7.6.1 Mean Rainfall

The annual mean spatial pattern of precipitation over Singapore is shown in Figure 7.20. The mean precipitation values range from 0-10mm/day. The kriged precipitation over the Singapore land grids uses 28 observational stations with continuous data availability during the analysis period (1995-2014) Figure 7.20a. Please see Chapter 9 Section 9.7.1 for more information on the kriged rainfall.

The SINGV-RCM simulations at 2 km resolution forced by SINGV-RCM 8 km obtained from forcing ERA5 reanalysis is shown in Figure 7.20b and the multi-model annual pattern of mean precipitation simulated using 5 GCMs is shown in Figure 7.20c. The bias in the simulated annual mean precipitation with respect to station kriged precipitation are shown in Figure 7.20d, and e for downscaled data using ERA5 and multi-model mean, respectively.

The overall pattern of precipitation over the Singapore land grid points are well captured in the 2km model downscaled using ERA5 and multi-model mean with respect to the kriged precipitation mean.

The annual mean precipitation bias for ERA5 downscaled simulation (Figure 7.20d) shows dry bias over the central land grids and exhibits dry biases over the coastal grids of Singapore. This may be due to the fact that the model sees those grids as Ocean grid points. Also there is a slight overestimation of precipitation over the northernmost land grid points. MMM downscaled simulations (Figure 7.20e) shows similar low bias over the central land grids and exhibit dry biases over the coastal grids of Singapore, and we don't find the overestimation of precipitation over the northernmost land grid points.

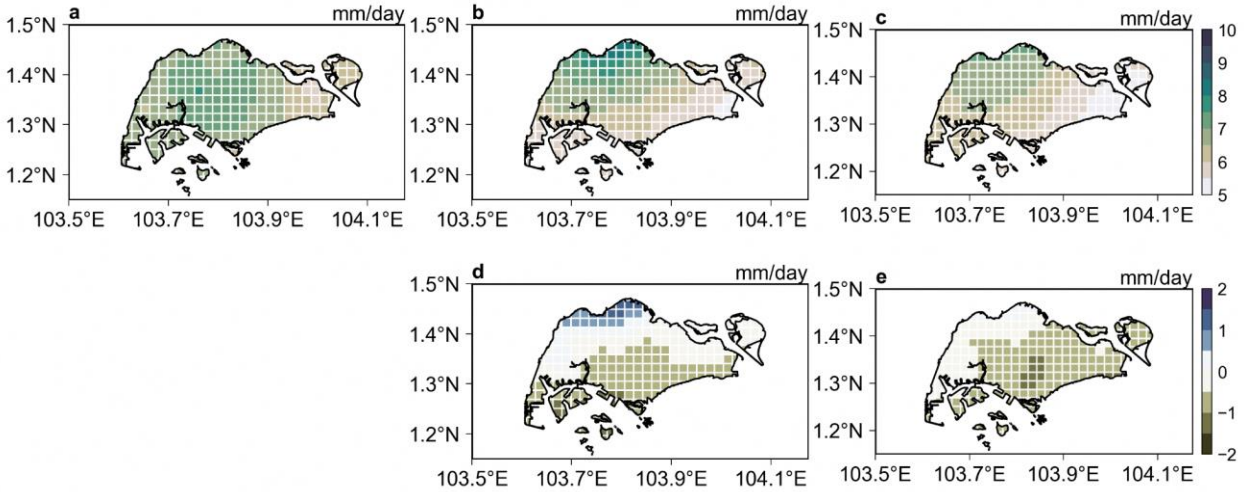

Figure 7.20: Annual mean precipitation in (a) Kriging gridded dataset, (b) ERA5 downscaled by SINGV (SINGV-ERA5) (c) Multimodel mean of downscaled GCM simulations with SINGV (SINGV-MMM). (d) shows the bias in SINGV-ERA5 (i.e. b -a), while (e) shows the bias in SINGV-MMM (i.e. c-a).

7.6.2 Rainfall Extremes

Extreme precipitation events are defined as the annual maximum daily maximum precipitation (Rx1day). The Annual RX1day spatial pattern of precipitation over Singapore is shown in Figure 7.21. The Annual RX1day in kriged precipitation ranges from 80 to 180 mm. There is a clear east-west contrast with east being wet and west being dry in the station observations Figure 7.21a.

The Annual RX1day of SINGV-RCM simulations at 2 km resolution from ERA5 is shown in figure 7.21b and the multi-model annual pattern of mean precipitation simulated using 5 GCMs is shown in Figure 7.21c.

The bias in the simulated Annual RX1day precipitation with respect to station kriged precipitation are shown in Figures 7.21d and 7.21e for downscaled using ERA5 and multi-model mean respectively. The Annual RX1day precipitation by 2km model downscaled using ERA5 shows upwards of 80mm in the grids over North-west of Singapore, while the 2km model downscaled using multi-model mean shows wet bias upwards of 80mm in grids over central-west land points of Singapore with respect to the kriged Annual RX1day precipitation.

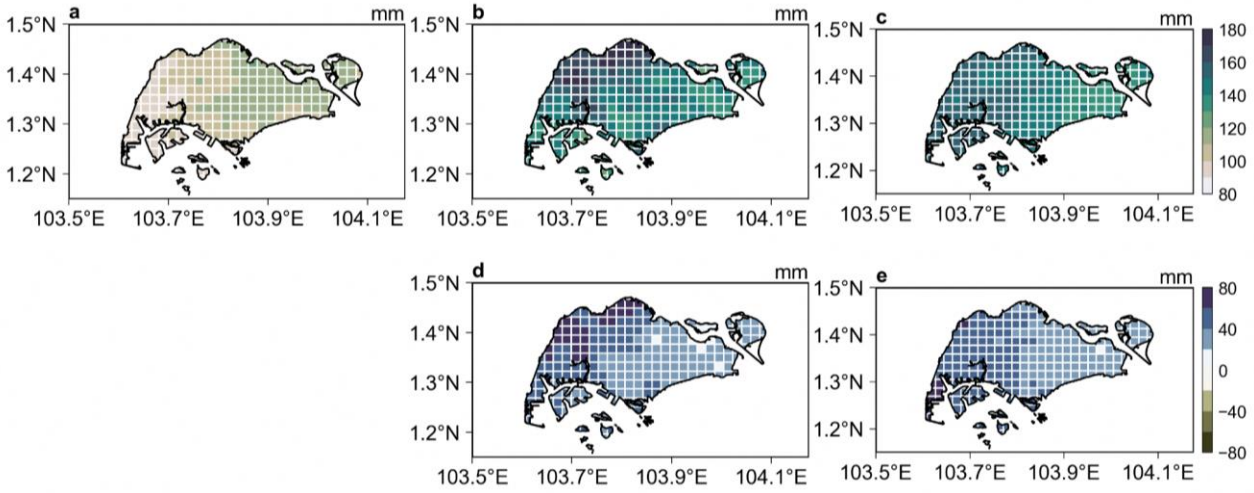

Figure 7.21: Annual RX1day in (a) kriged gridded dataset, (b) ERA5 downscaled by SINGV-RCM (SINGV-ERA5), (c) multimodel mean of downscaled GCM simulations with SINGV-RCM (SINGV-MMM). (d) Shows the bias in SINGV-ERA5 (i.e. b -a), while (e) shows the bias in SINGV-MMM (i.e. c-a).

7.6.3 Mean Temperature

The Annual spatial pattern of mean temperature over Singapore is shown in Figure 7.22. The mean annual temperature values range from 27-29 deg. Celsius.

The SINGV-RCM simulation of annual pattern of mean temperature at 2 km resolution forced by ERA5 reanalysis is shown in Figure 7.22a and the multi-model downscaled annual pattern of temperature simulated using 5 GCMs is shown in Figure 7.22b.

The overall pattern of annual Mean Temperatures over the Singapore land grid points are well captured in the 2km model downscaled using ERA5 and multi-model mean, with warm temperatures over the Central Business District (CBD) regions and cooler temperature over the less urbanized areas of North-West and Central regions.

Large warm biases are confined only over the coastal grid points and most grid points in the urbanized area are within the range of 0.1-0.3 deg. Celsius as shown in Figure 7.22c.

7.6.4 Temperature Extremes

Extreme Temperature events are defined as the highest maximum temperature (TXx) of the monthly maximum value of daily maximum temperature (TX). The Annual TXx spatial pattern of Temperature over Singapore is shown in Figure 7.23. The Annual TXx ranges from 30 to 38 deg. Celsius. The warmer temperature grids of above 36 deg. Celsius covers about 70-80% of Singapore land grid points in the ERA5 downscaled data as shown in Figure 7.23a.

The Annual TXx of SINGV-RCM simulations at 2 km resolution from ERA5 is shown in Figure 7.23a and the multi-model Annual TXx simulated using 5 GCMs is shown in Figure 7.23b.

The bias in the multi-model simulated (MMM) Annual TXx with respect to ERA5 downscaled data is shown in Figure 7.23c. The warm bias is between 1-2 deg. Celsius in the grids confined only over the northernmost land points and coastal land points of Singapore.

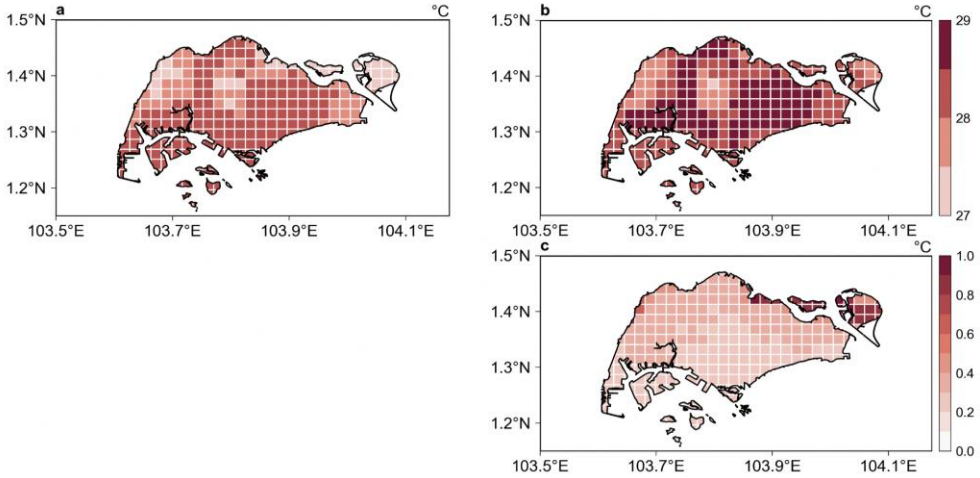

Figure 7.22: Annual mean temperature in (a) ERA5 downscaled by SINGV (SINGV-ERA5) (b) Multimodel mean of downscaled GCM simulations with SINGV (SINGV-MMM) and (c) shows the bias in SINGV-MMM relative to SINGV-ERA5 (i.e. b-a).

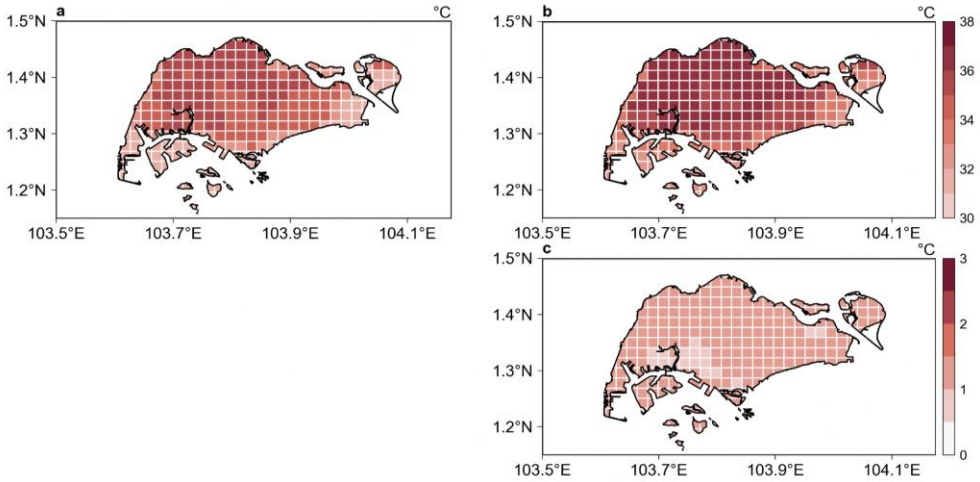

Figure 7.23: Annual TXx in (a) ERA5 downscaled by SINGV (SINGV-ERA5) (b) Multimodel mean of downscaled GCM simulations with SINGV (SINGV-MMM) and (c) shows the bias in SINGV-MMM relative to SINGV-ERA5 (i.e. b-a).

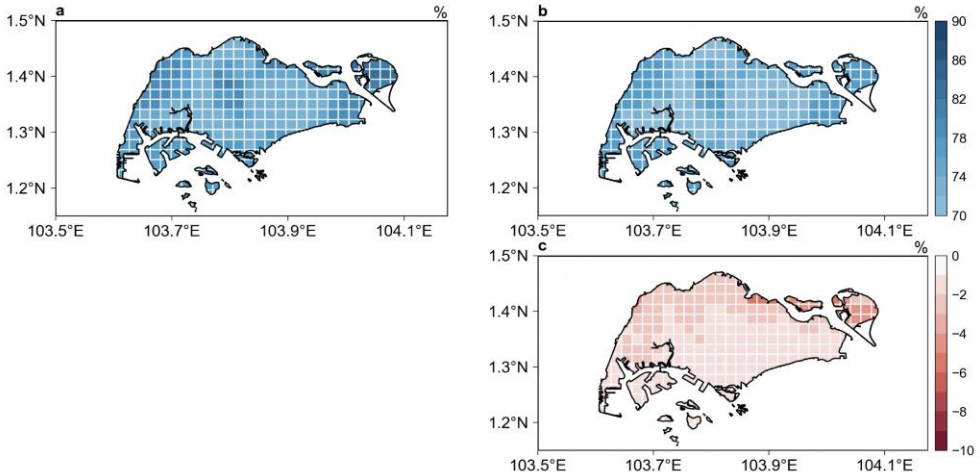

Figure 7.24: Annual mean relative humidity in (a) ERA5 downscaled by SINGV (SINGV-ERA5) (b) Multimodel mean of downscaled GCM simulations with SINGV (SINGV-MMM). (c) the bias in SINGV-MMM relative to SINGV-ERA5 (i.e. b -a).

7.6.5 Relative Humidity

The annual mean relative humidity over Singapore is shown in Figure 7.24. The mean relative values range from 70-90%, which is typical of a humid tropical location.

The SINGV-RCM simulations at 2 km resolution forced by SINGV-RCM 8 km obtained from forcing ERA5 reanalysis is shown in Figure 7.24a and the multi-model mean pattern of annual mean relative humidity simulated using 5 GCMs is shown in Figure 7.24b. The bias in the simulated annual mean relative humidity with respect to ERA5 downscaled dataset is shown in Figure 7.24c.

The annual mean relative humidity bias for MMM downscaled simulations (Figure 7.24c) shows negative bias over the east and west of central land grids and exhibits less biases over the southern coastal grids of Singapore.

7.6.6 Winds

The annual mean wind speed over Singapore is shown in Figure 7.25. The annual mean wind speed values range from 0-5 m/s.

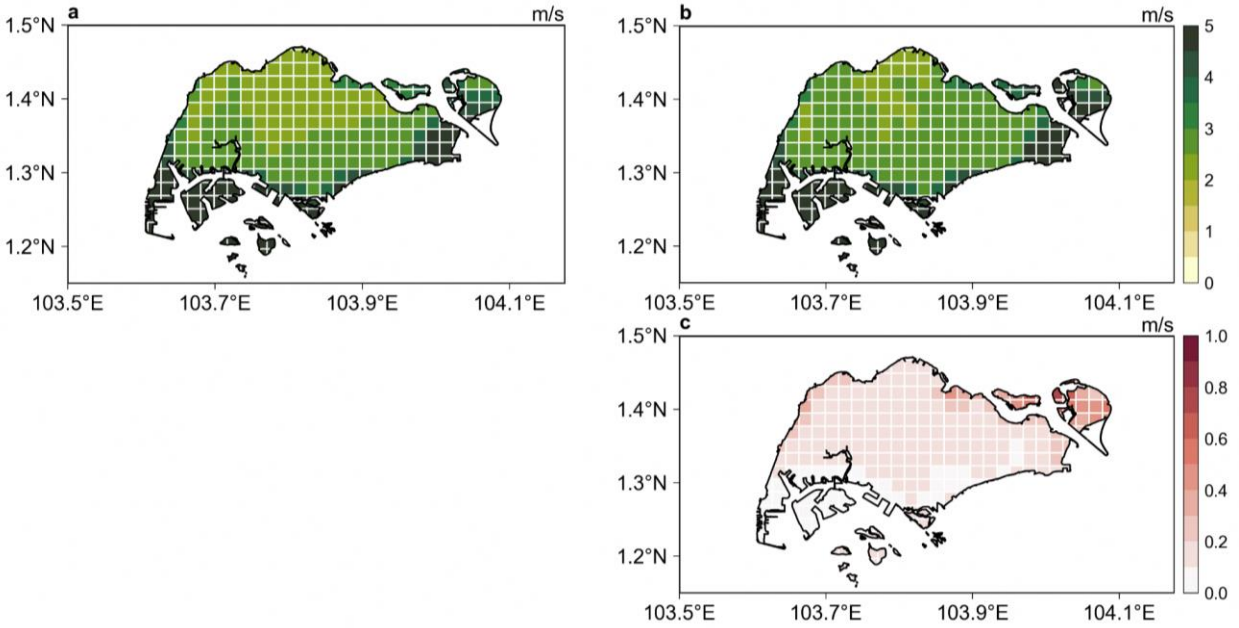

Figure 7.25: Annual mean wind speed in (a) ERA5 downscaled by SINGV (SINGV-ERA5) (b) Multimodel mean of downscaled GCM simulations with SINGV (SINGV-MMM). (c) the bias in SINGV-MMM relative to SINGV-ERA5 (i.e. b -a).

The SINGV-RCM simulations at 2 km resolution forced by SINGV-RCM 8 km obtained from forcing ERA5 reanalysis is shown in Figure 7.25a and the multi-model pattern of annual mean wind speed simulated using 5 GCMs is shown in Figure 7.25b. The bias in the simulated annual mean wind speed with respect to ERA5 downscaled dataset is shown in Figure 7.25c.

The annual mean wind speed bias for MMM downscaled simulations (Figure 7.25c) shows positive bias over the most of northern coastal grid points and exhibits less biases over the land grids of Singapore.

7.8 Summary

In summary, the downscaled simulations from ERA5 as well as 6 GCMs to 8 km resolution over South East Asia have shown added value in each variable compared to observations. Though the 2 km is not statistically different to 8 km over the western Maritime continent domain, to balance between very high computation costs and to benefit from high-resolution climate downscaling, we performed 2 km time slice simulations over the western Maritime continent domain in the historical as well as in the future for certain specific agency applications.

Following are some of the key summary points from this study:

1. We have clearly shown that there are added values in downscaling the coarse resolution driving models namely ERA-5 and 6 GCMs to 8 km and further to 2 km resolution.
2. We have clearly demonstrated the SINGV-RCM downscaling is consistent with the parent driving model and follows the long-term trends and variability of the parent driving model.
3. In this chapter, we evaluated the downscaled simulations of important meteorological parameters like precipitation, temperature, relative humidity as well as wind speed for different time scales of variability from diurnal to seasonal and their annual cycles are reproduced well in the model.
4. The important meteorological variables simulated by SINGV-RCM are compared with the available high-resolution regional observations like in situ (ground-based stations) and satellite merged products for establishing the model's skill in the historical period.
5. We have also brought out that the model is able to capture the regional climate drivers like remote teleconnection (ENSO-teleconnection) and processes like cold surges over this region by performing diagnostics with both observational data as well as simulated data.
6. Finally, the model is also evaluated over Singapore land grids using high resolution station observations in capturing the climate of the city state.

This chapter has documented the added value brought by the dynamical downscaling using SINGV-RCM to 8 km and 2 km resolution over SEA and WMC domains and the model's skill in capturing the different times scales of variability and also its ability to capture different regional processes. Further the usefulness of high-resolution 2km simulation in capturing the climate of a city state like Singapore is evident when compared with very high-resolution (both temporal as well as spatial) insitu station datasets.

References

Gelaro, R., and Coauthors, 2017: The Modern-Era Retrospective Analysis for Research and Applications, Version 2 (MERRA-2). J. Climate, 30, 5419–5454, https://doi.org/10.1175/JCLI-D-16-0758.1.

Hersbach, H, Bell, B, Berrisford, P, et al. The ERA5 global reanalysis. Q J R Meteorol Soc. 2020; 146: 1999– 2049. https://doi.org/10.1002/qj.3803.

Huffman, G.J.; Bolvin, D.T.; Braithwaite, D.; Hsu, K.; Joyce, R.; Kidd, C.; Nelkin, E.J.; Sorooshian, S.; Tan, J.; Xie, P. NASA Global Precipitation Measurement (GPM) Integrated Multi-satellitE Retrievals for GPM (IMERG). In Algorithm Theoretical Basis Document (ATBD) Version 06; NASA/GSFC: Greenbelt, MD, USA, 2019.

Huffman, George J., Bolvin, David T., Nelkin, Eric J., Wolff, David B., Adler, Robert F., Gu, Guojun, Hong, Yang, Bowman, Kenneth P., Stocker, Erich F.. 2007. The TRMM Multisatellite Precipitation Analysis (TMPA): Quasi-Global, Multiyear, Combined-Sensor Precipitation Estimates at Fine Scales. Journal of Hydrometeorology. Vol. 8, No. 1, pp. 38-55. DOI: 10.1175/JHM560.1 ISSN: 1525-755X, 1525-7541.

Morice, C. P., J. J. Kennedy, N. A. Rayner, and P. D. Jones (2012), Quantifying uncertainties in global and regional temperature change using an ensemble of observational estimates: The HadCRUT4 dataset, J. Geophys. Res., 117, D08101, doi:10.1029/2011JD017187.

Nguyen, P., E.J. Shearer, H. Tran, M. Ombadi, N. Hayatbini, T. Palacios, P. Huynh, G. Updegraff, K. Hsu, B. Kuligowski, W.S. Logan, and S. Sorooshian, The CHRS Data Portal, an easily accessible public repository for PERSIANN global satellite precipitation data, Nature Scientific Data, Vol. 6, Article 180296, 2019. doi: https://doi.org/10.1038/sdata.2018.296.

Roca, R., Alexander, L. V., Potter, G., Bador, M., Jucá, R., Contractor, S., Bosilovich, M. G., and Cloché, S.: FROGS: a daily 1° × 1° gridded precipitation database of rain gauge, satellite and reanalysis products, Earth Syst. Sci. Data, 11, 1017–1035, https://doi.org/10.5194/essd-11-1017-2019, 2019.

Rohde, R. A. and Hausfather, Z.: The Berkeley Earth Land/Ocean Temperature Record, Earth Syst. Sci. Data, 12, 3469–3479, https://doi.org/10.5194/essd-12-3469-2020, 2020.

Sadeghi, M., Nguyen, P., Naeini, M.R. et al. PERSIANN-CCS-CDR, a 3-hourly 0.04° global precipitation climate data record for heavy precipitation studies. Sci Data 8, 157 (2021). https://doi.org/10.1038/s41597-021-00940-9.

Shinya KOBAYASHI, Yukinari OTA, Yayoi HARADA, Ayataka EBITA, Masami MORIYA, Hirokatsu ONODA, Kazutoshi ONOGI, Hirotaka KAMAHORI, Chiaki KOBAYASHI, Hirokazu ENDO, Kengo MIYAOKA, Kiyotoshi TAKAHASHI, The JRA-55 Reanalysis: General Specifications and Basic Characteristics, Journal of the Meteorological Society of Japan. Ser. II, 2015, Volume 93, Issue 1, Pages 5-48, Released on J-STAGE March 18, 2015, Online ISSN 2186-9057, Print ISSN 0026-1165, https://doi.org/10.2151/jmsj.2015-001.

Torres-Alavez, J. A., F. Giorgi, F. Kucharski, E. Coppola, and L. Castro-García, 2021: ENSO teleconnections in an ensemble of CORDEX-CORE regional simulations. Clim. Dyn., 57, 1445–1461, https://doi.org/10.1007/s00382-020-05594-8.

Xie P, Joyce R, Wu S, Yoo S-H, Yarosh Y, Sun F and Lin R : 2017 Reprocessed, bias-corrected CMORPH global high-resolution precipitation estimates from 1998 J. Hydrometeorol. 18 1617–41.

Appendix

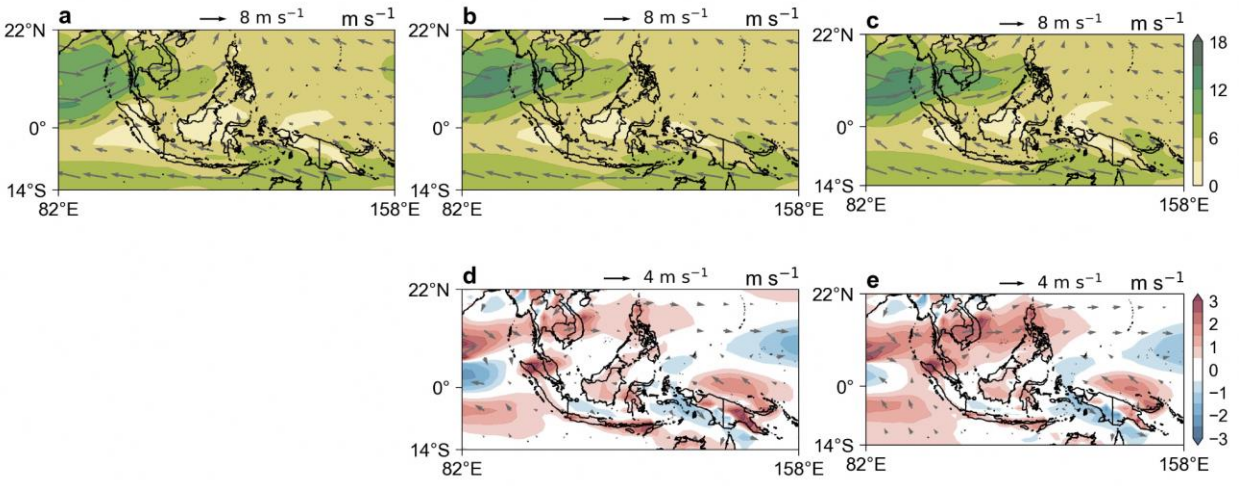

Figure A7.1: Mean JJA 850 hPa winds (quivers) and wind speed (shaded) in (a) ERA5, (b) Mutimodel mean of 49 CMIP6 models, (c) Multimodel mean of GCMs used in downscaling. (d) shows the bias of the 49 CMIP6 models (i.e. b-a), while (e) shows the bias in the GCMs used in downscaling (i.e. c-a). Data in these plots have been regridded to 1.5x1.5 degrees.

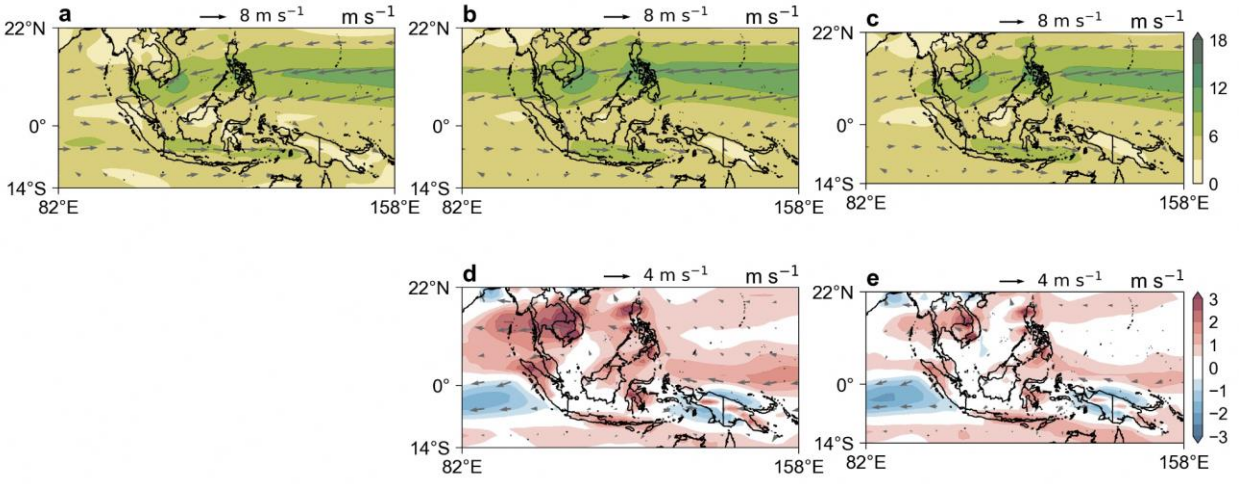

Figure A7.2: Mean DJF 850 hPa winds (quivers) and wind speed (shaded) in (a) ERA5, (b) Mutimodel mean of 49 CMIP6 models, (c) Multimodel mean of GCMs used in downscaling. (d) shows the bias of the 49 CMIP6 models (i.e. b-a), while (e) shows the bias in the GCMs used in downscaling (i.e. c-a). Data in these plots have been regridded to 1.5x1.5 degrees.

8

Regional Climate Change Projections

Authors:
Aurel Florian Moise, Sandeep Sahany, Muhammad Eeqmal Hassim, Chen Chen, Xin Rong Chua, Venkatraman Prasanna, Gerald Lim, Pavan Harika Raavi, Jianjun Yu, Fei Luo

METEOROLOGICAL SERVICE SINGAPORE
Centre for Climate Research Singapore

8.1 Introduction

In the V3 study, the SINGV-RCM has been used to dynamically downscale six sub-selected CMIP6 GCMs over the SEA domain at 8 km horizontal resolution for the historical period (1955-2014) and for the future (2015-2099) under 3 IPCC AR6 global warming scenarios (SSP1-2.6, SSP2-4.5 and SSP5-8.5). This dataset provides the most up-to-date and highest-resolution climate change projections over the SEA region when writing this report.

Although the regional climate change projections were also presented in Chapter 4 of this report using CMIP6 GCM outputs and from the existing literature, results presented in this chapter are based on the 8 km dynamically downscaled projections. The 8 km downscaled projections, although not expected to significantly deviate from the GCM-based projections when it comes to large-scale drivers, are still expected to add a lot more spatial details that cannot be seen from GCM data due to their coarser resolution.

This chapter presents the projections of means and extremes for key climate variables (rainfall, temperature, and relative humidity) over the region and key climate drivers (monsoons, northeast monsoon surges, and ENSO teleconnections). Where appropriate, we also discuss related changes reported in the literature.

8.2 Data and Methodology

This chapter makes use of the historical (1995-2014) and future (mid-century: 2040-2059 and end-century: 2080-2099) 8 km downscaled data over SEA under the 3 SSPs (SSP1-2.6, SSP2-4.5, and SSP5-8.5) to compute projected changes in means and extremes for some key climate variables and some key climate drivers.

Specifically, we compute the mean changes in rainfall and temperature on annual and seasonal timescales (DJF, MAM, JJA, and SON) for mid- and end-century under the 3 SSPs. In addition to the mean, we also compute the changes in temperature and rainfall extremes. For rainfall extremes, we compute changes in the annual maximum 1-day rainfall (RX1day) and annual maximum 5-day rainfall (RX5day), and for temperature extremes, we compute changes in the daily maximum and daily minimum temperatures. We also compute changes in the mean near-surface relative humidity on annual and seasonal timescales for mid- and end-century under the 3 SSPs.

Along with the computation of changes in key climate variables, we also compute changes in some of the important large-scale climate drivers over the region. As mentioned above, we don't expect any significant deviations in the projected changes of the large-scale climate drivers compared to the driving GCMs, except for more spatial details in the downscaled simulations. Specifically, (1) we compute projected changes in the 850hPa winds for each of the seasons mentioned above and, along with the seasonal mean rainfall changes, infer projected changes in the monsoon circulation and associated rainfall, (2) we compute the projected changes in 850 hPa winds and rainfall associated with the northeast monsoon surges, and (3) we present projected changes in the JJA ENSO-rainfall teleconnection by computing correlation coefficient of the 8 km downscaled rainfall with the Nino3.4 SSTs from the driving GCMs.

8.3 Climate Change Projections over the Maritime Continent

In this section, we present the projections of key climate variables (rainfall, temperature, and relative humidity) over the MC from the 8km downscaled projections.

8.3.1 Changes in annual mean rainfall

Figure 8.1 shows the projected changes in the annual mean rainfall over SEA (left panel) and SEA land-only points (right panel) in the mid-century and end-century relative to the historical baseline under the three SSP scenarios. They are also shown in tabular form in Tables 8.1 and 8.2 for readability.

Overall, there is a projected increase in annual mean domain-average rainfall over SEA during the mid and end centuries. Based on the multi-model mean, the end-century change is higher than the mid-century change for each of the scenarios. The inter-scenario spread is larger

during the end of the century (more than 3%) compared to the mid-century (within 1%). The multi-model end-century changes indicate larger increases in domain-average rainfall under scenarios with greater warming, i.e., change under SSP5-8.5 being higher than SSP2-4.5, which in turn is higher than SSP1-2.6.

We also find the projected end-century mean under SSP5-8.5 to be positively skewed due to an outlier model (see the difference between the thin line and the diamond in the left panel of Figure 8.1).

Table 8.1: Projected changes in annual mean rainfall (percent change) - SEA

ANN	Mid-Century (%)		End-Century (%)	
	Mean	Range	Mean	Range
SSP1-2.6	2.1	0.6 to 4.0	2.9	1.3 to 5.7
SSP2-4.5	3.0	1.2 to 4.9	4.0	1.7 to 5.6
SSP5-8.5	2.7	1.0 to 5.3	6.0	0.2 to 15

Table 8.2: Projected changes in annual mean rainfall (percent change) - SEA land regions

ANN	Mid-Century (%)		End-Century (%)	
	Mean	Range	Mean	Range
SSP1-2.6	2.9	0.4 to 4.5	3.9	2.6 to 5.5
SSP2-4.5	4.0	1.6 to 6.6	5.8	3.8 to 7.9
SSP5-8.5	4.0	0.5 to 6.3	8.7	4.2 to 13.4

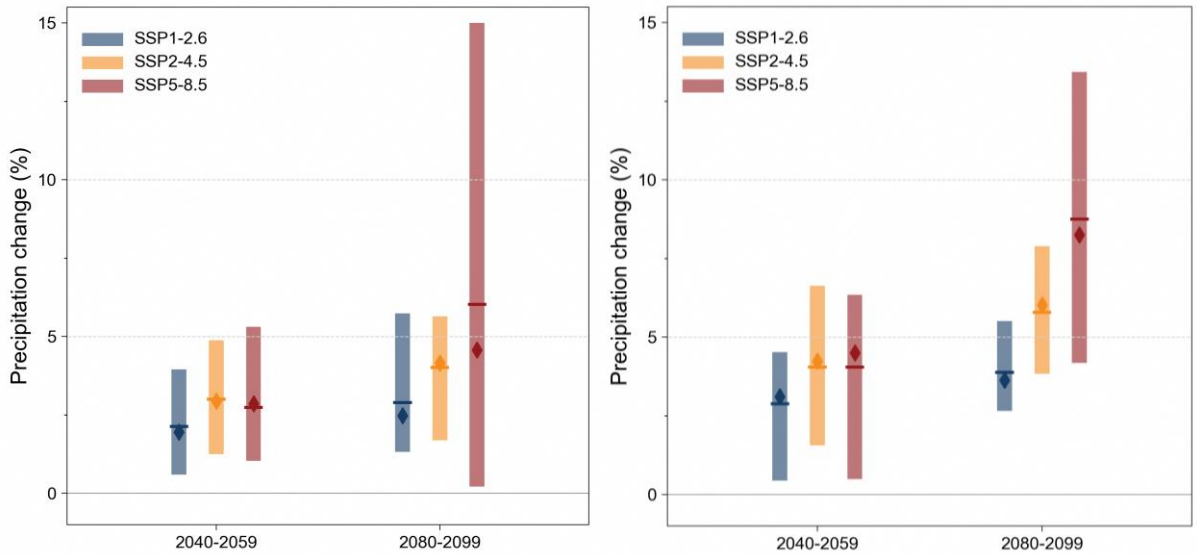

Figure 8.1: Percentage change of annual mean rainfall (pr) over the mid- (2040-59) and end-century (2080-99) period for the six downscaled GCMs (8km) over the SEA domain (left) and SEA land only (right) relative to the historical (1995-2014) baselines. The line and diamond represent the mean and median using the six models, respectively.

Over SEA land points, the projected changes show similar behaviour as the domain average. However, the projected change over land is higher than seen over the entire domain, suggesting higher rainfall changes over land than ocean points. Also, the positive skew seen in the projected end-century mean under SSP5-8.5 is less prominent for SEA land, suggesting that the outlier model projects significant positive changes over the ocean points.

8.3.2 Changes in seasonal mean rainfall

Figure. 8.2 shows the projected changes in the seasonal mean rainfall over SEA land in the mid-century and end century relative to the historical under three SSP scenarios using 8km downscaled GCM simulations. For readability, they are also shown in tabular form in Tables 8.3-8.6 for land. As seen in Figure 8.2, the projected seasonal multi-model mean rainfall is expected to increase both in mid-century and end century across different seasons. During the DJF season, the multi-model seasonal mean rainfall is projected to increase with warming both in mid-century and end century (Table 8.3). In the mid-century, the rainfall changes are similar in SSP1-2.6 (2.8%) and SSP2-4.5 (2.8%) but are larger under SSP5-8.5 (4.6%). In the end century, multi-model rainfall is projected to increase across all scenarios from SSP1-2.6 (2.4%), to SSP2-4.5

(5.0%), to SSP5-8.5(8.0%). The end-century multi-model mean rainfall projections are larger than the mid-century projections in SSP2-4.5 and SSP5-8.5 but slightly smaller in SSP1-2.6.

Table 8.3: Projected changes in seasonal mean rainfall (percent change) - DJF

DJF	Mid-Century (%)		End-Century (%)	
	Mean	Range	Mean	Range
SSP1-2.6	2.8	-1.4 to 5.8	2.4	-0.3 to 10.6
SSP2-4.5	2.8	-3.2 to 5.9	5.0	0 to 10.5
SSP5-8.5	4.6	1.2 to 8.5	8.0	2.5 to 14.5

For the MAM season, the rainfall is projected to increase over the SEA both in mid-century and end century compared to the historical period across all the scenarios. Both in the mid-century and end century, rainfall is projected to increase with warming from SSP1-2.6 to SSP5-8.5. The difference between mid-century and end-century changes is larger in SSP2-4.5 and SSP5-8.5 (~3%) than in SSP1-2.6 (~1.5%).

Table 8.4: Projected changes in seasonal mean rainfall (percent change) - MAM

MAM	Mid-Century (%)		End-Century (%)	
	Mean	Range	Mean	Range
SSP1-2.6	1.3	-3.1 to 4.2	2.8	0.2 to 5.8
SSP2-4.5	2.2	-1.5 to 6.3	5.3	0.4 to 10.6
SSP5-8.5	4.0	-0.9 to 6.6	7.5	0.2 to 16.8

Overall, the seasonal rainfall projections for the JJA seasons show an increase both in mid-century and end-century compared to the historical period. In the mid-century, there is a difference in the magnitude of the rainfall increases with the SSP2-4.5 scenario projecting higher percentage changes compared to the other two scenarios. Across the scenarios between mid-century and end century, the SSP5-8.5 scenario projects higher percentage increases in JJA rainfall compared to other two scenarios.

Table 8.5: Projected changes in seasonal mean rainfall (percent change) - JJA

JJA	Mid-Century (%)		End-Century (%)	
	Mean	Range	Mean	Range
SSP1-2.6	3.3	0.8 to 9.6	5.0	0.8 to 10.7
SSP2-4.5	5.3	3.1 to 10.2	5.1	-3.7 to 14.6
SSP5-8.5	2.7	-1.3 to 9.4	7.4	-1.7 to 13.4

For the SON season, the rainfall is projected to increase both in mid-century and end century compared to the historical with higher percentage changes in the end century. When moving across scenarios, at the end of the century there are higher percentage changes in the rainfall when moving from SSP2-4.5 to SSP5-8.5 scenario.

Table 8.6: Projected changes in seasonal mean rainfall (percent change) - SON

SON	Mid-Century (%)		End-Century (%)	
	Mean	Range	Mean	Range
SSP1-2.6	4.1	0.0 to 7.1	4.9	1.7 to 8.0
SSP2-4.5	5.5	-0.7 to 12.8	8.0	3.3 to 13.8
SSP5-8.5	5.4	0.8 to 11.5	12.7	5.1 to 19.0

Figure. 8.3 shows the percentage changes in the seasonal mean rainfall (ensemble mean) over SEA regions in the end century relative to the historical period under the SSP5-8.5 scenario. As seen in Figure 8.3, the seasonal mean rainfall changes vary with seasons over land and ocean regions. Increases in rainfall can be seen over parts of Indochina across the four seasons.

For the DJF season, there are large percentage increases (>90%) over the climatologically dry regions of Thailand and Cambodia (see Figure 7.4). In their analysis of changes of CORDEX RCMs over the end-century (2070-2099) relative to the historical (1976-2005), Tangang et al. (2020) noted increased rainfall of 10-20% over Indochina, which was consistent with the changes from GCMs.

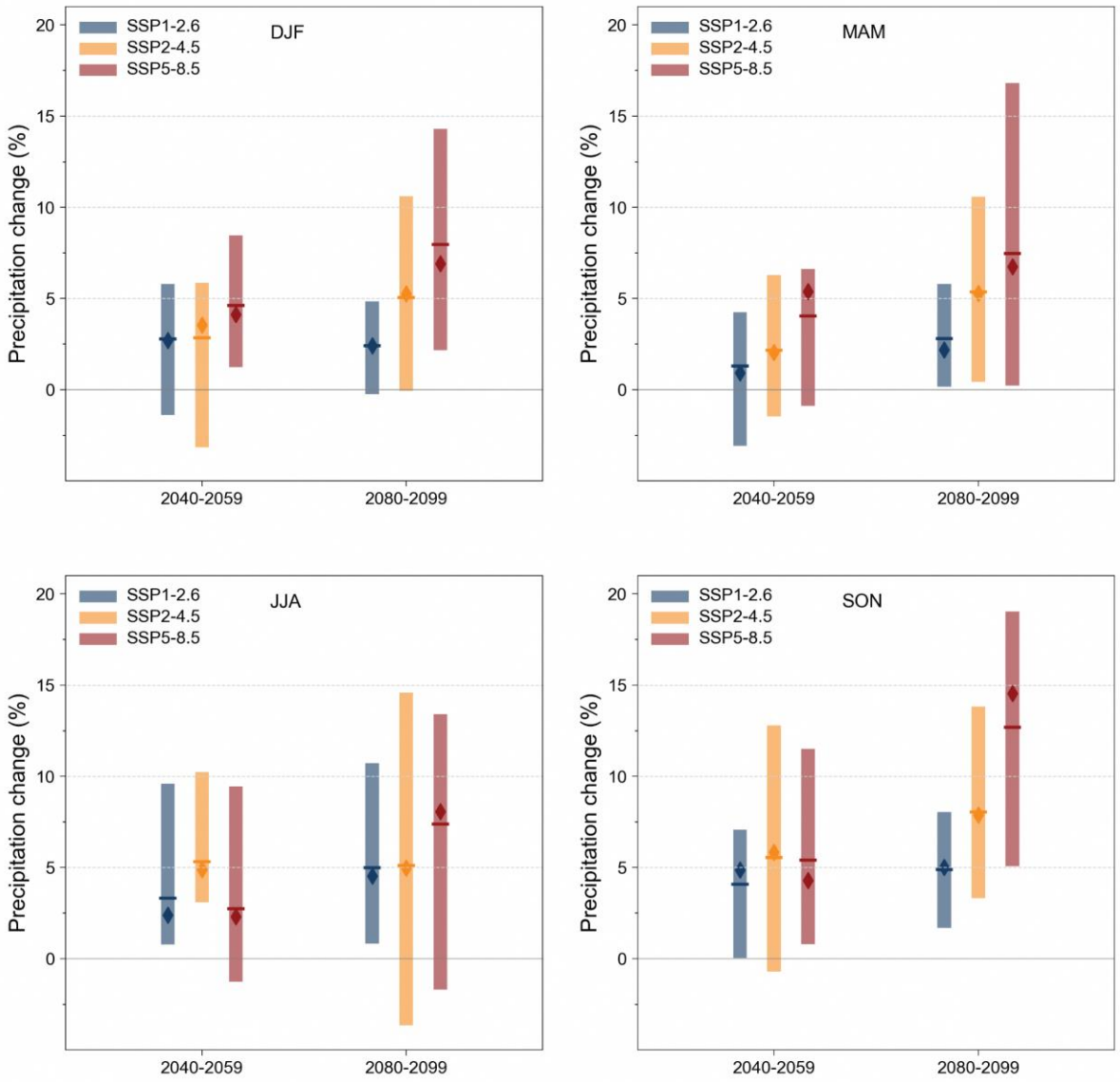

Figure 8.2: Percentage change of seasonal mean rainfall (pr) over the mid- (2040-59) and end-century (2080-99) period for the 6 downscaled GCMs (8km) over the SEA land relative to the historical (1995-2014) baselines. The line and diamond represent the mean and median using the 6 models, respectively.

During the MAM season, the seasonal mean rainfall is projected to increase (10-70%) over many SEA land regions. During the JJA season, the mean rainfall projections show increases (10-90%) over parts of Myanmar, Thailand, Malaysia, and around Java. Note that Java climatologically experiences little rainfall in JJA (see Figure 7.5) There is a percentage decrease (10-30%) in the mean rainfall over parts of Cambodia, Vietnam, Borneo, and New Guinea. For the SON season, the mean rainfall projections show percentage increases (10-90%) over the SEA nations with higher increases over Myanmar and around Nusa Tenggara. Tangang et al (2020) emphasize rainfall reduction of 10-30% in JJA, especially over Kalimantan and Sumatra and note that this drying has also been found in GCM simulations. They suggest it is linked to the equatorward contraction of the rising branch of the Hadley Circulation, the “deep tropical squeeze” discussed in Fu 2015. They also remark upon a reduction of 10-20% in mean rainfall over Cambodia, Vietnam, and eastern Thailand in the RCMs, which is not seen in the GCMs. These drying features are reflected in SINGV-MMM to some extent.

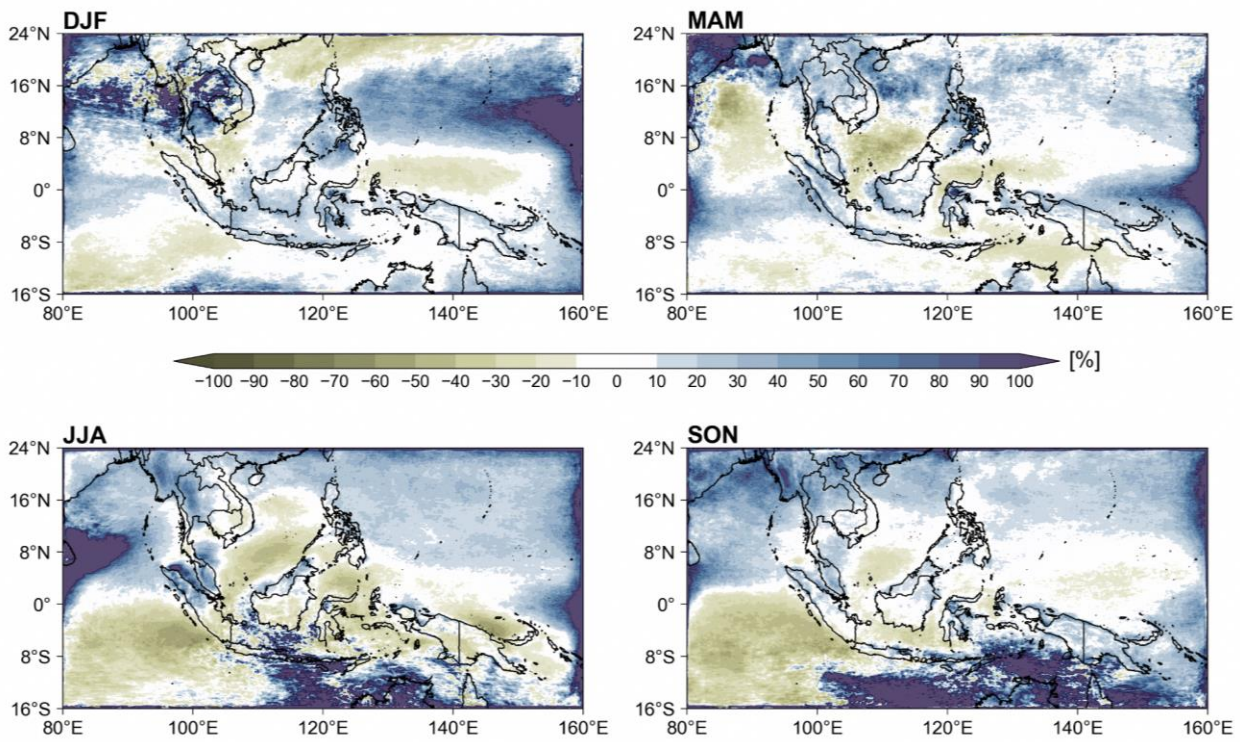

Figure 8.3: Percentage change of ensemble-mean downscaled (8km) changes in seasonal mean rainfall over end-century (2080-99) relative to the historical period (1995-2014) over the SEA domain under the SSP5-8.5 scenario.

8.3.3 Changes in rainfall extremes

Figure.8.4 shows the percentage changes in the maximum 1-day rainfall (RX1day) over SEA across different seasons in the end century relative to the historical under the SSP5-8.5 scenario. End-century RX1day is expected to increase in most of the SEA land regions across the four seasons.

During the DJF season, the projected RX1day percentage increases are largest over Thailand, Laos, and Cambodia. For the MAM season, the RX1day projections show increases (30%-70%) over the SEA land regions. During the JJA season, the projected RX1day increases (10%-100%) over most of the SEA land regions with decreases (-5% to -40%) around the Java sea. For the SON season, the RX1day projections increase (30%-100%) across the SEA land regions. Some of the largest percentage increases occur over climatologically dry regions (e.g. Indochina in DJF, around the Java sea in JJA).

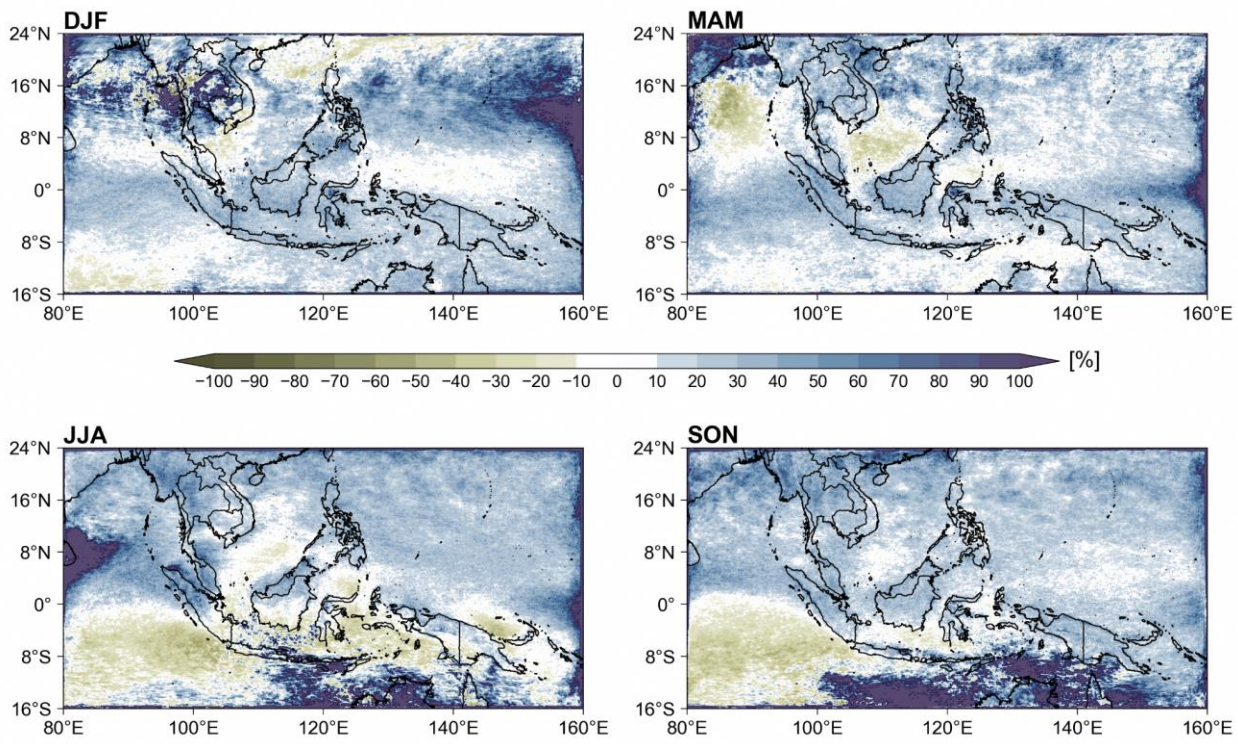

Figure 8.4: Percentage change of ensemble-mean downscaled (8km) changes in seasonal RX1day over end-century (2080-99) relative to the historical period (1995-2014) over the SEA domain under the SSP5-8.5 scenario.

Figure 8.5 shows the percentage changes in the maximum 5-day rainfall (RX5day) over SEA across different seasons in the end century relative to the historical under the high emission scenario (SSP5-8.5). RX5day is projected to increase with warming over much of SEA in most of the seasons, with features qualitatively similar to RX1day. During the DJF season, the RX5day projections show an increase (10%-100%) over much of the domain, with higher percentage increases over Thailand, Laos, and Cambodia. For the MAM season, the projected RX5day increases (30%-70%) across much of SEA land in the end century with some of the largest increases occurring west of Myanmar. During the JJA season, the projected RX5day increases with higher percentages (50%-90%) over the northern SEA nations. For the SON season, the RX5day projections show an increase (30%-100%) over most of the SEA nations.

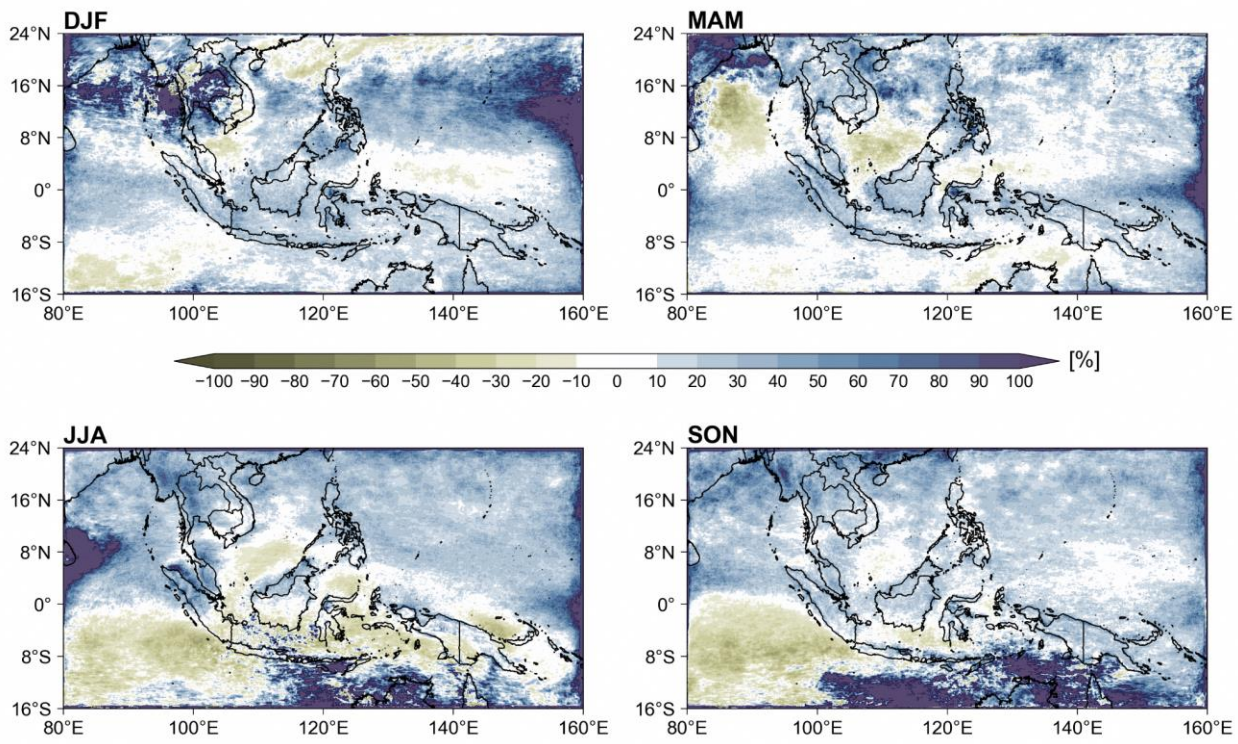

Figure 8.5: Percentage change of ensemble-mean downscaled (8km) changes in seasonal RX5day over end-century (2080-99) relative to the historical period (1995-2014) over the SEA domain under the SSP5-8.5 scenario.

8.3.4 Changes in annual mean temperature

Figure. 8.6 shows the projected changes in the annual mean near-surface air temperatures (tas) over SEA and SEA land regions during the mid-century (2040-59) and end century (2080-99) compared to historical (1995-2014) under three SSP scenarios using 8 km downscaled simulations. For readability, they are also shown in tabular form in Tables 8.7-8.8. Annual mean near-surface air temperatures increase over SEA and SEA land regions under different SSP scenarios. Over the SEA domain, the multi-model mean projected temperatures are expected to increase by at least 0.8ºC in the mid-century and by at least 1.0 ºC in the end century. Based on the multi-model mean projections, SEA land will experience increased warming as compared to the SEA domain by 0.1 ºC to 0.7 ºC (Tables 8.7 and 8.8) and up to 4.0 ºC by the end of the century. Land-amplified warming has been observed across multiple climate models, and can be explained by a simple analytical theory (Bryne and O'Gorman 2018)

Table 8.7: Projected changes in annual mean temperature - SEA

ANN	Mid-Century (ºC)		End-Century (ºC)	
	Mean	Range	Mean	Range
SSP1-2.6	0.8	0.6 to 1.1	1.0	0.5 to 1.4
SSP2-4.5	1.1	0.7 to 1.5	1.7	1.2 to 2.5
SSP5-8.5	1.4	0.9 to 1.9	3.3	2.4 to 4.4

Table 8.8: Projected changes in annual mean temperature - SEA land

ANN	Mid-Century (ºC)		End-Century (ºC)	
	Mean	Range	Mean	Range
SSP1-2.6	1.0	0.6 to 1.4	1.1	0.5 to 1.7
SSP2-4.5	1.2	0.8 to 1.8	2.1	1.4 to 3.0
SSP5-8.5	1.6	1.1 to 2.2	4.0	2.9 to 5.4

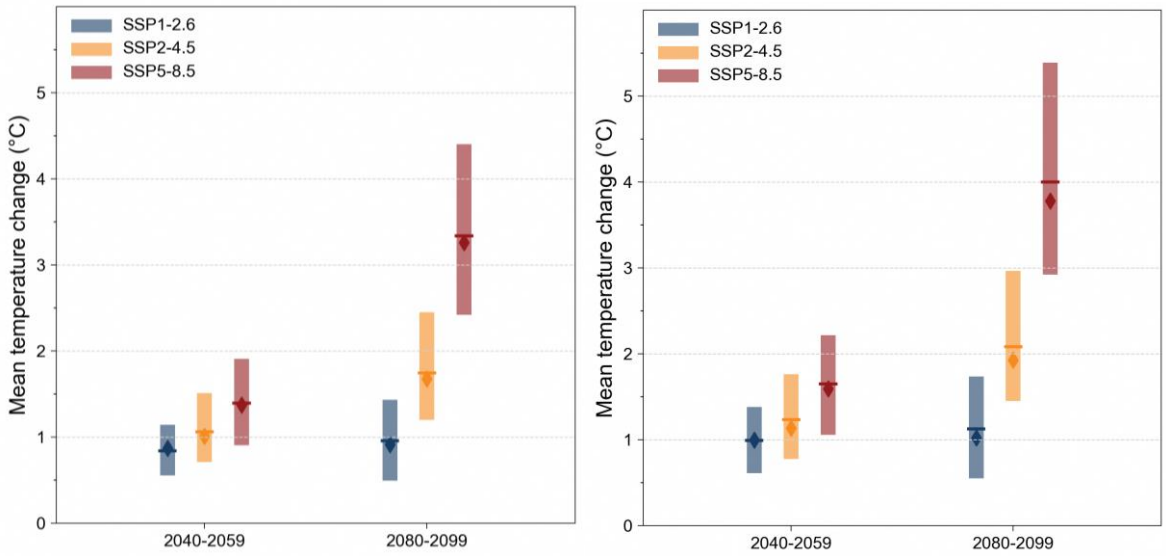

Figure 8.6: Average changes in annual mean near-surface air temperature (tas) over the mid- (2040-59) and end-century (2080-99) period for the 6 downscaled GCMs (8km) over the SEA domain (left) and SEA land only (right) relative to the historical (1995-2014) baselines. The line and diamond represent the mean and median using the 6 models, respectively.

Figure.8.7 shows the projected changes in the annual maximum (tasmax) and minimum near-surface air temperatures (tasmin) over SEA land regions in the mid-century and end century compared to historical under three SSP scenarios using 8 km downscaled GCM simulations. For readability, they are also shown in tabular form in Tables 8.9-8.10. As seen in Figure .8.7, the tasmax and tasmin temperatures over SEA land increase by similar amounts with warming across the different scenarios and time periods. There is a minimum increase of 1^{o}C of the tasmax and tasmin in mid and end century. Across the scenarios, towards the end century there is a higher degree of increases in tasmax and tasmin over SEA land regions under the SSP5-8.5 scenario. The qualitative changes in tasmax and tasmin are similar to those in tas (Figure 8.6).

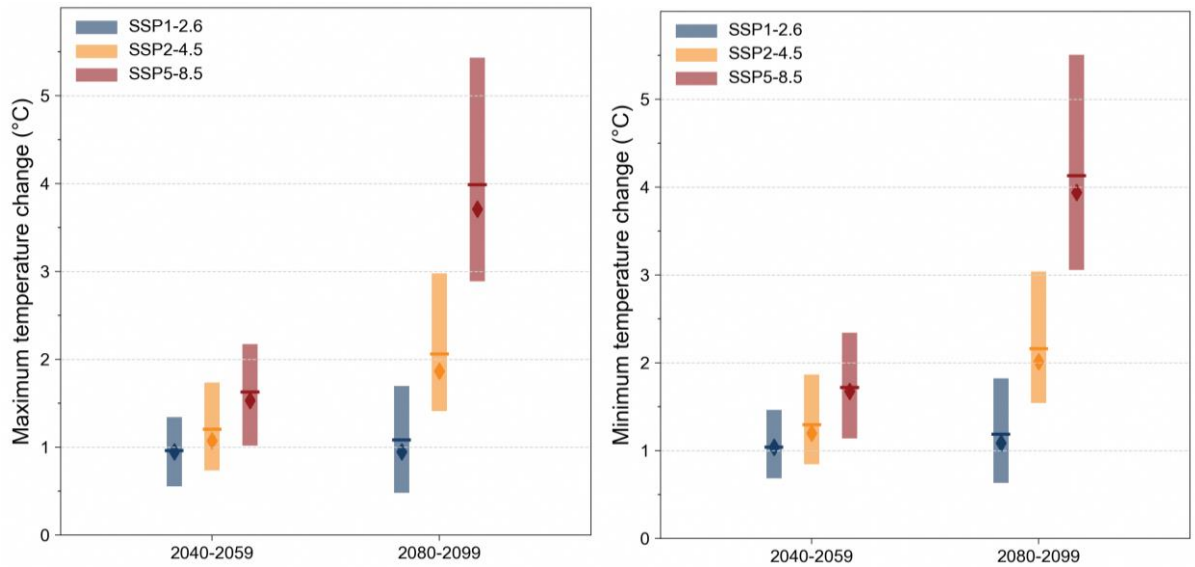

Figure 8.7: Average changes in annual maximum (tasmax) and minimum (tasmin) near-surface air temperature over the mid- (2040-59) and end-century (2080-99) period for the 6 downscaled GCMs (8km) over the SEA land relative to the historical (1995-2014) baselines. The line and diamond represent the mean and median using the 6 models, respectively.

Table 8.9: Projected changes in annual maximum temperature - SEA land

ANN	Mid-Century (ºC)		End-Century (ºC)	
	Mean	Range	Mean	Range
SSP1-2.6	1.0	0.6 to 1.3	1.1	0.5 to 1.7
SSP2-4.5	1.2	0.7 to 1.7	2.1	1.4 to 3.0
SSP5-8.5	1.6	1.0 to 2.2	4.0	2.9 to 5.4

Table 8.10: Projected changes in annual minimum temperature - SEA land

ANN	Mid-Century (ºC)		End-Century (ºC)	
	Mean	Range	Mean	Range
SSP1-2.6	1.0	0.7 to 1.5	1.2	0.6 to 1.8
SSP2-4.5	1.3	0.8 to 1.9	2.2	1.5 to 3.0
SSP5-8.5	1.7	1.1 to 2.3	4.1	3.1 to 5.5

8.3.5 Changes in seasonal mean temperature

Figure 8.8 shows the projected changes in the seasonal mean of daily maximum near surface temperatures (tasmax) over SEA land regions in the mid-century and end century relative to the historical under three SSP scenarios. For readability, they are also shown in tabular form in Tables 8.11-8.14. The projected tasmax temperatures increase with warming over SEA land regions across all the seasons. Across all seasons, the projected multi-model tasmax increases with warming in mid-century and end century. Across the scenarios, towards the end of the century there is an increased mean seasonal maximum temperature with higher increases under the SSP5-8.5 scenario (~3.9ºC). Based on the multi-model mean, across the seasons, mid-century tasmax would change from 0.9 ºC -1.7 ºC while end-century seasonal tasmax would change from 1.0 ºC -4.1 ºC.

Table 8.11: Projected changes in seasonal maximum temperature - DJF

DJF	Mid-Century (ºC)		End-Century (ºC)	
	Mean	Range	Mean	Range
SSP1-2.6	0.9	0.6 to 1.3	1.1	0.5 to 1.6
SSP2-4.5	1.2	0.6 to 1.6	2.0	1.2 to 2.8
SSP5-8.5	1.6	0.9 to 2.1	3.9	2.8 to 5.1

Table 8.12: Projected changes in seasonal maximum temperature - MAM

MAM	Mid-Century (ºC)		End-Century (ºC)	
	Mean	Range	Mean	Range
SSP1-2.6	1.1	0.6 to 1.4	1.2	0.5 to 1.9
SSP2-4.5	1.2	0.8 to 1.9	2.2	1.5 to 3.2
SSP5-8.5	1.7	1.0 to 2.2	4.1	2.9 to 5.7

Table 8.13: Projected changes in seasonal maximum temperature - JJA

JJA	Mid-Century (ºC)		End-Century (ºC)	
	Mean	Range	Mean	Range
SSP1-2.6	0.9	0.5 to 1.5	1.0	0.4 to 1.8
SSP2-4.5	1.2	0.8 to 1.9	2.1	1.3 to 3.2
SSP5-8.5	1.6	1.0 to 2.4	4.0	2.9 to 5.7

Table 8.14: Projected changes in seasonal maximum temperature - SON

SON	Mid-Century (ºC)		End-Century (ºC)	
	Mean	Range	Mean	Range
SSP1-2.6	0.9	0.5 to 1.2	1.0	0.4 to 1.6
SSP2-4.5	1.1	0.8 to 1.7	2.0	1.5 to 2.7
SSP5-8.5	1.6	1.2 to 2.1	3.9	2.8 to 5.3

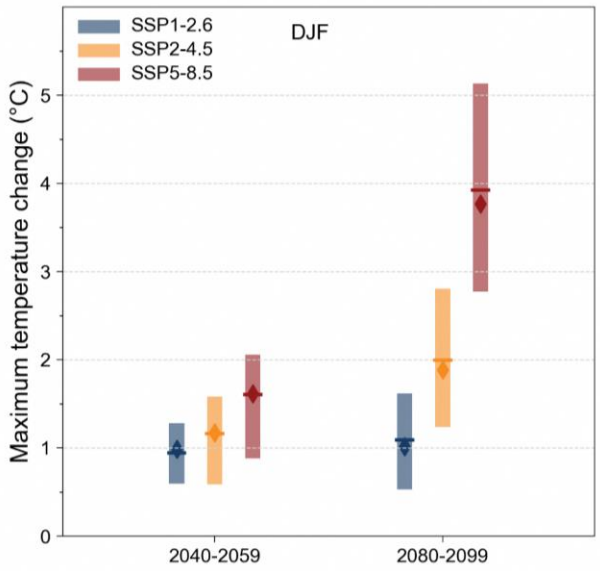

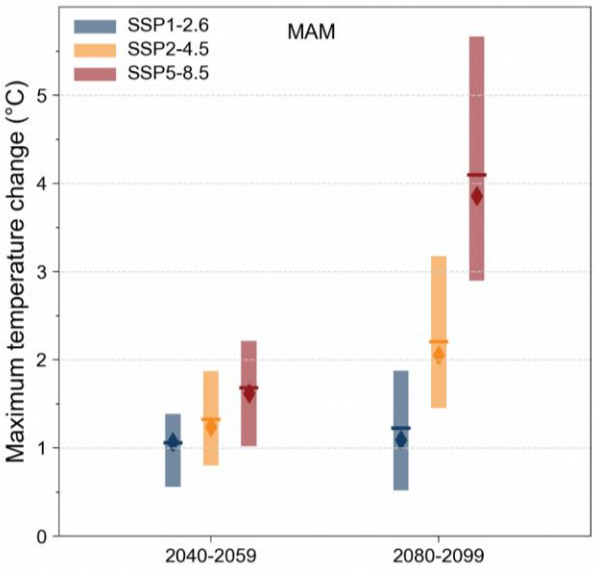

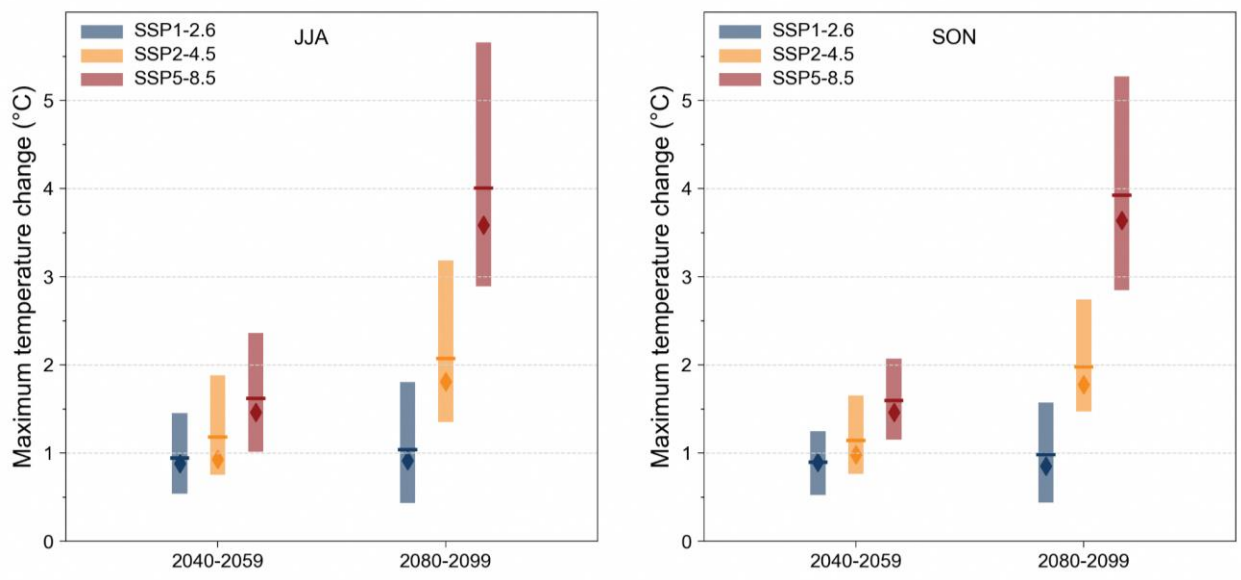

Figure 8.8: Average changes in seasonal maximum near-surface air temperature (tasmax) over the mid- (2040-59) and end-century (2080-99) period for the 6 downscaled GCMs (8km) over the SEA land relative to the historical (1995-2014) baselines. The line and diamond represent the mean and median using the 6 models, respectively.

Figure 8.9 shows the projected changes in the seasonal mean near-surface air temperatures over SEA in the end century (2080-99) relative to the historical (1995-2014) under the SSP5-8.5 scenario. The near-surface air temperatures are projected to increase in the end century over the SEA domain with higher increases over the land compared to the surrounding oceanic regions. During the DJF season, the projections of near-surface air temperatures increase in the range of 2.5 to 5.5^{o}C in the end century with higher values over Myanmar, Thailand, Laos and Cambodia. For the MAM season, the projected near-surface air temperatures increase by 2.5 to 6.0^{o}C in the end century with higher increases over Myanmar, Thailand and Laos. During the JJA season, the projected near-surface air temperatures increased in the range of 2.0 to 6.0^{o}C with higher increases over Laos, Vietnam, and Indonesia. The changes in JJA are of comparable magnitude to changes in JJA end-century (2070-2099) versus historical (1980-2009) temperatures in V2 (Chapter 5). For the SON season, the projections of near-surface air temperatures show increases by 2.0 to 5.0^{o}C in the end century.

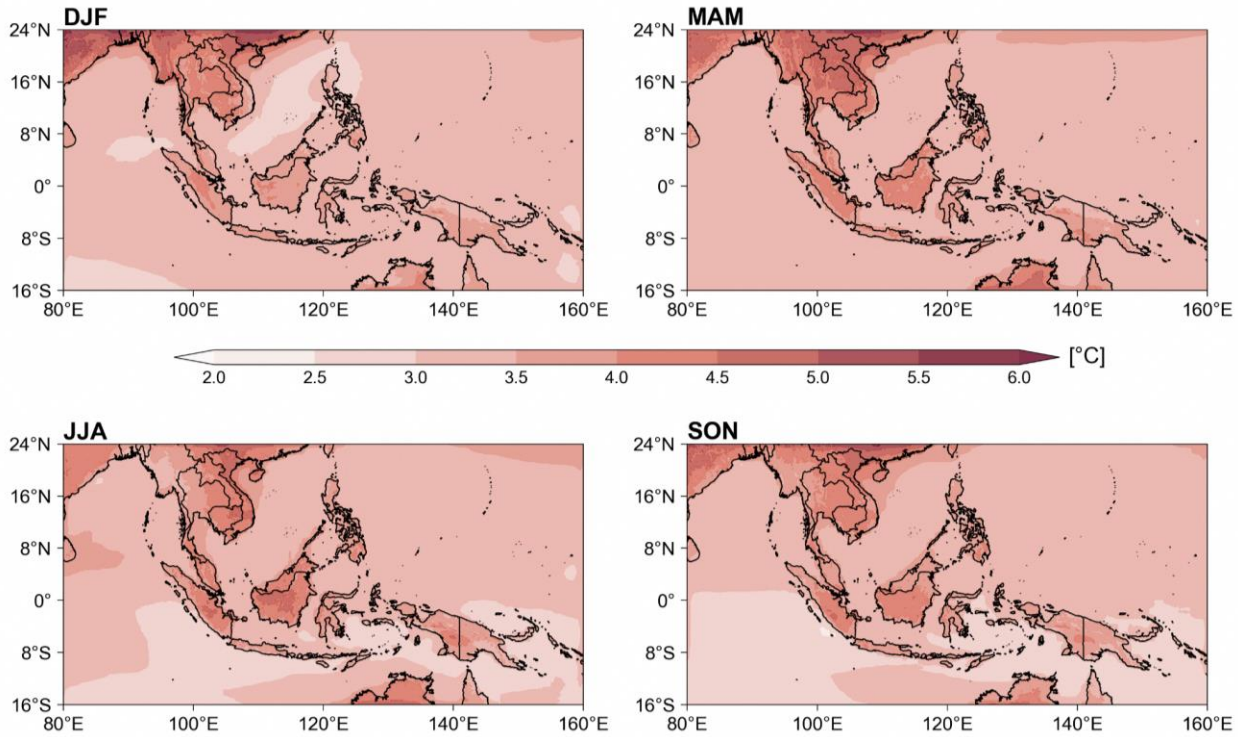

Figure 8.9: Ensemble-mean (6 downscaled GCMs 8 km) changes in seasonal mean near-surface air temperature over end-century (2080-99) relative to the historical period (1995-2014) over the SEA domain under the SSP5-8.5 scenario.

8.3.6 Changes in temperature extremes

Figure 8.10 shows the projected changes in the seasonal maximum of daily maximum temperatures (TXx) over the SEA domain in the end century relative to the historical under the SSP5-8.5 scenario. As seen in the Figure 8.10, the projected TXx increases over the SEA in the end century across the seasons with higher increases over the land regions compared to oceans. During the DJF season, the projected TXx increases in the range of 2.5 to 6.0ºC. For the MAM season, the projections of TXx show increases by 3.0 to 6.0ºC with higher increases over Laos, Vietnam, Borneo, Indonesia, and New Guinea. During the JJA season, the projected TXx increases in the range of 3.0 to 6.5ºC with higher increases over Thailand, Cambodia, Laos, Vietnam, Borneo, and Indonesia. For the SON season, the projected TXx increases by 3.0 to 6.0ºC with higher increases over Cambodia, Laos, Vietnam, Borneo, and Indonesia.

Figure 8.11 shows the projected changes in the seasonal minimum of daily minimum temperatures (TNn) over the SEA in the end century relative to the historical under the SSP5-8.5 scenario. Projected TNn increases over the SEA with higher increases over the land regions. During the DJF season, the projected TNn increases in the range of 3.0 to 6.0ºC with higher increases over Myanmar, Thailand, and Cambodia. For the MAM season, the projected TNn increases by 3.0 to 6.5ºC with higher increases over Myanmar, Thailand, and Cambodia. During the JJA season, the projected TNn increases in the range of 3.0 to 5.0ºC. For the SON season, the projected TNn increases in the range of 3.0 to 6.0ºC with higher increases over Myanmar, Thailand, and Cambodia.

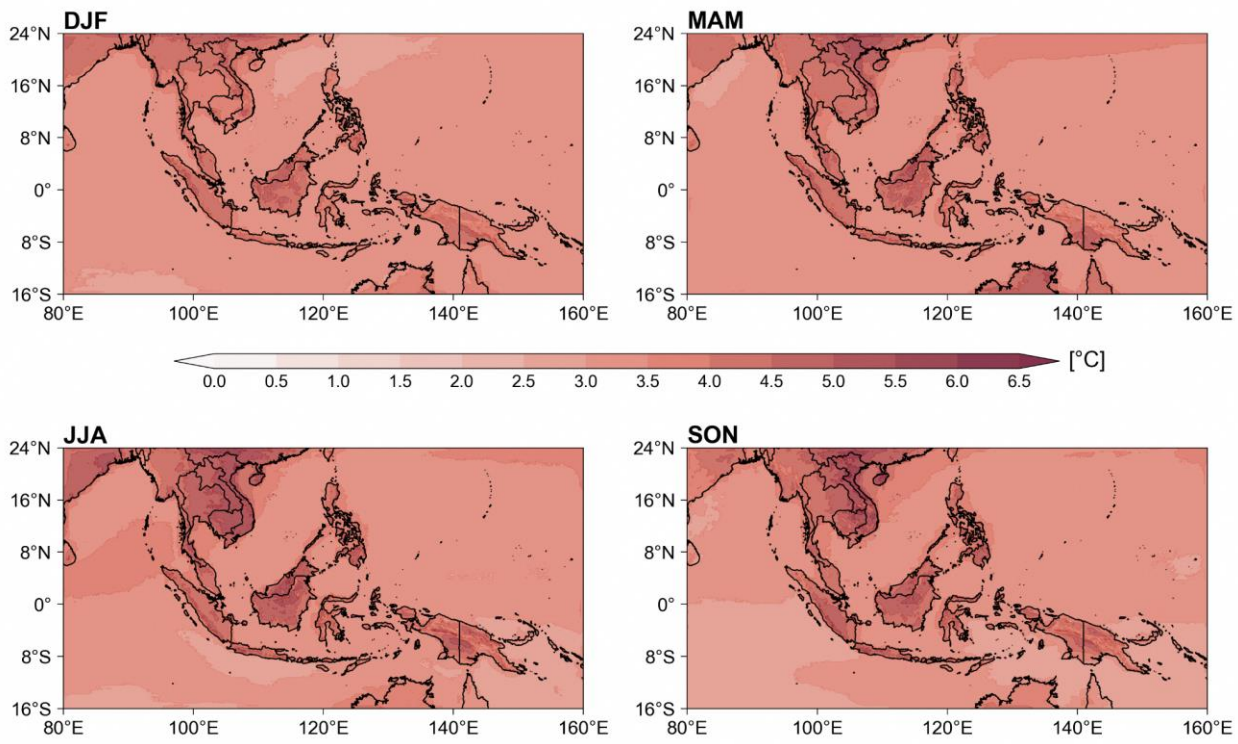

Figure 8.10: Ensemble-mean (6 downscaled GCMs 8 km) changes in seasonal maximum of daily maximum temperature (TXx) over end-century (2080-99) relative to the historical period (1995-2014) over the SEA domain under the SSP5-8.5 scenario.

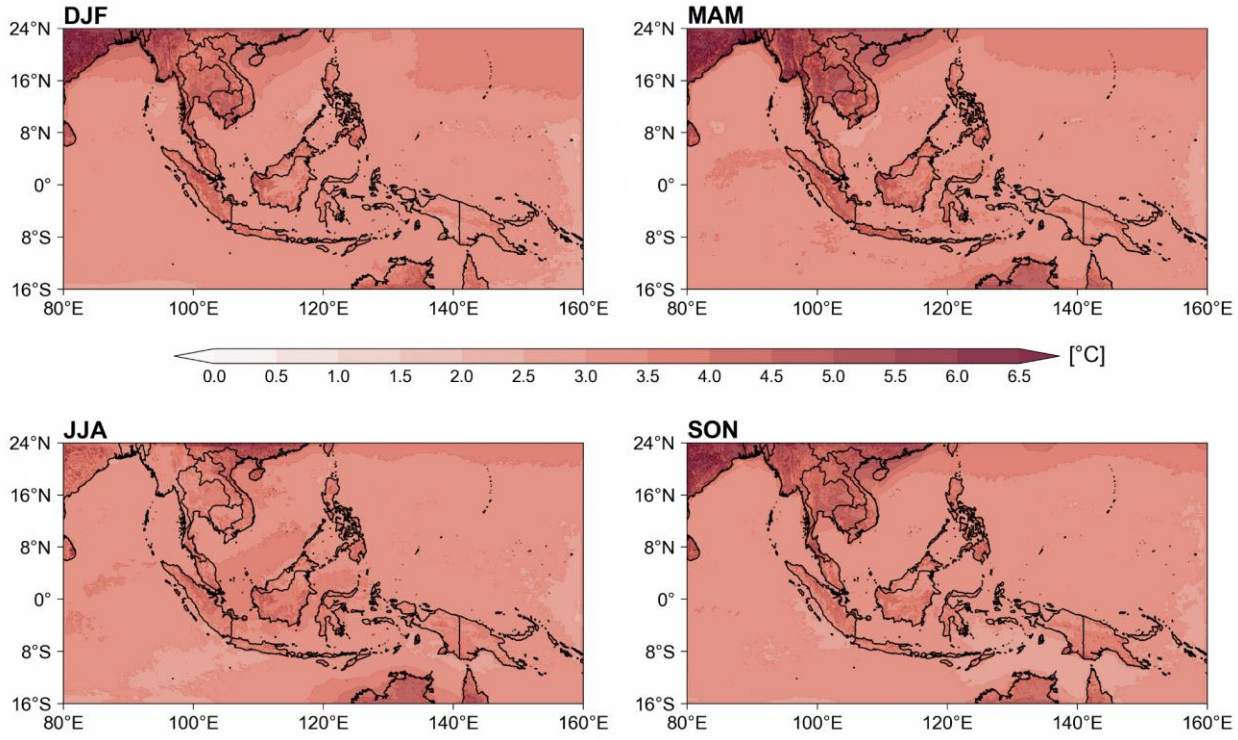

Figure 8.11: Ensemble-mean (6 downscaled GCMs 8 km) changes in seasonal minimum of daily minimum temperature (TNn) over end-century (2080-99) relative to the historical period (1995-2014) over the SEA domain under the SSP5-8.5 scenario.

8.3.7 Changes in relative humidity

Figure 8.12 shows the percentage changes in the annual mean near-surface relative humidity (hurs) over SEA and SEA land regions in the mid-century and end century relative to the historical under three SSP scenarios. For readability, they are also shown in tabular form in Tables 8.15-8.16. As seen in Figure 8.12, the multi-model mean indicates hurs increases over SEA and decreases over SEA land across scenarios and time periods. Similar to the warming over land, decreases in land hurs with warming have been reported in other studies and has some theoretical support (Byrne and O'Gorman 2018).

Table 8.15: Projected changes in annual mean near-surface relative humidity - SEA

ANN	Mid-Century (%)		End-Century (%)	
	Mean	Range	Mean	Range
SSP1-2.6	0.13	-0.05 to 0.27	0.10	-0.15 to 0.27
SSP2-4.5	0.22	0.03 to 0.41	0.29	0.07 to 0.53
SSP5-8.5	0.27	0.12 to 0.42	0.38	-0.09 to 0.83

Table 8.16: Projected changes in annual mean near-surface relative humidity - SEA land

ANN	Mid-Century (%)		End-Century (%)	
	Mean	Range	Mean	Range
SSP1-2.6	-0.20	-0.65 to 0.23	-0.21	-0.73 to 0.29
SSP2-4.5	-0.18	-0.84 to 0.21	-0.57	-1.20 to -0.07
SSP5-8.5	-0.32	-1.08 to 0.11	-1.35	-2.73 to -0.38

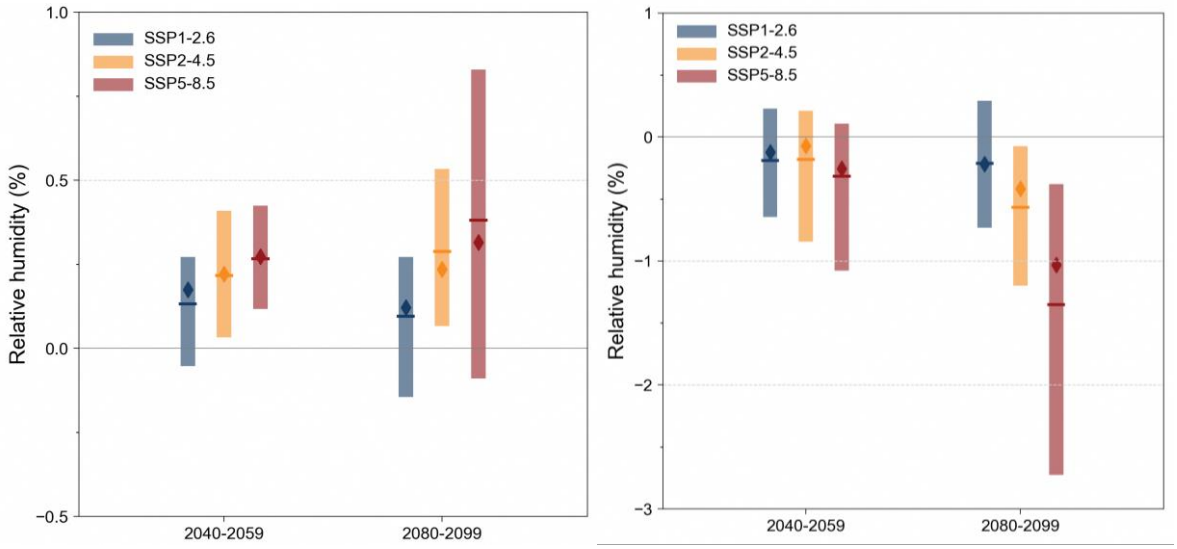

Figure 8.12: Average changes in annual mean near-surface relative humidity (hurs) over the mid- (2040-59) and end-century (2080-99) period for the 6 downscaled GCMs (8km) over the SEA domain (left) and SEA land only (right), with respect to their historical (1995-2014) baselines. The line and diamond represent the mean and median using the 6 models, respectively.

Figure 8.13 shows the percentage changes of seasonal mean hurs over SEA and SEA land regions in the mid-century and end century relative to the historical under three SSP scenarios. There are seasonal differences in the projected hurs over SEA and SEA land regions in mid-century and end century. In general, percentage changes in multi-model mean hurs over SEA land are either small or negative, ranging from 0 to -1.9%. For readability, they are also shown in tabular form in Tables 8.17-8.20.

During the DJF season, in the mid-century the projected multi-model mean hurs remained unchanged in all three scenarios. In the end century, the projected multi-model mean hurs decreased by 0.0 to -0.9%.

Table 8.17: Projected changes in seasonal mean near-surface relative humidity

DJF	Mid-Century (%)		End-Century (%)	
	Mean	Range	Mean	Range
SSP1-2.6	0.0	-0.4 to 0.6	0.0	-0.4 to 0.4
SSP2-4.5	0.0	-0.4 to 0.6	-0.3	-0.5 to 0.1
SSP5-8.5	0.0	-0.9 to 0.7	-0.9	-1.8 to -0.3

For the MAM season, in the mid-century the projected multi-model mean hurs decreases in the range of -0.4 % to -0.5%. In the end century, the

projected multi-model mean hurs decreases by -0.6% to -1.3%.

Table 8.18: Projected changes in seasonal mean near-surface relative humidity

MAM	Mid-Century (%)		End-Century (%)	
	Mean	Range	Mean	Range
SSP1-2.6	-0.4	-0.9 to 0.2	-0.6	-1.3 to 0.3
SSP2-4.5	-0.4	-1.2 to 0.1	-0.8	-1.6 to 0.2
SSP5-8.5	-0.5	-1.1 to 0.0	-1.3	-2.7 to -0.4

During the JJA season, in the mid-century the projected hurs decreases in the range of -0.2% to -0.6%. In the end century, the projected hurs decreases by -0.2% to -1.9%.

Table 8.19: Projected changes in seasonal mean near-surface relative humidity

JJA	Mid-Century (%)		End-Century (%)	
	Mean	Range	Mean	Range
SSP1-2.6	-0.2	-1.0 to 0.2	-0.2	-0.6 to 0.2
SSP2-4.5	-0.2	-1.1 to 0.3	-0.8	-1.9 to -0.1
SSP5-8.5	-0.6	-1.5 to 0.0	-1.9	-3.7 to -0.7

For the SON season, in the mid-century the projected hurs decreases in the range of -0.1 % to -0.2%. In the end century, the projected hurs changes range from 0% to -1.3%.

Table 8.20: Projected changes in seasonal mean near-surface relative humidity

SON	Mid-Century (%)		End-Century (%)	
	Mean	Range	Mean	Range
SSP1-2.6	-0.1	-0.9 to 0.5	0.0	-0.6 to 0.4
SSP2-4.5	-0.1	-0.9 to 0.6	-0.4	-1.3 to 0.2
SSP5-8.5	-0.2	-0.9 to 0.6	-1.3	-3.0 to 0.1

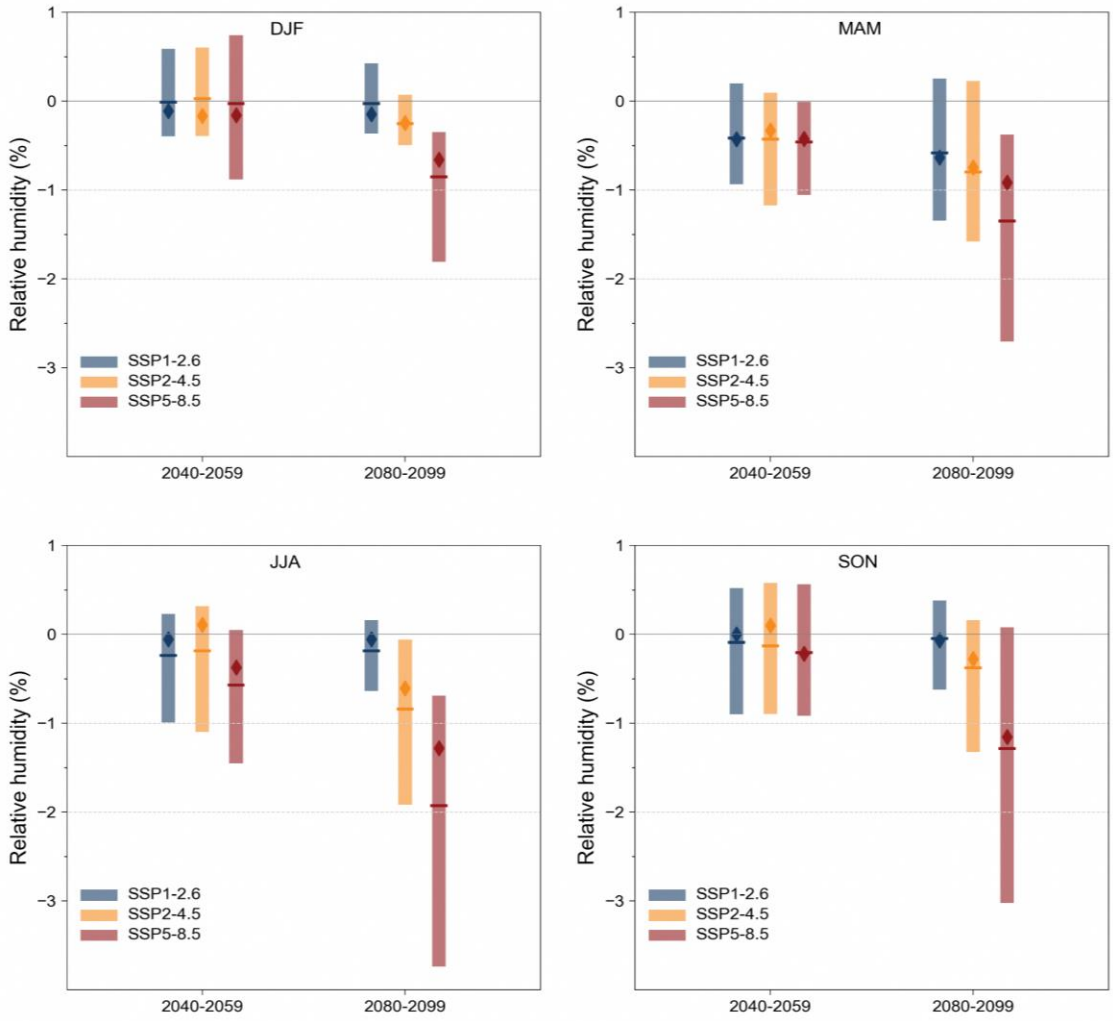

Figure 8.13: Average changes in seasonal mean near-surface relative humidity (hurs) over the mid- (2040-59) and end-century (2080-99) period for the 6 downscaled GCMs (8km) over the SEA land relative to the historical (1995-2014) baselines. The line and diamond represent the mean and median using the 6 models, respectively.

Figure 8.14 shows the multi-model mean percentage changes in the seasonal mean hurs over the SEA in the end century relative to the historical under the SSP5-8.5 scenario. As seen in Figure 8.14, there are seasonal differences in the hurs over the SEA land and ocean regions. During the DJF season, the projected hurs decreases (-1% to -6%) over most of the SEA land regions and increases (1% to 4%) over oceans in the end century.

For the MAM season, the projected hurs decreases in the range of -1% to -6% over the SEA land regions and slightly increases (1% to 3%) over the oceans.

During the JJA season, the projected hurs decreases (-1% to -9%) over the land regions with higher decreases over Cambodia, Vietnam, Indonesia, and New Guinea. The projected hurs over the oceanic regions increases (1% to 4%) during the JJA season. For the SON season, the projected hurs decreases (-1% to -7%) over the land regions and increases (1% to 6%) over the oceans.

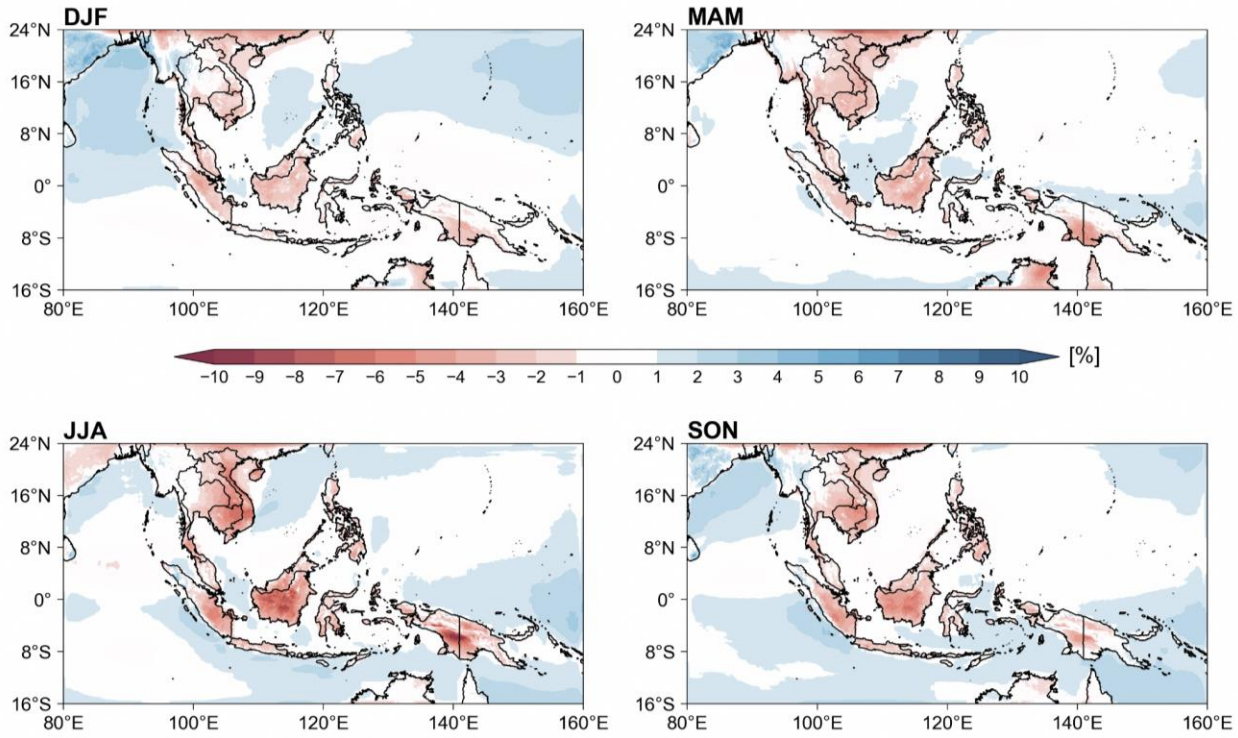

Figure 8.14: Ensemble-mean downscaled (8km) changes in seasonal mean near-surface relative humidity over end-century (2080-99) relative to the historical period (1995-2014) over the SEA domain under the SSP5-8.5 scenario.

8.4 Changes in Regional Climate Drivers

In this section we present projected changes in the important regional climate drivers discussed in Chapters 3, 4, 5, and 7. While we don't expect significant changes in the projected regional climate drivers in the downscaled simulations as compared to that seen from the driving GCMs, it is worth investigating if there are any notable differences.

8.4.1 Monsoons

In DJF (see Figure 8.15a), changes in wind speeds are small over the South China Sea, where some of the strongest climatological winds occur. There are anomalous westerlies east of the Philippines as well as anomalous easterlies west of Sumatra, representing a weakening of the climatological flow. Similar westerly and easterly anomalies can be seen in Tangang et al 2020, which examined changes in end-century (2071-2099) winds under RCP8.5 using the CORDEX ensemble, with changes over the South China

Sea being within 1 m/s. These westerly and easterly anomalies are also similar to those in SON (Figure 8.15d). The changes in winds in MAM are generally small (Figure 8.15b).

In JJA, (Figure 8.15c) there is a strengthening of the monsoon flow over Indochina, with an anomalous easterly flow over much of the western Maritime Continent. Tangang et al 2020 found a similar westerly flow over Indochina and easterly flow over Sumatra towards the Indian ocean. In all seasons, a weakening of the flow with anomalous easterlies over the Indian ocean can be seen. Overall, the wind anomalies are most notable in JJA.

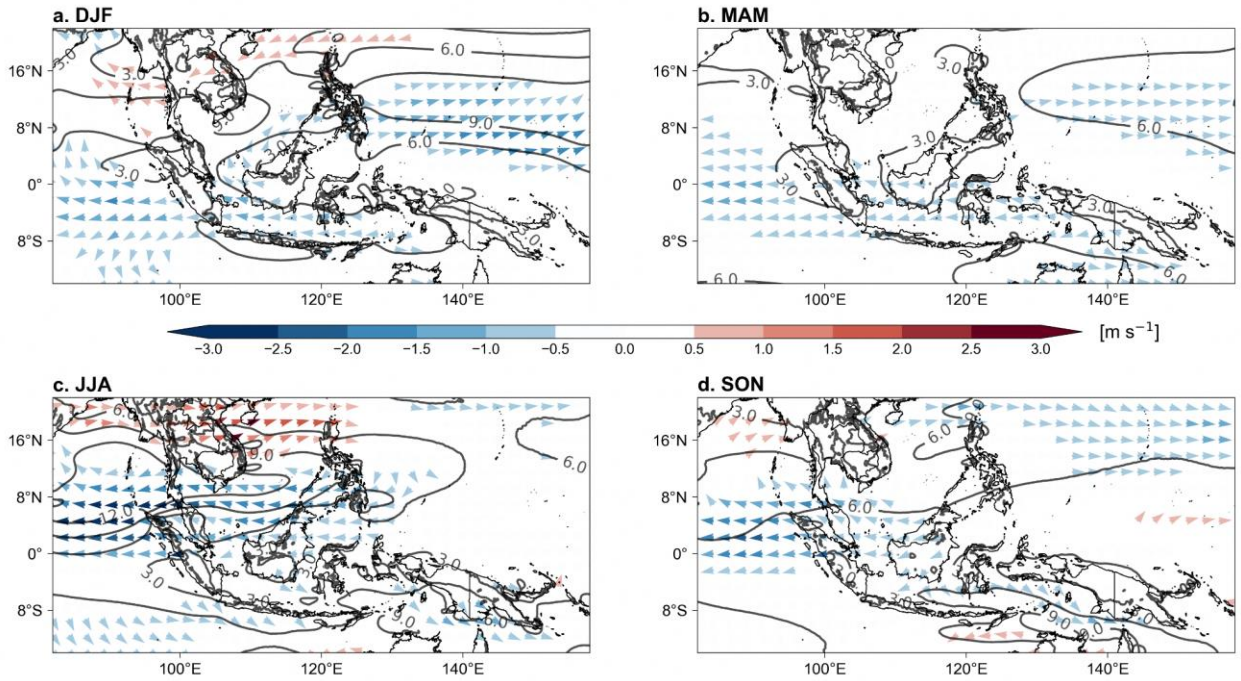

Figure 8.15: shows the change in 850 hPa wind direction (arrows, colors indicate magnitude) and climatological wind speeds (contours) over Southeast Asia during 2080-2099 in SSP5-8.5 with respect to 1995-2014 in SINGV-MMM (containing six 8km model outputs).

8.4.2 Northeast Monsoon surge

As highlighted in Section 4.5.5, monsoon cold surges are a key synoptic feature of the boreal winter circulation over the Maritime Continent and can lead to extreme rainfall. The cold surges can also be enhanced by the presence of a favorable phase of the MJO (e.g. Lim et al., 2017) and might also aid the MJO in its passage across the Maritime Continent (Pang et al., 2018). Given the importance of boreal winter monsoon cold surges to the weather and climate of SEA, it is important to analyse how the cold surges are projected to change under global warming in the V3 downscaled simulations. It is also important to check if there are any important differences in the downscaled projections of cold surges as compared to that seen in the driving CMIP6 GCMs (see Section 4.5.5 and Figure 4.10).

The changes over the Western Maritime Continent are relatively small (Figure 8.16). There is a weakening in surge winds over the Java Sea, and more rain over areas east of Borneo. There are also increased outflows towards Indochina. There are some similarities between changes in the composite over surge days (which occur in NDJF by definition) and the changes in wind speed over DJF - small changes over the South China Sea, anomalous westerlies east of the Philippines as well as anomalous easterlies west of Sumatra. The pattern of rainfall change is also similar to that of DJF rainfall e.g. increases over the Java sea and east of the Philippines.

Similar to the parent GCMs, the downscaled simulations predict easterly anomalies over Indochina and west of Sumatra, as well as westerly anomalies north of New Guinea. There is also an increase in multi-model surge frequency from 17% in historical to 18% in SSP5-8.5, similar to the parent GCMs, where surge frequency increases from 18% to 19%. In contrast, the magnitude of precipitation and rainfall changes in the downscaled simulations are also enhanced relative to the parent GCMs. There are also differences in the details of rainfall: the multimodel mean of the parent GCMs predicts rainfall increase over South Sumatra and Borneo, but the downscaled simulation places the rainfall increase primarily over the Java Sea.

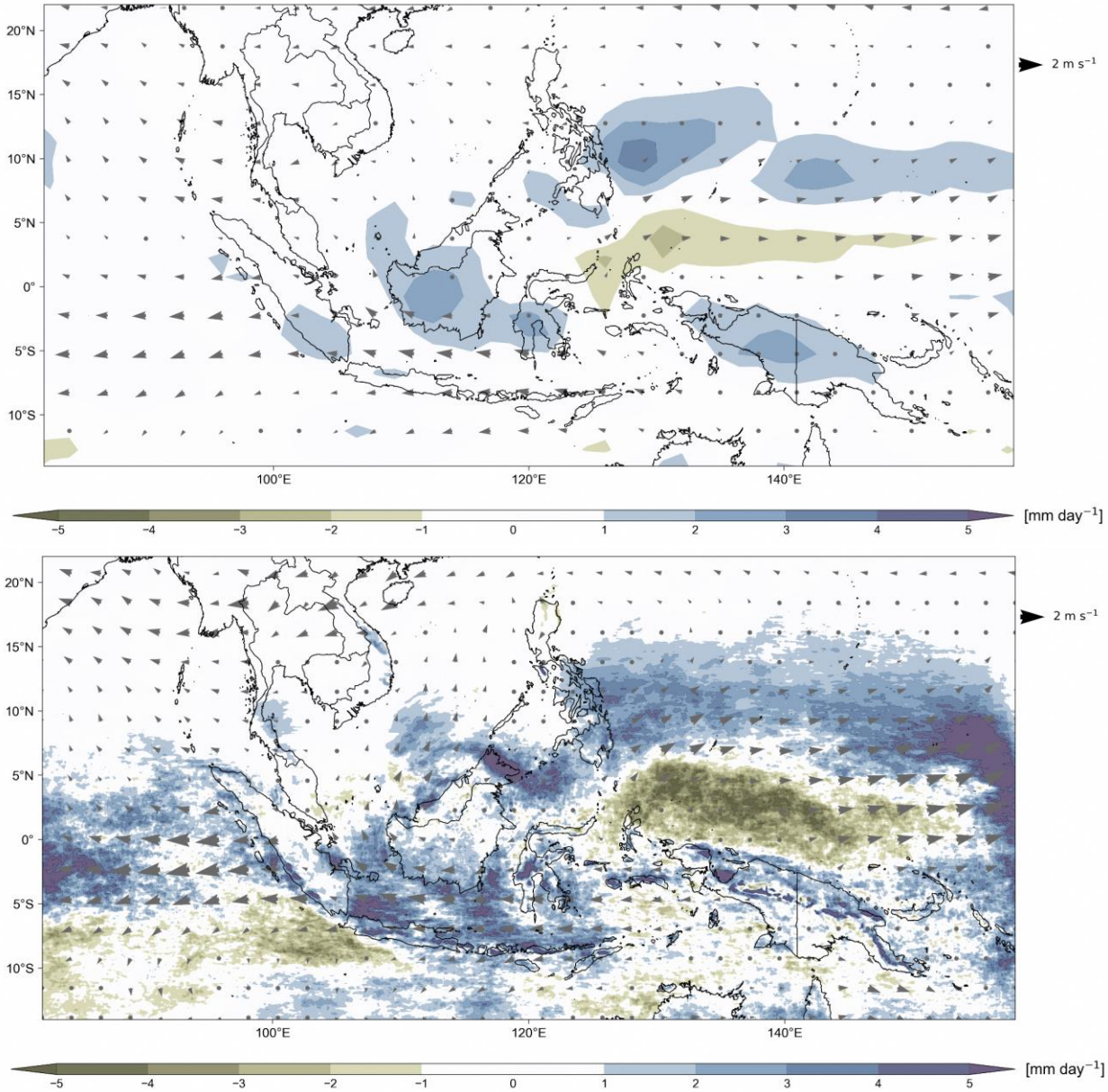

Figure 8.16: Upper panel shows the change in 850 hPa wind direction (arrows) and rainfall (shaded) composited over surge days from 2080-2099 in SSP5-8.5 with respect to 1995-2014 in 6 GCMs, regridded to 1.5 x1.5 (those used for downscaling). Lower panel shows the change in 850 hPa wind direction (arrows) and rainfall (shaded) composited over surge days from 2080-2099 in SSP5-8.5 with respect to 1995-2014 in SINGV-MMM (containing six 8km model outputs).

8.4.3 ENSO Teleconnection

Here in this section we focus on 6 SINGV-RCMs and their forcing GCMs to address changes in the ENSO teleconnection. Here we show that RCMs and GCMs produce very similar and consistent spatial patterns of the ENSO teleconnection (negative over the equatorial central MC and positive over the western Pacific) for both historical and future periods. The full results for the historical period are shown in chapter 7, section 7.5.3 Fig. 7.17. As to the future change (Figure 8.17), GCMs and RCMs both suggest that the negative correlation area over the equatorial MC is enlarged. The positive correlation area over the eastern MC and western Pacific are reduced, and the negative correlation extends to the east. These agree with the understanding that the whole zonal dipole pattern of the ENSO teleconnection shifts eastward, as shown by 32 GCMs in Chapter 4 and in our recent study (Chen et al. 2023).

Besides the large-scale consistency with GCMs, RCMs do offer additional detailed spatial representation of the ENSO teleconnection, especially over the mountainous islands (e.g. over New Guinea). Future studies may look into ENSO-induced rainfall variability at the local scale enabled by the high-resolution RCMs.

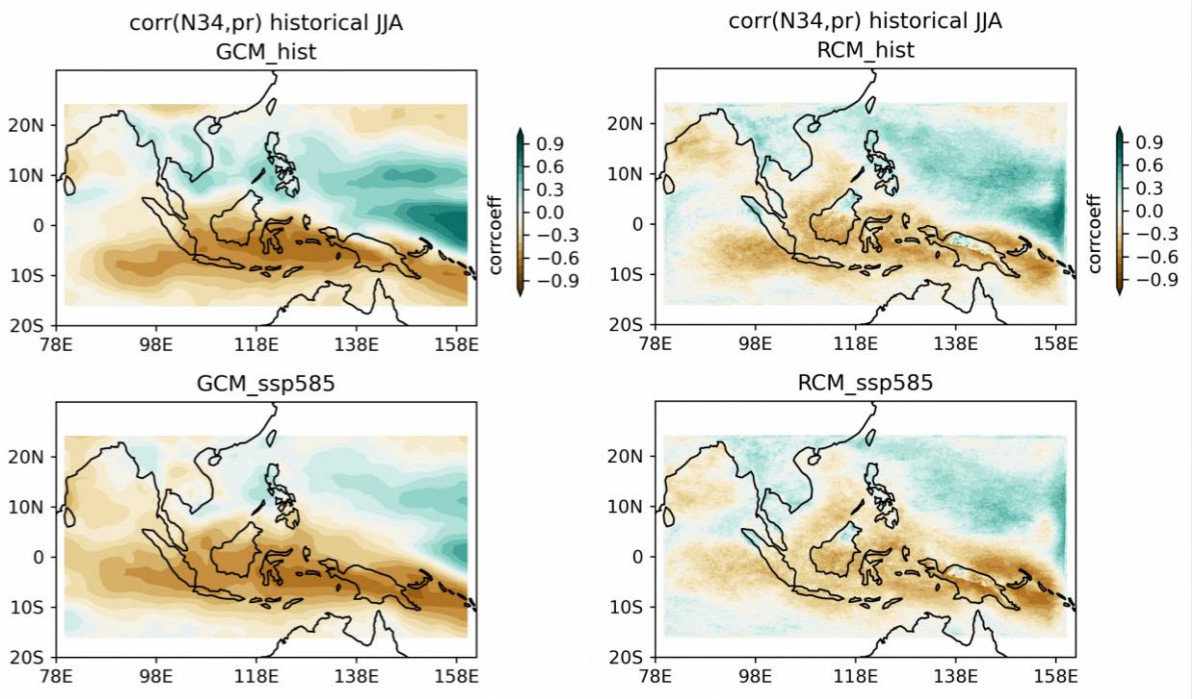

Figure 8.17: JJA ENSO-rainfall teleconnection (correlation coefficient) over the Maritime Continent (left: GCM mean, right: RCM mean. Upper: historical period (1995-2014) . Lower: future (2080-2099) in the SSP585 scenario).

8.5 Summary

This chapter uses projections of 6 CMIP6 GCMs downscaled by SINGV-RCM to examine climate change at regional scales. It examines changes in some important climate variables (e.g. temperature and rainfall). A comparison of the representation of some large-scale drivers are also provided to examine consistency with the GCMs.

Annual-mean domain-average rainfall over SEA is projected to increase both in the mid and end century. While the end-century change projected by the multi-model mean is higher than the mid-century change for each of the scenarios, the magnitude of the inter-model spread can be significant compared to differences in the multi-model mean. The increases noted in the annual mean occur as a result of spatially complex changes in the individual seasons. For example,

there are large percentage increases in climatologically dry periods (e.g. parts of Indochina in DJF and regions around the Java Sea in JJA), and drying over parts of the South China Sea in all seasons.

Extreme rainfall, as quantified by maximum 1-day rainfall (RX1day) and (RX5day), are expected to increase in most of the SEA land regions across the four seasons. Similar to changes in the mean rainfall, some of the largest percentage changes are seen over climatologically dry regions.

As for temperature, multi-model mean projected near-surface air temperatures over the SEA domain are expected to increase by at least 0.8^{o}C in the mid century and by at least 1.0^{o}C in the end century. Based on the multi-model mean projections, SEA land will experience increased warming as compared to the SEA domain by 0.1^{o}C to 0.7^{o}C in the mid-century (Tables 8.7 and 8.8) and up to 4.0^{o}C by the end of the century. This confirms the general expectation from existing studies that the land regions will experience more warming than ocean regions. Changes in annual maximum (tasmax) and annual minimum near-surface air-temperatures are qualitatively similar to those in tas. Based on the multi-model mean, across the seasons, mid-century tasmax would change from 0.9^{o}C-1.7^{o}C while end-century seasonal tasmax would change from 1.0^{o}C-4.1^{o}C.

Similarly, there are widespread increases in temperature extremes, as measured by changes in the seasonal maximum of daily maximum temperatures (TXx) over the SEA domain. The warming is larger over land areas as compared to ocean, exceeding 6^{o}C in parts of Indochina during JJA and SON. In addition, the seasonal minimum of daily minimum temperatures (TNn) increases over much of the domain.

Changes in multi-model seasonal mean near-surface relative humidity (hurs) are either small or negative over land, ranging from 0 to -1.9%, while increases in hurs can be observed over the oceans. Across seasons, the largest decreases can be seen in JJA, especially over Indochina, Borneo, and New Guinea. Similar to the enhanced land warming discussed above, the reduction in relative humidity over land is consistent with findings from existing studies.

Turning to the regional climate drivers, a weakening of the monsoonal flow with anomalous easterlies over the Indian ocean can be seen. Some of the largest changes occur in JJA, where there is also a strengthening of the monsoon flow over Indochina. The changes in the northeast monsoon cold surge are consistent with the GCM changes in terms of increased frequency, anomalous easterlies over Indochina and west of Sumatra, as well as anomalous westerlies north of New Guinea. In contrast, the magnitude of precipitation and rainfall changes in the downscaled simulations are also enhanced relative to the parent GCMs. There are also differences in the details of rainfall: the multimodel mean of the parent GCMs predicts rainfall increase over South Sumatra and Borneo, but the downscaled simulation places the rainfall increase primarily over the Java Sea.

The changes in ENSO teleconnections are consistent with those of the parent GCMs, showing an eastward shift of the zonal dipole pattern such that the negative correlation over the equatorial MC is enlarged while the positive correlation over the eastern MC and Western Pacific are reduced. The downscaled models also offer additional fine-scale spatial details of the ENSO teleconnection.

Overall, the downscaled projections indicate increases in temperature and temperature extremes, as well as rainfall extremes. Annual-mean domain-average rainfall over SEA is projected to increase both in the mid and end century.

Additionally, it's important to highlight the added value of future projections derived from high-resolution RCMs when compared to the coarse-resolution driving GCMs. In the Southeast Asia (SEA) domain, GCMs often exhibit smoothed spatial changes across islands in the equatorial Maritime Continents, attributed to their coarse resolutions at 1.5 degrees latitude/longitude. In contrast, high-resolution (8km) RCMs consistently produce large-scale changes similar to the driving GCMs, offering a more realistic representation of high rainfall variability in the high mountain areas of Java and Papua New Guinea. These enhancements prove crucial for advancing regional climate impact studies.

References

Byrne, M. P., & O'Gorman, P. A. (2018). Trends in continental temperature and humidity directly linked to ocean warming. Proceedings of the National Academy of Sciences, 115(19), 4863–4868. https://doi.org/10.1073/pnas.1722312115

Chen, C., Sahany, S., Moise, A. F., Chua, X. R., Hassim, M. E., Lim, G., & Prasanna, V. (2023). ENSO-rainfall teleconnection over the Maritime Continent enhances and shifts eastward under warming. Journal of Climate, 1(aop), 1–55. https://doi.org/10.1175/JCLI-D-23-0036.1

Tangang, F., Chung, J. X., Juneng, L., Supari, Salimun, E., Ngai, S. T., et al. (2020). Projected future changes in rainfall in Southeast Asia based on CORDEX–SEA multi-model simulations. Climate Dynamics, 55(5–6), 1247–1267. https://doi.org/10.1007/s00382-020-05322-2

9

Bias Adjustment for Singapore Climate Projections

Authors:
Chen Chen, Aurel Florian Moise, Sandeep Sahany, Muhammad Eeqmal Hassim, Xin Rong Chua, Venkatraman Prasanna, Gerald Lim, Shao-Yi Lee, Jianjun Yu, Anupam Kumar, Pavan Harika Raavi, Fei Luo

Meteorological Service Singapore
Centre for Climate Research Singapore

9.1 Introduction

The main objective of the V3 study is to generate accurate and realistic future climate projections in order to assess and adapt to the impacts of climate change in Singapore. To achieve this, a subset of the latest and most advanced CMIP6 GCMs that exhibit good performance over Southeast Asia has been carefully chosen to drive the regional dynamical downscaling simulations.

Despite improvements made in both the global models and the regional climate model SINGV-RCM, there are still residual biases present in the simulations, as shown in the evaluation chapter of the dynamical downscaling process (Chapter 7). In order to enhance the reliability of the climate change projections, it is necessary to adjust these biases. To achieve this, we conducted bias adjustments (BA) of the V3 downscaled simulations using the widely recognized ISIMIP3 bias adjustment method (Lange, 2019). We also performed rigorous methodology evaluations. The aim was to ensure that the adjusted outcomes effectively reduced biases and were physically realistic. This adjustment process plays a crucial role in producing more accurate and dependable climate projections, which are essential for addressing climate change impacts in Singapore.

By conducting bias adjustment of the V3 downscaled simulations, we aim to refine the results and ensure they align more closely with observed data. Here we used the following references: (1) For precipitation, we utilized a newly developed krigged rainfall dataset for Singapore. (2) For other variables, we utilized the latest version of high-resolution ERA5-driven simulation dataset (ERA5-RCM). This dataset underwent careful evaluation and was found suitable for our bias adjustment purposes.

In the data section, we will provide detailed information about the reference data and the model outputs used in our study. We will outline the sources and characteristics of the reference data as well as the specific model outputs from RCMs.

In the methods section, we will elaborate on the specific configurations we utilized for each variable. These configurations have undergone thorough evaluation using pseudo reality experiments and have consistently yielded realistic outcomes. We will explain the methodology and approaches employed to ensure the reliability and accuracy of our results.

Finally, in the results section, we will present the findings of the bias adjustment process for the model simulations, both in the historical period and in the future projections. Our bias adjustment techniques have demonstrated a very good performance. By applying these bias adjustments, we obtain more realistic RCM outputs, which are essential for conducting climate impact studies in the context of Singapore.

Table 9.1: List of downscaling simulations driven by sub-selected CMIP6 models

CMIP6 model	Ensemble ID	ECS (K)	GCM Resolution	RCM Resolution
ACCESS-CM2	r4i1p1f1	4.66	250km	8km, 2km
EC-Earth3	r1i1p1f1	4.26	100km	8km, 2km
MIROC6	r1i1p1f1	2.60	250km	8km
MPI-ESM1-2-HR	r1i1p1f1	2.98	100km	8km, 2km
NorESM2-MM	r1i1p1f1	2.49	100km	8km, 2km
UKESM1-0-LL	r1i1p1f2	5.36	250km	8km, 2km

9.2 Data

9.2.1 Simulations for bias adjustments

In our study, we performed bias adjustments for regional climate model (RCM) downscaling simulations driven by six CMIP6 global climate models (GCMs) as shown in Table 9.1. It is worth noting that the downscaling simulation using the MIROC6 GCM was conducted only for the 8km resolution.

Considering the availability of regional downscaling data (Table 9.2), we selected the 20-year period from 1995 to 2014 as the historical base period for our analysis. This time frame allows us to capture a representative snapshot of the recent past and establish a

baseline for comparison. For future projections, we focused on a 20-year period near the end of the 21st century to address the change, specifically from 2080 to 2099. By selecting these specific historical and future periods, we aimed to analyze and assess the changes in climate variables and their impacts over Singapore, providing valuable insights for climate change adaptation and planning in the region.

Table 9.2: Time period for model simulations

Scenarios	RCM @8km (SEA domain)	RCM @2km (WMC domain)
Historical	1955-2014 (60 yr)	1995-2014 (20 yr)
Future (SSP126)	2015-2099 (85 yr)	2040-2059 (20 yr), 2080-2099 (20 yr)
Future (SSP245)	2015-2099 (85 yr)	2040-2059 (20 yr), 2080-2099 (20 yr)
Future (SSP585)	2015-2099 (85 yr)	2040-2059 (20 yr), 2080-2099 (20 yr)

9.2.2 Domain for bias adjustments

In our study, we defined three specific regions for analysis: the South East Asia domain (SEA), the West Maritime Continent domain (WMC), and Singapore (SG) (Table 9.3). These regions are depicted in Figure 9.1 as D1 and D2 for SEA and WMC, respectively, and Figure 9.2 represents the SG domain. For the purpose of bias correction, we focused on conducting the adjustments specifically for the model simulations over the SG domain. To calculate Singapore-averaged results, we applied a landsea mask. This process enabled us to derive Singapore-specific climate information and assess the impacts of climate change on the country.

Table 9.3: List of defined domains

Domain	Latitude and Longitude	Grid info for 8km (lon) x (lat)	Grid info for 2km (lon) x (lat)	Remarks
SEA	18S-26N, 80W-160W	1120 x 560	N/A	8km model domain D1
WMC	7S-10N, 93-110W	237 x 236	936 x 943	2km model domain D2
SG	1.1N-1.54N, 103.5W-104.15W	10 x 7	36 x 24	bias adjustment domain

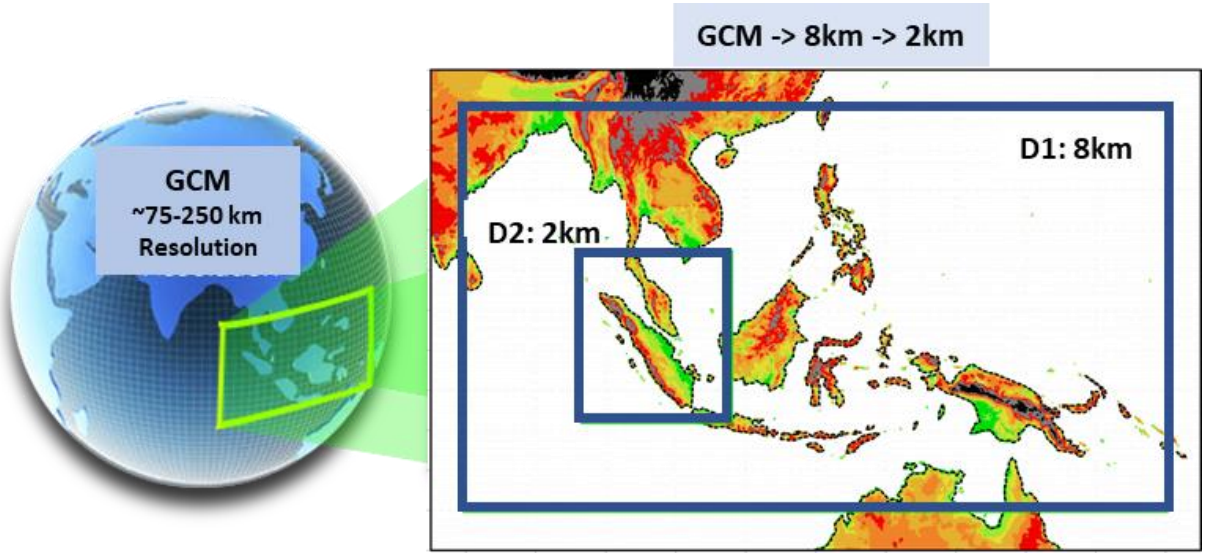

Figure 9.1: The V3 regional climate model domains. 8km resolution simulations are carried out over the D1 domain, and the 2km resolution simulations are carried out over the D2 domain.

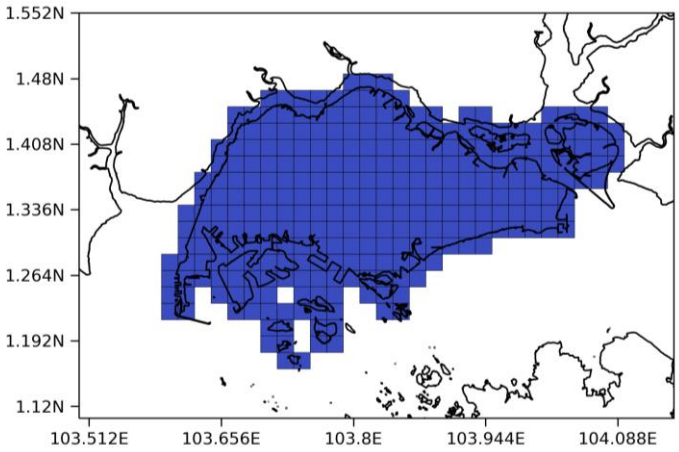

Figure 9.2: Landsea mask for the SG region in the 2km resolution

9.2.3 Variables for bias Adjustments

Here we focus on the following daily variables to carry out the bias adjustment given their relevance to possible future climate impact studies as raised by key stakeholder groups (Table 9.4).

Table 9.4: Variables for bias adjustment

Variable Name	Unit	Description	Relevance to impact studies
pr	mm/day	daily mean of precipitation	plays a crucial role in studying rainfall patterns, droughts, and wet spells
tas	°C	daily mean of near surface air temperature	essential factor in understanding and assessing climate conditions
tasmax	°C	daily maximum of near surface air temperature	providing insights into extreme heat events and temperature extremes
tasmin	°C	daily minimum of near surface air temperature	allowing for the analysis of cold spells and temperature variations
hurs	%	daily mean of near surface relative humidity	contributes to the understanding of moisture levels and atmospheric conditions
sfcWind	m/s	daily mean of 10m wind speed	important for studying wind patterns, gusts, and potential impacts on various sectors

9.2.4 Gridded reference for bias adjustments

To conduct bias adjustments, it is crucial to have gridded observations that cover Singapore and its surrounding area at a daily frequency and in spatial resolutions of 8km and 2km. However, it is challenging to find existing observation products that fully meet these requirements. As a result, additional efforts were undertaken to create suitable benchmark datasets for our study.

Here we employed different approaches for different variables, as outlined in Table 9.5. For precipitation, we utilized station data and applied advanced spatial interpolation methods, specifically Kriging, to generate a gridded precipitation product. This allowed us to convert the point station data into a spatially distributed precipitation dataset, providing a more comprehensive representation of precipitation patterns over Singapore. For the variables of temperature (tas, tasmax, tasmin), relative humidity (hurs), and surface wind speed (sfcWind), we used the ERA5-RCMs as the gridded references. ERA5-RCM is the ERA5-driven regional downscaling simulation using our own SINGV-RCM model (documented in the Chapter 6). By truncating the model outputs for the Singapore domain, we obtained gridded references that align with regional information provided by ERA5 reanalysis but focus on the

spatial extent of Singapore. These ERA5-RCM-based references were found to provide a realistic gridded representation of the selected variables over Singapore, exhibiting good agreement with the point station data across the region.

It is important to note that while efforts were made to create the best available observation benchmarks, observations are not perfect. As new observation products become available in the future, the observation benchmarks can be updated to further improve the accuracy and representativeness of the gridded references.

Table 9.5: Observation references

Resolution	Variable	Source	Period	Additional remarks
2km	pr	krig	1995-2014	using hourly rainfall from 28 stations
8km	pr	krig	1995-2014	using hourly rainfall from 28 stations
2km	tas, tasmax, tasmin, hurs, sfcWind	ERA5-RCM	1995-2014	using 2km daily output from ERA5-driven SINGV-RCM
8km	tas, tasmax, tasmin, hurs, sfcWind	ERA5-RCM	1995-2014	2km daily ERA5-RCM remapped to 8km resolution

9.3 Methods

9.3.1 Bias Adjustment methods

Bias adjustment is a common post-processing technique used in downscaling model applications. One may be aware of two basic “Delta” methods (e.g., Gleick, 1986, Hay et al., 2000). The model-observation “Delta” method calculates the historical model-observation “mean” bias and adds this difference to the future model simulation to correct the “mean” bias in the future projection. The “Delta” method aims to reduce the systematic errors and bring the model closer to the observed reality. The other historical - future “Delta” method calculates the “mean” change in the simulations from the historical to future period, and adds this change to the historical observation. By construction, these “Delta” methods preserve the “mean” future change. They are straightforward approaches and can be useful when more sophisticated bias correction methods are not feasible due to data limitations or computational resources.

Note that the delta method has its limitations. The delta method might not adequately capture biases in extreme events and high percentiles, given that the method assumes the model bias is constant across all quantiles. More advanced statistical methods like quantile mapping (QM) or distribution-based methods may be necessary to address more complex bias patterns and non-stationarities in the climate data. QM-based methods focus on correcting the cumulative distribution functions (CDFs) of climate variables, by acknowledging that the bias can vary across different parts of the distribution. The quantile mapping method corrects biases in both the mean and the shape of the distribution, making it more flexible in addressing complex bias patterns (Maraun, 2016).

The QM method itself has many developments over years and consists of a variety of implementation algorithms. By default, the conventional QM method (Pierce et al., 2015) does not preserve the future change (i.e., delta). The quantile delta mapping (QDM, Cannon et al. 2015) involves identifying the differences in quantiles between the future projections and historical simulations and then applying these delta differences to adjust the entire CDF of the observations. Cannon et al. (2015) discussed and compared several quantile mapping techniques including conventional QM, detrended quantile mapping (DQM), and quantile delta mapping (QDM) in correcting precipitation outputs from GCMs based on a few precipitation extreme indices. The study pointed out that the QDM method shows advantages in its effectiveness of detrending the projection data through multiple quantiles, and capability of dealing with extreme model projections which may be beyond the scope of the historical record by using a superimposing algorithm.

The basic delta method and the quantile mapping methods are both techniques used in statistical and climate modeling, particularly in the context of downscaling and bias correction. The choice between these methods depends on

the specific characteristics of the data and the research objectives. They are often employed to bridge the gap between coarse-scale climate model projections and finer-scale regional or local projections. More extensive review of bias-correction methods can be referred to Maraun (2016).

9.3.2 V3 bias adjustment: ISIMIP3 method

For the V3 study, we specifically sought a trend-preserving method suitable for climate change studies. Various advanced methods have been developed for this purpose, and a comprehensive survey conducted by Casanueva et al. 2020 highlighted several popular bias adjustment methods. The study demonstrated that quantile trend-preserving methods, such as quantile delta mapping (QDM, Cannon et al. 2015), scaled distribution mapping (SDM, Switanek et al. 2017), and the bias adjustment method from the third phase of the Intersectoral Impact Model Intercomparison Project (ISIMIP3, Lange 2019), tend to preserve the raw signals better for different indices and variables considered.

In line with these findings, for the V3 study, we have chosen to adopt the ISIMIP3 bias correction method. This method is designed to preserve the underlying trends and patterns in the data while effectively adjusting for biases, making them well-suited for our climate change analysis and ensuring the reliability and accuracy of our results.

The ISIMIP community has made significant advancements in the development and refinement of bias adjustment methods over the years. Starting from the ISIMIP Fast Track method introduced by Hempel et al. in 2013, they have made subsequent updates in ISIMIP2 (Frieler et al., 2017) and the most recent version, ISIMIP3 (Lange, 2019). These bias adjustment methods have been widely used in the climate impacts modeling community and have shown promising results. Researchers have employed ISIMIP2 in studies such as Peter et al. (2022), and ISIMIP3 has been utilized in the research conducted by Casanueva et al. (2020). These studies demonstrate the practical application and effectiveness of the ISIMIP bias adjustment methods in addressing biases in climate data for various modeling purposes. Furthermore, it is worth noting that the ISIMIP3 scripts are regularly updated to improve their functionality and performance. The updates from Version 1.0 to the current Version 2.5 are publicly available (https://doi.org/10.5281/zenodo.4686991), providing researchers with the most up-to-date tools for implementing bias adjustment in their climate modeling studies. These updates ensure that the bias adjustment methods stay relevant and incorporate the latest advancements in the field. The continuous development and refinement of the ISIMIP bias adjustment methods reflect the commitment of the scientific community to enhance the accuracy and reliability of climate impact assessments and improve our understanding of climate change effects.

One aspect of bias adjustment methods in climate modeling is to handle complex situations and address biases across various time scales and multivariate dependencies. Several studies have proposed advanced methods to handle such complexities and improve the performance of bias correction. For example, Mehrotra and Sharma (2016) developed a method to correct the duration of observed events using an auto-regressive model, which can be particularly useful when simulations fail to capture the realistic duration of events.

Additionally, Mehrotra and Sharma (2012) proposed recursive bias correction methods that can address biases across different time scales, ranging from daily to interannual, allowing for a comprehensive correction approach. In situations where there is a need to account for the multivariate dependence between variables, Cannon (2017) introduced multivariate methods that utilize lagged correlation and regression models. These approaches enable the correction of biases between variables such as precipitation (pr) and temperature (tas) at specific time scales, improving the overall fidelity of the simulation outputs. It's important to note that these advanced methods require sufficient high-quality data to robustly fit the parameters and achieve good performance. Overfitting can be a concern when data availability is limited, as it may lead to artifacts in the bias-corrected outcomes. Striking a balance between correcting biases and avoiding alterations to the fundamental physics represented in the raw simulations is crucial in order to maintain the integrity of the underlying climate models.

In this context, the ISIMIP3 method offers a well-balanced approach. It incorporates physical

considerations while maintaining a reasonable level of complexity that can be adequately fitted to available data. Although it may not completely eliminate biases, ISIMIP3 provides sufficient bias reduction and adjusts future projections closer to the expected future conditions. By adopting the ISIMIP3 method, the V3 study can strike an appropriate balance between reducing biases and preserving the underlying physics of the raw simulations, allowing for more accurate and dependable climate impact assessments. While raw simulations can still offer valuable insights into the "Delta" changes, bias-adjusted simulations are particularly useful for obtaining accurate information regarding the absolute values, variability, and complete distribution of the climate variables. This ensures that the adjusted simulations provide reliable data for conducting climate impact studies.

9.3.3 Bias adjustment configurations

The ISIMIP3 bias adjustment method offers a comprehensive approach to correct biases in various quantiles across the distribution of variables. Compared to basic delta methods, ISIMIP3's quantile mapping approach provides a more detailed and nuanced correction by considering every quantile individually. ISIMIP3 also allows for different fitting options, such as parametric fits or non-parametric fits, to ensure the best possible representation of the observed data. This flexibility enables the method to adapt to different variable characteristics and improve the accuracy of the bias-adjusted simulations. By adopting the configurations suggested by the ISIMIP3 paper (Table 9.6), our study ensures that the bias adjustments are carried out using recommended settings and approaches. This enhances the reliability and consistency of the bias-adjusted simulations for climate impact studies for Singapore.

Table 9.6: Bias adjustment configurations

Variable	Configurations
pr	python bias_adjustment.py --obs-hist=$FILE_OBS_HIST --sim-hist=$FILE_SIM_HIST --sim-fut=$FILE_SIM_PROJ --sim-fut-ba=$FILE_OUTPUT --variable=$VARNAME --halfwin-upper-bound-climatology 0 --lower-bound 0 --lower-threshold .1 --distribution gamma --trend-preservation mixed --adjust-p-values True
hurs	python bias_adjustment.py --obs-hist=$FILE_OBS_HIST --sim-hist=$FILE_SIM_HIST --sim-fut=$FILE_SIM_PROJ --sim-fut-ba=$FILE_OUTPUT --variable=$VARNAME --halfwin-upper-bound-climatology 0 --lower-bound 0 --lower-threshold .01 --upper-bound 100 --upper-threshold 99.99 --distribution beta --trend-preservation bounded --adjust-p-values True
sfcWind	python bias_adjustment.py --obs-hist=$FILE_OBS_HIST --sim-hist=$FILE_SIM_HIST --sim-fut=$FILE_SIM_PROJ --sim-fut-ba=$FILE_OUTPUT --variable=$VARNAME --halfwin-upper-bound-climatology 0 --lower-bound 0 --lower-threshold .01 --distribution weibull --trend-preservation mixed --adjust-p-values True
tas	python bias_adjustment.py --obs-hist=$FILE_OBS_HIST --sim-hist=$FILE_SIM_HIST --sim-fut=$FILE_SIM_PROJ --sim-fut-ba=$FILE_OUTPUT --variable=$VARNAME --halfwin-upper-bound-climatology 0 --distribution normal --trend-preservation additive --detrend True
tasrange	python bias_adjustment.py --obs-hist=$FILE_OBS_HIST --sim-hist=$FILE_SIM_HIST --sim-fut=$FILE_SIM_PROJ --sim-fut-ba=$FILE_OUTPUT --variable=$VARNAME --halfwin-upper-bound-climatology 0 --lower-bound 0 --lower-threshold .01 --distribution rice --trend-preservation mixed --adjust-p-values True
tasskew	python bias_adjustment.py --obs-hist=$FILE_OBS_HIST --sim-hist=$FILE_SIM_HIST --sim-fut=$FILE_SIM_PROJ --sim-fut-ba=$FILE_OUTPUT --variable=$VARNAME --halfwin-upper-bound-climatology 0 --lower-bound 0 --lower-threshold .0001 --upper-bound 1 --upper-threshold .9999 --distribution beta --trend-preservation bounded --adjust-p-values True
tasmin	tasmin = tas - tasskew x tasrange
tasmax	tasmax = tasrange + tasmin

One important aspect of climate change studies is the preservation of the embedded global warming trends in the variables, particularly in temperature (tas). ISIMIP3 takes this into account and ensures that the trend present in the raw simulations is preserved during the bias correction process. This is crucial for capturing the long-term changes in climate variables and their impacts on various sectors.

The 2-step procedure used by ISIMIP3 for bias adjustment of tasmax and tasmin variables ensures that the physical relationship between these variables is maintained during the correction process. In the first step, two intermediate variables, tasrange and tasskew, are derived. The tasrange represents the temperature range and is calculated as the difference between tasmax and tasmin (tasrange = tasmax - tasmin). Tasskew is a measure calculated as the ratio of the difference between tas and tasmin to tasrange (tasskew = (tas - tasmin) / tasrange). In the second step, bias adjustments are applied to tasrange and tasskew. Finally, using the bias-adjusted values of tasrange and tasskew, the bias-adjusted tasmin and tasmax are derived. The tasmin is calculated by subtracting the product of tasskew and tasrange from tas (tasmin = tas - tasskew x tasrange), and tasmax is obtained by adding tasrange to tasmin (tasmax = tasrange + tasmin). By incorporating this additional procedure, the ISIMIP3 method ensures that the physical consistency between tas, tasmax, and tasmin is preserved in the bias-adjusted simulations. This helps to maintain the appropriate temperature relationships and improves the overall realism of the corrected temperature variables.

For precipitation (pr), ISIMIP3 includes specific treatments to address certain issues in the simulations. It implements a lower bound at 0 mm/day to prevent negative (physically unrealistic) precipitation values. Additionally, a lower threshold at 0.1 mm/day is used to correct the drizzle issue commonly observed in simulations, where very low precipitation amounts are overestimated. These treatments improve the realism of the bias-adjusted precipitation simulations.

The bias_adjustment.py script, along with the utility_function.py script, forms the main components for conducting bias adjustment in the ISIMIP3 method. Here's a breakdown of their functionalities: 1. bias_adjustment.py: This script serves as the main function for the bias adjustment process. 2. utility_function.py: This script contains various subroutines and utility functions that support the bias adjustment process. It includes functions for data handling, interpolation, statistical calculations, and other necessary operations. By utilizing these scripts and their functionalities, the bias adjustment process can be carried out effectively and efficiently. The scripts automate the correction procedure for each grid cell or station, ensuring consistency and coherence in the bias-corrected data across space and time.

9.3.4 Combining 2km and 8km resolution bias-adjusted outputs

We conducted bias adjustments for both the 2km and 8km simulations in our study. The 2km simulations provide a detailed spatial pattern over Singapore and the West Maritime Continent, making them suitable for analyzing climate change on a local scale. However, it's important to note that the 2km simulations cover a shorter time period, specifically 1995-2014, 2040-2059, and 2080-2099. To address the long-term trend, we also utilized the 8km bias-corrected simulations, which cover a longer period from 1955 to 2014 for the historical period and from 2015 to 2099 for the future warming period. Although the 8km simulations give a coarser spatial resolution, they provide useful insights into the climate change over a broader time span.

It is worth mentioning that the information and conclusions based on both the 2km and 8km simulations are consistent. We combined the results from both resolutions to address the long-term changes and capture the detailed spatial structure over Singapore. By incorporating strengths of the 2km and 8km simulations, we gained a comprehensive understanding of the climate change trends and their local implications. This approach ensures the robustness of our analysis and enhances the reliability of our findings.

9.3.5 Advances from V2 to V3

In the V2 study, bias adjustment was briefly addressed in Chapter 5 (Climate Change Projections, Annexe 5a: Description of the Quantile Matching technique applied to provide bias-corrected RCM outputs over Singapore). Here we highlight the advances in the V3 bias

adjustment compared to the V2 study (Table 9.7). These advancements have led to more accurate and reliable simulations, providing improved data for climate impact studies over Singapore.

Table 9.7. Advances from V2 to V3 bias adjustment

Advances in V3	V2	V3
higher resolution	V2 study adjusted model output on the 12km resolution over singapore (8 grid cells)	V3 study provided higher resolution bias-adjusted outcome on the 8km (25 grid cells) and 2 km resolution (over 300 grid cells)
new observation reference	V2 used stations across Singapore to aggregate into one CDF as the reference. 3 stations for temperature and humidity, one station for wind, and 28 stations for rainfall. There is no spatial information in the observation reference.	V3 uses ERA5-RCM data to create gridded observational reference for temperature, humidity, and wind. V3 also uses 28 stations to create gridded rainfall reference. These efforts created gridded benchmarks for bias adjustment in the 8km and 2 km resolution.
customised distributions	V2 carried out the same configuration (i.e. multiplicative quantile mapping) to all the target variables.	V3 applied customised configurations for individual variables. e.g., temperature using normal distribution, precipitation using Gamma distribution, relative humidity using beta distribution, and wind using Weibull distribution.
trend-preserving	V2 didn't have treatments for the trend in the historical data and in the model simulations.	V3 has additional treatment to preserve the trend.
adjust rainfall frequency	V2 didn't have treatment for days with zero-rainfall and the low rainfall range.	V3 applies a threshold at 0.1mm/day to adjust the rainfall frequency.
flexible bins for CDF	V2 used 1 percentile bin size to group data in the cumulative distribution function (CDF).	V3 uses the default 0.5 percentile bin size for grouping. But it is adjusted automatically to make sure there are enough samples in each bin to handle zero-rain days.
updated base period	V2 used 1980-2009 30-year as the base period.	V3 uses 1995-2014 20-year as the baseline, which is inline with the IPCC AR6 guidelines.

9.4 Results: bias-adjustment for tas

Historical gridded reference: The evaluation depicted in Figure 9.3 demonstrates a good agreement between the 12-month climatology of the ERA5-RCM and the observed temperature (tas) from five manned stations in Singapore (locations shown in Figure 9.3a). This agreement indicates that the ERA5-RCM simulations can serve as a reasonably realistic gridded reference for temperature (tas) in Singapore for the bias correction process.

Bias-adjusted historical climatology: Figure 9.4 illustrates the historical surface air temperature (tas) over Singapore, showing temperature peaks typically occurring around May. While the models are generally able to capture the seasonal cycle, they tend to overestimate the temperature by approximately 1 degree Celsius. After applying the bias adjustment to the models, the corrected tas align much more closely with the observation reference, indicating a successful correction of the overestimation bias. The bias-adjusted simulations provide a more accurate representation of the observed temperature patterns over Singapore.

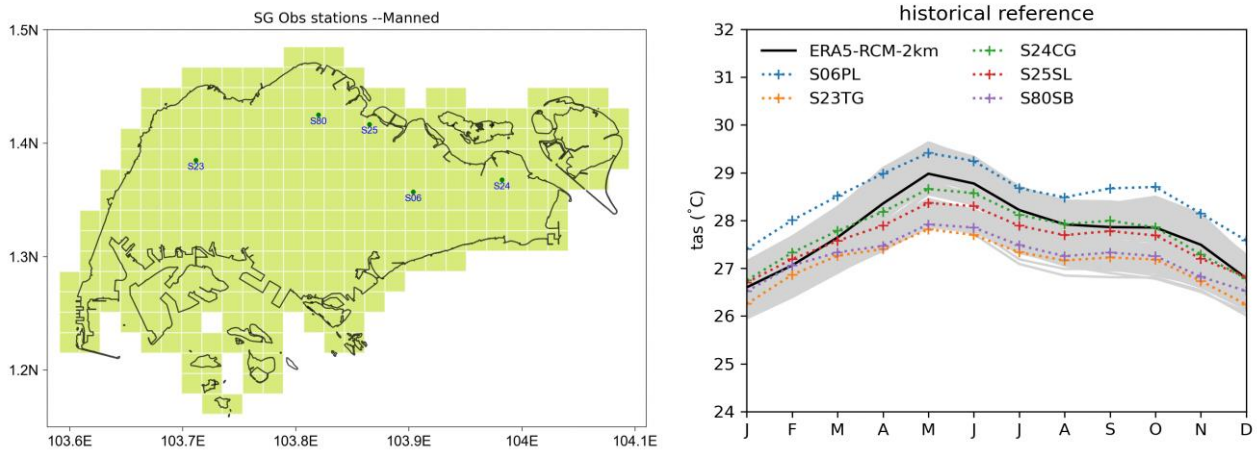

Figure 9.3. (a) map of manned station in Singapore. (b) 12-month climatology of tas in the historical period (1995-2014) from 5 manned stations (dotted) and from 2km-resolution ERA5-RCM gridcells across Singapaore (black is the gridcell mean)

Bias-adjusted future climatology: The models consistently exhibit a tendency to overestimate the surface air temperature by approximately 1 degree Celsius, both in the historical and future periods. After applying the bias adjustment based on the historical reference, the future tas projections are tuned down, bringing them into a more realistic range and better align with expectations based on the observational baseline. This bias adjustment helps to improve the accuracy of the future tas simulations. Figure 9.5 provides visual evidence of this improvement in the bias-adjusted future tas projections.

Future change largely preserved after bias adjustments: Figure 9.6 illustrates the projected changes in surface air temperature (tas) over Singapore. The results indicate a range of warming levels across models, ranging from approximately 2 to 5 degrees Celsius. On average, the models project a mean warming of around 4 degrees Celsius, representing a 15% increase in temperature. It is worth noting that these warming levels are consistent across seasons, indicating a relatively uniform temperature increase throughout the year.
The comparison between the bias-adjusted simulations and the original projections demonstrates that the warming signals are largely preserved after the bias adjustment process. This indicates that the adjustments successfully correct the systematic biases without significantly altering the projected changes in tas. The preserved warming signals in the bias-adjusted simulations provide a more reliable representation of the expected future climate conditions over Singapore.

Climate change patterns largely preserved by bias adjustments: Figure 9.7 illustrates the spatial pattern of projected warming signals across Singapore for both raw and bias-adjusted simulations from the UKESM1-0-LL model. It is evident that there are spatial differences in the projected warming, with northern Singapore exhibiting a larger warming signal compared to the southern parts of Singapore, which are closer to the open ocean.

The bias adjustment process aims to preserve the spatial features of the warming signals while reducing systematic biases in the model simulations. The comparison for UKESM1-0-LL shows that both raw and bias-adjusted simulations keep consistency in the magnitude of the warming signal. Furthermore, the bias adjustment successfully preserves the spatial differences in the warming patterns. The larger warming signal observed in northern Singapore, as seen in the raw simulations, is also maintained in the bias-adjusted simulations.

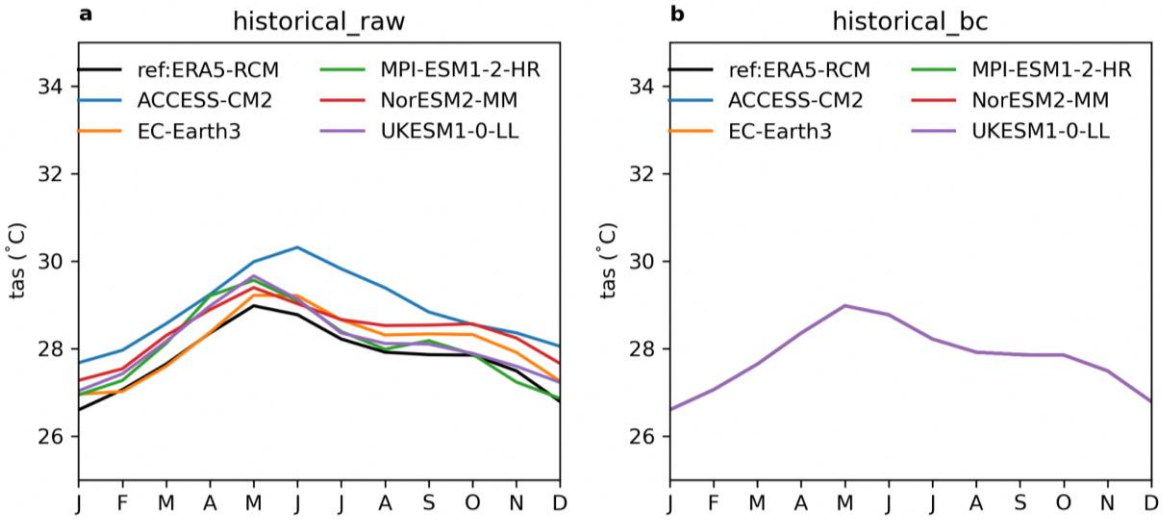

Figure 9.4: Singapore domain-averaged tas at the 2km resolution in the historical period (1995-2014). a. observation reference (ERA5-RCM) and raw simulations. b. similar to a, but plotting bias-adjusted simulations.

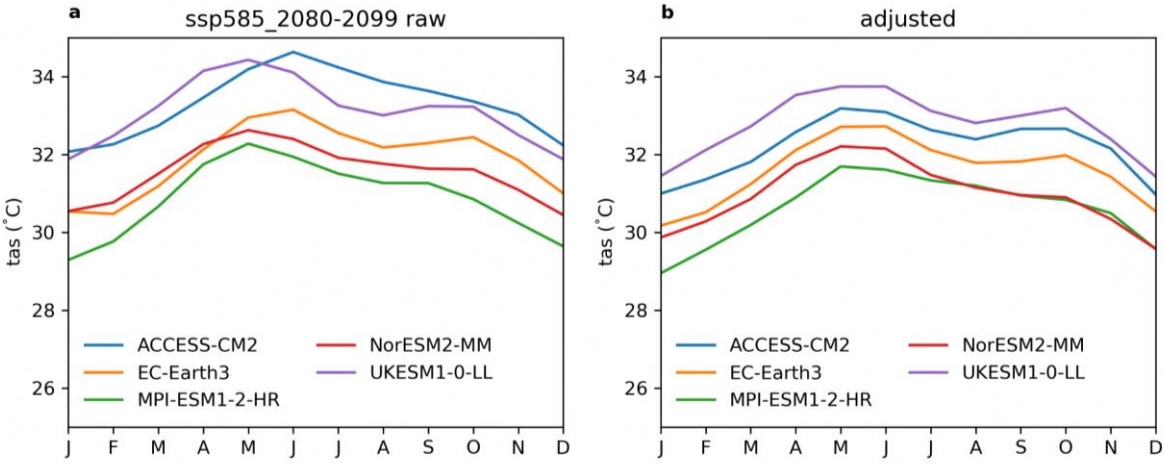

Figure 9.5: Singapore domain-averaged tas in the SSP585 future period (2080-2099) at the 2km resolution. a. raw simulations. b. bias-adjusted simulations.

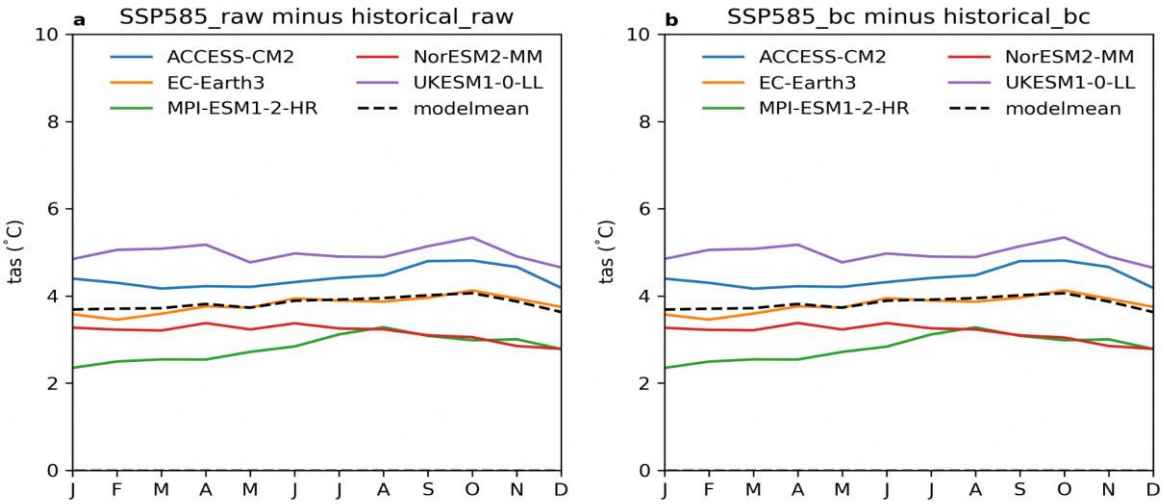

Figure 9.6: Changes in the Singapore domain-averaged tas from the historical period (1995-2014) to the future period (2080-2099) under the SSP585 scenario at the 2km resolution. a. raw simulations. b. bias-adjusted simulations.

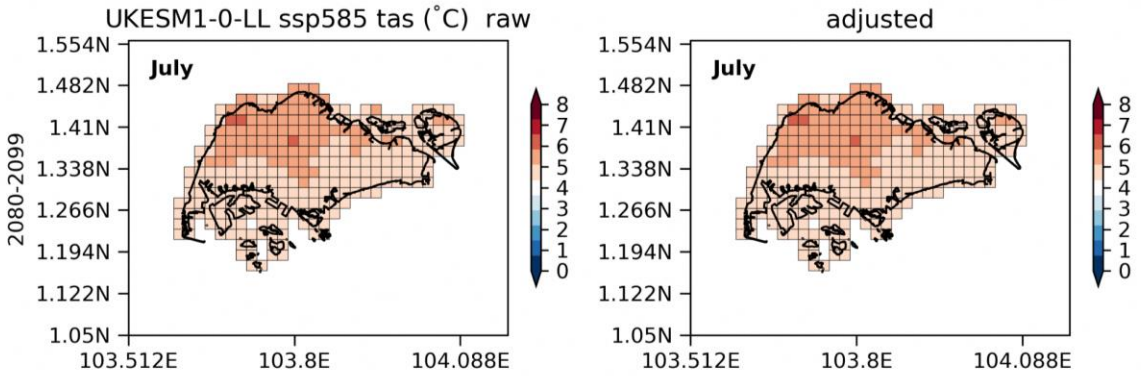

Figure 9.7: 2km resolution Singapore tas change in July from the historical period to the future period under the SSP585 scenario in the UKESM1-0-LL. a. raw simulations. b. bias-adjusted simulations.

Bias-adjusted distribution: Figure 9.8 presents the distributions of daily tas (surface air temperature) for both raw and bias-adjusted simulations from individual models, along with the reference distribution from ERA5-RCM. It is shown that the overall distribution of daily tas follows a normal distribution.

The bias adjustment process successfully brings the model simulations into better agreement with the observed distribution. Furthermore, when considering the effect of warming on tas, models that initially overestimate the warming are tuned down during the bias adjustment process. This can be observed in Figure 9.8b. This downshifted distribution reflects the adjustment made to bring the models' projected warming to a more realistic range. Overall, the bias adjustment method ensures that the bias-adjusted simulations provide a more accurate representation of the expected distribution of daily tas, considering both historical observations and projected future changes.

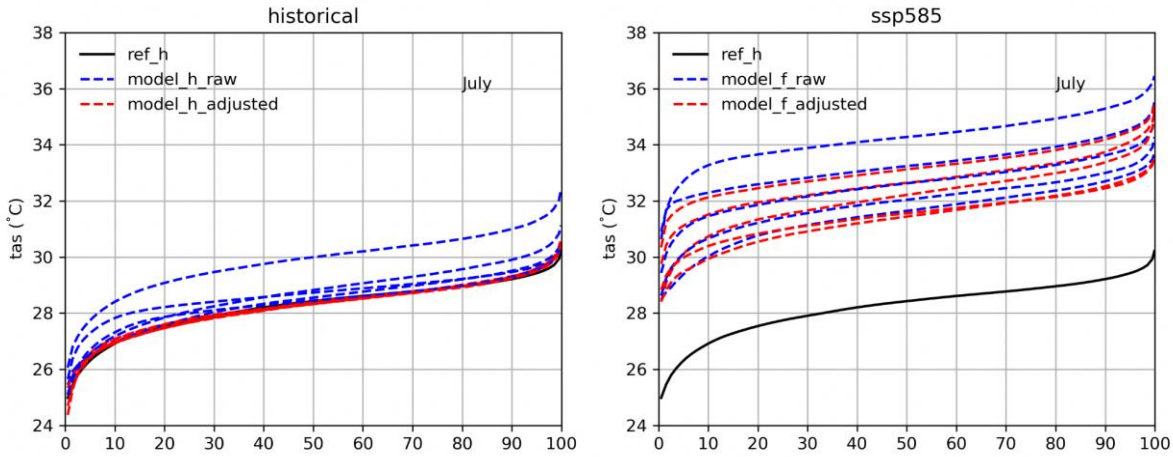

Figure 9.8: (a) July CDF of tas at gridcells across Singapore for the historical period (1995-2014). Here the ref_h is ERA5-RCM, model_h_raw are raw simulations, and model_h_adjusted are adjusted models. (b) July CDF for the future period (2080-2099) under the SSP585 scenario.

Trend in annual mean tas: Figure 9.9 highlights the climate change signal in tas (surface air temperature) and the performance of the bias-adjusted simulations in capturing this signal. It demonstrates that the bias-adjusted tas successfully preserves the warming trend associated with climate change.

In the historical period, the time series of tas in the models are adjusted to match the mean of the observed data. This adjustment ensures that the model simulations are consistent with the observed mean temperature, providing a more accurate representation of historical climate conditions. Furthermore, the variability range of the adjusted simulations in the historical period is similar to that of the observations. This suggests that the bias adjustment process not only corrects for biases in the mean tas but also addresses discrepancies in the variability, allowing the adjusted simulations to capture the observed range of temperature variations.

Looking into the future period, the bias-adjusted time series provide a more realistic projection of tas. The adjusted simulations not only capture the adjusted mean temperature but also maintain a realistic range of variability. Overall, the bias-adjusted tas preserves the important climate change signal by capturing the warming trend and matches the mean and variability of the observations in the historical period. In the future period, the adjusted simulations offer a more realistic projection of tas, ensuring that the bias adjustment process enhances the accuracy and reliability of the model outputs.

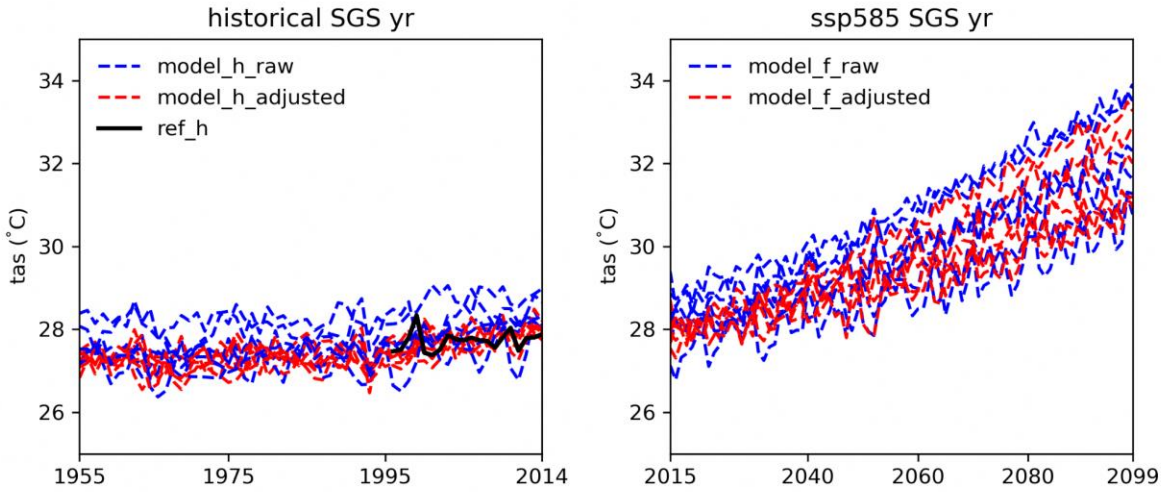

Figure 9.9: (a) 8km resolution Singapore domain-averaged tas in the historical period. (b) tas in the future period under the SSP585 scenario. Observation reference is in black (ERA5-RCM). Raw simulations are in blue, and bias-adjusted simulations are in red.

9.5 Results: bias-adjustment for tasmax

Historical gridded reference: Here we use ERA5-RCM as the historical reference. Comparison showed that the 12-month climatology of tasmax observations from 5 manned stations in Singapore are within the range of the climatology of tasmax at each gridcells from the ERA5-RCM (Figure 9.10). It indicates that ERA5-RCM can provide a reasonably realistic gridded reference for tasmax.

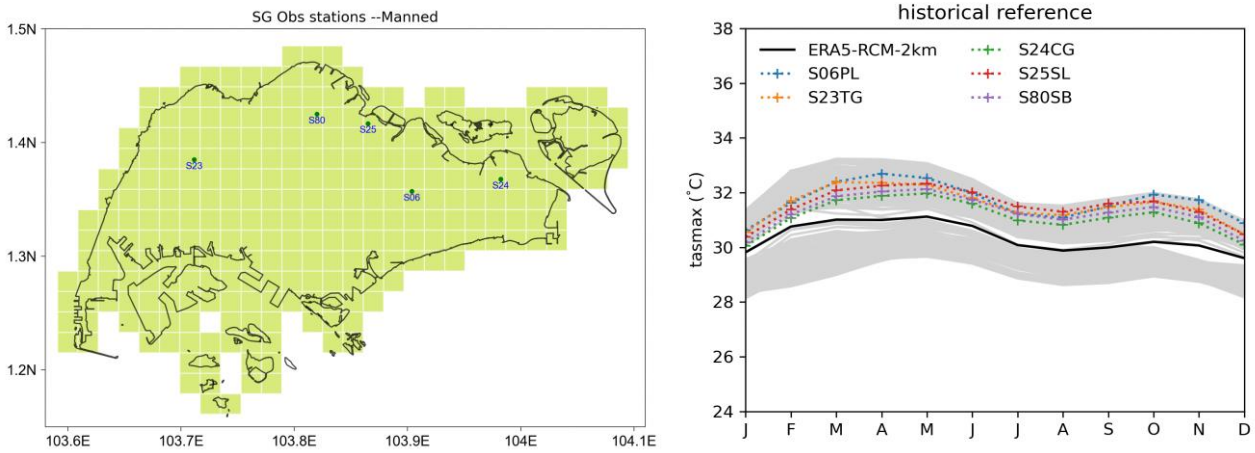

Figure 9.10. (a) Map of manned stations in Singapore. (b) 12-month climatology of tasmax from 5 manned stations (dotted) and from ERA5-RCM gridcells across Singapaore (black is the gridcell mean).

Bias-adjusted historical climatology: Historical tasmax over Singapore shows temperature peaks around March-April-May (Figure 9.11). Models are able to simulate the seasonal cycle but tend to overestimate the tas for ~1°C. Bias-adjusted simulations match with the observation reference (Figure 9.11).

Bias-adjusted future climatology: Models tend to overestimate the temperature in both historical and future period. Adjusted tasmax is tuned down to provide a more realistic future projection (Figure 9.12).

Climate change signal preserved by bias adjustments: As to the change, models project warming ranging from ~2.5 to ~5.5°C (Figure 9.13) with the mean around 4°C (~13% increase). The warming levels are similar across seasons. Bias adjustments largely preserve the warming.

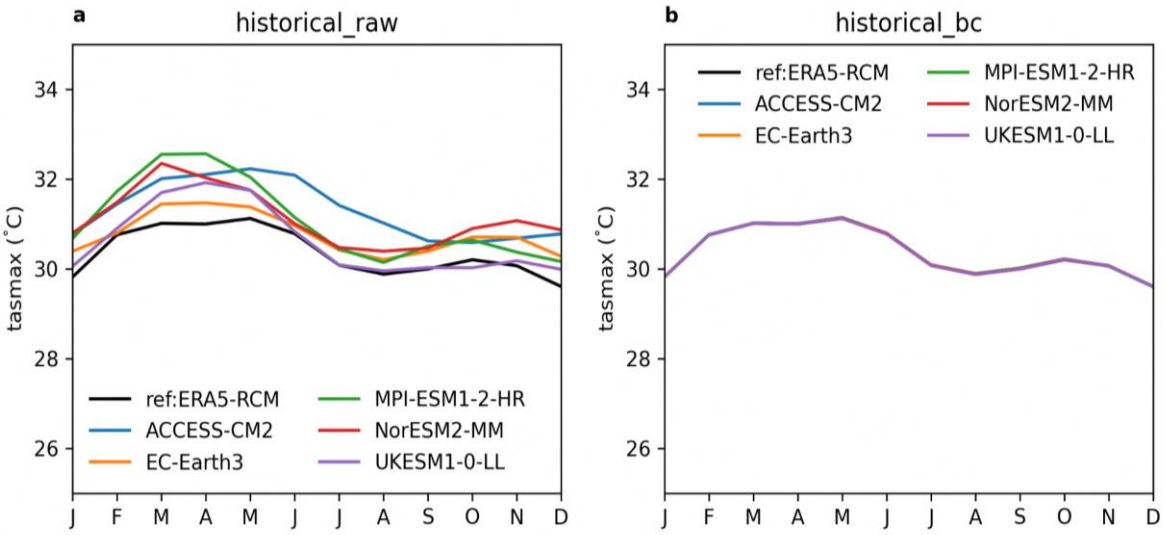

Figure 9.11: Singapore domain-averaged tasmax in the historical period (1995-2014). (a) observation reference (ERA5-RCM) and raw simulations. (b) similar to a, but plotting bias-adjusted simulations.

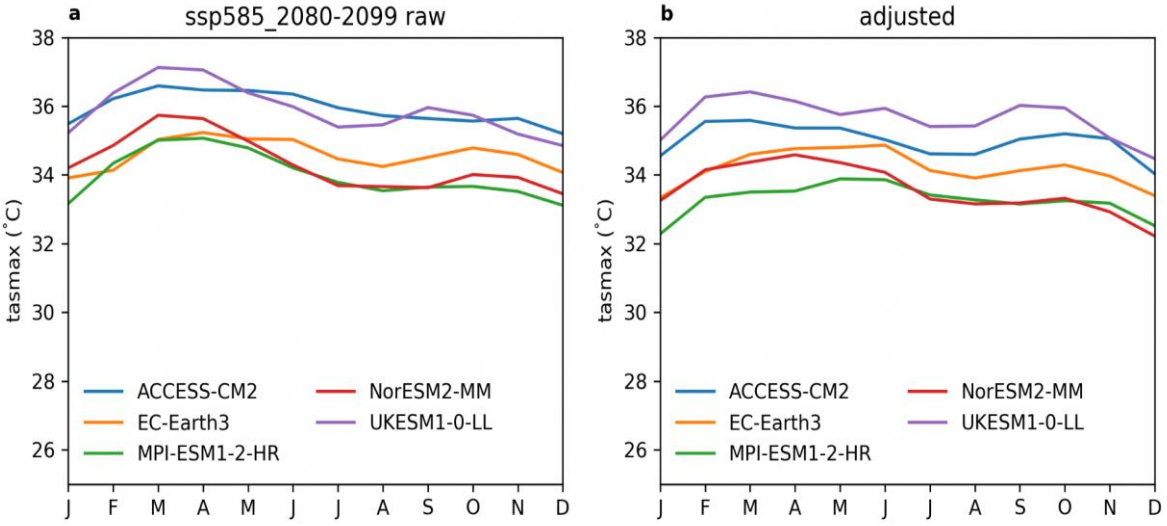

Figure 9.12: Singapore domain-averaged tasmax in the SSP585 future period (2080-2099) at a 2km resolution. a. raw simulations. b. bias-adjusted simulations.

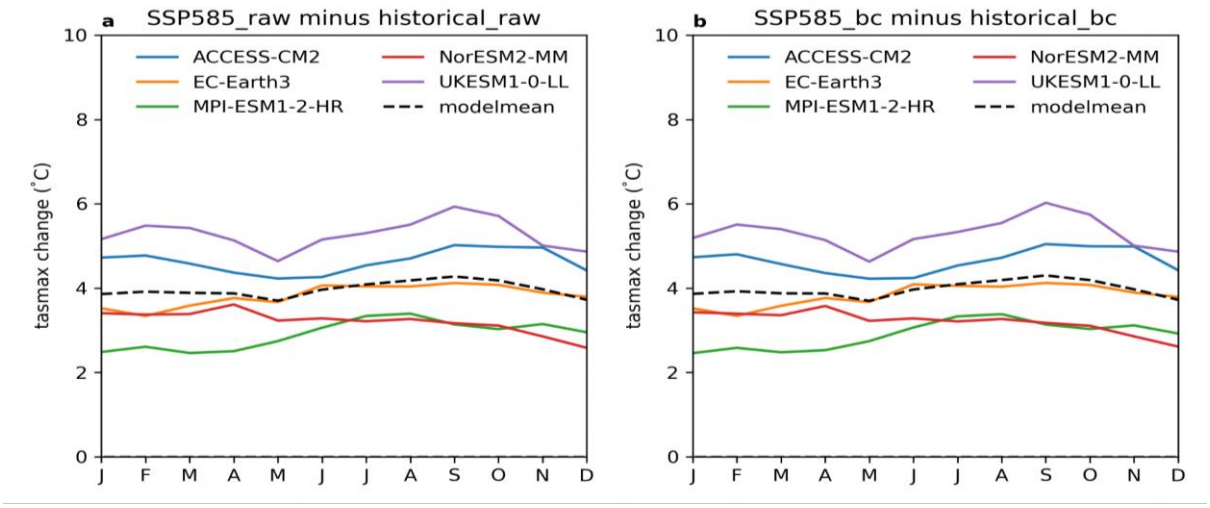

Figure 9.13: Changes in the Singapore domain-averaged tasmax from the historical period (1995-2014) to the future period (2080-2099) under the SSP585 scenario. a. raw simulations. b. bias-adjusted simulations.

Climate change patterns preserved by bias adjustments: Similar to the warming pattern of tas, future change of tasmax in both raw and adjusted simulations show a larger warming in the northern Singapore compared to the southern Singapore (Figure 9.14).

Bias-adjusted distribution: Distributions of modelled tasmax are adjusted to the reference distribution (ERA5-RCM) for the historical period (Figure 9.15). Under warming, distributions of tasmax are tuned down slightly.

Trend in annual mean tasmax: Here we show time series of tasmax in models are adjusted to match observation mean in the historical period (Figure 9.16). Also the variability range of the adjusted simulations is similar to the observation. In the future period, adjusted time series provide more realistic projection with adjusted mean and variability. Here bias adjustment preserved the warming trend in tasmax.

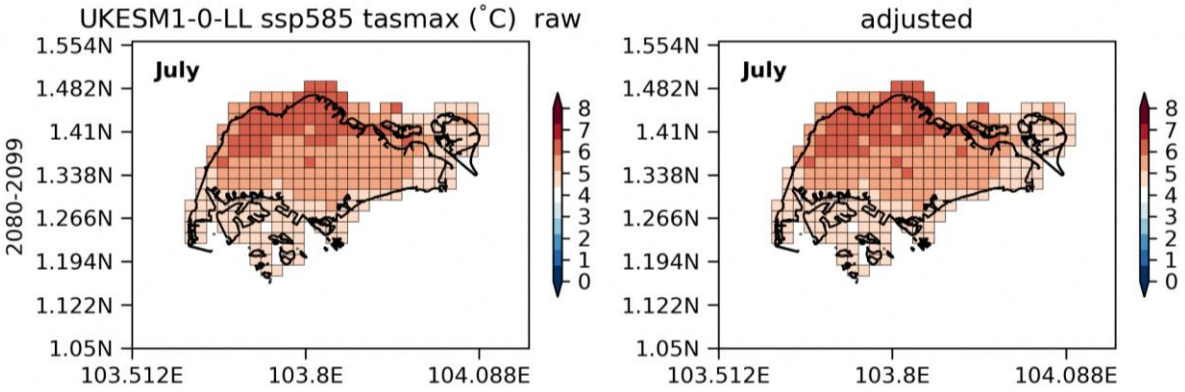

Figure 9.14: 2km resolution Singapore tas change in July from the historical period to the future period under the SSP585 scenario. a. raw simulations. b. bias-adjusted simulations.

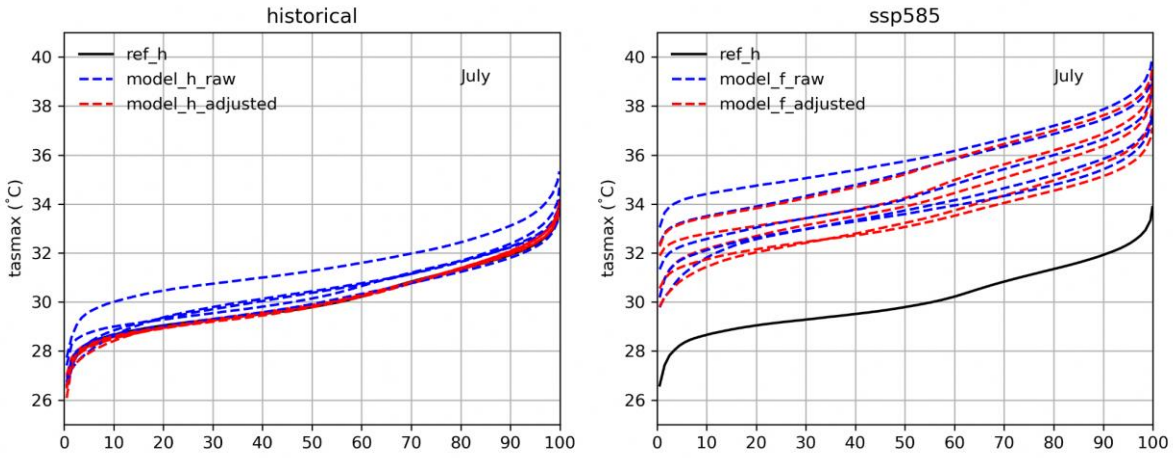

Figure 9.15: a. July CDF of tasmax at gridcells across Singapore for the historical period (1995-2014). Reference is the ERA5-RCM. b. July CDF for the future period (2080-2099) under the SSP585 scenario.

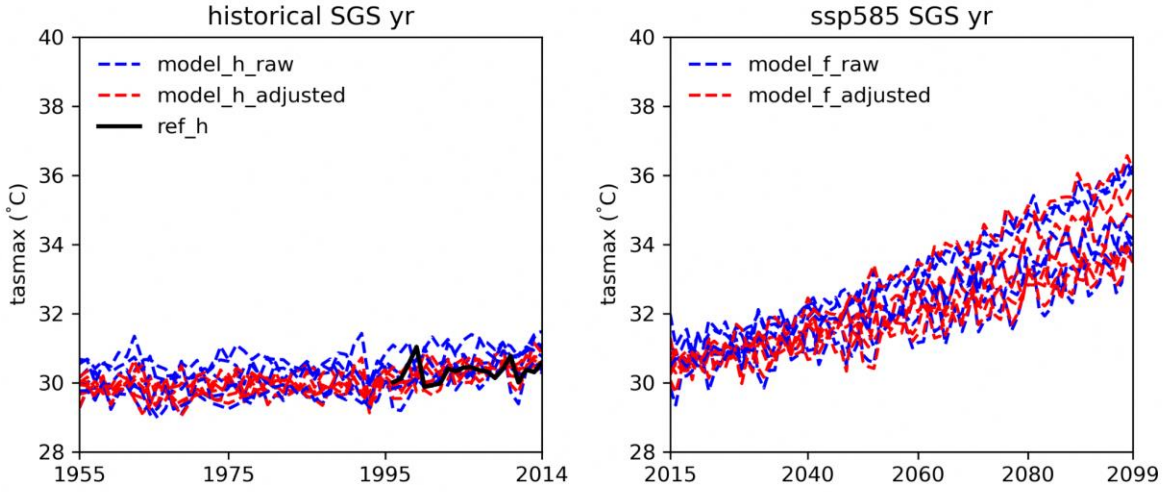

Figure 9.16: 8km resolution Singapore domain-averaged tasmax in the historical period (a) and in the future period (b) under the SSP585 scenario. Observation reference (ERA5-RCM) is in black. Raw simulations are in blue, and bias-adjusted simulations are in red.

9.6 Results: bias-adjustment for tasmin

Historical gridded reference: Here we use ERA5-RCM as the historical reference. We compared the 12-month climatology of the ERA5-RCM with tasmin observations from 5 manned stations in Singapore, and the results (Figure 9.17) show that ERA5-RCM can provide a reasonably realistic gridded reference.

Bias-adjusted historical climatology: The models exhibit similar overestimated biases for tasmin. After applying bias-adjustment techniques, the simulations better align with the observational reference, as shown in Figure 9.18.

Bias-adjusted future climatology: Models tend to slightly overestimate the tasmin in both historical and future period. Adjusted tasmin is tuned down to provide a more realistic future projection (Figure 9.19).

Climate change preserved by bias adjustments: As to the change of tasmin (Figure 9.20), models project warming ranging from ~2 to ~5°C with the mean warming around 4°C (~15% increase). The warming levels are similar across seasons. Bias adjustment can preserve the change signal.

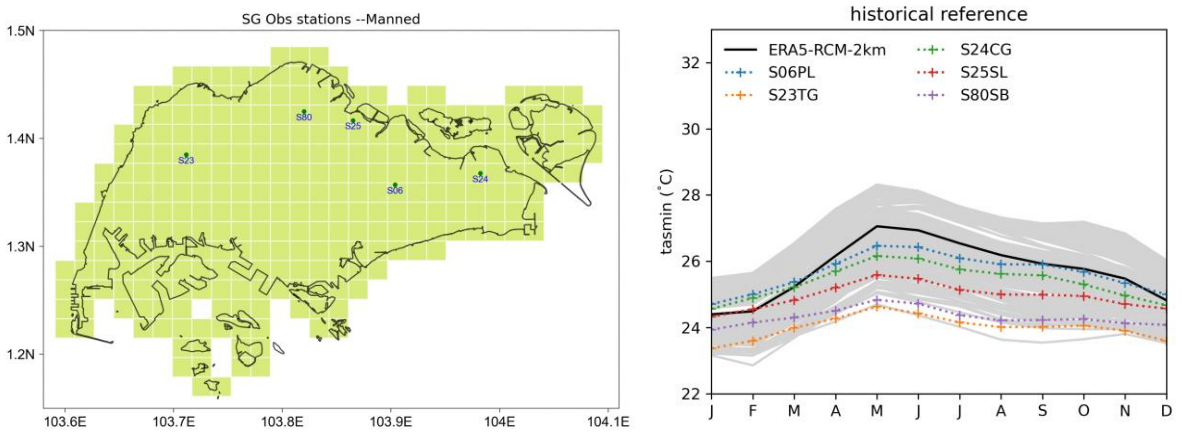

Figure 9.17. a. Map of manned stations in Singapore. b. 12-month climatology of tasmin in the historical period (1995-2014) from 5 manned stations (dotted) and from ERA5-RCM gridcells across Singapaore (black is the gridcell mean).

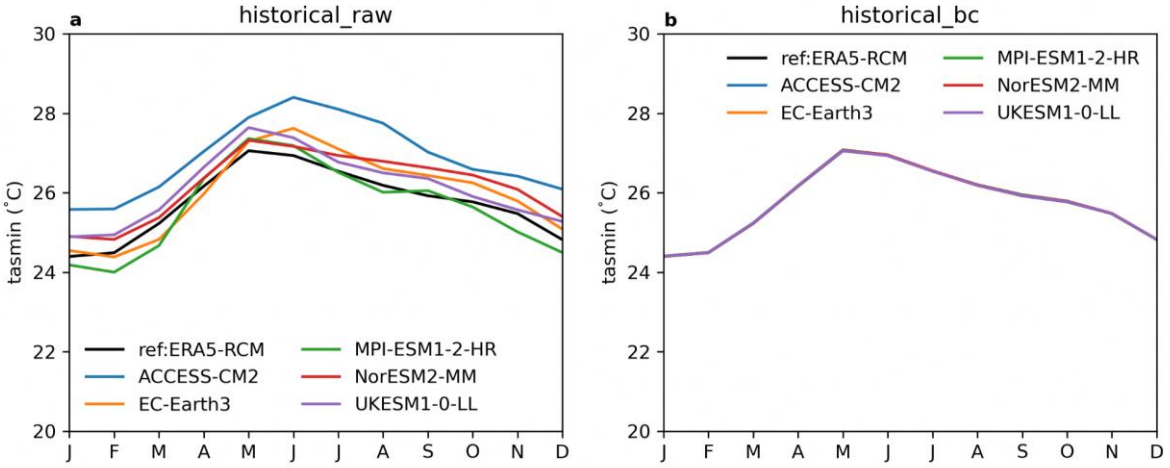

Figure 9.18: Singapore domain-averaged tasmin in the historical period (1995-2014) at a 2km resolution. a. observation reference (ERA5-RCM) and raw simulations. b. similar to a, but plotting bias-adjusted simulations.

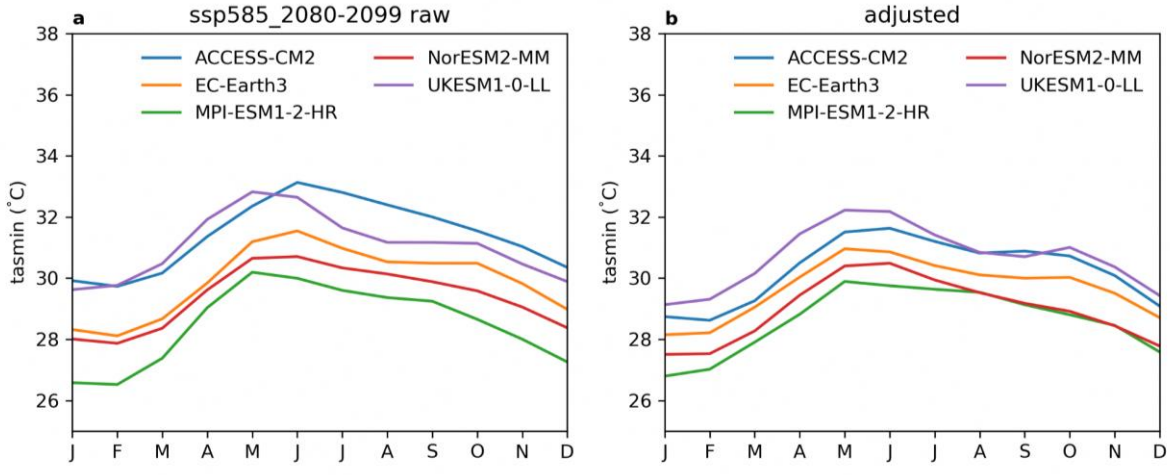

Figure 9.19: Singapore domain-averaged tasmin in the future period (2080-2099) under the SSP585 scenario at a 2km resolution. a. raw simulations. b. bias-adjusted simulations.

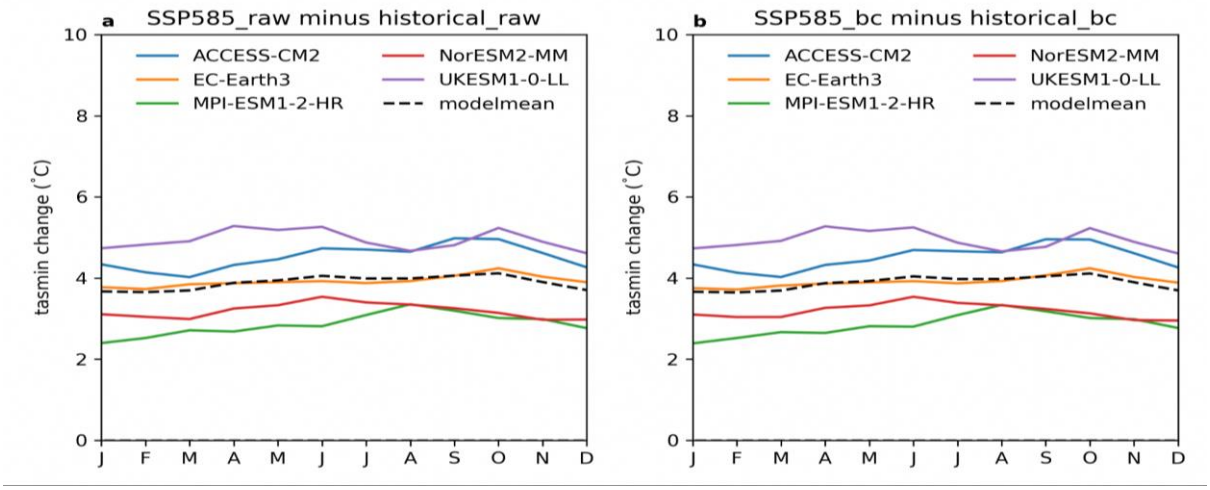

Figure 9.20: Changes in the Singapore domain-averaged tasmin from the historical period (1995-2014) to the future period (2080-2099) under the SSP585 scenario at a 2km resolution. a. raw simulations. b. bias-adjusted simulations.

Climate change patterns preserved by bias adjustments: Similar to the warming pattern of tas, future change of tasmin (Figure 9.21) in both raw and adjusted simulations show a larger warming in the northern Singapore compared to the southern Singapore.

Bias-adjusted distribution: Distributions of modeled tasmin are adjusted to the reference distribution (ERA5-RCM) for the historical period (Figure 9.22). Under warming, distributions of tasmin are tuned down to a more reasonable range of warming.

Trend in annual mean tasmin: Here we show time series of tasmin in models are adjusted to match observation mean in the historical period (Figure 9.23). Also the variability range of the adjusted simulations is similar to the observation. In the future period, adjusted time series provide more realistic projection with adjusted mean and variability. Bias adjustment preserves the warming trend.

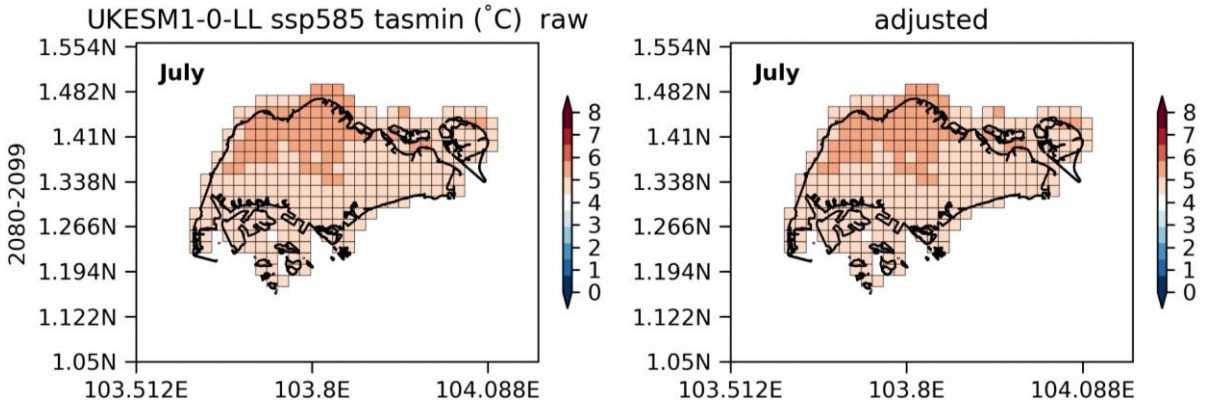

Figure 9.21: 2km resolution Singapore tasmin change in July from the historical period (1995-2014) to the future period (2080-2099) under the SSP585 scenario simulated by UKESM1-0-LL. a. raw simulations. b. bias-adjusted simulations.

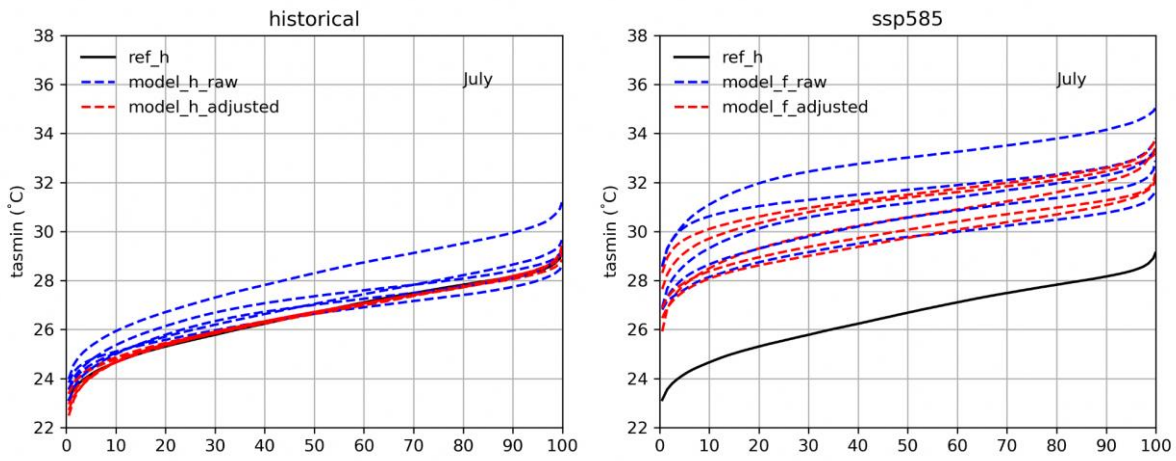

Figure 9.22: a. July CDF of tasmin at gridcells across Singapore for the historical period (1995-2014). b. July CDF for the future period (2080-2099) under the SSP585 scenario.

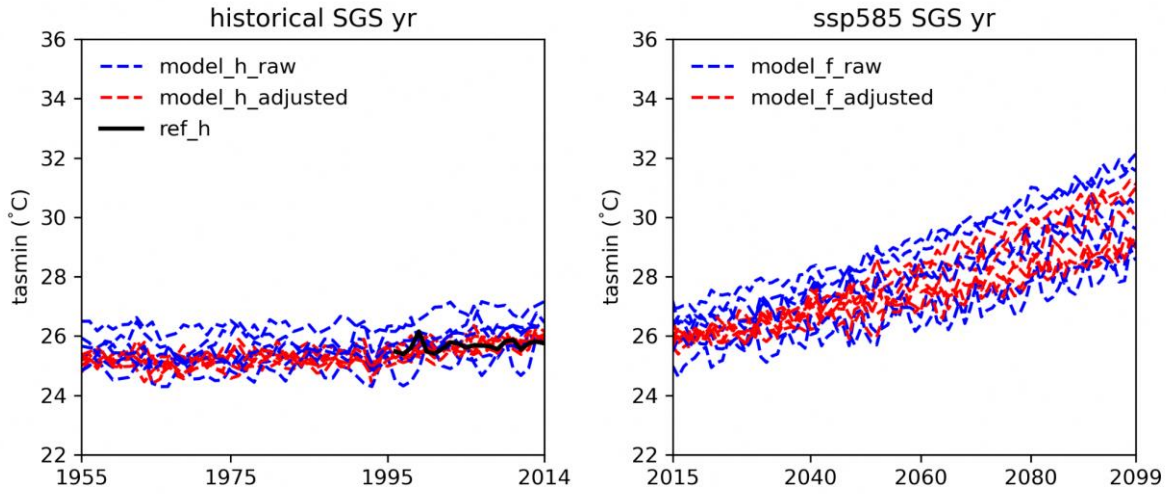

Figure 9.23: a. 8km resolution Singapore domain-averaged tasmin in the historical period. b. tasmin in the future period under the SSP585 scenario. Observation reference is in black (ERA5-RCM). Raw simulations are in blue, and bias-adjusted simulations are in red.

9.7 Results: bias-adjustment for pr

Historical gridded reference: The Meteorological Service Singapore (MSS) has established a network of 93 automatic weather stations (AWS) across Singapore since 2009. However, for long-term rainfall records, there are only around 28 rain-gauge stations available dating back to 1980. Figure 9.24 illustrates the locations of these rain gauges, revealing a limited spatial coverage particularly in western and eastern Singapore.

To overcome this spatial limitation, a gridded daily rainfall dataset was created using geostatistical interpolation techniques. The Python package PyKrige, as described by Murphy et al. (2020), was utilized for this purpose. The interpolation was performed on daily rainfall data aggregated from the hourly data collected at each station. Only days with at least one non-zero rainfall value were considered, while days with no rainfall were assigned a zero value. The geostatistical interpolation employed the concept of Ordinary Kriging, which is a spatial interpolation method based on variograms. A spherical semivariogram model was chosen to capture the spatial autocorrelation and variability of rainfall as a function of the separation distance between each pair of stations. The selection of the spherical model was based on the work of

Muhammad Ali and Othman (2017), who evaluated various semivariogram models and found the spherical model to be the most appropriate for the Kelang River basin in Peninsular Malaysia. By applying geostatistical interpolation using PyKrige and the spherical semivariogram model, the gridded daily rainfall dataset was generated, providing a more comprehensive representation of rainfall across Singapore. This dataset helps address the limited spatial coverage of rain-gauge stations and allows for a more accurate analysis and understanding of rainfall patterns and variability in the region.

The daily rainfall observations from 1980 to 2021 were subjected to spatial interpolation using kriging techniques, specifically applied to the SINGV-RCM 2-km and 8-km grid. This interpolation process resulted in a gridded representation of rainfall station data. For this study, the kriged rainfall observations for the period 1995-2014 were chosen as the reference dataset.

Comparisons between the kriged rainfall and individual rain gauges revealed good agreement in terms of climatological patterns. This agreement suggests that the kriged precipitation data can serve as a suitable gridded observation reference. By utilizing kriging interpolation, the study was able to fill in spatial gaps and provide a more comprehensive representation of rainfall across the region. Using the kriged rainfall observations as the reference, the study can effectively assess and analyze the model performance in capturing the spatial and temporal characteristics of precipitation.

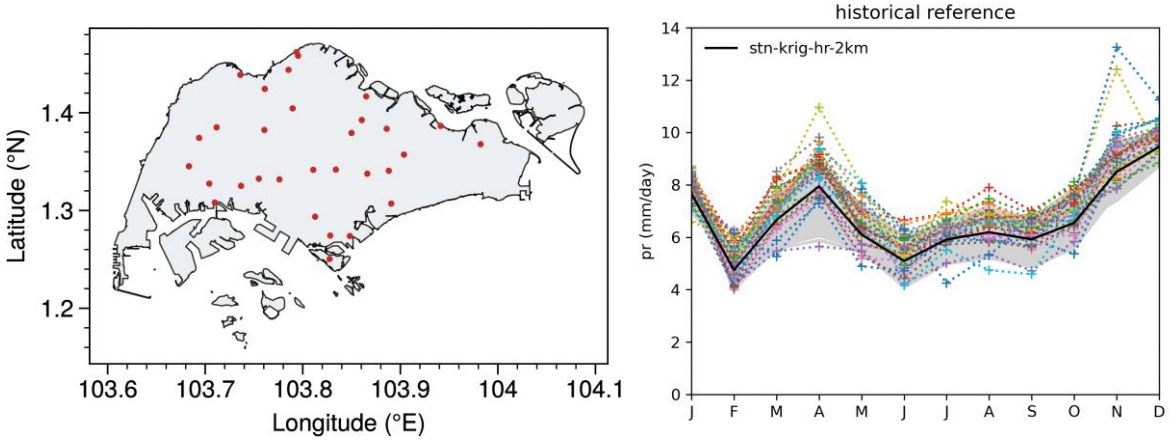

Figure 9.24: a. Map of 28 rain gauge stations in Singapore. b. 12-month climatology of pr in the historical period (1995-2014) from 28 pr stations (dotted) and from 2km-resolution krig gridcells across Singapore (black is the gridcell mean).

Bias-adjusted historical climatology: Historical rainfall over Singapore shows a seasonal transition between weather types (Figure 9.25). It starts from a wet winter due to the Northeast monsoon, followed by another wet April due to frequent squalls moving across Singapore. Then comes the dry summer and autumn due to Southwest monsoon. Here five SINGV RCM models show varying wet/dry biases compared to the observation reference. In particular, models appear to underestimate the January-March rainfall. Bias-adjusted simulations match closely with the reference (Figure 9.25).

Bias-adjusted future climatology: Here we show that (Figure 9.26) raw future rainfall is also low in Jan-Feb (systematic bias, similar to the historical rainfall, see Figure 9.25). After bias-adjustment, the Jan-Feb rainfall is more close to the magnitude of the observation reference.

Climate change overall preserved by bias adjustments: After bias adjustments, models tend to agree that SG may become drier (-3mm/day) by 25% (Figure 9.27) in Jan-Feb and July-Sept, while wetter (+2mm/day) by 20% in May and Nov-Dec. One may notice that the future rainfall changes are tuned down slightly after bias adjustments, unlike the changes in the surface air temperature. It is heavily due to the nonlinearity and skewed distribution in rainfall (Figure 9.29) compared to the relatively normal distribution in temperature (Figure 9.8). For

temperature, the biases are mainly in the mean instead of the shape of the distribution. However, the biases in rainfall are embedded in the whole distribution.

In the process of recalibrating historical and projected precipitation within these skewed distributions, the overall direction of change remains largely intact. However, there is potential for a minor adjustment in the magnitude of mean future changes. It is crucial to also recognize that raw future changes, when derived from biased simulations, do not inherently represent accurate projections. Consequently, changes after the bias adjustments could lead to alterations that are more aligned with realistic expectations. This bias adjustment practice does not alter the understanding and main conclusions as to the future changes.

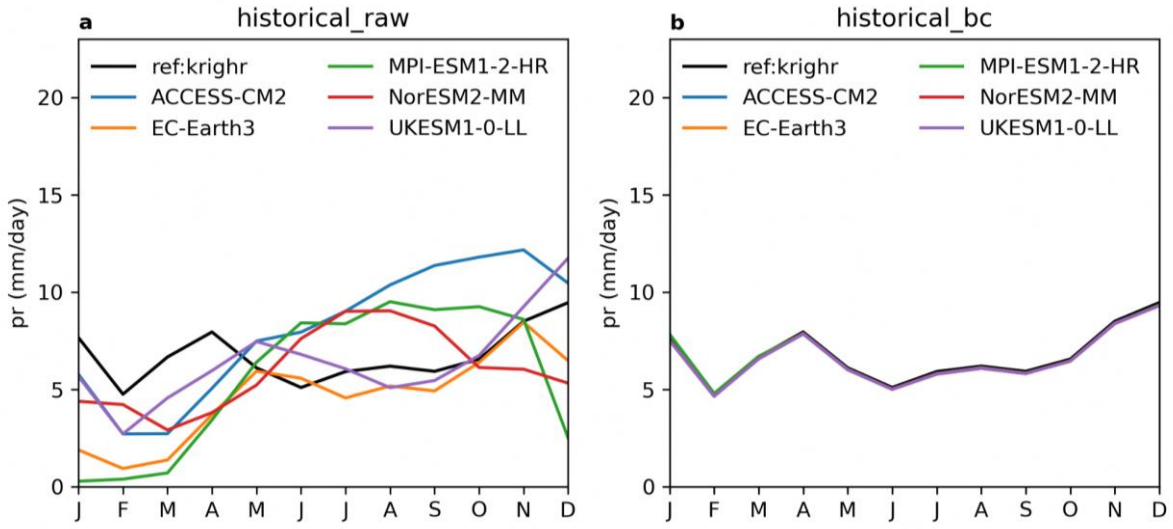

Figure 9.25: Singapore domain-averaged pr in the historical period (1995-2014) at a 2km resolution. a. observation reference (station krig pr) and raw simulations. b. similar to a, but plotting bias-adjusted simulations.

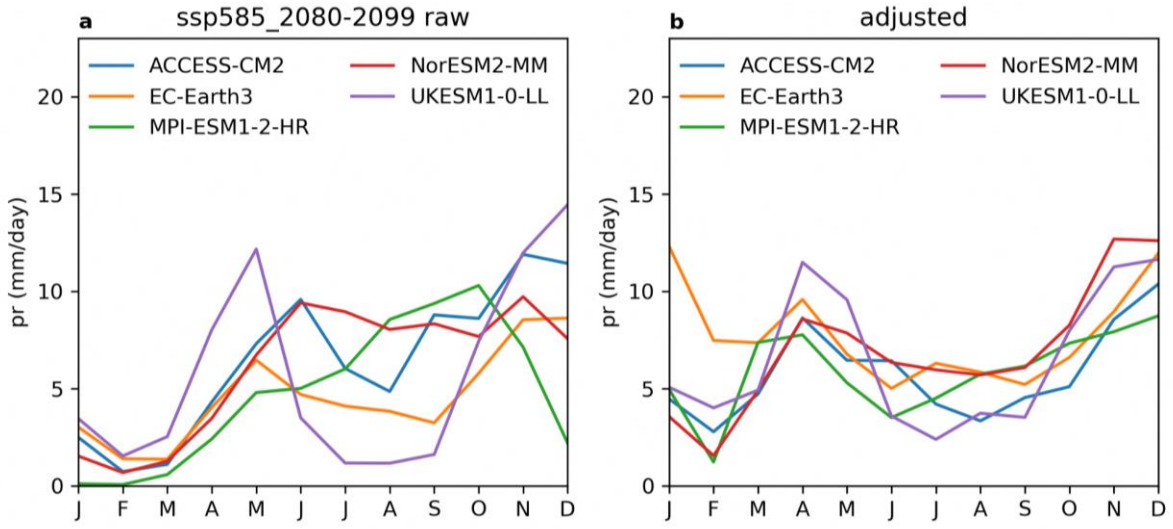

Figure 9.26: Singapore domain-averaged pr in the future period (2080-2099) under the SSP585 scenario. a. raw simulations. b. bias-adjusted simulations.

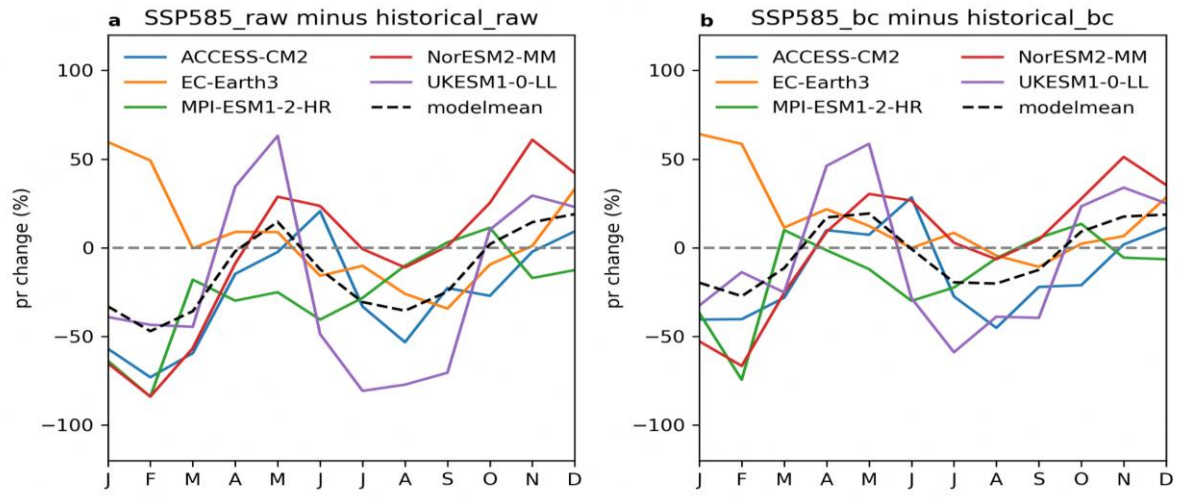

Figure 9.27: Percentage changes in the Singapore domain-averaged pr from the historical period (1995-2014) to the future period (2080-2099) under the SSP585 scenario at a 2km resolution. a. raw simulations. b. bias-adjusted simulations.

Climate change patterns preserved by bias adjustments: Singapore is controlled by southwest monsoon duing the JJAS season. Here future changes in pr projected by ACCESS-CM2 (Figure 9.28) in both raw and adjusted simulations show a larger reduction of rainfall in the south-western Singapore compared to the north-eastern Singapore. Note that bias adjustment still preserve the spatial feature of the change even though the change magnitude is reduced after bias adjustment.

Bias-adjusted distribution: Distributions of modeled pr (overestimated as to the reference) are adjusted to the reference distribution (station kriged) for the historical period (Figure 9.29). Under warming, distributions of overestimated July pr are tuned down.

Trend in annual mean pr: Here we show time series of rainfall in models are adjusted to match observation mean in the historical period (Figure 9.30). Also the variability range of the simulations is reduced to match the observation. In the future period, adjusted time series provide more realistic projection with adjusted mean and variability.

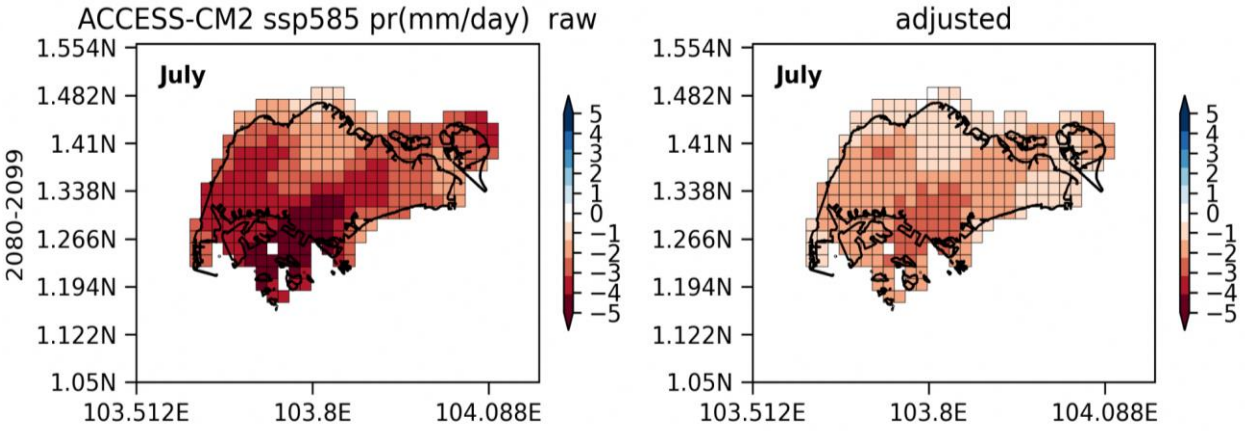

Figure 9.28: 2km resolution Singapore pr change in July from the historical period (1995-2014) to the future period (2080-2099) under the SSP585 scenario. a. raw simulations. b. bias-adjusted simulations.

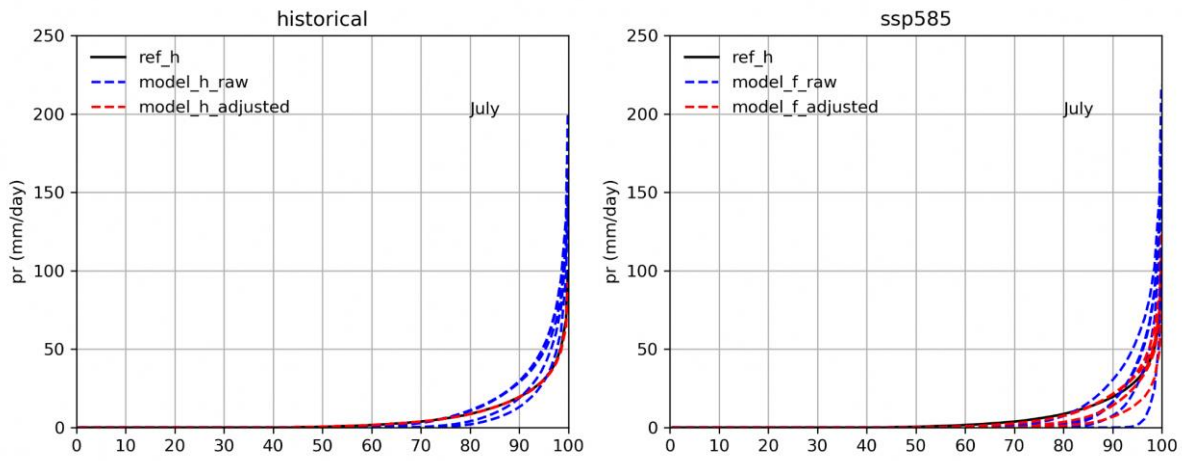

Figure 9.29: a. July CDF of pr at 2km resolution gridcells across Singapore for the historical period (1995-2014). b. July CDF for the future period (2080-2099) under the SSP585 scenario.

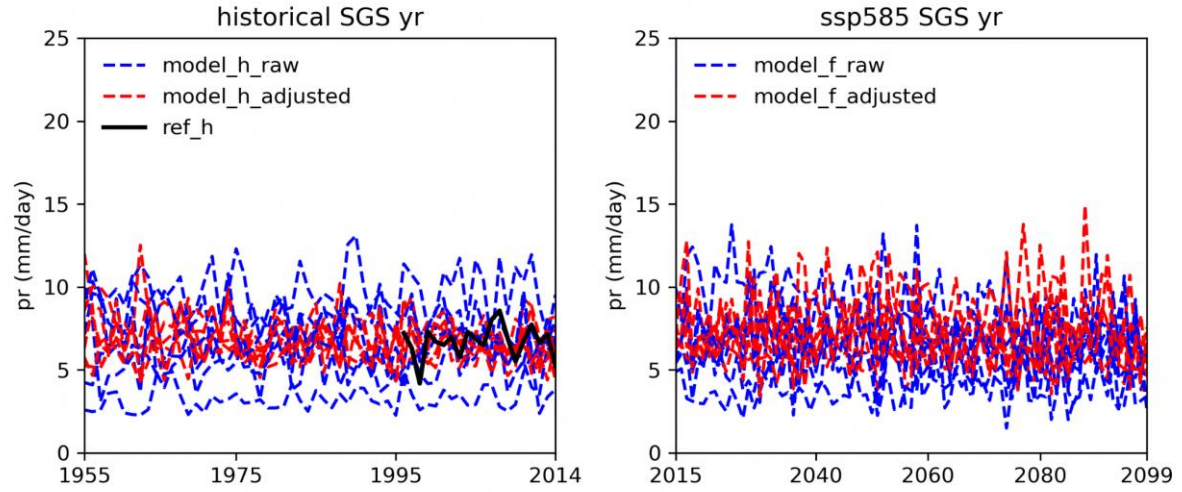

Figure 9.30: a. 8km resolution Singapore domain-averaged annual mean pr in the historical period. b. pr in the future period under the SSP585 scenario. Observation reference is in black (station krig pr). Raw simulations are in blue, and bias-adjusted simulations are in red.

9.8 Results: bias-adjustment for hurs

Historical gridded reference: Here we use ERA5-RCM as the historical reference. We compared the 12-month climatology of the ERA5-RCM with observations from 5 manned stations in Singapore, and the results (Figure 9.31) show that ERA5-RCM can provide a reasonably realistic gridded reference for hurs.

Bias-adjusted historical climatology: Models tend to underestimate the hurs in Jan-April, and bias-adjusted simulations match with the reference (Figure 9.32).

Bias-adjusted future climatology: Models tend to underestimate the magnitude in the future period during Jan- April. Adjusted simulations tune up the magnitude which becomes more realistic (Figure 9.33). Moreover, the seasonal cycle is adjusted to match better with the observation reference.

Climate change largely preserved by bias adjustments: Models tend to project reduction of the hurs (-2.5% in value as in Figure 9.34, -3% in percentage changes) across all seasons except in May. Bias adjustments largely preserve the change.

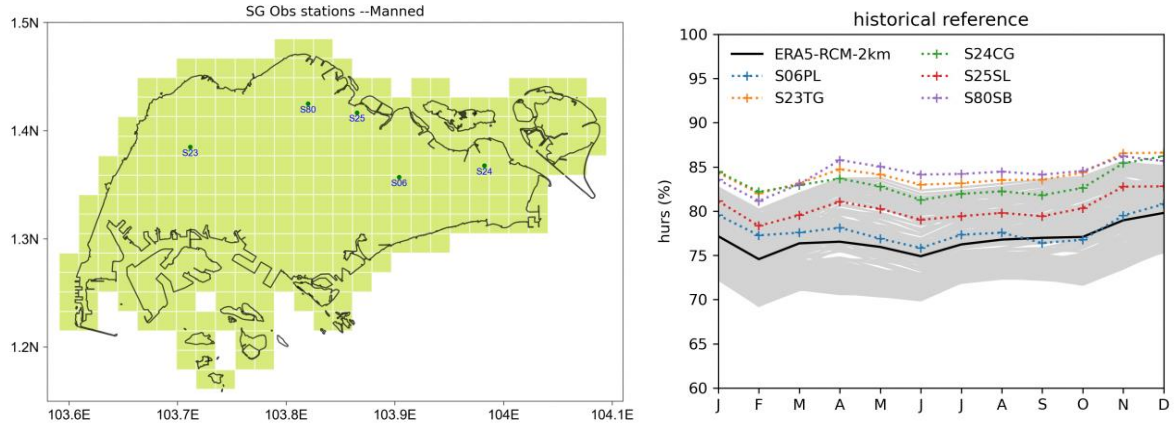

Figure 9.31. a. Map of manned stations in Singapore. b. 12-month climatology of hurs in the historical period (1995-2014) from 5 manned stations (dotted) and from ERA5-RCM gridcells across Singapore (black is the gridcell mean) at a 2km resolution.

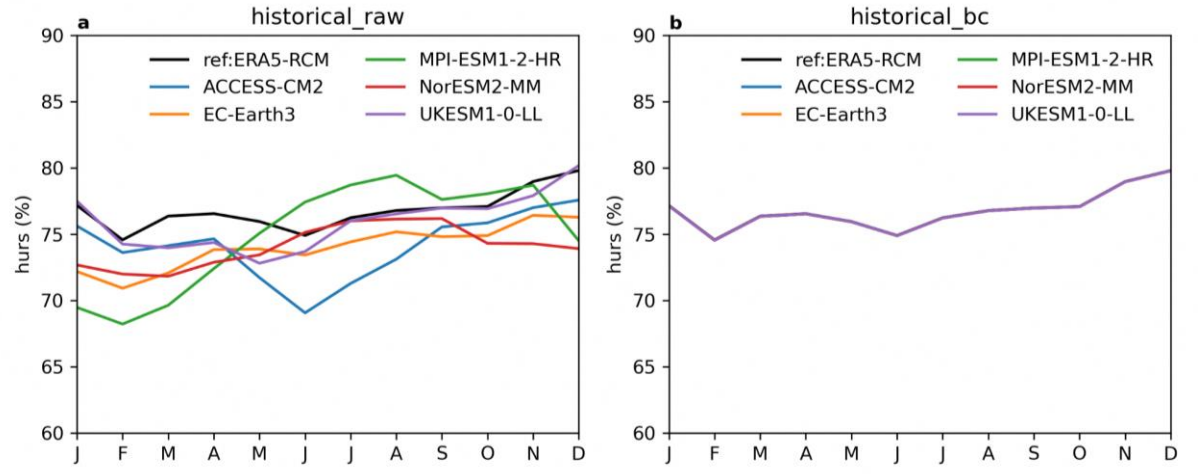

Figure 9.32: Singapore domain-averaged hurs in the historical period (1995-2014) at a 2km resolution. a. observation reference (ERA5-RCM) and raw simulations. b. similar to a, but plotting bias-adjusted simulations.

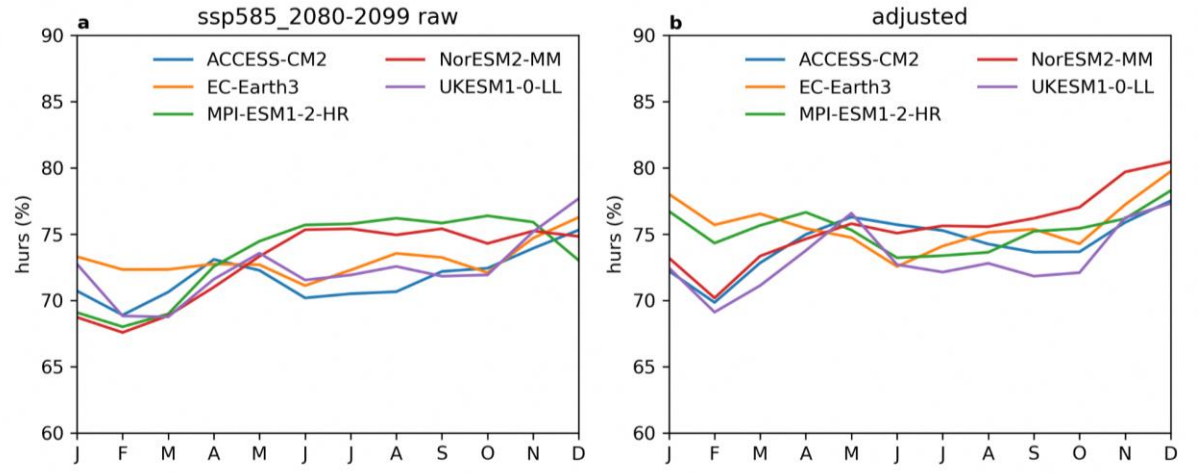

Figure 9.33: Singapore domain-averaged hurs in the future period (2080-2099) under the SSP585 scenario at a 2km resolution. a. raw simulations. b. bias-adjusted simulations.

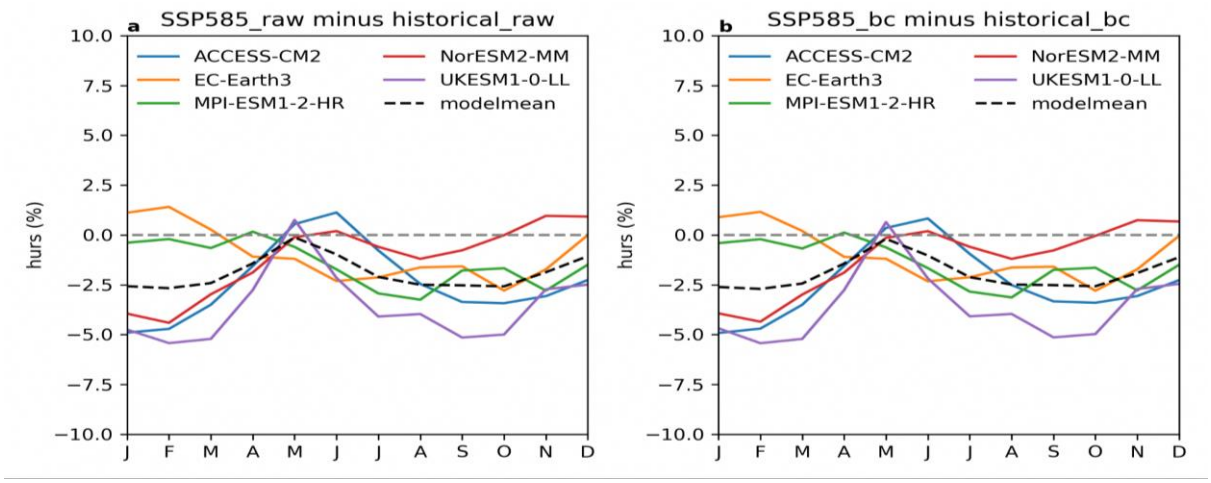

Figure 9.34: Changes in the Singapore domain-averaged hurs from the historical period (1995-2014) to the future period (2080-2099) under the SSP585 scenario at a 2km resolution. a. raw simulations. b. bias-adjusted simulations.

Climate change patterns preserved by bias adjustments: Here future change of hurs projected by UKESM1-0-LL (Figure 9.35) in both raw and adjusted simulations show a larger reduction of hurs in the north-western Singapore compared to the south-eastern Singapore. Note that bias adjustments preserve the spatial feature of the change.

Bias-adjusted distribution: Distributions of modeled hurs are adjusted to the reference distribution (ERA5-RCM) for the historical period (Figure 9.36). Under warming, distributions of overestimated and underestimated July hurs are all adjusted accordingly.

Trend in annual mean hurs: Here we show time series of hurs in models are adjusted up to match observation mean in the historical period (Figure 9.37). Also the variability range of simulations is reduced to match the observation. In the future period, adjusted time series provide more realistic projection with adjusted mean and variability. Bias adjustment also preserve the trend.

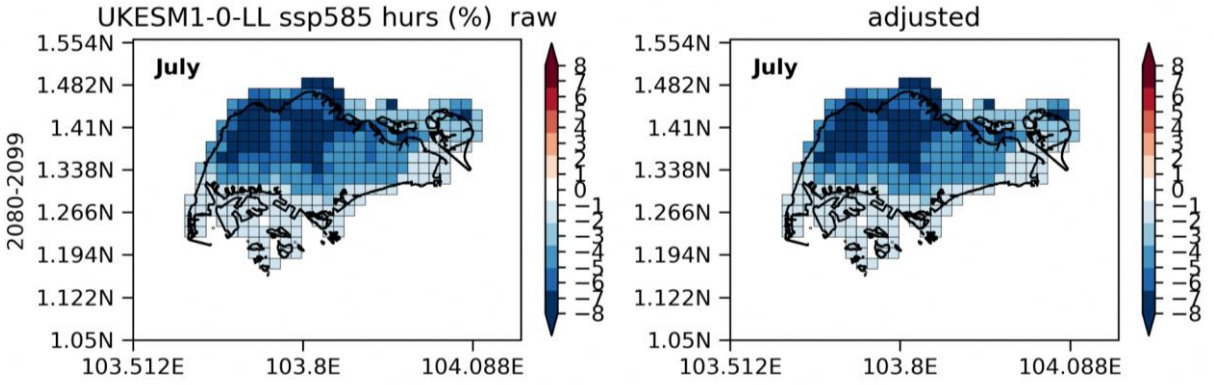

Figure 9.35: UKESM1-0-LL simulated 2km resolution Singapore July hurs change from the historical period (1995-2014) to the future period (2080-2099) under the SSP585 scenario. a. raw simulation. b. bias-adjusted simulations.

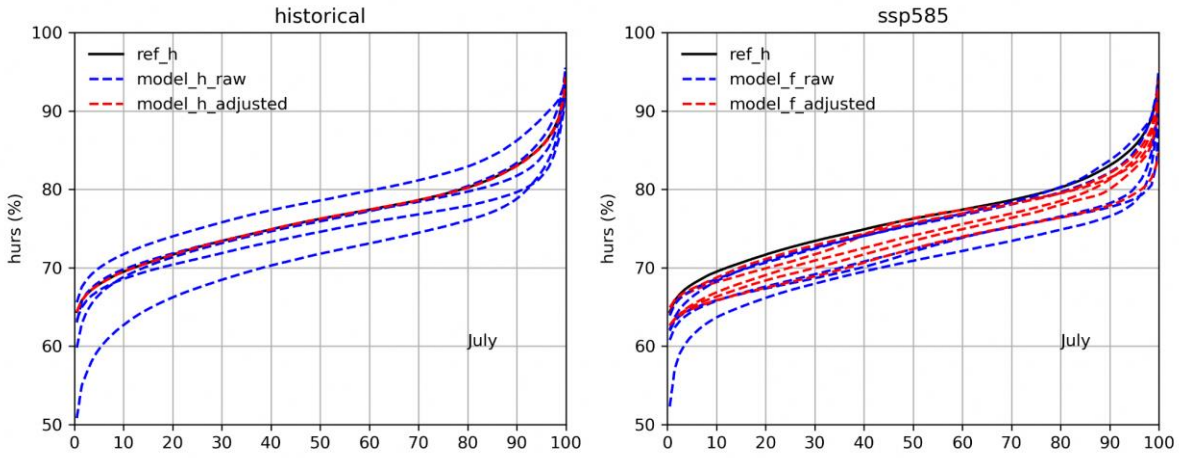

Figure 9.36: a. July CDF of hurs at 2km resolution gridcells across Singapore for the historical period (1995-2014). The reference is the station kriged rainfall. b. July CDF for the future period (2080-2099) under the SSP585 scenario.

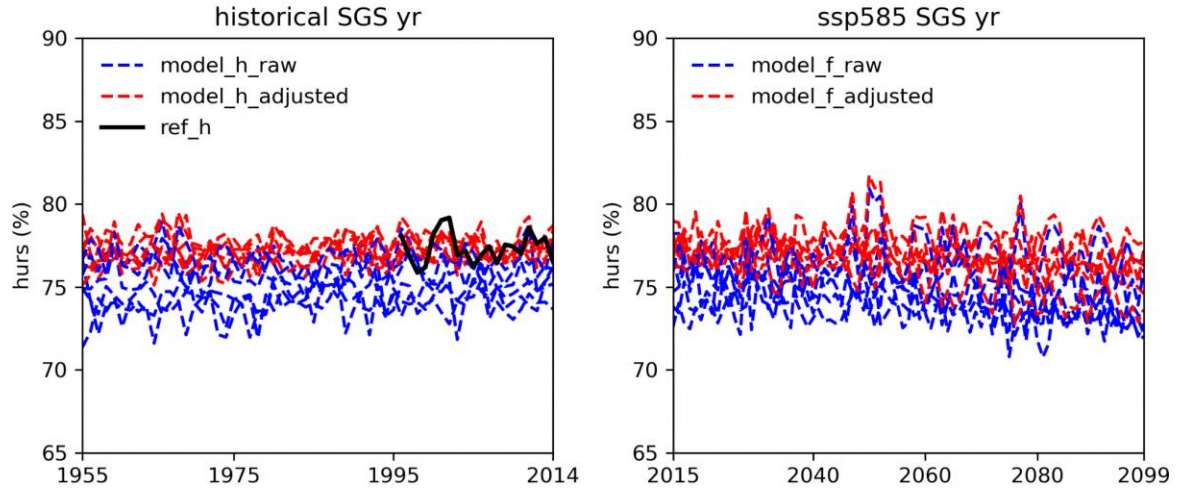

Figure 9.37: a. 8km resolution Singapore domain-averaged hurs in the historical period. b. hurs in the future period under the SSP585 scenario. Observation reference is in black. Raw simulations are in blue, and bias-adjusted simulations are in red.

9.9 Results: bias-adjustment for sfcWind

Historical gridded reference: We use the ERA5-RCM as the observation reference. We compared sfcWind climatology of all gridcells over Singapore from ERA5-RCM with 21 station data. Results (Figure 9.38) show that station sfcWind are largely within/overlap with the ERA5-RCM range, which suggests that ERA5-RCM data is a suitable product to provide a gridded estimate for sfcWind.

Bias-adjusted historical climatology: Surface wind speed over Singapore shows stronger wind during the monsoon seasons (Northeast and Southwest Monsoon season) and weaker wind during the intermonsoon transition period (Figure 9.39). Models overall overestimate the magnitude of sfcWind during the winter monsoon season. Bias-adjusted simulations match with the observation reference.

Bias-adjusted future climatology: Models overestimate the sfcWind in the winter monsoon season. Here adjusted future projection of sfcWind is tuned down for winter season (Figure 9.40).

Climate change preserved by bias adjustments: As to the future change, models project increase in the sfcWind (~0.5m/s in Figure 9. 41, or ~12% change) during the monsoon seasons (DJFM, and JJAS) except in the intermonsoon seasons (May, and Nov).

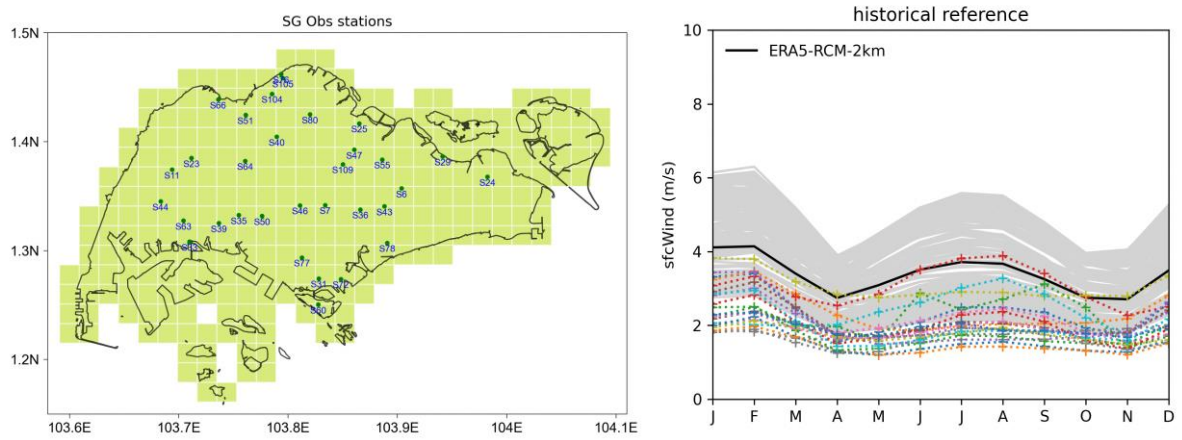

Figure.9.38 a. map of 21 stations on sfcWind. b. 12-month climatology in the historical period of station sfcWind (dotted) versus gridcells from ERA5-RCM (black is the gridcell mean) over Singapore.

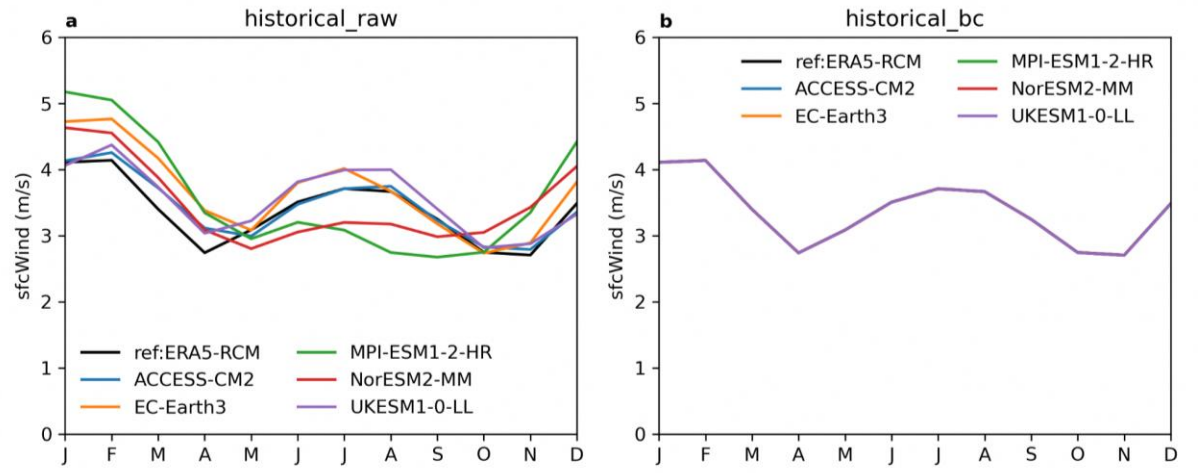

Figure 9.39: 12-month climatology of Singapore domain-averaged sfcWind in the historical period (1995-2014) at a 2km resolution. a. observation reference (ERA5-RCM, black) and raw simulations. b. similar to a, but plotting bias-adjusted simulations.

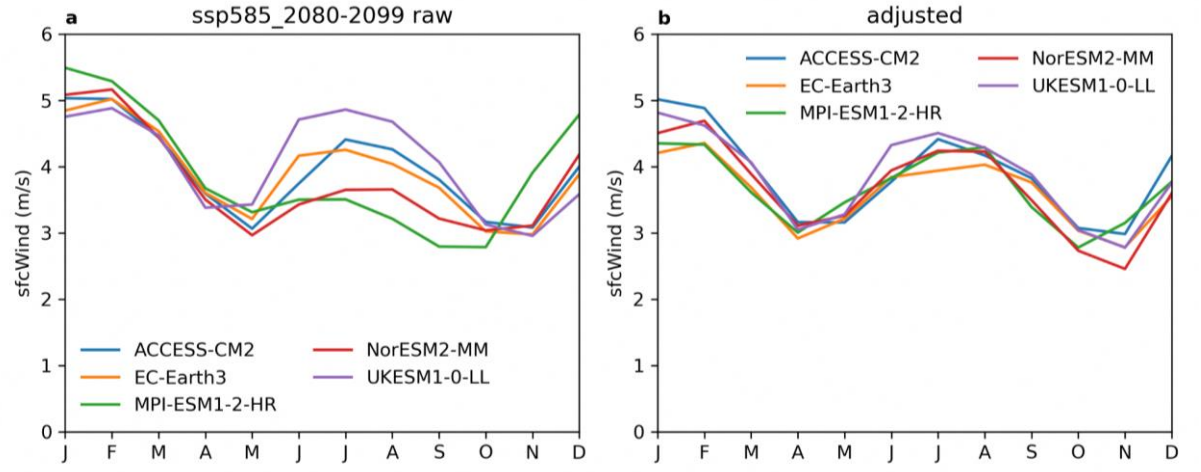

Figure 9.40: Singapore domain-averaged sfcWind in the future period (2080-2099) under the SSP585. a. raw simulations. b. bias-adjusted simulations.

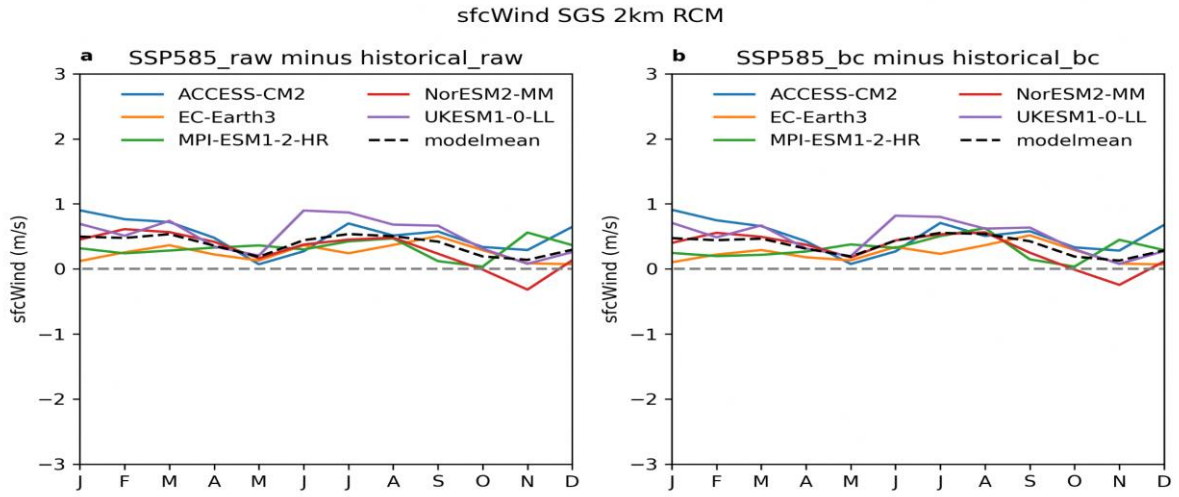

Figure 9.41: Percentage changes in the Singapore domain-averaged sfcWind from the historical period (1995-2014) to the future period (2080-2099) under the SSP585 scenario. a. raw simulations. b. bias-adjusted simulations.

Climate change patterns preserved by bias adjustments: Future change of sfcWind shows a larger increase at the coastal area of Singapore (Figure 9.42). Bias adjustment largely preserves the future change.

Bias-adjusted distribution: Distributions of modeled sfcWind are adjusted to the reference distribution (ERA5-RCM) for the historical period (Figure 9.43). Under warming, distributions of overestimated and underestimated July sfcWind are all adjusted accordingly.

Trend in annual mean sfcWind: Here we show the annual mean sfcWind in models are reduced to match observation mean in the historical period (Figure 9.44). Also the variability range of the adjusted simulations is similar to the observation. In the future period, adjusted time series provide more realistic projection with adjusted mean and variability. Bias adjustment also preserves the trend.

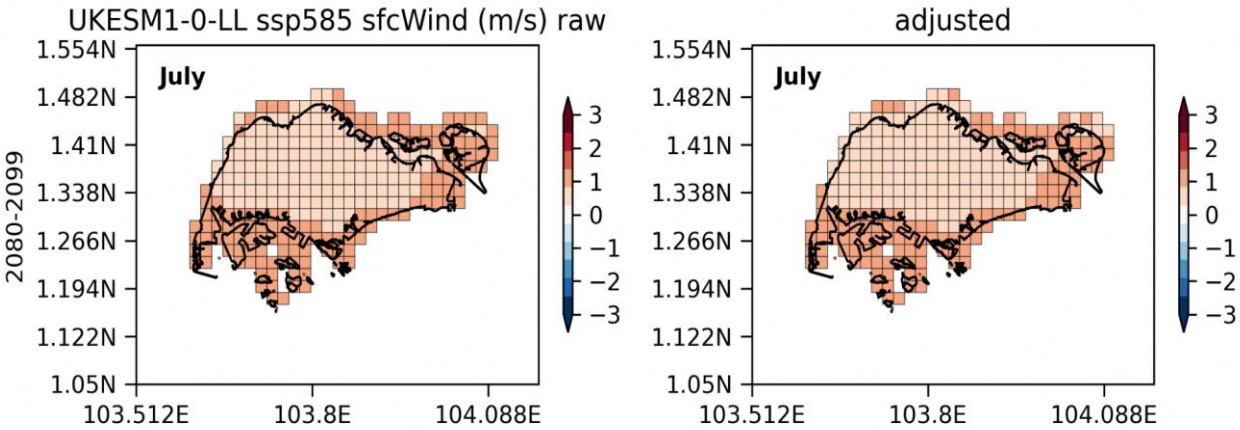

Figure 9.42: UKESM1-0-LL simulated 2km resolution Singapore July sfcWind change from the historical period to the future period under the SSP585 scenario. a. raw simulation. b. bias-adjusted simulations.

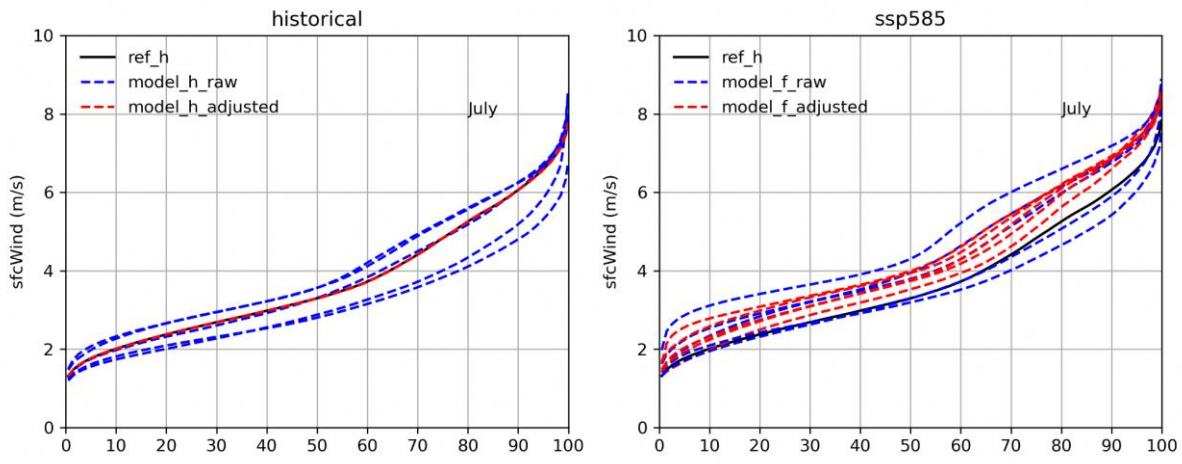

Figure 9.43: a. July CDF of sfcWind at 2km resolution gridcells across Singapore for the historical period (1995-2014). The reference is ERA5-RCM. b. July CDF for the future period (2080-2099) under the SSP585 scenario.

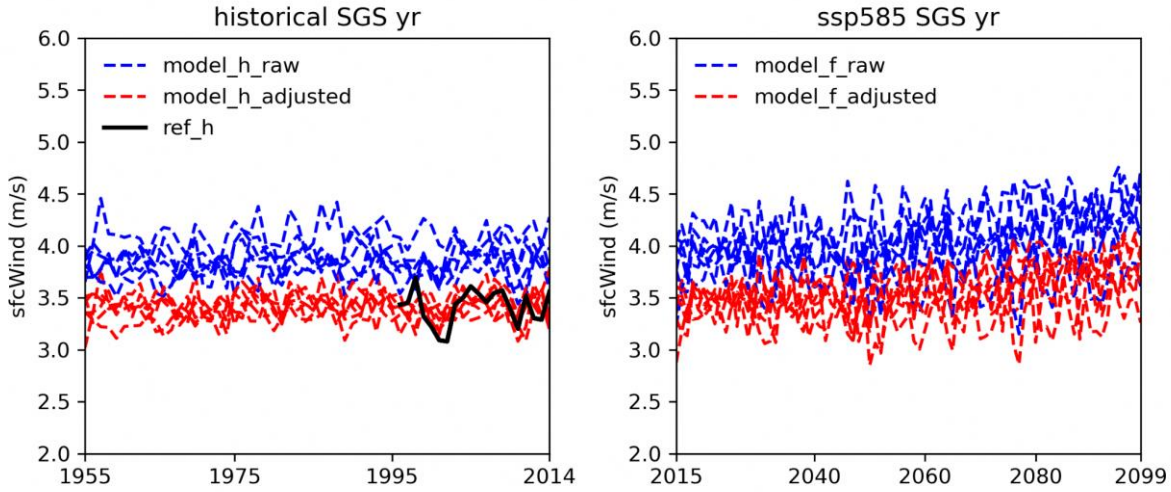

Figure 9.44: a. 8km resolution Singapore domain-averaged sfcWind in the historical period. sfcWind in the future period under the SSP585 scenario. Observation reference is in black. Raw simulations are in blue, and bias-adjusted simulations are in red.

9.10 Results: bias-adjusted climate impact indices

9.10.1 Derived extreme indices

Table 9.8 showcases the extreme indices calculated for impact studies based on essential variables, such as daily precipitation, maximum temperature, and minimum temperature.

The application of bias adjustments to those base variables leads to a substantial reduction in biases within the derived indices. This demonstrates that the bias adjustments not only enhance the accuracy and reliability of the raw model output but also ensure that the resulting indices accurately represent the desired characteristics of extreme events.

By mitigating biases in the derived indices, we can now have greater confidence in the validity and usefulness of the data for understanding and addressing extreme climate events. This improvement in data quality is of great importance in various fields, from climate research to policy-making and disaster preparedness.

Here we will show two examples of the derived frequency indices. One is the CWD (consecutive wet days), the other one is the R20mm (Number of very heavy precipitation days when pr>=20mm).

Table 9.8: Derived indices after the bias correction

Variables	Unit	Base variable	Description
RX1day	mm	pr	Maximum 1-day precipitation
RX5day	mm	pr	Maximum 5-day precipitation
PRCPTOT	mm	pr	Total precipitation during Wet Days
R10mm	days	pr	Number of heavy precipitation days (pr>=10mm)
R20mm	days	pr	Number of very heavy precipitation days (pr>=20mm)
CWD	days	pr	Maximum consecutive wet days (pr>=1mm)
CDD	days	pr	Maximum consecutive dry days (pr<1mm)
TXx	°C	tasmax	Maximum daily maximum temperature
TXn	°C	tasmax	Minimum daily maximum temperature
TNx	°C	tasmin	Maximum daily minimum temperature
TNn	°C	tasmin	Minimum daily minimum temperature

9.10.2 CWD and its future change

Let's consider the example of the consecutive wet days (CWD) index. It measures the maximum number of consecutive days with precipitation greater than or equal to 1mm, is an important measure of rainfall frequency. In Singapore, the CWD exhibits a seasonal cycle, with longer durations of wet days observed in April and during the winter monsoon season, and shorter durations during the dry (summer monsoon) season. This seasonal pattern generally aligns with the monthly mean rainfall climatology.

During the historical period, the SINGV-RCMs tend to underestimate the duration of wet days compared to the observation reference, with an average difference of around 3 days (observation reference: ~7 days). It is important to note that direct bias correction for the CWD index was not performed in this study, hence a perfect match is not expected. However, the bias-adjusted model simulations exhibit a much closer agreement with the observations (Figure 9.45), indicating that the bias adjustments have significantly improved the accuracy of the model outputs for the CWD index.

The close agreement between the bias-adjusted model simulations and the observation reference for the CWD index suggests that the bias correction approach employed in this study has effectively addressed the systematic biases in the SINGV-RCMs, leading to more reliable and realistic estimates of the duration of wet days.

As to the future change, raw model simulations also underestimate the CWD (Figure 9.46). And bias-adjusted simulations tuned up to show a more realistic magnitude of CWD for the future period.

The raw CWD shows a reduction (i.e., a shorter duration of wet days) under warming (Figure 9.47). After bias adjustments, the CWD values are tuned up, and the reduction range is also enlarged.

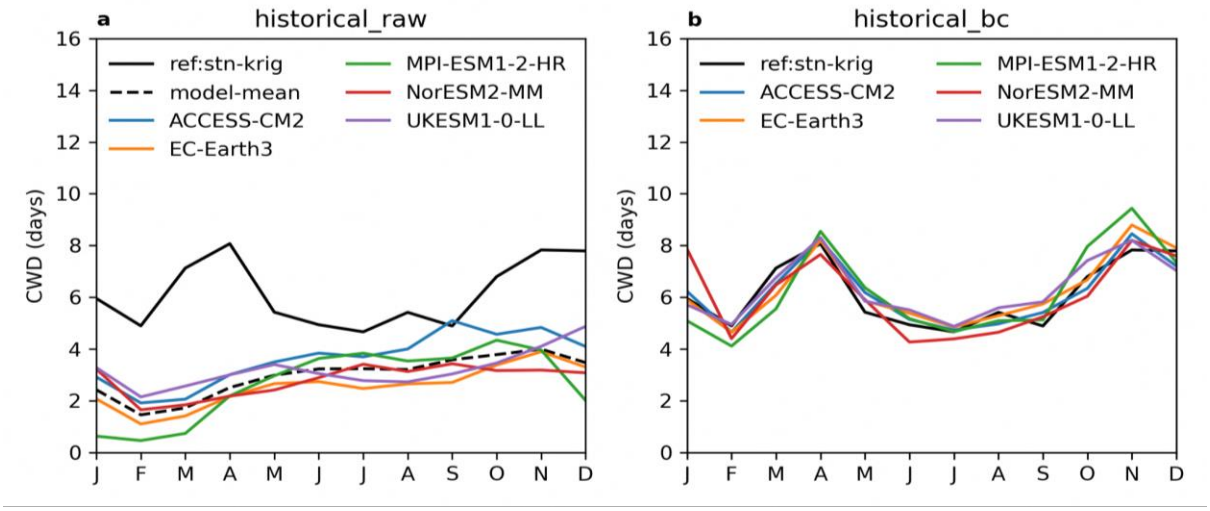

Figure 9.45: Singapore domain-averaged CWD in the historical period (1995-2014). a. observation reference (station krig pr) and raw simulations. b. similar to a, but plotting bias-adjusted simulations. Note that the value of CWD represents the wet days starting from individual month instead of truncated to the given month.

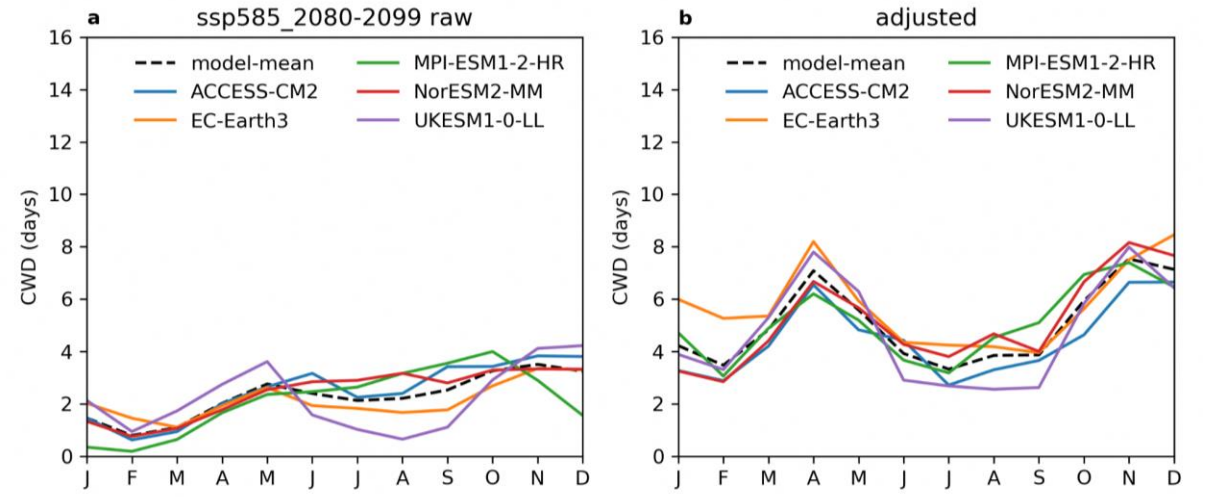

Figure 9.46: Singapore domain-averaged CWD in the SSP585 future period (2080-2099). a. raw simulations. b. bias-adjusted simulations.

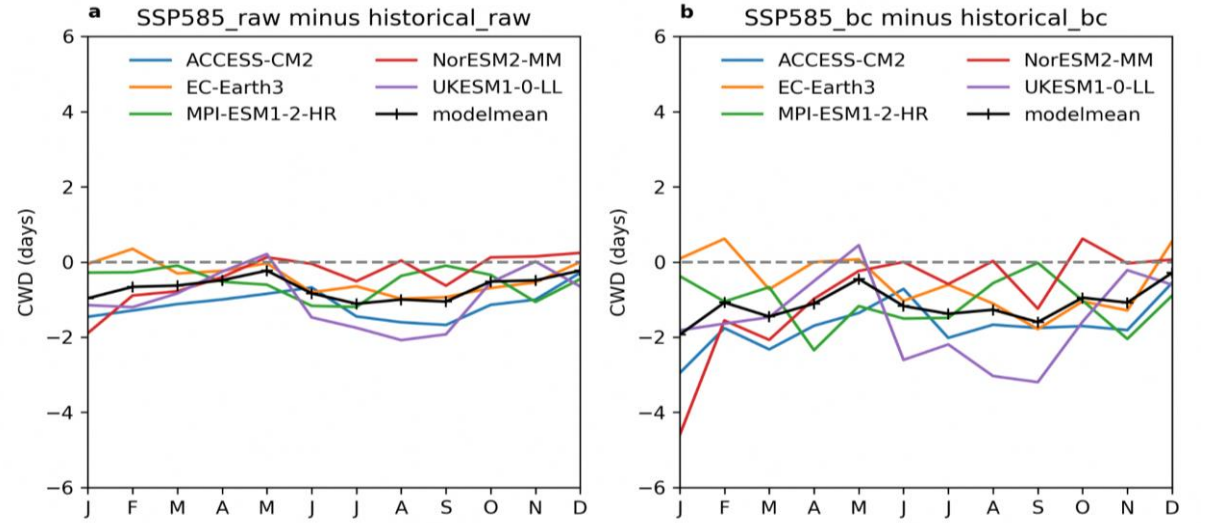

Figure 9.47: Changes in the Singapore domain-averaged CWD from the historical period (1995-2014) to the future period (2080-2099) under the SSP585 scenario. a. raw simulations. b. bias-adjusted simulations.

9.10.3 R20mm and its future changes

Here we show the other example of the frequency-based extreme index R20mm (Number of very heavy precipitation days (pr>=20mm), in days in unit). The dry season (JJAS) shows fewer days of the R20mm, while the wet season (NDJ and April) shows more days of R20mm. It overall follows the seasonal cycle of the mean rainfall.

Figure 9.48 shows that models tend to underestimate the R20mm in JFMA, but overestimate the R20mm in JJAS. The bias-adjusted simulations match R20mm with the observation very well. Note that the R20mm was not directly bias-adjusted but derived from the bias-adjusted pr. It indicates the bias adjustment in base variables like pr are successful and useful for impact studies.

Figure 9.49 showed the future R20mm under the SSP585 scenario. Future simulations tend to have similar biases as the historical period. After bias adjustments, JFMA season R20mm are tuned down, and the JJAS season R20mm are tuned down.

Figure 9.50 showed the future change of R20mm. The reduction in heavy rainfall days are mainly in the JJAS season. After the bias adjustment, the R20mm in the JJAS season are tuned down and the changes are also reduced.

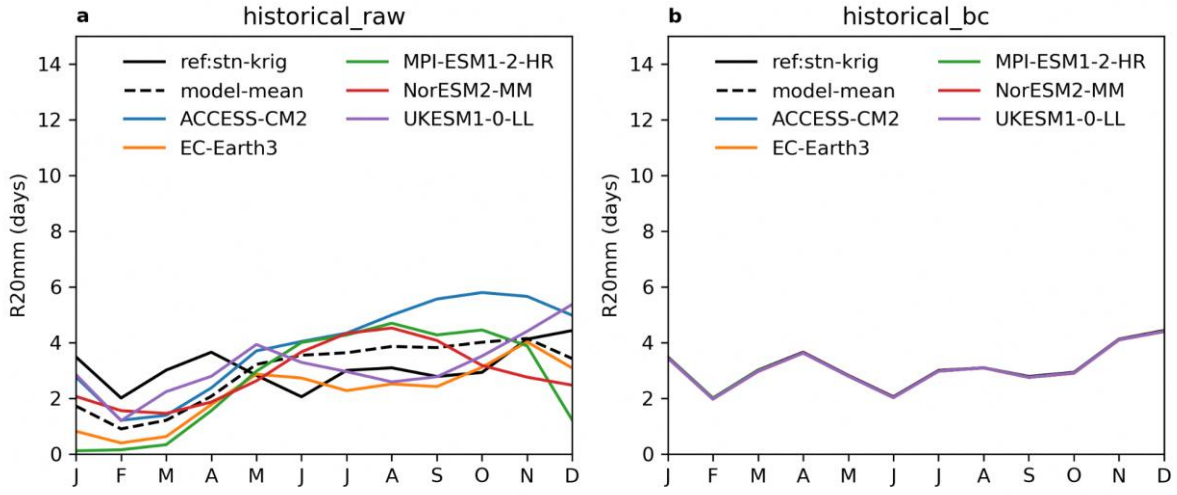

Figure 9.48: Singapore domain-averaged R20mm in the historical period (1995-2014) at a 2km resolution. a. observation reference (station krig pr) and raw simulations. b. similar to a, but plotting bias-adjusted simulations.

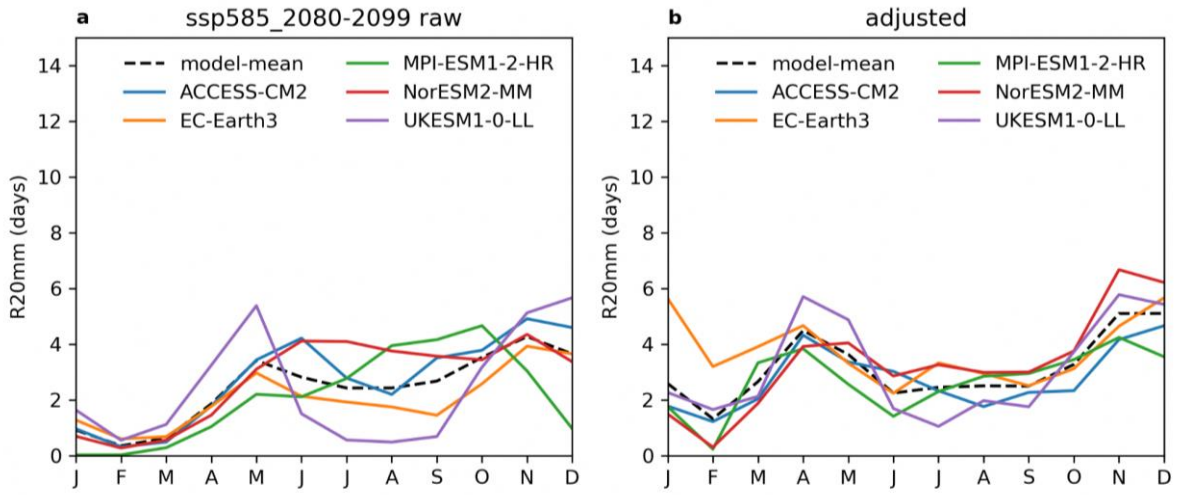

Figure 9.49: Singapore domain-averaged R20mm in the future period (2080-2099) under the SSP585 scenario. a. raw simulations. b. bias-adjusted simulations.

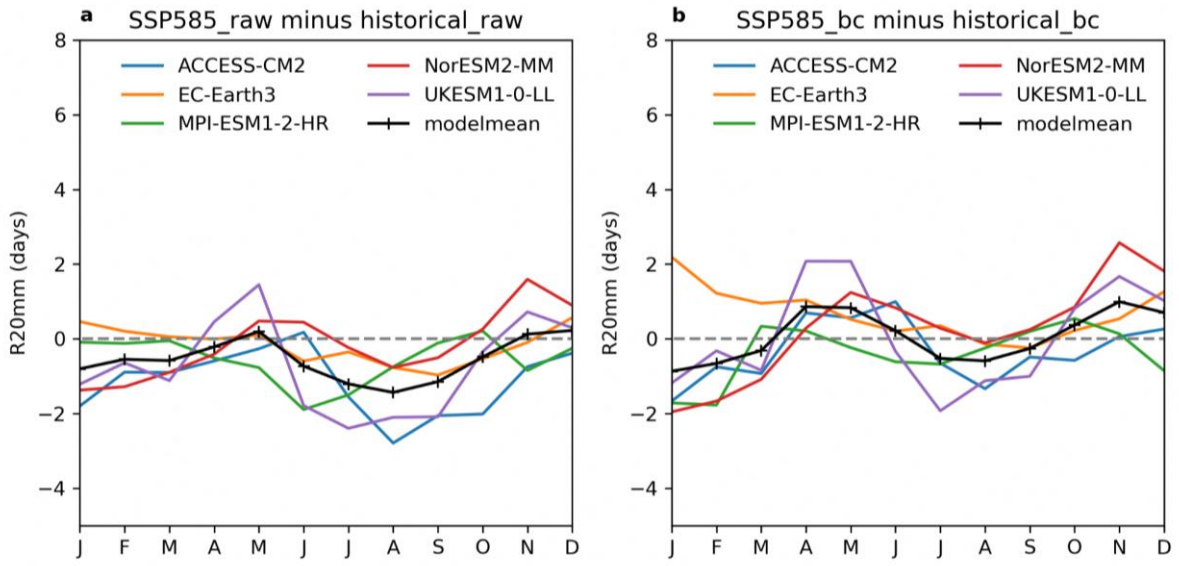

Figure 9.50: Percentage changes in the Singapore domain-averaged R20mm from the historical period (1995-2014) to the future period (2080-2099) under the SSP585 scenario at a 8km resolution. a. raw simulations. b. bias-adjusted simulations.

9.11 Evaluations using pseudo reality experiments

We showed in above results that bias adjustments are very useful to remove the systematic biases in models, provide more realistic simulations, and largely preserve the change and long-term trend. We have to acknowledge that bias-adjusted projections still have inevitable uncertainties given that we do not know what the actual future will look like in the reality. To provide more confidence, here we conduct an evaluation using a pseudo reality experiment. The main objective of this experiment was to assess the performance of the bias adjustment method by comparing the bias-adjusted simulations with a designated reference model that represents an alternative plausible reality.

The experiment involved selecting one CMIP6 model, specifically MPI-ESM1-2-HR, as the reference model, while the other four CMIP6 models were treated as test models (Table 9.9). The study domain focused on the West Maritime Continent (WMC) with a spatial extent of [7S-10N, 93-110W]. For the GCMs with a resolution of 1.5 degrees, this corresponds to a grid size of 12x12 cells. The historical period from 1995 to 2014 was chosen as the base period, while the future change period spanned from 2080 to 2099, considering the SSP585 scenario for analyzing the warming future.

The evaluation process involved comparing the differences between the reference model and the test models in both the historical period and future scenarios. The bias correction method was applied to the test models using the historical data from the reference model. The results demonstrated that the bias-adjusted simulations effectively reduced the biases present in the historical period, bringing them closer to the reference model. Furthermore, the adjusted future projections showed improved agreement with the actual future projections of the reference model.

The successful performance of the bias correction method in this evaluation, using the ISIMIP3 bias correction approach, provided increased confidence in the bias-adjusted downscaling outputs. This evaluation process contributes to reducing uncertainties associated with the bias adjustment procedure and enhances the reliability of the projections for the impact assessment and decision-making processes.

Table 9.9: CMIP6 model information for the bias adjustment tests

Category	CMIP6 model	ensemble ID	historical period	SSP585 period
reference model	MPI-ESM1-2-HR	r1i1p1f1	1850-2014	2015-2100
test model	ACCESS-CM2	r1i1p1f1	1850-2014	2015-2100
test model	EC-Earth3	r1i1p1f1	1850-2014	2015-2100
test model	MIROC6	r1i1p1f1	1850-2014	2015-2100
test model	NorESM2-MM	r1i1p1f1	1850-2014	2015-2100

9.11.1 Evaluation for the mean climatology

The WMC domain-averaged climatology for surface wind speed (sfcWind) from individual models was adjusted to match the reference model during the historical period, as shown in Figure 9.51d. The bias adjustment process aimed to correct the discrepancies between the individual models and the reference model. By applying the bias adjustment, the future projections of sfcWind from the test models became more aligned with the future projections of the reference model, as depicted in Figure 9.51d.

It is important to note that the specific adjustments for each model depended on the biases observed in the historical period. In the case of MIROC6, this model exhibited an underestimation of sfcWind compared to the reference model during the historical period. Consequently, the bias-adjusted future sfcWind in MIROC6 was shifted upwards from the raw climatology (green), bringing it closer to the actual future projections of the reference model (black). Furthermore, the bias-adjusted simulations demonstrated a significant preservation of the future changes of individual models, as illustrated in Figure 9.51f. This indicates that the bias adjustment process successfully retained the essential characteristics of the future changes projected by the models while reducing systematic biases.

Overall, the bias adjustment procedure effectively improved the realism and accuracy of the sfcWind projections from the test models, aligning them more closely with the reference model.

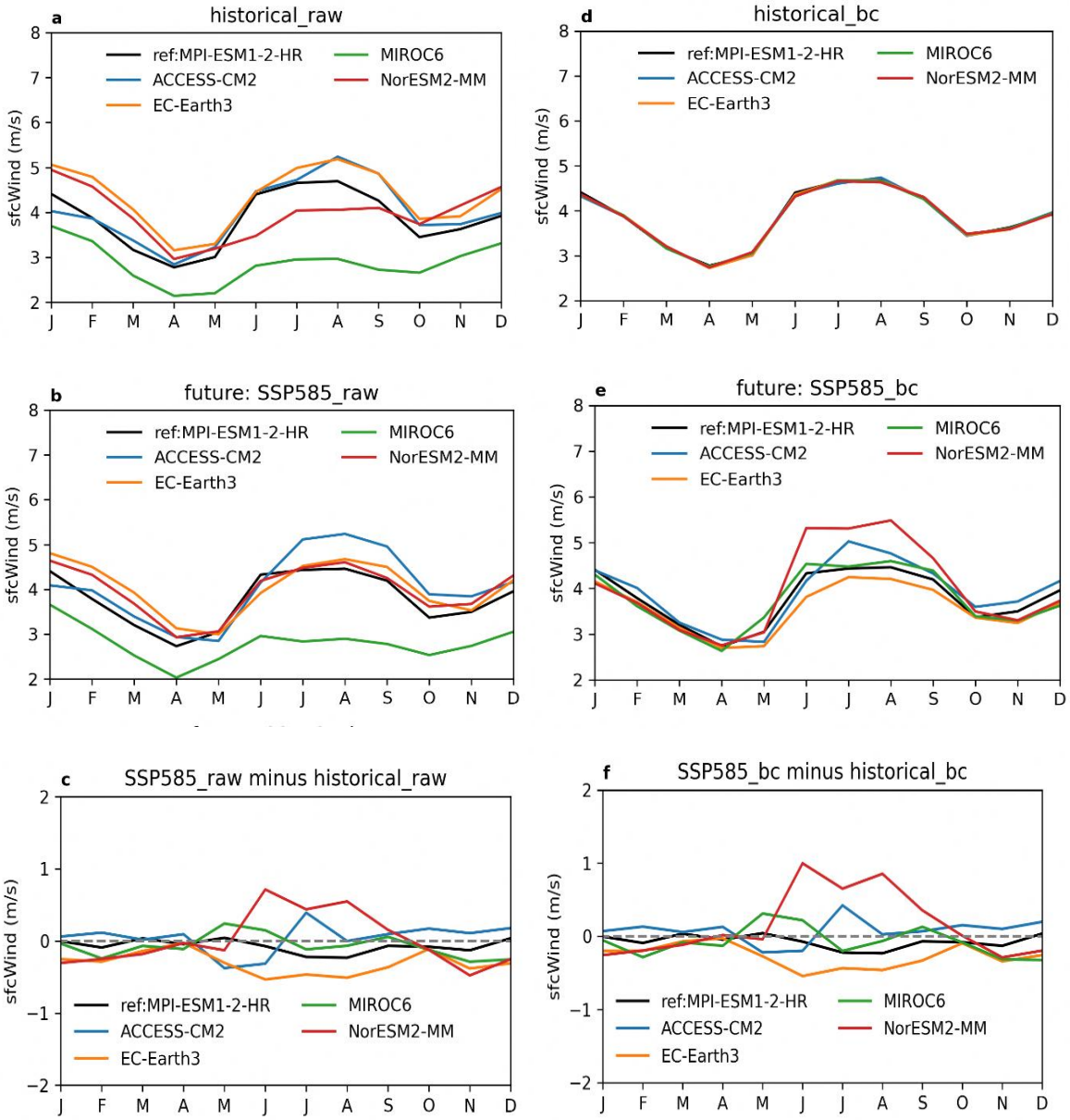

Figure 9.51: WMC domain averaged sfcWind in the historical period (a,d). Raw model outputs are in a. Bias corrected model outputs are in d. WMC domain averaged sfcWind in the future period (b,d). Raw model outputs are in b. Bias corrected model outputs are in d. WMC domain averaged sfcWind changes (2080-2099 minus 1995-2014) (c,f). Raw model outputs are in c. Bias corrected model outputs are in f.

9.11.2 Evaluation for the spatial pattern

The spatial pattern analysis of surface wind speed (sfcWind) in the WMC domain revealed certain characteristics for the month of July. Specifically, the central land area of the WMC tended to have lower wind speeds, while higher wind speeds were observed over the open ocean area, as depicted in Figure 9.52. This spatial distribution of wind speed is indicative of the prevailing atmospheric circulation patterns during that month.

Considering the future projections under warming from the reference model, a distinct change in the spatial pattern of sfcWind was observed. The reference model projected reduced sfcWind in the northern part of the WMC, indicating a weakening of wind speeds in that region. Conversely, enhanced sfcWind was projected near the equator, suggesting an increase in wind speeds in that area due to the influence of climate change, as illustrated in Figure 9.52.

This spatial pattern analysis provides insights into the potential changes in wind patterns and intensities within the WMC region under future warming scenarios. It demonstrates that the reference model's projections capture the expected shifts in wind speed distribution, allowing for a better understanding of the potential impacts of climate change on wind patterns in the WMC domain.

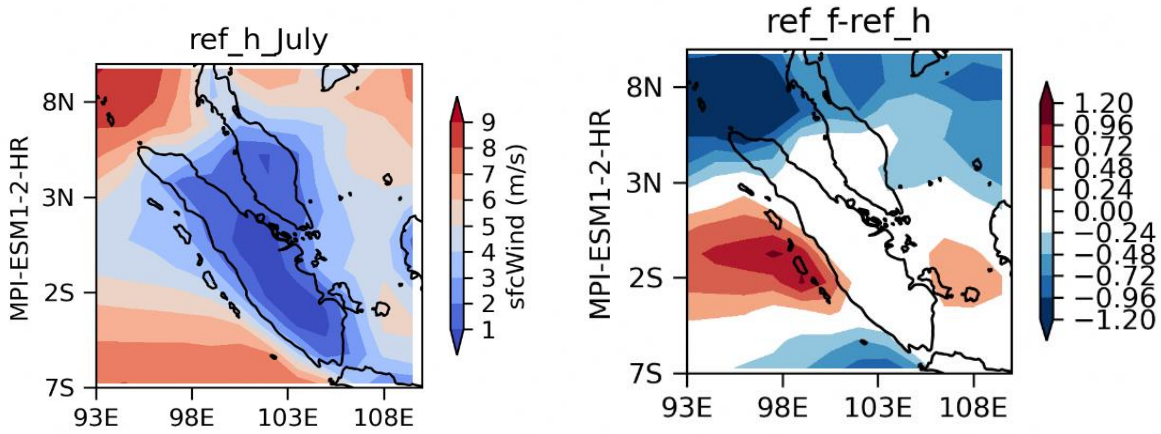

Figure 9.52: a. WMC domain sfcWind (July) in the historical period of the reference model (MPI-ESM1-2-HR). b. Future changes in WMC domain sfcWind projected by the reference model.

During the historical period, the four test models (including ACCESS-CM2) generally exhibit a similar spatial pattern of surface wind speed (sfcWind) compared to the reference model, with some variations in magnitude. In the case of ACCESS-CM2, it tends to overestimate sfcWind in the central WMC region, as illustrated in Figure 9.53.

To address the overestimation issue and improve the agreement with the reference model, bias adjustment was applied to the sfcWind simulations from ACCESS-CM2. The bias-adjusted sfcWind values demonstrate a better match with the reference model, indicating that the adjustment successfully mitigated the overestimation bias in the central WMC region. The comparison between raw and bias-adjusted sfcWind highlights the effectiveness of the bias adjustment method in reducing discrepancies and improving the agreement with the reference model. By correcting the systematic biases in the sfcWind simulations, the bias-adjusted results provide a more reliable representation of the historical wind patterns in the WMC domain.

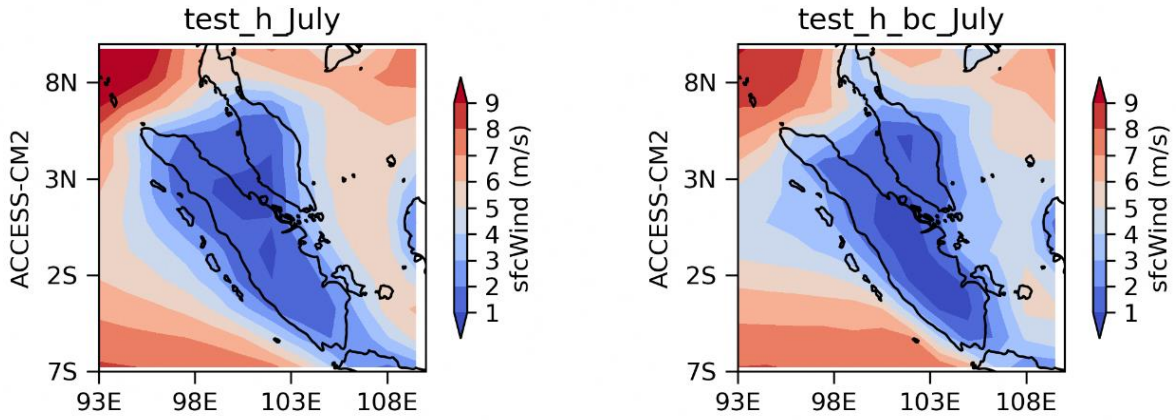

Figure 9.53: a. WMC domain sfcWind (July) in the historical period of raw test model (ACCESS-CM2). b. bias-adjusted test model.

In terms of the future changes in July surface wind speed (sfcWind) over the WMC, the four test models (including ACCESS-CM2) exhibit varying patterns. For instance, ACCESS-CM2 projects an enhanced sfcWind over the southeastern WMC region and a reduced sfcWind over the northwestern WMC region, as depicted in Figure 9.54.

After applying the bias adjustment to the sfcWind simulations from the test models, the spatial changes in sfcWind are largely preserved in the bias-adjusted results. This means that the bias adjustment process did not significantly alter the projected spatial pattern of sfcWind changes. The bias-adjusted simulations still reflect the enhanced sfcWind over the southeastern WMC and reduced sfcWind over the northwestern WMC, in line with the original model projections.

This preservation of the spatial changes in sfcWind after bias adjustment provides additional confidence in the reliability of the bias-adjusted simulations for assessing future wind patterns over the WMC. It suggests that the bias adjustment method successfully corrected the systematic biases in the models without introducing substantial distortions to the projected changes.

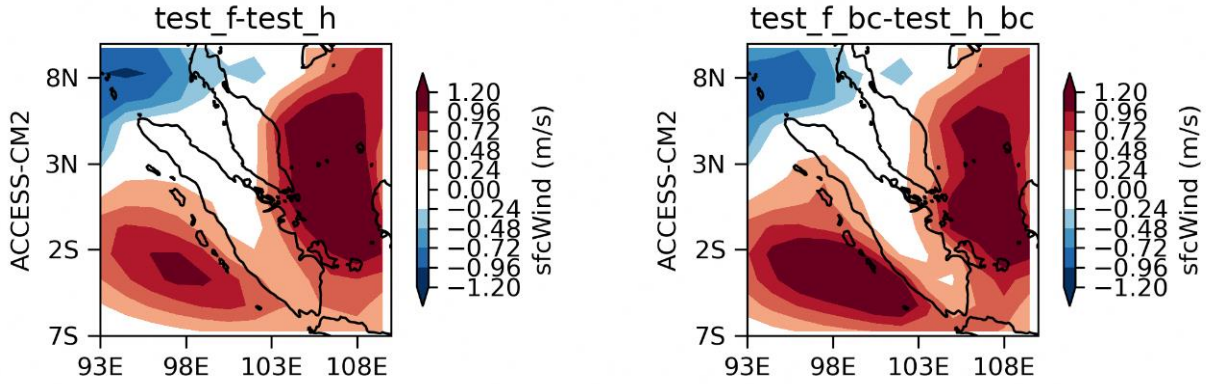

Figure 9.54: a. future changes in WMC domain sfcWind projected by raw the test model (ACCESS-CM2). b. bias-adjusted test model.

9.12 Summary

Our high-resolution regional climate model (RCM) simulations, conducted at resolutions of 8km and 2km, have demonstrated excellent performance over the Maritime Continent. However, these high-resolution RCMs exhibit slight model biases when compared to local observations specifically within Singapore. To ensure that we provide appropriate simulation data for local climate change impact studies, we have conducted bias adjustments for several key climate variables. These variables include tas (near-surface air temperature), tasmax (maximum air temperature), tasmin (minimum air temperature), pr (precipitation), hurs (relative humidity), and sfcWind (surface wind speed). By applying bias adjustments to these selected variables, we aim to align the RCM simulations more closely with the observed local climate conditions in Singapore.

In order to perform bias corrections, it is crucial to have gridded observation reference data that is specifically tailored to the high-resolution (8km and 2km) scale required for Singapore. However, finding existing observation products at such fine resolutions can be challenging. To overcome this limitation, we adopted a two-step approach. For rainfall (pr), we utilized data from 28 long-term rainfall stations to create gridded precipitation data at resolutions of 2km and 8km using advanced kriging techniques. This allowed us to generate gridded precipitation reference datasets that closely represent the spatial variability of rainfall in Singapore. Evaluations conducted on the kriged precipitation data demonstrated its suitability as a reference dataset, as it exhibited strong consistency with the station precipitation data. For other variables, such as temperature (tas, tasmax, tasmin), relative humidity (hurs), and surface wind speed (sfcWind), the number of available

long-term stations was insufficient for directly converting them into gridded products. Therefore, we used the 25km-resolution ERA5 reanalysis dataset to drive the 8km and 2km resolution RCMs. The output within the Singapore domain from the ERA5-RCM simulations served as the gridded reanalysis reference. Evaluations conducted on the ERA5-RCM data revealed its suitability as a reference dataset, as it demonstrated excellent consistency with the available station data across Singapore. These gridded reference datasets, derived from kriging of station data for precipitation and the ERA5-RCM simulations for other variables, currently represent the best options available for conducting bias corrections in our study. If new observation products become available at higher resolutions in the future, we can update the historical reference accordingly in subsequent studies.

For the bias adjustment process in the V3 study, we recognized the need for advanced features beyond the straightforward quantile-mapping based bias adjustment methods used in V2. These new requirements included preserving trends, correcting rainfall frequency, and customizing distribution fits for each variable, among others. To meet these demands, we implemented the latest and widely used ISIMIP3 bias adjustment methods. The results of the bias adjustment process demonstrated the successful removal of biases in the adjusted historical simulations. Additionally, the future simulations showed improved realism after the adjustments. Importantly, the adjustments were able to preserve the future change signals present in the raw simulations, ensuring that the projected climate changes remained intact. To provide further confidence in the reliability of the bias adjustments, we conducted pseudo reality experiments. In these experiments, we designated one model as the reference, with known historical and future data. We then applied bias adjustments to the other test models and assessed the performance and added value of the adjustments. The results of these tests revealed that the simulations after bias adjustments were more realistic compared to the raw simulations. By incorporating the advanced features and conducting rigorous evaluations, the bias adjustments performed in the V3 study produced more reliable and accurate climate simulations. These adjusted simulations provide greater confidence in their use for assessing climate change impacts in Singapore.

In addition to the main climate variables, we derived key extreme indices based on certain variables to assess the characteristics of extreme events. For example, we calculated the maximum consecutive wet days (CWD) using the precipitation (pr) data and the number of very heavy precipitation days (R20mm). Our findings indicate that these frequency-based indices (CWD and R20mm) calculated using the raw simulations exhibited biases. However, after applying the bias adjustments, the biases in the CWD and R20mm based on the adjusted simulations were largely removed. This demonstrates the effectiveness of the bias adjustments in improving the accuracy of extreme indices.

In conclusion, the bias adjustments conducted in our study have demonstrated very good performance. We consider bias adjustment to be a crucial step in the post-processing of regional downscaling simulations, as it significantly improves the realism and accuracy of the regional climate model (RCM) outputs. The successful implementation of bias adjustments enhances our confidence in the climate projections and their suitability for assessing and addressing the impacts of climate change in Singapore.

References

Cannon, A.J., Sobie, S.R. and Murdock, T.Q. (2015) Bias correction of GCM precipitation by Quantile mapping: how well do methods preserve changes in quantiles and extremes? J. Climate, 28, 6938–6959. https://doi.org/10.1175/JCLI-D-14-00754.1.

Cannon, A. J, 2017.: Multivariate quantile mapping bias correction: an N-dimensional probability density function transform for climate model simulations of multiple variables, Climate Dynamics, pp. 1–19, https://doi.org/10.1007/s00382-017-3580-6

Frieler, K., Lange, S., Piontek, F., Reyer, C. P. O., Schewe, J., Warszawski, L., Zhao, F., Chini, L., Denvil, S., Emanuel, K., Geiger, T., Halladay, K., Hurtt, G., Mengel, M., Murakami, D., Ostberg, S., Popp, A., Riva, R., Stevanovic, M., Suzuki, T., Volkholz, J., Burke, E., Ciais, P., Ebi, K., Eddy, T. D., Elliott, J., Galbraith, E., Gosling, S. N., Hattermann, F., Hickler, T., Hinkel, J., Hof, C., Huber, V., Jägermeyr, J., Krysanova, V., Marcé, R., Müller Schmied, H., Mouratiadou, I., Pierson, D., Tittensor, D. P., Vautard, R., van Vliet, M., Biber, M. F., Betts, R. A., Bodirsky, B. L., Deryng, D., Frolking, S., Jones, C. D., Lotze, H. K., Lotze- Campen, H., Sahajpal, R., Thonicke, K., Tian, H., and Yamagata, Y., 2017: Assessing the impacts of 1.5 ◦C global warming simulation protocol of the Inter-Sectoral Impact Model Intercomparison Project (ISIMIP2b), Geosci. Model Dev., 10, 4321–4345, https://doi.org/10.5194/gmd-10-4321-2017

Gleick, P. H. (1986). Methods for evaluating the regional hydrologic impacts of global climatic changes. *Journal of Hydrology*, *88*(1–2), 97–116. https://doi.org/10.1016/0022-1694(86)90199-X

Hay, L. E., Wilby, R. L., & Leavesley, G. H. (2000). A COMPARISON OF DELTA CHANGE AND DOWNSCALED GCM SCENARIOS FOR THREE MOUNTAINOUS BASINS IN THE UNITED STATES 1. *JAWRA Journal of the American Water Resources Association*, *36*(2), 387–397. https://doi.org/10.1111/j.1752-1688.2000.tb04276.x

Hempel, S., K. Frieler, L. Warszawski, J. Schewe, and F. Piontek, 2013: A trend-preserving bias correction: The ISI-MIP approach. Earth Syst. Dyn., 4, 219–236, https://doi.org/10.5194/esd-4-219-2013.

Lange, S. (2019). Trend-preserving bias adjustment and statistical downscaling with ISIMIP3BASD (v1.0). Geoscientific Model Development, 12(7), 3055–3070. https://doi.org/10.5194/gmd-12-3055-2019

Lange, S. 2021: ISIMIP3BASD v2.5.0, https://doi.org/10.5281/zenodo.4686991

Maraun, D. (2016). Bias Correcting Climate Change Simulations - a Critical Review. *Current Climate Change Reports*, *2*(4), 211–220. https://doi.org/10.1007/s40641-016-0050-x

Mehrotra, R., & Sharma, A. (2012). An improved standardization procedure to remove systematic low frequency variability biases in GCM simulations. *Water Resources Research*, *48*(12), 1–8. https://doi.org/10.1029/2012WR012446

Mehrotra, R., & Sharma, A. (2016). A Multivariate Quantile-Matching Bias Correction Approach with Auto- and Cross-Dependence across Multiple Time Scales: Implications for Downscaling. *Journal of Climate*, *29*(10), 3519–3539. https://doi.org/10.1175/JCLI-D-15-0356.1

Muhamad Ali, M. M. A., & Othman, F. (2017). Selection of variogram model for spatial rainfall mapping using Analytical Hierarchy Procedure (AHP). Scientia Iranica, 24(1), 28-39. https://doi.org/10.24200/sci.2017.2374.

Benjamin Murphy, Roman Yurchak, & Sebastian Müller. (2022). GeoStat-Framework/PyKrige: v1.7.0 (v1.7.0). Zenodo. https://doi.org/10.5281/zenodo.7008206

Peter, J., Vogel, E., Sharples, W., Bende-Michl, U., Wilson, L., Hope, P., Dowdy, A., Kociuba, G., Srikanthan, S., Duong, V. C., Roussis, J., Matic, V., Khan, Z., Oke, A., Turner, M., Baron-Hay, S., Johnson, F., Mehrotra, R., Sharma, A., Thatcher, M., Azarvinand, A., Thomas, S., Boschat, G., Donnelly, C., and Argent, R. 2023: Continental-scale bias-corrected climate and hydrological projections for Australia, Geosci. Model Dev. Discuss. [preprint], https://doi.org/10.5194/gmd-2023-7.

Pierce, D. W., Cayan, D. R., Maurer, E. P., Abatzoglou, J. T., & Hegewisch, K. C. (2015). Improved Bias Correction Techniques for Hydrological Simulations of Climate Change. *Journal of Hydrometeorology*, *16*(6), 2421–2442. https://doi.org/10.1175/JHM-D-14-0236.1

Switanek, M.B., Troch, P.A., Castro, C.L., Leuprecht, A., Chang, H.- I., Mukherjee, R. and Demaria, E.M.C. (2017) Scaled distribution mapping: a bias correction method that preserves raw climate model projected changes. Hydrology and Earth System Sciences, 21, 2649–2666. https://doi.org/10.5194/hess-21-2649-2017.

Bias-Adjusted Climate Change Projections over Singapore

10

Authors:
Aurel Florian Moise, Sandeep Sahany, Muhammad Eeqmal Hassim, Chen Chen, Xin Rong Chua, Venkatraman Prasanna, Gerald Lim, Pavan Harika Raavi, Jianjun Yu, Fei Luo

METEOROLOGICAL SERVICE SINGAPORE
Centre for Climate Research Singapore

10.1 Introduction

In this chapter, we present the climate change projections over Singapore using the 2km dynamically downscaled simulations that have been bias-adjusted to reduce systematic biases reported in Chapter 7 of this report. As discussed in Chapter 9, the 8km and 2km downscaled projections over Singapore were bias-adjusted using one of the advanced techniques recommended by ISIMIP3 (Lange, S. 2019).

Singapore's climate change projections are presented for annual and seasonal scales. For the seasons, 5 periods corresponding to Singapore's monsoon and intermonsoon transition seasons were selected: the northeast monsoon season, the southwest monsoon season and both the intermonsoons. The northeast monsoon season is further divided into the wet phase comprising the months of December and January, and the dry phase comprising the months February and March. The southwest monsoon season comprises the months of June through September, and the first and second intermonsoon periods occur in April-May and October-November respectively.

Specifically, we present changes in the mean state and extremes of some key variables under the three SSP scenarios for the mid- and end-century 20-year periods:

Changes in rainfall: For mean rainfall, we present changes in the annual and seasonal mean rainfall. For rainfall extremes, we present changes in the maximum daily rainfall (RX1day), maximum 5-day rainfall (RX5day), the 95th and 99.9th percentiles in each season and for the annual timescale. Changes are only shown for the end-century period under the SSP5-8.5 scenario.

Changes in temperature: For mean temperature, we present changes in the annual and seasonal mean temperature, and for temperature extremes we present changes in the daily maximum temperature, daily minimum temperature, annual maximum temperature, annual minimum temperature, the 95th and 99.9th percentiles.

Changes in heat stress: For heat stress index, we present changes in the wet bulb globe temperature (WBGT) for annual and various seasons.

Changes in relative humidity: For relative humidity, we present changes in the 2m relative humidity for annual and various seasons.

Changes in near- surface winds: For winds, we present changes in the 10m wind speed for annual and various seasons. For wind gusts we present changes in wind gusts during the mid- and end-century for SSP5-8.5.

Finally, we also compare the similarities and differences in the projected rainfall and temperature changes over Singapore from the 8 km bias-adjusted data with the 2 km bias-adjusted data.

In the figures where we show projected changes for the mid- and end-century for the 3 SSPs, we document the changes for each of the periods by referring to the changes shown by the multi-model mean (thin line) in the 3 SSPs followed by the range (lowest projected change to highest projected change) within each SSP shown in brackets.

10.2 Changes in Mean Rainfall

Figure 10.1 shows the projected changes in the mean rainfall, area-averaged over Singapore, under the 3 SSP scenarios for the entire year (annual) and different seasonal periods as presented in Section 10.1.

10.2.1 Annual Rainfall

Overall, across all scenarios, the multi-model average in annual mean rainfall is projected to increase or remain the same both in the mid- and end-century. However, the magnitude of change varies going from mid-century to end-century between the scenarios (Table 10.1, Figure 10.1): an increase is projected in SSP1-2.6 (5% to 11%), almost no change is projected for SSP2-4.5 (i.e. remaining at 5%), and a decrease is projected in SSP5-8.5 (from 10% to 0%). The large drop in projected mean change in SSP5-8.5 from the mid-to-end century is largely due to the increased spread between the models (i.e. lack of model

consensus in the sign of change by the end-century). The differences seen between the scenarios indicate that the local change in annual mean rainfall change does not necessarily scale with global warming, unlike the global average as reported in IPCC AR6. There can be significant differences on regional and local scales, as seen for Singapore.

Table 10.1: Projected changes in annual mean rainfall (percent change)

Scenario	Mid-Century Annual Rainfall Change (%)		End-Century Annual Rainfall Change (%)	
	Mean	Range	Mean	Range
SSP1-2.6	5	-2 to 8	11	0 to 24
SSP2-4.5	5	-2 to 12	5	-6 to 12
SSP5-8.5	10	-5 to 19	0	-12 to 17

While there is a similar annual mean rainfall by 2100, we observe that the year-to-year variation has increased over time, particularly towards the second half of the 21st century (not shown). The change in variability is most likely related to the change in ENSO behavior in the future. New evidence suggests that ENSO variability will likely increase in the future i.e., more extreme El Ninos and La Niñas (Cai et al., 2014, 2021).

Although the annual mean rainfall is projected to increase/remain same both in the mid- and end-century across all scenarios, the seasonal mean changes differ across seasons. Based on the multi-model mean changes in SSP5-8.5, there are increases in wet months (e.g. DJ) and decreases in dry months (e.g. FM, JJAS) at the end of the century. This increased contrast between seasons was noted in the 2nd National Climate Change Study (V2), and might be linked to the narrowing of the ITCZ projected by global models (e.g. Byrne and Schneider., 2016). We discuss these changes in detail below.

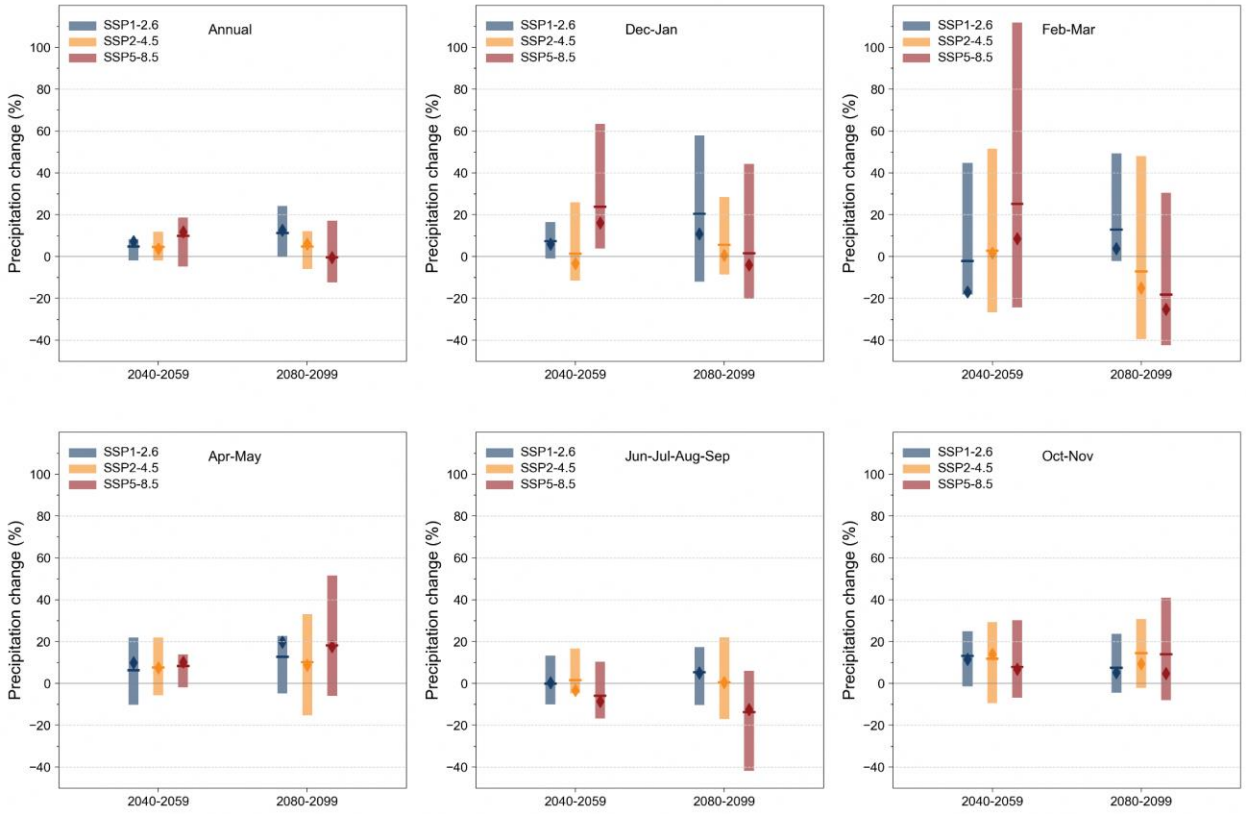

Figure 10.1: Percentage change of rainfall total (pr) in the Annual, December–January, February–March, April–May, June–July–August–September, and October–November for mid- (2040–2059) and end-century (2080–2099) periods from the 5 bias-

adjusted downscaled GCMs (2 km) over Singapore relative to the baseline (1995–2014). The line and diamond represent the mean and median using the 5 models, respectively. For readability, the values are available in Tables 10.1-10.6.

10.2.2 December-January (DJ) rainfall (wet phase of NE monsoon)

The projected changes in DJ rainfall follow a similar pattern to the change in mean annual rainfall. Overall, DJ rainfall is projected to increase by the end of the century across all scenarios. However, the magnitude of change differs between the scenarios. While the average DJ rainfall is projected to increase even more under SSP1-2.6 (from 7% in mid-century to 20% in end-century), the projected changes are considerably smaller under SSP2-4.5 and especially in SSP5-8.5 (24% in mid-century to only 2% in end-century). This suggests that local DJ rainfall changes over Singapore do not scale with the level of global warming. In chapter 8, we noted a slight increase in the frequency of NE monsoon surges from November to February (NDJF), with small changes in the magnitude of rainfall during surge days. It is possible that the changes would be different in other scenarios, or even in DJ as opposed to NDJF.

Table 10.2: Projected Changes in DJ Mean Rainfall (percent change)

DJ	Mid-Century Dec-Jan Rainfall Change (%)		End-Century Dec-Jan Rainfall Change(%)	
	Mean	Range	Mean	Range
SSP1-2.6	7	-1 to 16	20	-12 to 58
SSP2-4.5	1	-12 to 26	6	-9 to 28
SSP5-8.5	24	4 to 63	2	-20 to 44

However, there is a general agreement among the model projections for the wet phase of the NE monsoon season to become slightly wetter, consistent with the finding in the 2nd National Climate Change Study (V2). This could be due to a multitude of factors such as changing characteristics of Borneo Vortices, which could become less frequent but bring more rainfall (Liang et al., 2021), an increase in MJO-related rainfall from the second half of the 21st century (Bui et al., 2023) and/or the occurrence of more El Ninos (Cai et al., 2021; Geng et al., 2022). Note that while El Nino is known to reduce rainfall across many parts of the region during NE monsoon season, historical climatological records show that local December rainfall for Singapore actually increases during El Nino events and decreases during La Nina events, compared to ENSO-neutral conditions (no El Nino or La Nina in the Pacific).

10.2.3 February-March (FM) rainfall (dry phase of NE monsoon)

The projections for February-March mean rainfall indicate a drying tendency for the 2nd half of the 21st century under the moderate (SSP2-4.5) and high warming (SSP5-8.5) scenarios. This is in contrast to a projected increase under the low warming (SSP1-2.6) scenario (-2% mid-century to 13% end-century). The reasons for the difference in the sign of change between the scenarios by the end of the century are unclear at this stage but could be related to the differences in the timing, magnitude and regional impacts of decadal-scale variability between the scenarios (Johnson et al., 2020). In addition, the high mean change value for the mid-century under the SSP5-8.5 scenarios (25%) is positively skewed by an outlier model (c.f. mid-century range is -24 to 112 %). Likewise, the projected mid-century mean change under SSP1-2.6 is also positively skewed by an outlier model (c.f. the separation between the median diamond and mean thin line markers, Figure 10.1).

Nonetheless, the signs of the end-century projected changes under SSP2-4.5 and SSP5-8.5 reported here are consistent with the end-century changes projected in V2 for the same months. Under the RCP8.5 scenario, six out of nine models projected a statistically significant decreasing signal of more than 30% change in mean February rainfall towards the end of the century (Figure 5.23, Marzin et al. 2015). This suggests that the projected drying trend in the

drier phase of the NE monsoon is likely to be robust and could be associated with stronger cross-equatorial flow in the future (Liang et al., 2022). Cross-equatorial northerly surges are a feature during the drier phase of the NE monsoon. These tend to shift the rainband south of the equator and into the Java Sea, thereby reducing rainfall over Singapore.

Overall, the findings here suggest that NE monsoon could experience a much greater intra-seasonal contrast in the future by the end of the century with the wet phase of the NE monsoon projected to become slightly wetter and the drier phase NE monsoon likely to become drier.

Table 10.3: Projected Changes in FM Mean Rainfall (percent change)

FM	Mid-Century Feb-Mar Rainfall Change (%)		End-Century Feb-Mar Rainfall Change (%)	
	Mean	Range	Mean	Range
SSP1-2.6	-2	-18 to 45	13	-2 to 49
SSP2-4.5	3	-27 to 52	-7	-39 to 48
SSP5-8.5	25	-24 to 112	-18	-43 to 30

10.2.4 April-May (AM) and October-November (ON) rainfall (first and second intermonsoon periods)

The first (AM) and second (ON) intermonsoon periods both exhibit very similar positive changes both in the mid-century and end-century. Overall, both intermonsoon periods show increased mean rainfall by the end of the century across the scenarios, although there is a slight reduction in the positive change of ON mean rainfall under SSP1-2.6 (from 13% to 8%). Under SSP1-2.6, most of the warming in global mean and local Singapore temperatures takes place by mid-century. As such, there is not expected to be much additional influence of warming on rainfall from mid-century to end-century. As such, the reduction in the magnitude of the positive change from mid-century to end-century in ON rainfall is more likely due to decadal variability. This is also most likely the case for AM mean rainfall.

In contrast, the magnitude of change under SSP2-4.5 and SSP5-8.5 for AM and ON mean rainfall both increase by the end of the century, and are likely to be governed more by the climate change signal. Both the scenarios show increases of mean rainfall with warming from mid- to end-century, albeit at different rates (e.g. from 12% to 14% under SSP2-4.5, and from 8% to 14% under SSP5-8.5 for ON rainfall, see Table 10.5).

Table 10.4: Projected Changes in AM Mean Rainfall (percent change)

AM	Mid-Century Apr-May Rainfall Change (%)		End-Century Apr-May Rainfall Change (%)	
	Mean	Range	Mean	Range
SSP1-2.6	6	-10 to 22	13	-5 to 23
SSP2-4.5	8	-6 to 22	10	-15 to 33
SSP5-8.5	8	-2 to 14	18	-6 to 52

Table 10.5: Projected Changes in ON Mean Rainfall (percent change)

ON	Mid-Century Oct-Nov Rainfall Change (%)		End-Century Oct-Nov Rainfall Change (%)	
	Mean	Range	Mean	Range
SSP1-2.6	13	-1 to 25	8	-4 to 24
SSP2-4.5	12	-9 to 29	14	-2 to 31
SSP5-8.5	8	-7 to 30	14	-8 to 41

10.2.5 June-September (JJAS) rainfall (SW monsoon)

As in FM rainfall, the SW monsoon season only shows an increase in mean JJAS rainfall from mid- to end-century under the SSP1-2.6 scenario, while the other scenarios show slight change

(SSP2-4.5) or a reduction in rainfall (SSP5-8.5). The behavior under SSP1-2.6 is likely again to be associated with decadal variability while the response under SSPs 2-4.5 and 5-8.5 are more likely related to the warming climate, with JJAS rainfall potentially reducing by an average of 14% by 2100.

The mechanism for this drying trend could be related to how SST warming patterns in the tropical Pacific might change in the future to become more El Nino-like. Such changes are known to greatly affect the southwestern Maritime Continent region (Ghosh & Shepherd, 2023).

Recent work by CCRS suggests that seasonal rainfall totals are likely to fluctuate even more in the future due to the stronger relationship that ENSO exerts over rainfall in the Western Maritime Continent region during the Southwest Monsoon season (Chen et al., 2023). For the influence of ENSO, we also showed in Chapter 8 section 8.4.3 that GCMs and RCMs both suggest that ENSO-induced negative teleconnection area over the equatorial MC is enlarged under warming.

An even drier JJAS season increases the risk of peatland and forest fires and thus transboundary haze for this highly vulnerable region. The drying signal is considered robust since it further supports the findings from V2 (in which four of nine models showed statistically significant decreases in mean rainfall at the end of the 21st century under the RCP 8.5 scenario, see Figure 5.22b, Marzin et al., 2015).

Overall, we find that the projected mean rainfall change varies in sign and magnitude across the seasons for both mid- and end-century periods and for all scenarios. The largest range in probable outcomes is shown for February-March (due to an outlier).

Table 10.6: Projected Changes in JJAS Mean Rainfall (percent change)

JJAS	Mid-Century Jun-Sep Rainfall Change (%)		End-Century Jun-Sep Rainfall Change (%)	
	Mean	Range	Mean	Range
SSP1-2.6	0	-10 to 13	5	-10 to 17
SSP2-4.5	2	-5 to 17	0	-17 to 22
SSP5-8.5	-6	-17 to 10	-14	-42 to 6

The end-century changes under SSP1-2.6 are more likely to be related to decadal variability while the projected changes under SSP2-4.5 and especially SSP5-8.5 are likely a response to the increased warming brought by increasing greenhouse gas emissions.

10.3 Changes in Rainfall Extremes

Extreme rainfall – as represented by the average maximum 1-day and 5-day totals on annual and seasonal time scales – is expected to increase considerably by the end of the 21st century. In Chapter 8 Section 8.3.3, we showed that extreme rainfall changes across Southeast Asia. Here in this section of Chapter 10, we focus on Singapore to address changes in the rainfall extremes. The increases in both extreme rainfall metrics occur for all seasons and across all of Singapore except for February and March, in which a reduction in the average intensity of RX1day and RX5day is projected over the northern, central and southern parts of Singapore (Figure 10.2 and Figure 10.3). Interestingly, increases in average RX1day and RX5day rainfall (10-45%) are still projected for the easternmost and westernmost areas of Singapore during the dry phase of the NE monsoon.

The areas with the highest projected percentage increases vary with season. Overall, the largest values occur during the intermonsoon periods. Specifically, the biggest changes (40-50% relative to the 1995-2014 baseline) are seen over the western and central areas during the first inter monsoon period (April-May), while these are concentrated to the far east of Singapore during the second intermonsoon (October-November).

In contrast, the wet NE monsoon (December-January) and the SW monsoon periods show smaller projected increases across Singapore. There is a southwest-to-northeast gradient in the pattern of intensity change during the SW

monsoon (June-September) with relatively higher percentage increases projected in mean RX1day and RX5day for the northeastern areas and lower in the southwest portions of the country. The spatial pattern of percentage increases is more heterogeneous during the wet phase of the NE monsoon.

Notably, the spatial pattern of both RX1day and RX5day average intensity changes are very similar. This suggests that RX5day extremes are dominated by the extreme rainfall amounts on daily time scales. The overall increase in both average RX1day and RX5day intensities in all seasons except for the NE monsoon dry period is consistent with the expectation that rainfall (wet) extremes will become more severe in a warming world (Seneviratne et al., 2021).

The increases in mean RX1day and RX5day imply that there are changes to the future characteristics of extreme precipitation events typical for the season. For the two intermonsoon periods, daily rainfall is often dominated by the frequent diurnal occurrence of afternoon convective thunderstorms. The strong increase in mean RX1Day rainfall suggests that future convective thunderstorms are either more intense and/or lasting longer, on average, than those in the current climate.

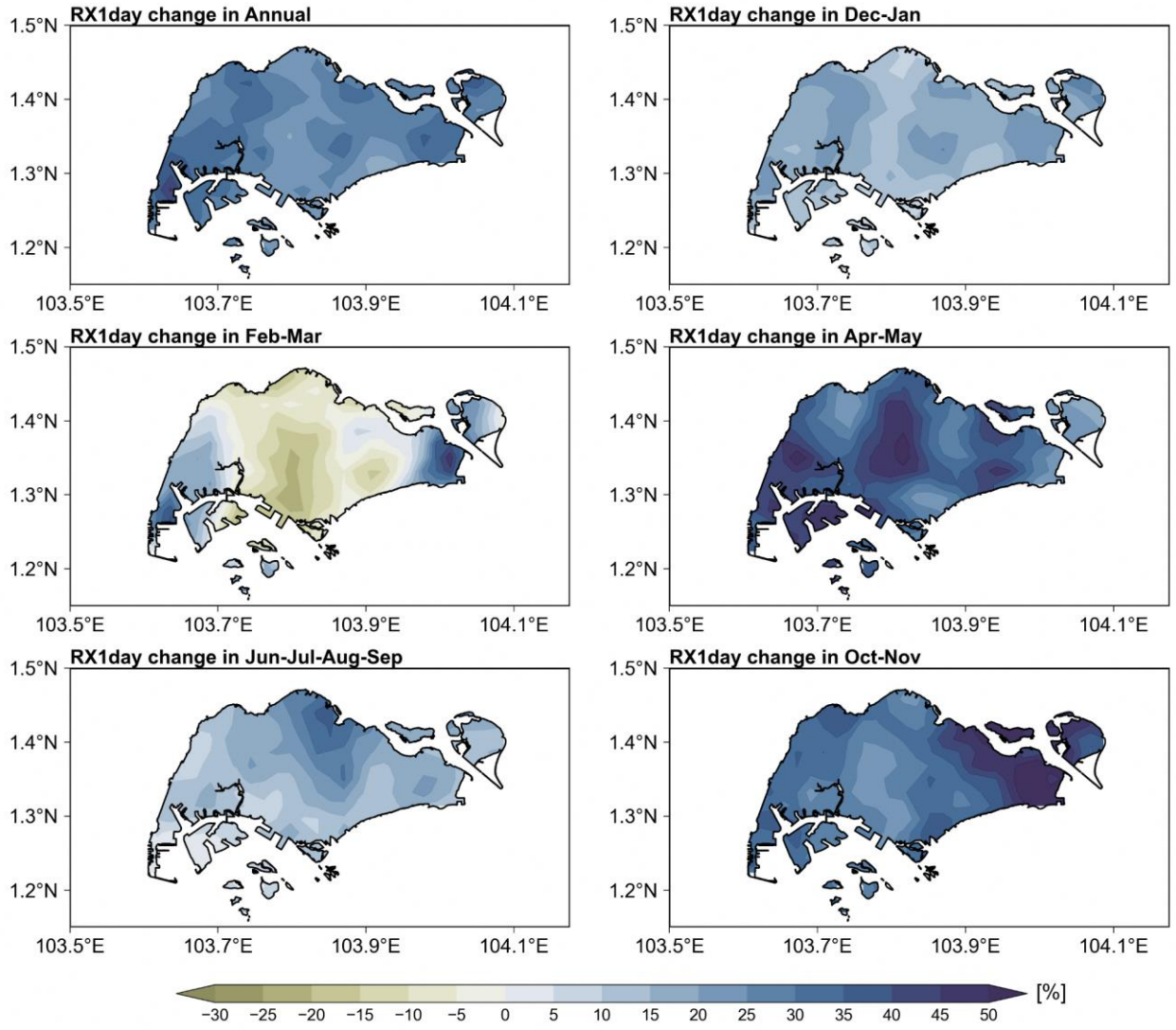

Figure 10.2: Ensemble mean (5 bias-adjusted 2km downscaled GCMs) percentage change of maximum 1-day (Rx1day) precipitation in annual, December–January, February–March, April–May, June–July–August–September, and October–

November months during end-century (2080–2099) period relative to the baseline (1995–2014) over Singapore under the SSP5-8.5 scenario.

For the NE monsoon wet phase, extreme daily rainfall values in the historical observations are likely caused by strong monsoon surges. The projected increases in mean RX1day and RX5day for the two intermonsoons and the wet NE monsoon phase suggest that rainfall associated with strong monsoon surges have become more severe (i.e. more total rainfall associated with them).

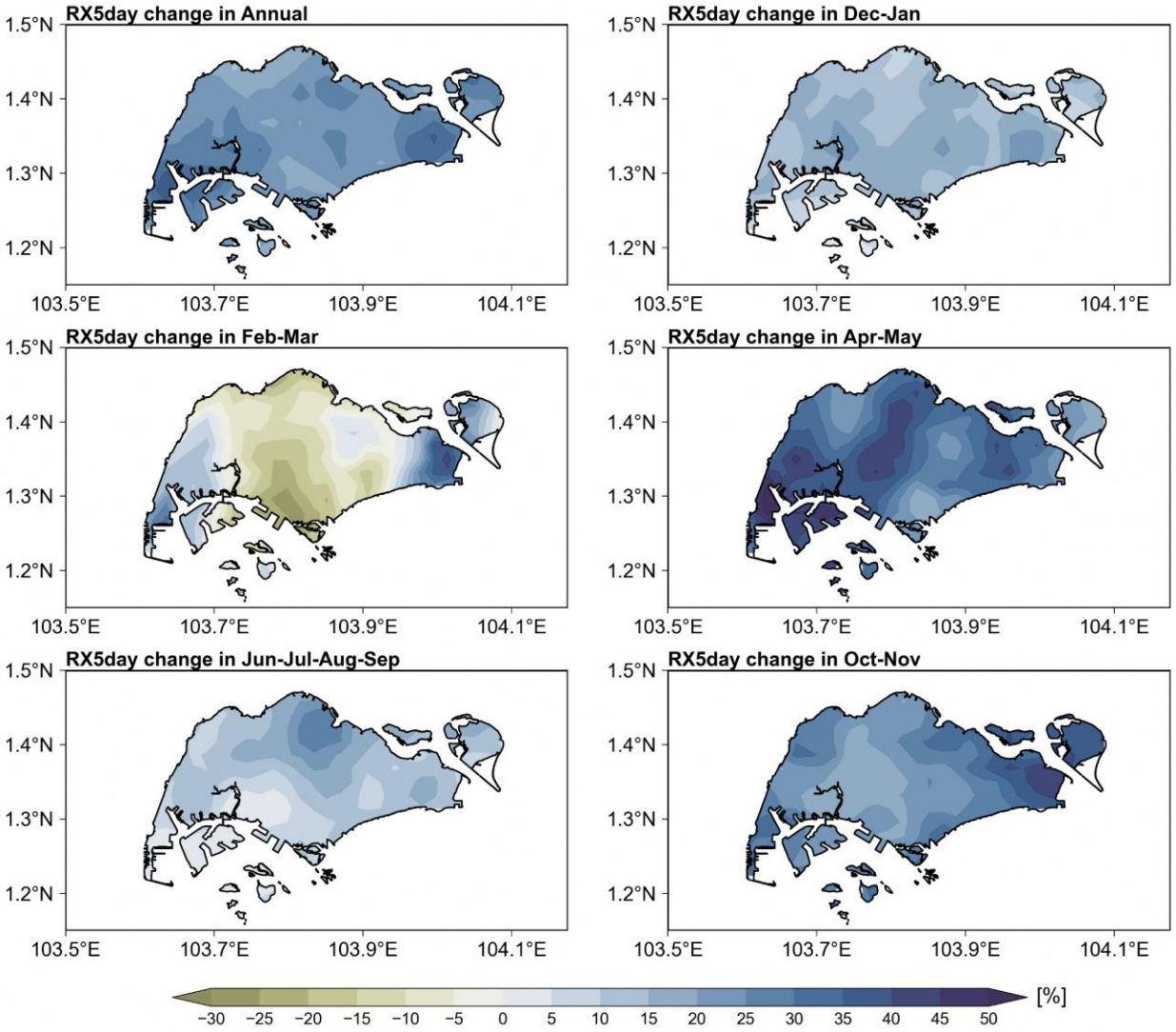

Figure 10.3: Ensemble mean (5 bias-adjusted 2km downscaled GCMs) percentage change of annual maximum 5-day (Rx5day) precipitation in annual, December–January, February–March, April–May, June–July–August–September, and October–November months during end-century (2080–2099) period relative to the baseline (1995–2014) over Singapore under the SSP5-8.5 scenario.

Note that, as we showed in Chapter 8 Section 8.3, Singapore is in between regions of increase and decrease for both mean rainfall and extremes in all seasons, so it is likely that a small shift in either direction could change the sign of the projected change over Singapore. Therefore, we need to be careful to interpret the detailed spatial changes across Singapore.

Precipitation extremes over the entire Singapore are measured using the 95th and 99.9th percentiles of daily rainfall distributions. Figure

10.4 shows the percentage changes in the extreme rainfall percentiles (95th and 99.9th) in the mid-century and end century under SSP5-8.5 scenario relative to historical period at annual and seasonal time scales. As seen in the figure, the extreme rainfall is projected to increase but vary at annual and seasonal time scales both in mid and end century.

At annual time scales (Table 10.7), both the multi-model mean 95th and 99.9th percentile of daily rainfall experience larger rises in the mid-century compared to the end-century period.

Table 10.7: Projected percentage changes in extreme daily rainfall percentiles (ANN)

ANN	Percentage change in annual extreme Rainfall (SSP5-8.5)			
	95th Percentile		99.9th Percentile	
	Mean	Range	Mean	Range
Mid century	15.6	0.6 to 24.2	39.4	9.3 to 64.6
End century	11.9	-0.3 to 21	26.4	12.7 to 43

During the northeast monsoon wet season (DJ; Table 10.8), 95th percentile rainfall in the mid century has a larger range compared to the end-century values; both the 95th and 99.9th percentile rainfall show reductions from their mid-century values to smaller increases in the end-century.

For the northeast monsoon dry season (FM; Table 10.9 and Fig. 10.4), the 95th and 99.9th percentile rainfall in the mid century has the largest range among the models. Towards the end of the century, both the 95th and 99.9th percentiles reduced from their mid-century values.

Table 10.8: Projected changes in extreme daily rainfall percentiles (DJ)

DJ	Percentage change in Dec-Jan extreme Rainfall (SSP5-8.5)			
	95th Percentile		99.9th Percentile	
	Mean	Range	Mean	Range
Mid century	31.5	6 to 92.8	50.6	28.6 to 88.2
End century	11.7	-17.1 to 50.9	36.2	26.3 to 42.9

Table 10.9: Projected changes in extreme daily rainfall percentiles (FM)

FM	Percentage change in Feb-Mar extreme Rainfall (SSP5-8.5)			
	95th Percentile		99.9th Percentile	
	Mean	Range	Mean	Range
Mid century	31.8	-19.6 to 118.5	47.6	-3.8 to 144.2
End century	-11.1	-40 to 29.5	20.2	-10.6 to 50.9

In contrast to the northeast monsoon season, the multi-model mean precipitation extremes (95th and 99.9th) over the first intermonsoon (AM; Table 10.10, and second intermonsoon (ON; Table 10.12) season rise towards the end of the century.

The southwest monsoon season shows a small decrease in the multi-model mean 95th percentile but 50 % increase (from 19.4 to 29.3 % change) for the 99.9th percentile.

Table 10.10: Projected changes in extreme daily rainfall percentiles (AM)

AM	Percentage change in Apr-May extreme Rainfall (SSP5-8.5)			
	95th Percentile		99.9th Percentile	
	Mean	Range	Mean	Range
Mid century	12.2	3.3 to 19	25.7	10 to 41.9

End century	27.4	5.3 to 58.3	53.4	21.6 to 91.6

Table 10.11: Projected changes in extreme daily rainfall percentiles (ON)

ON	Percentage change in Oct-Nov extreme Rainfall (SSP5-8.5)			
	95th Percentile		99.9th Percentile	
	Mean	Range	Mean	Range
Mid century	13.5	-0.3 to 27.9	23.7	9.2 to 38.7
End century	26.0	8.5 to 48.3	46.8	31.3 to 75.0

Table 10.12: Projected changes in extreme daily rainfall percentiles (JJAS)

JJAS	Percentage change in Jun-Sep extreme Rainfall (SSP5-8.5)			
	95th Percentile		99.9th Percentile	
	Mean	Range	Mean	Range
Mid century	0.8	-10.9 to 14.1	19.4	10.9 to 29.6
End century	0.2	-25.7 to 16.5	29.3	18.9 to 36.9

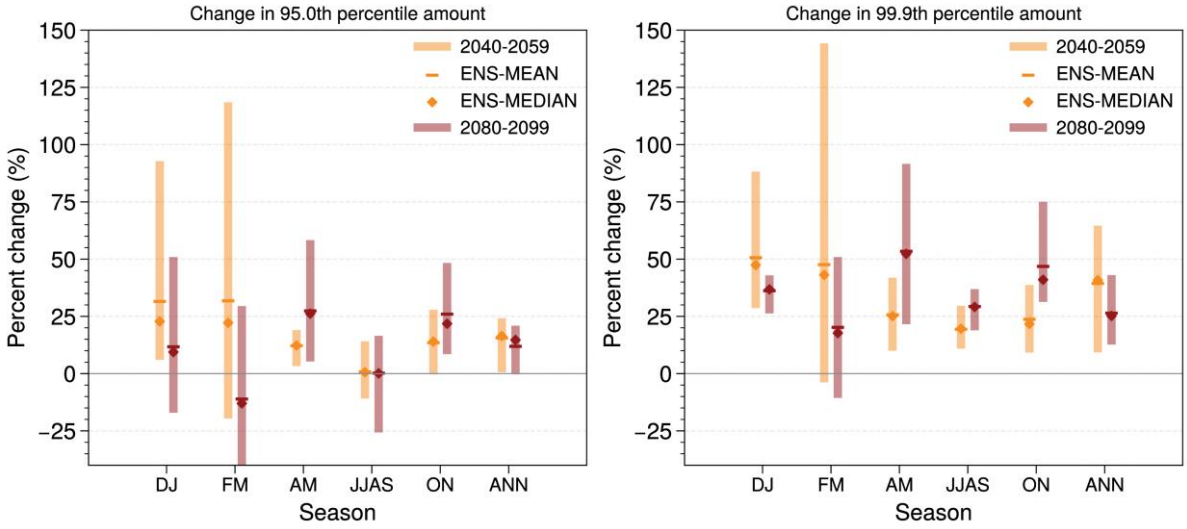

Figure 10.4: Percentage changes in 95th and 99.99th daily rainfall percentile amounts for annual and various seasons from the 2-km bias-adjusted SINGV-RCM simulations during the mid- (orange) and end-century (red) for SSP5-8.5. The line and diamond represent the mean and median using the 5 models, respectively. Rainfall percentiles are based on all days, pooled over all Singapore grid points; each percentile uses the nearest corresponding daily rainfall value. For readability, the values have been provided in Table 10.7-10.12.

The drought conditions over a region are measured using the maximum number of consecutive dry days (dry spell length). Figure 10.5 shows the annual maximum dry spell length (i.e. consecutive dry days) over Singapore in historical (1995-2014) and future (i.e. mid-century (2040-59) and end century (2080-99) under three SSP scenarios) time periods. As seen in Figure 10.5 and Table 10.13, the multi-model mean dry spell length in SSP5-8.5 increases with warming in the mid-century (~21 days) and end century (~23 days) relative to historical periods (Table 10.13). The increased dry spell length in a future warmer climate could put more stress on the water resources and energy consumption of Singapore.

Table 10.13: Historical and projected annual maximum dry spell length

	Mean dry spell length (days)	Dry spell length range (days)
Historical	21.1	18.5 to 22.3

Future	Mid-Century		End-Century	
	Mean	Range	Mean	Range
SSP1-2.6	22.3	21 to 25	21	20.3 to 22
SSP2-4.5	21.7	18.5 to 24.2	23	20.8 to 25.7
SSP5-8.5	21.8	18.7 to 24.8	23.3	18.7 to 25.7

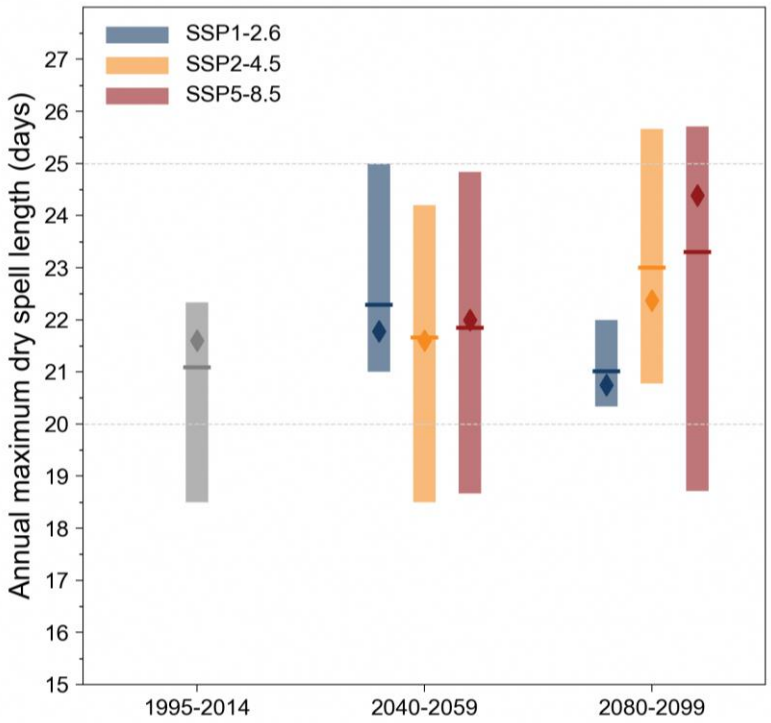

Figure 10.5: Historical and future annual maximum dry spell length for mid- (2040–2059) and end-century (2080–2099) periods from the 5 bias-adjusted downscaled GCMs (2 km) over Singapore relative to the baseline (1995–2014). The line and diamond represent the mean and median using the 5 models, respectively. For readability, the values are available in Tables 10.13.

Figure 10.6 shows the annual number of dry spells for more than 5 consecutive dry days over Singapore in historical and future (i.e. mid-century and end century under three SSP scenarios) time periods. As seen in Figure 10.6 and Table 10.14, the multi-model mean annual dry spell numbers under the SSP5-8.5 scenario are projected to increase in mid-century (~0.4) and end century (~0.7) compared to historical periods. On average, Singapore could experience a dry spell from once every ten months (1/1.2 multiplied by 12) to once every sixty months (1/0.2 multiplied by 12). The increased number of dry spells would be expected to increase the frequency of droughts over Singapore.

Table 10.14: Historical and projected changes in annual dry spell (length >= 15 days) numbers

	Mean dry Spell number (count)		Dry spell number range (count)	
Historical	0.2		0.1 to 0.3	
Future	Mid-Century		End-Century	
	Mean	Range	Mean	Range
SSP1-2.6	0.3	0.2 to 0.7	0.3	0.2 to 0.5
SSP2-4.5	0.3	0.25 to 0.35	0.6	0.45 to 0.75
SSP5-8.5	0.4	0.2 to 0.6	0.7	0.4 to 1.2

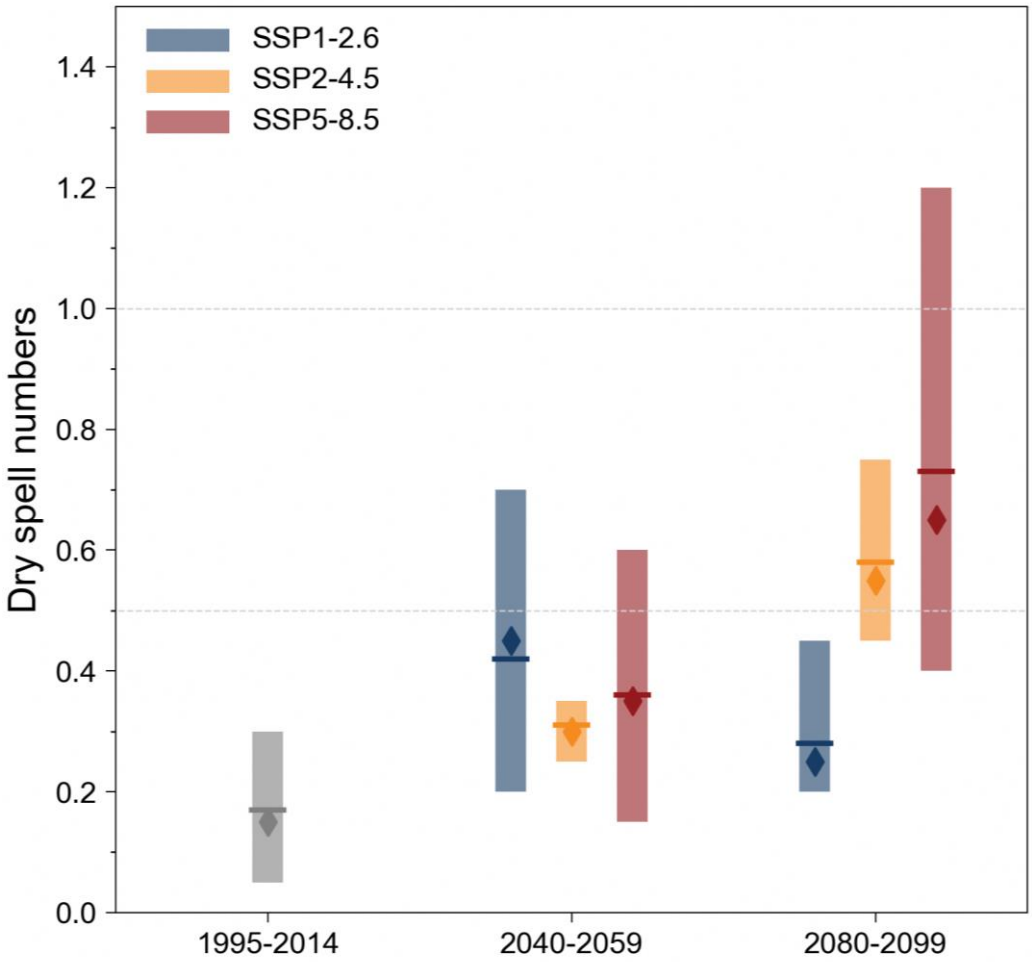

Figure 10.6: Historical and future annual number of dry spells for mid- (2040–2059) and end-century (2080–2099) periods from the 5 bias-adjusted downscaled GCMs (2 km) over Singapore relative to the baseline (1995–2014). The line and diamond represent the mean and median using the 5 models, respectively. For readability, the values are available in Tables 10.14.

10.4 Changes in Mean Temperature

Figure 10.7 shows the projected changes in the mean temperatures over Singapore under 3 SSP scenarios at different timescales in the mid- (2040-2059) and end-century (2080-2099) relative to the historical (1995-2014). As seen in Figure 10.7, the mean temperatures are projected to increase under the three scenarios both in mid- and end-century at annual (Table 10.15) and seasonal time scales (Table 10.16-10.20). The southwest monsoon (JJAS) and the second intermonsoon period (ON) seasons noted the biggest rises in surface temperatures at the end of the century, each by 3.9ºC and 4.0ºC, respectively. At the end of the century, the annual mean surface temperatures are projected to increase by 1.1ºC, 2.0ºC, 3.8ºC under the SSP1-2.6, SSP2-4.5, and SSP5-8.5 respectively. Also note that, for each scenario and time period, the changes for each season are very similar to one another.

From these projections we can infer that under the low-emission scenario of SSP1-2.6, temperature over Singapore will generally rise further by at least 1 degree during both mid- and end-century.

Table 10.15: Projected changes in annual mean near-surface air temperature

ANN	Mid-Century (°C)		End-Century (°C)	
	Mean	Range	Mean	Range
SSP1-2.6	1.0	0.6 to 1.3	1.1	0.6 to 1.6
SSP2-4.5	1.2	0.8 to 1.7	2.0	1.4 to 2.8
SSP5-8.5	1.6	0.9 to 2.2	3.8	2.8 to 5.0

Table 10.16: Projected changes in DJ mean near-surface air temperature

DJ	Mid-Century (°C)		End-Century (°C)	
	Mean	Range	Mean	Range
SSP1-2.6	0.9	0.6 to 1.2	1.0	0.5 to 1.6
SSP2-4.5	1.1	0.7 to 1.6	1.9	1.3 to 2.7
SSP5-8.5	1.5	0.9 to 2.1	3.7	2.6 to 4.7

Table 10.17: Projected changes in FM mean near-surface air temperature

FM	Mid-Century (°C)		End-Century (°C)	
	Mean	Range	Mean	Range
SSP1-2.6	1.0	0.5 to 1.4	1.1	0.5 to 1.7
SSP2-4.5	1.2	0.7 to 1.7	2.0	1.2 to 2.8
SSP5-8.5	1.5	0.8 to 2.1	3.7	2.5 to 5.1

Table 10.18: Projected changes in AM mean near-surface air temperature

AM	Mid-Century (°C)		End-Century (°C)	
	Mean	Range	Mean	Range
SSP1-2.6	1.0	0.6 to 1.3	1.2	0.6 to 1.7
SSP2-4.5	1.3	0.7 to 1.7	2.1	1.3 to 2.8
SSP5-8.5	1.5	0.8 to 2.1	3.8	2.6 to 5.0

Table 10.19: Projected changes in ON mean near-surface air temperature

ON	Mid-Century (°C)		End-Century (°C)	
	Mean	Range	Mean	Range
SSP1-2.6	0.9	0.7 to 1.3	1.1	0.6 to 1.6
SSP2-4.5	1.2	0.9 to 1.7	2.0	1.4 to 2.8
SSP5-8.5	1.6	1.1 to 2.2	4.0	2.9 to 5.1

Table 10.20: Projected changes in JJAS mean near-surface air temperature

JJAS	Mid-Century (°C)		End-Century (°C)	
	Mean	Range	Mean	Range
SSP1-2.6	1.0	0.7 to 1.3	1.1	0.6 to 1.6
SSP2-4.5	1.2	0.8 to 1.7	2.1	1.5 to 2.8
SSP5-8.5	1.6	0.9 to 2.2	3.9	3.1 to 5.0

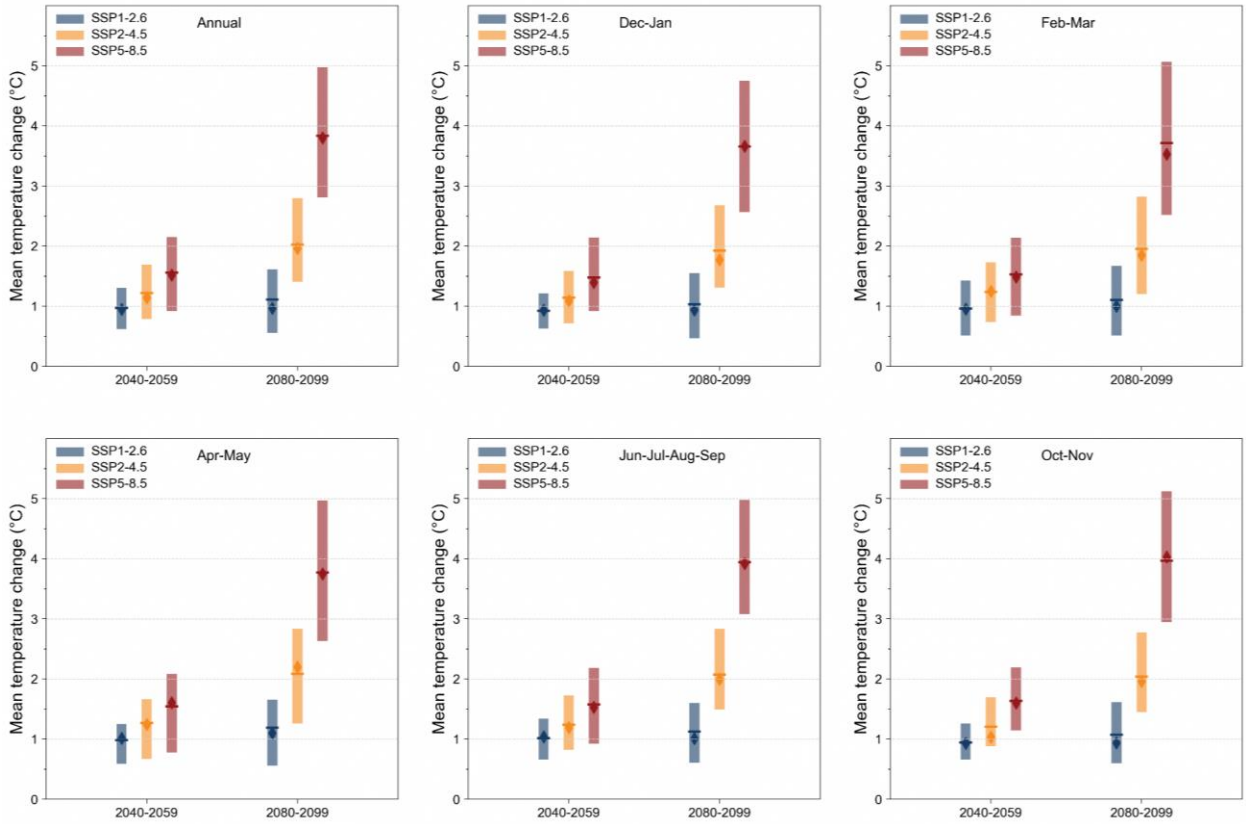

Figure 10.7: Change in mean daily near-surface air temperature in annual, December–January, February–March, April–May, June–July–August–September, and October–November during mid- (2040–2059) and end-century (2080–2099) periods from the 5 bias-adjusted downscaled GCMs (2 km) over Singapore relative to the baseline (1995–2014). The line and thin diamond represent the mean and median from the 5 models, respectively. For readability, the values are available in Tables 10.15-10.20.

10.5 Changes in Temperature Extremes

Temperature extremes of a region can be determined using the mean daily maximum and mean daily minimum temperatures. Figure 10.8 shows the projected changes in the extreme temperatures across Singapore under the three SSPs in the mid-century (2040-2059) and the end-century (2080-2099). As seen in Figure 10.8, Singapore's daily maximum (Table 10.21) and daily minimum temperatures (10.22) are projected to increase under the three scenarios both in the mid- and end-century. In the mid century, the daily maximum and daily minimum temperatures can increase by 1.6°C under the SSP5-8.5 scenario. Towards the end of the century, the daily maximum and daily minimum temperatures can increase by 4.0°C under the SSP5-8.5 scenario.

Table 10.21: Projected changes in annual mean daily maximum temperature

ANN	Mid-Century (°C)		End-Century (°C)	
	Mean	Range	Mean	Range
SSP1-2.6	1.0	0.6 to 1.4	1.1	0.5 to 1.7
SSP2-4.5	1.2	0.8 to 1.8	2.1	1.4 to 3.0
SSP5-8.5	1.6	0.9 to 2.2	4.0	2.9 to 5.3

Table 10.22: Projected changes in annual mean daily minimum temperature

ANN	Mid-Century (°C)		End-Century (°C)	
	Mean	Range	Mean	Range

SSP1-2.6	1.0	0.6 to 1.3	1.1	0.6 to 1.6
SSP2-4.5	1.2	0.8 to 1.7	2.1	1.5 to 2.8
SSP5-8.5	1.6	1.0 to 2.2	3.9	2.9 to 4.9

It is to be noted that even a resolution of 2 km is coarse to model urban effects and hence the projected maximum and minimum temperatures do not take into account the impact of the Urban Heat Island (UHI), and hence the current projections of absolute temperatures may be considered as an underestimation, although there could be a much lesser impact on the projected changes. Hence, follow up studies are being planned by CCRS that will further downscale the 2 km model simulations to 300 m (or 100 m if feasible) resolution over Singapore using the urban version of the SINGV model (uSINGV) that takes into account the urban impacts on climate variables at local scales. Daily maximum and daily minimum temperatures in Singapore are indicated by the multi-model mean to increase by at least 1°C under the low emission scenario (SSP1-2.6).

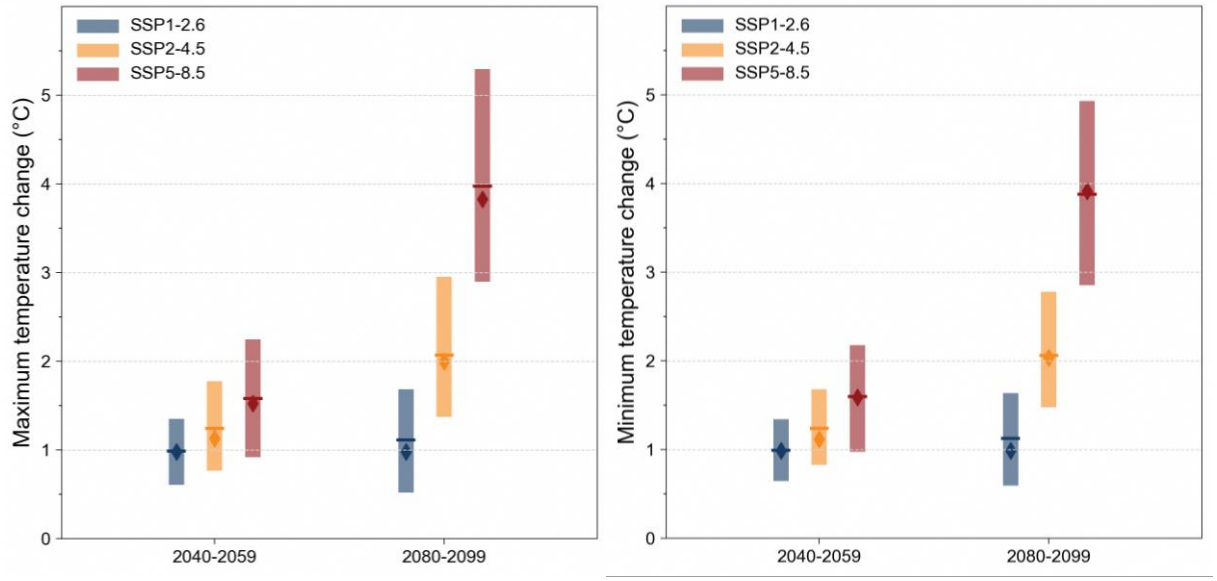

Figure 10.8: Change in mean daily minimum (tasmin) and maximum (tasmax) near-surface air temperature during mid-century (2040–2059) and end-century (2080–2099) period for the 5 bias-adjusted downscaled GCMs (2 km) over Singapore relative to the baseline (1995–2014). The line and thin diamond represent the mean and median over the 5 models, respectively. For readability, the values are available in Tables 10.21-10.22.

Temperature extremes can also be estimated using the 95th and 99.9th percentiles of the daily maximum temperatures of a region. Figure 10.9 shows the projected changes in the extreme temperature percentiles (95th & 99.9th) in the mid-century and end century under the SSP5-8.5 scenario at annual and seasonal time scales. As seen in Figure 10.9, the extreme temperatures (95th and 99.9th percentiles) are expected to increase during mid and end century under the SSP5-8.5 at annual (Table 10.23) and seasonal time scales (Table 10.24-10.28). Towards the end of the 21st century (2100) under the SSP5-8.5 scenario, the temperature extremes are projected to significantly increase (>4°C) across annual and seasonal time scales. Based on the multi-model mean, the second inter monsoon season (ON) is expected to experience the highest increases of about 4.7°C in the extreme temperatures (95th and 99.9th percentile) at the end of the century.

Table 10.23: Projected changes in extreme temperature percentiles (ANN)

ANN	Absolute changes (SSP5-8.5) compared to historical period (°C)			
	95th Percentile		99.9th Percentile	
	Mean	Range	Mean	Range
Mid century	1.8	1.0 to 2.5	2.0	1.0 to 2.8
End century	4.4	3.0 to 5.7	4.5	3.0 to 5.9

Table 10.24: Projected changes in extreme temperature percentiles (DJ)

DJ	Absolute changes (SSP5-8.5) compared to historical period (°C)			
	95th Percentile		99.9th Percentile	
	Mean	Range	Mean	Range
Mid century	1.5	0.5 to 2.6	1.8	1.0 to 2.9
End century	4.1	3.0 to 5.3	4.3	3.0 to 5.8

Table 10.25: Projected changes in extreme temperature percentiles (FM)

FM	Absolute changes (SSP5-8.5) compared to historical period (°C)			
	95th Percentile		99.9th Percentile	
	Mean	Range	Mean	Range
Mid century	1.8	1.0 to 2.6	2.0	1.0 to 2.9
End century	4.3	2.7 to 5.8	4.5	2.9 to 6.0

Table 10.26: Projected changes in extreme temperature percentiles (AM)

AM	Absolute changes (SSP5-8.5) compared to historical period (°C)			
	95th Percentile		99.9th Percentile	
	Mean	Range	Mean	Range
Mid century	1.7	1.0 to 2.3	1.8	1.2 to 2.3
End century	4.2	3.0 to 5.3	4.3	3.0 to 5.4

Table 10.27: Projected changes in extreme temperature percentiles (ON)

ON	Absolute changes (SSP5-8.5) compared to historical period (°C)			
	95th Percentile		99.9th Percentile	
	Mean	Range	Mean	Range
Mid century	1.9	1.3 to 2.6	2.1	1.5 to 2.8
End century	4.5	3.3 to 6.0	4.7	3.3 to 6.3

Table 10.28: Projected changes in extreme temperature percentiles (JJAS)

JJAS	Absolute changes (SSP5-8.5) compared to historical period (°C)			
	95th Percentile		99.9th Percentile	
	Mean	Range	Mean	Range
Mid century	1.8	1.3 to 3.0	2.0	1.5 to 3.3
End century	4.5	3.3 to 6.0	4.5	3.0 to 6.3

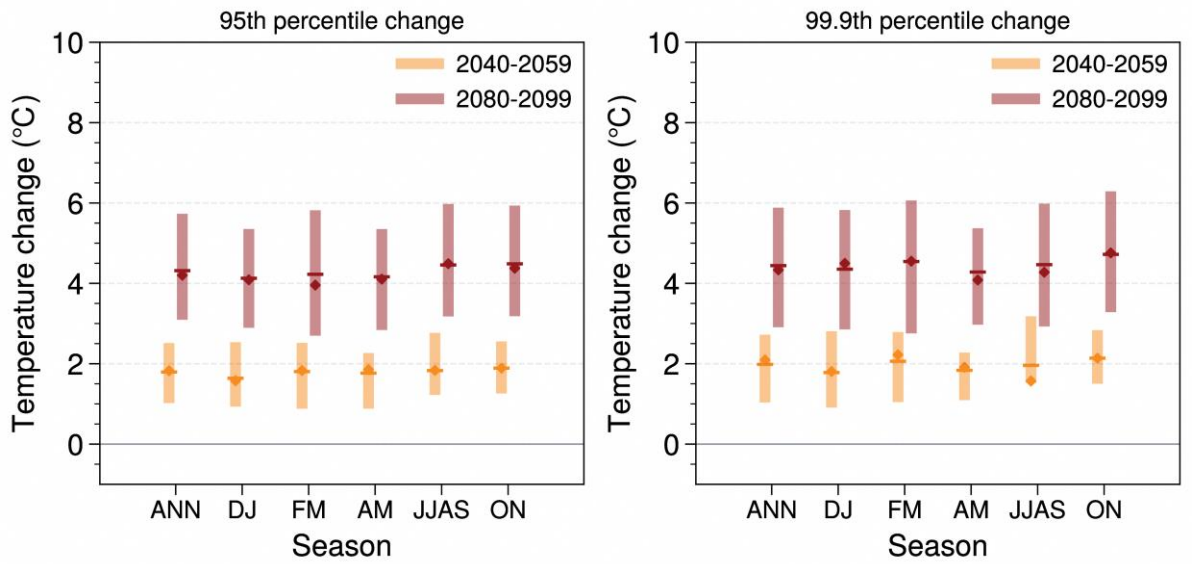

Figure 10.9: Changes in 95th and 99.99th daily maximum temperature percentile amounts for annual and various seasons from the 2-km bias-adjusted SINGV-RCM simulations during the mid- (left) and end-century (right) for SSP5-8.5. Percentiles are calculated after pooling all Singapore grid points. The line and diamond represent the mean and median using the 5 models, respectively. For readability, the values are available in Tables 10.23-10.28.

Temperature extremes of location can also be estimated using the monthly maximum of daily maximum temperatures (TXx) and monthly minimum of daily minimum temperatures (TNn). Figure 10.10 shows the multi-model mean projections of TXx over Singapore across annual and monthly timescales under the SSP5-8.5 scenario. As seen in Figure 10.10, the TXx is expected to increase on annual and monthly timescales in the end-century. The annual projections of TXx show an increase in a range of 3.3 to 4.6°C with higher range (4.4 to 4.6°C) in the western part of Singapore.

During the northeast monsoon season, for the Dec-Jan months, the TXx increases in a range of 3.2 to 4.2°C over Singapore with around 0.4°C lower in the eastern part. For the Feb-Mar months, the TXx tends to rise in a range of 3.4 to 4.8°C with higher values over western, central and northern parts.

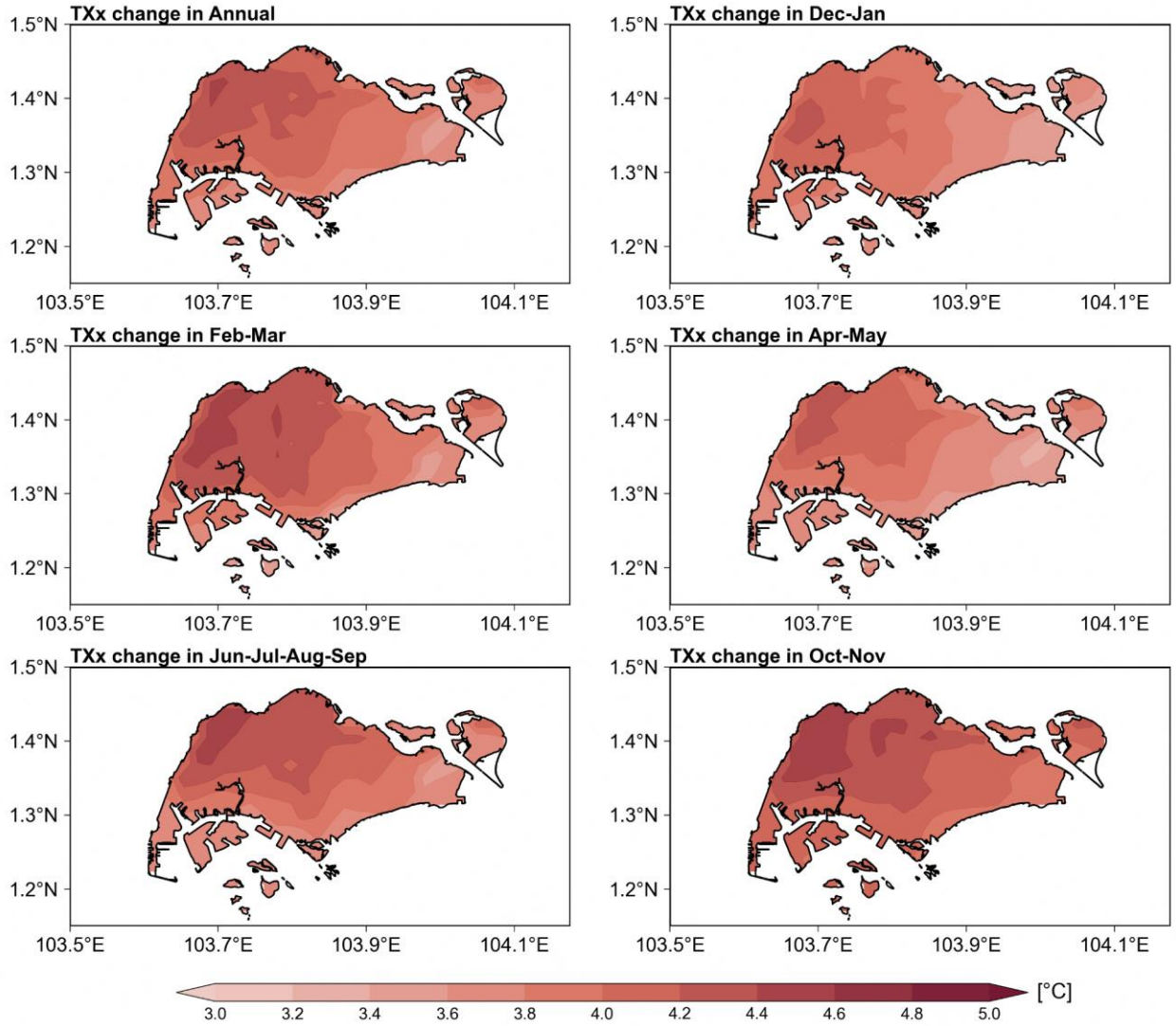

Figure 10.10: Ensemble mean (5 bias-adjusted 2km downscaled GCMs) change in monthly maximum of daily maximum temperature (TXx) for annual, December–January, February–March, April–May, June–July–August–September, and October–November during the end-century (2080–2099) period relative to the baseline (1995–2014) over Singapore under the SSP5-8.5 scenario.

During intermonsoons, for the Apr-May months, the TXx is projected to increase between 3.2 to 4.2^{o}C. For the Oct-Nov months, the TXx is projected to increase in a range of 4.0 to 5.0^{o}C over Singapore.

During the southwest monsoon season (Jun-Sep), the TXx is projected to increase between 3.4 to 4.8^{o}C with a higher increase in the northern part of Singapore. According to the projections of TXx, Oct-Nov are the months with the highest increase throughout Singapore during the end-century.

The TXx is expected to increase by 3.0 to 5.0^{o}C with warming across Singapore at annual and seasonal time scales with higher increases over the northern, central, and western parts of Singapore. Projections for very hot days and warm nights are shown in Appendix C.

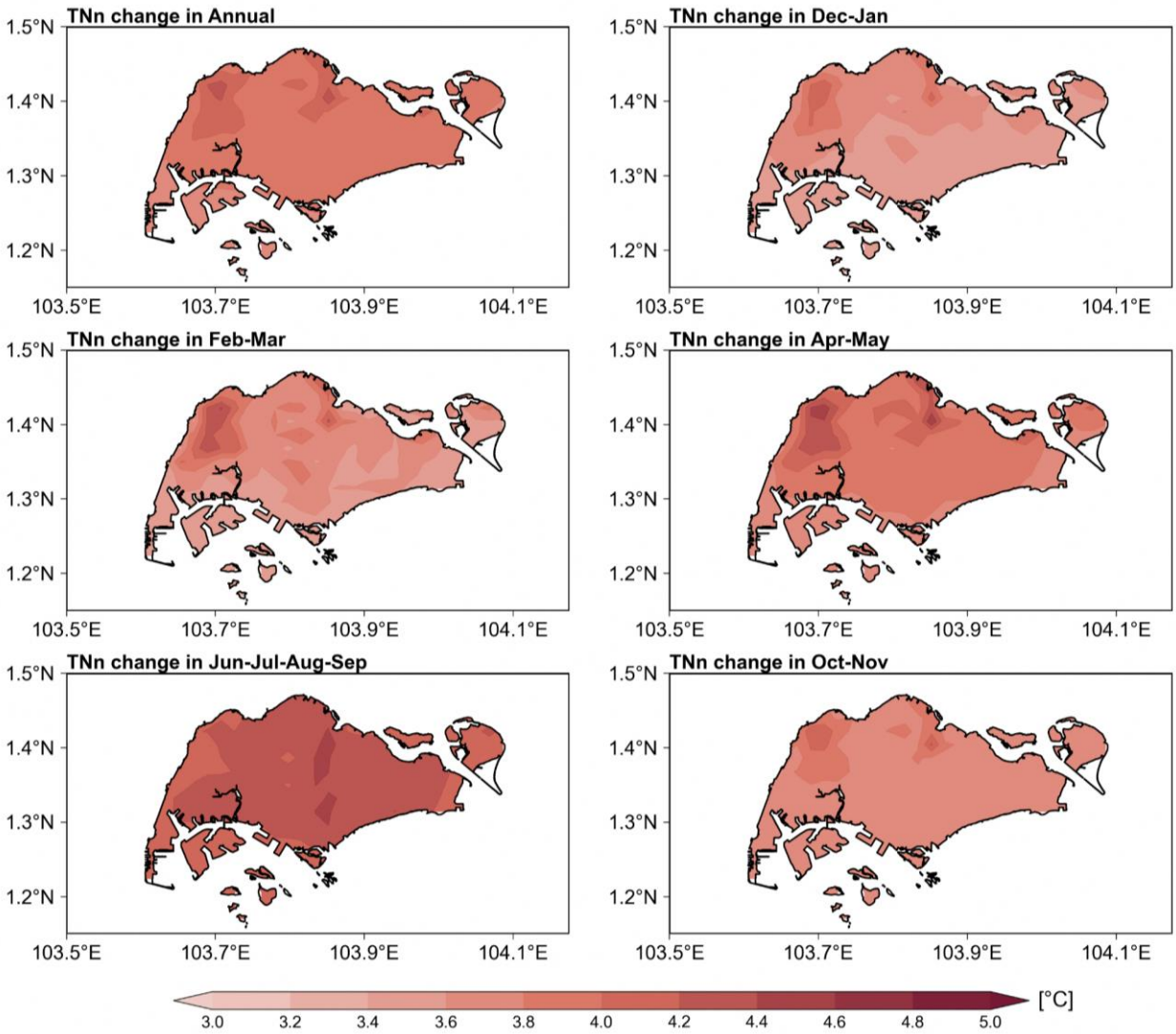

Figure 10.11: Ensemble mean (5 bias-adjusted 2km downscaled GCMs) change in monthly minimum of daily minimum temperature (TNn) for annual, December–January, February–March, April–May, June–July–August–September, and October–November during end-century (2080–2099) period relative to the baseline (1995–2014) over Singapore under the SSP5-8.5 scenario.

Figure 10.11 shows the multi-model mean projections of TNn across Singapore in the end-century under the SSP5-8.5 scenario. TNn is projected to increase on annual and monthly timescales across Singapore towards the end century under a very high emission scenario. The annual projections of TNn show an increase of 3.4 to 4.2^{o}C.

During the northeast monsoon season, for Dec-Jan months, the TNn is projected to increase between 3.2 to 4.0^{o}C across Singapore. For the Feb-Mar months, the TNn is projected to increase between 3.4 to 4.2^{o}C.

During intermonsoons, for the Apr-May months, the TNn is projected to increase in a range of 3.6 to 4.8^{o}C. For the Oct-Nov months, the TNn is projected to increase between 3.4 to 4.2^{o}C.

During the southwest monsoons (Jun-Sep), the TNn is projected to increase between 4.0 to 5.0^{o}C. In the end century, the TNn is projected to increase (3.2 to 5.0^{o}C) across Singapore with higher increases over the Jun-Sep season (4.2 to 5.0^{o}C).

Overall, the TNn is projected to increase by 3.0-5.0^{o}C across Singapore at annual and seasonal

time scales with higher increases (>4.0°C) during the southwest monsoon season.

10.6 Changes in Heat Stress Index

According to the factsheet on Heat and Health by the UN World Health Organization, population exposure to heat is increasing due to climate change, and this trend will continue. In the backdrop of global warming, heat stress is becoming an increasingly important topic around the world, including Singapore. Although there are various metrics that can be used as indicators of heat stress, in this report we use the Wet Bulb Globe Temperature (WBGT) as a heat stress indicator and assess the future change in this indicator under 3 SSP scenarios for the mid- and end-century. Based on the hourly near-surface air temperature, wind speed, relative humidity and net incoming solar radiation, we used Liljegren's model (Liljegren, 2008) to obtain the hourly WBGT and select the daily maximum WBGT as the heat stress indicator. The WBGT is calculated as the weighted sum of the natural wet bulb temperature Tw, the globe temperature Tg, and the dry bulb temperature Tas:

$$WBGT = 0.7\,Tw + 0.2\,Tg + 0.1\,Tas$$

Figure 10.12 shows the multi-model projections of WBGT under three SSP scenarios in the mid century and end century. As seen in Figure 10.12, the daily maximum WBGT is projected to increase with warming across Singapore at annual (Table 10.29) and seasonal time scales (Table 10.29-10.33). Towards the end of the current century, the annual mean daily maximum WBGT can increase by 0.5°C (SSP1-2.6) to 4.0°C (SSP5-8.5).

Table 10.29: Projected changes in annual mean daily maximum WBGT

ANN	Mid-Century (°C)		End-Century (°C)	
	Mean	Range	Mean	Range
SSP1-2.6	0.8	0.5 to 1.1	0.9	0.5 to 1.3
SSP2-4.5	1.0	0.7 to 1.4	1.7	1.2 to 2.2
SSP5-8.5	1.4	1.0 to 1.8	3.3	2.3 to 4.0

Table 10.30: Projected changes in DJ mean daily maximum WBGT

DJ	Mid-Century (°C)		End-Century (°C)	
	Mean	Range	Mean	Range
SSP1-2.6	0.8	0.6 to 1.0	0.9	0.6 to 1.3
SSP2-4.5	0.9	0.6 to 1.1	1.7	1.1 to 2.1
SSP5-8.5	1.3	0.9 to 1.8	3.1	2.1 to 3.8

Table 10.31: Projected changes in FM mean daily maximum WBGT

FM	Mid-Century (°C)		End-Century (°C)	
	Mean	Range	Mean	Range
SSP1-2.6	0.6	0.3 to 1.0	0.8	0.4 to 1.2
SSP2-4.5	1.0	0.7 to 1.3	1.4	1.0 to 1.9
SSP5-8.5	1.3	0.9 to 1.6	2.9	2.0 to 3.8

Table 10.32: Projected changes in AM mean daily maximum WBGT

AM	Mid-Century (°C)		End-Century (°C)	
	Mean	Range	Mean	Range
SSP1-2.6	0.8	0.4 to 1.1	0.9	0.4 to 1.3
SSP2-4.5	1.1	0.6 to 1.5	1.8	1.1 to 2.3
SSP5-8.5	1.3	0.8 to 1.8	3.2	2.1 to 4.1

Table 10.33: Projected changes in ON mean daily maximum WBGT

ON	Mid-Century (°C)	End-Century (°C)

	Mean	Range	Mean	Range
SSP1-2.6	0.9	0.5 to 1.2	1.0	0.5 to 1.5
SSP2-4.5	1.0	0.6 to 1.4	1.8	1.3 to 2.4
SSP5-8.5	1.8	1.3 to 2.4	3.4	2.4 to 4.1

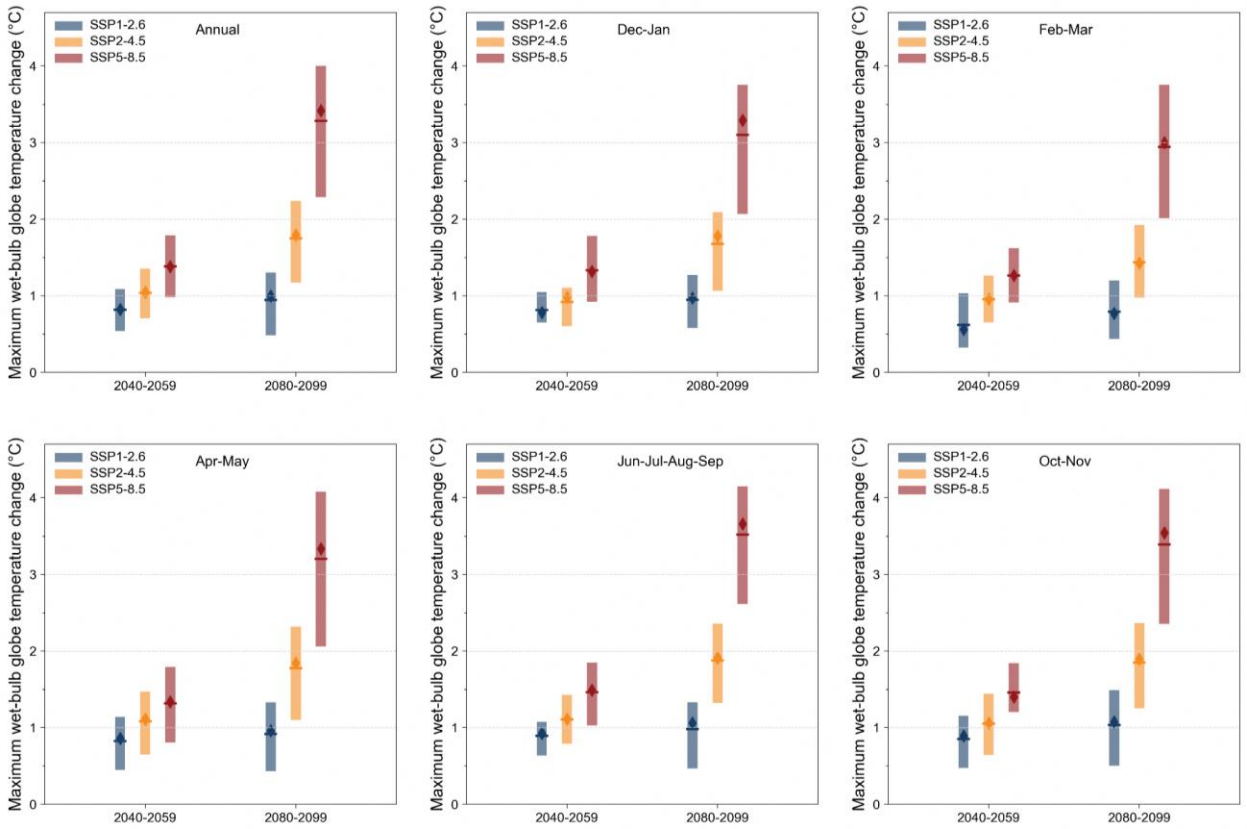

Figure 10.12: Change in daily maximum wet-bulb globe temperature (WBGT) for annual, December–January, February–March, April–May, June–July–August–September, and October–November during mid- (2040–2059) and end-century (2080–2099) periods from the 5 bias-adjusted downscaled GCMs (2 km) over Singapore relative to the baseline (1995–2014). The line and thin diamond represent the mean and median over the 5 models, respectively.For readability, the values are available in Tables 10.29-10.34.

Table 10.34: Projected changes in JJAS mean daily maximum WBGT

JJAS	Mid-Century (°C)		End-Century (°C)	
	Mean	Range	Mean	Range
SSP1-2.6	0.9	0.6 to 1.1	1.0	0.5 to 1.3
SSP2-4.5	1.1	0.8 to 1.4	1.9	1.3 to 2.4
SSP5-8.5	1.5	1.0 to 1.8	3.5	2.6 to 4.2

In the baseline period from 1995-2014, the climate models predict an annual average of 35.9 days featuring maximum WBGT above 33°C, ranging from 20.5 to 57.2 days among various models. Looking ahead, the number of days with WBGT surpassing this critical threshold is projected to rise significantly. By mid-century, under the scenarios of SSP1-2.6, SSP2-4.5 and SSP5-8.5 scenarios, we anticipate 74.9 days (ranging from 52.8 to 111.8), 87.2 days (ranging from 60.5 to 131.2), and 112.7 days (ranging from 85.8 to 154.6), respectively. The frequency of days exceeding WBGT of 33°C escalates even further, reaching 80.7 days (ranging from 54.4 to 134.6) for SSP1-2.6, 141.5 days (ranging from 107 to 204.7) for SSP2-4.5, and 269.6 days (ranging

from 207.4 to 326.1) SSP5-8.5. The projections underscore the growing heat stress challenges that lie ahead in Singapore, which requires proactive preparation for the intensified risk of heat-related illness, potential shortage of healthcare resources, and the threats to economic stability in industrial sectors relying on outdoor labors and tourism.

Figure 10.12 shows the spatial changes in the ensemble mean of monthly maximum WBGT across Singapore in the mid-century and end century under the SSP5-8.5 scenario compared to the historical period. The WBGT is expected to rise with warming at both annual and seasonal time scales over Singapore in a range of 2.8 to 3.8^{o}C. The southwest monsoon season (July to September) has higher WBGT increases (3.5 to 3.8^{o}C) and the dry phase of the northeast monsoon season increases WBGT in the range of 2.8 to 3.0^{o}C. Overall the heat stress (WBGT) which is projected to increase across Singapore in the future warmer climate can thereby influence the socio-economic conditions across the nation.

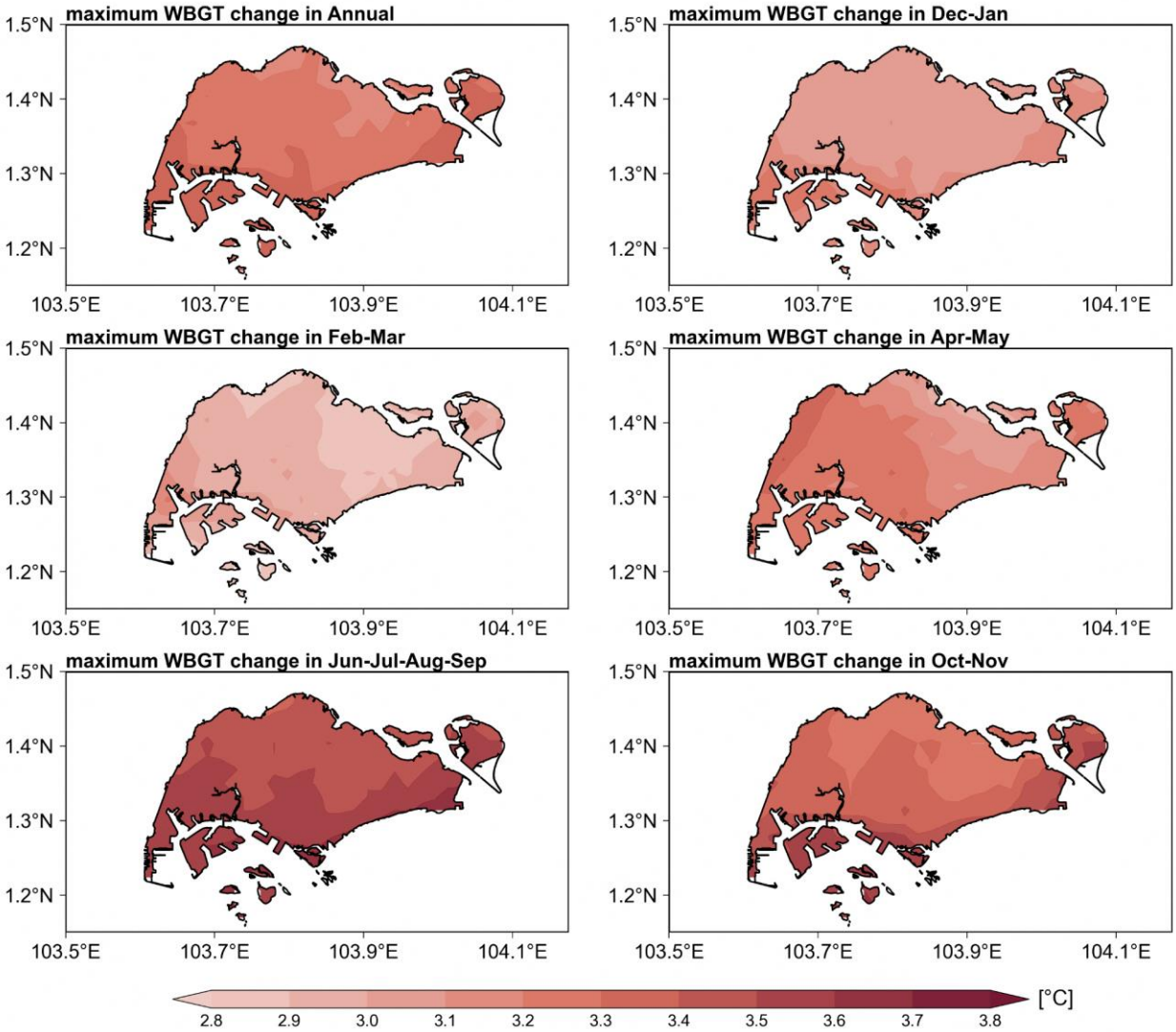

Figure 10.12: Ensemble mean (5 bias-adjusted 2km downscaled GCMs) change in monthly maximum WBGT for annual, December–January, February–March, April–May, June–July–August–September, and October–November during end-century (2080–2099) period relative to the baseline (1995–2014) over Singapore under the SSP5-8.5 scenario.

10.7 Changes in 10m relative humidity

Relative humidity is expressed as a percentage and is a measure of how saturated the air is. It

includes the combined effect of temperature and water vapour in the air. In simple terms, it is an indicator of how much water vapour the air contains compared to the maximum it could contain at a given temperature and pressure.

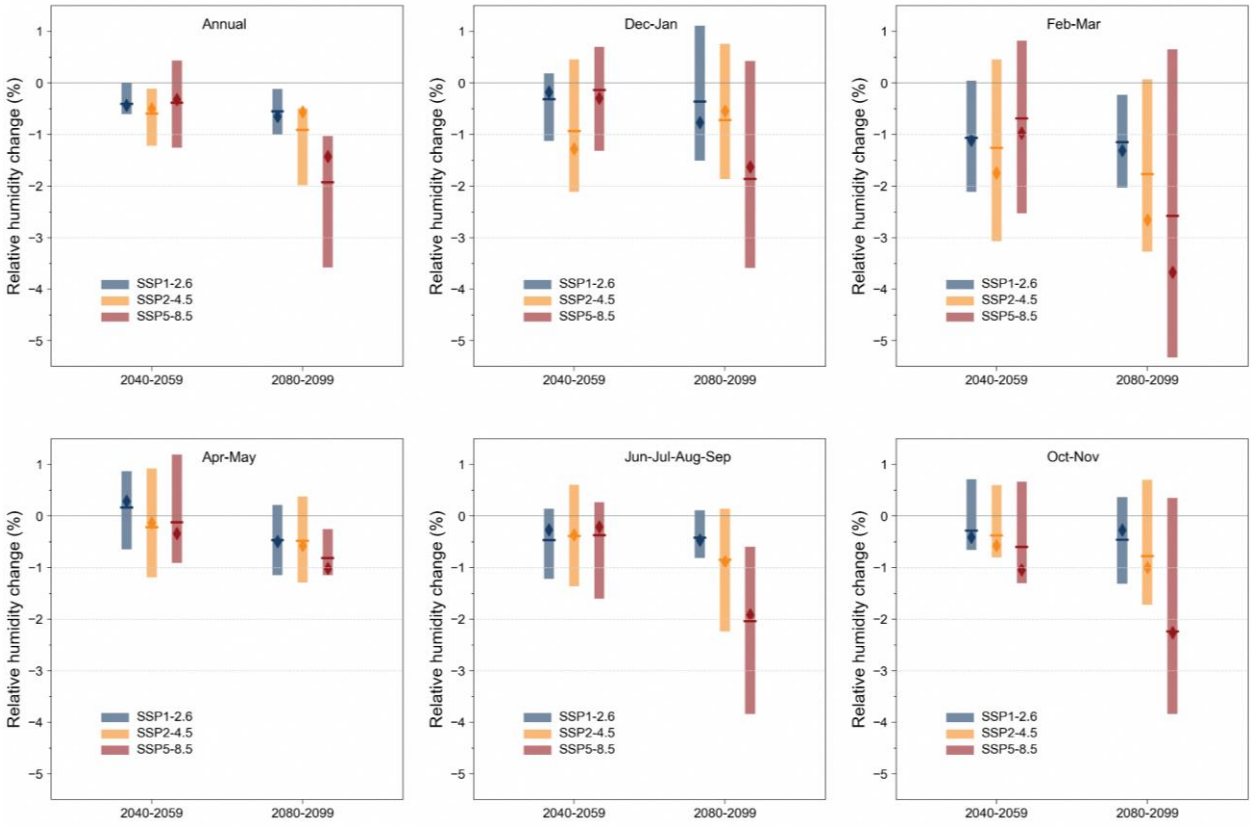

Figure 10.13: Change in mean relative humidity (hurs) for annual, December–January, February–March, April–May, June–July–August–September, and October–November during mid- (2040–2059) and end-century (2080–2099) periods for the 5 bias-adjusted downscaled GCMs (2 km) over Singapore relative to the baseline (1995–2014). The line and thin diamond represent the mean and median over the 5 models, respectively. For readability, the values are available in Tables 10.35-10.40.

With increase in temperature, the amount of water vapour in the air is expected to increase. This is because of the Clausius-Clapeyron (CC) equation, which implies that the air can generally hold around 7% more moisture for every 1°C increase in air temperature. Therefore, under global warming, for the relative humidity to be constant the water vapour content in the air should increase at the same rate i.e., 7% increase for every 1°C increase in air temperature. However, from Singapore's observation records we find that there is a decreasing trend in relative humidity. This also matches with what was projected in V2. The reasons for this is (1) there is a limited supply of moisture in the land unlike oceans, and (2) the land surface has been warming at a faster rate than oceans. Hence, neither the local evaporation over land, nor the advected moisture from the oceans is enough to increase the water vapour over land at the CC rate.

Figure 10.13 shows the multi-model mean projections of RH under three SSP scenarios in the mid and end century at annual and seasonal time scales. As seen in Figure 10.13, the RH is projected to decrease over Singapore at annual and seasonal time scales in mid century and end century. Towards the end of the century, the annual mean RH is projected to decrease by 0.5% (SSP1-2.6) to 1.9% (SSP5-8.5). When compared to other seasons, the northeast monsoon dry phase (Feb-Mar) project decreased RH by 1.2% (SSP1-2.6) and 2.6% (SSP5-8.5) in the end century. Additionally, the projected changes in RH

during the dry phase of the northeast monsoon show significant inter-model variation.

Table 10.35: Projected changes in annual mean RH

ANN	Mid-Century (%)		End-Century (%)	
	Mean	Range	Mean	Range
SSP1-2.6	-0.4	-0.6 to 0.0	-0.5	-1.2 to -0.1
SSP2-4.5	-0.6	-1.2 to -0.1	-0.9	-2.0 to -0.5
SSP5-8.5	-0.4	-1.3 to 0.4	-1.9	-3.6 to -1.0

Table 10.36: Projected changes in DJ mean RH

DJ	Mid-Century (%)		End-Century (%)	
	Mean	Range	Mean	Range
SSP1-2.6	-0.3	-1.1 to 0.2	-0.4	-1.5 to 1.1
SSP2-4.5	-0.9	-2.1 to 0.5	-0.7	-1.9 to 0.8
SSP5-8.5	-0.1	-1.3 to 0.7	-1.9	-3.6 to 0.4

Table 10.37: Projected changes in FM mean RH

FM	Mid-Century (%)		End-Century (%)	
	Mean	Range	Mean	Range
SSP1-2.6	-1.1	-2.1 to 0.0	-1.2	-2.0 to -0.2
SSP2-4.5	-1.3	-3.1 to 0.5	-1.8	-3.3 to 0.1
SSP5-8.5	-0.7	-2.5 to 0.8	-2.6	-5.3 to 0.7

Table 10.38: Projected changes in AM mean RH

AM	Mid-Century (%)		End-Century (%)	
	Mean	Range	Mean	Range
SSP1-2.6	0.2	-0.6 to 0.9	-0.5	-1.1 to 0.2
SSP2-4.5	-0.2	-1.2 to 0.9	-0.5	-1.3 to 0.4
SSP5-8.5	-0.1	-0.9 to 1.2	-0.8	-1.1 to -0.3

Table 10.39: Projected changes in ON mean RH

ON	Mid-Century (%)		End-Century (%)	
	Mean	Range	Mean	Range
SSP1-2.6	-0.3	-0.7 to 0.7	-0.5	-1.3 to 0.4
SSP2-4.5	-0.4	-0.8 to 0.6	-0.8	-1.7 to 0.7
SSP5-8.5	-0.6	-1.3 to 0.7	-2.2	-3.9 to 0.3

Table 10.40: Projected changes in JJAS mean RH

ANN	Mid-Century (%)		End-Century (%)	
	Mean	Range	Mean	Range
SSP1-2.6	-0.5	-1.2 to 0.7	-0.5	-1.3 to 0.4
SSP2-4.5	-0.4	-1.4 to 0.6	-0.9	-2.2 to 0.1
SSP5-8.5	-0.4	-1.6 to 0.3	-2.0	-3.8 to -0.6

10.8 Changes in 10m wind speed

This section presents the annual cycle of mean surface wind speeds in the historical and 2 km downscaled SINGV simulations under the SSP5-8.5 scenario in the mid and end century. We also present the projected changes in the mean surface wind speed for three SSP scenarios at annual and seasonal time scales in mid and end century.

Figure 10.14 shows the annual cycle of surface wind speeds over Singapore during historical, mid-century (SSP5-8.5), and end-century (SSP5-8.5). In all three time periods, the annual cycle comprises higher wind speeds in the northeast and southwest monsoon seasons and lower wind speeds in the intermonsoon seasons. Relative to the historical simulations, there is not much change in the mid-century for most of the year, but by the end of the century, the mean surface wind speeds exceed those of historical throughout the year, especially in Jan-Sep, where there is high model agreement on the increases.

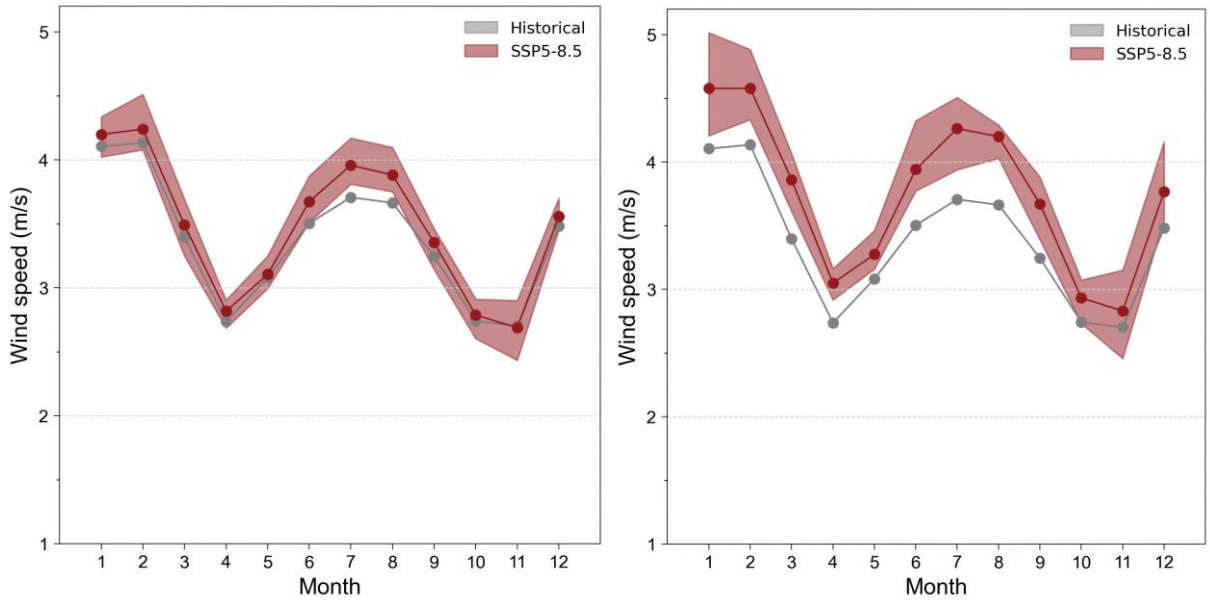

Figure 10.14: Annual cycle of historical and future winds under mid- (left) and end-century (right).

Projected changes in surface wind speed for mid- and end-century under the 3 SSP scenarios are shown in Figure 10.15. As seen in the figure, projected mean surface wind speed changes over Singapore varies on annual (Table 10.41) and monthly scales (Table 10.42-10.46). At annual time scales, the mean wind speeds are projected to increase by 0.1 m/s (SSP1-2.6) to 0.37 m/s (SSP5-8.5). Under the SSP5-8.5 scenario, the northeast monsoon and southwest monsoon seasons are projected to experience greater increases in mean wind speeds in the end of the century.

Table 10.41: Projected changes in annual mean 10m wind speed

ANN	Mid-Century (m/s)		End-Century (m/s)	
	Mean	Range	Mean	Range
SSP1-2.6	0.10	0.02 to 0.16	0.10	0.0 to 0.17
SSP2-4.5	0.12	0.03 to 0.19	0.19	0.09 to 0.28
SSP5-8.5	0.10	-0.03 to 0.24	0.37	0.23 to 0.51

Table 10.42: Projected changes in DJ mean 10m wind speed

DJ	Mid-Century (m/s)		End-Century (m/s)	
	Mean	Range	Mean	Range

SSP1-2.6	0.03	-0.05 to 0.20	0.09	-0.06 to 0.22
SSP2-4.5	0.14	-0.02 to 0.31	0.16	0.00 to 0.36
SSP5-8.5	0.08	-0.05 to 0.22	0.38	0.09 to 0.80

Table 10.43: Projected changes in FM mean 10m wind speed

FM	Mid-Century (m/s)		End-Century (m/s)	
	Mean	Range	Mean	Range
SSP1-2.6	0.18	0.00 to 0.43	0.14	-0.02 to 0.33
SSP2-4.5	0.16	0.01 to 0.33	0.33	0.07 to 0.54
SSP5-8.5	0.10	-0.10 to 0.33	0.45	0.21 to 0.70

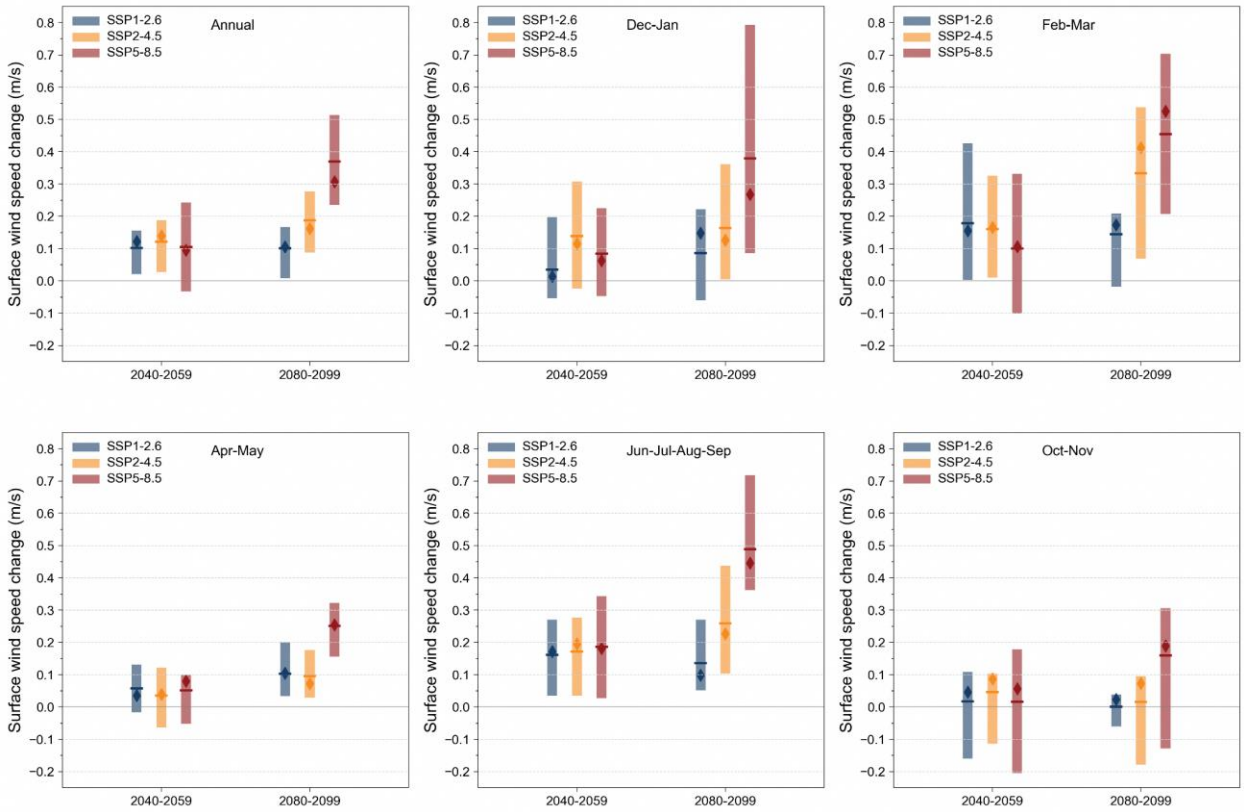

Figure 10.15: Changes in mean 10m wind speed for annual, December–January, February–March, April–May, June–July–August–September, and October–November during mid- (2040–2059) and end-century (2080–2099) periods for the 5 bias-adjusted downscaled GCMs (2 km) over Singapore relative to the baseline (1995–2014). The line and thin diamond represent the mean and median over the 5 models, respectively. For readability, the values are available in Tables 10.41-10.46.

Table 10.44: Projected changes in AM mean 10m wind speed

AM	Mid-Century (m/s)		End-Century (m/s)	
	Mean	Range	Mean	Range
SSP1-2.6	0.06	-0.02 to 0.13	0.10	0.03 to 0.20
SSP2-4.5	0.04	-0.06 to 0.12	0.10	0.03 to 0.18
SSP5-8.5	0.05	-0.05 to 0.10	0.25	0.16 to 0.32

Table 10.45: Projected changes in ON mean 10m wind speed

ON	Mid-Century (m/s)		End-Century (m/s)	
	Mean	Range	Mean	Range

SSP1-2.6	0.02	-0.16 to 0.11	0.0	-0.06 to 0.04
SSP2-4.5	0.05	-0.11 to 0.10	0.01	-0.19 to 0.09
SSP5-8.5	0.02	-0.20 to 0.18	0.16	-0.13 to 0.31

Table 10.46: Projected changes in JJAS mean 10m wind speed

JJAS	Mid-Century (m/s)		End-Century (m/s)	
	Mean	Range	Mean	Range
SSP1-2.6	0.16	0.03 to 0.27	0.14	0.05 to 0.27
SSP2-4.5	0.17	0.03 to 0.28	0.26	0.10 to 0.44
SSP5-8.5	0.19	0.03 to 0.34	0.49	0.36 to 0.72

10.9 Changes in Wind Gusts

In this section, we present the projected changes in daily maximum wind gust under warming. Strong wind gusts are often associated with thunderstorms and squall lines and can potentially cause substantial damage to Singapore's infrastructure (buildings and roads), uprooting of trees, and threat to the safety of human beings. While in V2, due to the use of a coarser spatial resolution model (12km grid size), thunderstorms and squall lines could not be simulated well. Hence, wind gust changes were projected using a single model run at 1.5km resolution for the last decade of the 21st century for the RCP8.5 scenario. In V3 there is a significant improvement in the simulation of the processes causing strong wind gusts due to the use of an advanced numerical model (SINGV-RCM) and higher resolution (2km), and we have more confidence in the wind gust projections.

Figure 10.16 shows the spatial distribution of multi-model mean of the percentages changes in the wind gust speed in the mid- and end-century from the 2 km simulations under SSP5-8.5. It can be seen from the figure that the increase in mid-century is less than 3%, and that during the end-century is less than 10%. This is consistent with the projections from V2 that showed a future end-century increase under RCP8.5 by 5-10%.

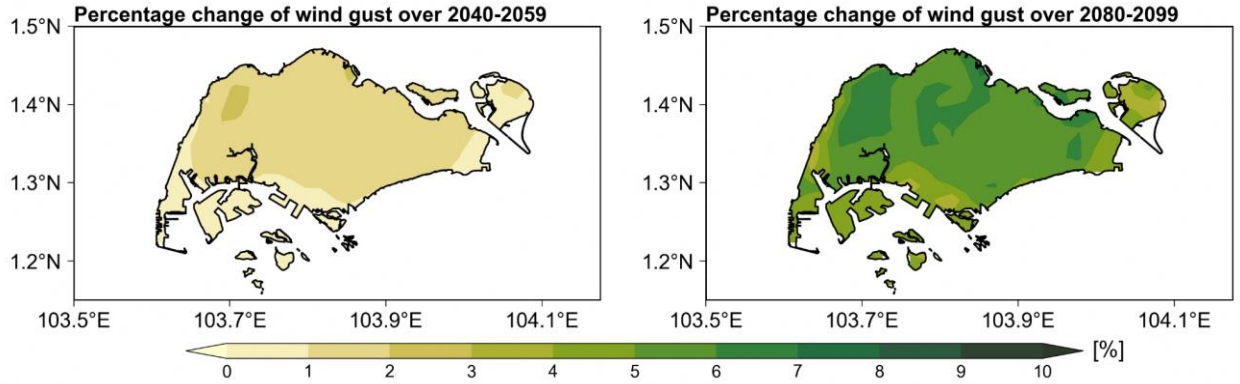

Figure 10.16: Ensemble mean (5 bias-adjusted 2km downscaled GCMs) percentage change in wind gust (10m daily maximum wind speed) during mid- (2040–2059) and end-century (2080–2099) relative to the baseline (1995–2014) over Singapore under SSP5-8.5 scenario.

10.10 Comparison of 2km and 8km Projections

In this section we compare the projections of rainfall and temperature over Singapore from the

bias-adjusted 8km and 2km downscaled simulations. For brevity, we present results only for temperature and rainfall and for the SSP5-8.5 scenario.

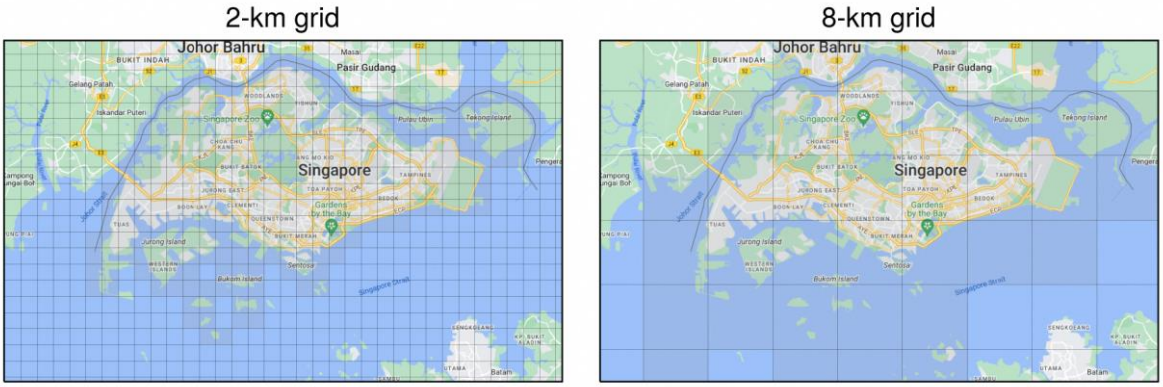

Figure 10.17: The two SINGV-RCM grids over the Singapore region. (Left) 2-km grid. (Right) 8-km grid.

While we are making this comparison only over Singapore (25 grid points in the 8km model and 286 grid points in the 2km model), results over the broader region could be more similar due to the fact that the 8km model provides the driving conditions and hence large-scale constraints for the 2km simulations. Also, the 2km simulations can better resolve some of the local climate drivers such as squall lines, thunderstorms, and land-sea breeze circulation, so we would expect improved rainfall projections, especially extremes.

The multi-model annual and seasonal mean rainfall and temperature projections over Singapore using 2 km and 8 km downscaled GCM simulations during the end century under SSP5-8.5 scenario were analysed (figures in Appendix A). It was found that the 2 km and 8 km projections largely agree both in magnitude and spatial pattern, although one may find small local variations and higher spatial granularity in the 2 km simulations due to the higher resolution. Although the local variations may appear small, aggregated together in space they could lead to larger differences between the 8 km and the 2 km projections. For example, as can be seen in Fig A10.3, the percentage change in 99.9th percentile projected in the 8 km simulations is ~10% whereas that in the 2 km projections is ~40%.

10.11 Summary

This chapter uses bias-adjusted projections of 6 CMIP6 GCMs downscaled by SINGV-RCM to examine climate change over Singapore. The results are presented for both annual and seasonal scales, using periods corresponding to Singapore's monsoon and intermonsoon seasons. Changes in rainfall, temperature, wet bulb globe temperature as a measure of what stress, relative humidity, and near-surface winds and wind gusts are presented.

Multi-model annual mean rainfall is projected to remain the same or increase by the end of the century over Singapore (11% across scenarios), although there are individual models that project reductions in rainfall. Similar to the regional case, the changes in annual means are not uniformly distributed over seasons. In the case of SSP5-8.5, by the end-century, there are signs of greater contrasts between the wet (e.g. Dec-Jan), and dry (e.g. Feb-Mar, Jun-Sep), or a 'wet-get-wetter' and 'dry-get-drier' type behavior.

In the end of the century under SSP5-8.5, there are generally increases in precipitation extremes as measured by annual maximum 1-day and 5-day precipitation (RX1day and RX5day) of up to 50% across different seasons. The main exception is Feb-Mar, where large parts of Singapore show a decrease in both RX1day and RX5day. Models project an increase across seasons in the 99.9th percentile of rainfall in both mid-century and end-century in SSP5-8.5. The multi-model mean length of dry spells (measured by consecutive dry days) increases in all

scenarios in both the mid-century and end-century periods.

Annual mean near-surface air temperatures are projected to increase in a range of 0.6-5.0^{o}C by the end of the century under SSP5-8.5. Models robustly agree on an increase in temperature across all seasons, with all seasons showing similar increases in temperature. Annual mean daily maximum temperatures are also projected to increase across models, with a range of 0.5-5.3^{o}C. Annual average daily mean wet-bulb globe temperature is projected to increase in the range of 0.5-4.3^{o}C. There is also a decrease in multi-model mean near-surface relative humidity. The reduction in relative humidity has a compensating effect on enhanced heat stress under warming.

No major changes are expected in wind-related variables. Changes in near-surface winds are generally small (within 1 m/s). By the end of the century, the multi-model mean winds are expected to increase in all seasons under SSP5-8.5. Changes in wind gusts are expected to be within 10% under SSP5-8.5, even up till the end of the century.

A discussion of the comparison of the 2km and 8km simulations indicate that the spatial pattern simulated by the model at the two resolutions are broadly similar, but the differences can lead to noticeable differences in domain-wide statistics. In this case, we would tend to trust the 2km model, which at a higher resolution is better able to resolve key physical processes which drive and organize convection.

In summary, the models predict increases in temperature and heat stress over Singapore, together with greater variability of rainfall and rainfall extremes. This includes greater occurrences and duration of drought conditions, as well as increases in extreme rainfall.

References

WHO (2020) https://www.who.int/news-room/fact-sheets/detail/climate-change-heat-and-health

Bui, H. X., Li, Y.-X., Maloney, E. D., Kim, J.-E., Lee, S.-S., & Yu, J.-Y. (2023). Emergence of Madden-Julian oscillation precipitation and wind amplitude changes in a warming climate. *Npj Climate and Atmospheric Science*, *6*(1), 1–6. https://doi.org/10.1038/s41612-023-00344-z

Byrne, M. P., & Schneider, T. (2016). Narrowing of the ITCZ in a warming climate: Physical mechanisms. *Geophysical Research Letters*, *43*(21), 11,350-11,357. https://doi.org/10.1002/2016GL070396

Cai, W., Borlace, S., Lengaigne, M., van Rensch, P., Collins, M., Vecchi, G., et al. (2014). Increasing frequency of extreme El Niño events due to greenhouse warming. *Nature Climate Change*, *4*(2), 111–116. https://doi.org/10.1038/nclimate2100

Cai, W., Santoso, A., Collins, M., Dewitte, B., Karamperidou, C., Kug, J.-S., et al. (2021). Changing El Niño–Southern Oscillation in a warming climate. *Nature Reviews Earth & Environment*, 1–17. https://doi.org/10.1038/s43017-021-00199-z

Chen, C., Sahany, S., Moise, A. F., Chua, X. R., Hassim, M. E., Lim, G., & Prasanna, V. (2023). ENSO-rainfall teleconnection over the Maritime Continent enhances and shifts eastward under warming. *Journal of Climate*, *1*(aop), 1–55. https://doi.org/10.1175/JCLI-D-23-0036.1

Geng, T., Cai, W., Wu, L., Santoso, A., Wang, G., Jing, Z., et al. (2022). Emergence of changing Central-Pacific and Eastern-Pacific El Niño-Southern Oscillation in a warming climate. *Nature Communications*, *13*(1), 6616. https://doi.org/10.1038/s41467-022-33930-5

Ghosh, R., & Shepherd, T. G. (2023). Storylines of Maritime Continent dry period precipitation changes under global warming. *Environmental Research Letters*, *18*(3), 034017. https://doi.org/10.1088/1748-9326/acb788

James C. Liljegren, Richard A. Carhart, Philip Lawday, Stephen Tschopp & Robert Sharp (2008). Modeling the Wet Bulb Globe Temperature Using Standard Meteorological Measurements. *Journal of Occupational and Environmental Hygiene*, 5:10, 645-655, https://doi.org/10.1080/15459620802310770

Johnson, N. C., Amaya, D. J., Ding, Q., Kosaka, Y., Tokinaga, H., & Xie, S.-P. (2020). Multidecadal modulations of key metrics of global climate change. *Global and Planetary Change*, *188*, 103149. https://doi.org/10.1016/j.gloplacha.2020.103149

Lange, S. (2019). Trend-preserving bias adjustment and statistical downscaling with ISIMIP3BASD (v1.0). Geoscientific Model Development, 12(7), 3055–3070. https://doi.org/10.5194/gmd-12-3055-2019

Liang, J., Catto, J. L., Hawcroft, M., Hodges, K. I., Tan, M. L., & Haywood, J. M. (2021). Climatology of Borneo Vortices in the HadGEM3-GC3.1 General Circulation Model. *Journal of Climate*, *34*(9), 3401–3419. https://doi.org/10.1175/JCLI-D-20-0604.1

Liang, J., Tan, M. L., Catto, J. L., Hawcroft, M. K., Hodges, K. I., & Haywood, J. M. (2022). Projected near-term changes in monsoon precipitation over Peninsular Malaysia in the HighResMIP multi-model ensembles. *Climate Dynamics*. https://doi.org/10.1007/s00382-022-06363-5

Appendix A - Comparison of Rainfall and Temperature Changes in the 8km and 2km projections

Rainfall

Figure A10.1 shows the spatial mean projections of daily mean and extreme rainfall percentiles over Singapore in the mid and end century on annual and seasonal time scales.

For the Dec-Jan months, the mid-century projections of mean rainfall show an increase of 17% and extreme rainfall percentiles increase with a range of (12-40%). In the end century, the daily mean rainfall projections show an increase of 10% and extreme rainfall increase with a range of (11-35%). During the Feb-Mar months, in the mid-century the mean rainfall increases by 25% and extreme rainfall shows an increasing trend with a range of (0-38%). In the end century, the projections of the mean rainfall shows neutral changes and extreme rainfall varies with a range of (-20-15%).

During the Apr-May months, the projections of daily mean rainfall increases by 5% and extreme rainfall rises with a range of (3-20%). In the end century, the mean rainfall increases by 17% and extreme rainfall increases with a range of 0-50%. For the Jun-Sep period, the mid-century projections of the mean show an increase of 5% and extreme rainfall varies with a range of (-4-30%). In the end century, mean rainfall increases by 15% and extreme rainfall projections vary with a range of (-4 to 26%).

During the Oct-Nov months, in the mid-century mean rainfall increases by 9% and extreme rainfall increases with a range of (5-26%). Over the end century, mean rainfall rises by 14% and extreme rainfall enhances with a range of (5-60%). These results suggest that there are variations in the projections of the daily mean and extreme rainfall of Singapore in the mid-century and the end century across annual and monthly timescales.

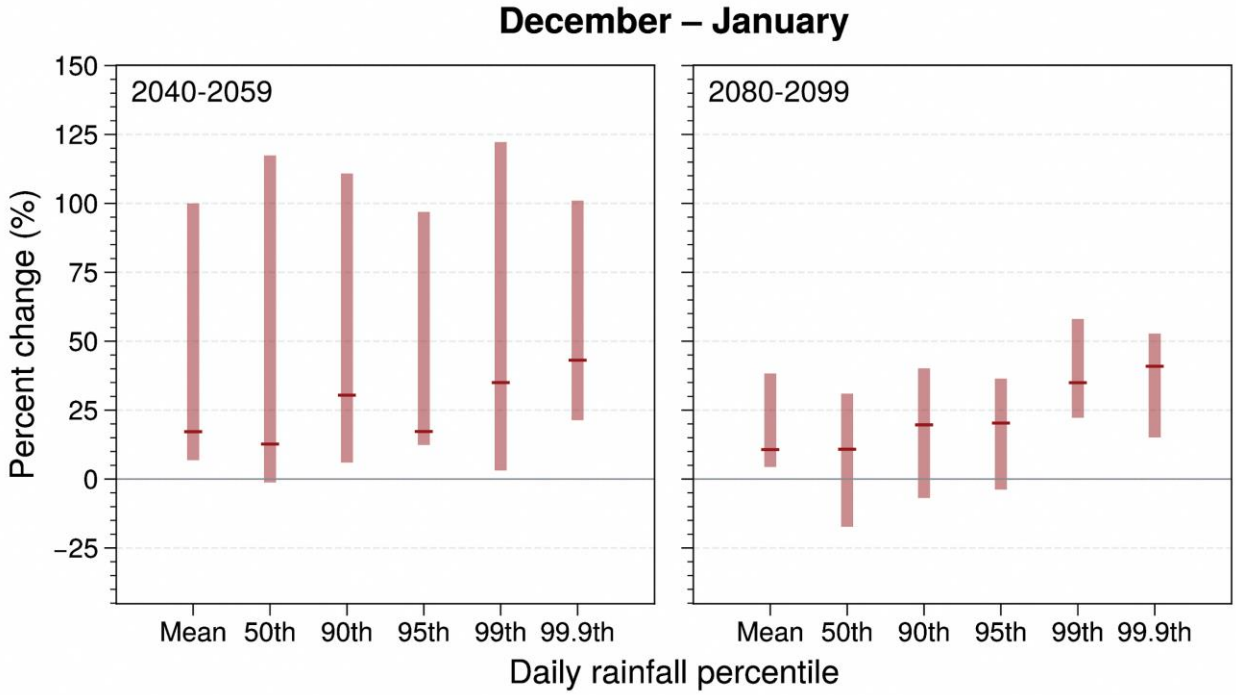

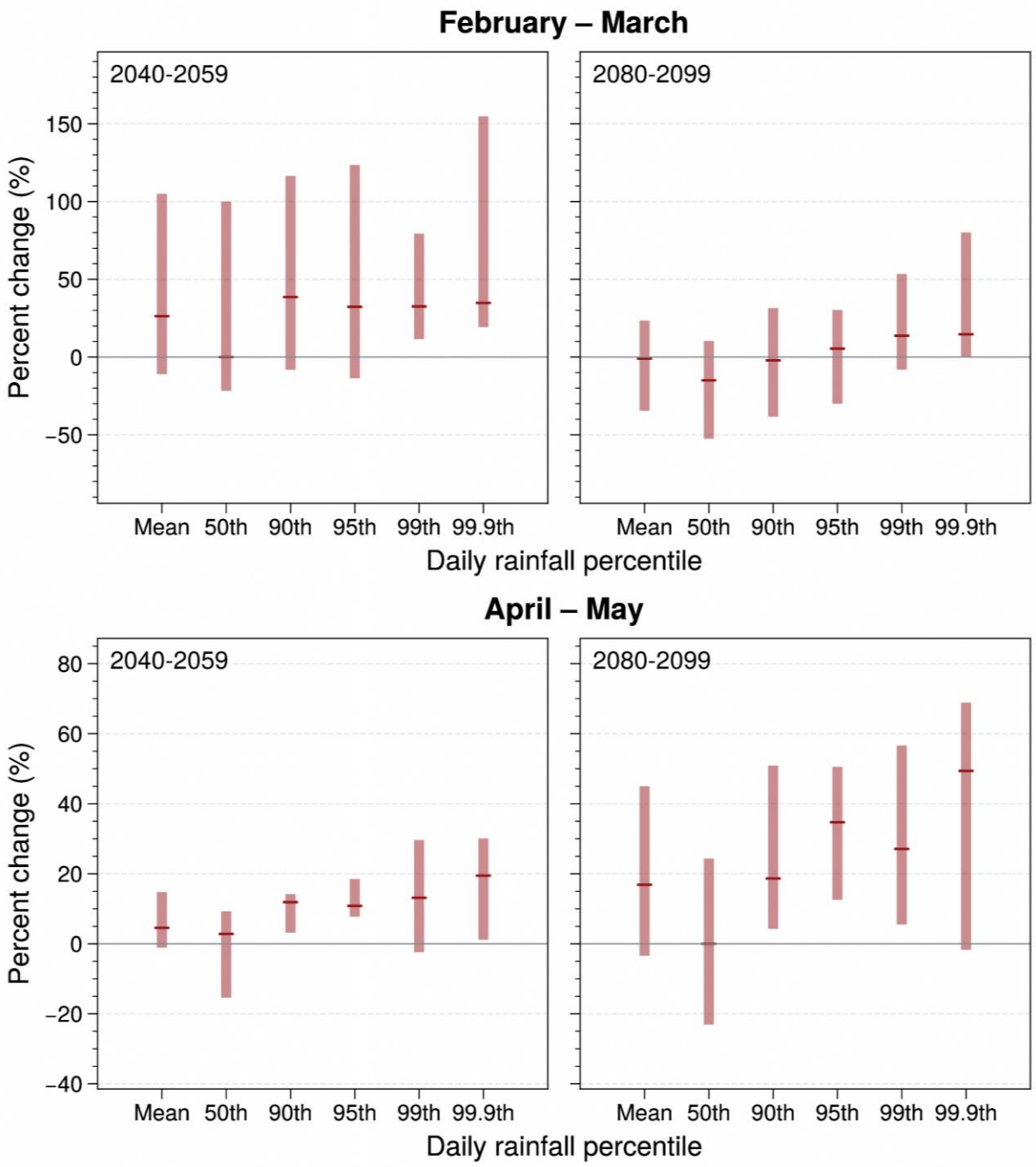
February – March
2040-2059
2080-2099
Percent change (%)
150
100
50
0
−50
Mean
50th
90th
95th
99th
99.9th
Daily rainfall percentile
April – May
2040-2059
2080-2099
Percent change (%)
80
60
40
20
0
−20
−40
Mean
50th
90th
95th
99th
99.9th
Daily rainfall percentile

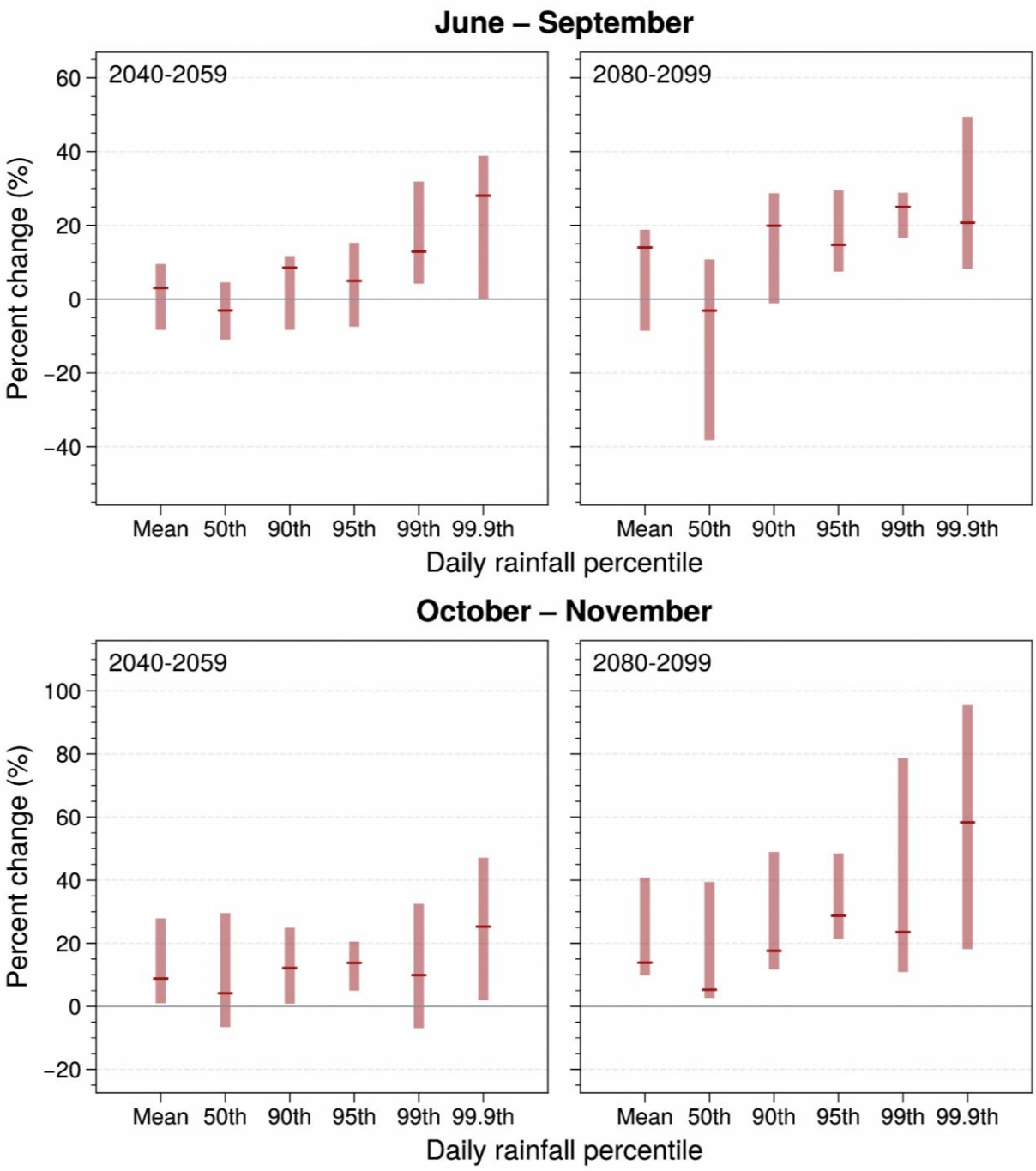

Figure A10.1: Range of percentage changes in mean and extreme daily rainfall percentile amounts for various seasons (December-January, wet NE monsoon; February-March, dry NE monsoon; April-May, first intermonsoon; June-September; SW monsoon) from the 2-km SINGV-RCM simulations over Singapore. The median value in the range of percentage changes for each percentile is denoted by the dark red horizontal line. Rainfall percentiles are based on wet days only (defined as any day when rainfall >= 1mm/day); each percentile uses the nearest corresponding daily rainfall value.

As seen in Figure A10.2 the mean and extremes are projected to rise in the mid-century but with a higher magnitude in the end century.

Temperature

For the Dec-Jan months, the daily maximum mean temperatures are expected to increase by 1.4 degrees and extremes increase with a range of 1.3 to 1.7 degrees in the mid century. In the end century, the mean daily maximum

temperatures are projected to increase by 3.6 degrees and extremes increase with a range of 3.6 to 4.4 degrees. During Feb-Mar months, in the mid-century the mean daily maximum temperatures are projected to increase by 1.5 degrees and extremes increase with a range of 1.4 to 1.8 degrees. In the end century, the mean temperatures are projected to increase by 3.5 degrees and extremes increase with a range of 3.5 to 4.2 degrees.

During the Apr-May months, the mean temperatures are expected to increase by 1.6 degrees and extremes increase with a range of 1.6 to 1.8 degrees. In the end century the mean temperatures are projected to rise by 3.6 degrees and extremes increase with a range of 3.6 to 4.1 degrees. For the Jun-Sep period, in the mid-century the mean temperatures are expected to rise by 1.6 degrees and extremes increase with a range of 1.5 to 1.7 degrees. In the end century, the mean temperatures projected to increase by 4.1 degrees and extremes increase with a range 4.1 to 4.4 degrees.

During the Oct-Nov months, in the mid-century the mean temperatures are projected to increase by 1.6 degrees and extremes increase with a range of 1.5 to 1.9 degrees. In the end century, the mean temperatures are expected to rise by 4 degrees and extremes increase with a range of 4.0 to 4.5 degrees.

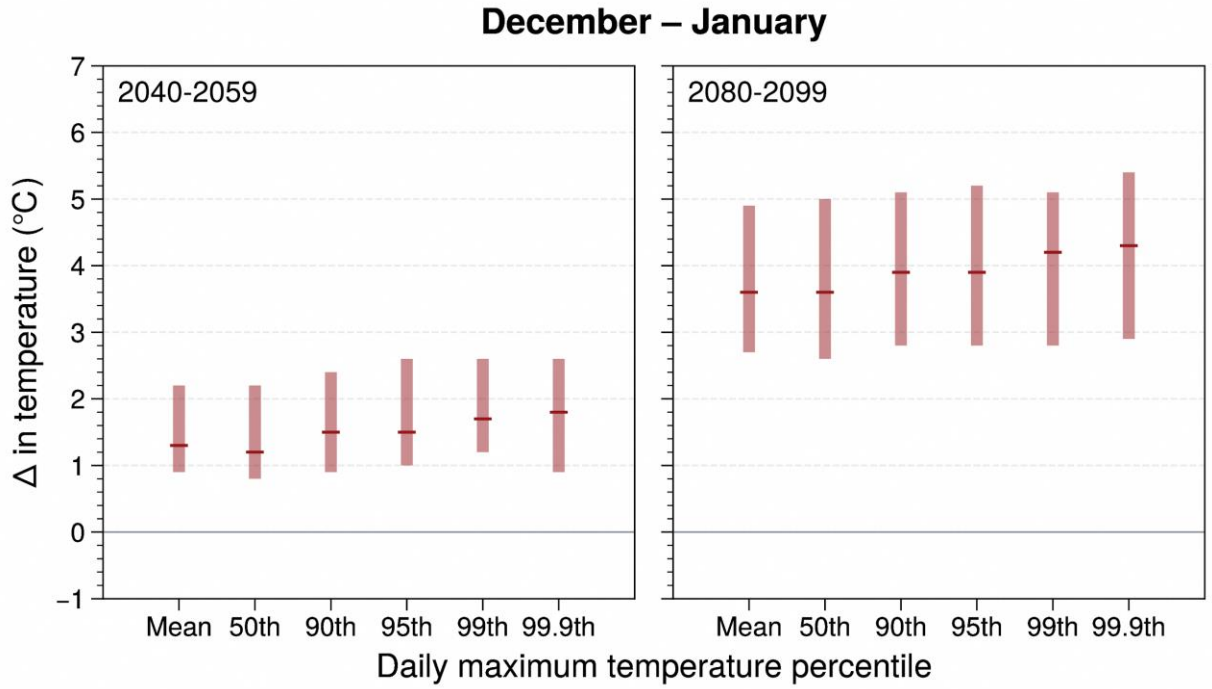

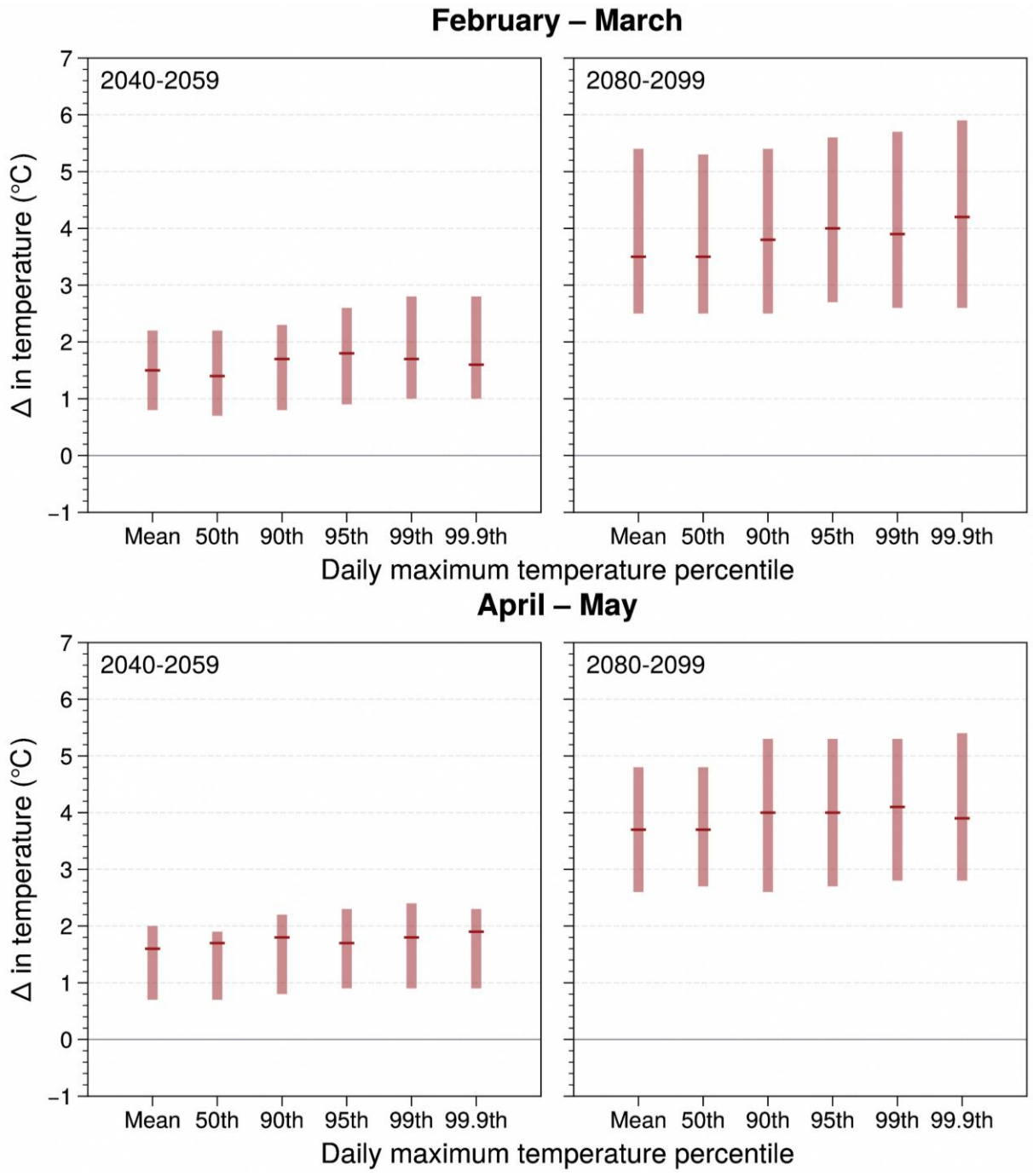
February – March
2040-2059
2080-2099
Δ in temperature (°C)
7
6
5
4
3
2
1
0
−1
Mean
50th
90th
95th
99th
99.9th
Daily maximum temperature percentile
April – May
2040-2059
2080-2099
Δ in temperature (°C)
Mean
50th
90th
95th
99th
99.9th
Daily maximum temperature percentile

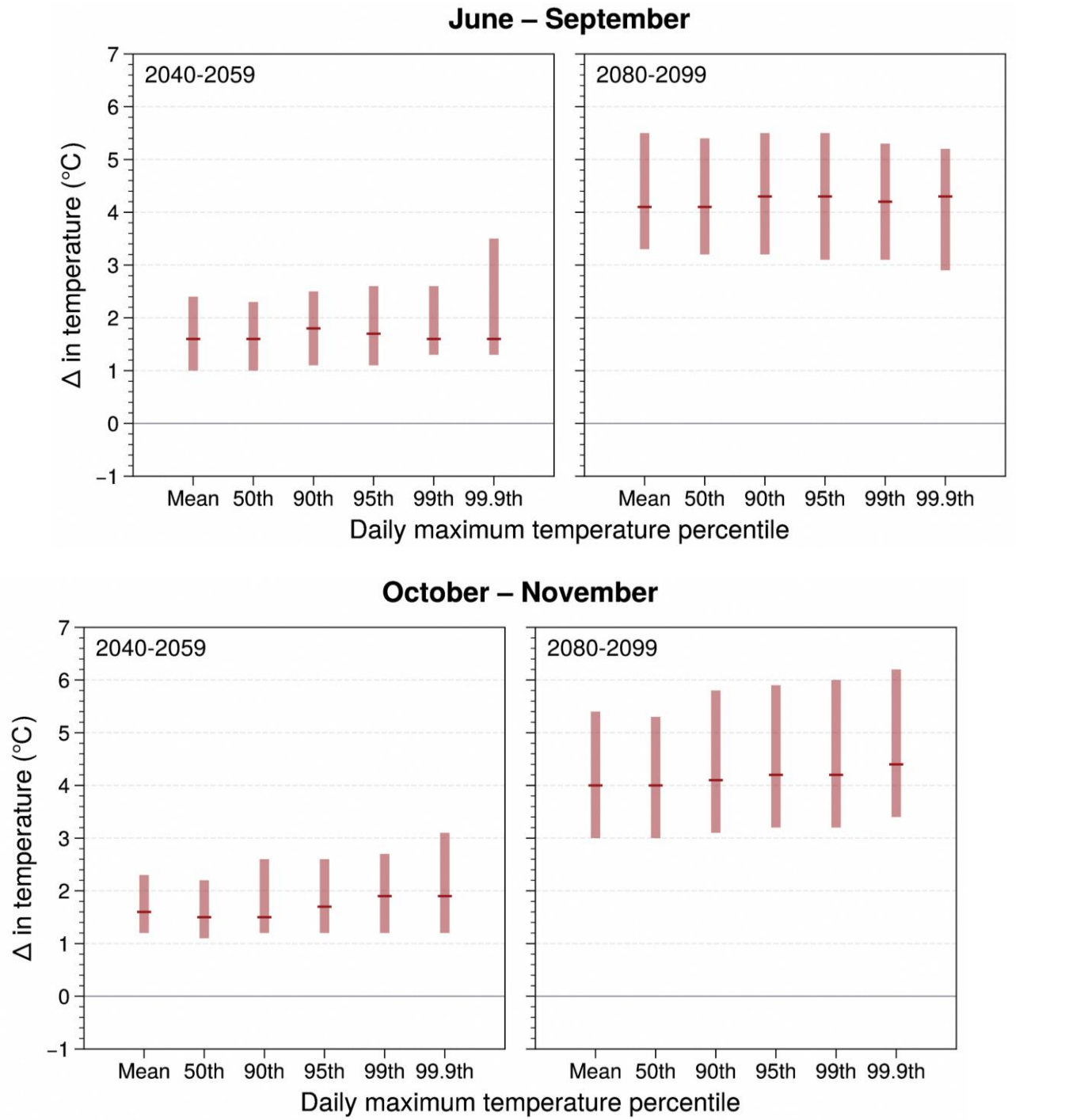

Figure A10.2: Range of changes in mean and extreme daily maximum temperature percentile amounts for various seasons (December-January, wet NE monsoon; February-March, dry NE monsoon; April-May, first intermonsoon; June-September; SW monsoon) from the 2-km SINGV-RCM simulations over Singapore. The median value in the range of percentage changes for each percentile is denoted by the dark red horizontal line. Each percentile uses the nearest corresponding daily maximum temperature value.

Figure A10.3 shows the projected changes of daily mean and extreme rainfall percentiles for Dec-Jan months over Singapore using 2 km and 8 km downscaled simulations in mid-century and end century. In a 2km simulation, the mid-century's mean rainfall increased by 18% and extreme rainfall increased in the range of 15-35%. The mid-century mean rainfall from 8 km

simulation increased by 8% and extreme rainfall increased in the range of 3-20%. According to a 2 km simulation, the average rainfall increased by 10% at the end of the century, while extreme rainfall increased by 10% to 40%. In the end century from the 8 km simulations, the mean rainfall increased by 3% and extreme rainfall varied in the range of -18 to 22%. During Dec-Jan months, the 2 km simulation had higher percentage increases in the mid and end century mean and extreme rainfall than the 8 km simulation.

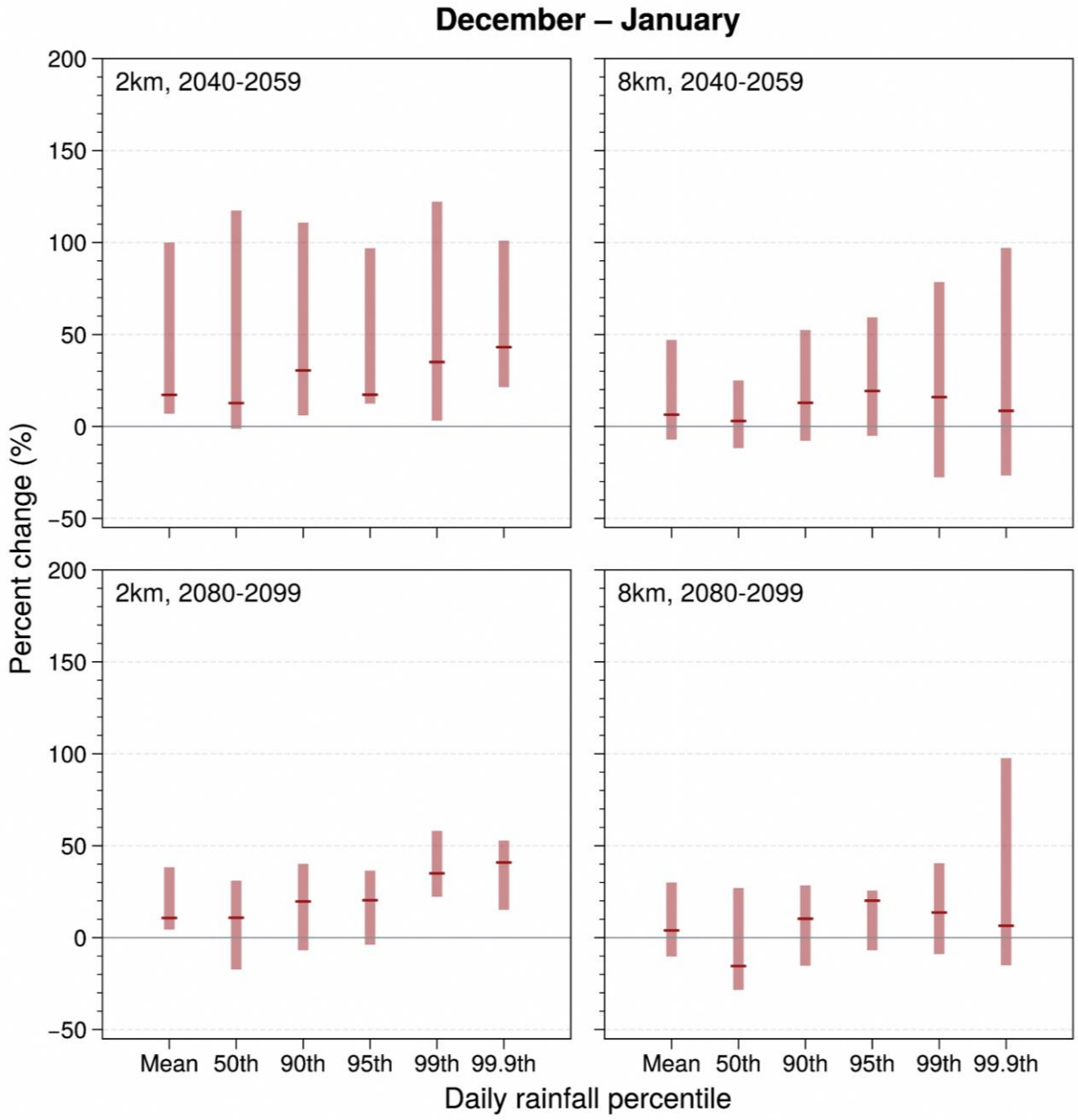

Fig A10.3: Changes in Singapore average daily rainfall amount during December - January (wet phase of NE monsoon) for the mid-century (2040-2059; top row) and end-century (2080-2099; bottom row) periods from SINGV-RCM downscaled simulations at 2-km (left) and 8-km (right). Shown are the percentage changes in the mean and at different percentiles (50th, 90th, 95th, 99th and 99.9th) under the SSP5-8.5 scenario. The mean and percentile values are derived only from wet days (rainfall >= 1mm/day); each percentile uses the nearest corresponding daily rainfall value.

Figure A10.4 shows the projected changes of daily mean and extreme rainfall percentiles for Feb-Mar months over Singapore using 2km and 8km downscaled simulations in mid-century and end century. In the mid-century, the 2km simulation showed that mean rainfall increased by 25% and extreme rainfall increased in the range of 0-38%. In the 8 km simulation, the mid-century's mean rainfall increased by 25% and extreme rainfall increased in the range of 5-45%. In the end century, the mean rainfall remained neutral and extreme rainfall varied in the range of -18 to 17% from 2 km simulation. The mean rainfall in the end century from the 8 km simulations remained unchanged whereas extreme rainfall varied in the range of -18 to 25%. The 2 km and 8 km simulation's mean and extreme rainfall projections often vary by almost the same amount for the months of February and March.

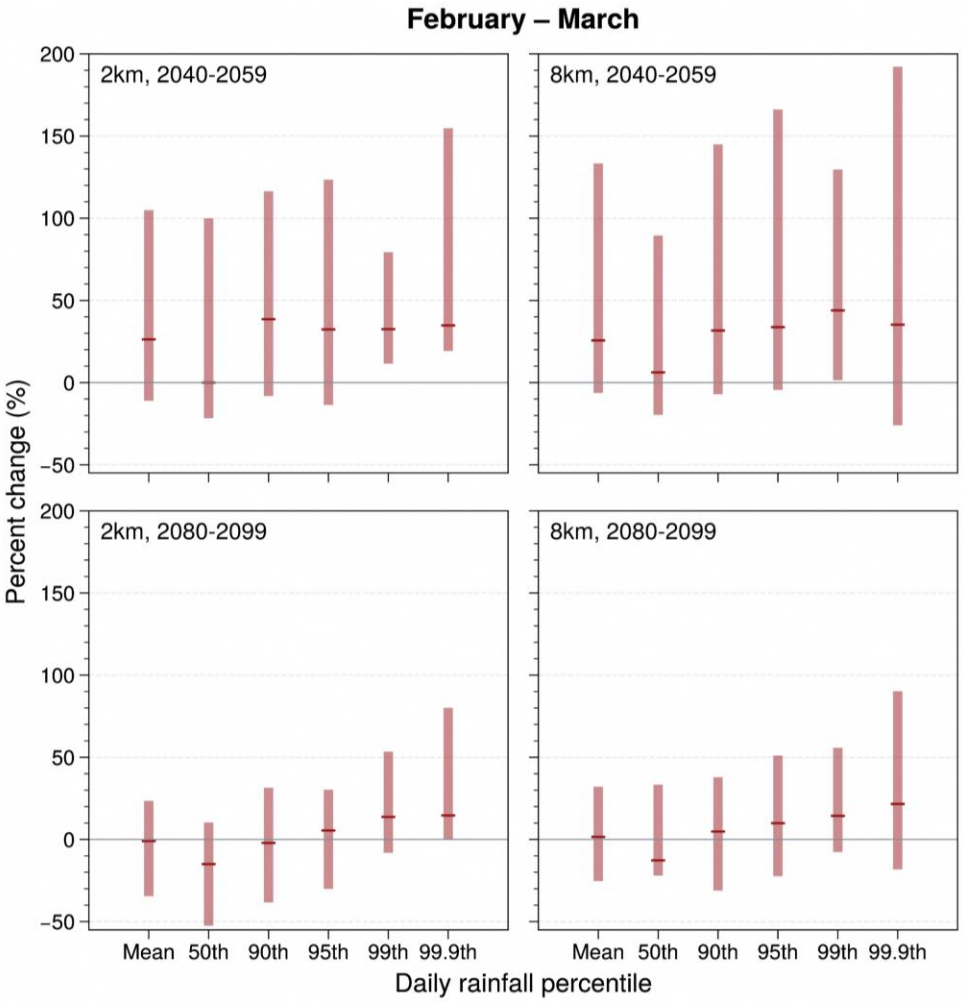

Figure A10.4: As in Figure A10.3 but for February - March (Dry phase of NE monsoon).

Figure A10.5 shows the projected changes of daily mean and extreme rainfall percentiles for Apr-May months over Singapore using 2 km and 8 km downscaled simulations in mid-century and end century. In a 2km simulation, the mid-century's mean rainfall increased by 5% and extreme rainfall increased in the range of 4-20%. The mid-century mean rainfall from 8 km simulation increased by 5% and extreme rainfall increased in the range of 0-15%. According to a 2 km simulation, the average rainfall increased by 18% at the end of the century, while extreme rainfall increased by 0- 50%. In the end century from the 8 km simulations, the mean rainfall increased by 15% and extreme rainfall increased in the range of 0 to 25%. During Apr-May months,

the 2 km simulation had higher percentage increases in the mid and end century extreme rainfall than the 8 km simulation.

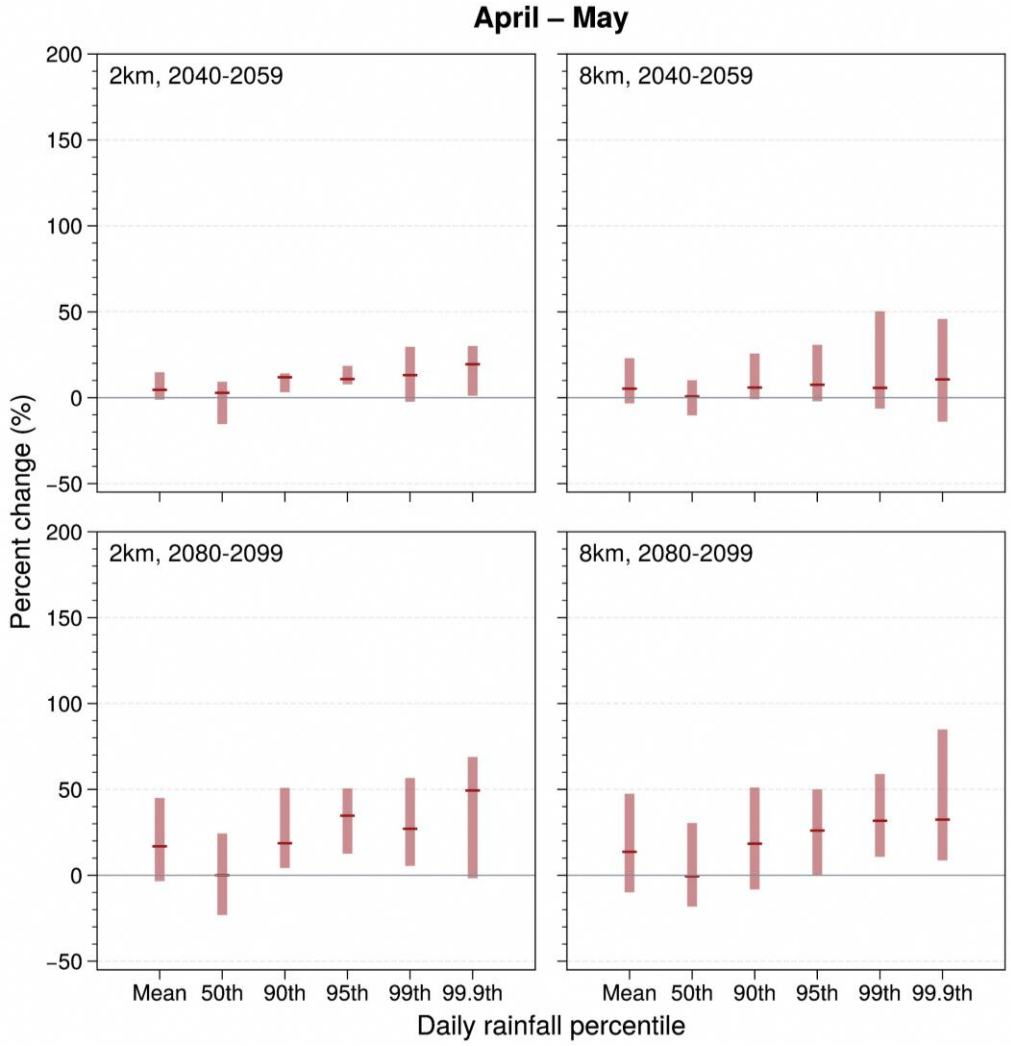

Figure A10.5: As in Figure A10.3 but for April-May

Figure A10.6 shows the projected changes of daily mean and extreme rainfall percentiles for Jun-Sep period over Singapore using 2km and 8km downscaled simulations in mid-century and end century. In the mid-century, the 2km simulation showed that mean rainfall increased by 2% and extreme rainfall varied in the range of -2 to 30%. In the 8 km simulation, the mid-century's mean rainfall increased by 1% and extreme rainfall varied in the range of -2 to 15%. In the end century, the mean rainfall increased by 15% and extreme rainfall varied in the range of -2 to 25% from 2 km simulation. The mean rainfall in the end century from the 8 km simulations increased by 13% whereas extreme rainfall varied in the range of 0 to 20%. Similar to the Apr-May months, the 2 km simulation has higher percentage changes in the extreme rainfall than the 8 km simulation.

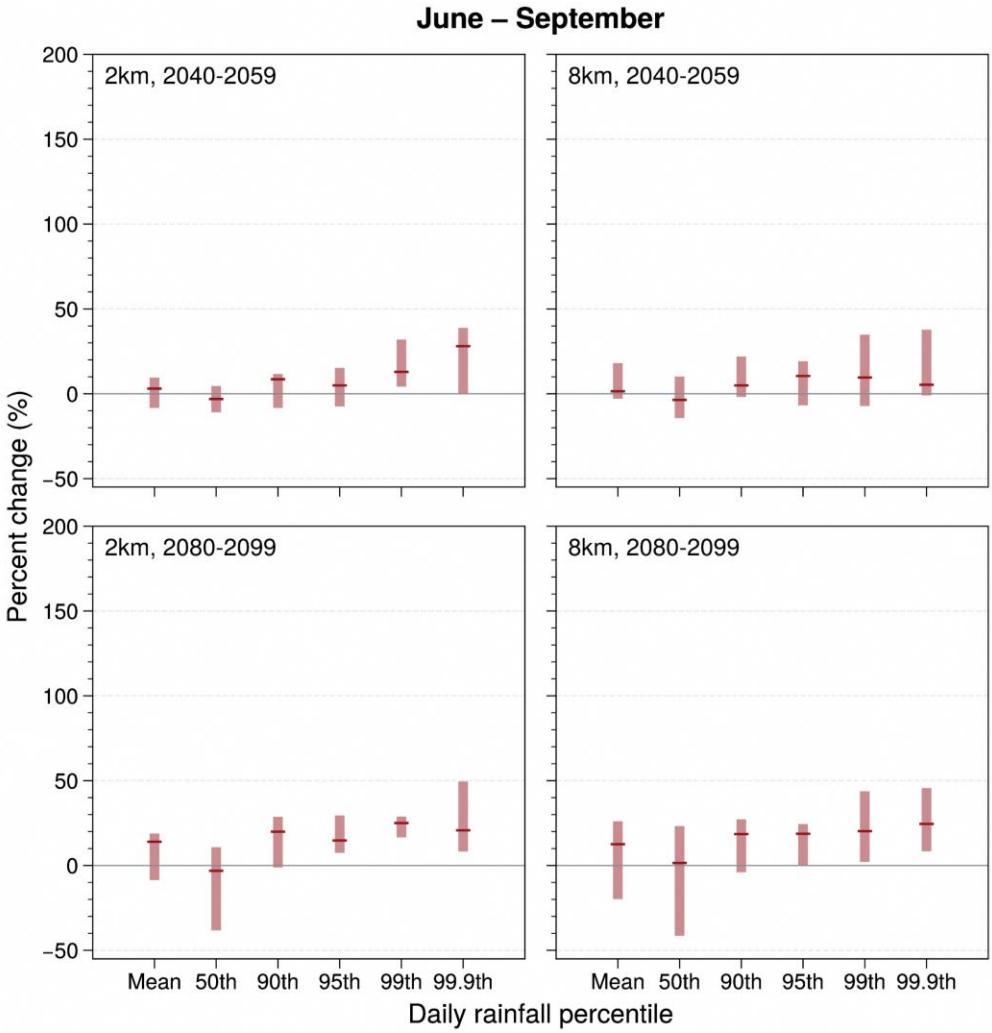

Figure A10.6: As in Figure A10.3 but for June - September (SW monsoon period).

Figure A10.7 shows the projected changes of daily mean and extreme rainfall percentiles for Oct-Nov months over Singapore using 2 km and 8 km downscaled simulations in mid-century and end century. In a 2km simulation, the mid-century's mean rainfall increased by 10% and extreme rainfall increased in the range of 5-25%. The mid-century mean rainfall from 8 km simulation increased by 17% and extreme rainfall increased in the range of 15-25%. According to a 2 km simulation, the average rainfall increased by 15% at the end of the century, while extreme rainfall increased by 5- 60%. In the end century from the 8 km simulations, the mean rainfall increased by 22% and extreme rainfall increased in the range of 10 to 55%. In contrast to the other months, in Oct-Nov months the 8 km simulation had higher percentage changes in the mean and extreme rainfall.

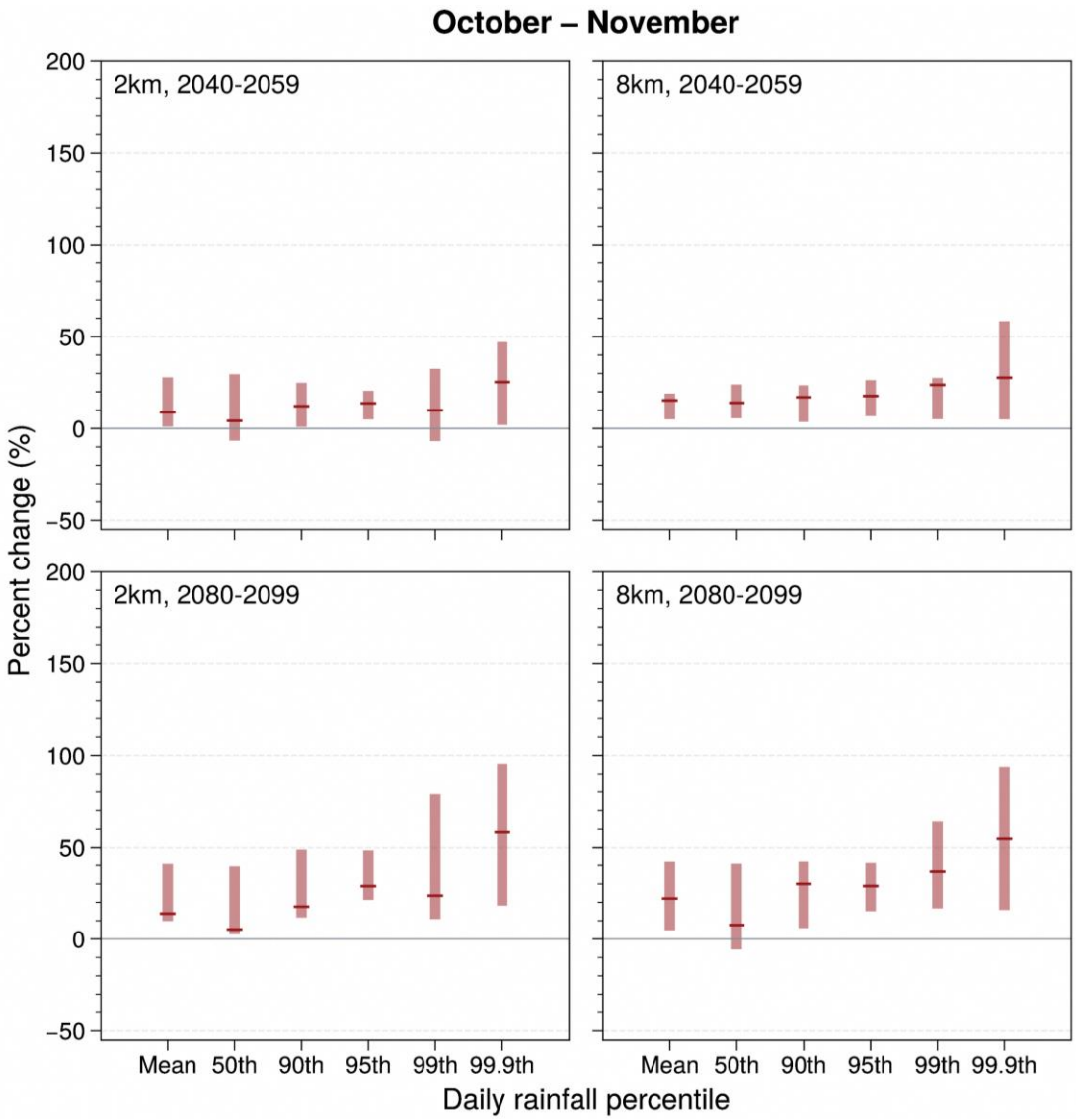

Figure A10.7: As in Figure A10.3 but for October-November (2nd intermonsoon)

Temperature

Figure A10.8 shows the projected changes of daily mean and extreme temperature percentiles for Dec-Jan months over Singapore using 2km and 8km downscaled simulations in mid-century and end century. In the mid-century, the 2km simulation showed that mean temperature is projected to increase by 1.3°C and extreme temperatures could increase in the range of 1.2°C to 1.7°C. In the 8 km simulations, in the mid-century the mean temperature is projected to increase by 1.4°C and extreme temperature is projected to increase in the range of 1.4°C to 1.7°C. In the end century, for the 2 km simulation the mean temperature is projected to increase by 3.6°C and extreme temperature is projected to increase in the range of 3.6°C to 4.3°C. The mean temperature in the end century from the 8 km simulations is projected to increase by 3.4°C, whereas extreme temperature is projected to increase in the range of 3.4°C to 3.6°C. The mean and extreme temperature variations at the mid-century and end-of-century time frames vary only slightly across 2 km and 8 km simulations.

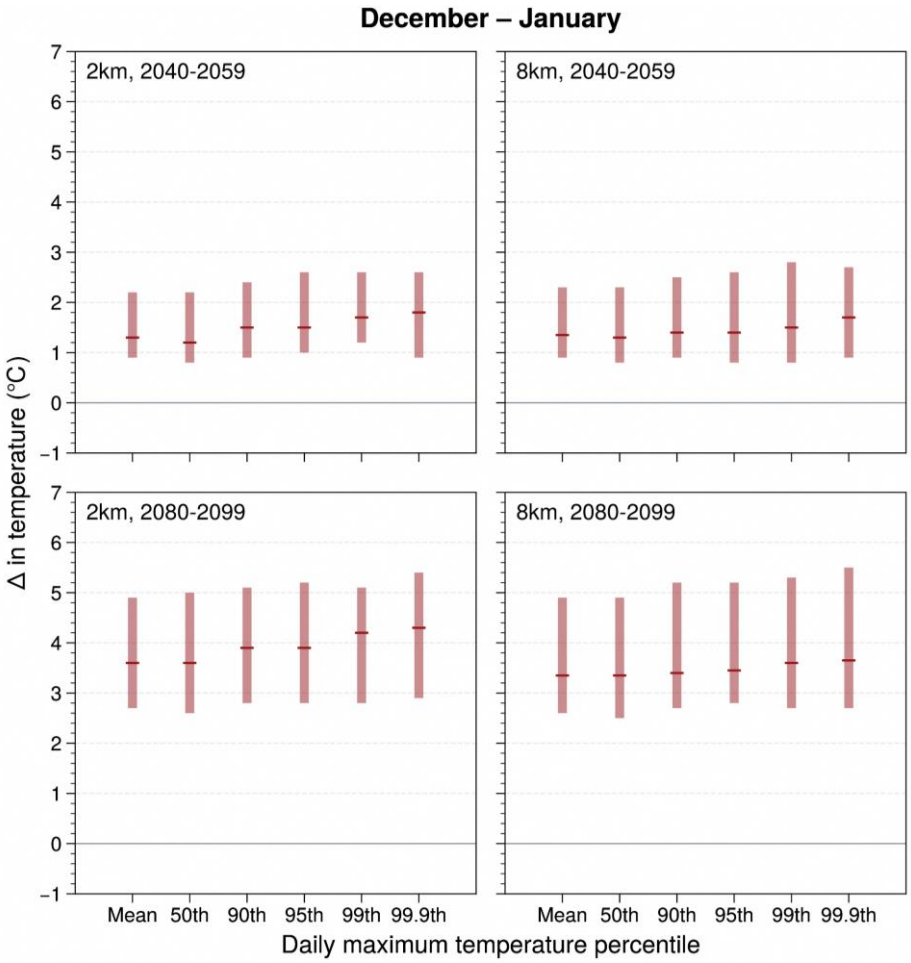

Figure A10.8: Changes in Singapore average daily maximum temperature during December - January (wet phase of NE monsoon) for the mid-century (2040-2059; top row) and end-century (2080-2099; bottom row) periods from SINGV-RCM downscaled simulations at 2-km (left) and 8-km (right). Shown are the percentage changes in the mean and at different percentiles (50th, 90th, 95th, 99th and 99.9th) under the SSP5-8.5 scenario. Each percentile uses the nearest corresponding daily maximum temperature value.

Figure A10.9 shows the projected changes of daily mean and extreme temperature percentiles for Feb-Mar months over Singapore using 2 km and 8 km downscaled simulations in mid-century and end century. In the 2km simulations, the mid-century mean temperature is projected to increase by 1.5^{o}C and extreme temperature is projected to increase in the range of 1.4^{o}C to 1.6^{o}C. The mid-century mean temperature from 8 km simulations is projected to increase by 1.3^{o}C and extreme temperature is projected to increase in the range of 1.3^{o}C to 1.6^{o}C. Based on the 2 km simulations, the mean temperature is projected to increase by 3.5^{o}C at the end of the century, while extreme temperature is projected to increase in the range of 3.5^{o}C - 4.3^{o}C. In the end century, from the 8 km simulations, the mean temperature is projected to increase by 3.4^{o}C and extreme temperature is projected to increase in the range of 3.4^{o}C to 3.8^{o}C.

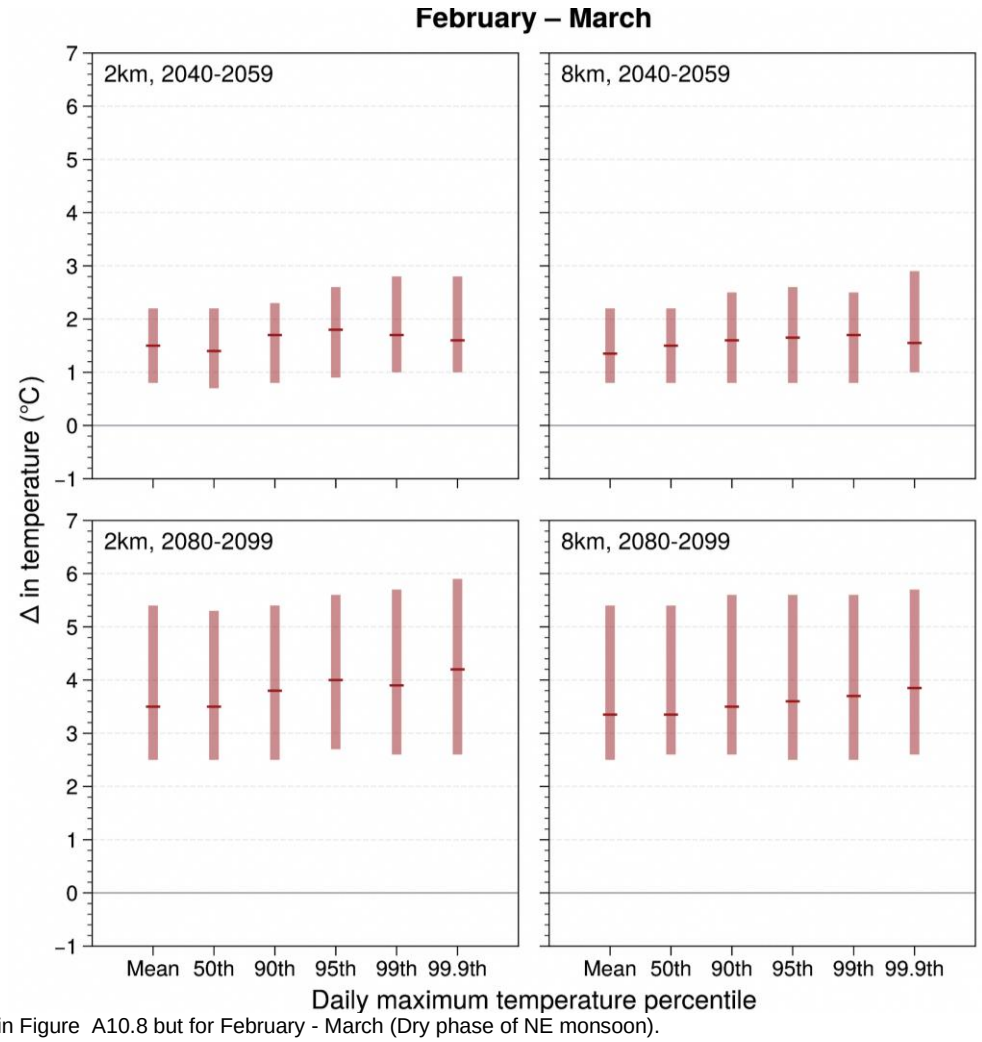

Figure A10.9: As in Figure A10.8 but for February - March (Dry phase of NE monsoon).

Figure A10.10 shows the projected changes of daily mean and extreme temperature percentiles for Apr-May months over Singapore using 2km and 8km downscaled simulations in mid-century and end century. In the mid-century, the 2km simulation showed that mean temperature is projected to increase by 1.3ºC and extreme temperature is projected to increase in the range of 1.2ºC to 1.7ºC. In the 8 km simulation, the mid-century's mean temperature is projected to increase by 1.4ºC and extreme temperature is projected to increase in the range of 1.4ºC to 1.7ºC. In the end century, for the 2 km simulation the mean temperature is projected to increase by 3.6ºC and extreme temperature is projected to increase in the range of 3.6ºC to 4.3ºC. The mean temperature in the end century from the 8 km simulations is projected to increase by 3.4ºC, whereas extreme temperature is projected to increase in the range of 3.4ºC to 3.6ºC.

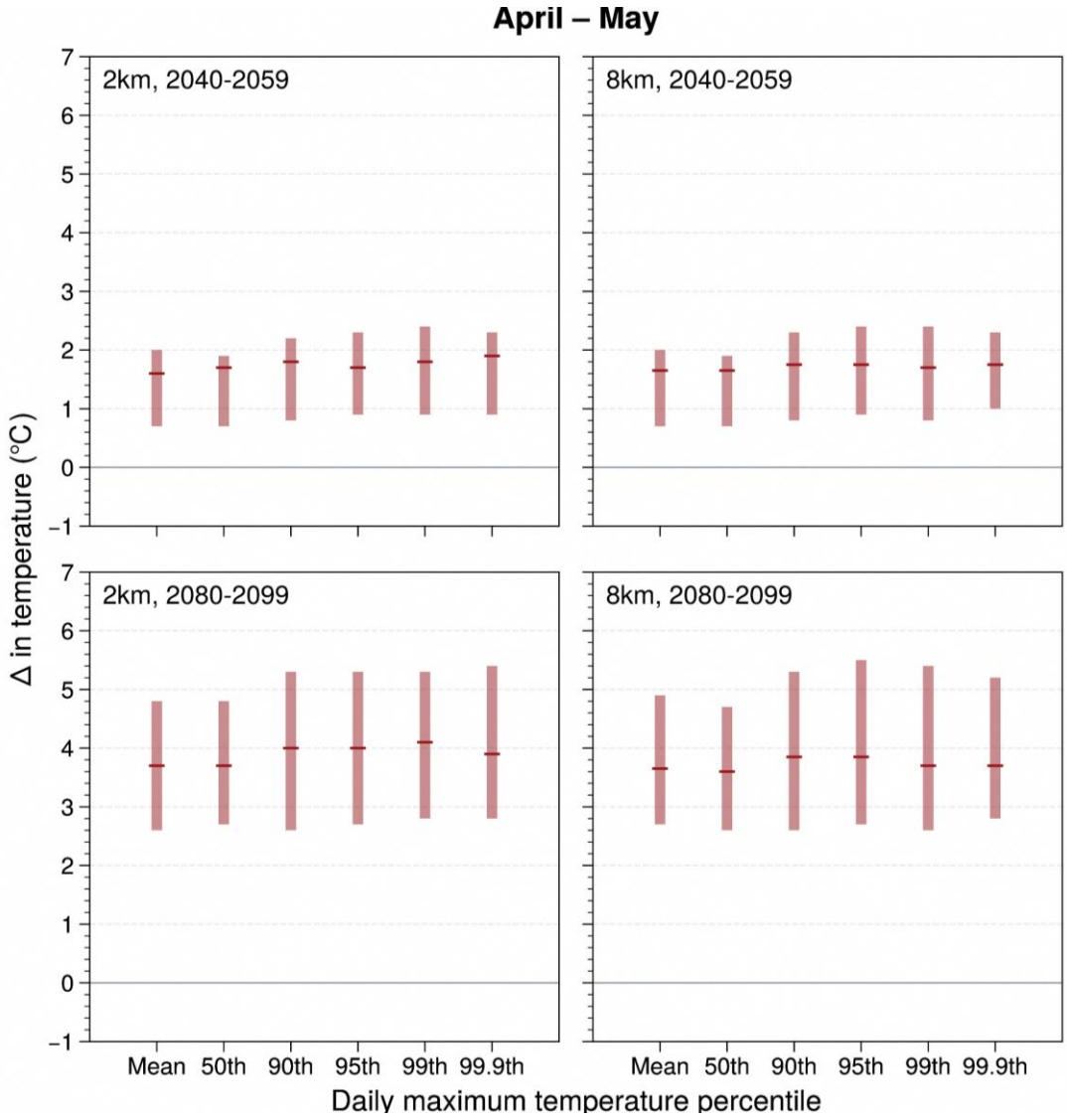

Figure A10.10: As in Figure 10.8 but for April-May

Figure A10.11 shows the projected changes in daily mean and extreme temperature percentiles for Jun-Sep period over Singapore using 2 km and 8 km downscaled simulations during mid-century and end century. Based on 2 km simulations, the mid-century's mean temperature is projected to increase by 1.6ºC and extreme temperature is projected to increase in the range of 1.6ºC to 1.8ºC. The mid-century mean temperature, from 8 km simulations is projected to increase by 1.5ºC and extreme temperature is projected to increase in the range of 1.5ºC to 1.6ºC. Based on 2 km simulations, the mean temperature is projected to increase by 4.1ºC at the end of the century, while extreme temperature is projected to increase in the range of 4.1ºC - 4.4ºC. In the end century, from the 8 km simulations, the mean temperature is projected to increase by 3.7ºC and extreme temperature is projected to increase in the range of 3.7ºC to 3.9ºC.

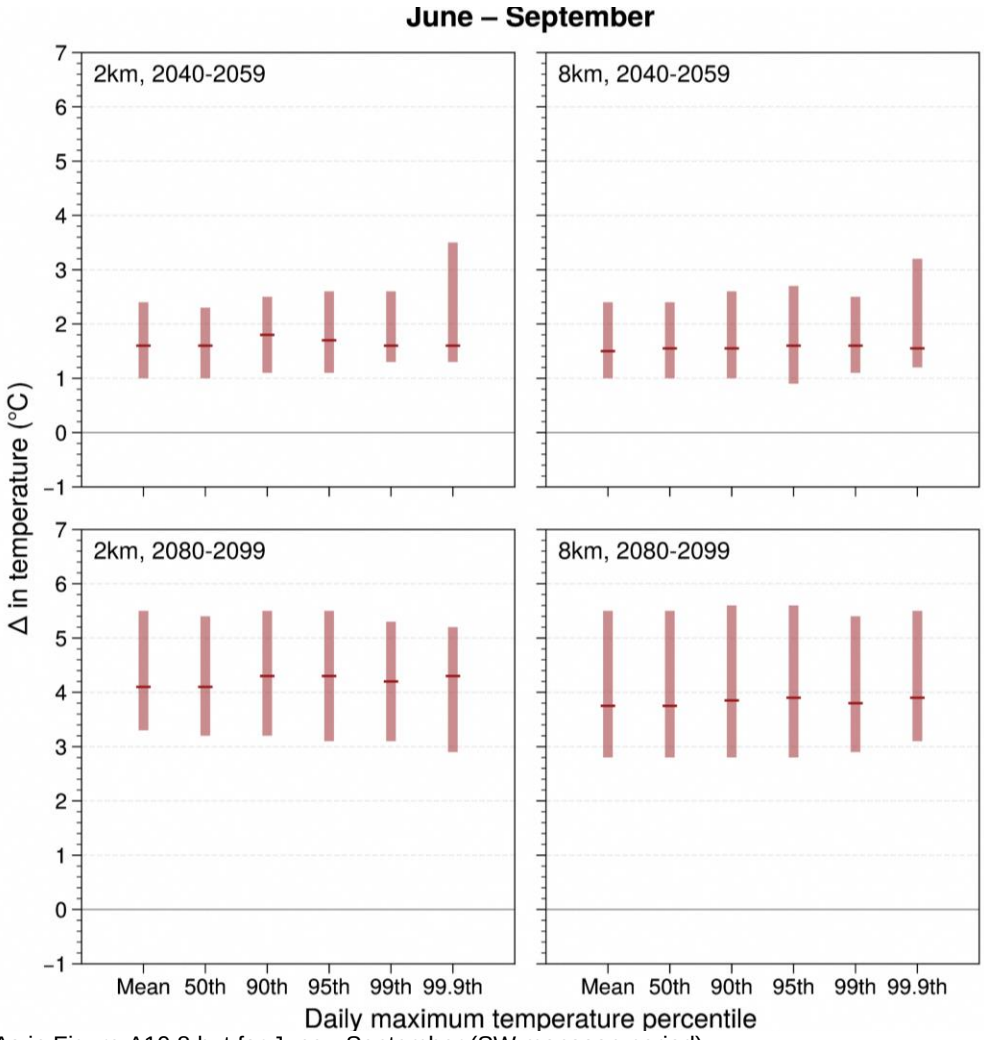

Figure A10.11: As in Figure A10.8 but for June - September (SW monsoon period).

Figure A10.12 shows the projected changes of daily mean and extreme temperature percentiles for Oct-Nov months over Singapore using 2km and 8km downscaled simulations in mid-century and end century. In the mid-century, the 2km simulation showed that mean temperature is projected to increase by 1.6^{o}C and extreme temperature is projected to increase in the range of 1.5^{o}C to 1.9^{o}C. In the 8 km simulations, the mid-century's mean temperature is projected to increase by 1.3^{o}C and extreme temperature is projected to increase in the range of 1.3^{o}C to 1.7^{o}C. In the end century, from the 2 km simulations the mean temperature is projected to increase by 4.0^{o}C and extreme temperature is projected to increase in the range of 4.0^{o}C to 4.5^{o}C. The mean temperature in the end century from the 8 km simulations is projected to increase by 3.4^{o}C, whereas extreme temperature is projected to increase in the range of 3.4^{o}C to 4.1^{o}C. Between 2 km and 8 km simulations, there are modest differences in the mean and extreme temperature changes at the mid-century and end-of-century.

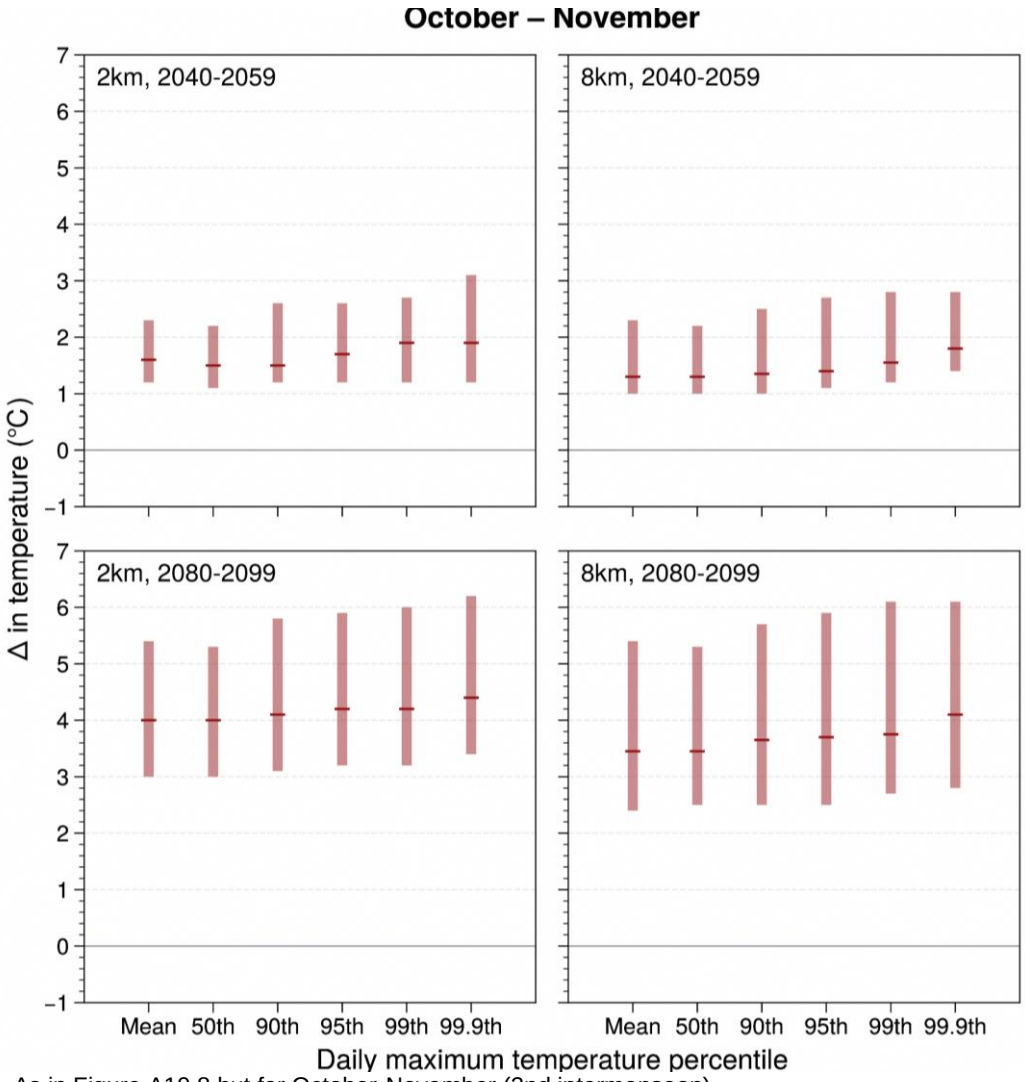

Figure A10.12: As in Figure A10.8 but for October-November (2nd intermonsoon)

Appendix B - Changes in winds over the WMC domain

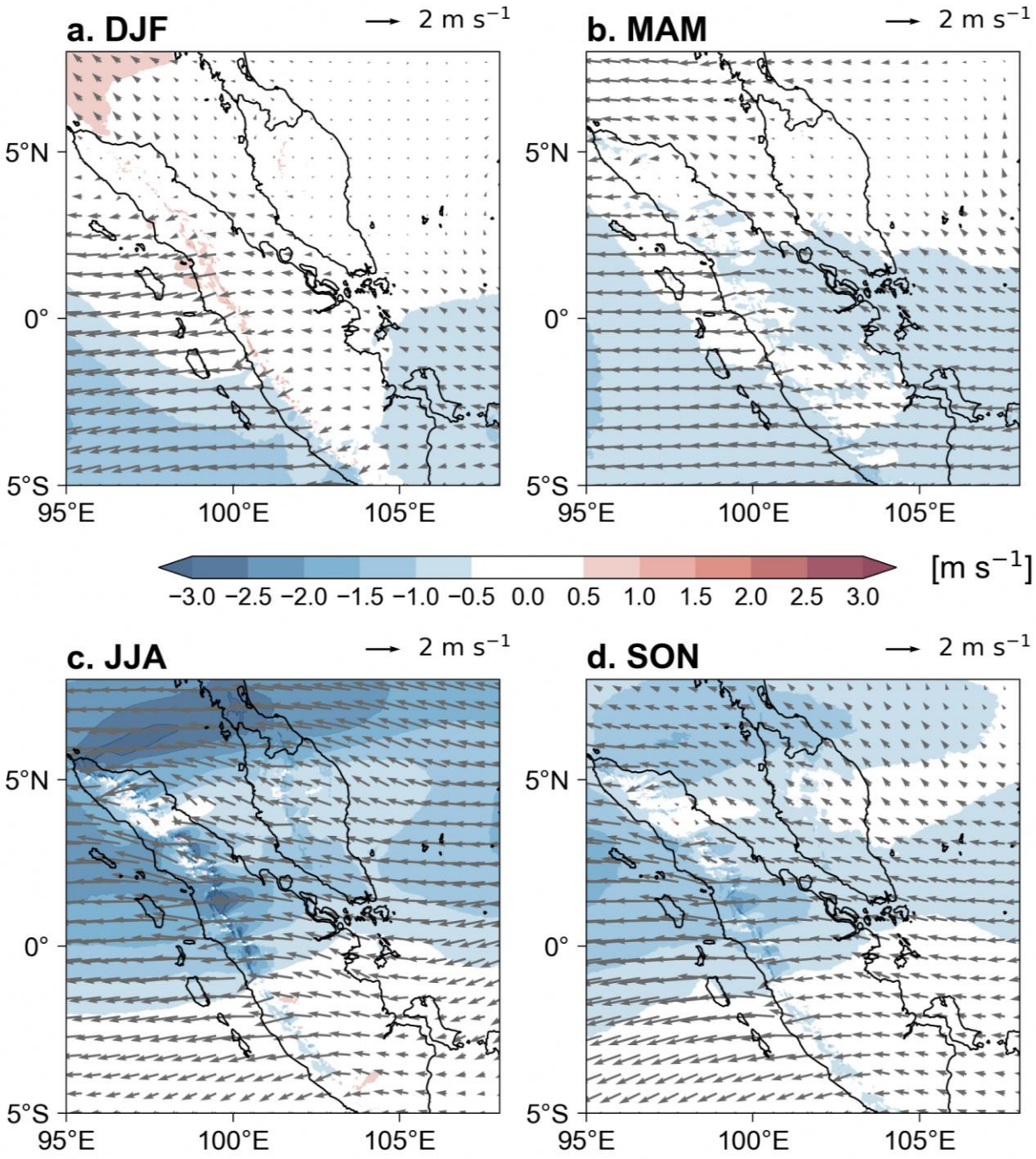

Figure B10.1: Changes in 850 hPa wind direction and climatological wind speeds (colors) in (a) DJF, (b) MAM, (c) JJA, (d) SON over Southeast Asia during 2080-2099 in SSP5-8.5 with respect to 1995-2014 in SINGV-MMM (containing five 2km model outputs).

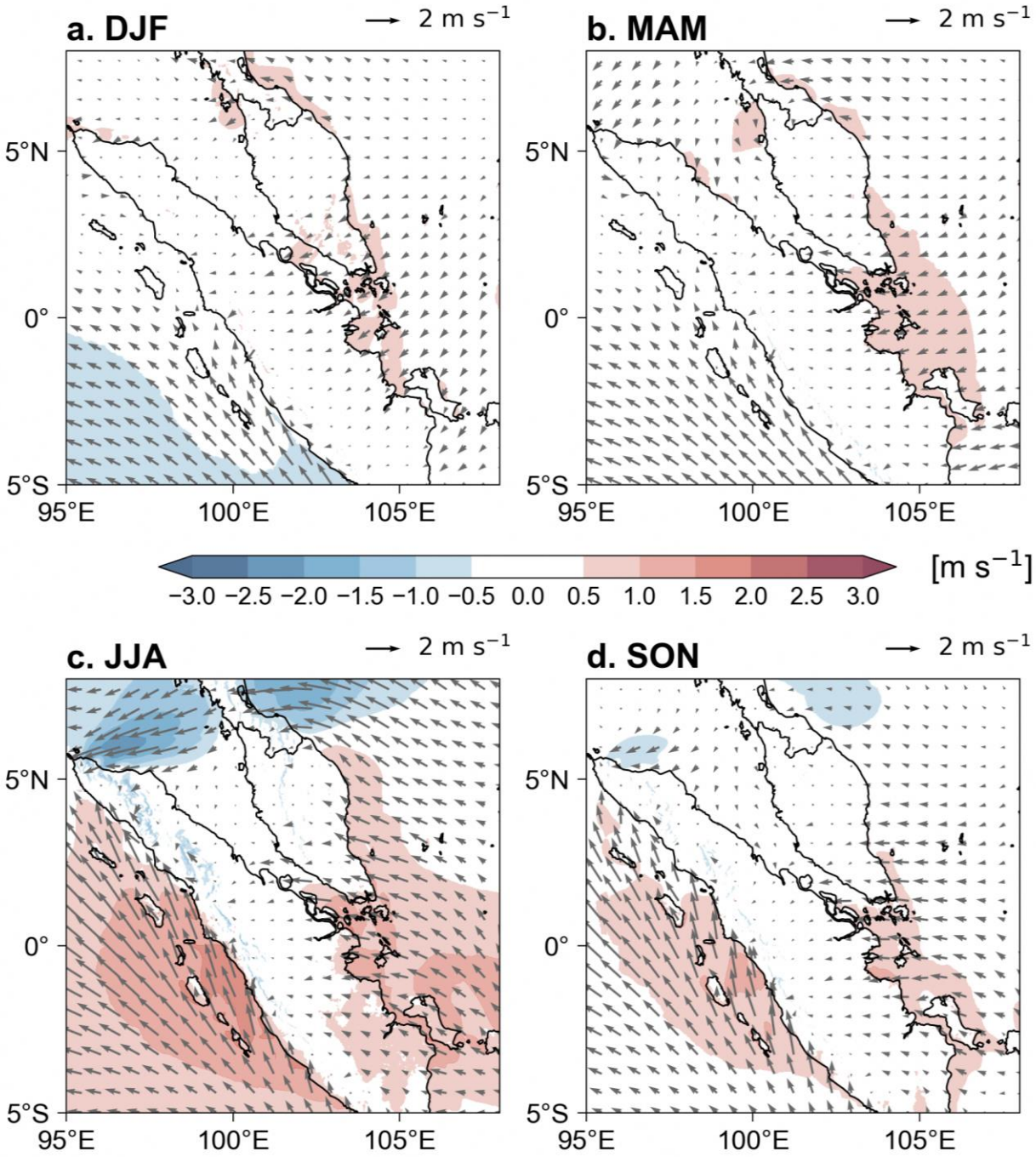

Figure B10.2: As in Figure B10.1 but for near-surface winds.

Appendix C – Changes in warm nights and very hot days

C10.1 How will the annual occurrence of warm nights change?

The frequency of occurrence of warm nights (daily minimum temperature equal to or exceeding 26.3 °C) is projected to increase in the future. Based on the observations record, Singapore has around 76 warm nights annually, and this number is projected to increase in the future, with warm nights becoming an everyday occurrence, by end-century, under the high emissions scenario. Projected changes for the mid- and end-century for all SSPs are shown in Table C10.1.

Table C10.1: Observed and projected number of warm nights annually, during mid- and end-century under the 3 SSP scenarios.

Scenario	Number of warm nights annually	
Observations	76 nights	
Future	Mid-Century	End-Century
SSP1-2.6	336 (317 to 352)	342 (312 to 361)
SSP2-4.5	347 (327 to 360)	362 (360 to 365)
SSP5-8.5	354 (335 to 364)	365 (365)

C10.2 How will the annual occurrence of very hot days change?

Very hot days are defined as days with daily maximum temperature exceeding 35 °C, based on the 99th percentile of daily maximum temperature. Historically, the average annual occurrence of very hot days are 21.4 days.

The frequency of occurrence of very hot days is projected to increase in the future. Based on the observations record, Singapore has around 21 very hot days annually, and this number is projected to increase in the future, with the worst case of almost every day being a very hot day by the end century under the high emissions scenario. Projected changes for the mid- and end-century for all SSPs are shown in Table C10.2.

Table C10.2: Observed and projected number of very hot days annually, during mid- and end-century under the three SSP scenarios.

Scenario	Number of very hot days annually	
Observed	*21.4 days*	
Future	Mid-Century	End-Century
SSP1-2.6	73 (47 to 93)	85 (41 to 125)
SSP2-4.5	95 (63 to 134)	173 (103 to 261)
SSP5-8.5	129 (76 to 189)	305 (252 to 351)

Uncertainty Quantification of Climate Change Projections

11

Authors:
Aurel Florian Moise, Sandeep Sahany, Muhammad Eeqmal Hassim, Chen Chen, Xin Rong Chua, Venkatraman Prasanna, Gerald Lim, Jianjun Yu, Pavan Harika Raavi, Fei Luo

METEOROLOGICAL SERVICE SINGAPORE
Centre for Climate Research Singapore

11.1 Introduction

The importance of uncertainty in climate change projections and its communication to stakeholders is well recognised by the IPCC as can be seen from the assessment reports. Uncertainty in regional climate change projections further cascades to uncertainties in impacts (hydrology, agriculture, etc.), and it gives a hard time to the decision makers to come up with necessary adaptation measures, as the adaptation plans and corresponding costs can significantly be affected due to these uncertainties. Hence, there are efforts by the scientific community to reduce uncertainty in climate change projections to the extent possible.

With regard to the communication of uncertainty to stakeholders, the IPCC AR6, similar to AR5, uses a "calibrated language" in various statements published in the reports. The 2 terms that are used to communicate uncertainty in the IPCC reports are "confidence" and "likelihood". IPCC uses a rather detailed methodology to assess and communicate uncertainty as can be seen in Figure 11.1 taken from the AR6 WG-I report.

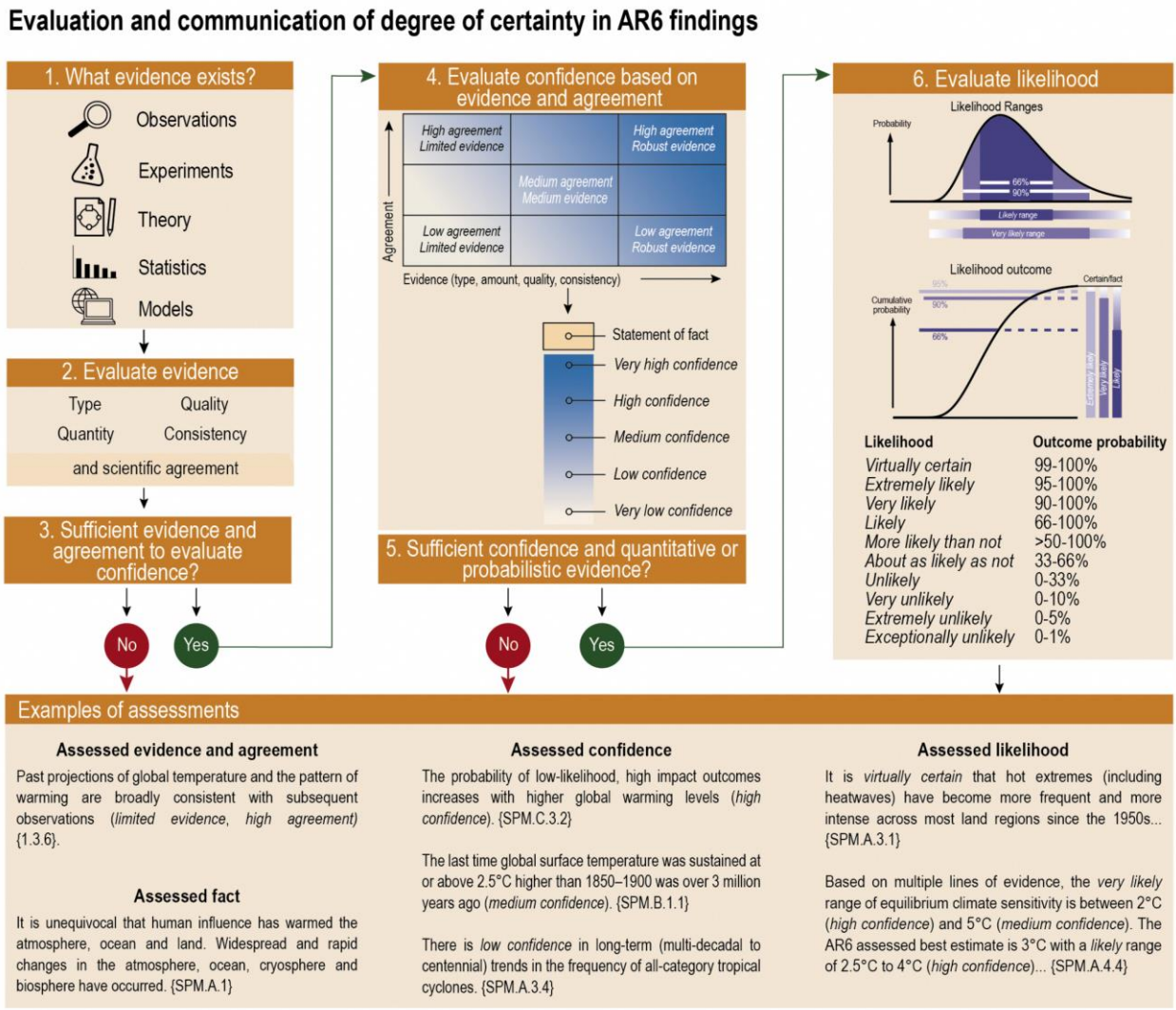

Figure 11.1: The IPCC AR6 approach for characterizing understanding and uncertainty in assessment findings. This diagram illustrates the step-by-step process authors use to evaluate and communicate the state of knowledge in their assessment (Mastrandrea et al., 2011). Box 1.1, Fig. 1, IPCC AR6.

11.2 Sources of uncertainties in Climate Change Projections

There are 3 distinct sources of uncertainty in global climate change projections - (1) internal variability uncertainty, (2) model uncertainty, and (3) scenario uncertainty (e.g., Hawkins and Sutton 2009).

Internal variability uncertainty: As evident from the name, this is due to the internal variability or natural fluctuations of the climate system that arise in the absence of any radiative forcing on the earth system.

Model uncertainty: This is also known as a response uncertainty. Each model has its own representation of the processes in the climate system. As such, different models respond differently to the same forcing and hence produce somewhat different climate change projections at global and regional levels.

Scenario uncertainty: This is the difference in response of a given model that can arise due to differences in the external forcing, e.g., greenhouse gas emissions under different pathways, leading to different responses and hence different climate change projections.

Dynamical downscaling uncertainty: In the case of regional climate change projections via dynamical downscaling an additional uncertainty factor arises that is associated with the different downscalers (regional climate models) used for downscaling. For example, for a given CMIP6 GCM and for a given scenario, 2 different regional climate models used for dynamical downscaling will produce somewhat different regional climate change projections. This is called the dynamical downscaling uncertainty.

The relative importance of each of the uncertainty factors changes with the time and space scale of interest. Hawkins and Sutton (2009) compared the roles of internal variability uncertainty, model uncertainty, and scenario uncertainty. Their work indicates that for time horizons of many decades or longer, the dominant sources of uncertainty at regional or larger spatial scales are model uncertainty and scenario uncertainty. However, for time horizons of a decade or two, the dominant sources of uncertainty on regional scales are model uncertainty and internal variability. In general, the importance of internal variability increases at smaller spatial scales and shorter time scales.

In Figure 11.2 we have shown the total variance and fractional variance of near-surface air temperature (tas) from CMIP6 GCMs over the V3 8 km domain, split into 3 sources of uncertainty, i.e., internal variability, model uncertainty, and scenario uncertainty, following the methodology of Hawkins and Sutton 2009. It can be seen from the left panel that the internal variability remains almost constant in time, the model uncertainty shows a steady increase in time but at a slow rate, whereas the scenario uncertainty non-linearly increases with time.

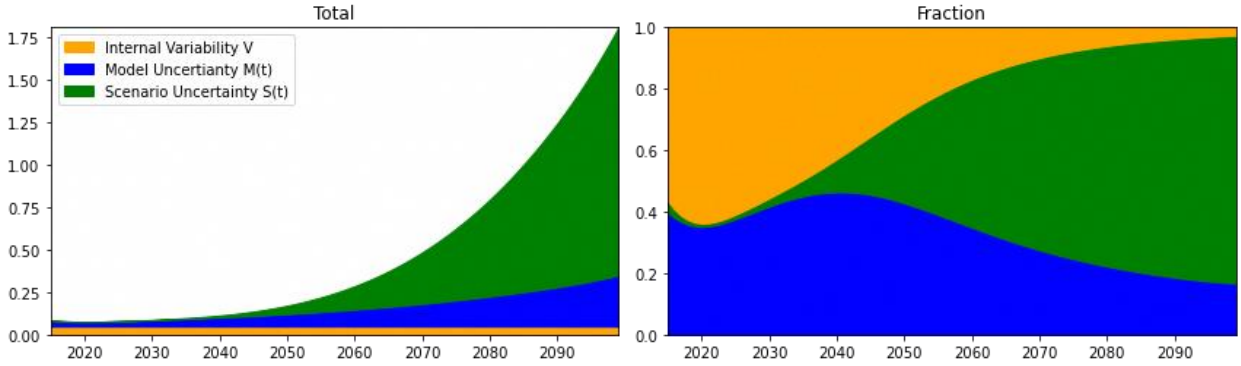

Figure 11.2: Total and fractional variance of surface air temperature over the V3 8 km domain using CMIP6 GCMs data.

From the right panel, as expected from the findings of Hawkins and Sutton (2009), on timescales of 1-2 decades the dominant sources of uncertainty are internal variability and model

uncertainty, whereas on longer timescales (beyond 2 decades) scenario uncertainty is the dominant mode of uncertainty.

11.3 Methods to constrain uncertainties

While there are uncertainties in climate changes projections, there are methods to reduce the range of uncertainty by applying constraints. For example, one of the methods that was used to constrain the climate change projections in IPCC AR6 was the use of emulators. As highlighted in Chapter 4 (Section 4.2.1), many CMIP6 models exhibit an equilibrium climate sensitivity (ECS) of 5°C or higher (Zelinka et al., 2020), much higher than the upper value of the CMIP5 range of 4.5°C. Sherwood et al. (2020) constrained the likely and very likely ranges of ECS in CMIP6 models to 2.5°C - 4.0°C and 2.0°C - 5.0°C, respectively. Hence, the IPCC adopted the approach of employing an emulator for constraining temperature and all parameters scaling with temperature, based on the analysis of Sherwood et al. (2020).

There have been studies that have used other methods to constrain the uncertainty in climate change projections. For example, Tokarska et al. (2020) used past warming trends to constrain future warming in CMIP6 models. They reported that projected future warming is correlated with the simulated warming trend during recent decades across CMIP5 and CMIP6 models, and hence can be used to constrain future warming based on consistency with the observed warming.

Emergent constraint (Hall et al., 2019), defined as a statistical relationship, across a model ensemble, between a measurable aspect of the present-day climate (the predictor) and an aspect of future projected climate change (the predictand) is another method which is promising and being widely researched and used to constrain future climate change projections.

Another alternative method to constrain climate change projections is the storyline approach discussed in Shepherd et al. (2018). This method, although inherently subjective, provides a powerful way of interpreting climate change projections based on storylines, and either accepting or discarding the projected changes based on the confidence in the associated projected storyline.

11.4 Uncertainty in V3

The 4 types of uncertainty discussed above are also present in the V3 climate change projections presented in this report, which we explore further in this subsection.

Scenario uncertainty

The role of scenario uncertainty is shown in Figure 11.3. It shows the range (across the 3 SSPs) of changes in precipitation (%) and changes in temperature (°C) for each of the 2 km simulations over Singapore for mid- and end-century. We see from the figure that, in general, the scenario uncertainty increases in time from mid-century to end-century, as expected. However, the actual magnitude of scenario uncertainty is model-dependent. This is because the scenario uncertainty is governed by the response of a given model to different forcings, and since the differences in responses to different forcings is dependent on the model the scenario uncertainty is also dependent on the model. For example, in one of the models the scenario uncertainty in precipitation change is as high as 25% during the end-century, and similarly the scenario uncertainty in temperature projections for one of the models during the end-century is as high as 3.5°C.

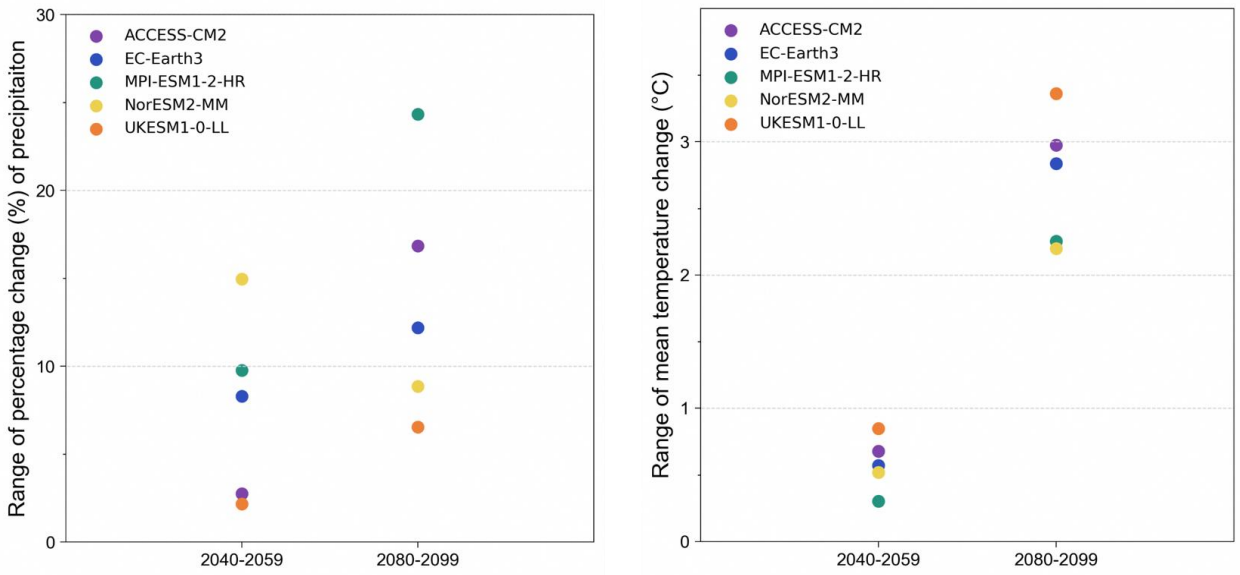

Figure 11.3: Projected range of precipitation change (%; left panel) and temperature change (ºC; right panel) across SSP scenarios during mid-century (2040-2059) and end-century (2080-2099) for the five 2 km downscaled simulations over Singapore. Each dot represents the difference between the minimum and maximum values (across the 3 SSPs) for the individual models.

Model uncertainty

The next source of uncertainty we look at is the model uncertainty. Figure 11.4 shows the future range of precipitation change and temperature change across models during mid-century (2040-2059) and end-century (2080-2099) under the 3 SSPs for the five 2 km downscaled simulations over Singapore.

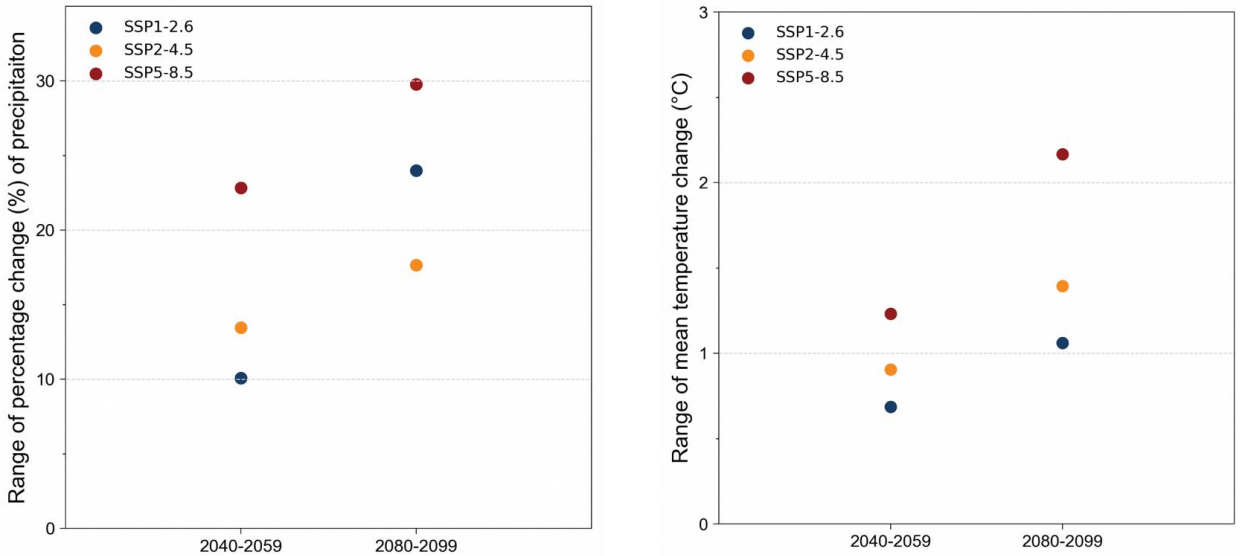

Figure 11.4: Projected range of precipitation change (%; left panel) and temperature change (ºC; right panel) across models during mid-century (2040-2059) and end-century (2080-2099) under the 3 SSPs for the five 2 km downscaled simulations over Singapore. Each dot represents the difference between the minimum and maximum values (across the 5 models) for the individual SSPs.

We see from the figure that, in general, the model uncertainty increases with time and is higher in the end-century as compared to the mid-century. We also find that the model uncertainty is highest for the SSP5-8.5 scenario. For example, the model uncertainty in projected precipitation change over Singapore could be as high as 30% under SSP5-8.5 during the end-century, and that for projected temperature change could be as high as 2.2°C under SSP5-8.5 during the end-century.

Dynamical downscaling uncertainty

Next, we turn to the dynamical downscaling uncertainty. Another dynamical downscaling model, the Weather and Research Forecasting (WRF) model, was used to perform a parallel version of a subset of the simulation conducted with SINGV-RCM, making use of two global models (EC-Earth3 and MPI-ESM1-2-HR) and three time periods (historical, SSP2-4.5, and SSP5-8.5).

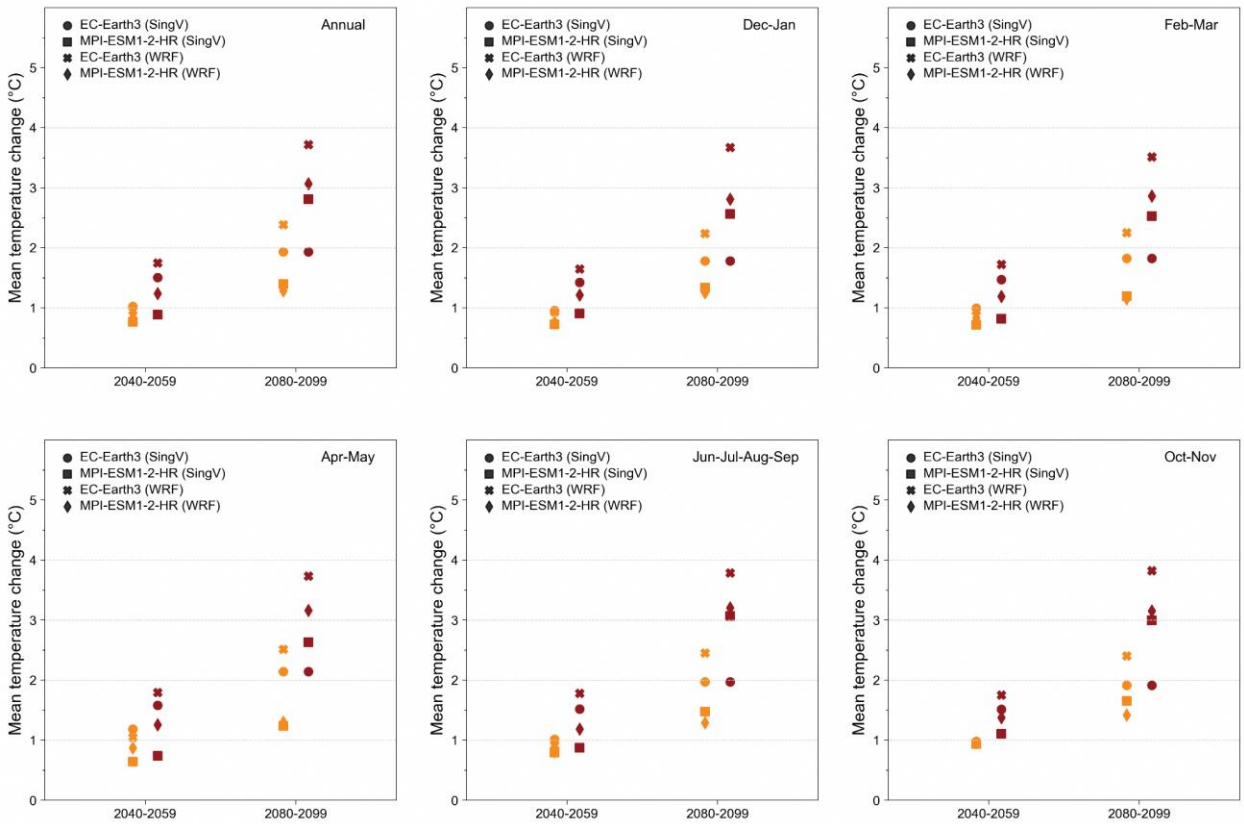

Figure 11.5: Comparison of projected change in mean near-surface air temperature over Singapore in the SSP2-4.5 (orange) and SSP5-8.5 (deep red) scenarios using SINGV-RCM and WRF downscaled from EC-Earth3 and MPI-ESM1-2-HR for mid and end century at 8km resolution.

Figure 11.5 shows the projected percentage change of near-surface air temperature over Singapore in the SSP2-4.5 (orange) and SSP5-8.5 (deep red) scenarios using SINGV-RCM and WRF downscaled from EC-Earth3 and MPI-ESM1-2-HR for mid and end century at 8 km resolution. Across the scenarios and time periods, near-surface air temperature downscaled from WRF are generally warmer, with differences within ~2°C. Note that the uncertainty is a nonlinear combination of both the parent GCM and downscaler; for example, relative to SINGV-RCM, WRF amplifies the warming in Dec-Jan at the end-of the century for EC-Earth3 much more than it does for MPI-ESM1-2-HR. The spread also increases in SSP5-8.5 as compared to SSP2-4.5, and in many cases in the end-century as compared to the mid-century. The results increase our confidence in the projection of warming over Singapore in the future under the SSP scenarios.

Figure 11.6 shows the projected percentage change of precipitation over Singapore in the SSP2-4.5 (orange) and SSP5-8.5 (deep red) scenarios using SINGV-RCM and WRF downscaled from EC-Earth3 and MPI-ESM1-2-HR for mid and end century at 8 km resolution. Even when downscaled with forcings from the same GCM, RCMs can predict different signs of change (e.g., downscaling of EC-Earth3 over annual timescales in the end of the century, shown by the crosses versus circles). The percentage change can be larger for Feb-Mar, which is a climatologically dry month. Similarly, using two different GCM forcings on the same downscaler can give projections of opposing signs (e.g., downscaling using WRF over annual timescales for SSP5-8.5, as seen by the cross and diamonds). It is not obvious whether the spread in RCM or spread in GCM contributes more to the overall uncertainty. For example, in the end-century in Feb-Mar under SSP5-8.5, the uncertainty from considering the additional regional model WRF (circle and cross) is smaller than that of considering an additional GCM (circle and square), but the opposite is true for its mid-century counterpart. Considering the analysis of Figure 11.5 and Figure 11.6 reveals that we have a high certainty in future warming over Singapore as compared to changes in rainfall.

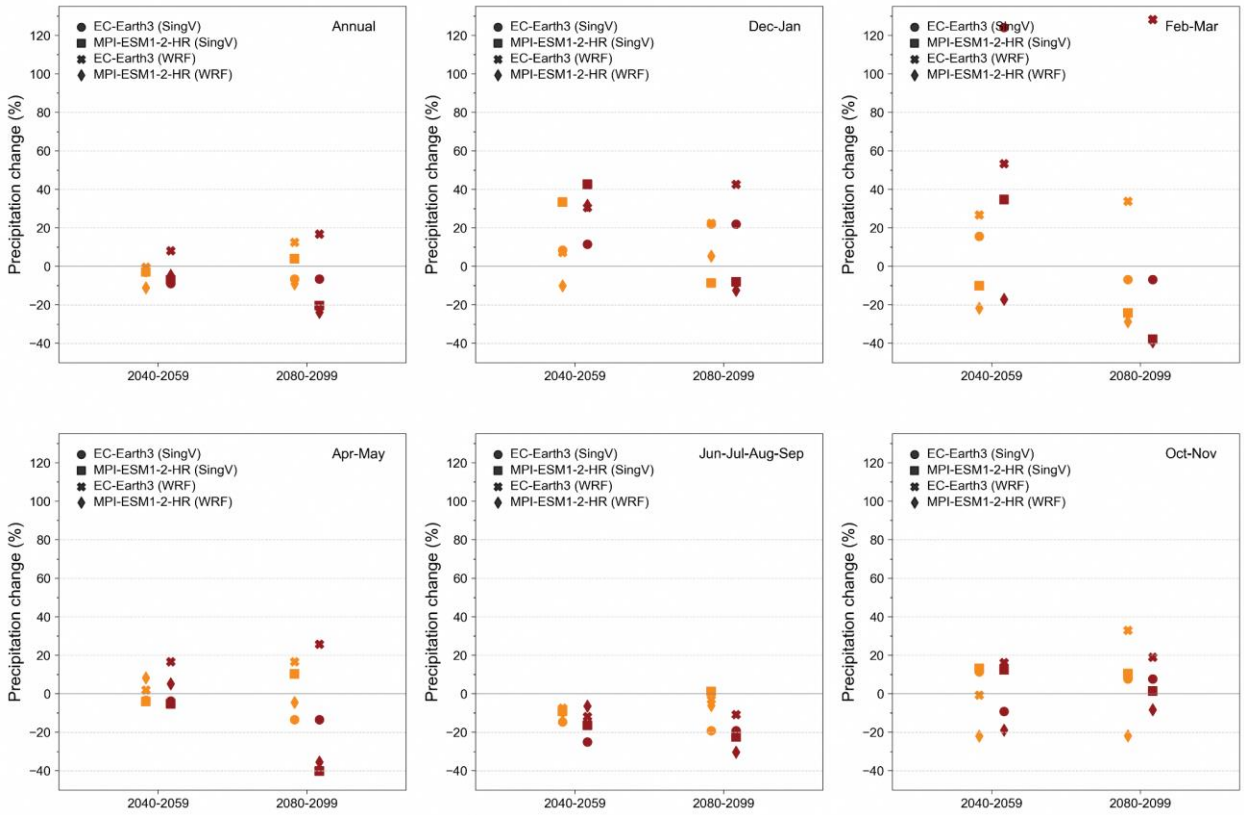

Figure 11.6: Comparison of projected percentage change of precipitation over Singapore in the SSP2-4.5 (orange) and SSP5-8.5 (deep red) scenarios using SINGV-RCM and WRF downscaled from EC-Earth3 and MPI-ESM1-2-HR for mid and end century at 8km resolution.

Internal variability uncertainty

As explained in Section 11.2, internal variability is inherent within the climate system. As such, in addition to being present in GCMs, this variability is present within all the downscaling results and observed trends shown in this report. By presenting climatological averages over twenty years, we aim to reduce the impact on variability in assessing the potential of changes in the middle or end of the century. Nevertheless, decadal

variability from the models could still influence the results. The role of such variability becomes particularly important over small spatial scales, such as local changes over Singapore (Chapter 10).

11.5 Summary

Future climate projection for Singapore is challenging. In particular, Singapore is located in between two much larger areas where increases in rainfall are projected on one side and decreases on the other for most of the seasons. This is related to the complex and seasonally-varying regional climate drivers in the SEA region, and surely makes projections of rainfall change particularly challenging for Singapore, especially given its small size.

The contents of this chapter aim to provide guidance to the users of the bias-adjusted projections over Singapore (Chapter 10) about the reliability and robustness of the projections, given the uncertainties inherent in climate projections.

Our analysis shows that the scenario uncertainty increases in time from mid-century to end-century, while also being model-dependent. For example, in one of the models the scenario uncertainty in precipitation change is as high as 25% during the end-century, and similarly the scenario uncertainty in temperature projections for one of the models during the end-century is as high as 3.5°C.

Model uncertainty also increases with time and is larger in the end-century as compared to the mid-century. Model uncertainty is also largest for the SSP5-8.5 scenario. For example, the model uncertainty under SSP5-8.5 during the end-century can be as high as 30% for projected precipitation change and 2.2°C for projected temperature change.

Dynamical downscaling uncertainty can affect the change in sign of precipitation change for individual models, and lead to temperature changes within ~2°C.

Given the presence of the sources of uncertainty described in Section 11.2, we are more confident in the projections that remain qualitatively similar despite the time period/scenario/model used in the analysis. We are also more confident in changes that are consistent with the changes in the regional and global climate system, especially if they are supported by theoretical understanding.

For the purpose of using the model results, the mean or median of the multi-model ensemble could be used to provide an indication of the change. However, for robust decision making, it may be useful to consider the full multi-model range of the variables of interest.

References

Mastrandrea, M. D., Mach, K. J., Plattner, G.-K., Edenhofer, O., Stocker, T. F., Field, C. B., et al. (2011). The IPCC AR5 guidance note on consistent treatment of uncertainties: a common approach across the working groups. *Climatic Change*, *108*(4), 675. https://doi.org/10.1007/s10584-011-0178-6

Hawkins, E., & Sutton, R. (2009). The Potential to Narrow Uncertainty in Regional Climate Predictions. Bulletin of the American Meteorological Society, 90(8), 1095–1108. https://doi.org/10.1175/2009BAMS2607.1

Katarzyna B. Tokarska, et al., Past warming trend constrains future warming in CMIP6 models.*Sci. Adv.***6**,eaaz9549(2020).DOI:10.1126/sciadv.aaz9549

Hall, A., R. Cox, C. Huntingford, and S. Klein, 2019: Progressing emergent constraints on future climate change. Nat. Climate Change, 9, 269–278, https://doi.org/10.1038/s41558-019-0436-6.

Shepherd, T. G., and Coauthors, 2018: Storylines: An alternative approach to representing uncertainty in physical aspects of climate change. *Climatic Change*, **151**, 555–571, https://doi.org/10.1007/s10584-018-2317-9.

12 Past and Future Sea Level Change

Authors:
Trina Ng, Nidheesh Gangadharan, Aurel Florian Moise, Matthew Palmer

Meteorological Service Singapore
Centre for Climate Research Singapore

Summary

This chapter discusses observed and projected mean sea-level rise around Singapore and the wider Southeast Asian region. Various physical mechanisms and processes driving past and future mean sea-level rise around Singapore are discussed here. Our findings specifically highlight vertical land movement (VLM) as an important driving process of relative sea-level rise in many parts of Southeast Asia.

We found that the rate of observed and future mean sea-level rise around Singapore is comparable to the global-mean rate. Past sea-level change in Singapore is shown at ten tide-gauge locations whilst future sea-level change in Singapore is shown at six of these ten tide-gauge locations.

Relative mean sea level has been rising at a rate of 3.6 mm/yr off Singapore (average rate across four tide-gauges with rate varies between 3.27 - 3.77 mm/yr) for the 1993 - 2021 period, and is projected to continue rising at different rates depending on the future emission pathways. We show that the relative mean sea level is *likely* to reach up to 0.74 m under the low emissions scenario (SSP1-2.6) and up to 1.24 m under the high emissions scenario (SSP5-8.5) by 2100 (relative to 1995-2014) at a particular location in the southern coast of Singapore (Sultan Shoal). Projected relative sea-level rise at this location could *likely* increase to 1.15 m (SSP1-2.6) and 2.12 m (SSP5-8.5) by 2150.

We show that the contemporary mass redistribution (CMR) between the oceans and the land, which refers to freshwater from ice sheets, glaciers and other terrestrial water storages, is the main driver of observed sea-level rise around Singapore during the 1993 - 2021 period (70% of the total rise). On the other hand, manometric sea-level, or in other words the ocean internal mass distribution, drives a large part of the sterodynamic sea-level rise (~23% of the total rise) in Singapore with a very weak contribution from steric sea-level rise. Our findings indicate that nearly 90% of the observed sea-level rise off Singapore is “mass-driven” and highlights the importance of having a bottom pressure recorder in the shelf region of Singapore to assist future studies of mean sea-level changes around Singapore.

We present the contribution from six driving components to mean sea-level change in Singapore by 2100 and 2150 under the low and high emission scenarios: Antarctic and Greenland ice sheets, glaciers, land water storage, ocean sterodynamics. Our projections show that mass changes in the Antarctic ice sheet are projected to *likely* contribute the most significantly to the projected sea-level rise in Singapore (Sultan Shoal) by 2100 and 2150 regardless of emission scenarios.

Low confidence sea-level projections for Singapore and the global mean up to 2300 are also presented in this chapter. These projections follow single paths of low-likelihood high-impact scenarios consistent with unstable ice sheet feedback processes such as marine ice cliff instability (MICI) and marine ice shelf instability (MISI). Despite their low confidence, these projections offer a more comprehensive view of potential future climate scenarios, providing essential information for stakeholder planning. It is, however, important to use these projections cautiously, with awareness of their inherent uncertainties.

This chapter centers on mean sea level in Singapore and the surrounding region, excluding an analysis of extreme sea level. Coastal water level fluctuations are also contributed from tides, storm surges, and waves. For robust mitigation and adaptation and planning in response to sea-level rise, an understanding of extreme sea levels is as vital as comprehending mean sea-level change. The mean sea-level change projections outlined in this chapter hence provide a foundation for future studies on extreme sea levels, aiding in comprehensive coastal sea-level change studies.

The availability of coastal observational systems and data is very sparse in many parts of the Southeast Asian region, including Singapore. Sustaining the existing observing networks (e.g. tide gauges) and initiating coordinated ocean observational programmes (e.g., coastal hydrographic measurements) is fundamental in addressing sea-level rise in the Southeast Asian seas. The complexity of understanding the drivers behind mean sea-level rise also calls for

developing modeling frameworks for the Southeast Asian region encompassing high-resolution regional and coastal hydrodynamic models. This will aid sea-level-rise-induced coastal impact assessments (e.g., inundation, erosion and land/infrastructure loss).

12.1 Introduction

Global mean sea-level rise is one of the most significant consequences of climate change, with the potential to impact coastal communities worldwide. Over the past century, global-mean sea level rose by an average rate of 1.8 mm per year, and this rate is expected to increase in the coming decades due to increased mass loss of ice sheets and glaciers and the thermal expansion of ocean waters (Fox-Kemper et al. 2021). Countries in southeast Asia are particularly vulnerable to sea-level rise due to the large population living in low-lying coastal areas (Nicholls and Cazenave, 2010; Nicholls et al. 2021; Asian Development Bank, 2018) and making robust estimates of sea-level rise and its coastal impacts is challenging for this region mainly due to sparse observational data and complex oceanographic and climatic features of the region as illustrated in Figure 12.1. Situated at the southern tip of the Malay Peninsula, Singapore is particularly at risk from sea-level rise impacts such as inundation, erosion and coastal flooding (Ministry of Sustainability and the Environment, 2021; Figure 12.2). The coastal sea-level rise and associated impacts indeed pose significant challenges to Singapore's public safety, infrastructure, and economy (National Climate Change Secretariat, 2018).

Singapore Prime Minister Lee Hsien Loong, in his National Day Rally speech in 2019, emphasised the importance of addressing sea-level rise around Singapore, highlighting the government's commitment to tackling this critical issue over the coming years (Prime Minister’s Office Singapore, 2019). To address the challenges posed by sea-level rise, the Singapore government has implemented various measures that collectively enhance state resilience to climate change. For example, the Coastal and Flood Protection Fund was established in 2018 as part of the Climate Action Plan, with an initial budget of SGD 5 billion to support coastal adaptation measures (National Climate Change Secretariat, 2018). Additionally, to enhance research in understanding sea-level rise and its impacts around Southeast Asia, which includes seas around Singapore, the National Sea Level Programme (NSLP) was launched by the Singapore government in 2019 with an initial budget of SGD 10 million (Ministry of Sustainability and the Environment, 2020).

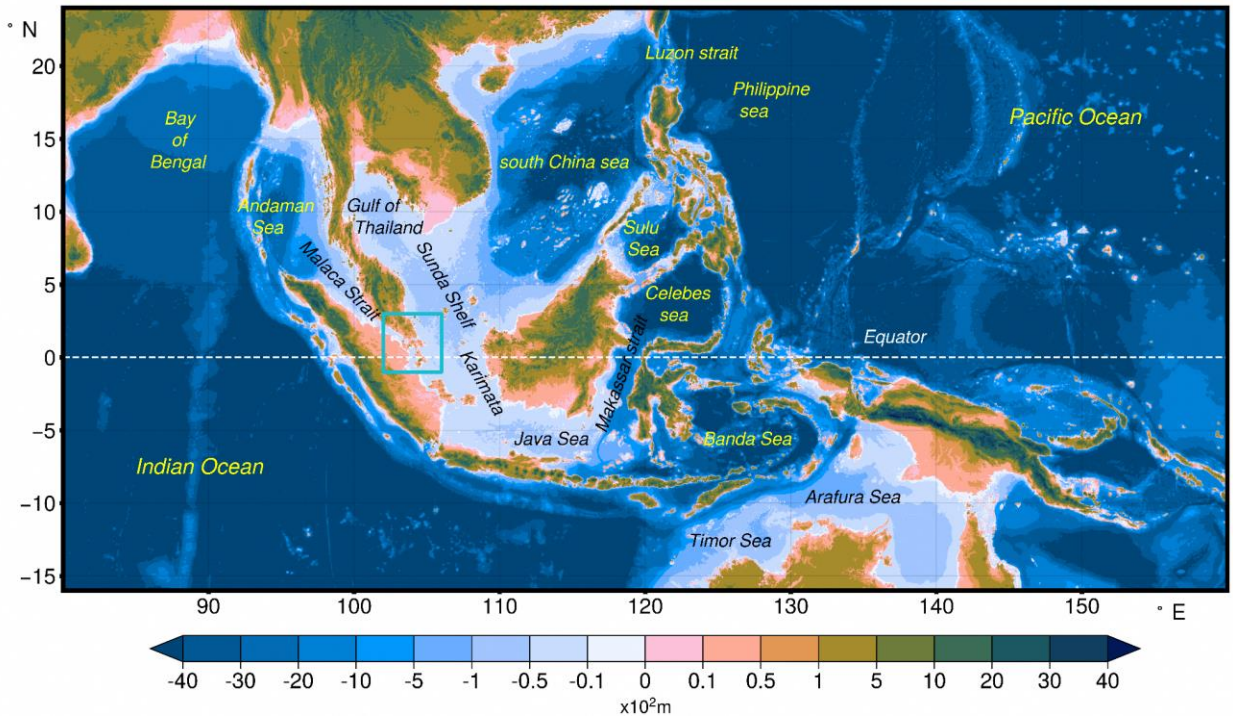

Figure 12.1: Land surface elevation and sea-floor depth relative to mean sea level of the Southeast Asian region. Major seas, shelves, and straits are shown and the geographic location of Singapore is marked by a rectangle. Units are 10^2 m, e.g., 0.1 = 10 m above sea level. Data source: General Bathymetric Chart of the Oceans (GEBCO_2022 Grid).

Changes in coastal water level can occur either through changes in regional relative mean sea-level or by means of changes caused by tides and extreme weather processes (waves, storm surges) or some combination of both.

Singapore's Second National Climate Change Study - by evaluating both time-mean sea level and sea-level extremes using different physical models - indicated that the projected coastal water levels around Singapore by the end of this century are predominantly driven by mean sea-level rise and changes in extreme sea levels are not so significant.

Hence, in this report, we focus mainly on how and why relative mean sea level rose around Singapore and the wider southeast Asian region over the historical period (Sections 12.3 and 12.4) and provide robust estimates of projected mean sea levels around Singapore for this century for different emission scenarios, using IPCC sea-level projection methodology.

In the following sections, we provide a general description for main drivers of coastal sea level following the historical sea-level change for Southeast Asia and Singapore using observational data, and subsequently discuss future sea-level change for these regions based on the Intergovernmental Panel on Climate Change (IPCC) Sixth Assessment Report of Working Group I (AR6).

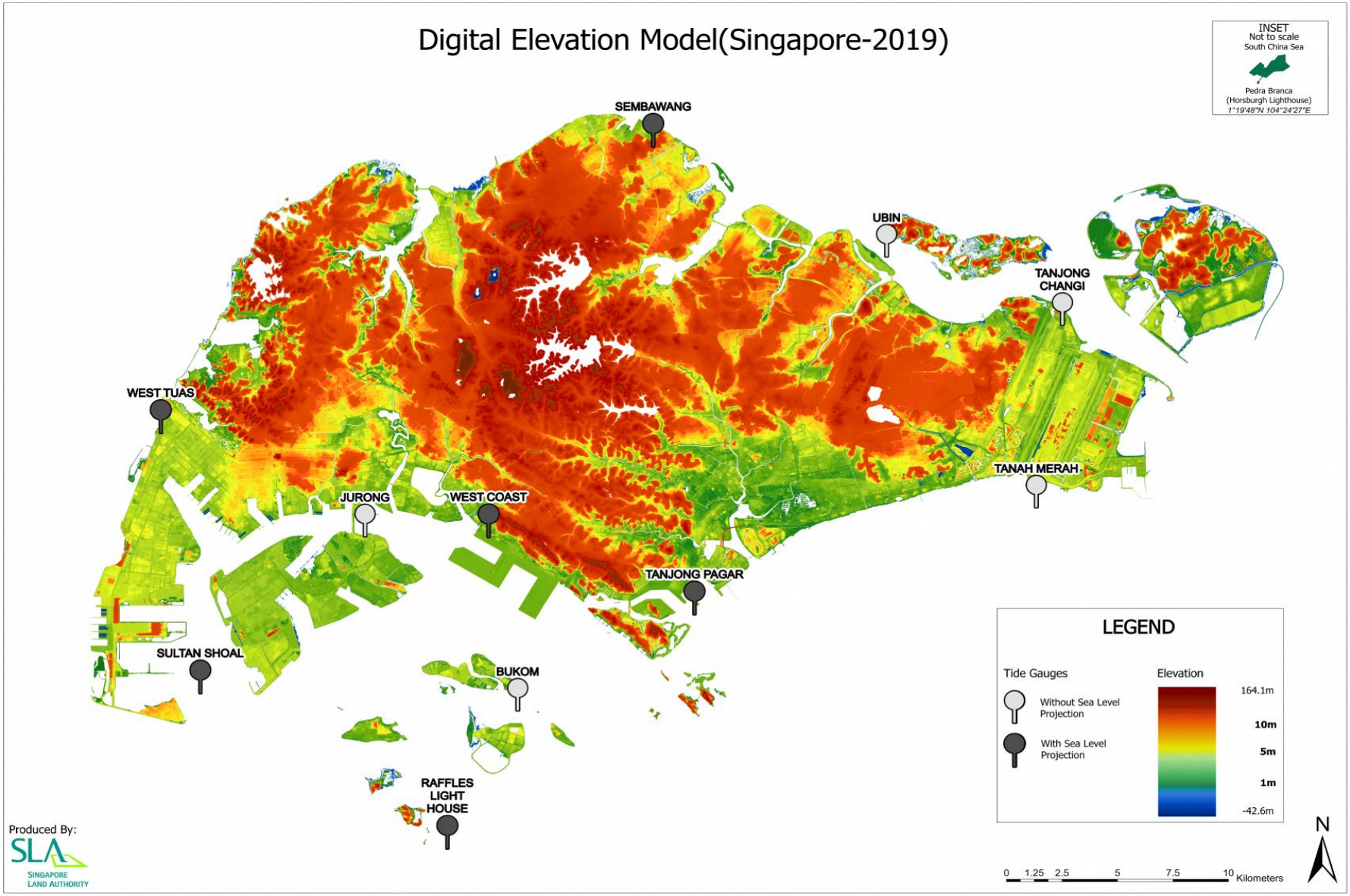

Figure 12.2: Map of elevation of Singapore (provided by Singapore Land Authority). Units are meters relative to mean sea level.

12.2 Drivers of sea-level change

Sea level varies over a wide range of spatial (from a point to global scale) and time (from seconds to millennia) scales. Sea level is an integrative ocean variable, meaning it integrates changes over the entire ocean depth and also reflects changes in other components of the climate system such as land, atmosphere and cryosphere. Therefore, sea level seldom settles down to a steady state (a condition in which no sea-level change occurs over time), but it constantly changes under the influence of several geophysical processes as shown in Figure 12.3.

Mean sea level at a given location is usually defined as the average of sea surface height over a certain period. It is the annual average water level at the coast upon which shorter-term variations from tides, surges and waves are superimposed. The averaging period could vary and hence, it is crucial to note that the rate of MSL could differ significantly if not compared over identical periods of time.

For a given location, subtracting the mean sea level from the original sea-level measurements would yield sea-level anomalies, which represent deviations of sea surface from a mean level due to several processes operating at different spatial and time scales, as illustrated in Figure 12.3.

Sea level can be measured with respect to a reference level, or also known as the datum, which is either fixed to the land (e.g., tide-gauge sea-level measurements) or based on Earth's center (e.g. satellite observations). Tide-gauge measured sea-level changes are hence affected by (or include information of) local vertical land movement (VLM) at the tide-gauge location, and hence called relative sea-level (RSL) changes.

Global-mean sea level[1] (GMSL) is the area-weighted average of sea surface height over the global oceans. Consequently, temporal changes in GMSL indicate a net change in the global ocean volume caused by ocean thermal expansion and/or exchange of water between other components of the Earth (e.g., mass balance changes in ice sheets, glaciers and terrestrial water storages). GMSL change due to the net mass change of the ocean is known as global-mean barystatic sea-level change, and that is caused by a net change in the global ocean heat content is called global-mean thermosteric sea-level change (Gregory et al., 2019).

[1] Mean sea level averaged over the global oceans. Refer to the Glossary for a complete list of sea level terminology definitions.

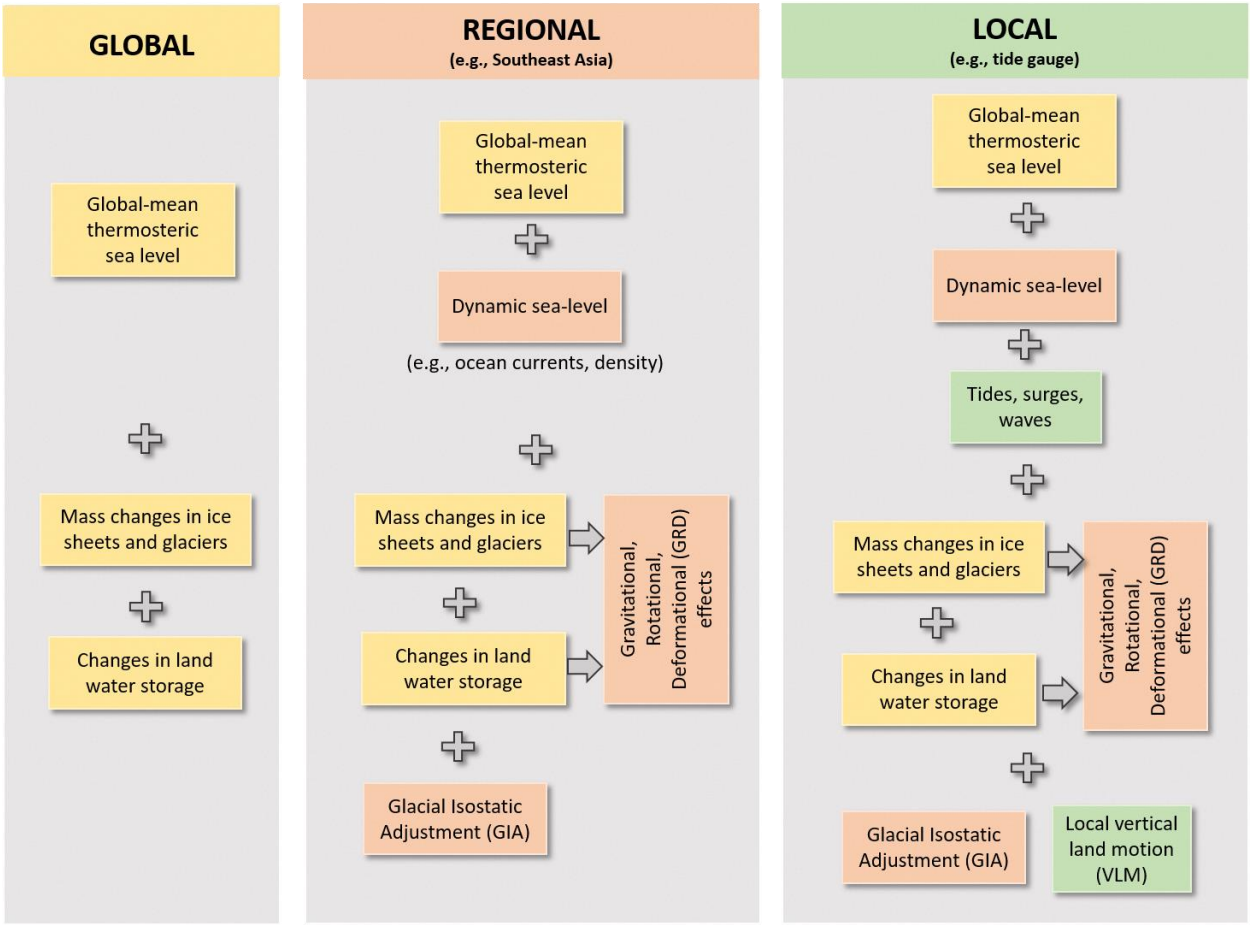

Figure 12.3: Schematic of different geophysical processes contributing to global, regional and local sea-level change. Note, the color-coding reflects the spatial scales on which the different processes operate, as per the column titles and that these are treated additively as we progress to smaller scales (left-to-right).

Regional and local sea-level changes can deviate from the global mean due to a number of processes (e.g. ocean circulation and tides) as summarised in Figure 12.3. By definition, these regional processes do not contribute to GMSL change since averaging their contributions over the entire ocean surface results in zero net change. The key processes that induce regional sea-level changes are ocean circulation (dynamic sea-level change) and the regional sea-level variations associated with freshwater exchange between the oceans and the land.

In the following sections, we focus on the drivers of mean sea level that occur on different temporal and spatial scales with a few contextual remarks for the sea-level changes around Singapore. We separate and discuss the drivers contributing to global, regional and local mean sea level.

12.2.1 Global drivers

GMSL rise is one of the major consequences of anthropogenic global warming. The earth system gained substantial energy during the last fifty from increased greenhouse gas emissions and associated positive radiative forcing. This surplus energy is closely linked to GMSL rise through the global ocean thermal expansion (Fox-Kemper et al., 2021). For instance, the GMSL rise (1.2 – 1.5 mm/yr ; Figure 12.4a) in the 20th century (e.g. Hay et al., 2015; Frederikse et al., 2020) is linked to the fact that nearly 90% of the excessive radiative heating of the climate system, due to greenhouse gas emission, has been stored in the

oceans (e.g. von Schuckmann et al., 2016, 2023; Church et al., 2013; Zanna et al., 2019; Meyssignac et al., 2019).

Global-mean thermosteric sea-level (GMTSL) rise accounts for nearly 90% of the observed energy increase since 1971 with much smaller amounts going into melting of ice (3%) and heating of the land (5%) and atmosphere (1%). Notably, majority of the ocean warming (~ 60%) is confined in the upper 700 meters of the oceans, causing about 4 - 5 cm of GMSL rise since 1971 and such rapid warming of the ocean (thermosteric sea-level rise) is shown to be indeed unprecedented over the last two thousand years (Fox-Kemper et al., 2021; Nidheesh et al., 2022). Nevertheless, it is important to note that the thermosteric sea-level rise is not spatially uniform across the oceans and in fact the thermal expansion is almost negligible over the shallow shelf regions like Singapore, leading to additional oceanic processes balancing the spatial variations as discussed in Section 12.3.

The remaining heat due to global warming (~10%), although small compared to what is being stored in the oceans, is in fact more efficient in changing the GMSL via changing the mass balance of land-based ice (i.e., polar ice sheets and glaciers) and the global hydrological cycle (Forster et al. 2021; WCRP Global sea Level Budget Group, 2018; von Schuckmann et al. 2020; Fox-Kemper et al. 2021). For instance, Figure 12.4a clearly shows that the GMSL change due to the redistribution of mass between the oceans and land is nearly twice the GMTSL change over the entire twentieth century, and the rates of global-mean barystatic and thermosteric sea-level rise are almost equal in magnitude during 1971 - 2018 (Fox-Kemper et al., 2021). More specifically, the GMSL rise over 1971 - 2018 (7.3 - 14.6 cm with a central estimate of 10.96 cm) can be closed with largest contribution comes from ocean thermal expansion (3.4 - 6.1 cm with a central estimate of 4.75 cm) and remaining contributions from glaciers (2.1 cm [1 - 3.2 cm]), Greenland ice sheet (1.2 cm [0.8 - 1.6 cm]), Antarctic ice sheet (0.67 cm [-0.4 - 1.7 cm]) and terrestrial water storage (0.73 cm [-0.2 - 1.7 cm]).

Additionally, a number of recent studies (e.g. Nerem et al., 2018; Dangendorf et al., 2019) pointed out that there is an apparent acceleration in the rate of GMSL rise, as evident in the higher rate of satellite-measured GMSL rise (~ 3.4 mm/yr since 1993), possibly related to accelerating levels of anthropogenic forcings in the climate system. Satellite-based observations and other in-situ measurements also suggest that mass loss from glaciers and the polar ice sheets has increased over recent decades, and can potentially become large sources of sea-level change in the current century (Fox-Kemper et al., 2021).

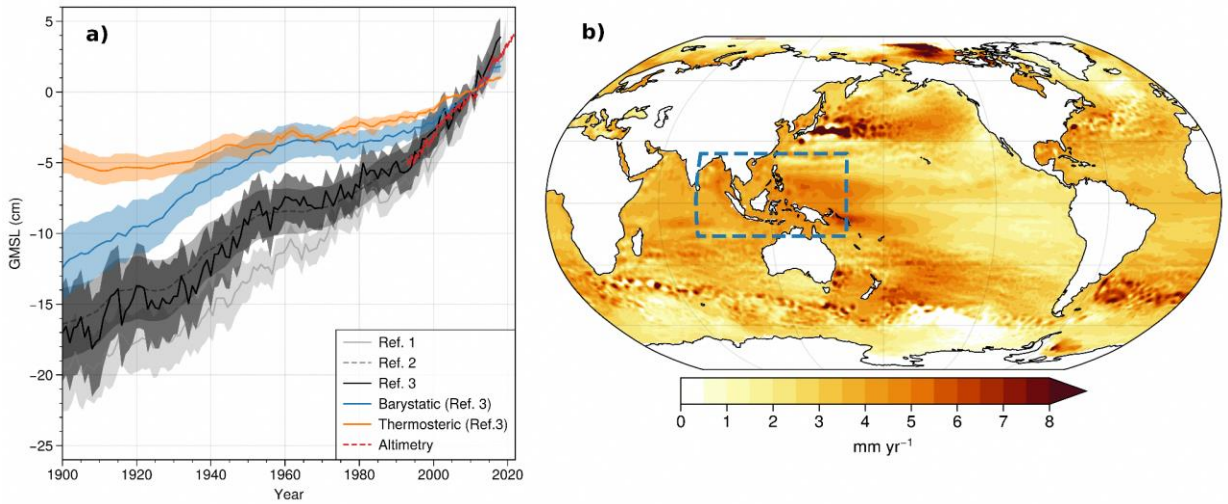

Figure 12.4: (a) Estimates of twentieth-century global-mean sea-level (GMSL) rise from different sources: Commonwealth Scientific and Industrial Research Organization (CSIRO; Ref. 1), Hay et al. 2015 (Ref. 2) and Frederikse et al. 2020 (Ref. 3). The two major components - thermosteric and barystatic contributions - of the GMSL are also shown from Frederikse et al. (2020). GMSL curve from satellite altimetry is also shown. (b) Spatial map of mean sea-level rise trend for the period 1993 -

2021 estimated from satellite altimetry. The southeast Asian region is highlighted by a rectangle [Note that satellite-observed sea-level rise does not include the effects of vertical land motion].

12.2.2 Regional drivers

Sea-level rise is not spatially uniform (Figure 12.4b). For instance, the rate of satellite-observed sea-level rise in the far western Pacific (about 5-6 mm yr−1 is clearly larger than the GMSL rate over the same period. Mean sea-level rise is generally higher (lower) than the global-mean in the Southern Ocean mid-latitudes (eastern tropical Pacific), as seen in Figure 12.4b. This spatially non-uniform sea-level rise, or also known as dynamic sea-level change, is primarily caused by ocean circulation, which redistributes water mass and heat within the ocean basins under the influence of winds and density differences.

For example, strengthened trade winds in the Pacific during the falling phase of Interdecadal Pacific Oscillation (IPO) since 1990s have resulted in increased ocean heat uptake by the equatorial Pacific and warm water accumulation in the west (e.g. England et al. 2014), causing a higher (lower) rate of mean sea-level rise in the western (eastern) tropical Pacific as seen in Figure 12.4b. Regional sea-level changes are often driven by surface winds and spatially varying atmospheric heat and freshwater fluxes, often associated with regional climate modes. For instance, the sea-level changes in the Atlantic ocean is primarily driven by wind and heat flux variations associated with the North Atlantic Oscillation (NAO) and changes in ocean heat transport associated with the Atlantic Meridional Overturning Circulation (AMOC; Oppenheimer et al. 2019). Similarly, the high rates of sea-level rise in the north Indian Ocean during the second half of the 20th century was linked to the weakening of Indian Monsoon circulation (Swapna et al. 2017).

Such natural variability in the climate system is very efficient in channelising non-uniform distribution of heat, salt and water masses within the ocean and to lead non-uniform sea-level changes at different oceanic regions. Ocean general circulation models are widely used to understand this ‘circulation-induced’ sea-level variations, known as ‘dynamic’ sea-level changes (Gregory et al. 2019). The global-mean density of the ocean can vary in time and contributes to regional as well as global-mean sea-level changes. The regional sea-level change due to the combined effects of dynamic sea-level change and global-mean thermosteric sea-level change is called ‘sterodynamic’ sea-level changes (Gregory et al. 2019).

Understanding the natural climate variability and ocean circulation is a key aspect in the understanding of climate-change-induced regional sea-level rise. For instance, several studies have examined the sea-level rise in the tropical Pacific and showed that accounting for natural climate variability (i.e., ENSO and/or IPO) could substantially modify the observed sea-level rise pattern. This is useful in detecting the trends originating from anthropogenic warming (e.g. Royston et al. 2018). Sea-level rise in the Southeast Asian seas could also be influenced by low-frequency natural climate variability rooted in both Indian and Pacific oceans. Understanding what drives regional variability in sea level is also key for deriving robust sea-level projections.

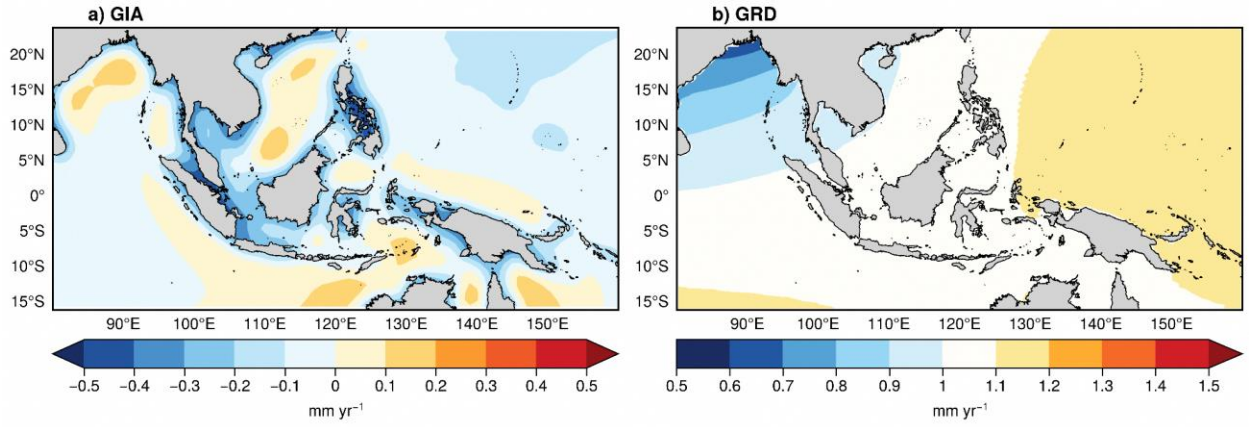

Figure 12.5: Relative sea-level rise in the southeast Asian region due to GIA (a) and GRD (b) effects. The rate of GIA-induced sea-level change is taken from the ICE-6G_C (VM5a) model (Peltier et al. 2015). The GRD fingerprint (b) represents the relative sea-level rise caused by mass redistribution between the oceans and ice sheets (Antarctic and Greenland), mountain glaciers and terrestrial water storages for the period 1900 - 2018, as described in Frederikse et al. (2020).

Sea-level change in response to land-ice melting and changes in land water storage is also not uniform across the oceans. The associated changes in Earth's **g**ravity, **r**otation and crustal **d**eformations impose characteristic patterns of regional sea-level change (Farrel and Clarke, 1976), collectively referred to as GRD fingerprints. GRD effects on sea level can be due to past changes (e.g. changes occur over glacial cycles) in land-ice storage, which is known as glacial isostatic adjustment or GIA. GRD effect could also be due to ongoing changes in the land-ice or land water storages, which is termed contemporary GRD effects. Observed RSL rise is affected by both GIA and GRD effects. For example, on average, the ocean basins are slightly subsiding (uplifting) due to the loading (unloading) of sea water since the Last Glacial Maximum that occurred about 20,000 years ago. On the other hand, mass loss from the Greenland ice sheet over the last few decades has caused a sea-level fall around Greenland by a few centimeters as a response to changes in the local gravitational field (e.g. Coulson et al. 2022) while sea level rose over most of the tropical oceans in response to that melting.

While the GRD sea-level fingerprints impose large spatial gradients in RSL near glaciated regions (e.g. the northeast US coasts or Greenland ice sheet), those effects are relatively small in the tropics (Wang et al. 2021). For example, Figure 12.5 illustrates the current rate of RSL rise due to GIA (Figure 12.5a) and GRD (Figure 12.5b) from Peltier et al. (2015; GIA rate) and Frederikse et al. (2020; GRD), respectively in the Southeast Asian region. The GIA-induced sea-level rise represents the sea-level response to deglaciation history over the last 25,000 years from an updated GIA model (ICE-6G_C (VM5a); Argus et al. 2014). Figure 12.5a suggests that RSL falls with rates ranging from -0.1 to -0.4 mm/yr at many of the coastal locations in the Southeast Asia due to GIA, including Singapore (Table 12.5 for GIA-induced RSL change at tide-gauge stations around Singapore).

Figure 12.5b indicates the RSL change due to the net mass balance changes in the ice sheets, glaciers and land water storage for the period 1900 - 2018 (Frederikse et al., 2020). The GRD-induced sea-level rise is mostly uniform around Singapore and the wider south China sea region (~1 mm/yr) for the 1900 - 2018 period (Figure 12.5b).

12.2.3 Local drivers

In addition to the factors discussed in the previous sections, sea-level rise at the coasts is further affected by various physical processes such as tides, storm surges and waves, changes in coastal morphology, and VLM. VLM is one of the most important yet often understudied issues in the detection of RSL rise at many coastal regions. As we will see in Section 12.3, many of the coastal

locations in the Southeast Asian region indeed experience significant local VLM that exacerbates the climate-change-driven sea-level rise.

For instance, Indonesia's capital city Jakarta, is subsiding at an alarming rate of a few centimeters per year (e.g., Bott et al. 2021), and the country is moving its capital to mitigate the associated risks. The Solomon Islands, a low-lying island nation in the western tropical Pacific, has lost at least five of its reef islands to the rising seas and intense wave action, and many of the small islands in the archipelago await a similar fate (Albert et al. 2016).

Factors such as tectonic activities and anthropogenic subsidence potentially cause significant RSL changes in the Southeast Asian seas. Monitoring and understanding those factors are critical to understanding RSL rise in the region.

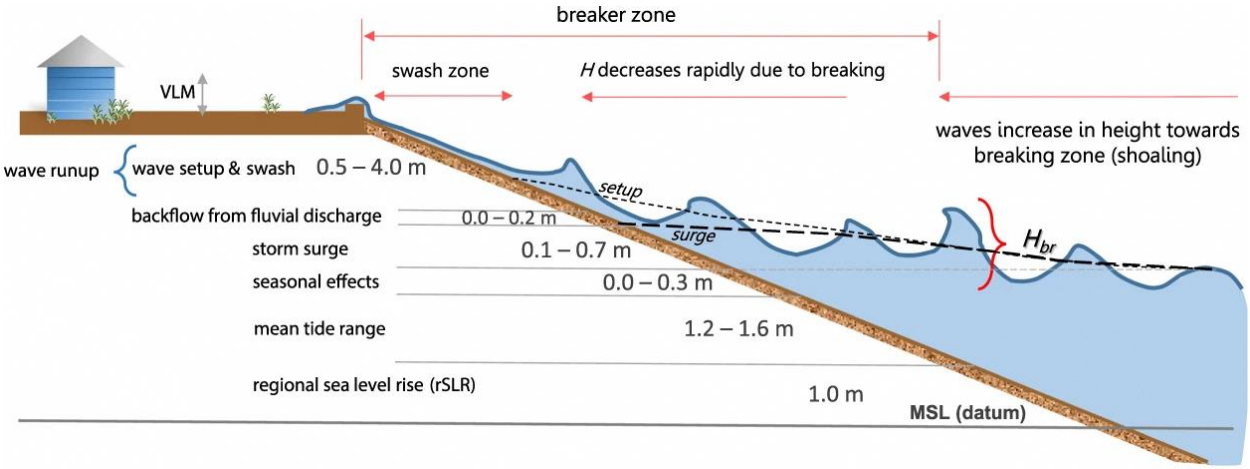

Figure 12.6: An illustration for California for 1 m of sea level rise of the significant water level components that comprise total water levels on a beach during a storm resulting in potential flooding. The range of values are based on observations and modeling conducted for California as described in Barnard et al. (2019). (H = wave height, H_{br} = breaking wave height). The total water level at the coast is a combined effect of regional sea-level rise and other coastal phenomena (e.g. tides, storm surges, seasonal effects and waves). Adapted from Barnard et al. 2019).

At the coasts, tides, storm surges and waves constitute the major processes, coupled with mean sea-level change, that contribute to significant water level oscillations at the coasts (Figure 12.6). Consequentially, this results in extreme sea level change.

Tides around Singapore are typically mixed diurnal and semidiurnal with a range around 2 – 3 m. Cyclonic storm activities around Singapore are weak due to its proximity to the equator. However, sea-level seasonal variations associated with monsoons are substantial (~ 20 cm amplitude; see appendix A1). The monsoon-driven wind-setup drives high (low) sea levels during the northeast (southwest) monsoon and the extreme sea-level anomalies around Singapore indeed tend to occur during the northeast monsoon (Tkalich et al. 2009). A key finding of Singapore's Second National Climate Change study was indeed that the projected changes in surges or waves are dominated by projected mean sea-level rise. Cannaby et al. (2016) pointed that the highest recorded surge level in the Singapore Strait (~ 84 cm) lies between the central and upper estimates of mean sea-level rise by 2100, highlighting the role of mean sea-level rise in driving the extreme water levels at the coasts and the vulnerability of the region.

For the southeast Asian region, the lack of long-term, spatially dense ocean and coastal observations is one of the main challenges in improving understanding of sea-level rise. Ideally, each tide-gauge installation should include a complementary Global Navigation Satellite System (GNSS) receiver to directly monitor VLM. Spatial monitoring of VLM with InSAR (Synthetic

Aperture Radar interferometry) techniques provides another means of estimating the VLM for coastal regions (e.g. Catalao et al. 2020, Tay et al., 2022). Temperature, salinity and current measurements are also fundamental in understanding coastal ocean dynamics and sea-level changes. By analysing observed and model-based sea-level data, this report indicates that the sea-level rise around Singapore is essentially "mass-driven" (Section 12.3). The deployment of a bottom pressure recorder in the shelf region around Singapore would significantly help to observe and interpret the sea-level changes here. However, the availability of such complementary observational systems and data is very sparse in many parts of the Southeast Asian region, including Singapore. Sustaining the existing observing networks (e.g. tide gauges, LIDAR) and initiating coordinated ocean observational programmes would hence be an important step forward in addressing sea-level rise in the SEA region.

The complexity of fully comprehending local sea-level change on varied timescales (Figure 12.3) also calls for developing modeling frameworks for the Southeast Asian region encompassing high-resolution regional ocean modeling and coastal hydrodynamic models, which are essential tools to translate the sea-level rise information into coastal impacts (e.g., inundation, erosion and land/infrastructure loss).

12.3. Observed sea-level rise in Southeast Asia

Tide-gauges have been the key observational records of coastal sea-level changes, and a large body of literature has discussed the mean sea-level changes using those records, at both global and regional scales (e.g. Peltier and Tushingham, 1991; Douglas, 2001; Jevrejeva et al. 2008; Church and White, 2011; Gregory et al. 2013; Hay et al. 2015; Wyrtki, 1987; Mitchum and Wyrtki, 1988; Unnikrishnan and Shankar, 2007; Feng et al. 2004; Woodworth et al. 2019; Nidheesh et al. 2013; Royston et al. 2022). Tide-gauge measures local sea-level changes relative to the land to which the gauge is fixed. A number of oceanic and land processes can thus affect tide-gauge readings as illustrated in Figure 12.3.

Although tide-gauges possess data over multi-decadal periods, a natural limitation of tide-gauges lies in their sparse and uneven geographical distribution. Extreme care has been given in most literature to minimise the biases originating from sparse spatial coverage while estimating global and regional sea-level-rise trends from those records (e.g. Hay et al. 2015; Unnikrishnan and Shankar, 2007). In addition, the record length of sea-level data varies across gauges. Many of the records across the world suffer from substantial data gaps, and this includes many coastal regions in Southeast Asia. Few studies have attempted to quantify the mean sea-level rise in the South China sea and the adjacent shallow shelves using tide gauges (e.g. Tkalich et al. 2013), although a large body of literature has addressed tide-gauge-based sea-level rise estimates in the western Pacific ocean (e.g. Merrifield, 2011; Feng and Meyers, 2004).

Ideally, the VLM-corrected mean sea-level change estimate from tide-gauges is expected to closely match the mean sea-level change measured by satellite altimetry at the same location (Section 12.2). As we will see in the following section, synergising the estimates of mean sea-level rise from tide-gauges and satellite altimetry could provide better insights on local mean sea-level change and potentially indicate the rates of VLM over their overlapping period. Satellite altimetry provides global-scale, gridded sea-level measurements and has greatly aided the understanding of open ocean variability since 1993. A few studies in the past have shown that employing satellite sea-level data in conjunction with tide-gauge records can provide meaningful information on regional and coastal sea-level rise (e.g. Vinogradov and Ponte, 2011; Unnikrishnan et al. 2015; Allison et al. 2022).

In the following section, we describe the observed sea-level rise in Southeast Asian seas (SEAS) by analysing sea-level data from selected tide-gauges and satellite altimetry for the 1993 - 2021 period.

12.3.1 Sea-level rise from satellite altimetry and tide gauges

Monthly sea-level data from tide-gauge records are obtained from the Permanent Service for Mean Sea Level (PSMSL) repository (Holgate et al., 2013; PSMSL, 2022). All the records used in this report are the 'revised local reference' records to assure that the sea-level heights at all stations are referenced to a common datum. More details can be seen in the PSMSL website (https://psmsl.org). Satellite-measured sea-level anomaly (with respect to mean sea-surface height for the period 1993 - 2012) data from the Copernicus Marine Environment Monitoring Service (CMEMS) are another key observational data used in this report, which is based on a merged product from multiple satellite missions (TOPEX/Poseidon, ERS-1/2, Jason-1, Jason-2, and Envisat). The monthly-mean sea-level data have global coverage and are available at a spatial resolution of 0.25° × 0.25°. We analyzed the data for the period 1993 - 2021, for this report. We considered 12 tide-gauge records in the SEAS (Figure 12.7 and Table 12.1), each of them having at least 90% of data coverage during the altimetry period (1993 - 2021). Note that all the twelve gauges, as shown in Figure 12.8, do not extend to the entire satellite period, but some of them do not have a couple of years of data at the end of the period (Malakal [1993 - 2019], Kota Kinabalu [1993 - 2019], Zhapo [1993 - 2020], Sultan Shoal [1993 - 2020], Tanjung Geylang [1993 - 2019], and Ko Taphao Noi [1993 - 2020]). As we focus on long-term trends, the sea-level seasonal cycle is removed for both tide-gauge and satellite monthly data. Hence, all the sea-level data analysed in this report, including the reanalysis data, are anomalies with respect to 1993 - 2012 time-mean sea level and seasonal climatology estimated over the period of analysis (1993 - 2021). The sea-level trends are estimated through a linear regression of the sea-level data in time, and the standard error of the trend is provided as a measure of trend uncertainty.

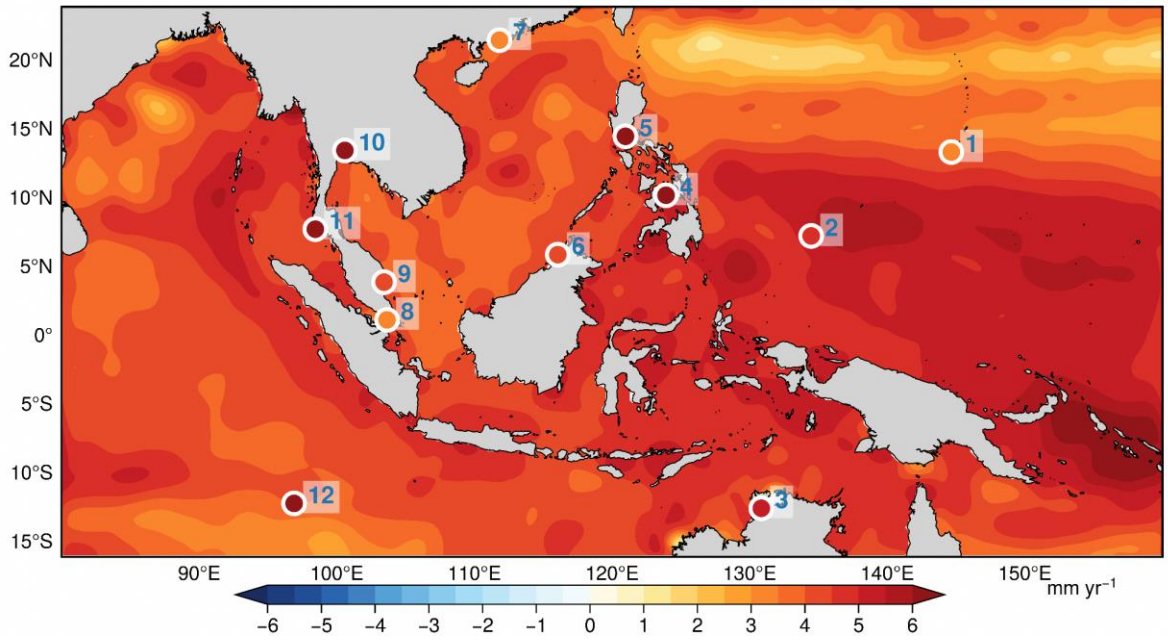

Figure 12.7: Observed sea-level trend from satellite altimetry (spatial map) and tide gauge records (circle) for the period 1993 - 2021. The selected tide gauges are, from east to west: 1. Pago Bay (Guam); 2. Malakal (Palau); 3. Darwin (Australia); 4. Cebu (Philippines); 5. Manila (Philippines); 6. Kota Kinabalu (Malaysia); 7. Zhapo (China); 8. Sultan Shoal (Singapore); 9. Tanjung Gelang (Malaysia); 10. Fort Phrachula Chomklao (Thailand); 11. Ko Taphao Noi (Thailand); 12. Home Island (Cocos Islands).

Satellite sea-level trend map for the period 1993 - 2021 shows that mean sea level is rising almost everywhere in the Southeast Asian region, with a regional-mean rate of ~ 4.4 mm/yr (Figure 12.7). The rate of sea-level rise is not the same everywhere in the region and exhibits deviations from the regional-mean and the global-mean rate (~3.4 mm/yr). For instance, the rates are higher in the western equatorial Pacific (4 - 6 mm/yr) and the eastern Indian Ocean (off the Andaman Islands) whereas relatively weak sea-level rise (0 - 2 mm/yr) is observed in the tropical northwest Pacific (Figure 12.7).

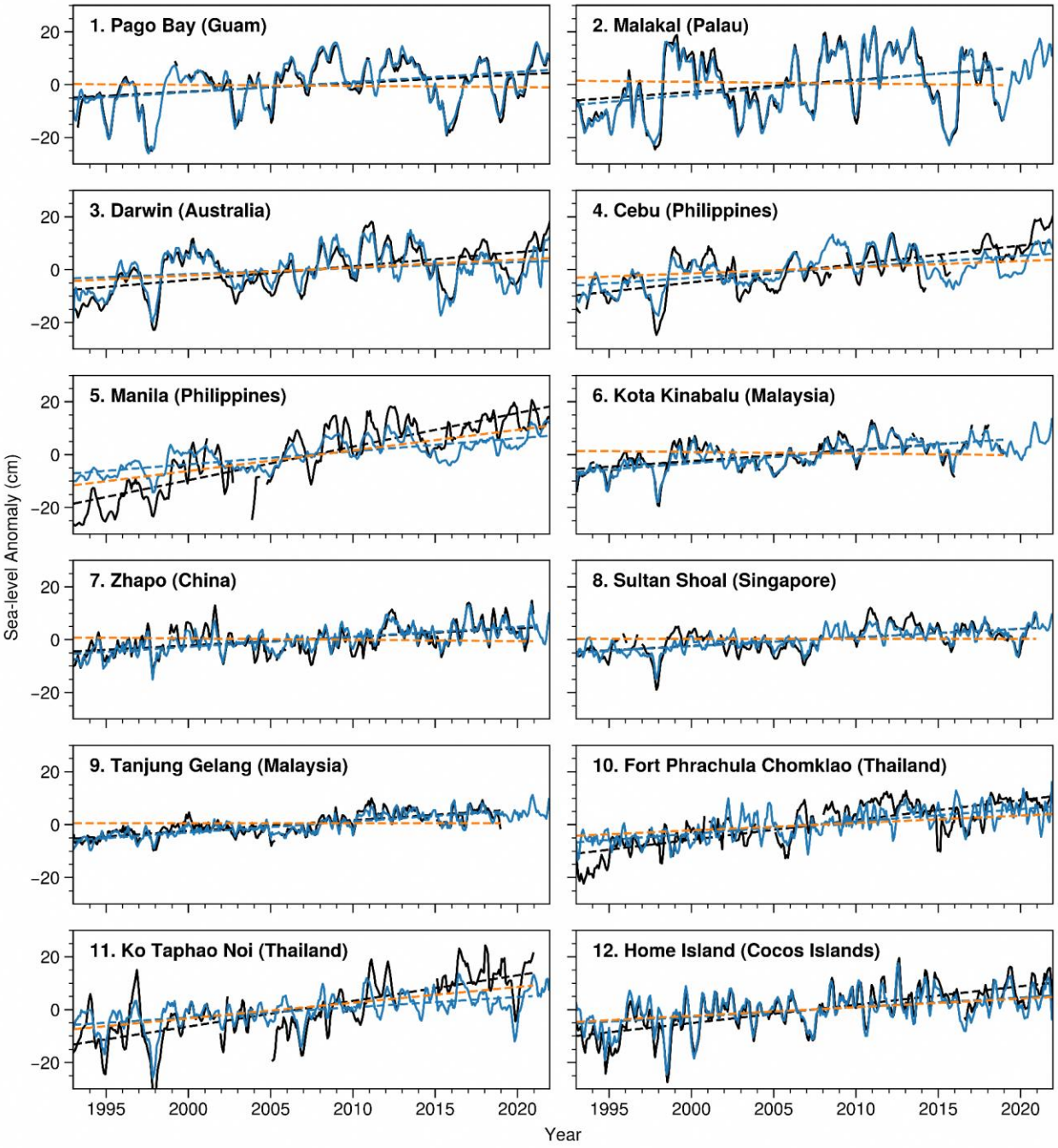

Figure 12.8: Time series of sea-level anomalies from tide gauges (black) and satellite altimetry (blue, averaged over 1 degree around each gauge location shown in Figure 12.5). The difference between the tide-gauge and satellite time series is also shown (orange). A linear trend based on the least-square method is also plotted as a dashed line over each time series with the same color. The trend and corresponding standard error for each tide-gauge is given in Table 12.1.

Note that the rate of mean sea-level rise in the South China sea (SCS) and off Singapore is close to the global-mean rate. Regional deviations in the rate of sea-level change can arise through various geophysical processes, such as the regional ocean circulation and GRD effects (c.f. Figure 12.3). We will come to these points in the following sections.

Rate of sea-level rise across selected tide-gauge records in the SEAS (locations of gauges are shown in Figure 12.7 with color indicating the sea-level trend) also show similar spatial variations. Notably, the tide-gauge trends differ significantly from satellite-based trend estimates (Figures 12.7 & 12.8, Table 12.1) at six locations, namely - Darwin (Australia), Cebu (Philippines), Manila (Philippines), Fort Phrachula Chomklao (Thailand), Ko Taphao Noi (Thailand), and Home Island (Cocos Islands). As explained in section 12.2, the difference in the rates of sea-level rise between altimetry and tide gauge at a given location provide an indication of the local VLM (Woppelmann and Marcos, 2016).

Table 12.1 also suggests that the Sultan Shoal (Singapore) does not have significant local VLM compared to other coastal locations in the SEA region (also refer to Sections 12.4 and 12.6). As detailed in Section 12.6, the GIA-induced VLM in Singapore drives a land uplift (RSL fall) which may counter any local land subsidence due to other factors. Two of the Malaysian gauges (Kota Kinabalu and Tanjung Gelang), as shown in Figure 12.8, stopped recording sea-level change around 2018. This accentuates the importance of sustaining tide-gauge for monitoring and improved understanding of long-term sea-level rise at coastal regions. Ideally, tide-gauge measurements should be supplemented with direct VLM estimates (e.g. using GNSS; Martinez-Asensio et al. 2019), which are absent at many of these tide gauge locations. We call for joint programs to monitor the VLM in Singapore and other vulnerable locations in the Southeast Asian region toward reliable future sea-level projections and coastal adaptation procedures.

Table 12.1: Sea-level trend and standard error for the selected tide-gauge records in the SEAS. Satellite sea-level is averaged at a 1-degree area surrounding each tide-gauge station and the trend of this satellite time series is also given. The trend estimates for the difference time series (i.e. tide-gauge - altimetry) is shown in the last column. Unit is in mm/yr.

	Tide Gauge	Lon (E)	Lat (N)	Tide gauge	Satellite	Difference
1	Pago Bay (Guam)	144.65	13.44	3.20 ± 0.55	3.84 ± 0.52	-0.42 ± 0.10
2	Malakal (Palau)	134.47	7.33	4.59 ± 0.87	5.35 ± 0.82	-0.63 ± 0.11
3	Darwin (Australia)	130.85	-12.47	5.26 ± 0.45	2.27 ± 0.45	2.99 ± 0.20
4	Cebu (Philippines)	123.92	10.3	6.96 ± 0.40	4.18 ± 0.33	2.33 ± 0.30
5	Manila (Philippines)	120.97	14.58	12.71 ± 0.41	4.92 ± 0.25	7.78 ± 0.30
6	Kota Kinabalu (Malaysia)	116.06	5.98	4.28 ± 0.41	4.74 ± 0.28	-0.6 ± 0.14
7	Zhapo (China)	111.82	21.58	3.23 ± 0.31	3.79 ± 0.23	-0.51 ± 0.16
8	Sultan Shoal (Singapore)	103.65	1.23	3.26 ± 0.29	3.34 ± 0.20	-0.01 ± 0.19

9	Tanjung Gelang (Malaysia)	103.43	3.97	4.11 ± 0.21	4.19 ± 0.17	-0.04 ± 0.13
10	Fort Phrachula Chomklao (Thailand)	100.58	13.55	7.49 ± 0.33	4.67 ± 0.25	2.8 ± 0.35
11	Ko Taphao Noi (Thailand)	98.43	7.83	9.69 ± 0.53	3.89 ± 0.33	5.93 ± 0.35
12	Home Island (Cocos Islands)	96.89	-12.12	6.96 ± 0.38	3.66 ± 0.36	3.26 ± 0.09

12.3.2 Decomposition of observed sea-level rise

The sea-level trend from satellite altimetry can be decomposed into two main sources. First, the sea-level trend which is caused by ongoing freshwater exchange between the ocean and land (this includes ice mass changes in grounded ice sheets and glaciers and changes in terrestrial water storages). Following Harvey et al. (2021), we call this source (component) “contemporary mass redistribution” (CMR). Note that, in our definition, the CMR sea-level trend includes both global-mean barystatic sea-level trend and the associated regional GRD fingerprints (Gregory et al. 2019). Second, the sea-level trend caused by ocean sterodynamic changes reflects the sea-level change caused by ocean circulation and seawater density variations (Section 12.2.2). Satellite sea level is also affected by GIA, and hence, we have corrected the satellite trend for GIA by subtracting GIA (GSL) solutions from ICE-5G (Peltier, 2004; Appendix A2) to focus on the remaining two contributions - sterodynamic and CMR. We can hence write the GIA-corrected sea-level rise (SLR) from altimetry as:

SLR (altimeter) = Sterodynamic + CMR + residual

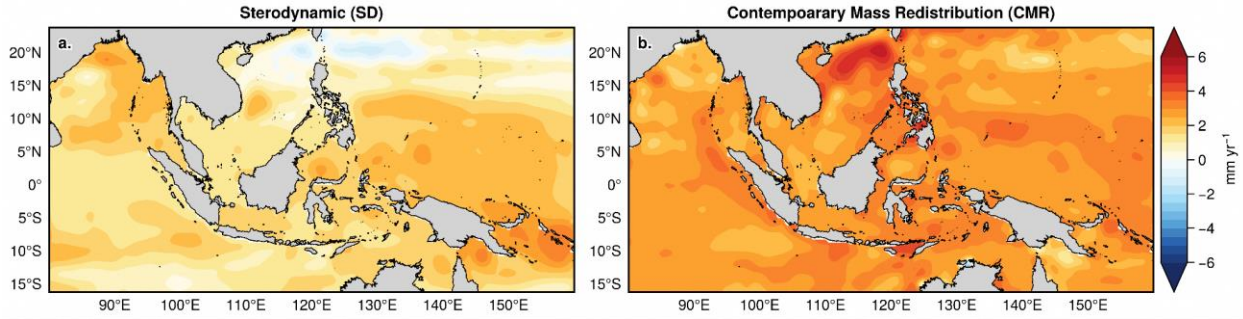

Figure 12.9: a) Sterodynamic sea-level rise (which includes the effects of ocean density variations and regional circulation) for the period 1993 - 2021. b) Sea-level rise trend estimated from the residual signal (i.e. satellite sea level - minus - sterodynamic sea level), considered here as an estimate of sea-level trend caused by contemporary mass redistribution (CMR) between the ocean and land (i.e. sea-level rise caused by ice-melting from ice sheets and glaciers, and terrestrial water storage changes).

The ocean sterodynamic sea-level trend is estimated from the European Centre for Medium-Range Weather Forecasts (ECMWF) Ocean Reanalysis System 5 (ORAS5; Zuo et al. 2019) sea surface height for the satellite period (1993 - 2021). Since ORAS5 is constrained to satellite sea-level trend, we have subtracted the global-mean sea level (estimated from the ORAS5 sea level) from each grid-point and then added back the global-mean thermosteric sea level (GMTSL; estimated from ORAS5 ocean temperature and salinity), to obtain the sterodynamic sea level. The

sterodynamic sea-level rise hence represents both dynamic sea-level rise (due to changes in regional ocean circulation) and the global-mean thermosteric sea-level rise. We subtracted the sterodynamic sea level from altimeter sea level to obtain the “residual signals'', which are approximated to be representative of the sea-level change due to CMR (assuming the uncertainties in the sterodynamic sea level is small as our period of analysis is well constrained by observational data). This exercise provides us a unique way to detect CMR-induced sea-level changes in the SEAS without independent estimates of the GRD fingerprints.

The sterodynamic sea-level rise in the SEAS is positive and rather uniform (with a regional-mean rate of ~ 1.5 mm/yr), except for a few regions (Figure 12.9a) showing deviation from the regional-mean rate. For instance, the sterodynamic sea-level rise in the western equatorial Pacific and the eastern Bay of Bengal (BoB) is slightly higher compared to other regions, and there is a narrow zonal belt of slightly negative (1 - 2 mm/yr in magnitude) rate in the northwest Pacific (~20°N). The higher values in the western equatorial Pacific could be linked to the enhanced trade winds associated with the negative phase of Interdecadal Pacific Oscillation (IPO, see England et al. 2014) during the first decade of the altimeter period. The higher rates along the eastern rim of BoB are also attributed to natural wind variations in the equatorial Indian Ocean (Nidheesh et al. 2013; Unnikrishnan et al. 2015), over recent decades. The sterodynamic sea-level rise in the SCS varies between 1 - 2 mm/yr, with a notable higher rate in the central SCS (Figure 12.9a).

The CMR-driven sea-level rise, in general, is spatially uniform and higher than the sterodynamic sea-level rise almost everywhere in the SEAS (Figure 12.9b). The regional-mean rate due to CMR is ~ 2.9 mm/yr which is nearly twice the regional-mean rate due to sterodynamic sea-level rise (~ 1.5 mm/yr). Note that the sterodynamic and CMR sea-level rise includes sea-level rise due to global-mean thermosteric sea-level rise (~1.2 mm/yr) and global-mean barystatic sea-level rise (~ 2.1 mm/yr) respectively, for the 1993 - 2021 period. Figure 12.9 hence suggests that about two-thirds of net sea-level rise in the SEAS is caused by CMR. The sterodynamic sea-level rise is mostly contributed by GMTSL rise, indicating that the dynamic sea-level rise is weak and confined to a few regions (western equatorial Pacific and eastern BoB) over the satellite period. In the following sections, we will further decompose the sterodynamic sea-level rise into contributions from local density (steric sea-level rise) and local mass changes (manometric sea-level rise, see Gregory et al. 2019), and will discuss how these different processes contribute differently in the SEAS.

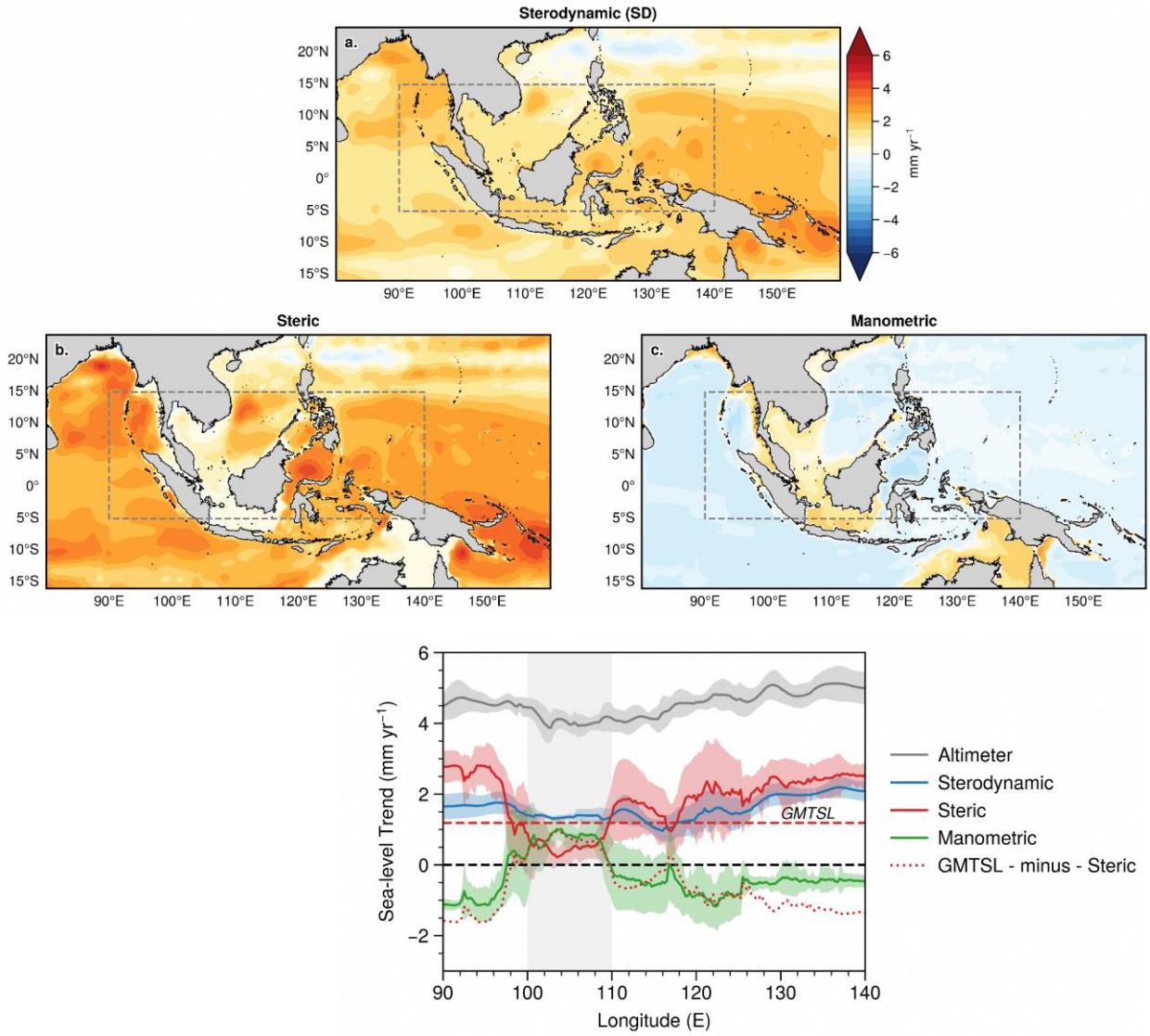

Figure 12.10: (a) Sterodynamic (SD) sea-level rise trend decomposed into, b) steric and c) manometric sea-level rise, estimated from high-resolution ocean reanalysis system (ORAS5). A sub-domain in the SEAS encompassing Sunda shelf, south China sea and the eastern Indian and western Pacific Oceans (gray-dashed rectangle) is shown to highlight the respective contribution of steric and manometric components to sterodynamic sea level change d) Different components of sterodynamic sea-level rise, latitudinally-averaged over the region highlighted by rectangle in panels a, b, and c. The correspondence between the trends of steric anomalies (with respect to global-mean thermosteric sea level - red-dotted curve) and the manometric solution (green) is also shown. The number of valid grid-points in the latitudinal averaging (panel d) is given in Appendix A3.

In principle, the sterodynamic sea-level change can be viewed as a combined response to two different physical processes: the sea-level change caused by local density (steric sea-level change) and the sea-level change due to sea-water (mass) redistribution (manometric sea-level change); i.e.

$$\frac{\vartheta\eta}{\vartheta t} = \frac{1}{g\rho_0}\frac{\vartheta(p_b - p_a)}{\vartheta t} - \frac{1}{\rho_0}\int_{-H}^{\eta}\frac{\vartheta\rho}{\vartheta t}dz \qquad (12.1)$$

The first term in the RHS represents the sea-level change due to ocean mass variations which can be estimated from ocean bottom pressure changes (Pb) corrected for atmospheric loading (Pa). Note that Pa is the local sea-level pressure (SLP) anomaly with respect to the instantaneous average of SLP over the global ocean (Gregory et al. 2019). This term has been known as the bottom pressure sea level in the past literature and renamed to manometric sea-level change in

Gregory et al. (2019). And, the second term in the RHS represents the steric sea-level change estimated as the time-derivative of seawater density. We estimated steric sea-level changes from ocean temperature and salinity from ORAS5, using the equation of state (Jacket and Mcdougal, 1995). The manometric sea-level is obtained by subtracting the steric sea level from the sterodynamic sea level (Eqn. 12.1).

Figure 12.10b and 12.10c show the steric and manometric sea-level rise in the SEAS respectively. Steric sea-level rise contributes the sterodynamic sea-level rise mainly over deep oceans (Figure 12.10b and c.f. Figure 12.1 showing the water depth) while manometric rise is more prominent over shallow shelf regions in the SEAS (Figure 12.10c). This “depth-dependent” contribution of steric and manometric sea-level change has been reported earlier (e.g. Landerer et al. 2007a).

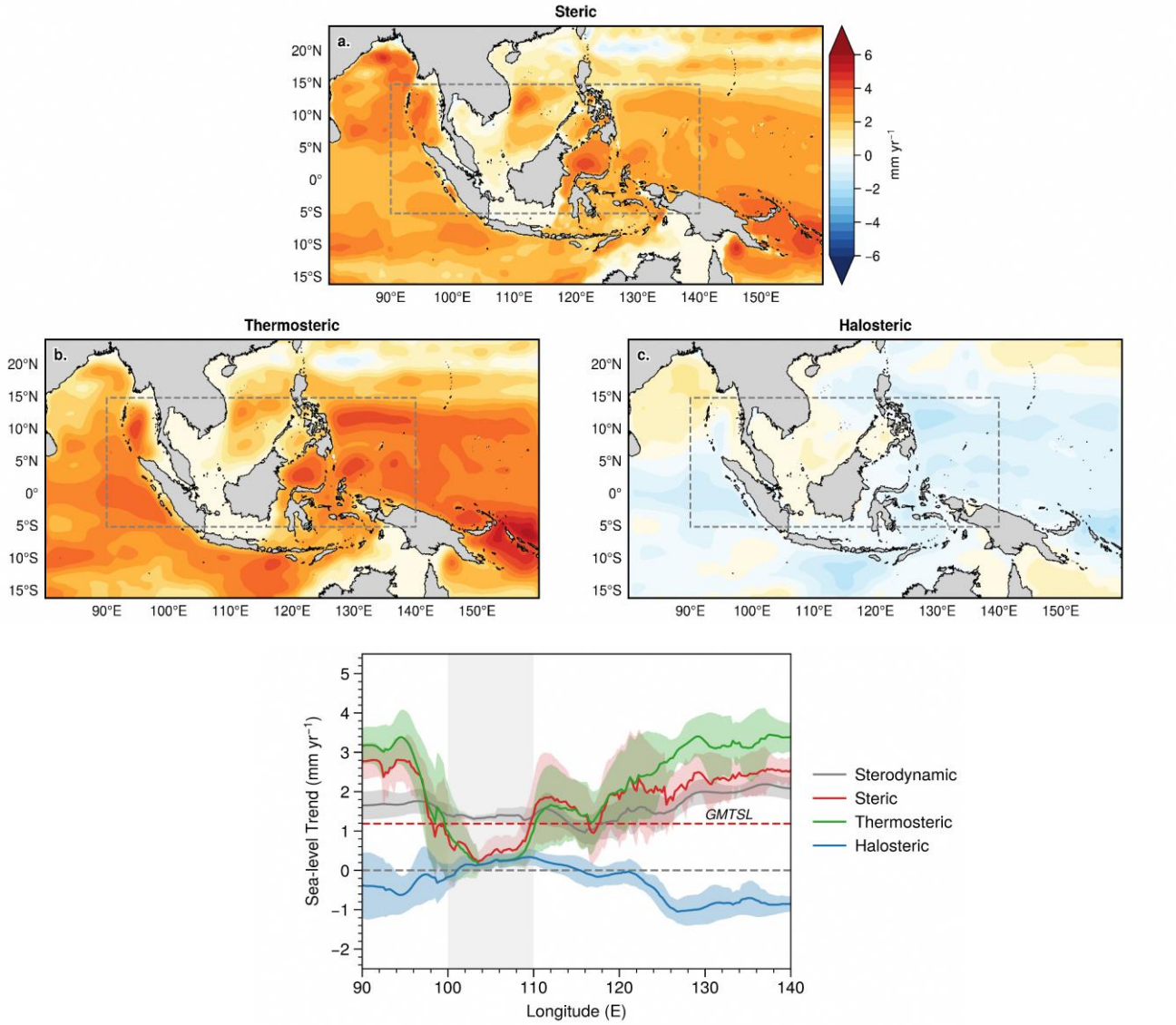

Figure 12.11: (a) Steric sea-level-rise trend decomposed into, b) thermosteric and c) halosteric sea-level rise in the SEAS estimated from high-resolution ocean reanalysis system (ORAS5). A sub-domain encompassing Sunda shelf, south China sea

and the western Indian and eastern Pacific Oceans (gray rectangle) is shown to highlight the contribution of respective components to steric sea-level rise d) Components of steric sea-level rise, latitudinally-averaged over the region highlighted by rectangle in panels a, b, and c. Red dashed line indicates the global-mean thermosteric sea-level trend for the period 1993 - 2021, estimated from ORAS5 ocean temperature and salinity (1.2 mm/yr).

As the deep ocean is more efficient in storing heat than shallow waters, the former experiences more thermosteric sea-level rise (Figure 12.11b) which leads to more steric sea-level rise over deep oceanic regions. At the same time, those enhanced deep ocean expansion would create a strong steric gradient (surface pressure gradient) between the deep and shallow regions leading to a redistribution of water to shelves, causing significant manometric sea-level rise over the shallow regions, as seen in Figure 12.10c. Readers may refer to Landerer et al. (2007b) to see more details of such mass redistribution process. Figure 12.11b indeed suggests that the steric sea-level rise in the SEAS is mostly driven by ocean thermal expansion and contribution from salinity changes (halosteric sea-level changes) is relatively weak (Figure 12.11c).

To understand the relative role of steric and manometric sea-level rise to sterodynamic sea-level change in our region better, let us focus over a small subdomain as highlighted by dashed rectangles on Figures 12.10 and 12.11. The selected region encompasses the shallow Sunda shelf (sea around Singapore) at its center and deep basins either side of it.

A meridionally-averaged distribution of sea-level trend, as shown in Figures 12.10d and Figure 12.11d, clearly shows how steric and manometric sea-level change contribute differently over deep and shallow regions in the SEAS. The steric sea-level trend drops significantly (falls close to zero) over the Sunda shelf and then rises at either side of the shelf where water depth increases sharply (off to the continental slope, c.f. Figure 12.1). The manometric sea-level trend appears to be a mirror of the steric sea-level trend (green and red curves in Figure 12.10d), supporting the notion that the ocean adjusts to the spatially non-uniform steric sea-level rise by redistributing the ocean mass from regions of larger steric sea-level rise to regions of smaller steric sea-level rise (Landerer et al. 2007b). Even though the exact physical mechanism through which this mass transfer occurs is rather complex and not understood fully (see Bingham and Hughes, 2012), it is interesting to note that the sterodynamic sea-level rise in the Sunda shelf and off Singapore is primarily associated with “ocean internal mass redistribution”. Figure 12.10d also suggests that the manometric sea-level rise could be driven by the gradient in steric sea-level anomalies with respect to global-mean thermosteric change (red-dotted curve in Figure 12.10d), rather than by the actual steric sea-level rise.

As mentioned above, the steric sea-level rise in the SEAS is mostly contributed by thermosteric changes as seen in Figures 12.11b and 12.11c. Even though the contribution of halosteric sea-level rise is weak compared to thermosteric changes, it is worth noting that the salinity contribution is positive in the SCS region and negative in the western Pacific and eastern Indian Ocean (Figures 12.11c and 12.11d). This spatial variability indicates the freshening of seawater in the SCS over the recent decades compared to the western Pacific for which the depth-integrated salinity seems increased. The physical processes that contribute to the halosteric sea-level rise in the SCS is not examined further for this report, but this will be an important perspective for CCRS research activities in future.

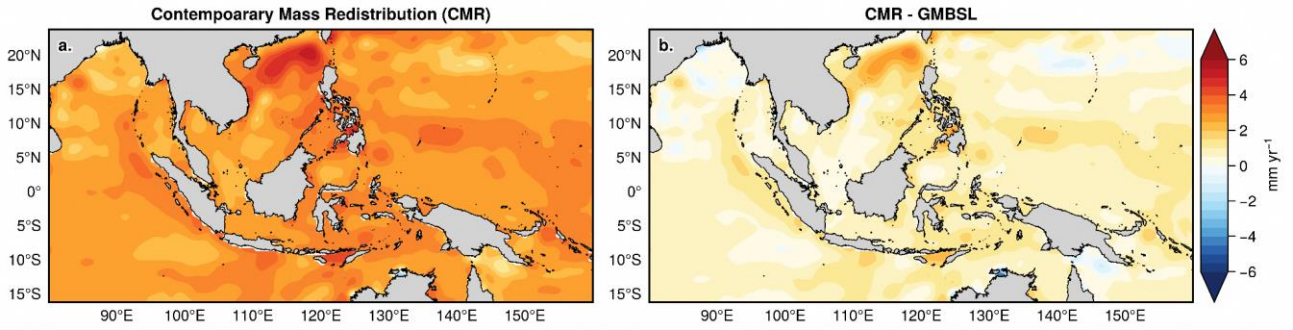

Figure 12.12: a) Sea-level rise trend from contemporary mass redistribution (CMR, as shown in Figure 12.9) estimated as the difference between altimeter and sterodynamic sea-level. Global-mean barystatic sea-level rise for the period 1993 - 2021 (2.1 mm/yr) is subtracted from CMR-driven sea-level rise (panel a) to highlight the GRD effects in the SEAS and shown in b.

We noted earlier that the CMR-driven sea-level rise (Figure 12.12a) includes the global-mean barystatic sea-level rise (GMBSL; ~2.1 mm/yr) and the regional deviations associated with the GRD effects. We have subtracted the GMBSL rate from the CMR sea-level trend to see if there are any notable deviations in the SEAS (Figure 12.12b). No significant deviations from GMBSL rate observed in the SEAS, except for a noticeable pattern in the northern SCS (Figure 12.12b). A few of the previous studies indicated that the GRD effects in the tropical regions are rather uniform (e.g. Frederikse et al. 2020; Wang et al. 2021), and hence, the anomalous CMR pattern seen in the northern SCS (Figure 12.12a) would probably be related to either any "uncaptured" sterodynamic signal in the ORAS5 or some other processes which may not be accounted for by the GRD effects. To investigate this further, we compared the dynamic sea-level (DSL) rise from other two reanalyses - GECCO3 (German contribution of the Estimating the Circulation and Climate of the Ocean; Köhl, A. 2020) and GLORYS 12V1 (Global Ocean Physics Reanalysis; Supplementary figure A12.4) over the same period, and found that the DSL rise in the northern SCS in those products conforms each other but differ to that from ORAS5. This indicates that the anomalous CMR signal in the northern SCS (Figure 12.5a) might be originating from uncertainties in SD sea-level change in this region as represented in reanalyses. We do not go into further details on it in this report. In general, Figure 12.12 suggests that the CMR related mean sea-level rise in the SEAS is predominantly driven by GMBSL rise and the GRD effects are negligible as suggested by earlier studies mentioned above.

As we have seen at the beginning of this section, the residual sea-level signal, i.e. signal obtained once the sterodynamic sea-level change is subtracted from GIA-corrected altimeter sea level, is considered an approximation to the contribution of CMR to sea-level rise over the satellite period in the SEAS (shown in Figure 12.12a). This approximated CMR contribution should be understood within the context of uncertainties associated with the sterodynamic sea-level changes, any other processes that contribute to the observed sea-level change, and the uncertainties in the altimeter measurements itself. Our sterodynamic sea-level estimate comes from a recently updated ocean reanalysis which encompasses the latest updates and advances in base ocean model and observational data assimilation for the post-altimetry era (see Zuo et al. 2019), and hence offer minimum uncertainties in the sea-level and other ocean state variables used in this report (ocean temperature and salinity). However, an exact assessment of the CMR driven sea-level rise should follow an independent estimate of GRD sea-level fingerprints using geodetic models (e.g. Harvey et al. 2021; Coulson et al. 2022). Such an exercise would also reveal the contribution of individual mass sources (e.g. Greenland ice sheet and mountain glaciers) to the observed sea-level rise in the SEAS. We are currently developing this analysis to include such independent CMR contributions using latest mass balance estimates from different sources (e.g. data from the Ice

Sheet Mass Balance Inter-comparison Exercise - IMBIE; Otosaka et al. 2023), which would complement the findings presented in this report in the near future.

12.4. Observed sea-level rise around Singapore

The vertical datum for all height measurements in Singapore (called Singapore Height Datum) is set to mean sea level at 0.0 m, which is taken as the average water level from the historical tide-gauge record at the Victoria Dock for the 1935 - 1937 period (Singapore Land Authority, Singapore). As we have seen in the introduction, a large portion of the Singapore mainland (especially the coastal zones) lies well below five meters of MSL. MSL changes, ranging from seasonal to long-term (over a period of 100 years), hence have great concern for the coastal regions of Singapore as it could adversely affect Singapore's coastal infrastructures.

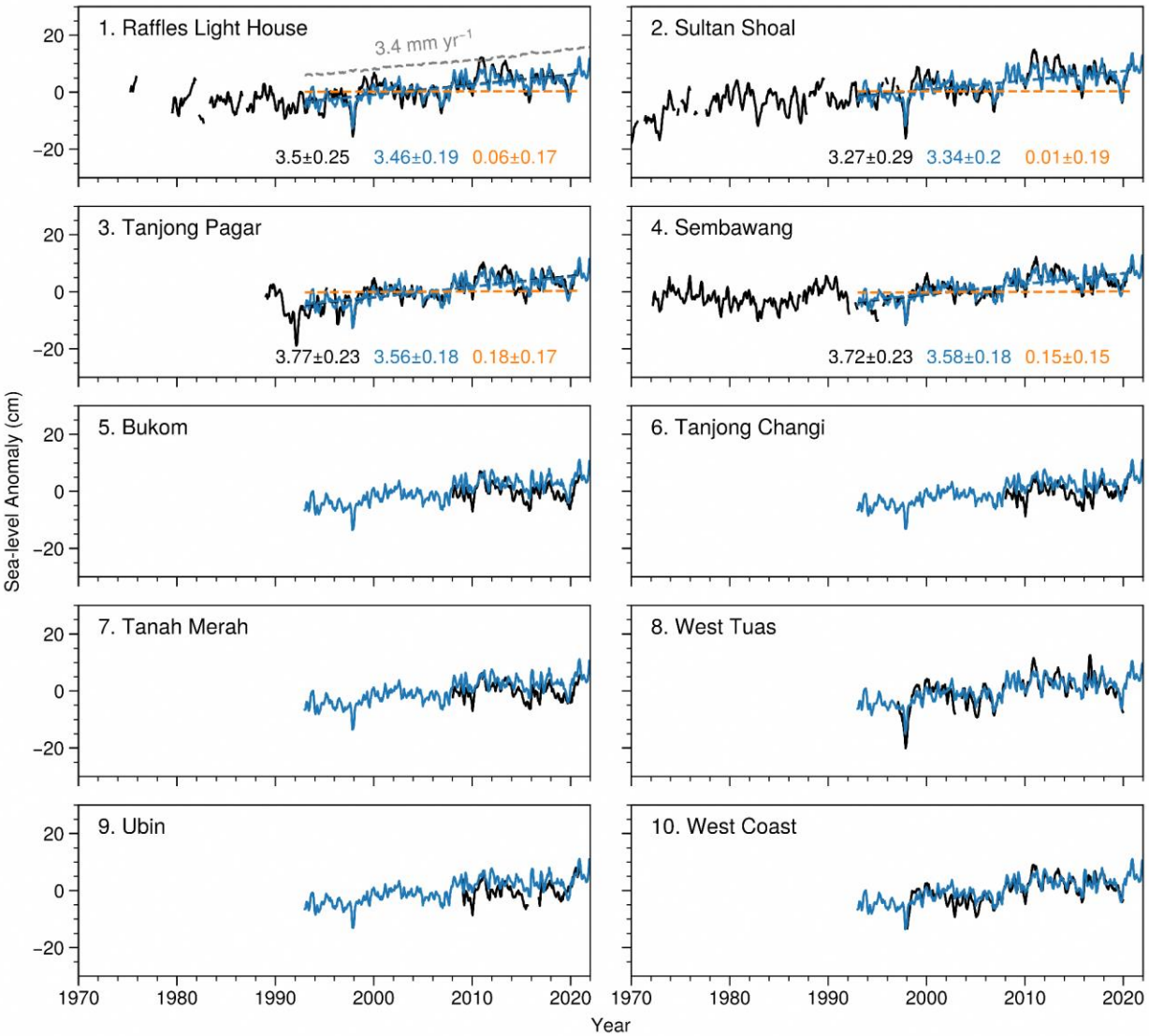

Figure 12.13: Time series of sea-level anomalies from tide gauges (black) and satellite altimetry (blue, averaged over 1 degree around each tide-gauge location). The difference between the tide-gauge and satellite time series is taken for the first four tide-

gauge records which have more than 90% of data during the satellite period (1993 - 2021). A linear trend based on the least-square method is also plotted as a dashed line over those four records (black - tide-gauge, blue - satellite, orange - difference. Units are mm/yr). The slope and standard error corresponding to each trend line are also given. The global-mean sea level from satellite altimetry (trend ~ 3.4 mm yr-1) is shown for a comparison in panel a (gray dashed curve), indicating that the mean sea-level rise off Singapore over the last three decades is consistent with the rate of global-mean sea-level rise.

Sea-level time series from ten tide-gauge records around Singapore are shown in Figure 12.13. Satellite sea-level data (¼ degree resolution) averaged at a 1-degree square domain around each tide-gauge record is also shown (blue curve). Note that, mean seasonal cycle (seasonal climatology) is removed from both satellite and tide-gauge data. There is a good level of agreement between tide gauge and altimeter time series at interannual periods (Figure 12.13), providing confidence on comparing their respective trends. Four out of ten records (Raffles Light House, Sultan Shoal, Tanjong Pagar and Sembawang) have more than 90% data over the altimeter period (1993 - 2021) and the trend estimates are given for those four records (Figure 12.13). As we have seen in section 12.3 and for Figure 12.8, difference in sea-level rise trend estimates between tide-gauge record and altimeter sea level could indicate rate of local VLM, which is shown for those four records.

Rate of sea-level rise around Singapore varies between 3.27 (Sultan Shoal) to 3.77 (Tanjong Pagar) with a mean rate (average rate for the four stations) of 3.56 mm/yr during 1993 - 2021. The mean rate from corresponding altimeter data (3.48 mm/yr) is close to tide-gauge measured sea-level rise. Figure 12.13 shows that the rates of sea-level rise from tide-gauge and satellite at the four tide-gauge stations agree well with each other. This agreement between tide-gauge and altimeter sea-level trends indicates that the rate of local VLM in Singapore might be weak (< 0.2 mm/yr) compared to other coastal locations in the southeast Asian region (see Figure 12.8). Local VLM consists of VLM caused by GIA and other processes (local subsidence, tectonics, etc). As shown in section 12.6 (Table 12.5), the GIA-induced land uplift rate is ~0.2 mm/yr. There is no consensus on the local subsidence or movements related to tectonics due to limited observations. See Section 12.6 for a detailed note on the VLM in Singapore.

Figure 12.13 also suggests that the rate of mean sea-level rise around Singapore is consistent with the rate of GMSL rise (~ 3.4 mm/yr) over the satellite period. However, it is worth noting a few points on the processes that drive sea-level changes around Singapore as discussed in section 12.3. Contemporary mass redistribution (CMR) turns out to be the main driver of observed sea level rise around Singapore (explains about 70% of the net observed rise). The CMR contribution mostly comes from the GMBSL rise over the 1993 - 2021 period which is about 2.1 mm/yr (Figure 12.12). On the other hand, manometric sea-level (ocean internal mass distribution) drives large part of the sterodynamic sea-level rise (~23% of the total rise) with a very weak contribution from steric sea-level rise (due to the fact that shallow shelf does not support large steric changes compared to deep ocean).

The combined contribution of both CMR and manometric sea-level suggests that nearly 90% of the observed sea-level rise off Singapore is “mass-driven”. The dominating contribution of CMR on sea-level rise around Singapore indicates how land ice melting from remote locations (mostly from mountain glaciers in mid-to-high latitudes) can impact low-lying countries in the equatorial regions. Also, the role of manometric sea level indicates that the dynamic sea-level changes off Singapore are essentially linked to ocean circulation, highlighting the importance of accurately resolving the circulation features in climate models to better predict the sterodynamic sea-level rise for the region. The coarse resolution of the current global climate models cannot resolve the narrow straits and coastal currents adequately, and our findings stress the need for high-resolution ocean modeling and dynamical downscaling of the ocean climate and sea level to obtain better future projections.

12.5 Sea-level projections

Sections 12.3 and 12.4 provide an overview of the historical sea-level change in Singapore and the Southeast Asian region, and important contextual

information on driving mechanisms that are also relevant to the spatio-temporal evolution of future sea-level rise in this region. In the following sections, we present future sea-level projections for both Singapore and Southeast Asia for several tide gauge locations. We also discuss the strengths and limitations of the projections in order to promote well-informed coastal protection planning measures.

The Intergovernmental Panel for Climate Change Sixth Assessment Report (IPCC AR6) (Fox-Kemper et al., 2021; Garner et al., 2021) published in 2021 produced global and local sea-level projections using state-of-the-art methodologies. Major advances in the sea-level projections in AR6 compared to previous IPCC reports (i.e., AR5 and SROCC) include: (i) the use of emulators to provide sea-level projections consistent with the AR6 assessment of equilibrium climate sensitivity and global surface temperature rise (Forster et al, 2021; Fox-Kemper et al, 2021; Slangen et al., 2022); (ii) the explicit consideration of accelerated sea-level associated with poorly-understood ice sheet instability mechanisms through high-end storylines (Fox-Kemper et al, 2021). One key difference is also the usage of historical tide gauge data in the AR6 methods of projecting vertical land movement, which contributes to RSL rise on a regional and local scale. This is the first time the non-climatic background component contributing to RSL rise has been included in the IPCC sea-level projections, using tide gauges. In this light, the following sections present sea-level projections from AR6 at the various tide gauges in Singapore and Southeast Asia.

We follow the calibrated uncertainty terminology used in the IPCC AR6 here, in which scientific confidence levels (low, medium, high) represent a qualitative assessment of the number of lines of evidence and level of agreement among studies, whereas the likelihood of any projected value of sea-level rise (e.g., *likely* range) is a quantitative measure of uncertainty, expressed as probabilities. Other sea level terminology used in this chapter follows that of Gregory et al. (2019). We focus on three Shared Socioeconomic Pathways (SSPs): SSP1-2.6, SSP2-4.5 and SSP5-8.5 for all the sea-level projections shown in the following sections, to be consistent with the climate projections presented in the other chapters of this report.

12.5.1 Data and methods

Here we outline the main methodology utilised in the IPCC AR6 projections and our V3 projections for sea level. But for more technical details, do refer to the detailed report (Chapter 9 of IPCC AR6 WGI).

AR6 methodology

Sea-level projections from the IPCC AR6 are produced using the Framework for Assessing Changes to Sea-level (FACTS; Kopp et al, 2023). FACTS employs a Monte Carlo approach across the various drivers of GMSL rise and includes localisation of these global projections using GRD patterns, information of sterodynamic sea-level change from CMIP6 models and vertical land motion (including the effect of GIA) based on Kopp et al (2014). In AR6, medium confidence sea-level projections are tabulated until 2150, whereas thereafter until 2300 are considered low confidence sea-level projections. The type and number of models used, combined with expert judgment assessments, vary largely across the individual drivers. No single method was used to derive the projected sea level change by the different drivers for a homogeneous time period (e.g., 2020 to 2150). Table 12.2 below summarises the methodology used to estimate each driver of the IPCC AR6 sea-level projections.

Table 12.2: Summarised methodologies respective to the sea level drivers according to 3 timelines: projections up till 2100, beyond 2100 till 2150 and till 2300. Heavily referenced from IPCC AR6 Chapter 9 and Table 1 from Slangen et al. (2022); refer to AR6 for full reference.

	Sea level driver	Projection for 2014-2100 (*medium confidence*)	Projection for 2100-2150 (*medium confidence*)	Projections for 2150-2300 (*low confidence*)

1	Thermal expansion	Two-layer emulator with climate sensitivity calibrated to the AR6 assessment and expansion coefficients calibrated to emulate CMIP6 models.	
2	Ocean dynamic sea level	Multivariate *t*-distribution fitted to ocean dynamic sea level produced from CMIP6 models. This distribution is derived from CMIP6 ensemble *zos* field after linear drift removal, then combined with the emulator-based global mean thermosteric projections.	
3	Glaciers	Gaussian process emulated glacier model: GlacierMIP (Marzeion et al., 2020; Edwards et al., 2021)	AR5 parametric model re-fit to GlacierMIP (Marzeion et al., 2020).
4	Greenland Ice Sheets	Medium confidence processes up to 2100: Emulated ISMIP6 simulations (Box 9.3) (Edwards et al., 2021)	Medium confidence processes: Parametric model fit to ISMIP6 simulations up to 2100 extrapolated based on either constant post-2100 rates or a quadratic interpolation to the multimodel assessed 2300 range. Assumption of constant rates of mass change after 2100. Low confidence processes: Structured expert judgement (Bamber et al., 2019)
5	Antarctic Ice Sheets	Medium confidence processes up to 2100: p-box including (1) Emulated ISMIP6 simulations (Edwards et al., 2021) and (2) LARMIP-2 simulations (Levermann et al., 2020) augmented by AR5 surface mass balance model. Processes considered are surface mass balance and ice dynamics, which includes marine ice sheet instability (MISI).	Medium confidence processes after 2100: p-box including (1) AR5 parametric AIS model and (2) LARMIP-2 simulations augmented by AR5 surface mass balance model, with both methods extrapolated based on either constant post-2100 rates or a quadratic interpolation to the multimodel assessed 2300 range. Low confidence processes: (1) Single ice-sheet-model ensemble simulations incorporating Marine Ice Cliff Instability (MICI) (DeConto et al., 2021) and (2) structured expert judgement (Bamber et al., 2019)
6	Land Water Storage	Statistical relationships between population and anthropogenic causes of changes in land water storage are determined: (1) Population and groundwater depletion relationship calibrated based on Konikow (2011), Wada et al., (2012) and Wada et al., (2016). (2) Population and dam impoundment relationship calibrated based on Chao et al., (2008), and adjusted to scenario-dependent based on the different SSP's population variations (Kopp et al., 2014).	

7	Vertical Land Motion	Using a Gaussian process spatiotemporal model based on tide-gauge data (updated from Kopp et al., (2014)) and GIA model, linear rates of VLM are derived.
8	Gravitational, rotational, and deformational (GRD) effects	Sea-level equation solver (Slangen et al., 2014a) driven by projections of ice sheet, glacier, and land water storage changes is used to compute annual sea-level fingerprints for each mass change contribution.

Deriving V3 sea-level projections for Singapore

The IPCC AR6 provided RSL projections for Singapore at 6 tide-gauges. These six tide-gauges are Sultan Shoal, Sembawang, Raffles Light House, Tanjong Pagar, West Coast and West Tuas. Although there are a total of 13 running tide gauges in Singapore that are managed by the Marine Port Authority (MPA), only the above-mentioned 6 tide gauges have records that span at least 15 years, which was the criteria for generating sea-level projections at tide gauges in AR6 (Kopp et al., 2014).

Annual tide-gauge data from the Permanent Service for Mean Sea-Level (PSMSL) play a crucial role in the AR6 sea-level projections for vertical land movement (VLM)—a component that distinguishes local sea level projections from regional and global projections. As part of the IPCC methodology, the tidal data is processed through a spatiotemporal Gaussian model developed by Kopp et al. (2014) to estimate VLM. This analysis generates a linear projected rate of VLM, along with a corresponding standard deviation (Kopp et al., 2014).

However, during our quality checks on the Singapore tide-gauge data in the PSMSL, we identified errors in the Sembawang annual tide-gauge data. Specifically, we discovered that the data from the 1950s preceding a data gap was not referenced to the same benchmark as the rest of the dataset (Figure 12.14). The erroneous data associated with the Sembawang tide-gauge was subsequently revised and improved by PSMSL. The improved dataset was reprocessed using the Kopp et al. (2014) model.

This step allowed us to generate revised VLM projections and update the AR6 sea level projections for the six tide gauges in Singapore. The AR6 projections without the VLM component were obtained from the IPCC authors (Garner et al., 2022). In accordance with the AR6 methodology, we added our revised VLM projections with the AR6 projections that do not contain the VLM component and generated the total projected RSL for all six locations in Singapore.

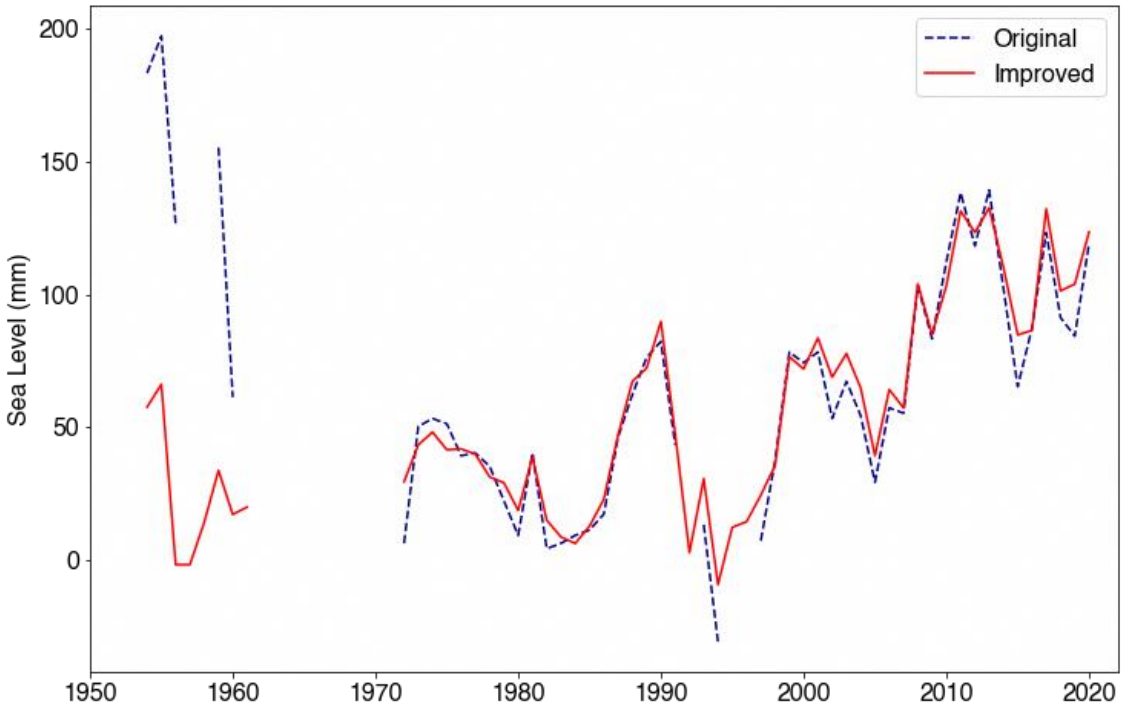

Figure 12.14: Annual tide-gauge data at Sembawang. Shown in dashed blue is the original data on PSMSL and red is the corrected data.

12.5.2 Global-mean sea level projections

According to the IPCC AR6 WGI Report, global-mean sea-level (GMSL) is projected to rise across all future climate scenarios. Until 2050, in accordance with the AR5 and Special Report on the Ocean and Cryosphere in a Changing Climate (SROCC) reports, the projected GMSL rise shows little variation depending on different scenarios. However, after 2050, the scenarios start to show more significant differences (Fox-Kemper et al., 2021).

There is medium confidence in these projections, with a *likely* GMSL rise of 0.19 (0.16–0.25) m under SSP1-2.6 and 0.23 (0.20–0.30) m under SSP5-8.5 by 2100 (Figure 12.15).

The IPCC AR6 suggests an alternative approach to addressing uncertainty in future GMSL rise by factoring in the uncertainty associated with the timing of specific sea-level rise thresholds. Focusing on projections that only incorporate processes with medium confidence, it is *likely* that GMSL will surpass 0.5 m sometime between 2080 and 2170 under SSP1-2.6 and between 2070 and 2090 under SSP5-8.5.

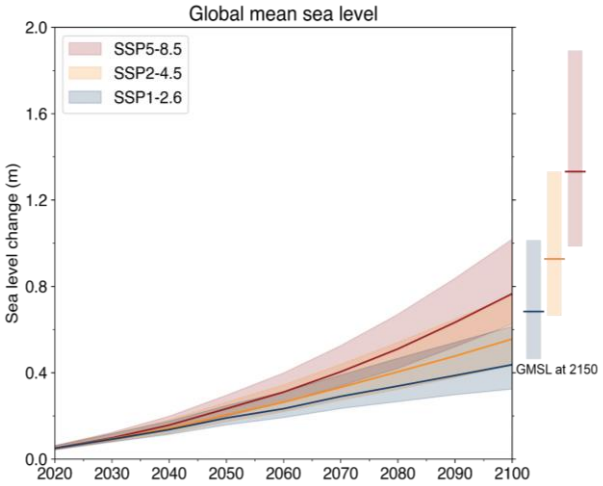

Figure 12.15: Projected rise in global-mean sea-level up to 2150, relative to IPCC AR6 baseline 1995 - 2014, under three emission scenarios (SSP1-2.6, SSP2-4.5 and SSP5-8.5). Solid curves represent the median

(50th percentile), whilst the shaded bands represent the *likely* range (17th to 83rd percentile).

It is *likely* that GMSL will exceed 1.0 m between 2150 and beyond 2300 under SSP1-2.6, and between 2100 and 2150 under SSP5-8.5. However, it is *unlikely* to surpass 2.0 m until after 2300 under SSP1-2.6, whereas it is *likely* to do so between 2160 and 2300 under SSP5-8.5 (Fox-Kemper et al., 2021).

12.5.3 Sea-level projections for Singapore

In the following subsections, we provide a comprehensive analysis of our sea-level projections. Our findings encompass both medium and low confidence projections, offering valuable insights for planning and decision-making. The medium confidence sea-level projections extend up to the year 2150 (Section 12.5.3.1). These projections serve as a robust basis for mitigation planning, providing stakeholders with a reliable framework for addressing potential sea-level rise impacts within a reasonable timeframe. Additionally, we present low confidence sea-level projections that extend beyond 2150, up until 2300 (Section 12.5.3.2). Despite their lower confidence level, these projections hold significance as they represent potential outcomes that cannot be entirely disregarded. By including these projections, we aim to equip stakeholders with a more comprehensive understanding of the range of possibilities, enabling them to make better-informed decisions.

12.5.3.1 Medium-confidence sea-level projections to 2150

Here we present sea-level projections at the six tide gauges in two ways: (i) continuous projections for the period 2014-2100; and (ii) projected ranges at 2150 (Figure 12.16 and 12.17). Figure 12.16 provides a timeseries visualisation of the projected change in mean sea level at the six locations, whilst Figure 12.17 summarises the projections by 2150 under the low, medium and high emission scenario on a map of Singapore.

A consistent methodology was used in the AR6 sea-level projections for the period 2014-2100, so we show these as continuous time series. For the period from 2100 to 2150, additional methodological assumptions were made that resulted in discontinuities in the time series. Therefore, we show only the projected ranges at 2150. All sea-level projections are expressed relative to the AR6 baseline period of 1995-2014.

Annual tide-gauge records of the change in RSL as recorded by these tide gauges prior to 2020 are also shown in Figure 12.17. See Table 12.3 for values of the median and *likely* range of sea-level projections at these gauges for three scenarios.

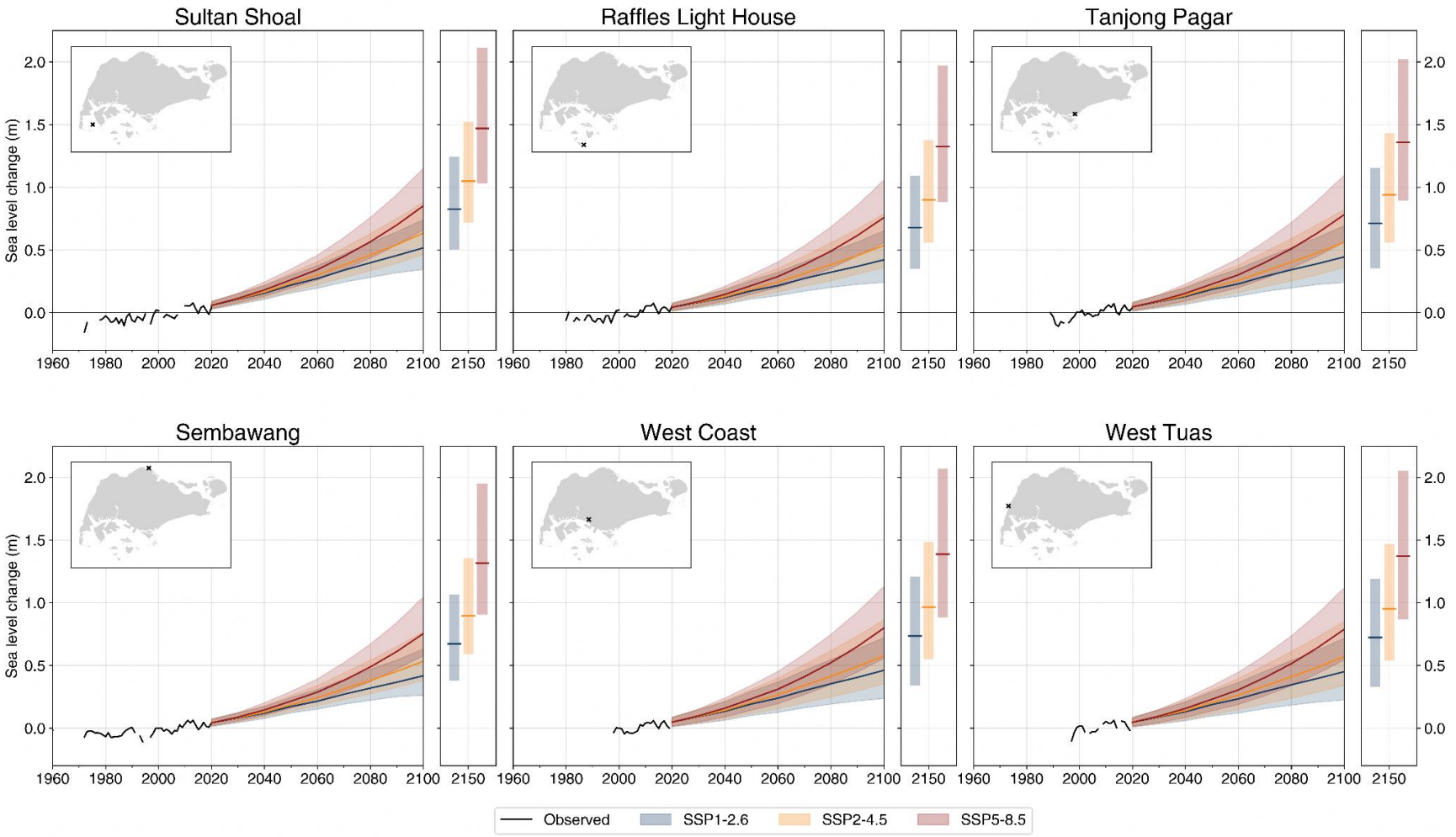

Figure 12.16: Time series of relative sea level change at the six primary Singapore tide gauges. Black solid line before 2020 shows observed relative sea level using annual tide gauge data taken from PSMSL. After 2020, continuous mean sea level projections up till 2100 and at 2150 for 3 SSPs (SSP1-2.6, SSP2-4.5, SSP5-8.5) are shown. Median (colored solid lines) and *likely* range (shaded regions) of the projections are shown. Projections at Sembawang have been adjusted with the new VLM projections taken into consideration. Both observed and projections are relative to the baseline 1995 – 2014. Individual locations of these tide gauges, indicated with a black cross, are shown on a map of Singapore on the top right corner.

Figure 12.17: Projected relative sea-level rise in Singapore at six tide-gauges (Sembawang, West Tuas, West Coast, Tanjong Pagar, Raffles Light House and Sultan Shoal) by 2150 under three emission scenarios (SSP1-2.6, SSP2-4.5 and SSP5-8.5). Values shown reflect the median (*likely* range) projected sea-level change by 2150 relative to the IPCC AR6 baseline 1995 - 2014.

Tide Gauges	SSP1-2.6		SSP2-4.5		SSP5-8.5	
	2100	**2150**	**2100**	**2150**	**2100**	**2150**
Sultan Shoal	0.51 (0.34 – 0.74)	0.82 (0.50 – 1.24)	0.63 (0.46 – 0.88)	1.05 (0.72 – 1.52)	0.85 (0.66 – 1.15)	1.47 (1.03 – 2.12)
Sembawang	0.42 (0.26 – 0.63)	0.67 (0.38 – 1.07)	0.53 (0.38 – 0.77)	0.9 (0.59 – 1.36)	0.75 (0.58 – 1.04)	1.32 (0.90 – 1.95)
Raffles Light House	0.42 (0.24 – 0.65)	0.68 (0.35 – 1.09)	0.54 (0.36 – 0.79)	0.9 (0.56 – 1.38)	0.76 (0.56 – 1.06)	1.32 (0.88 – 1.97)
Tanjong Pagar	0.44 (0.24 – 0.69)	0.71 (0.35 – 1.16)	0.56 (0.36 – 0.82)	0.94 (0.56 – 1.43)	0.78 (0.56 – 1.10)	1.36 (0.89 – 2.02)
West Coast	0.46 (0.24 – 0.72)	0.74 (0.34 – 1.21)	0.58 (0.35 – 0.86)	0.97 (0.55 – 1.49)	0.80 (0.55 – 1.13)	1.39 (0.88 – 2.07)
West Tuas	0.45 (0.23 – 0.72)	0.72 (0.33 – 1.19)	0.57 (0.34 – 0.85)	0.95 (0.54 – 1.47)	0.79 (0.54 – 1.12)	1.37 (0.87 – 2.05)
Local mean	0.45 ± 0.03	0.72 ± 0.05	0.57 ± 0.04	0.95 ± 0.06	0.79 ± 0.04	1.37 ± 0.06
Global mean	**0.44 (0.32 – 0.62)**	**0.68 (0.46 – 0.99)**	**0.56 (0.44 – 0.76)**	**0.92 (0.66 – 1.33)**	**0.77 (0.63 – 1.01)**	**1.32 (0.98 – 1.88)**

Table 12.3: Relative sea-level rise projections by 2100 in meters (relative to baseline 1995-2014) for 6 of Singapore's gauges and the global mean. Values at each tide-gauge correspond to the median projection (*likely* range). Local mean is the average of the median values across all six locations.

The spatial variability of projected RSL rise across the tide gauges in Singapore is found to be relatively small, with a variation of ± 3 - 6 cm by 2100 and 2150 (Table 12.3). Among these tide gauges, Sultan Shoal exhibits the highest projected RSL rise with 0.51 (0.34 - 0.74) m by 2100 under SSP1-2.6 and 0.85 (0.66 - 1.15) m under SSP5-8.5. By 2150, the projected rise at Sultan Shoal reaches 0.82 (0.50 - 1.24) m under SSP1-2.6 and 1.47 (1.03 - 2.12) m under SSP5-8.5. This information could be of relevance to stakeholders engaged in conservative mitigation planning for Singapore's shorelines. By referencing the estimates at Sultan Shoal, stakeholders can obtain a valuable indication for setting their mitigation strategies.

To gain a comprehensive understanding of the factors influencing sea-level change, the IPCC AR6 incorporates estimates from six key components: Antarctic Ice Sheet (AIS), Greenland Ice Sheet (GIS), Glaciers, Land Water Storage (LWS), Ocean Sterodynamic (OS) and Vertical Land Motion (VLM). The contribution of these processes to sea-level rise at Singapore's tide gauges at 2100 and 2150 are shown in Figures 12.18 and 12.19 (median and *likely* range). The methodology behind the derivation of these individual processes in the IPCC AR6 is described above in Section 12.5.1, Table 12.2.

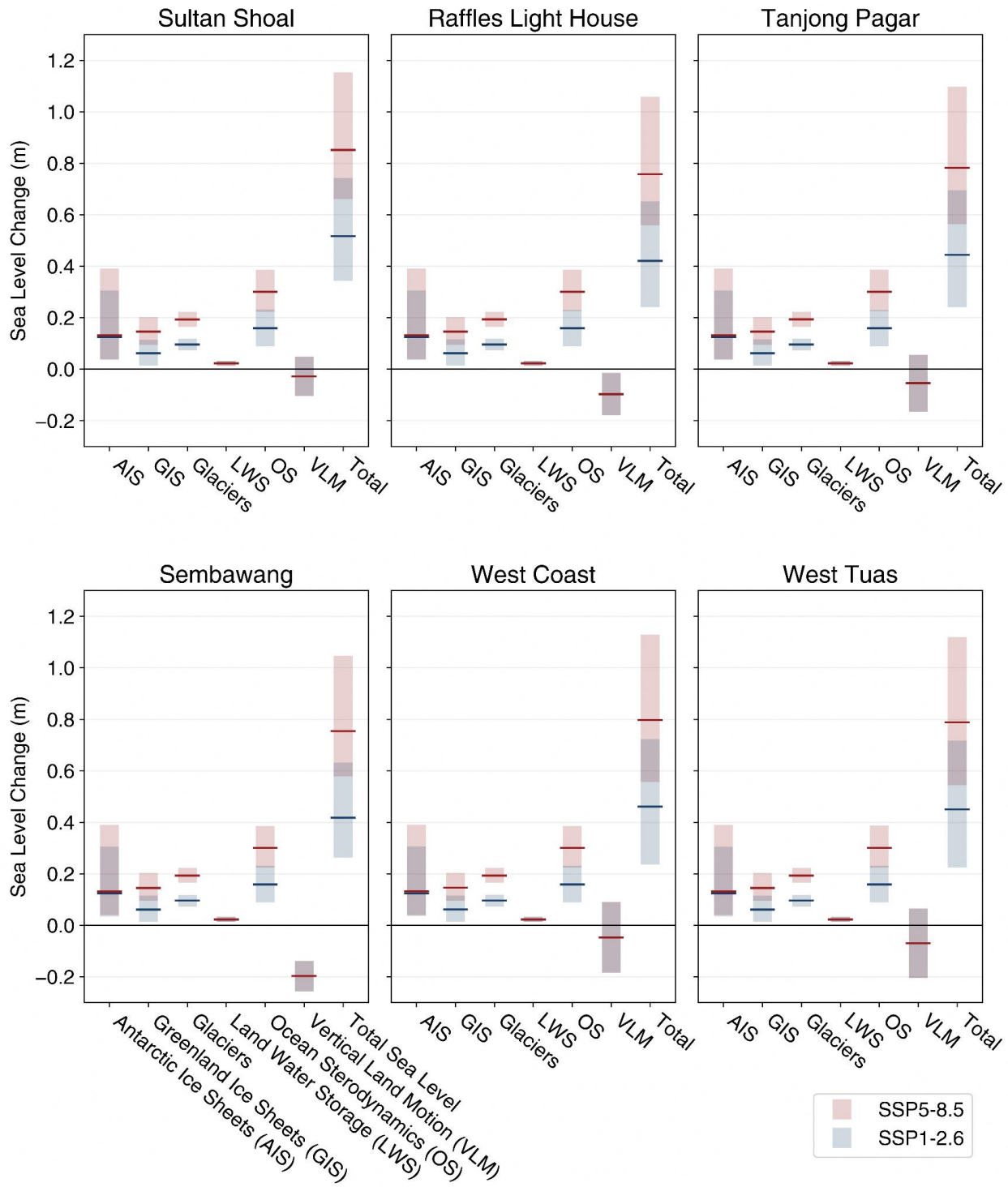

Figure 12.18: Antarctic Ice Sheet (AIS), Greenland Ice Sheet (GIS), Glaciers, Land Water Storage (LWS), Ocean Sterodynamics (OS) and Vertical Land Motion (VLM) contributions to the Total Sea Level rise in centimeters at 6 of Singapore's tide gauges by 2100 under SSP5-8.5 (red) and SSP1-2.6 (blue). *Likely* ranges (17th to 83rd percentile) are indicated with the shaded boxes. Bold, horizontal solid lines represent the median (50th percentile).

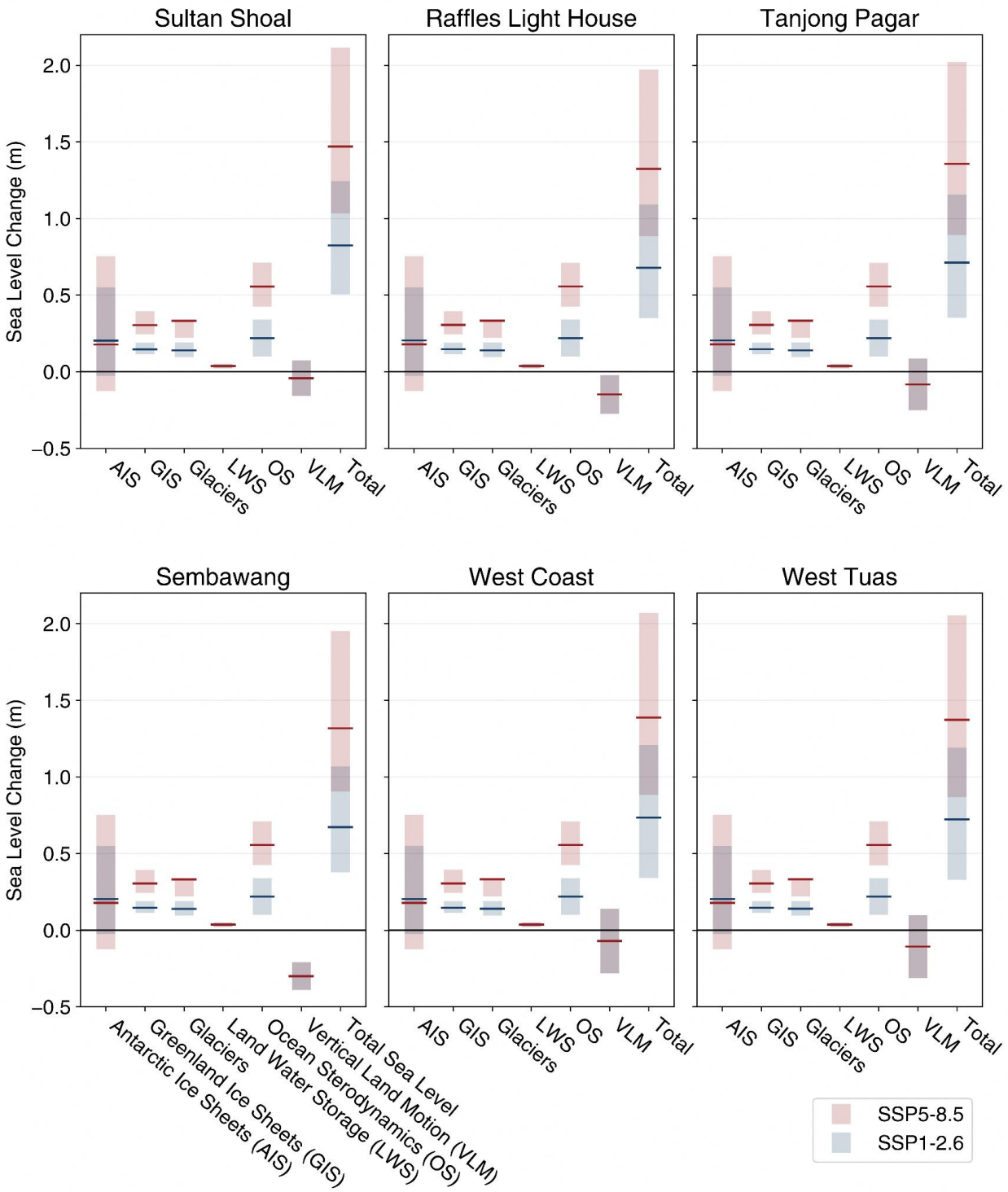

Figure 12.19: Antarctic Ice Sheet (AIS), Greenland Ice Sheet (GIS), Glaciers, Land Water Storage (LWS), Ocean Sterodynamics (OS) and Vertical Land Motion (VLM) contributions to the Total Sea Level rise in centimeters at 6 of Singapore's tide gauges by 2150 under SSP5-8.5 (red) and SSP1-2.6 (blue). *Likely* ranges (17th to 83rd percentile) are indicated with the shaded boxes. Bold, horizontal solid lines represent the median (50th percentile).

Contributor	SSP1-2.6	SSP2-4.5	SSP5-8.5	SSP5-8.5 (Global)
Ocean Sterodynamics	0.16 (0.09 – 0.23)	0.20 (0.15 – 0.26)	0.30 (0.22 – 0.39)	0.30 (0.24 – 0.36)
Greenland Ice	0.06 (0.01 – 0.12)	0.09 (0.05 – 0.15)	0.15 (0.10 – 0.20)	0.13 (0.09 – 0.18)
Antarctica Ice	0.12 (0.04 – 0.31)	0.13 (0.03 – 0.33)	0.13 (0.04 – 0.39)	0.12 (0.03 – 0.34)
Glaciers	0.10 (0.07 – 0.12)	0.13 (0.11 – 0.16)	0.19 (0.17 – 0.22)	0.18 (0.15 – 0.20)
Land Water Storage	0.02 (0.01 – 0.03)	0.02 (0.01 – 0.04)	0.02 (0.01 – 0.03)	0.03 (0.02 – 0.04)
Vertical Land Movement	0.03 (-0.04 – 0.10)	0.03 (-0.04 – 0.10)	0.03 (-0.07 – 0.10)	
Total	**0.51 (0.35 – 0.73)**	**0.63 (0.47 – 0.87)**	**0.85 (0.66 – 1.13)**	**0.77 (0.63 – 1.01)**

Table 12.4: Mean sea level projections under SSP1-2.6, SSP2-4.5 and SSP5-8.5 at Sultan Shoal, relative to baseline of 1995-2014, in meters by 2100. Individual contributions of the six components driving sea-level change and the total mean sea level are shown. Median values (*likely* range) are shown. Global mean sea level projections are shown on the far right column for the highest emission scenario SSP5-8.5.

Regardless of the emission scenario (SSP1-2.6 or SSP5-8.5), the AIS is projected to contribute the most to the uncertainty of total projected mean sea-level rise in Singapore by 2100 and 2150. Although the projected median values of sterodynamic sea-level change by 2100 and 2150 are larger than the projected median values of AIS, AIS could *likely* (83rd percentile) contribute more or just as much to the total mean sea level rise in Singapore (Table 12.4).

The changes in land water storage contributing to local sea-level rise in Singapore are almost negligible (median and *likely* range). In general, total sea-level rise (median) is projected to be higher for the worst-case scenario SSP5-8.5, with a larger *likely* range of uncertainties too. We see here that projected local sea-level rise in Singapore is largely scenario-dependent, with the exception of the contribution from the AIS and VLM, which was carefully explained in the IPCC AR6 Chapter 9 for projected global mean sea-level.

Unlike most of the other sea-level drivers, the *likely* range in the contribution of AIS to sea-level rise grows beyond 2100, as seen most significantly under SSP5-8.5. The IPCC AR6 emphasises that there is *low agreement* on the relationship between scenario-dependence and the net AIS contribution to sea level. The net changes in ice sheets are broadly driven by two processes: surface mass balance and ice dynamics. A possible reason behind a higher, albeit minimal, median sea-level rise driven by AIS under SSP1-2.6 as compared to SSP5-8.5 by 2150 (Figure 12.17) could be because of a negative contribution to sea-level rise from the Antarctic surface mass balance over the 21st century (Fox-Kemper et al., 2021). Warmer temperatures are associated with increased snowfall, and hence a fall in sea level. There is medium confidence that future contribution of the Antarctic surface mass balance to sea level will be negative under all emissions scenarios. However, it is *likely* that mass loss from the AIS from ice dynamic processes, which contributes positively to sea-level rise, will dominate in the longer term.

12.5.3.2 Low-confidence sea-level projections to 2300

In this subsection, we present a long-term perspective on sea-level rise in Singapore, focusing on one particular tide gauge: Sultan Shoal. In addition, we consider highly uncertain

ice sheet processes that could result in substantially larger sea-level rise than seen in the IPCC AR6 medium confidence projections. Sea-level projections beyond 2150 and/or that included uncertain ice-sheet feedback processes (e.g. Marine Ice Cliff Instability (MICI); DeConto and Pollard, 2016) were assessed by IPCC AR6 as having low confidence, i.e., there was low agreement and/or limited evidence to inform their assessment. However, the low confidence projections presented in this section provide important information for longer planning time-horizons and more fully represent the full range of potential future outcomes.

Essentially, there are two types of information on low confidence sea-level projections presented in IPCC AR6: (i) assessed ranges of GMSL rise at 2300 under the SSP1-2.6 and SSP5-8.5 emissions scenarios that do not include highly uncertain ice sheet feedback processes; (ii) low-likelihood high-impact storylines that include highly uncertain ice sheet feedback processes (such as MICI). Note that the storylines are presented as singular trajectories of sea-level rise that are available as local projections up to 2150. A qualitative description of the low-likelihood storylines presented in AR6 is presented in Box 9.4 (Fox-Kemper et al, 2021). The key storyline elements are: a strong warming scenario (e.g. linked to high real-world climate sensitivity); faster-than-projected disintegration of marine ice shelves and subsequent widespread onset of ice sheet instability processes in Antarctica; more frequent and severe melt events than expected for the Greenland ice sheet.

The main physical process considered in the LLHI storyline (low confidence) that is not included in the medium confidence projections presented in Sections 12.5.3.1 is the marine ice cliff instability (MICI). MICI is a process whereby ice cliffs at the edge of marine-terminating glaciers (such as in the Antarctic) become unstable and rapidly collapse. This process is a mechanism that could contribute to the potential collapse of the West Antarctic ice sheet, which could add to several meters of global sea-level rise by 2100 (e.g., DeConto and Pollard, 2016).

Figure 12.20 shows the single trajectories of LLHI storylines (83rd and 95 percentiles) at Sultan Shoal until 2300 and the low confidence projected GMSL by 2300 (17th to 83rd percentile, low confidence) that does not include the MICI processes.

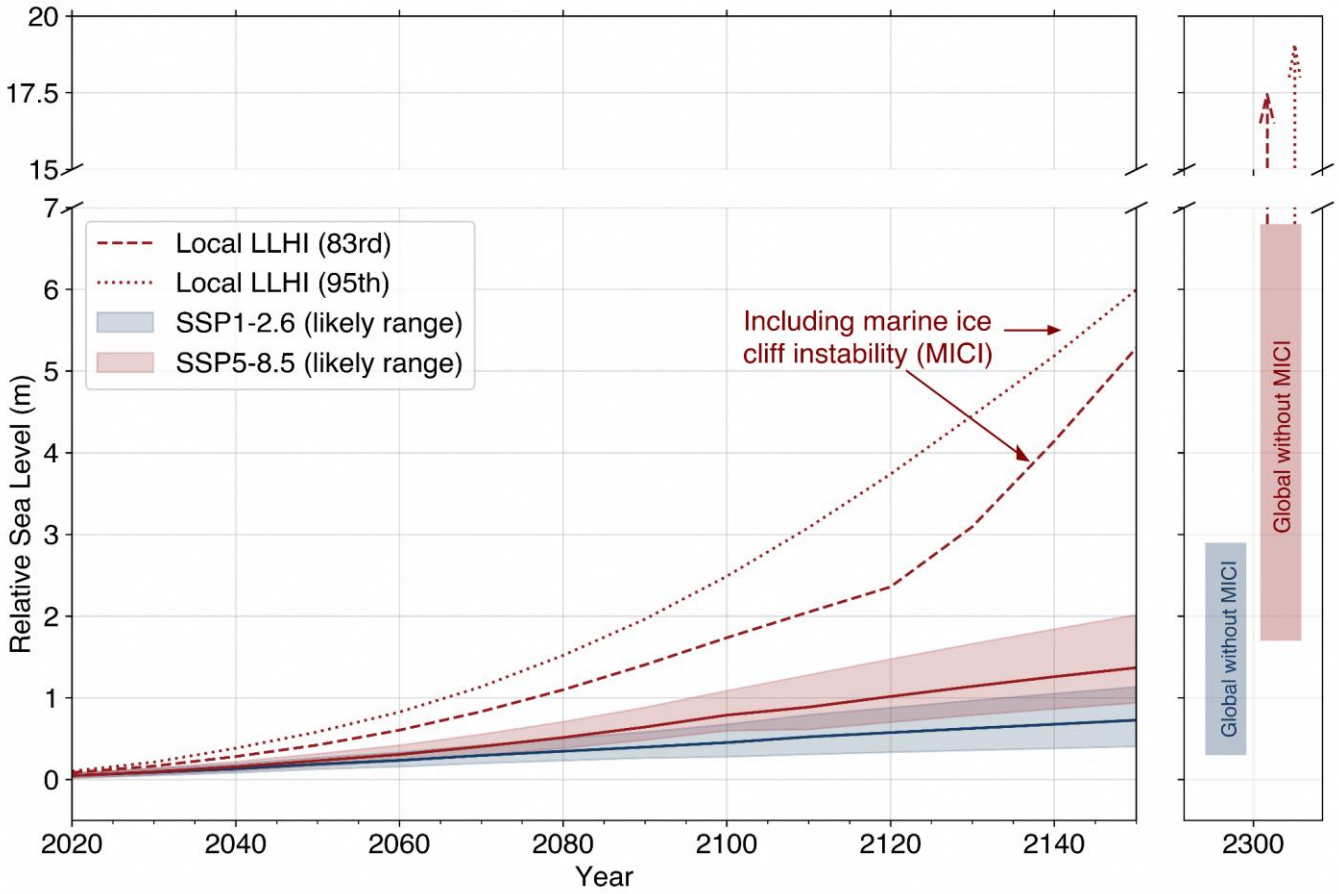

Figure 12.20: Low confidence total relative sea-level change at Sultan Shoal (Singapore) until 2300 (relative to 1995-2014 baseline) that include low-likelihood, high-impact (LLHI) ice sheet processes (i.e., MICI) that cannot be ruled out. Shaded regions before 2150 are medium confidence projections (median and *likely* range). Dashed (83rd percentile) and dotted (95th percentile) lines until 2150 and at 2300 (arrows) represent the low confidence LLHI storylines that include the unstable ice sheet processes. Low confidence projected global-mean sea-level change at 2300 that do not include MICI are shown with the shaded vertical bars. The future pathways shown are SSP1-2.6 (blue) and SSP5-8.5 (red).

The low confidence projected GMSL under SSP5-8.5 at 2300 could *likely* reach ~7 m (83rd percentile). However, if coupled with the highly uncertain ice sheet feedback processes such as MICI, 7 m of sea-level rise is projected to be obtained in Singapore just after 2150 under SSP5-8.5.

Based on the single trajectories of LLHI storylines for Singapore until 2300 (dashed and dotted lines in Figure 12.18), projected RSL rise could reach 6 m by 2150 and almost 20 m by 2300 under SSP5-8.5.

While it is not possible to provide robust likelihood information on any of the low confidence sea-level projections, we know that the assessed ranges at 2300 are much more *likely* to be reached than the LLHI storylines. Therefore, we recommend that decision makers treat the assessed ranges at 2300 as indicative of the committed sea-level rise under low and high emissions. The LLHI storylines represent much more severe outcomes that cannot be ruled out based on the current level of scientific knowledge. Choice and use of these storylines will depend on the risk appetite of adaptation planners depending on the sector and application. It is important to note that there is no single community-agreed definition of a plausible maximum sea-level rise scenario and stakeholders may wish to consider other estimates in the literature, such as Dayan et al (2021) and van de Wal et al (2022).

12.5.3.3 Differences in V3 compared to V2

Prior to the release of the AR6 sea level projections, mean sea level projections for Singapore are found in the Second National Climate Change Study for Singapore (V2) Chapter 8 'Changes in Time Mean Sea Level'. Released in 2015, this chapter was led by the UK Met Office. The V2 methods were based on the IPCC Fifth Assessment Report (AR5) sea-level projections, which represented the state-of-the-art at that time.

V2 provided only one set of medium confidence sea-level projections for Singapore based on moderate (RCP4.5) and high (RCP8.5) greenhouse gas emissions scenarios. V2 combined the *likely* range of global sea level rise from the IPCC AR5 with non-uniform spatial patterns of sea level change ("fingerprints") from Slangen et al. (2014) to derive a median and *likely* range of projected mean sea level rise for the same processes shown in V3 (i.e., ocean dynamics, Greenland and Antarctic ice sheets, glaciers and land water). Following AR5, V2 used the Representative Concentration Pathways (RCPs) climate change scenarios instead of the SSPs presented in AR6. RCP4.5 is comparable to SSP2-4.5 andRCP8.5 to SSP5-8.5. V2 provided medium confidence projections up until 2100.

The total mean sea-level rise shown in V2 under RCP4.5 was 0.53 (0.30 - 0.74) m and 0.73 (0.45 - 1.02) m under RCP8.5 at 2100. The median projected value under RCP4.5 is comparable to the average projected sea-level rise by 2100 under SSP2-4.5 in V3 (0.57 ± 0.04 m). Conversely, the median projected sea-level rise under RCP8.5 in V2 is slightly lower than the average projected sea-level rise by 2100 under SSSP5-8.5 in V3 (0.79 ± 0.04 m).

The V2 and V3 projections are relative to different baselines. The projections in V3 are relative to a different baseline 1995-2014 while the V2 projections are relative to 1986-2005. AR6 quantified the baseline adjustment as +0.03 m if adjusting the global-mean sea-level projections from AR5 to the AR6 baseline. As Singapore's rate of mean sea-level change is similar to the global mean (more in Section 12.4), we adopt this adjustment for the V2 sea-level projections as reflected in Figure 12.21.

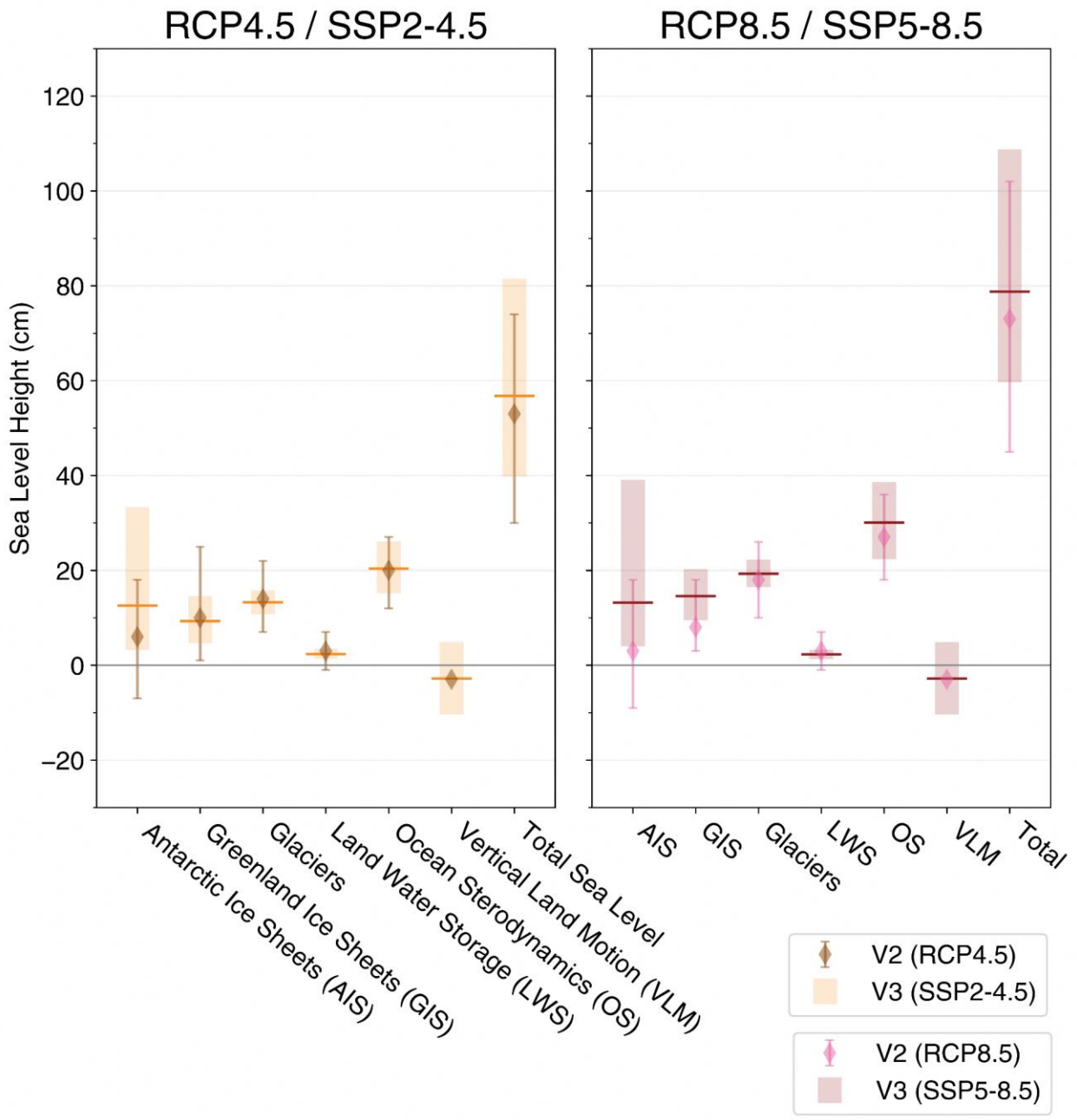

Figure 12.21: Summary of the sea-level projections given in V2 and V3 at 2100. Median (horizontal, bold lines for V3 and diamonds for V2) and *likely* range (shaded bars for V3 and error bars with caps for V2) shown from both V2 and V3. The projections from V3 shown here are at Sultan Shoal, whereas only one set of projections were given from V2.

The V2 projections show that sterodynamic sea-level change is arguably one of the largest, if not the largest (RCP8.5), component that contributes to the total projected sea-level rise. Both the median and *likely* range of the projected contribution of the AIS component had significantly increased in the V3 projections under both scenarios. Projected sea-level rise due to mass loss from glaciers and Greenland ice sheet and land water storage have reduced uncertainties in V3, stemming from improved modelling techniques and incorporation of more ice processes and feedback than the AR5 models which V2 projections were based on.

In the V3 projections, estimates of vertical land motion (VLM) contributing to RSL rise now consider more potential outcomes and non-climatic processes as compared to V2, where only one process—glacial isostatic adjustment—was considered (Kopp et al., 2014, Marzin et al., 2015). Therefore, this led to a larger range of uncertainties of RSL rise caused by VLM under all scenarios.

12.5.3.4 Coastal Vulnerability Analysis

Visualising and communicating coastal vulnerability is a crucial step in assessing the potential impacts of rising sea levels. One approach involves the use of digital elevation maps that depict specific elevations above a reference height, aligned with projected sea-level rise scenarios. These maps highlight areas that are at greater risk of inundation and can serve as valuable tools for decision-making and urban planning. However, it is important to note that this method represents just one way of assessing coastal vulnerability. Other approaches include assessing vulnerability based on socio-economic factors, ecological sensitivity, infrastructure exposure, and community resilience.

The Singapore Land Authority (SLA) provided digital elevation maps that visually depict elevations below 1 m, 2 m, and 5 m in Singapore, represented by dark blue shading (Figures 12.22, 12.23, and 12.24).

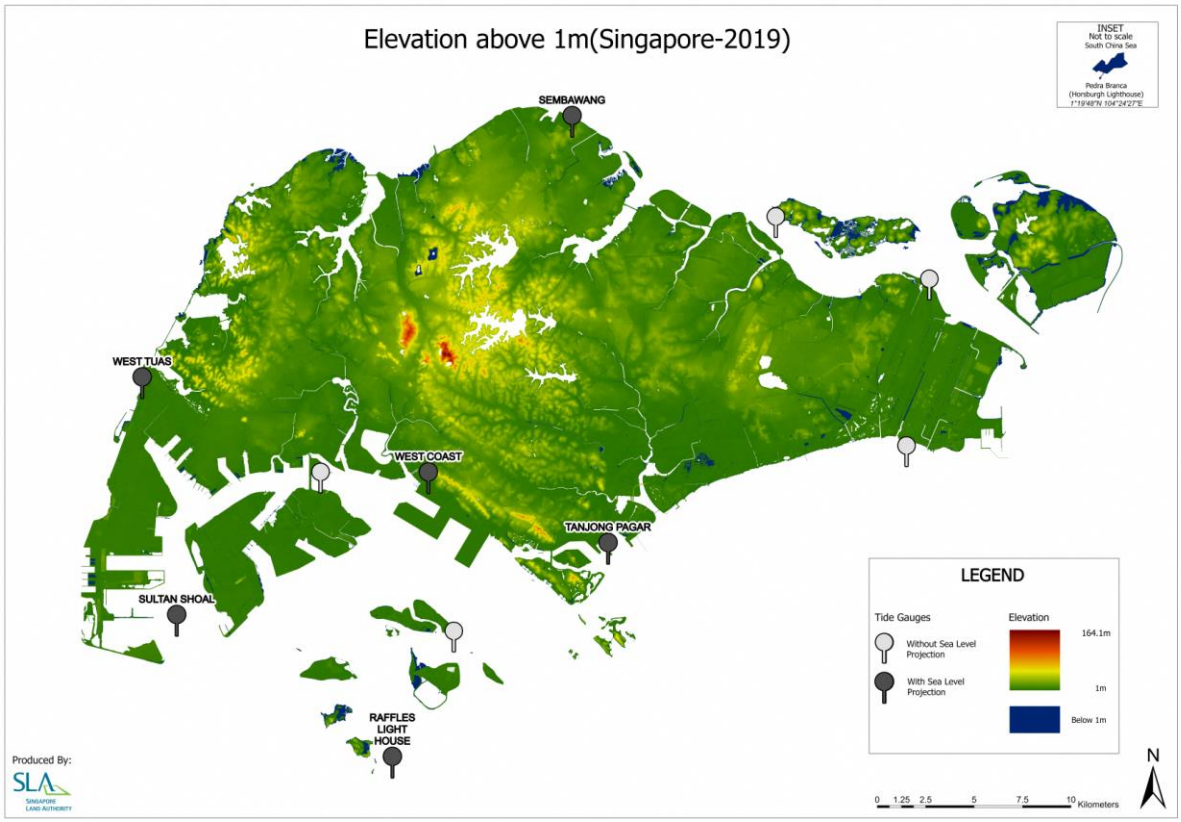

Figure 12.22: Digital Elevation Map of Singapore above mean sea level, with all elevations below 1 m indicated in dark blue.

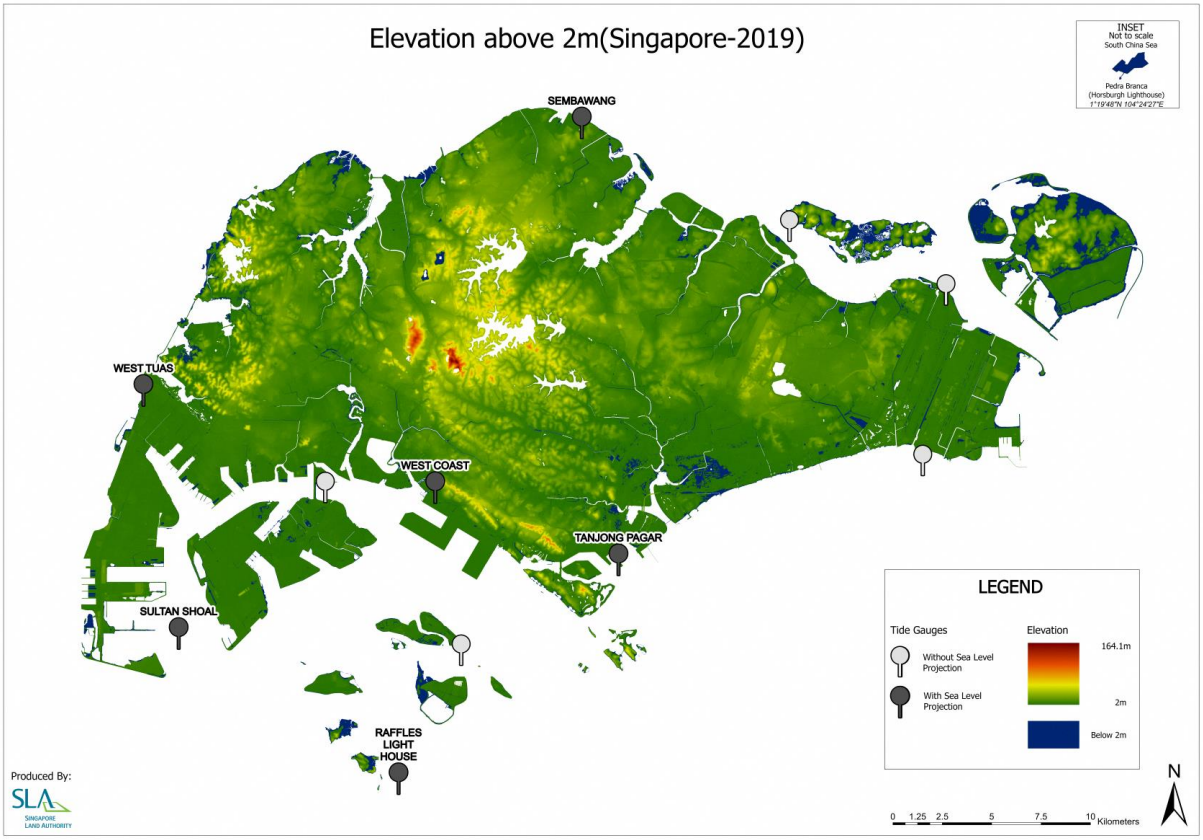

Figure 12.23: Digital Elevation Map of Singapore above mean sea level, with all elevations below 2 m indicated in dark blue.

These elevation thresholds correspond to key sea-level rise projections for specific time horizons. For instance, the 1-meter elevation represents the upper limit of the *likely* range projected for 2100 (medium confidence), while the 2-meter elevation corresponds to the upper limit of the *likely* range projected for 2150 (medium confidence). Additionally, the 5-meter elevation represents the upper limit of the *likely* range in a high-end scenario (low confidence) for 2150. All these projections are based on the worst-case future pathway SSP5-8.5. These digital elevation maps provide valuable insights into the potential impacts of sea-level rise in Singapore.

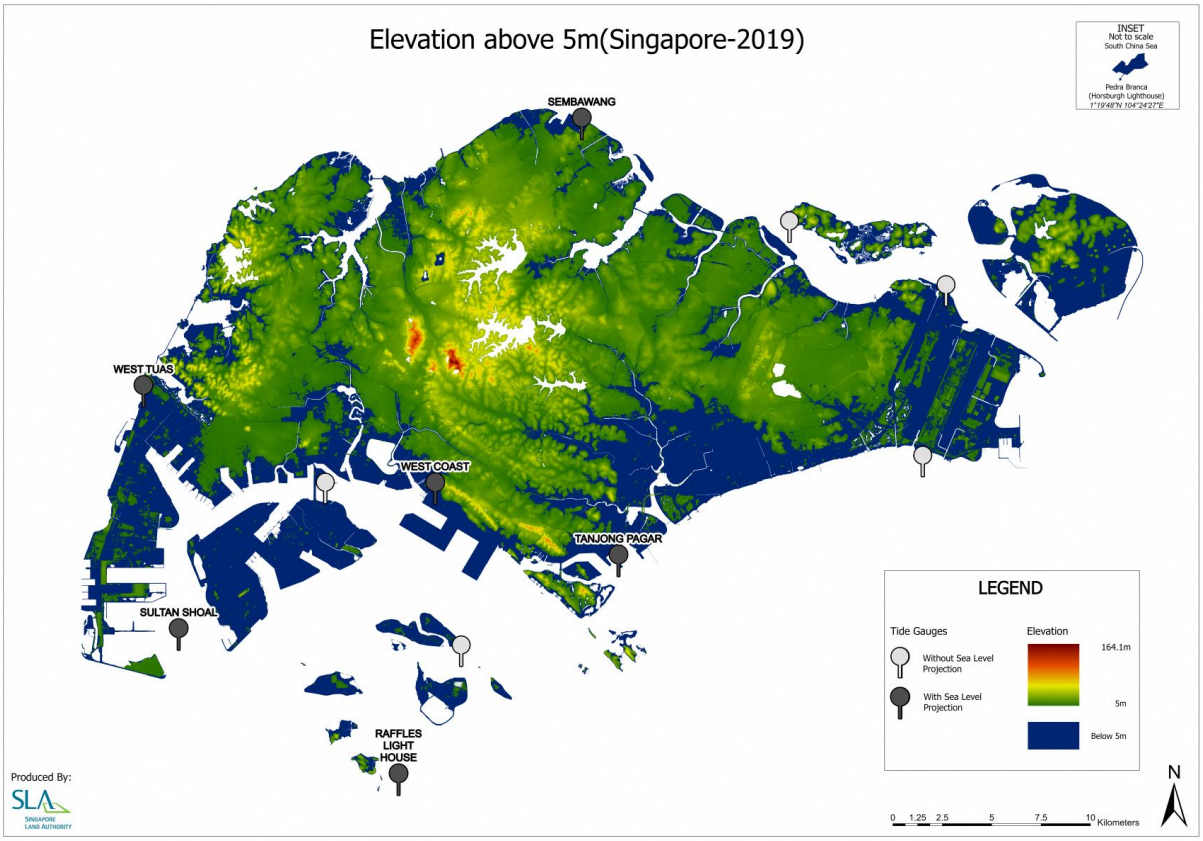

Figure 12.24: Digital Elevation Map of Singapore above mean sea level, with all elevations below 5 m indicated in dark blue.

Figure 12.24 presents a striking depiction of coastal vulnerability in Singapore, highlighting areas below 5 meters that could potentially be inundated. While this scenario is considered low-likelihood, it carries the potential for significant economic losses.

The vulnerable areas primarily encompass the southern shores of Singapore, including the Central Business District located near the southeastern coast. It is worth noting that further research is required to gain a more comprehensive understanding of this situation. Interestingly, the areas at risk of inundation, as indicated by the dark blue shading, appear to align with the reclaimed land in Singapore. This observation underscores the need for continued investigation and assessment of coastal vulnerability in relation to land reclamation efforts.

12.5.4 Sea-level projections in Southeast Asia

Here we present sea-level projections until 2150 (median and *likely* range) from the IPCC AR6 at some tide-gauge locations in Southeast Asia shown in Section 12.3. Time series of the projected RSL rise at a subset of the tide-gauges discussed in Section 12.3 are shown in Figure 12.25 in a bid to provide an evolution of sea level change. However, not all the tide-gauges shown in Section 12.3 passed the IPCC AR6 criteria to generate sea level projections.

Additional tide-gauge stations with sea-level projections are included here (i.e., additional cities in Southeast Asia; Table 12.5, Figure 12.26, Figure 12.27).

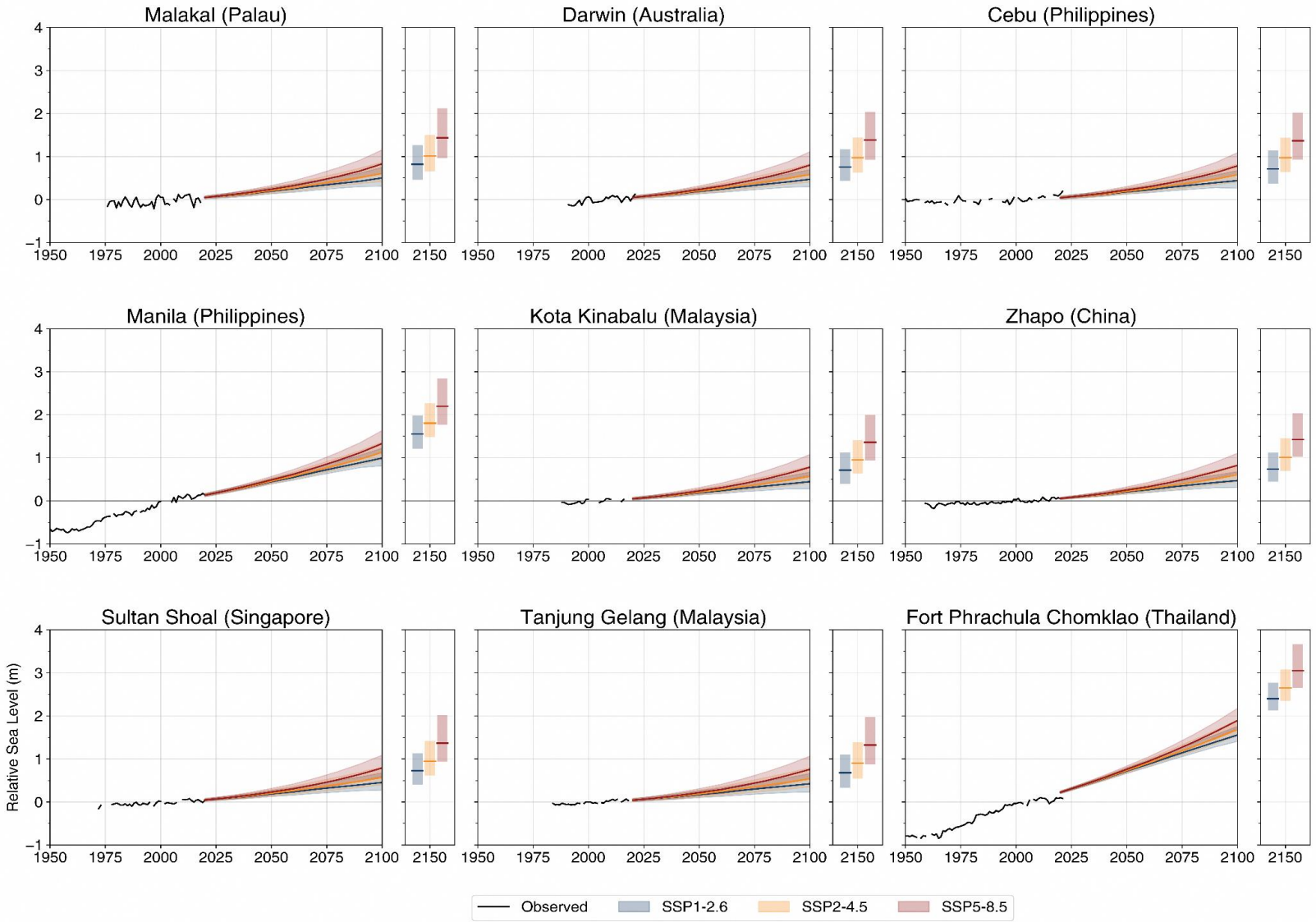

Figure 12.25: Time series plots of relative sea-level change in the past and projected future at a subset of tide gauges (country) discussed in Section 12.3. Shown in solid black are the annual tide gauge data taken from PSMSL at the respective tide gauges; shown in the other various colours with the shaded bands are the projected sea-level rise till 2100 under the different SSPs from the IPCC AR6. Observations and projections are relative to the baseline period 1995-2014.

	City/State (tide-gauge name)	SSP1-2.6		SSP2-4.5		SSP5-8.5	
		2100	2150	2100	2150	2100	2150
1	Cebu City (Cebu)	0.44 (0.26 - 0.68)	0.72 (0.37 - 1.15)	0.58 (0.41 - 0.83)	0.97 (0.64 - 1.44)	0.78 (0.58 - 1.09)	1.37 (0.92 - 2.02)
2	Manila (Manila, S. Harbour)	0.99 (0.81 - 1.22)	1.55 (1.21 - 1.98)	1.12 (0.96 - 1.37)	1.80 (1.49 - 2.26)	1.33 (1.13 - 1.63)	2.20 (1.77 - 2.85)
3	Phuket (Ko Taphao Noi)	0.50 (0.33 - 0.72)	0.80 (0.48 - 1.21)	0.60 (0.45 - 0.84)	1.00 (0.69 - 1.46)	0.82 (0.62 - 1.12)	1.42 (0.99 - 2.06)
4	Bangkok (Fort Phrachula Chomklao)	1.56 (1.41 - 1.76)	2.40 (2.13 - 2.77)	1.68 (1.54 - 1.91)	2.65 (2.35 - 3.09)	1.89 (1.71 - 2.18)	3.05 (2.65 - 3.67)
5	Johor Bahru (Johor Bahru)	0.43 (0.23 - 0.68)	0.70 (0.34 - 1.14)	0.55 (0.35 - 0.82)	0.93 (0.55 - 1.43)	0.77 (0.55 - 1.09)	1.34 (0.87 - 2.01)
6	Kuantan (Tanjung Gelang)	0.42 (0.23 - 0.66)	0.68 (0.33 - 1.1)	0.54 (0.35 - 0.8)	0.91 (0.55 - 1.39)	0.76 (0.55 - 1.06)	1.32 (0.87 - 1.98)
7	Kota Kinabalu (Kota Kinabalu)	0.44 (0.28 - 0.66)	0.71 (0.39 - 1.12)	0.56 (0.41 - 0.8)	0.95 (0.63 - 1.41)	0.78 (0.60 - 1.08)	1.36 (0.94 - 2.00)
8	Penang (Pulau Pinang)	0.39 (0.19 - 0.64)	0.64 (0.26 - 1.08)	0.5 (0.3 - 0.76)	0.85 (0.47 - 1.34)	0.71 (0.49 - 1.03)	1.25 (0.79 - 1.92)
9	Da Nang (Danang)	0.50 (0.32 - 0.74)	0.80 (0.45 - 1.22)	0.63 (0.44 - 0.89)	1.05 (0.69 - 1.52)	0.84 (0.64 - 1.14)	1.46 (1.02 - 2.09)
10	Yangon (Rangoon)	0.62 (0.43 - 0.84)	0.98 (0.64 - 1.40)	0.71 (0.53 - 0.96)	1.17 (0.83 - 1.62)	0.93 (0.72 - 1.23)	1.58 (1.14 - 2.21)
11	Palau (Malakal)	0.50 (0.31 - 0.75)	0.82 (0.46 - 1.27)	0.60 (0.42 - 0.87)	1.01 (0.65 - 1.51)	0.83 (0.61 - 1.16)	1.44 (0.96 - 2.12)
12	Darwin (Darwin)	0.47 (0.30 - 0.70)	0.76 (0.43 - 1.17)	0.58 (0.41 - 0.83)	0.97 (0.62 - 1.44)	0.80 (0.59 - 1.11)	1.38 (0.92 - 2.04)
13	Zhapo (Zhapo)	0.47 (0.31 - 0.68)	0.74 (0.44 - 1.12)	0.61 (0.45 - 0.84)	1.01 (0.70 - 1.46)	0.82 (0.64 - 1.11)	1.42 (1.02 - 2.03)
14	Singapore (Sultan Shoal)	0.51 (0.34 – 0.74)	0.82 (0.50 – 1.24)	0.63 (0.46 – 0.88)	1.05 (0.72 – 1.52)	0.85 (0.66 – 1.15)	1.47 (1.03 – 2.12)
	Global mean	**0.44 (0.32 – 0.62)**	**0.68 (0.46 – 0.99)**	**0.56 (0.44 – 0.76)**	**0.92 (0.66 – 1.33)**	**0.77 (0.63 – 1.01)**	**1.32 (0.98 – 1.88)**

Table 12.5: Projected relative sea level rise by 2100 and 2150 under SSP1-2.6, SSP2-4.5 and SSP5-8.5 at various locations in Southeast Asia and some peripheral locations (i.e., Zhapo, Darwin and Palau; Figure 12.26). The values shown are meters of sea-level change relative to baseline 1995-2014. Median (*likely* range) are presented. Projections of global mean sea level rise are also shown here, relative to the same baseline.

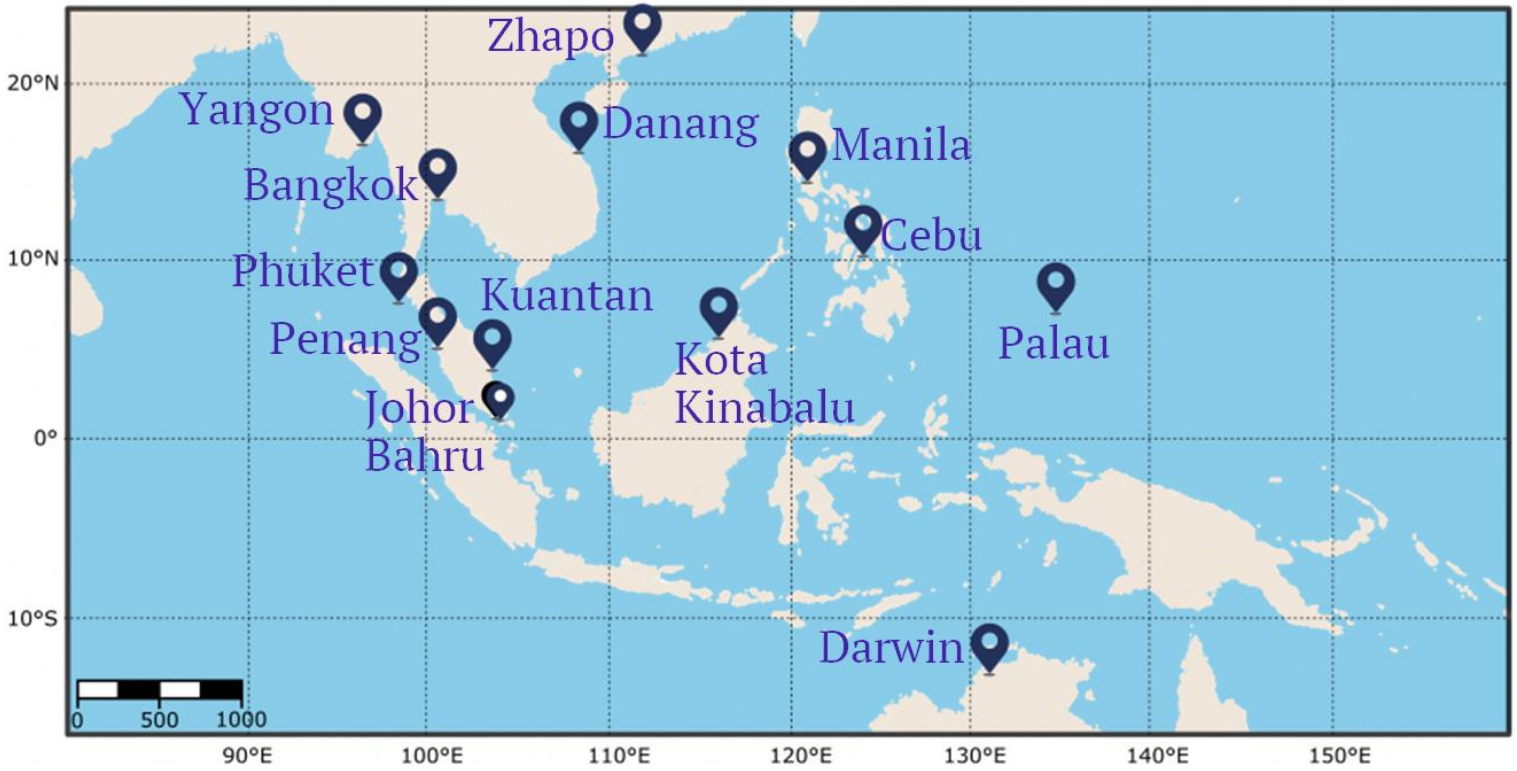

Figure 12.26: Location of the 13 tide-gauges in the various Southeast Asian cities and countries listed in Table 12.5. Labels on the map indicate the city names.

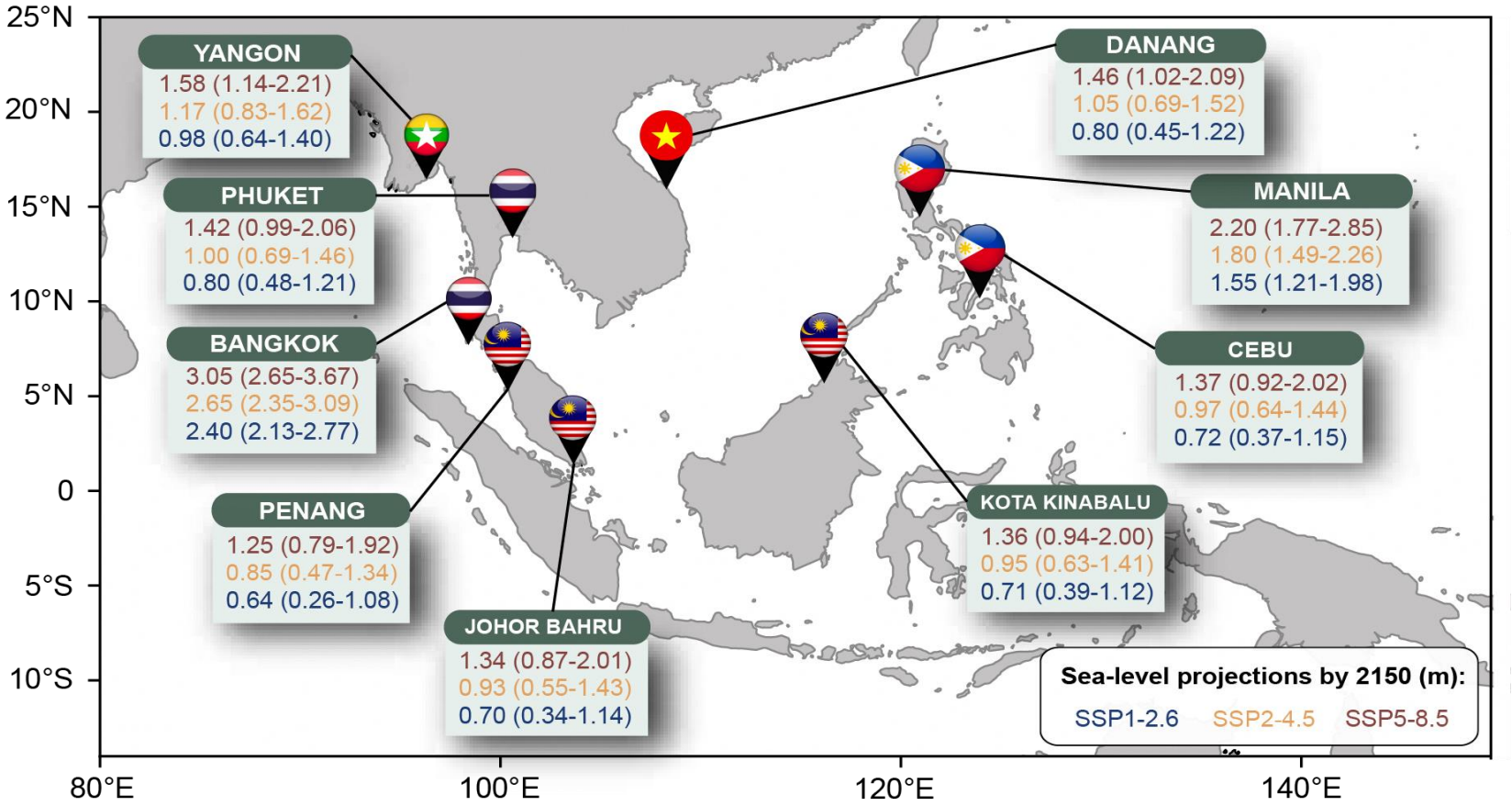

Figure 12.27: Projected relative sea-level rise at some of the most densely populated Southeast Asian cities by 2150 under all emission scenarios considered in V3. Projections are relative to the baseline period 1995–2014.

Over this century, RSL is projected to rise at all the tide gauges listed in Table 12.5 regardless of the future emissions scenarios by 2100 and 2150 (Figure 12.27). Similar to Singapore, RSL rise at most of these locations is *likely* to reach ~1 m by 2100 under the high greenhouse gas emissions scenario (SSP5-8.5).

However, this is with the exception of Manila and Fort Phrachula Chomklao, which will be addressed as 'Bangkok' from hereon as the tide gauge is located less than 10 km away from the populated city. By the end of the century (i.e., 2100), Manila and Bangkok are *likely* to experience RSL rise of more than 1.5 m and 2 m respectively under SSP5-8.5. Under the low emissions scenario, RSL rise could *likely* reach up to 1 m in most of these cities and up to 2 to 3 m in Manila and Bangkok by 2150 (Figure 12.27). Under the high emissions scenario RSL rise could *likely* reach up to 2 m in most cities and exceed 3m in Bangkok by 2150 (Figure 12.27).

Land subsidence due to excessive groundwater withdrawal has been a well-established factor causing RSL rise since the 1970s (e.g., Ahmed et al., 2020; Siringan et al., 2019, Niesters et al., 2021). In Bangkok, groundwater withdrawal has been attributed with land subsidence, with rates reaching up to 120 mm/yr in some areas (Aobpaet et al., 2013).

Several studies have also reported subsidence rates up to centimeters per year in some coastal areas around Manila due to groundwater extraction (Rodolfo et al., 2020; Kim et al., 2019). In both cases of Manila and Bangkok, the extraction of groundwater has outpaced the natural recharge rate of the aquifers. As water is pumped out, the pressure in the aquifer decreases, causing the soil and rock layers above it to compact and settle. Over time, this causes the land surface to sink, leading to subsidence (Galloway et al., 2011).

12.6 Vertical Land Movement

While global sea-level rise is driven primarily by the thermal expansion of oceans and the melting of land ice, the RSL changes experienced at specific locations are influenced by a range of additional factors (IPCC, 2021). One of the most significant factors is vertical land movement, or vertical land motion (VLM, which can cause the land to sink or rise relative to sea level (Church et al., 2013). This motion can result from a variety of natural and anthropogenic processes, including tectonic activity, sediment compaction, groundwater withdrawal, and human-made structures (Kench et al., 2018).

VLM is particularly important in regions such as Southeast Asia, where it can cause significant variations in local sea levels and exacerbate the impacts of global sea-level rise on coastal communities and infrastructure (Koh et al., 2021). In this section, we explore the factors of VLM and its importance for understanding RSL changes in the region. We use the term 'vertical land movement' in this section as referenced to Gregory et al. (2019), and the term 'vertical land motion' used in Section 12.5 is in accordance with the IPCC AR6 Chapter 9 terminology. The terms are often used interchangeably in publications, and do not have different physical meanings.

VLM describes the change in the height of the sea floor or land surface (Gregory et al., 2019) and it affects RSL change. The need for understanding and quantifying VLM is crucial for producing robust sea-level projections. Vertical displacements of the ground could either cause a fall or rise in mean sea level relative to the occupants on land, given that the mean geocentric sea level remains constant.

12.6.1 Factors causing vertical land movement

The rate of VLM and the extent to which it affects RSL change varies temporally and spatially. These factors can be natural and/or human-induced, and are able to have an impact on the land for up to millions of years (Figure 12.28).

One factor causing VLM arises due to changes in mass redistributions within the atmosphere, ocean and continents caused by natural or anthropogenic mechanisms (Pfeffer et al., 2017). The solid Earth is still in a state of isostatic disequilibrium and continues to respond to the loss of ice sheets during the Last Glacial Maximum about 21 thousand years ago (e.g., King et al., 2010). This ongoing GIA results in varied rates of vertical displacements across the globe.

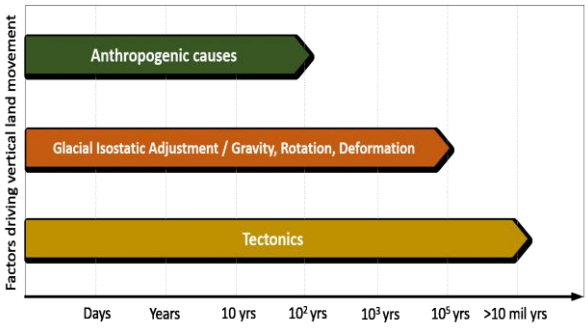

Figure 12.28: Significant factors driving vertical land movement (VLM) in Southeast Asia that are explained in Section 12.6.1. The temporal extent to which these factors affect VLM vary from days to millions of years (tectonics). Graphic and information is referenced to Pfeffer et la. (2017).

Similarly, ongoing contemporary changes in land-based ice sheets (e.g., melting Antarctic and Greenland ice sheets) and land water storage results in instantaneous changes in the geoid and VLM that must be considered. Together, these effects affect the rate of VLM and contribute to RSL change.

Other natural factors that can also cause VLM include seismic activity such as earthquakes (Wöppelmann et al., 2016). Earthquakes occur when tectonic plates in the earth's crust shift, causing a sudden release of energy that creates seismic waves. This movement can result in uplift or subsidence of the land, which can affect local RSL rise (Wöppelmann et al., 2016; Shirzaei et al., 2021). At different stages of the earthquake cycle, which includes interseismic, coseismic, and postseismic periods, there are different rates and spatio-temporal extent of land movement (Pollitz et al., 2018). The extent of subsidence or uplift in the land near the fault depends on several factors, including the magnitude and duration of the earthquake, the location of the fault, and the properties of the surrounding geology (Pollitz et al., 2018).

There are also anthropogenic factors such as groundwater withdrawal that can have significant impacts on VLM. Groundwater withdrawal causes the water table to drop, leading to a reduction in pore water pressure and compaction of sediment layers, which can cause subsidence (Galloway et al., 2019). Some of the cities that are most severely-affected by groundwater withdrawal-induced land subsidence include Mexico City, Bangkok and Jakarta (Galloway et al., 2019; Wassmann et al., 2016; Firman et al., 2019). In addition to groundwater extraction, there are other anthropogenic factors such as oil and gas extraction, mining, and the construction of large dams that can result in land subsidence (Zhang et al., 2018).

12.6.2 Observed vertical land movement in Singapore

Understanding the past and present state of VLM in Singapore is crucial for accurately assessing and predicting future sea-level rise impacts on low-lying coastal areas. In this section, we examine the current knowledge of observed VLM in Singapore from published sources and some existing global positioning system (GPS) and/or global navigation satellite system (GNSS) data.

VLM is often measured either using radar sensors or in situ GPS/GNSS stations. Studies such as Catalao and Fernandes (2013) and Catalao et al. (2020) had previously presented VLM rates in Singapore using the former technique. Both studies found greatest subsidence rates near the southeastern coasts of Singapore (-2 to -13 mm/yr, from 2011 to 2016, Catalao et al., 2020). Catalao et al. (2020) suggested that a correlation between the geological setting of Singapore and subsidence rates exists, due to lower subsidence rates observed for unconsolidated material as compared to higher subsidence rates for consolidated sand. However, this relationship is still understudied, and the period over which VLM rates were presented in Catalao et al. (2020) (i.e., 6 years) may be insufficient to robustly conclude the associated correlation with varied bedrock.

Another way of examining VLM is using GPS data. Figure 12.26 shows the time series of recorded land movement at two of Singapore's GPS/GNSS stations, named SIN1 and SING (Figure 12.26), taken from Nevada Geodetic Lab (Blewitt et al., 2018). Linear trends of the measurements were taken over different segments of time (i.e., before/after a data gap or shift) to approximately quantify the rate of VLM in Singapore over the last decade or so. SIN1 shows negligible VLM, with arguably little subsidence of -0.4 to -0.5 mm/yr

over the past ~10 years. On the other hand, a vertical downward shift was recorded at SING on 5 November 2015, with missing data the day before.

According to the Singapore Land Authority (SLA), the recorded subsidence of ~5 cm was likely caused by the earthquake that occurred in Indonesia on 4 November 2015 ("GPS Station at Bukit Timah Base Recorded Subsidence", 2015). Due to Singapore's close proximity to the Sunda megathrust fault that borders the Indonesian archipelago, land subsidence in Singapore due to any significant future seismic activity is yet again plausible (Gee et al., 2010; Hermawan et al., 2020). Such a phenomenon is not uncommon around the world. For instance, the 2011 Tohoku earthquake in Japan caused significant subsidence in coastal areas, while the 2010 earthquake in Haiti caused up to 20 cm of subsidence in some areas ("Earthquake-Induced Land Subsidence," 2018).

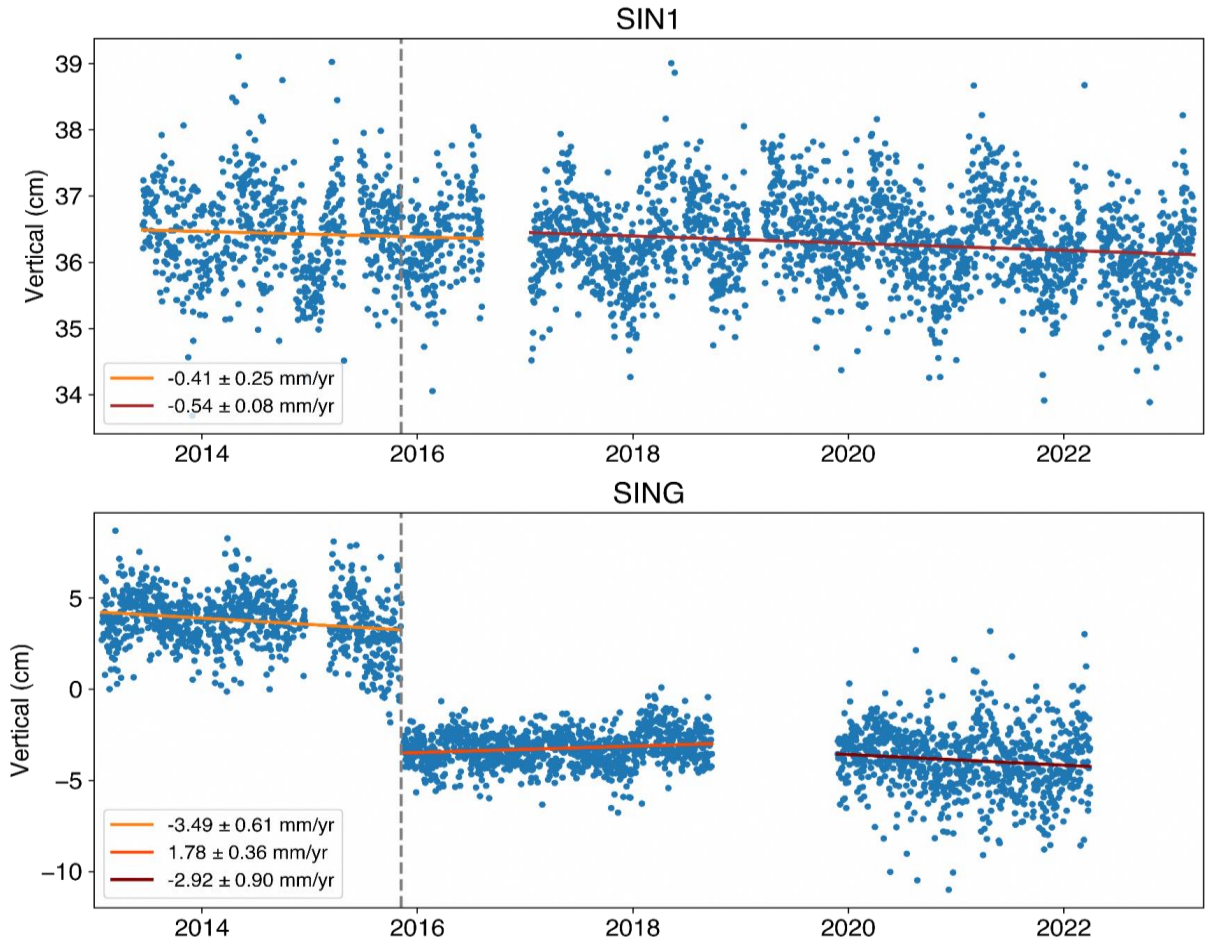

Figure 12.29: GNSS stations in Singapore (SIN1 and SING) showing the processed vertical component in centimeters (blue points). Linear trends were also plotted (in shades of orange and red) over different time periods in an attempt to show the rate of VLM observed in Singapore at these stations. Vertical dashed line represents an earthquake occurrence that most likely explains the vertical shift in measurements at SING. Data taken from the Nevada Geodetic Lab (Blewitt et al., 2018).

However, subsidence was not observed at the other station, SIN1. A number of factors could have explained this discrepancy, given that Singapore is a comparatively small island-state. GPS stations are designed to detect changes in the position of the ground, which can be caused by a variety of factors, including tectonic movement, subsidence, and even human activity (Bock et al., 2016).

The accuracy and sensitivity of GPS measurements can vary depending on factors

such as the location of the station, the type of equipment used, and the surrounding geology (Hashimoto et al., 2011; Ozawa et al., 2008). In the case of the November 4 2015 earthquake, it is possible that the other GPS station in Singapore was located further away from the epicenter of the earthquake, or was situated in an area where the ground was less susceptible to subsidence (Dragert et al., 2001). Additionally, variations in local geological conditions, such as soil composition and depth, can also influence the magnitude of subsidence recorded at different GPS stations (Hu and Wang, 2019).

It is also important to note that subsidence is not always a uniform phenomenon and can vary in magnitude and location depending on the specific conditions of the area affected by the earthquake (Bock et al., 2016). Therefore, it is possible that the lack of subsidence recorded at the other GPS station in Singapore may be due to a combination of factors related to the site, the earthquake, and the measurement equipment used (Ozawa et al., 2008).

While GPS measurements can be a powerful tool for monitoring VLM, earthquakes can introduce a level of uncertainty into these measurements due to a range of factors. For example, the magnitude and type of earthquake can influence the magnitude and distribution of vertical land movement, while the sensitivity and accuracy of GPS equipment can vary depending on the specific site conditions. As a result, it can be challenging to accurately quantify vertical land movement and associated uncertainties in the aftermath of an earthquake.

12.6.3 Future vertical land movement and its associated uncertainties to relative sea-level rise in Singapore

As shown above, the GPS data suggests that different parts of Singapore experience different rates of VLM over the past few years. Although more detailed study needs to be done for accurate conclusions, we could nonetheless hypothesize that land is subsiding in some parts of Singapore over the past few years (Tay et al., 2022). This has important implications for research on past and future sea-level studies, as stakeholders should be ultimately concerned about the relative rise in sea-level with VLM taken into account.

Tide Gauge	Rate of vertical land movement due to GIA (VLM in mm/yr)	Rate of sea-level change due to GIA (mm/yr)
Sultan Shoal	0.21	-0.38
Sembawang	0.19	-0.35
Raffles Light House	0.20	-0.37
Tanjong Pagar	0.19	-0.36
West Coast	0.20	-0.37
West Tuas	0.21	-0.38

Table 12.6: Rates of vertical land movement due to GIA and sea-level change due to GIA component of VLM. Results taken from ICE6G_C (Peltier et al., 2015).

As of 2022, the IPCC AR6 projections of VLM at tide gauges are the only set of projections that consider more than vertical deformation due to GIA. The projections are derived using a Gaussian process model that sums the global, regional and local fields, whereby the local component is generated based on a GIA model and historical tide-gauge data, in a bid to include non-climatic background factors (Kopp, 2013). Tide-gauges record changes in RSL and hence,

the measurements are inclusive of any net changes in VLM.

VLM is projected to cause a fall in sea level in Singapore by 2150 (median) at almost all the tide gauges (Section 12.5.3.1, Figure 12.17). This could be largely dominated by the effects of GIA, which are causing multi-millennium rates of land uplift (Table 12.6). However, the range of uncertainties in the VLM projections (Figure 12.16 and 12.17; Table 12.4) include the possibility of VLM adding to sea-level rise in Singapore (upper bound of *likely* range), instead of a fall (median). Additionally, tectonic activity is another factor that was not accounted for in the AR6 VLM projections, which increases the quantitative and qualitative uncertainties associated with future VLM in Singapore. The prediction of earthquakes alone with any degree of accuracy, for example, remains elusive and a challenging task for scientists (e.g., Jordan, 2011; McGuire, 2014).

Site-specific analyses of VLM for Singapore play a crucial role in strengthening the knowledge base for informed coastal decision making. Comprehensively understanding the local sea-level budget at coastal locations in terms of the driving processes is a high scientific priority for addressing the challenges posed by RSL rise.

Acknowledgements

We thank the Permanent Service for Mean Sea Level (PMSL) and the National Oceanographic Centre (NOC), UK for maintaining the platform for continuous usage of monthly and annual tide-gauge data. Specifically, we want to acknowledge Peter Hogarth from PSMSL/NOC for assisting us with the correction of erroneous tide-gauge data at Sembawang.

We acknowledge the Copernicus Marine Service (CMS) for redistributing the gridded sea surface height data from satellite altimetry and also for providing Global Ocean Physics Reanalysis data (GLORYS12V1). We dually acknowledge ocean reanalysis groups (ORAS5, GECCO3) for making their ocean state estimates publicly available.

Finally we thank all the external reviewers for their suggestions and comments which helped to improve this chapter significantly.

Appendix

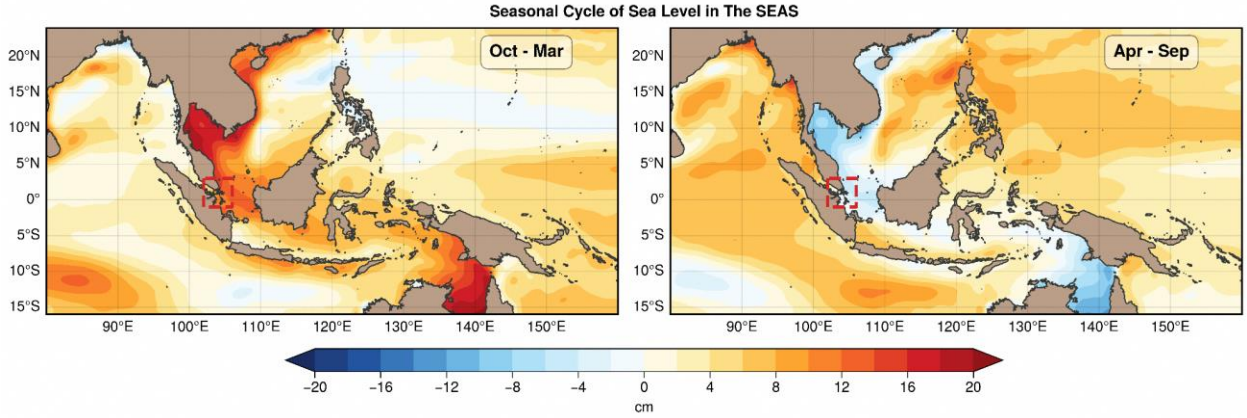

Figure A12.1: Seasonal cycle of sea level in the southeast Asian seas computed from satellite data for the period 1993 - 2021.

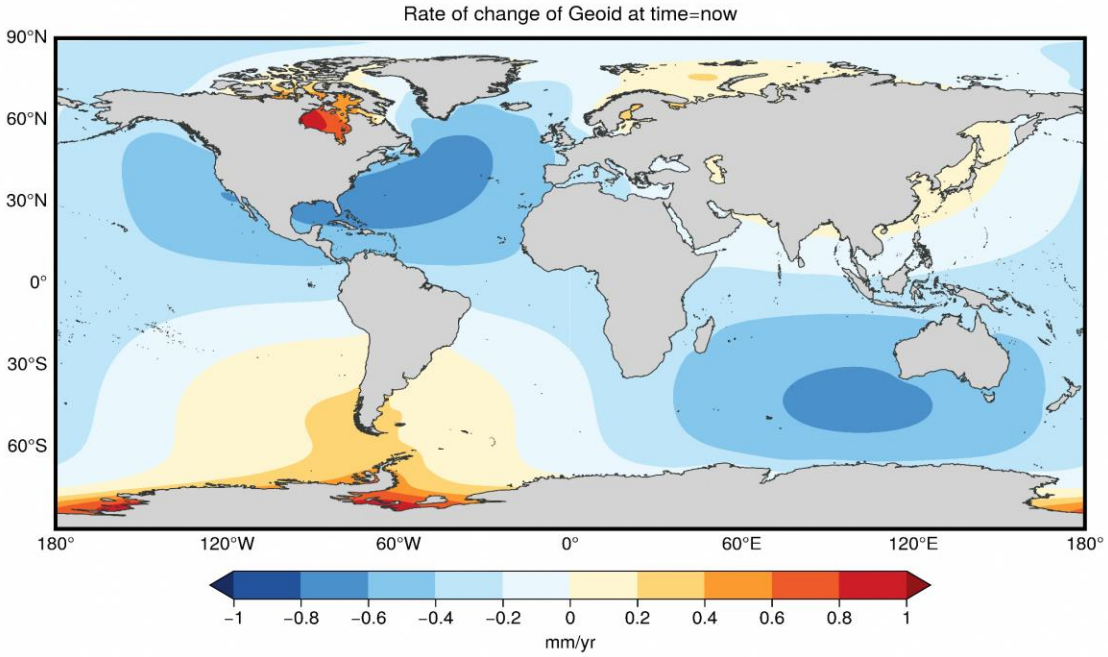

Figure A12.2: Sea surface height change due to changes in gravity (Geoid) associated with GIA from ICE-5G (Peltier et al. 2004).

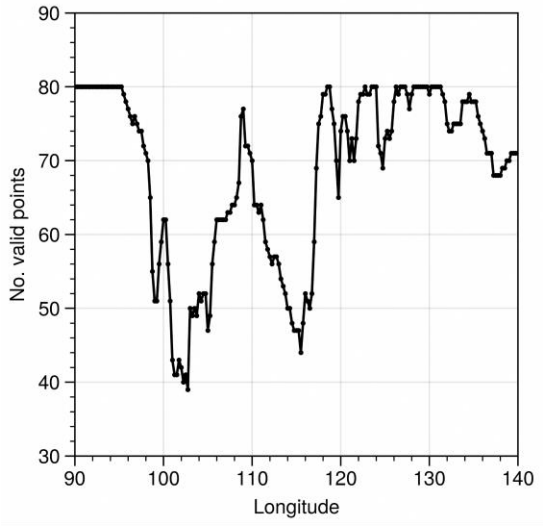

Figure A12.3: Number of valid grid-points (i.e. ocean grid points) used in the latitudinal averaging of sea-level trends shown in Figures 12.7 and 8.

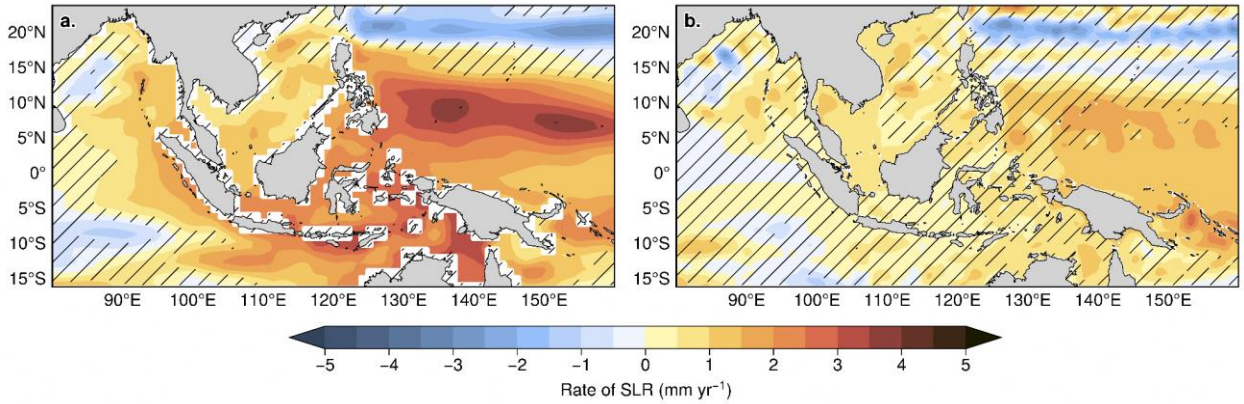

Figure A12.4: Dynamic sea-level rise trend from GECCO3 (German contribution of the Estimating the Circulation and Climate of the Ocean) and GLORYS 12V1 (Global Ocean Physics Reanalysis; https://doi.org/10.48670/moi-00021). For GECCO (GLORYS), the trend estimation covers the period 1993 - 2018 (1993 - 2020). The patches on each panel indicate the trends which are not significant at 95% confidence level.

References

ABC News. (2015, November 4). Magnitude 6.3 earthquake strikes eastern Indonesia. https://abcnews.go.com/International/wireStory/magnitude-63-earthquake-strikes-eastern-indonesia-34915559

Ahmed, A., Khan, M. S., Abdullah, S. A., & Shoaib, M. (2020). Land subsidence and sea level rise impact on Jakarta coastal areas. Environmental Science and Pollution Research, 27(22), 27955-27968.

Albert *et al.* (2016) Interactions between sea-level rise and wave exposure on reef island dynamics in the Solomon Islands. *Environ. Res. Lett.* **11** 054011, https://doi:10.1088/1748-9326/11/5/054011

Alley, R. B., & Alley, K. E. (2018). The rise and fall of ice sheets. Scientific American, 319(5), 54-61. (This article provides a general introduction to ice sheet dynamics and the role of marine ice cliff instability in the collapse of the West Antarctic ice sheet.)

Allison, L.C., Palmer, M.D., Haigh, I.D., (2022), Projections of 21st century sea level rise for the coast of South Africa, *Environ. Res. Commun.* **4** 025001, 10.1088/2515-7620/ac4a90

Aobpaet, Anuphao & Caro Cuenca, Miguel & Hooper, Andy & Trisirisatayawong, Itthi. (2013). InSAR time-series analysis of land subsidence in Bangkok, Thailand. International Journal of Remote Sensing. 34. 2969-2982. 10.1080/01431161.2012.756596.

Argus, D. F., Peltier, W. R., Drummond, R. and Moore, A..W., (2014) The Antarctica component of postglacial rebound model ICE-6G_C (VM5a) based upon GPS positioning, exposure age dating of ice thicknesses, and relative sea level histories. Geophys. J. Int., 198(1), 537-563, doi:10.1093/gji/ggu140.

Asian Development Bank. (2018). Addressing Climate Change and Migration in Asia and the Pacific. Retrieved from https://www.adb.org/sites/default/files/publication/446576/addressing-climate-change-migration-asia-pacific.pdf

Bamber, J.L., M. Oppenheimer, R.E. Kopp, W.P. Aspinall, and R.M. Cooke (2019) Ice sheet contributions to future sea-level rise from structured expert judgment. Proceedings of the National Academy of Sciences, 116(23), 11195–11200, doi:10.1073/pnas.1817205116

Barnard, P.L., Erikson, L.H., Foxgrover, A.C. *et al.* (2019) Dynamic flood modeling essential to assess the coastal impacts of climate change. *Sci Rep* **9**, 4309. https://doi.org/10.1038/s41598-019-40742-z

Blewitt, G., W.C. Hammond, C. Kreemer (2018), Harnessing the GPS Data Explosion for Interdisciplinary Science, Eos, 99, https://doi.org/10.1029/2018EO104623 (link).

Bingham, R. J., and Hughes, C. W. (2012), Local diagnostics to estimate density-induced sea level variations over topography and along coastlines, *J. Geophys. Res.*, 117, C01013, doi:10.1029/2011JC007276.

Bock, Y., Melgar, D., Crowell, B. W., & Haase, J. S. (2016). Real-time seismology and earthquake damage mitigation. Annals of Geophysics, 59(1), S0101. https://doi.org/10.4401/ag-7102.

Bott L.-M., Schöne T., Illigner J., Haghshenas Haghighi M., Gisevius K., Braun B. (2021) Land subsidence in Jakarta and Semarang Bay – The relationship between physical processes, risk perception, and household adaptation Ocean Coast Manag. 211 pp 105775.

Cannaby, H., Palmer, M. D., Howard, T., Bricheno, L., Calvert, D., Krijnen, J., Wood, R., Tinker, J., Bunney, C., Harle, J., Saulter, A., O'Neill, C., Bellingham, C., and Lowe, J. (2016) Projected sea level rise and changes in extreme storm surge and wave events during the 21st century in the region of Singapore, Ocean Sci., 12, 613–632, https://doi.org/10.5194/os-12-613-2016.

Catalao, J., D. Raju, and R. Fernandes (2013) Mapping vertical land movement in Singapore using INSAR and GPS.

Catalao, J., D. Raju, and G. Nico. (2020) INSAR maps of land subsidence and sea level scenarios to quantify the flood inundation risk in coastal cities: The case of Singapore. Remote Sensing, 12(2):296.

Chao, B.F., Y.H. Wu, and Y.S. Li (2008) Impact of artificial reservoir water impoundment on global sea level.. Science (New York, N.Y.), 320(5873), 212–4, doi:10.1126/science.1154580.

Church, J. A. and White, N. J. (2011) Sea-level rise from the late 19th to the early 21st century, Surv. Geophys., 32, 585–602, https://doi.org/10.1007/s10712-011-9119-1.

Church, J. A., Clark, P. U., Cazenave, A., Gregory, J. M., Jevrejeva, S., Levermann, A., ... & Unnikrishnan, A. S. (2013). Sea level change. In Climate Change 2013: The Physical Science Basis. Contribution of Working

Group I to the Fifth Assessment Report of the Intergovernmental Panel on Climate Change (pp. 1137-1216). Cambridge University Press.

Church, J. A., Clark, P. U., Cazenave, A., Gregory, J. M., Jevrejeva, S., Levermann, A., Merrifield, M. A., Milne, G. A., Nerem, R. S., Nunn, P. D., Payne, A. J., Pfeffer, W. T., Stammer, D., and Unnikrishnan, A. S.: Sea-level change, in: Climate Change 2013: The Physical Science Basis, Contribution of Working Group I to the Fifth Assessment Report of the Intergovernmental Panel on Climate Change, edited by: Stocker, T. F., Qin, D. D., Plattner, G. K., Tignor, M., Allen, S. K., Boschung, J., Nauels, A., Xia, Y., Bex, V., and Midgley, P. M., Cambridge University Press, https://doi.org/10.1017/CBO9781107415324.

DeConto, R.M. et al., (2021) The Paris Climate Agreement and future sea-level rise from Antarctica. Nature, in press.

Coulson, S. et al. (2022) A detection of the sea level fingerprint of Greenland Ice Sheet melt. *Science* **377**, 1550-1554. DOI:10.1126/science.abo0926

Dangendorf, S., Hay, C., Calafat, F. M., Marcos, M., Piecuch, C. G., Berk, K., & Jensen, J. (2019). Persistent acceleration in global sea-level rise since the 1960s. *Nature Climate Change*, 9, 705– 710.

Dayan, Hugo & Le Cozannet, Goneri & Sabrina, Speich & Thieblemont, Remi. (2021). High-End Scenarios of Sea-Level Rise for Coastal Risk-Averse Stakeholders. Frontiers in Marine Science. 8. 10.3389/fmars.2021.569992.

DeConto, R. M., & Pollard, D. (2016). Contribution of Antarctica to past and future sea-level rise. Nature, 531(7596), 591-597.

Dieng, H. B., Delcroix, T., Arnault, S., & Cazenave, A. (2021). Revisiting global sea level budget since 1961: importance of vertical land motion. Scientific reports, 11(1), 1-11.

Douglas, B., (2001) Chapter 3 Sea level change in the era of the recording tide gauge, Sea Level Rise - History and Consequences, 10.1016/S0074-6142(01)80006-1, (37-64).

Dragert, H., Wang, K., & James, T. S. (2001). A silent slip event on the deeper Cascadia subduction interface. Science, 292(5521), 1525-1528. https://doi.org/10.1126/science.1058715

Earthquake-Induced Land Subsidence. (2018, May 2). USGS. https://www.usgs.gov/natural-hazards/earthquake-hazards/science/earthquake-induced-land-subsidence

Edwards, T.T.L. et al., (2021) Projecting the land ice contribution to sea level rise this century. Nature, in press.

England M et al. (2014) Recent intensification of wind-driven circulation in the Pacific and the ongoing warming hiatus. Nat Clim Chang 4:222–227

Farrell , W.E., Clark, J.A. (1976) On Postglacial Sea Level, *Geophysical Journal International*, Volume 46, Issue 3, 647–667, https://doi.org/10.1111/j.1365-246X.1976.tb01252.x

Feng M, Li Y, Meyers G (2004) Multi-decadal variations of Fremantle sea level: footprint of climate variability in the tropical Pacific. Geophys Res Lett 31:L16302.

Firman, T., Sofyan, H., & Novirman, J. (2019). The Challenge of Groundwater Overexploitation and Land Subsidence in Jakarta. Journal of Urban Affairs, 41(4), 451-463.

Forster, P., Storelvmo, T., Armour, K., Collins, W., Dufresne, J.-L., Frame, D., Lunt, D. J., Mauritsen, T., Palmer, M. D., Watanabe, M., Wild, M., and Zhang, H.: The Earth's Energy Budget, Climate Feedbacks, and Climate Sensitivity, in: Climate Change 2021: The Physical Science Basis. Contribution of Working Group I to the Sixth Assessment Report of the Intergovernmental Panel on Climate Change, edited by: Masson-Delmotte, V., Zhai, P., Pirani, A., Connors, S. L., Péan, C., Berger, S., Caud, N., Chen, Y., Goldfarb, L., Gomis, M. I., Huang, M., Leitzell, K., Lonnoy, E., Matthews, J. B. R., Maycock, T. K., Waterfield, T., Yelekçi, O., Yu, R., and Zhou, B., Cambridge University Press, Cambridge, United Kingdom and New York, NY, USA, Cambridge, United Kingdom and New York, NY, USA, 923–1054, https://doi.org/10.1017/9781009157896.009.

Fox-Kemper, B., H.T. Hewitt, C. Xiao, G. Aðalgeirsdóttir, S.S. Drijfhout, T.L. Edwards, N.R. Golledge, M. Hemer, R.E. Kopp, G. Krinner, A. Mix, D. Notz, S. Nowicki, I.S. Nurhati, L. Ruiz, J.-B. Sallée, A.B.A. Slangen, and Y. Yu, (2021): Ocean, Cryosphere and Sea Level Change. In Climate Change 2021: The Physical Science Basis. Contribution of Working Group I to the Sixth Assessment Report of the Intergovernmental Panel on Climate Change [Masson-Delmotte, V., P. Zhai, A. Pirani, S.L. Connors, C. Péan, S. Berger, N. Caud, Y. Chen, L. Goldfarb, M.I. Gomis, M. Huang, K. Leitzell, E. Lonnoy, J.B.R. Matthews, T.K. Maycock, T. Waterfield, O. Yelekçi, R. Yu, and B. Zhou (eds.)]. Cambridge University Press, Cambridge, United Kingdom and New York, NY, USA, pp. 1211–1362, doi:10.1017/9781009157896.011.

Frederikse, T., Landerer, F., Caron, L. et al. (2020) The causes of sea-level rise since 1900. *Nature* **584**, 393–397. https://doi.org/10.1038/s41586-020-2591-3

Freymueller, J. T., Haeussler, P. J., & Elliott, J. (2018). Active tectonics of Alaska. University of Alaska Press.

Galloway, D. L., Jones, D. R., & Ingebritsen, S. E. (2019). Land subsidence in the United States. US Geological Survey.

Galloway, D. L., et al. (2011). Land subsidence: natural causes, human-induced, and an evolving legacy. Environmental and Engineering Geoscience, 17(2), 227-251.

Gangadharan, N., Goosse, H., Parkes, D., Goelzer, H., Maussion, F., and Marzeion, B. (2022) Process-based estimate of global-mean sea-level changes in the Common Era, Earth Syst. Dynam., 13, 1417–1435, https://doi.org/10.5194/esd-13-1417-2022.

Garner, G. G., T. Hermans, R. E. Kopp, A. B. A. Slangen, T. L. Edwards, A. Levermann, S. Nowikci, M. D. Palmer, C. Smith, B. Fox-Kemper, H. T. Hewitt, C. Xiao, G. Aðalgeirsdóttir, S. S. Drijfhout, T. L. Edwards, N. R. Golledge, M. Hemer, G. Krinner, A. Mix, D. Notz, S. Nowicki, I. S. Nurhati, L. Ruiz, J-B. Sallée, Y. Yu, L. Hua, T. Palmer, B. Pearson, (2021). IPCC AR6 Global Mean Sea-Level Rise Projections. Version 20210809. Dataset accessed [YYYY-MM-DD] at https://doi.org/10.5281/zenodo.5914709.

GEBCO Bathymetric Compilation Group 2022 (2022) The GEBCO_2022 Grid - a continuous terrain model of the global oceans and land. NERC EDS British Oceanographic Data Centre NOC. doi:10.5285/e0f0bb80-ab44-2739-e053-6c86abc0289c

Gee, M. J. R., et al. (2010) The 2004 Indian Ocean tsunami in Indonesia: Observations on the northern limit in the Indian Ocean and Andaman Sea. Earth and Planetary Science Letters, 297(3-4), 634-642.

Gomez, N., & Warner, R. C. (2018) Marine ice cliff instability: Recent progress and future prospects. Earth-Science Reviews, 177, 709-720. (This review article provides a more detailed examination of marine ice cliff instability and its implications for sea level rise.)

Gregory, J.M., Griffies, S.M., Hughes, C.W. et al. (2019) Concepts and Terminology for Sea Level: Mean, Variability and Change, Both Local and Global. Surv Geophys 40, 1251–1289. https://doi.org/10.1007/s10712-019-09525-z

Gregory, J. M., and Coauthors (2013) Twentieth-Century Global-Mean Sea Level Rise: Is the Whole Greater than the Sum of the Parts?. *J. Climate*, **26**, 4476–4499, https://doi.org/10.1175/JCLI-D-12-00319.1.

Hashimoto, M., Fukuda, J., & Matsu'ura, M. (2011). Why do some GPS stations detect non-tectonic velocity transients?—Comparison of GPS observation and geologic information. Earth and Planetary Science Letters, 312(1-2), 171-182. https://doi.org/10.1016/j.epsl.2011.10.018

Hay, C. C., Morrow, E., Kopp, R. E. & Mitrovica, J. X. (2015) Probabilistic reanalysis of twentieth-century sea-level rise. *Nature* **517**, 481–484; erratum **552**, 278 (2017).

Harvey, T.C., Hamlington, B.D., Frederikse, T. et al. (2021) Ocean mass, sterodynamic effects, and vertical land motion largely explain US coast relative sea level rise. *Commun Earth Environ* **2**, 233. https://doi.org/10.1038/s43247-021-00300-w

Hermawan, I., et al. (2020). Megathrust Earthquakes along the Indonesian Sunda Megathrust Fault: A Review on Seismic Hazard Assessment. Geosciences, 10(8), 287.

Holgate, S.J.; Matthews, A.; Woodworth, P.L.; Rickards, L.J.; Tamisiea, M.E.; Bradshaw, E. (2013) Foden, P.R.; Gordon, K.M.; Jevrejeva, S., and Pugh, J., New data systems and products at the Permanent Service for Mean Sea Level. *Journal of Coastal Research*, 29 (3): 493–504.

Hu, J. C., & Wang, Y. (2019). Dynamic Characteristics of GPS Monitoring Sites and Its Influence on Seismic Deformation Observations. Journal of Earth Science, 30(2), 424-433. https://doi.org/10.1007/s12583-018-0843-2

IPCC. (2021). Climate change 2021: The physical science basis. Contribution of Working Group I to the Sixth Assessment Report of the Intergovernmental Panel on Climate Change. Cambridge University Press.

Jackett DR, McDougall TJ (1995) Minimal adjustment of hydrographic profiles to achieve static stability. J Atmos Ocean Technol 12(4):381–389

Jevrejeva, S., Moore, J. C., Grinsted, A., and Woodworth, P. L. (2008), Recent global sea level acceleration started over 200 years ago? *Geophys. Res. Lett.*, 35, L08715, doi:10.1029/2008GL033611.

Jordan, T. H. (2011). Earthquake predictability, brick by brick. Seismological Research Letters, 82(2), 181-186. https://doi.org/10.1785/gssrl.82.2.181

Kench, P. S., McLean, R. F., Brander, R. W., Nichol, S. L., Smithers, S. G., Ford, M. R., ... & Aslam, M. (2018). Geological effects of tsunami on reef islands result in

coral cover decline and volume and shoreline changes. Earth Surface Processes and Landforms, 43(3), 648-663.

Koh, H. L., Teo, S. C., Caballero-Anthony, M., & Esteban, M. (2021). Southeast Asia's coastal challenge: Managing seas in the era of climate change. Springer Nature.

Konikow, L.F. (2011) Contribution of global groundwater depletion since 1900 to sea-level rise. Geophysical Research Letters, 38(17), doi:10.1029/2011gl048604

Kopp, R.E. et al. (2014) Probabilistic 21st and 22nd century sea-level projections at a global network of tide gauge sites. Earth's Future, 2, 383–406, doi:10.1002/2014ef000239.

Kopp, R.E. et al. (2017) Evolving Understanding of Antarctic Ice-Sheet Physics and Ambiguity in Probabilistic Sea-Level Projections. Earth's Future, 5(12), 1217–1233, doi:10.1002/2017ef000663

Kopp, R. (2013). Does the mid-Atlantic United States sea level acceleration hot spot reflect ocean dynamic variability?. Geophysical Research Letters. 40. 10.1002/grl.50781.

Kopp, R., Garner, G., Hermans, T., Jha, S., Kumar, P., Slangen, A., Turilli, M., Edwards, T., Gregory, J., Koubbe, G., Levermann, A., Merzky, A. Nowicki, S. Palmer, M., and C. Smith (2023). The Framework for Assessing Changes To Sea-level (FACTS) v1.0-rc: A platform for characterizing parametric and structural uncertainty in future global, relative, and extreme sea-level change. 10.5194/egusphere-2023-14.

King, Matt & Altamimi, Zuheir & Boehm, Johannes & Bos, Machiel & Dach, Rolf & Elosegui, Pedro & Fund, F. & Pajares, Manuel & Lavallée, David & Cerveira, Paulo & Penna, Nigel & Riva, Riccardo & Steigenberger, Peter & Van Dam, Tonie & Vittuari, L. & Williams, Simon & Willis, Pascal. (2010). Improved Constraints on Models of Glacial Isostatic Adjustment: A Review of the Contribution of Ground-Based Geodetic Observations. Surveys in Geophysics. 31. 465-507. 10.1007/s10712-010-9100-4.

Landerer, F. W., J. H. Jungclaus, and J. Marotzke (2007a), Regional dynamic and steric sea level change in response to the IPCC-A1B scenario, *J. Phys. Oceanogr.*, 37(2), 296– 312.

Landerer, F., J. H. Jungclaus, and J. Marotzke (2007b), Ocean bottom pressure changes lead to a decreasing length-of-day in a warming climate, *Geophys. Res. Lett.*, 34, L06307, doi:10.1029/2006GL029106

Landerer, F. W., Jevrejeva, S., & Riva, R. E. M. (2015). Coastal sea level rise with warming above 2 °C. Proceedings of the National Academy of Sciences, 112(45), 14239-14244.

Levermann, A. et al. (2020) Projecting Antarctica's contribution to future sea level rise from basal ice shelf melt using linear response functions of ice sheet models (LARMIP-2). Earth System Dynamics, 11(1), 35–76, doi:10.5194/esd-11-35-2020

Martinez-Asensio, A., Wöppelmann, G., Ballu, V., Becker, M., Testut, L., Magnan, A.K. et al. (2019) Relative Sea-level rise and the influence of vertical land motion at tropical Pacific Islands. *Global and Planetary Change*, 176, 132– 143.

Marzeion, B. et al. (2020) Partitioning the Uncertainty of Ensemble Projections of Global Glacier Mass Change. Earth's Future, 8(7), doi:10.1029/2019ef001470

Marzin, C., R. Rahmat, D. Bernie, L. Bricheno, E. Buonomo, D. Calvert, H. Cannaby, S. Chan, M. Chattopadhyay, W. K. Cheong, M. E. Hassim, L. Gohar, N. Golding, C. Gordon, J. Gregory, D. Hein, A. Hines, T. Howard, T. Janes, R. Jones, E. Kendon, J. Krijnen, S. Y. Lee, S. Y. Lim, C. F. Lo, J. Lowe, G. Martin, K. McBeath, K. McInness, C. McSweeney, M. Mizielinski, J. Murphy, C. O'Neill, M. Palmer, G. Redmond, C. Roberts, S. Sahany, M. Sanderson, C. Scannell, D. Sexton, F. Shaw, J. Slingo, X. Sun, J. Tinker, S. Tucker, C. Wang, S. Webster, S. Wilson, R. Wood, S. Zhang (2015) Singapore's Second National Climate Change Study – Phase 1. [Web link: http://ccrs.weather.gov.sg/publications-second-National-Climate-Change-Study-Science-Reports]

McGuire, R. K. (2014). The tragedy of earthquake prediction in the United States: A historical examination. Seismological Research Letters, 85(6), 1163-1172. https://doi.org/10.1785/0220140071

Merrifield, M. A. (2011). A Shift in Western Tropical Pacific Sea Level Trends during the 1990s. *Journal of Climate*, 24(15), 4126– 4138. https://doi.org/10.1175/2011jcli3932.1

Meyssignac, B., Boyer, T., Zhao, Z., Hakuba, M. Z., Landerer, F. W., Stammer, D., Köhl, A., Kato, S., L'Ecuyer, T., Ablain, M., Abraham, J. P., Blazquez, A., Cazenave, A., Church, J. A., Cowley, R., Cheng, L., Domingues, C. M., Giglio, D., Gouretski, V., Ishii, M., Johnson, G. C., Killick, R. E., Legler, D., Llovel, W., Lyman, J., Palmer, M. D., Piotrowicz, S., Purkey, S. G., Roemmich, D., Roca, R., Savita, A., Schuckmann, K., Speich, S., Stephens, G., Wang, G., Wijffels, S. E., and Zilberman, N. (2019) Measuring Global Ocean Heat Content to Estimate the Earth Energy Imbalance,

Front. Mar. Sci., 6, 432, https://doi.org/10.3389/fmars.2019.00432, 2019.

Ministry of Sustainability and the Environment. (2021) Climate Change in Singapore. Retrieved from https://www.mse.gov.sg/climate-change/climate-change-in-singapore

Mitchum, G.T., & Wyrtki, K. (1988) Overview of Pacific sea level variability, Marine Geodesy, 12:4, 235-245, DOI: 10.1080/15210608809379595

Nerem, R. S., Beckley, B. D., Fasullo, J. T., Hamlington, B. D., Masters, D., & Mitchum, G. T. (2018). Climate-change–driven accelerated sea-level rise detected in the altimeter era. *Proceedings of the National Academy of Sciences*, 115(9), 2022– 2025.

Niesters, Lisa-Michéle & Schöne, Tilo & Illigner, Julia & Haghshenas Haghighi, Mahmud & Gisevius, Konstantin & Braun, Boris. (2021). Land subsidence in Jakarta and Semarang Bay -The relationship between physical processes, risk perception, and household adaptation. Ocean & Coastal Management. 211. 105775. 10.1016/j.ocecoaman.2021.105775.

Nicholls, R.J., Lincke, D., Hinkel, J. et al. A global analysis of subsidence, relative sea-level change and coastal flood exposure. Nat. Clim. Chang. 11, 338–342 (2021). https://doi.org/10.1038/s41558-021-00993-z

Nicholls, Robert & Cazenave, Anny. (2010). Sea-Level Rise and Its Impact on Coastal Zones. Science (New York, N.Y.). 328. 1517-20. 10.1126/science.1185782.

Nidheesh, A. G., Lengaigne, M., Vialard, J., Unnikrishnan, A. S. and Dayan, H. (2013) Decadal and long-term sea level variability in the tropical Indo-Pacific Ocean. Climate Dyn., 41(2), 381–402.

Okem, A., J. Petzold, B. Rama, and N. Weyer (eds.)]. In Press, pp. 321–445, www.ipcc.ch/srocc/chapter/chapter-4-sea-level-rise-and-implications-for-low-lying-islands-coasts-and-communities/.

Oppenheimer, M. et al. (2019) Sea Level Rise and Implications for Low Lying Islands, Coasts and Communities. In: IPCC Special Report on the Ocean and Cryosphere in a Changing Climate [Pörtner, H.-O., D.C. Roberts, V. Masson-Delmotte, P. Zhai, M. Tignor, E. Poloczanska, K. Mintenbeck, M. Nicolai,

Otosaka, I. N., Shepherd, A., Ivins, E. R., Schlegel, N.-J., Amory, C., van den Broeke, M. R., Horwath, M., Joughin, I., King, M. D., Krinner, G., Nowicki, S., Payne, A. J., Rignot, E., Scambos, T., Simon, K. M., Smith, B. E., Sørensen, L. S., Velicogna, I., Whitehouse, P. L., A, G., Agosta, C., Ahlstrøm, A. P., Blazquez, A., Colgan, W., Engdahl, M. E., Fettweis, X., Forsberg, R., Gallée, H., Gardner, A., Gilbert, L., Gourmelen, N., Groh, A., Gunter, B. C., Harig, C., Helm, V., Khan, S. A., Kittel, C., Konrad, H., Langen, P. L., Lecavalier, B. S., Liang, C.-C., Loomis, B. D., McMillan, M., Melini, D., Mernild, S. H., Mottram, R., Mouginot, J., Nilsson, J., Noël, B., Pattle, M. E., Peltier, W. R., Pie, N., Roca, M., Sasgen, I., Save, H. V., Seo, K.-W., Scheuchl, B., Schrama, E. J. O., Schröder, L., Simonsen, S. B., Slater, T., Spada, G., Sutterley, T. C., Vishwakarma, B. D., van Wessem, J. M., Wiese, D., van der Wal, W., and Wouters, B. (2023) Mass balance of the Greenland and Antarctic ice sheets from 1992 to 2020, Earth Syst. Sci. Data, 15, 1597–1616, https://doi.org/10.5194/essd-15-1597-2023.

Ozawa, S., Murakami, M., Kaidzu, M., Tada, T., & Sagiya, T. (2008). Anomalously large crustal deformation before the Niigata-Ken Chuetsu earthquake in 2007 detected by GEONET. Geophysical Research Letters, 35(22), L22303. https://doi.org/10.1029/2008gl035596

Peltier, W.R, Argus, D.F. and Drummond, R. (2015) Space geodesy constraints ice-age terminal deglaciation: The global ICE-6G_C (VM5a) model. J. Geophys. Res. Solid Earth, 120, 450-487, doi:10.1002/2014JB011176.

Peltier, W.R., (2004). Global Glacial Isostasy and the Surface of the Ice-Age Earth: The ICE-5G (VM2) Model and GRACE, Ann. Rev. Earth and Planet. Sci., 32, 111-149. https://doi.org/10.1146/annurev.earth.32.082503.144359

Peltier, W. R., and Tushingham, A. M. (1991), Influence of glacial isostatic adjustment on tide gauge measurements of secular sea level change, *J. Geophys. Res.*, 96(B4), 6779– 6796, doi:10.1029/90JB02067.

Permanent Service for Mean Sea Level (PSMSL), (2023) "Tide Gauge Data", Retrieved Aug 2022 from http://www.psmsl.org/data/obtaining/.

Pfeffer, J., Spada, G., A. Mémin, J.-P. Boy, P. Allemand, Decoding the origins of vertical land motions observed today at coasts, Geophysical Journal International, Volume 210, Issue 1, July 2017, Pages 148–165, https://doi.org/10.1093/gji/ggx142

Pollitz, F. F., Bürgmann, R., Banerjee, P., & Nagarajan, B. (2018). Earthquake cycle deformation, transient detection, and geodetic slip rates in subduction zones. Journal of Geophysical Research: Solid Earth, 123(3), 1893-1909.

Rodolfo, Kelvin & Eco, Rodrigo & Sulapas, Joyce & Morales, Anieri & Lagmay, Alfredo Mahar & Amelung, Falk. (2020). Disaster in Slow Motion: Widespread Land Subsidence in and Around Metro Manila,

Philippines Quantified By Insar Time-Series Analysis. 1068.

Royston, S. et al. (2018) Sea-Level Trend Uncertainty With Pacific Climatic Variability and Temporally-Correlated Noise. Journal of Geophysical Research: Oceans, 123(3), 1978–1993, doi:10.1002/2017jc013655.

Royston, S., Bingham, R. J., and Bamber, J. L. (2022) Attributing decadal climate variability in coastal sea-level trends, Ocean Sci., 18, 1093–1107, https://doi.org/10.5194/os-18-1093-2022.

Slangen A. B. A., Palmer M. D., Camargo C. M. L., Church J. A., Edwards T. L., Hermans T. H. J., Hewitt H. T., Garner G. G., Gregory J. M., Kopp R. E., Santos V. M. and van de Wal R. S. W. (2023). The evolution of 21st century sea-level projections from IPCC AR5 to AR6 and beyond. Cambridge Prisms: Coastal Futures, 1, E7. doi:10.1017/cft.2022.8.

Slangen, A.B.A., J.A. Church, X. Zhang, and D. Monselesan, (2014) Detection and attribution of global mean thermosteric sea-level change. Geophysical Research Letters, 41(16), 5951–5959, doi:10.1002/2014gl061356.

Shirzaei, M., Freymueller, J., Törnqvist, T.E. et al. Measuring, modelling and projecting coastal land subsidence. Nat Rev Earth Environ 2, 40–58 (2021). https://doi.org/10.1038/s43017-020-00115-x

Smith, C.J. et al. (2018) FAIR v1. 3: A simple emissions-based impulse response and carbon cycle model. Geoscientific Model Development, 11(6), 2273–2297.

Siringan, F. P., Taniguchi, M., Shimada, J., & Lapus, M. R. (2019). Land subsidence, aquifer system compaction and sea-level rise in the coastal aquifers of Manila Bay and Bangkok. Science of the Total Environment, 655, 843-856.

Swapna, P., J. Jyoti, R. Krishnan, N. Sandeep, and S.M. Griffies (2017) Multidecadal Weakening of Indian Summer Monsoon Circulation Induces an Increasing Northern Indian Ocean Sea Level. Geophysical Research Letters, 44(20), 10560–10572, doi:10.1002/2017gl074706.

Tamisiea, M.E., and J.X. Mitrovica (2011) The moving boundaries of sea level change: Understanding the origins of geographic variability. Oceanography 24(2):24–39, doi:10.5670/oceanog.2011.25.

Tay, C., Lindsey, E.O., Chin, S.T. et al. Sea-level rise from land subsidence in major coastal cities. Nat Sustain 5, 1049–1057 (2022). https://doi.org/10.1038/s41893-022-00947-z

Tkalich, P., Vethamony, P., Babu, M. T., and Pokratath, R. (2009) Seasonal sea level variability and anomalies in the Singapore Strait, Proceedings of International Conference in Ocean Eng., ICOE 2009 IIT Madras, Chennai, India.

Tkalich, P., Vethamony, P., Luu, Q.-H., and Babu, M. T. (2013) Sea level trend and variability in the Singapore Strait, Ocean Sci., 9, 293–300, https://doi.org/10.5194/os-9-293-2013.

Unnikrishnan A., Nidheesh G., Lengaigne M. (2015) Sea-level-rise trends off the Indian coasts during the last two decades. Curr Sci 108:966–971.

Wal, R.S.W. & Nicholls, R. & Behar, David & McInnes, K. & Stammer, D. & Lowe, Jason & Church, J. & DeConto, R. & Fettweis, Xavier & Goelzer, Heiko & Haasnoot, M. & Haigh, I. & Hinkel, Jochen & Horton, B. & James, T. & Jenkins, Adrian & LeCozannet, G. & Levermann, Anders & Lipscomb, W. & White, K.. (2022). A High-End Estimate of Sea Level Rise for Practitioners. Earth's Future. 10. 10.1029/2022EF002751.

Vinogradov, S. V., and Ponte, R. M. (2011), Low-frequency variability in coastal sea level from tide gauges and altimetry, *J. Geophys. Res.*, 116, C07006, doi:10.1029/2011JC007034.

von Schuckmann, K., Cheng, L., Palmer, M. D., Hansen, J., Tassone, C., Aich, V., Adusumilli, S., Beltrami, H., Boyer, T., Cuesta-Valero, F. J., Desbruyères, D., Domingues, C., García-García, A., Gentine, P., Gilson, J., Gorfer, M., Haimberger, L., Ishii, M., Johnson, G. C., Killick, R., King, B. A., Kirchengast, G., Kolodziejczyk, N., Lyman, J., Marzeion, B., Mayer, M., Monier, M., Monselesan, D. P., Purkey, S., Roemmich, D., Schweiger, A., Seneviratne, S. I., Shepherd, A., Slater, D. A., Steiner, A. K., Straneo, F., Timmermans, M.-L., and Wijffels, S. E. (2020) Heat stored in the Earth system: where does the energy go?, Earth Syst. Sci. Data, 12, 2013–2041, https://doi.org/10.5194/essd-12-2013-2020.

von Schuckmann, K., Minière, A., Gues, F., Cuesta-Valero, F. J., Kirchengast, G., Adusumilli, S., Straneo, F., Ablain, M., Allan, R. P., Barker, P. M., Beltrami, H., Blazquez, A., Boyer, T., Cheng, L., Church, J., Desbruyeres, D., Dolman, H., Domingues, C. M., García-García, A., Giglio, D., Gilson, J. E., Gorfer, M., Haimberger, L., Hakuba, M. Z., Hendricks, S., Hosoda, S., Johnson, G. C., Killick, R., King, B., Kolodziejczyk, N., Korosov, A., Krinner, G., Kuusela, M., Landerer, F. W., Langer, M., Lavergne, T., Lawrence, I., Li, Y., Lyman, J., Marti, F., Marzeion, B., Mayer, M., MacDougall, A. H., McDougall, T., Monselesan, D. P., Nitzbon, J., Otosaka, I., Peng, J., Purkey, S., Roemmich, D., Sato, K., Sato, K., Savita, A.,

Schweiger, A., Shepherd, A., Seneviratne, S. I., Simons, L., Slater, D. A., Slater, T., Steiner, A. K., Suga, T., Szekely, T., Thiery, W., Timmermans, M.-L., Vanderkelen, I., Wjiffels, S. E., Wu, T., and Zemp, M. (2023) Heat stored in the Earth system 1960–2020: where does the energy go?, Earth Syst. Sci. Data, 15, 1675–1709, https://doi.org/10.5194/essd-15-1675-2023.

von Schuckmann, K., Palmer, M.D., Trenberth, K.E., Cazenave, A., Chambers, D., Champollion, N., Hansen, J., Josey, S.A., Loeb, N., Mathieu, P-P., Meyssignac, B., and Wild, M. (2016) An imperative to monitor Earth's energy imbalance, Nat. Clim. Change, 6, 138–144, https://doi.org/10.1038/nclimate2876.

Wada, Y. et al. (2016) Fate of water pumped from underground and contributions to sea-level rise. Nature Climate Change, doi:10.1038/nclimate3001.

Wada, Y. et al. (2012) Past and future contribution of global groundwater depletion to sea-level rise. Geophysical Research Letters, 39(9), doi:10.1029/2012gl051230.

Wang, J., Church, J. A., Zhang, X., Gregory, J. M., Zanna, L., & Chen, X. (2021). Evaluation of the local sea-level budget at tide gauges since 1958. *Geophysical Research Letters*, 48, e2021GL094502. https://doi.org/10.1029/2021GL094502

Wassmann, R., Thevs, N., & Bandholtz, T. (2016). Bangkok's sinking realities: impacts and adaptations. Climate and Development, 8(4), 328-337.

WCRP Global Sea Level Budget Group: Global sea-level budget 1993–present (2018) Earth Syst. Sci. Data, 10, 1551–1590, https://doi.org/10.5194/essd-10-1551-2018.

Woodworth, P. L., Melet, A., Marcos, M., Ray, R. D., Wöppelmann, G., Sasaki, Y. N., Cirano, M., Hibbert, A., Huthnance, J. M., Monserrat, S., and Merrifield, M. A.(2019) Forcing Factors Affecting Sea Level Changes at the Coast, Surv. Geophys., 40, 1351–1397, https://doi.org/10.1007/s10712-019-09531-1.

Woppelmann, Guy & Marcos, Marta. (2015). Vertical land motion as a key to understanding sea level change and variability. Reviews of Geophysics. 54. n/a-n/a. 10.1002/2015RG000502.

Wyrtki, K. (1987), Indonesian through flow and the associated pressure gradient, *J. Geophys. Res.*, 92(C12), 12941– 12946, doi:10.1029/JC092iC12p12941.

Zanna, L., S. Khatiwala, J.M. Gregory, J. Ison, and P. Heimbach (2019) Global reconstruction of historical ocean heat storage and transport. Proceedings of the National Academy of Sciences, 116(4), 1126–1131, doi:10.1073/pnas.1808838115.

Zhang, P., Liu, J., Zhang, Z., Xu, Z., Zhao, W., & Wang, H. (2018) The effects of human activities on vertical land motion in the Beijing plain, China. Environmental Earth Sciences, 77(8), 310.

Zuo, H., Balmaseda, M. A., Tietsche, S., Mogensen, K., and Mayer, M. (2019) The ECMWF operational ensemble reanalysis–analysis system for ocean and sea ice: a description of the system and assessment, Ocean Sci., 15, 779–808, https://doi.org/10.5194/os-15-779-2019.

13 High Performance Computing Aspects

Authors:
Aurel Florian Moise,
Sandeep Sahany,
Venkatraman Prasanna,
Xin Rong Chua,
Bernard Tan (NSCC)

Meteorological Service Singapore
Centre for Climate Research Singapore

13.1 Introduction

The dynamical downscaling of CMIP6 GCMs from coarse resolution of ~75 km - 200 km to 8 km resolution over the SEA domain and further downscaling to 2 km resolution over the western Maritime Continent domain was the most time and resource consuming aspect of the entire V3 study. The high-performance computing (HPC) dimension of V3 documented in this chapter will not only serve as a benchmark for the next set of national climate change projections for Singapore (V4) but will also provide useful information for other similar efforts worldwide and to the HPC community in Singapore and elsewhere.

In this chapter we present numerical details of V3 dynamical downscaling simulations, such as details of the regional model used for downscaling, number of grid points in the 8 km and 2 km domains, and the time step size used for each of the resolutions in section 13.2. In the subsequent section (section 13.3) we present details of the 3 HPC systems (Koppen, and ASPIRE 2A at Singapore's National Supercomputing Centre NSCC, and Gadi at Australia's National Computational Infrastructure NCI) used for carrying out the dynamical downscaling simulations. In section 13.4 we present some details about the computing and storage requirements of the V3 study. Scalability tests that were carried out to design workflow of simulations such as length of each simulation chunk and number of parallel chunks are presented in section 13.5.

13.2 Numerical Details of V3 downscaling

The Singapore Variable Resolution (SINGV) model is the numerical weather prediction (NWP) model of the Meteorological Service Singapore that was developed in 2020 (Dipankar et al. 2020). This NWP version of the SINGV model domain covers Singapore, the Malay Peninsula and the Indonesian island of Sumatra, with a grid-resolution of 1.5 km, having 1,092 points in longitude and 1,026 points in latitude. Since the SINGV model was designed to run in an NWP mode, it could not be used as-is in climate mode to run long-term climate simulations. Hence, the SINGV model was tailored to run as a climate model and the climate version is called the SINGV Regional Climate Model (SINGV-RCM). Notably, the diurnal cycle of the sea surface temperatures (SSTs) was implemented in the SINGV-RCM for which the SST fields are interpolated from the driving model grid resolution to the SINGV-RCM grid resolution and updated every 6 hours. Further details of the evolution from SINGV to SINGV-RCM can be found in Chapter 5 of this report.

All numerical models of the atmosphere have a dynamical core, which is responsible for solving the governing equations of atmospheric motion. The dynamical cores used by all operational configurations of the UM prior to July 2014 are called "New-Dynamics" (Davies et al., 2005). Following the implementation of New Dynamics, the Met Office initiated the development of "ENDGame" (Even Newer Dynamics for General atmospheric modelling of the environment) (Wood et al., 2014). ENDGame is an evolution of New Dynamics designed to maintain its benefits, whilst improving its accuracy, stability and scalability. ENDGame uses a semi-Lagrangian advection scheme and a semi-implicit scheme for the temporal discretization of the non-hydrostatic, deep-atmosphere equations of motion (Wood et al., 2014). The V3 8km domain has 1120 points in longitude and 560 points in latitude, and a timestep size of 240s, whereas, the 2km domain has 960 points in longitude and 960 points in latitude, and a timestep size of 120s. The 8km and 2km downscaling domains are shown in Figure 13.1 below.

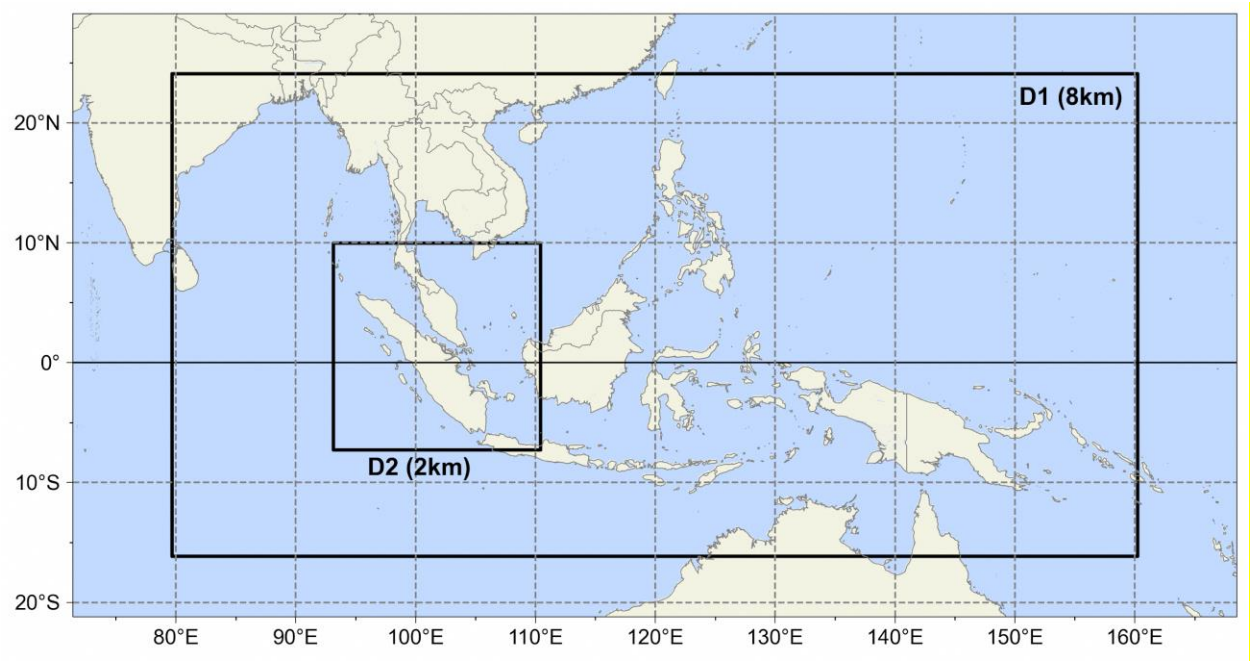

Figure 13.1: V3 downscaling domain

After an extensive period of testing the new SINGV-RCM and conducting various sensitivity experiments (see Chapter 6), the final version and configuration was decided in late 2019 and the initial simulations for V3 projections commenced in early 2020. Since then, V3 simulations were coordinated across 3 HPC systems and 2 continents for a period of 3 years. Final simulations stopped in March 2023. Using effectively tuned HPC resources, it took 1 month to conduct 10 years of 8km resolution simulations and 2 months for 10 years of 2km resolution. Because of the scaling properties of the UM model, simulations also had to be run in chunks of 10 years (for 2km simulations) and 30 years (for 8km simulations) only. Running all of this sequentially, this would have taken over 29 years to complete all V3 simulations. Because of running many simulations simultaneously in parallel, the time was reduced by a factor of 10. However, this took an enormous effort on every staff contributing to V3 to monitor all the parallel simulations, including restarting, trouble-shooting, house-keeping and post-processing.

13.3 HPC Systems Used

The V3 production runs were carried out on 3 HPC systems across 2 continents, two at NSCC (Koppen and Aspire 2A [A2A]), and one at NCI (Gadi) in Australia (refer Figure 13.2). NCI is made available through NSCC's network and arrangements.

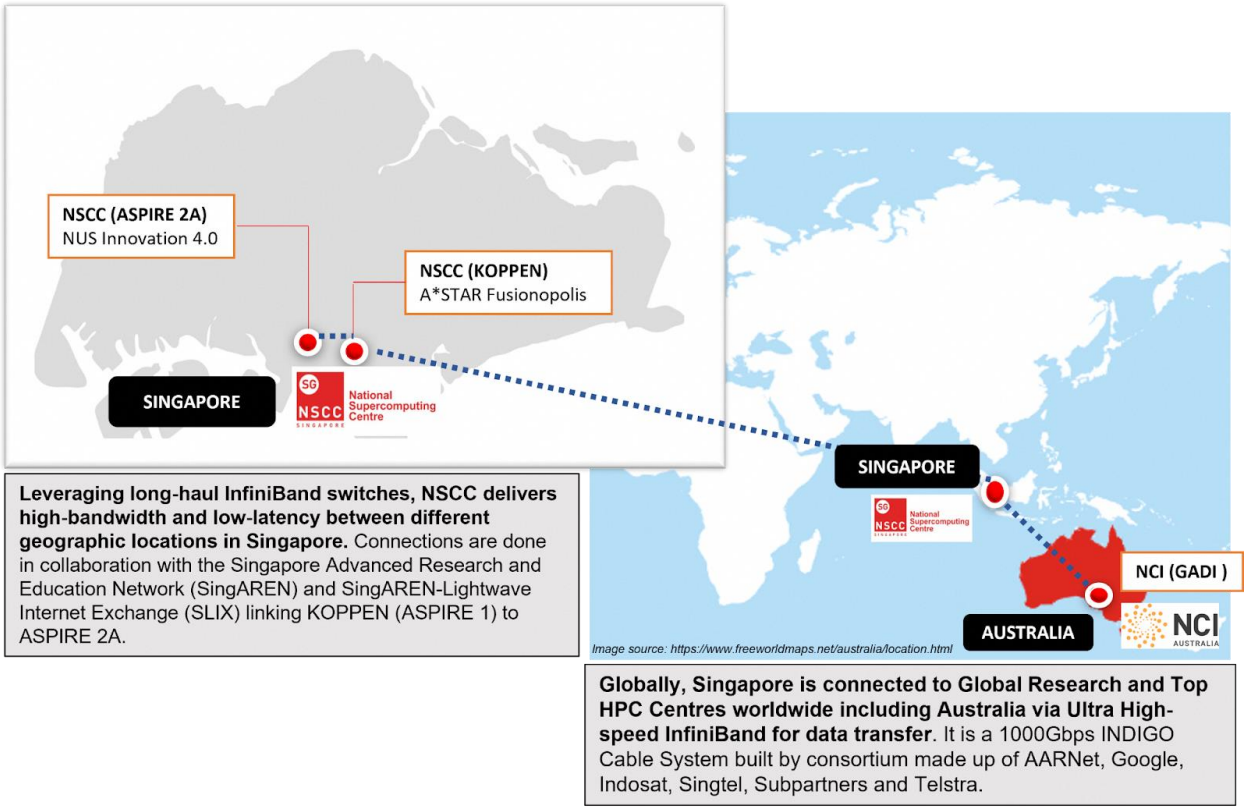

Figure 13.2: Geographical Distribution across 3 HPC Systems

The initial plan was to carry out the initial set of simulations on Koppen in 2020 and then later conduct the majority of the runs on A2A starting February 2021. However, due to COVID-19 related supply chain disruptions in the availability of semiconductor chips during 2020 and beyond, the A2A delivery was delayed by almost 15 months.

To mitigate the potential delay, NSCC proactively employed a multi-pronged strategy to address this matter. At the request of CCRS, NSCC purchased an additional 1 PB of storage equipment (valued at SGD400K) to upgrade Koppen storage from the initial 1 PB to 2 PB to support the V3 project on Koppen.

NSCC also engaged their international partner in Australia, National Computational Infrastructure (NCI), to secure 15 million CPU core-hours/month and 5 PB of storage/month, on their Gadi supercomputer (15 PFlops) for a period of 12 months, starting from July 2021. As a result, NSCC brought the V3 project up to speed within 5 months avoiding a potential 15 months delay due to A2A's late delivery.

Once A2A hardware is available, NSCC made special provisions by providing dedicated access to half of the entire A2A design capacity, and allocated 35 million CPU core-hours/month and 10 PB/month of storage, starting from June 2022 till Dec 2022, to accelerate the V3 research work.

In total, over the 3 supercomputers, NSCC has provided 306M CPU core-hours and 144 PB of storage from July 2021 till Dec 2022. This is about 12 M CPU core-hours and 108 PB more than what CCRS is entitled, based on the original arrangement which is 295 M CPU core-hours and 36 PB of storage over a 12 months period. The additional HPC resources, worth about SGD 3.06M, is provided by NSCC at a goodwill basis at no additional cost to CCRS.

The distribution of V3 simulations across the 3 HPC systems is shown in Table 13.1. As can be seen, almost two-thirds of the simulations were carried out in Singapore, and the remaining one-third in Australia.

Table 13.1: Distribution of Simulations across 3 HPC Systems

V3 Simulations	NSCC Koppen	NCI Gadi	NSCC A2A
ERA5_8km, ERA5_2km	X		
MIROC6_8km	X		
MPI_8km, MPI_2km		X	
NorESM_8km, NorESM_2km		X	
UKESM_8km		X	
UKESM_2km			X
ACCESS_8km, ACCESS_2km			X
EC-Earth_8km, EC-Earth_2km			X

Following is a description of the three HPC systems used for producing all V3 simulations.

Koppen: NSCC Koppen is specifically designed to support HPC research activities in climate and environment research in areas such as advanced modelling and simulation and weather pattern analysis. It is a Cray XC50 supercomputer system with 160 TFLOPS computing capacity, consisting of 52 nodes and 1.2 PB of lustre storage.

The special features of the Cray XC50 supercomputer include:

- the industry-leading Aries network interconnect, which is designed specifically to meet the performance requirements seen in today's emerging class of data center GPU accelerated applications, where high node-to-node communication performance is critical;
- a Dragonfly network topology tightly integrated with Aries that reduces communication latency for scale-out applications that rely heavily on the Message Passing Interface;
- optional SSD-enabled DataWarp I/O accelerator technology, enabling software-defined provisioning of application data for improved performance;
- innovative cooling systems to lower customers' total cost of ownership;
- the next-generation of the high performance and tightly integrated Cray Linux Environment that supports a wide range of applications;
- image-based systems management for easy upgrades, less downtime, and field-tested large-scale system deployment;
- enhancements to Cray's HPC optimized programming environment for improved performance and programmability of GPU environments;
- support for next-generation Intel Xeon and Intel Xeon Phi processors.

The detailed Koppen system information can be found in the Table below:

Table 13.2: Koppen HPC Systems details

Cray XC50-AC		
System peak performance		166.4 TFLOPS
Total system memory (compute node only)		12 TB
Compute nodes	Number of compute blades/nodes	13/(48*+4*=52)
	Processor type	Intel Xeon Cascade Lake 6248 20-core 2.5GHz
	Number of cores per socket/node	20/40
	Peak performance per socket/node	1,600 / 3,200 GFLOPS
	Memory type	*48 nodes with 16 GB DDR4-2933 DIMM *4 nodes with 64 GB DDR4-2933 DIMM
	Memory per socket/node	*48 nodes with 96/192 GB *4 nodes with 384/768 GB
	Memory bandwidth per node (peak)	281.6 GB/s
	Memory capacity per core	48 nodes with 4.8 GB per core (4.65 GB usable) 4 nodes with 19.2 GB per core
Inter-connection	Technology	Cray Aries
	Topology	Dragonfly
	Injection bandwidth	16 GB/s
	Node bandwidth	157.5 Gb/s (per direction, single cabinet of XC50-AC)
	Global bandwidth	1,260 GB/s
	Bi-sectional bandwidth	672 GB/s
Login Node	2 nodes of elogin	elogin1, elogin2

Storage System	
Model	Cray ClusterStor L300N with NXD flash accelerator
Parallel File System	Lustre
Number of System Management Unit	2
Raw Capacity	1,640 TB
Usable Capacity	Approximately 1,200 TB
Sustained I/O Bandwidth	10 GB/s
Connectivity	InfiniBand EDR

A simplified layout of the Koppen system is shown in Figure 13.3 below.

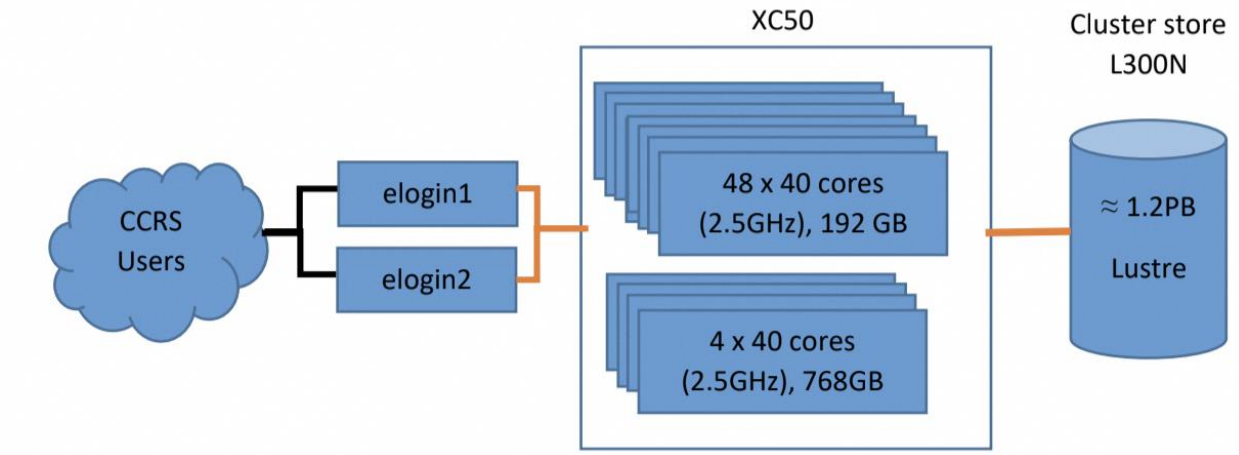

Figure 13.3: Simplified layout of Koppen (credit: NSCC)

ASPIRE 2A: NSCC ASPIRE 2A's (Figure 13.4) core computing capabilities deliver a level of performance and flexibility needed to support a multifaceted array of HPC applications. The computational components are balanced with high-speed storage subsystems and a low latency high speed interconnect that ensures to deliver the highest levels of performance across a broad spectrum of applications. It is an AMD-Based Cray EX supercomputer with 8 PB of GPFS FS and 10 PB of Lustre FS storage and Slingshot interconnect.

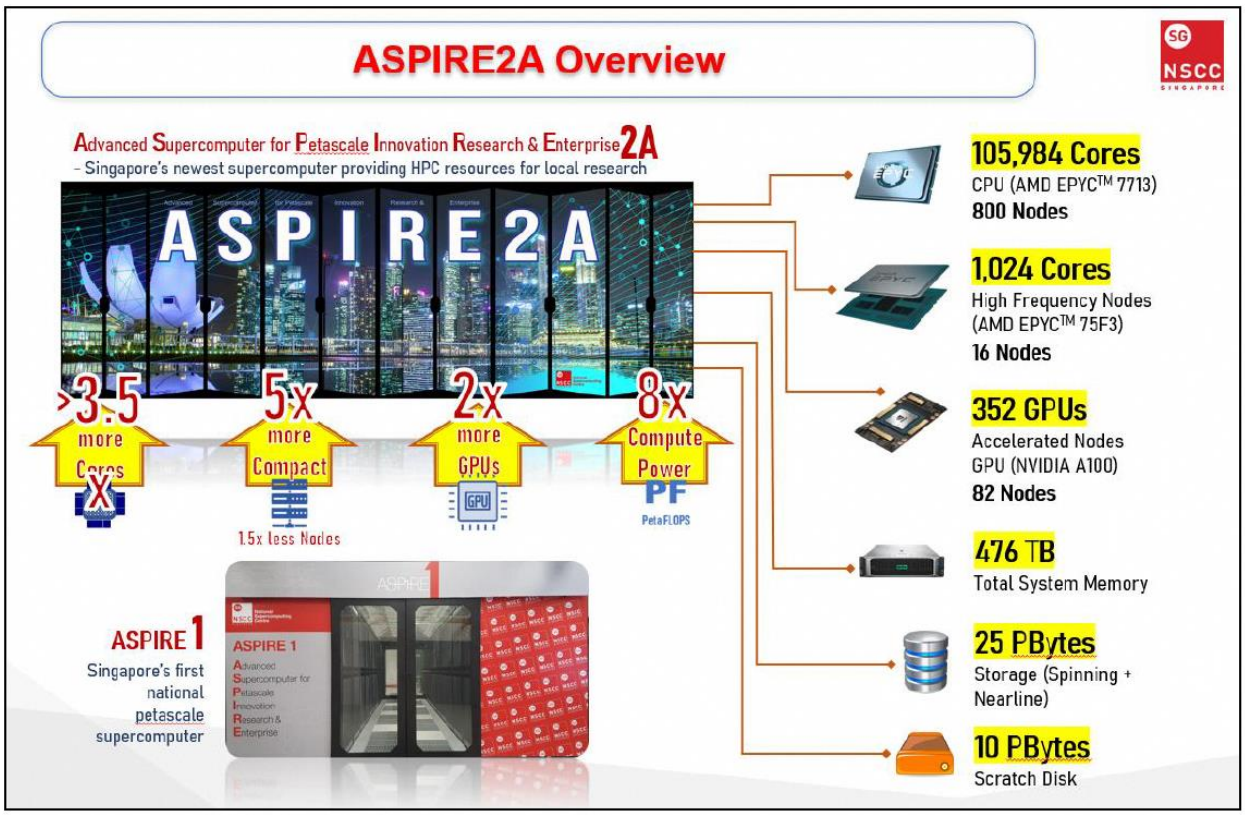

Figure 13.4: ASPIRE 2A specifications (credit: NSCC).

The building block of the HPE Cray EX supercomputer is the liquid cooled cabinet, a sealed unit that uses closed-loop cooling technology. (Figure 13.5) Each EX cabinet holds eight compute chassis and a total of 64 blades with eight Slingshot injection ports per blade. Each blade supports four dual-CPU nodes for a total of 512 processors per cabinet.

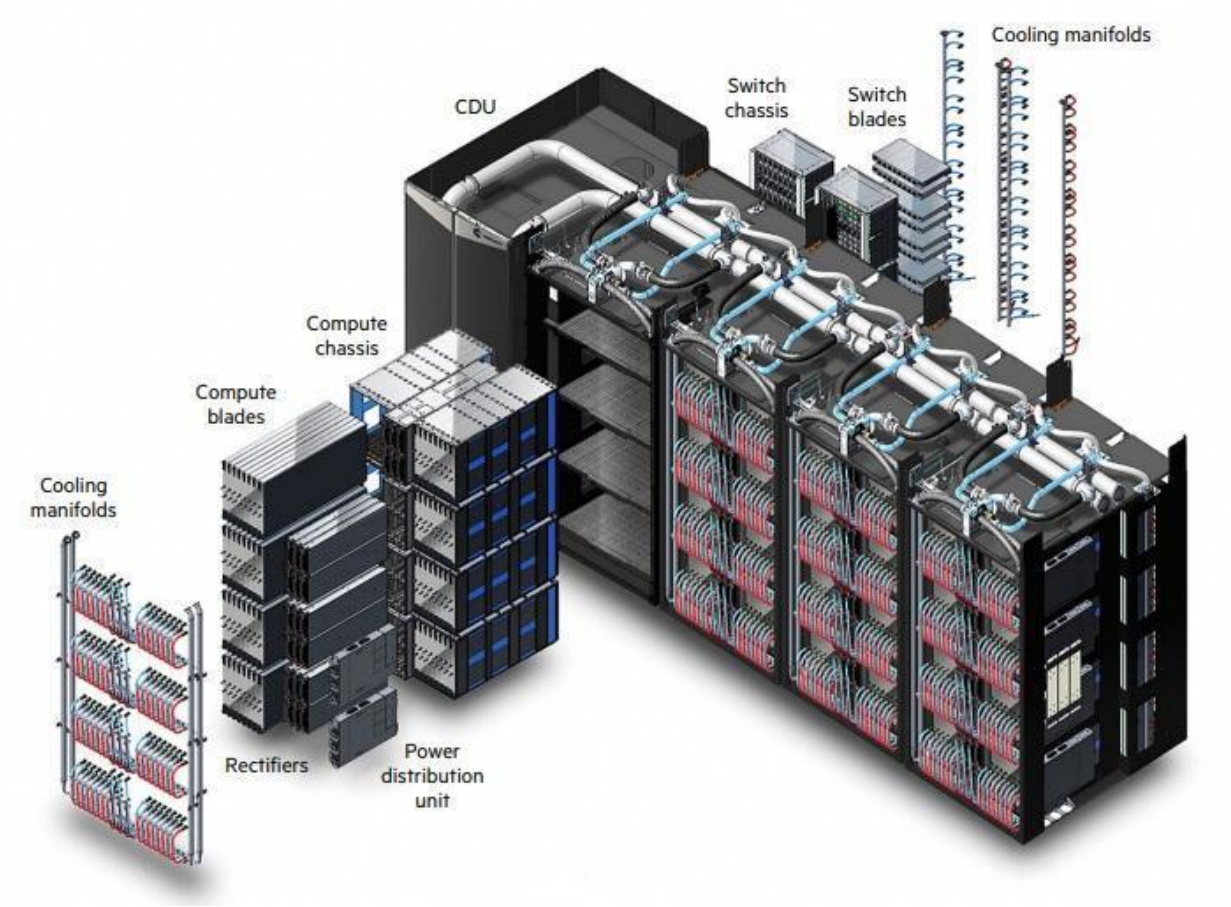

Figure 13.5: Building Block of HPE Cray EX supercomputer

This NSCC HPC **ASPIRE2A** system comprises of the following:

1. HPE Cray EX 2x AMD EPYC Millan 7713 providing total compute capacity of up to 10 PFlops, 512 GB memory and 128 cores per node. This includes a GPU compute capability with 4 x NVIDIA A100-40G SXM per node.
2. AI System: Total of 18 AI GPU nodes. This is divided into 12 nodes with 4x Nvidia A100 40GB and 12 TB nvme local storage; and further 6 nodes with 8x Nvidia A100 40GB and 14TB nvme local storage. The access to the AI systems is via ASPIRE2A “ai” queue.
3. High Frequency: 16 DL385 High Frequency Nodes. These are supported by a Dual-CPU AMD 75F3 (32 cores/CPU + 32 cores/CPU = 64 cores in a node). Additional components are a 100G High speed network, and 512GB DDR4 ECC RAM (User accessible RAM = 500 GB). The operating system is running Red Hat Enterprise Linux-8.
4. High Speed Network Interconnect (HPE Slingshot): All nodes are connected with HPE Slingshot Interconnect (Dragonfly Topology). HPE Slingshot provides a modern, high-performance interconnect for HPC and AI clusters that delivers high-bandwidth and low-latency for HPC, ML, and analytics applications.
5. Additional Features: Remote extended network connections to the A*STAR, NUS, NTU, SUTD and NEA sites; a parallel file system (Lustre & PFSS); Liquid cooled high-density Cray EX cabinets; Air cooled racks (specialized AI, Large memory, storage, login nodes) and an Altair Workload Manager.

NCI Gadi: Gadi (see Figure 13.6 below) is NCI’s peak supercomputer and Australia's most powerful CPU-based research supercomputer. It

is a 4,962 node supercomputer comprising Intel Sapphire Rapids, Cascade Lake, Skylake and Broadwell CPUs and NVIDIA V100 and DGX A100 GPUs, Gadi supports diverse workloads with well over 10 petaflops of peak performance.

Figure 13.6: NCI Gadi

Gadi contains more than 250,000 CPU cores, 930 Terabytes of memory and 640 GPUs. The technical specifications of Gadi are:

- **3,074 nodes** each containing **two 24-core Intel Xeon Scalable 'Cascade Lake' processors** and *192 Gigabytes of memory*
  - This includes 50 nodes each offering 1.5 Terabytes of Intel Optane DC Persistent memory
- **720 nodes** each with **two 52-core Intel Xeon Scalable 'Sapphire Rapids' processors** and *512 Gigabytes of memory*
- **804 nodes** each with **two 14-core Intel 'Broadwell' processors**
- **192 nodes** each with **two 16-core Intel 'Skylake' processors**
- **160 nodes** each containing **four Nvidia V100 GPUs** and two 24-core Intel Xeon Scalable 'Cascade Lake' processors.
- **10 nodes** each with **two 14-core Intel 'Broadwell' processors** and *512 Gigabytes of memory*
- **2 nodes** of the **NVIDIA DGX A100** system, with 8 A100 GPUs per node.
- Linking the storage systems and Gadi is Mellanox Technologies' latest generation HDR InfiniBand technology in a Dragonfly+ topology, capable of transferring data at up to 200 Gb/s.

.

13.4 Computing and Storage Requirements

Given that V3 involved running very high-resolution long-term simulations (a total of ~2000 model years at 8 km resolution and ~750 model years at 2 km resolution) for multiple GCMs (6 for 8 km runs and 5 for 2 km runs) and multiple scenarios (historical plus 3 SSP's), this required a large amount of computing and storage.

Considering the needs and available resources, both storage and compute was regularly monitored and adjusted throughout the project in close collaboration with NSCC (see Table 13.2). Monthly meetings assured that any issues were promptly dealt with and simulations were not significantly affected.

Although the required amount of computing and storage varied across the time span of the production runs which lasted for more than 3 years, the peak computing usage was around 35 million core-hours per month on A2A and around 15 million core-hours per month on Gadi.

The peak storage was around 12 PB on A2A and around 5PB on Gadi. The peak computing usage on Koppen was around 1.2 million core-hours per month, and for storage it was around 2 PB.

After the completion of the simulations on Gadi in Australia, around 4 PB of data was transferred back to Singapore (A2A) with the help of NSCC and the Singapore Advanced Research and Education Network (SingAREN). After employing parallel transfers, we obtained peak throughputs on the order of 1 Gbps

	Jun-21	Jul-21	Aug-21	Sep-21	Oct-21	Nov-21	Dec-21	Jan-22	Feb-22	Mar-22	Apr-22	May-22	Jun-22	Jul-22	Aug-22	Sep-22	Oct-22	Nov-22	Dec-22
NCI-Australia																			
Million Core-Hours	Testing **	Testing **	12.50	12.50	12.50	15	15	15	15	15	15	15	15	15					
PFLOPS	0.00	0.00	1.43	1.43	1.43	1.72	1.72	1.72	1.72	1.72	1.72	1.72	1.72	1.72					
Storage (Project) in PB	0.5	0.5	2.0	2.0	4.5	4.5	4.5	5.0	7.0	7.5	8.0	8.5	9.0	9.5	5.0	5.0			
Storage (Scratch) in PB	0.2	0.2	1.0	1.0	1.5	1.5	1.5	1.5	1.5	1.5	1.5	1.5	1.5	1.5	1.5	1.5			
Aspire2A-NSCC																			
Million Core-Hours												Testing **	35	35	35	35	35	35	35
PFLOPS												0.00	4	4	4	4	4	4	4
Storage (Project) in PB												6	10	10	10	10	10	10	10
Storage (Scratch) in PB												1	2.0	2.0	2.0	2.0	2.0	2.0	2.0
Koppen-NSCC																			
Million Core-Hours	1.40	1.40	1.40	1.40	1.40	1.40	1.40	1.40	1.40	1.40	1.40	1.40	1.40	1.40	1.40	1.40	1.40		
PFLOPS	0.16	0.16	0.16	0.16	0.16	0.16	0.16	0.16	0.16	0.16	0.16	0.16	0.16	0.16	0.16	0.16	0.16		
Storage (Total) in PB	1.5	1.5	1.5	2.0	2.0	2.0	2.0	2.0	2.0	2.0	2.0	2.0	2.0	2.0	2.0	2.0	2.0		

	Jan-23	Feb-23	Mar-23	Apr-23	May-23	Jun-23	Jul-23	Aug-23	Sep-23										
Aspire2A-NSCC																			
Million Core-Hours	35	35	Postprocessing and analysis																
PFLOPS	4	4																	
Storage (Project) in PB	10	10	10	10	10	10													
Storage (Scratch) in PB	2.0	2.0	2.0																

Table 13.2: Screenshot of a resource table projecting the V3 computing and storage estimates on the 3 HPC systems from one of the monthly MSS-NSCC monthly meetings held on 08th March 2022.

After the processing of all the level-0 data to levels 1, 2, and 3, and final housekeeping, around 5-6 PB of storage would still be needed, with a large fraction of this data stored in tapes and the rest as readily accessible live storage for the purpose of data sharing with stakeholders and for further analysis by CCRS.

13.5 Scalability

Scalability is the process optimisation for running compute-heavy simulations on HPC. This optimisation could significantly affect both timing and costs of resources.

Carrying out scalability tests by changing the number of CPUs and parallelization options (e.g. Message Passing Interface [MPI], threading such as OpenMP) to design the workflow of model simulations is standard practice when producing long-term climate change projections in order to optimise computational resource utilisation. As a part of V3 workflow design, systematic scalability tests were carried out for both the 8km and 2km model configurations.

Two metrics were used to measure scalability - minutes per simulated day (MPSD) and the scalability factor (SF). While MPSD is defined as the wall-clock (real) time required to complete 1 day of model simulation (model time), SF is defined as the ratio of theoretical MPSD based on linear scaling with the number of CPUs to actual MPSD. The results from the performed scalability test for the 8 km and 2 km resolutions are shown in Tables 13.3 and 13.4, respectively. The optimisation process tries to minimise MPSD while making sure the SF is sufficiently high. Typically, SF should be at least 0.9 while aiming for a low MPSD.

The tables show the total number of nodes used, the number of CPUs along the x direction of the domain (zonal direction) denoted by Xprocs, the number of CPUs in the y direction of the domain (meridional direction) denoted by Yprocs, number of threads used by each process, MPSD and SF.

Table 13.3: 8 km Scalability Test

Number of compute nodes used for simulation	Number of CPUs used for longitude computes	Number of CPUs used for latitude computes	Minutes per simulated day	Scalability factor
6	16	48	15.7	1
9	30	38	11.3	0.92
10	28	42	11.3	0.83
10	30	42	10.3	0.91
15	30	62	50.7	0.12

It is to be noted that although we tried the multithreading option, and the model showed improved scalability performance with this option, the results failed bit-reproducibility tests considered an important criteria to carry out long-term simulations, and hence we had to use the single thread option for our simulations. This behaviour originates from the actual core model used (UM) and couldn't be adjusted.

Based on the results of the scalability tests shown in Tables 13.3 and 13.4, it was decided to use 10 nodes (1260 CPUs) for each chunk of the 8km simulation and 14 nodes (1764 CPUs) for each chunk of the 2km simulation.

Table 13.4: 2 km Scalability Test

Number of compute nodes used for simulation	Number of CPUs used for longitude computes	Number of CPUs used for latitude computes	Minutes per simulated day	Scalability factor

8	32	32	33	1
10	40	32	29.3	0.9
12	48	32	23	0.96
14	42	42	21	0.9
18	48	48	17.7	0.83

13.6 Summary

In summary, a total of ~2000 model years of dynamical downscaling simulations covering almost entire SEA at 8 km resolution and ~750 model years of dynamical downscaling simulations covering the western Maritime Continent at 2 km resolution using the SINGV-RCM were carried out for the current and future climates as a part of V3.

Based on the availability of computing resources and V3 timelines, the simulations had to be carried out on 3 different HPC systems spanning 2 continents, 2 systems in Singapore (NSCC Koppen and A2A) and 1 in Australia (NCI Gadi). Although the computing and storage requirements kept varying throughout the simulation period, the peak computing exceeded ~35 million core-hours per month and peak storage went as high as ~12 PB.

In addition, around 4PB of data was transferred over from Australia to Singapore at peak transfer speeds of ~1 Gbps with the help of NSCC and SingAREN.

Overall, the HPC journey to accomplish the V3 simulations was challenging and adventurous, comprising significant resources from CCRS staff and dedicated time for managing the resources and simulations. With dedicated teamwork within MSS/CCRS and support from NSCC, NCI and SingAREN, along with the hard work by the V3 team at CCRS, the challenges were successfully maneuvered, and the desired outcome was achieved in time to be able to meet the V3 delivery timelines.

14

Communication and Dissemination of V3 Data and Products

Authors:
Aurel Florian Moise, Sandeep Sahany, Muhammad Eeqmal Hassim, Gerald Lim, Tammy Chin, Chen Chen, Xin Rong Chua, Venkatraman Prasanna, Jianjun Yu, Pavan Harika Raavi, Fei Luo, Trina Ng, Nidheesh Gangadharan

Meteorological Service Singapore
Centre for Climate Research Singapore

14.1 Introduction

It is now well recognised in the national and international community that the gap between scientific data producers and users needs to be reduced in order to make climate science information more usable for various stakeholders ranging from policymakers to the public. In this chapter, we present the various elements of the V3 communications and dissemination plan. Communicating the key messages, data, and products is an essential dimension of the V3 study. For the V2 study, we did not have a systematic communication plan, and hence, having such a plan is an important addition to the overall V3 planning and delivery process.

The V3 communications strategy has various dimensions:

1. Topical Brochures and Videos
2. Infographics
3. Scientific Publications
4. V3-Data Sharing and Visualisation Portal
5. V3 Public Release
6. Engagement with Singapore Ministries
7. Engagement with Singapore Government Agencies
8. Engagement with Singapore Media Houses
9. Engagement with Regional and International Media Houses
10. International Engagement

14.2 Topical Brochures and Videos

As a part of the V3 communications plan, topical brochures and videos have been planned on the following eight topics:

1. V3 Explained
2. Climate Change - From Global to Local
3. Past and Future Sea-level Change
4. Understanding Climate Extremes
5. Using Climate Change Projections in Risk Assessments
6. Probabilistic Climate Change Projections Explained
7. Weather and Climate Drivers for Singapore Explained
8. Application-ready Datasets Explained

Out of the eight brochures, the first three are already completed and are presented below.

14.2.1 V3 Explained

Figures 14.1 to 14.4 show the thumbnails of the 'V3 Explained' brochure. The cover page gives a high-level introduction to the context in which V3 is carried out and its importance (Figure 14.1). To give readers a more comprehensive overview of the V3 project, the rest of the brochure presents:

- Key outputs of V3
- Main areas of climate change impact research underpinned by V3
- Value proposition compared with V2
- Various stages in the V3 project
- Types of data and products that readers can expect
- Data and product categories and how the data will be disseminated

Definitions of SSPs, along with some abbreviations and acronyms used in the brochure, are provided for readers who are unfamiliar with the terminology (e.g., stakeholder agencies).

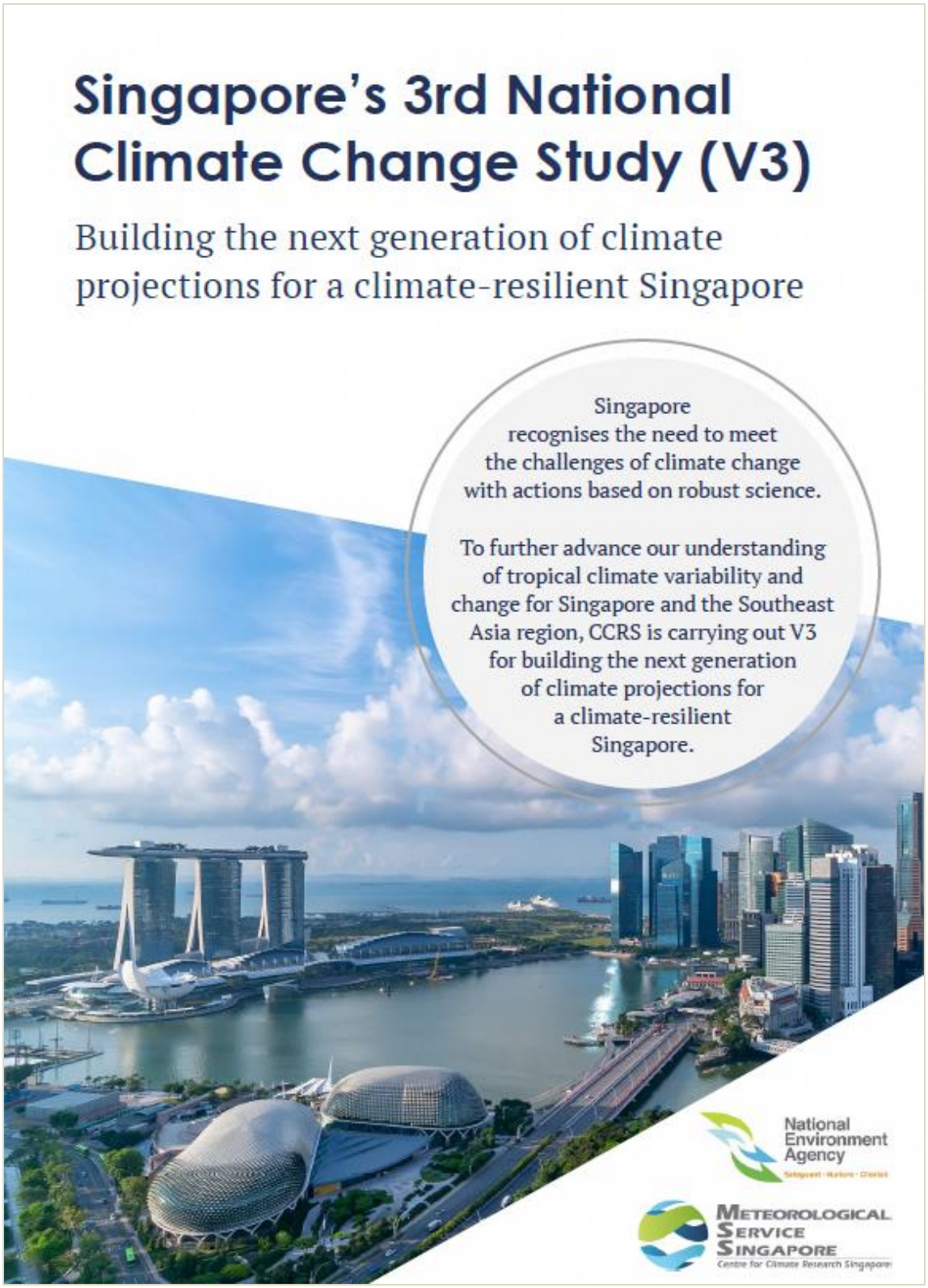

Figure 14.1: Cover page of the 'V3 Explained' brochure

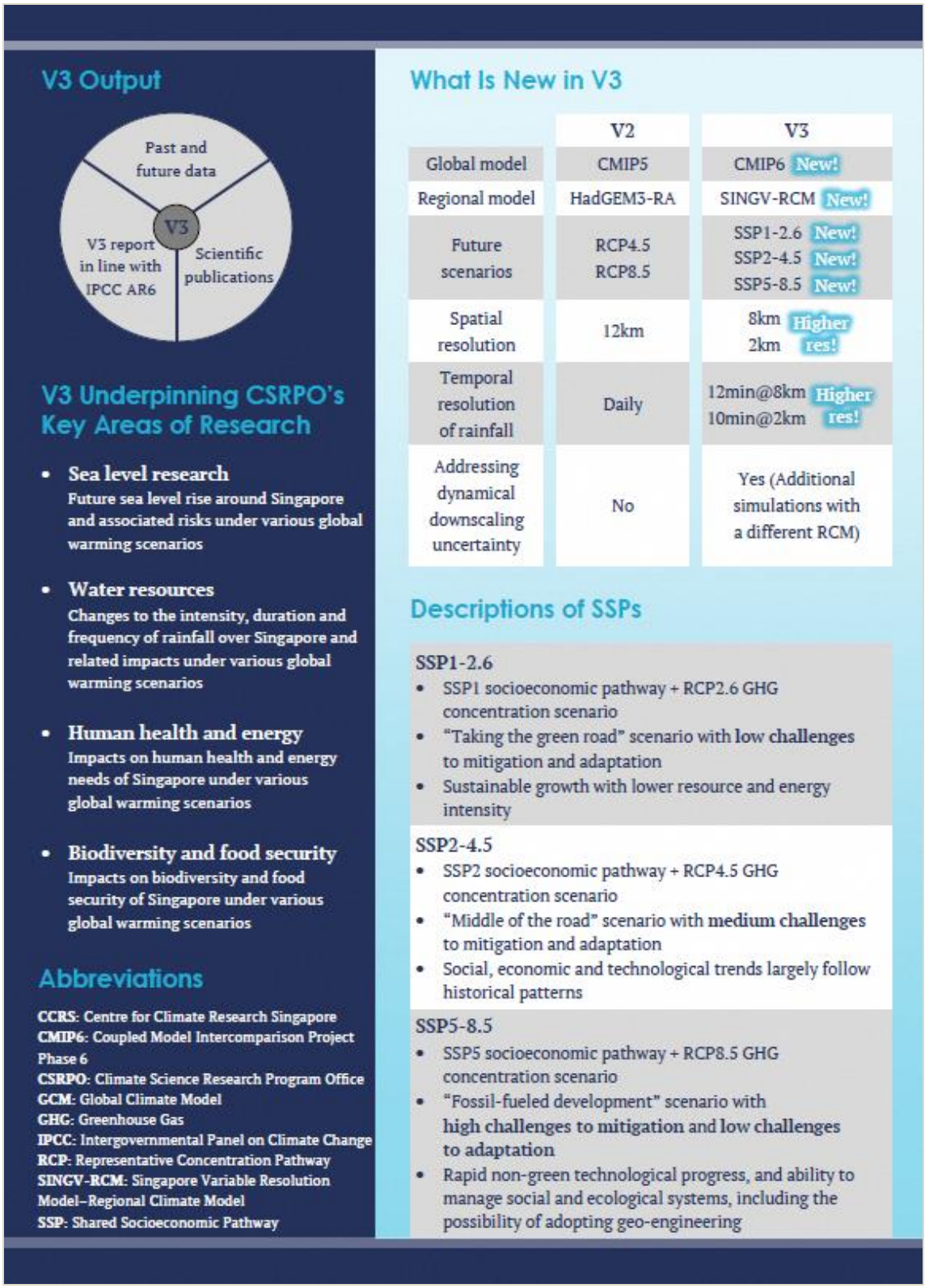

Figure 14.2: The 'V3 Explained' brochure shows the key outputs of V3, key areas of research that it underpins, and key differences from V2. Definitions of SSPs, along with some abbreviations used, are provided for readers who are unfamiliar with the terminology.

Processes in V3

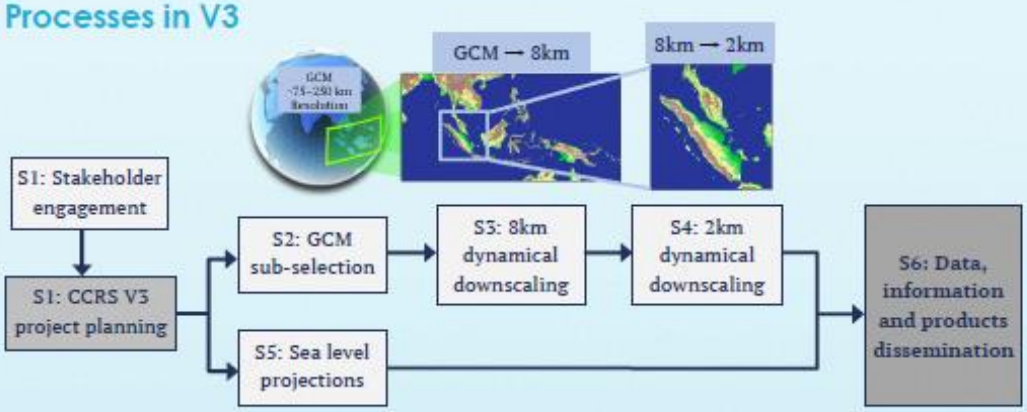

Expected V3 Data

	Rainfall	Temperature	Winds	Relative humidity
Domain (Resolution)	SG (8km, 2km)			
Models	5 CMIP6 GCMs downscaled by SINGV-RCM			
Scenarios	Historical, SSP1-2.6, SSP2-4.5, SSP5-8.5			
Timeline	1955–2100 @ 8km resolution; 1995–2014, 2040–2060, 2080–2100 @ 2km resolution			
Temporal resolution	• 12 min @8km • 10 min @2km • 1 hr @8km & 2km • Daily mean @8km & 2km • Monthly mean @8km & 2km	• Daily mean • Daily maximum • Daily minimum • Monthly mean • Monthly mean profiles (pressure levels)	• Daily mean 10m wind speed • Daily maximum 10m wind speed • Daily mean 10m wind direction • Monthly mean wind profiles (pressure levels) • Daily maximum wind gusts	• Daily mean • Daily maximum • Daily minimum • Monthly mean • Monthly mean profiles (pressure levels)
Vertical levels	Surface	1.5m (daily) Pressure levels (monthly)	10m (daily) Pressure levels (monthly)	1.5m (daily) Pressure levels (monthly)
Products	• Frequency and intensity of extreme rainfall events • Dry spells • Wet spells	Frequency and intensity of extreme temperature events (e.g. hot days, warm nights)	Frequency and intensity of extreme winds	—
Solar radiation	Projections of net incoming solar radiation will be provided for SSP1-2.6, SSP2-4.5 and SSP5-8.5 scenarios at daily frequency over Singapore at 8km and 2km spatial resolutions.			
Sea level projections	Probabilistic sea level projections with SSP1-2.6, SSP2-4.5 and SSP5-8.5 scenarios. Projections of wave and storm surge will be made available as a part of V3+ (pending additional resources).			

Figure 14.3: The 'V3 Explained' brochure presents the various stages in the V3 project, as well as the types of data and products that readers can expect.

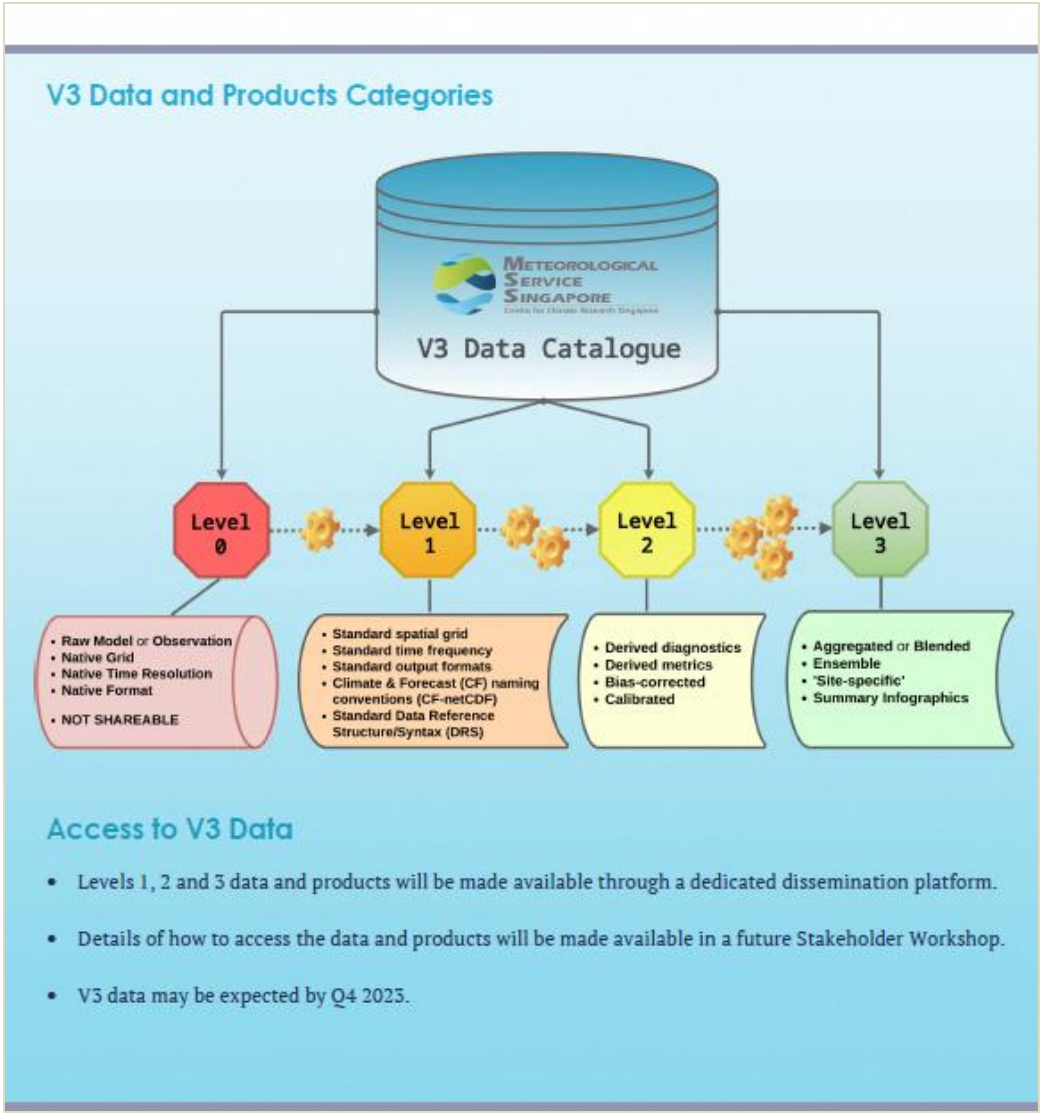

Figure 14.4: The 'V3 Explained' brochure gives an overview of the data and product categories and explains how the data can be accessed.

14.2.2 Climate Change - From Global to Local

Climate model downscaling is a scientific concept that is challenging to grasp for readers and stakeholders with whom CCRS has been engaging. There are various downscaling methods. For targeted communications with key stakeholders to enhance their understanding, a brochure is developed to specifically explain dynamical downscaling, the method adopted in the V3 project.

Figures 14.5 to 14.8 show the thumbnails of the 'Climate Change - From Local to Global' brochure. The cover of the brochure visually illustrates the idea of transforming global climate information to regional and then local climate information, with the subtitle reinforcing the key message that the V3 project plays a critical role in building a climate-resilient Singapore. The brochure first introduces what GCMs are and how their limitations lead to the need for finer-resolution regional and local climate information, which is required for climate change adaptation planning in Singapore and the surrounding region. Readers are then introduced to dynamical downscaling using the V3 project as an example, in line with the objective of the brochure. Finally, the brochure presents the two-

stage downscaling process in V3 (i.e. from global to 8km resolution to 2km resolution) and explains how the reliability and robustness of V3 climate change projections are demonstrated by comparing V3 climate simulations with observational data and ERA-5 data.

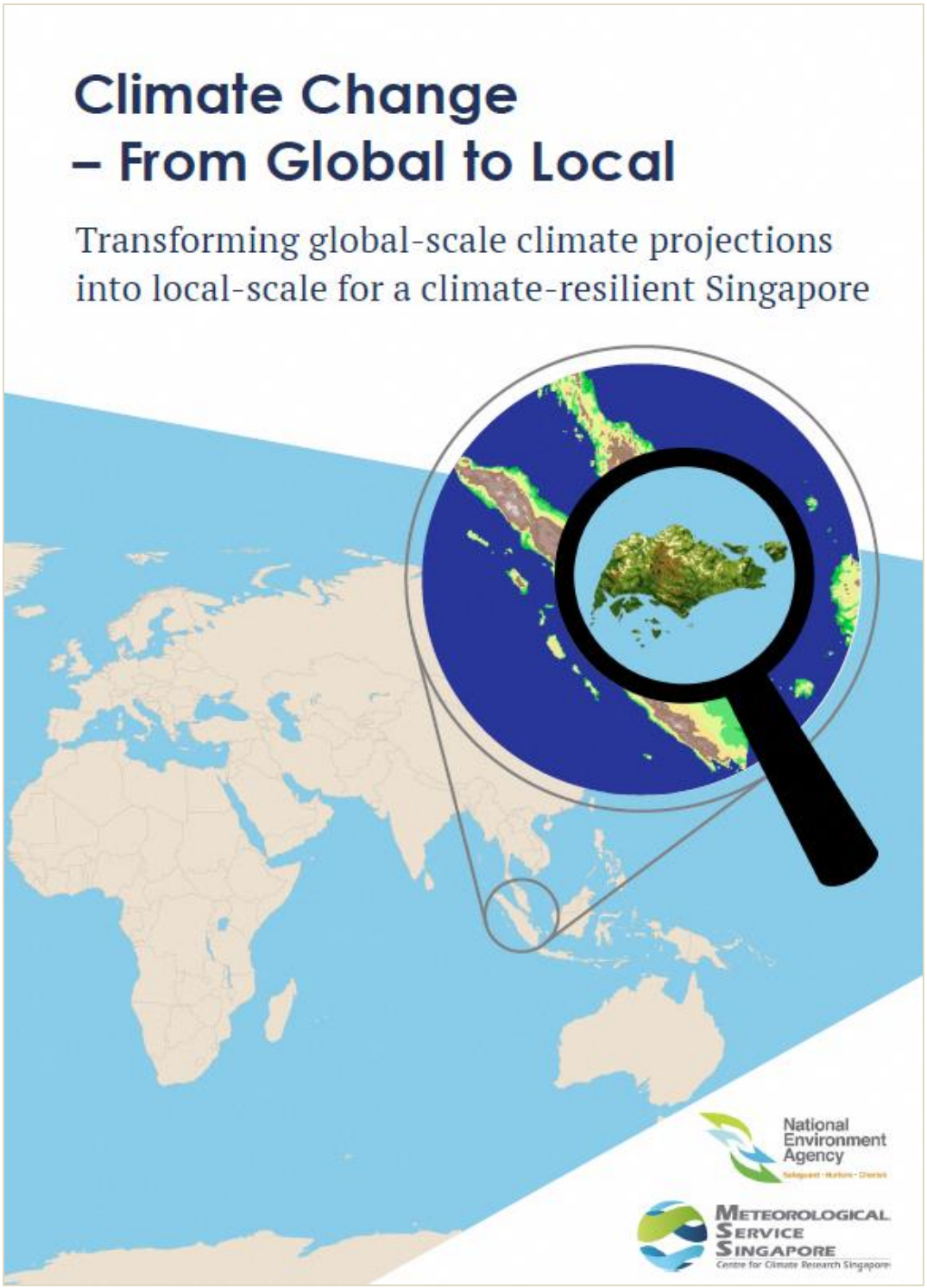

Figure 14.5: Cover page of the 'Climate Change - From Global to Local' brochure

Global Climate Models

- Developed by leading climate research centres around the world, global climate models (GCMs) consist of computer code that solves mathematical equations used to represent the physical processes in Earth's climate system.
- Generally, the latest GCMs have a resolution of 75–250 km, which means that Earth's atmosphere is divided into grid cells that are 75–250 km along each side.

- GCMs are the primary tools for providing climate projections. Once a climate simulation has been initiated, mathematical equations are solved by supercomputers over a number of time-steps to project future climate.

The Need for Finer-resolution Regional and Local Climate Information

- Most climate change impacts (especially those resulting from extreme events) take place at regional and/or local scale.
- Due to the coarse resolution of GCMs, they cannot be used to understand details of climate processes occurring at more modest regional and local scales.
- For scientists to understand climate change and its impacts at regional and local scales in order to inform climate change adaptation, downscaling GCMs using a higher-resolution regional climate model (RCM) to obtain more details is necessary. The RCM output can be further processed to provide even more local info, such as impact of buildings and hills (illustrated on the right).
- Typically, GCMs are also unable to capture rainfall and temperature extremes. The ability to predict and project these extremes is important for climate change adaptation in Southeast Asia (SEA) due to the region's topography, complex coastlines, and thousands of small islands. RCMs are often much more skilful in capturing extreme events.

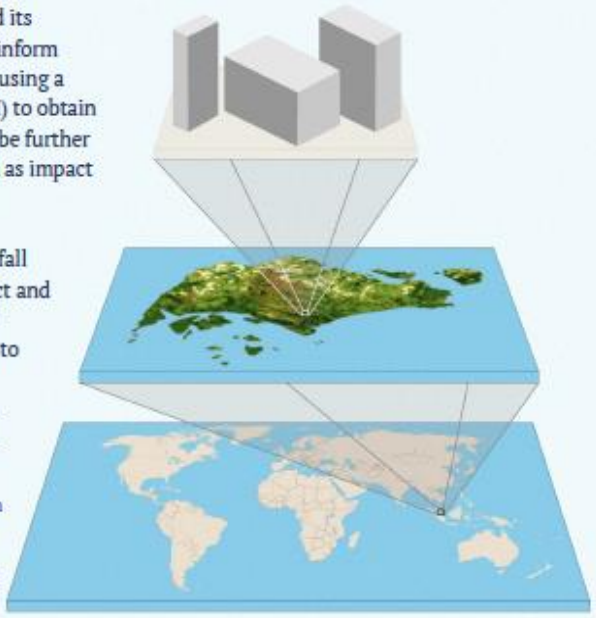

A schematic of how coarse-scale climate information from a GCM can be translated to fine-scale regional and local information through downscaling. This is done using a RCM that can represent more details (e.g. topography and coastlines) and the corresponding physical processes.

Figure 14.6: The 'Climate Change - From Global to Local' brochure begins with a brief introduction to GCMs and their limitations, explaining the need for finer-resolution climate information for climate change adaptation.

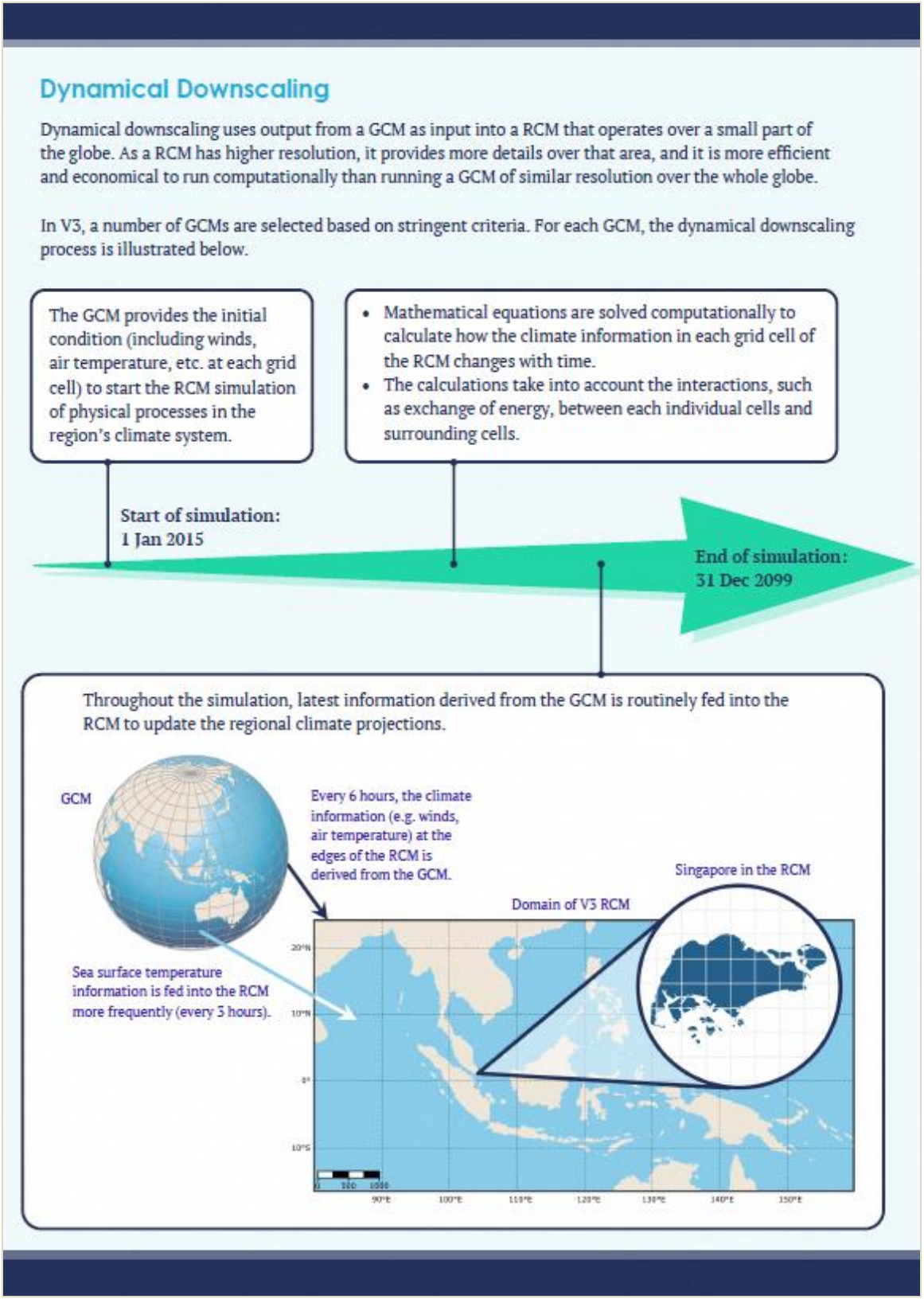

Figure 14.7: The 'Climate Change - From Global to Local' brochure introduces the concept of dynamical downscaling, using the V3 project as an example to illustrate the concept.

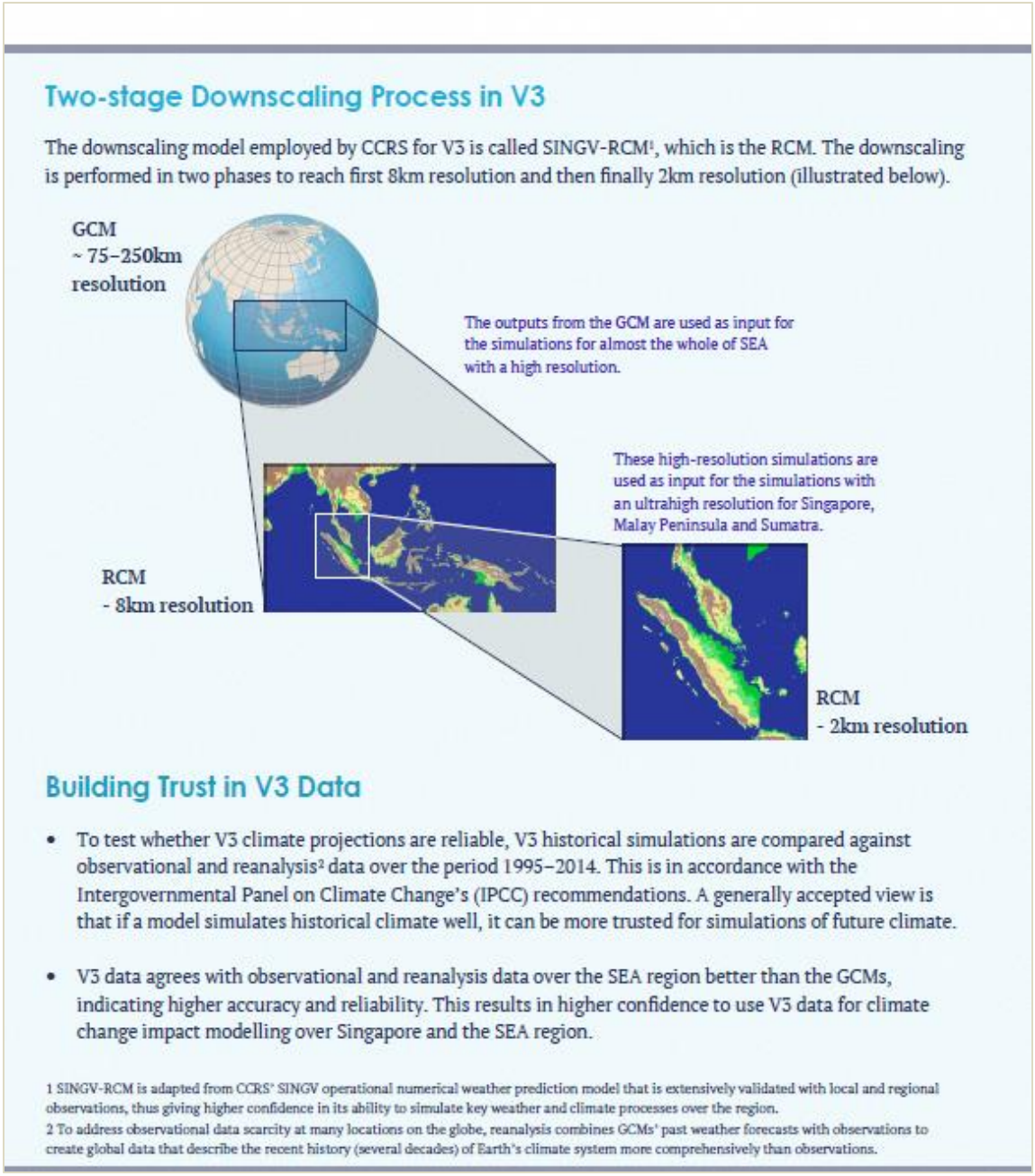

Figure 14.8: The 'Climate Change - From Global to Local' brochure presents the two-stage downscaling process in V3 and explains how the reliability and robustness of V3 projections are demonstrated.

14.2.3 Past and Future Sea-level Change

As a low-lying island country, Singapore is particularly vulnerable to sea-level rise. While this fact is widely accepted in Singapore, understanding the various drivers of sea-level change, especially at the local and regional scale, is generally lacking. PUB, Singapore's national coastal protection agency, has been leading the efforts to save Singapore's shores through different measures such as sea walls and mangroves. V3 sea-level projections in the Singapore region are essential to inform the adaptation design parameters. To enhance readers' knowledge of sea-level drivers and raise awareness of the type of sea-level information

available in V3, a brochure 'Past and Future Sea-level Change' is developed.

Figures 14.9 to 14.12 show the thumbnails of the brochure. The photo on the cover visually conveys Singapore's vulnerability to sea-level rise, with the subtitle reiterating V3's position in building a nation resilient to climate change. The brochure begins by listing several impacts of sea-level rise on Singapore to set the context and remind readers of the dire consequences. Some visually appealing illustrations are then used to explain the drivers of sea-level change at the global, regional and local scale, to raise awareness of the lesser-known drivers such as land water storage and dynamical sea-level change. The brochure ends with an overview of the past and future sea-level information that will be provided by V3, such as the locations at which data sets are available.

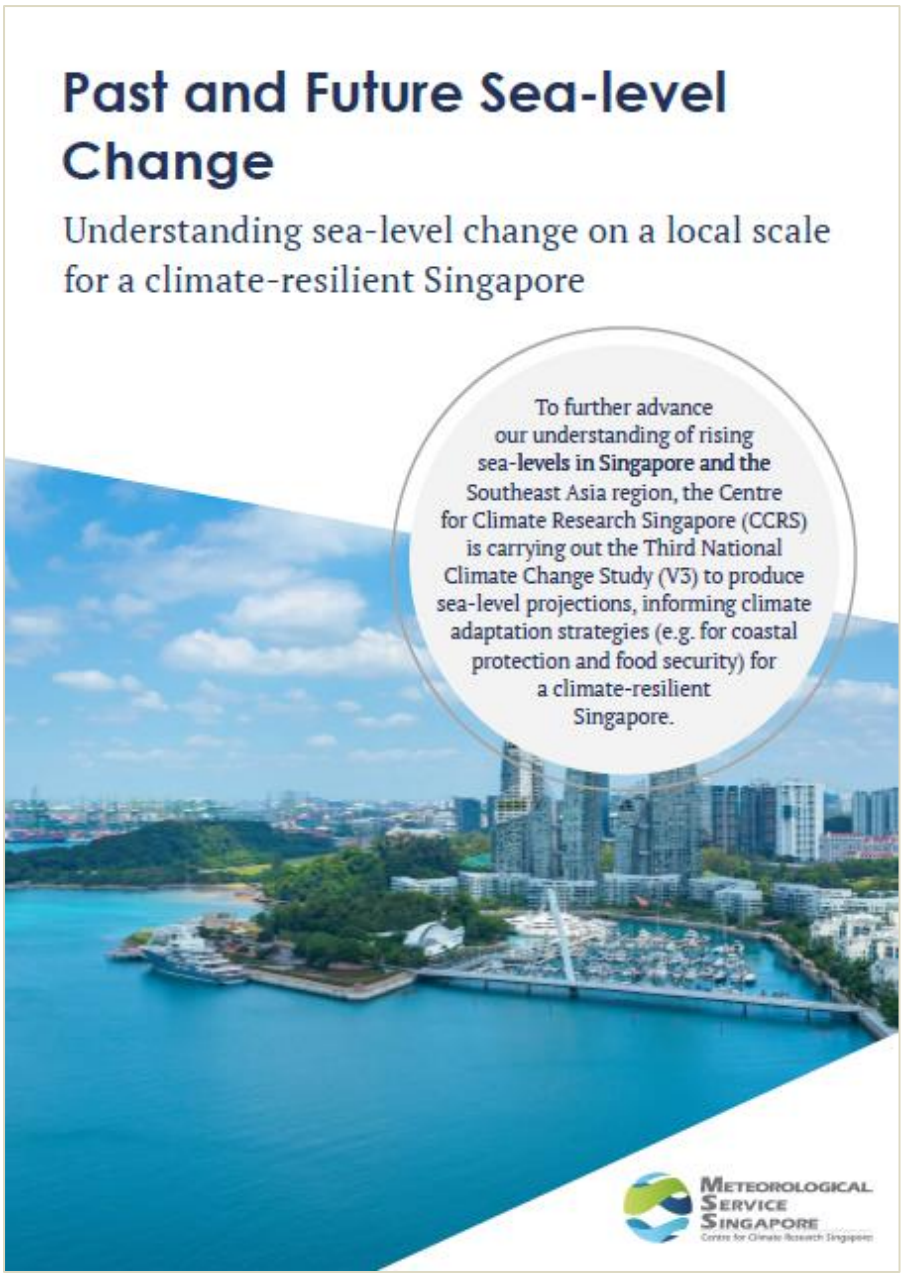

Figure 14.9: Cover of the 'Past and Future Sea-level Change' brochure

Figure 14.10: To set the context, the 'Past and Future Sea-level Change' brochure begins with some examples of sea-level rise impacts on Singapore before explaining the drivers of global sea-level rise.

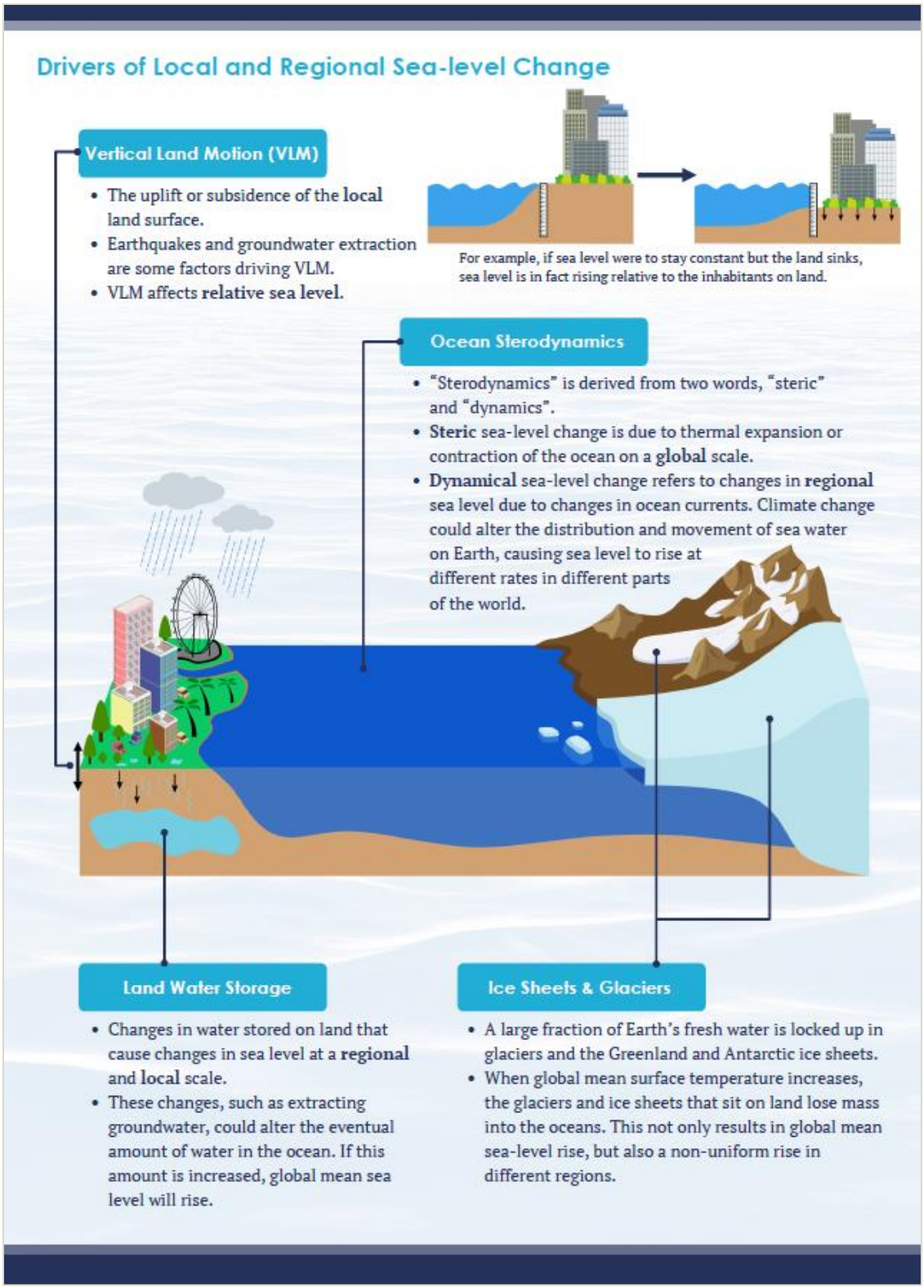

Figure 14.11: The 'Past and Future Sea-level Change' brochure explains the drivers of local and regional sea-level change that are less commonly known.

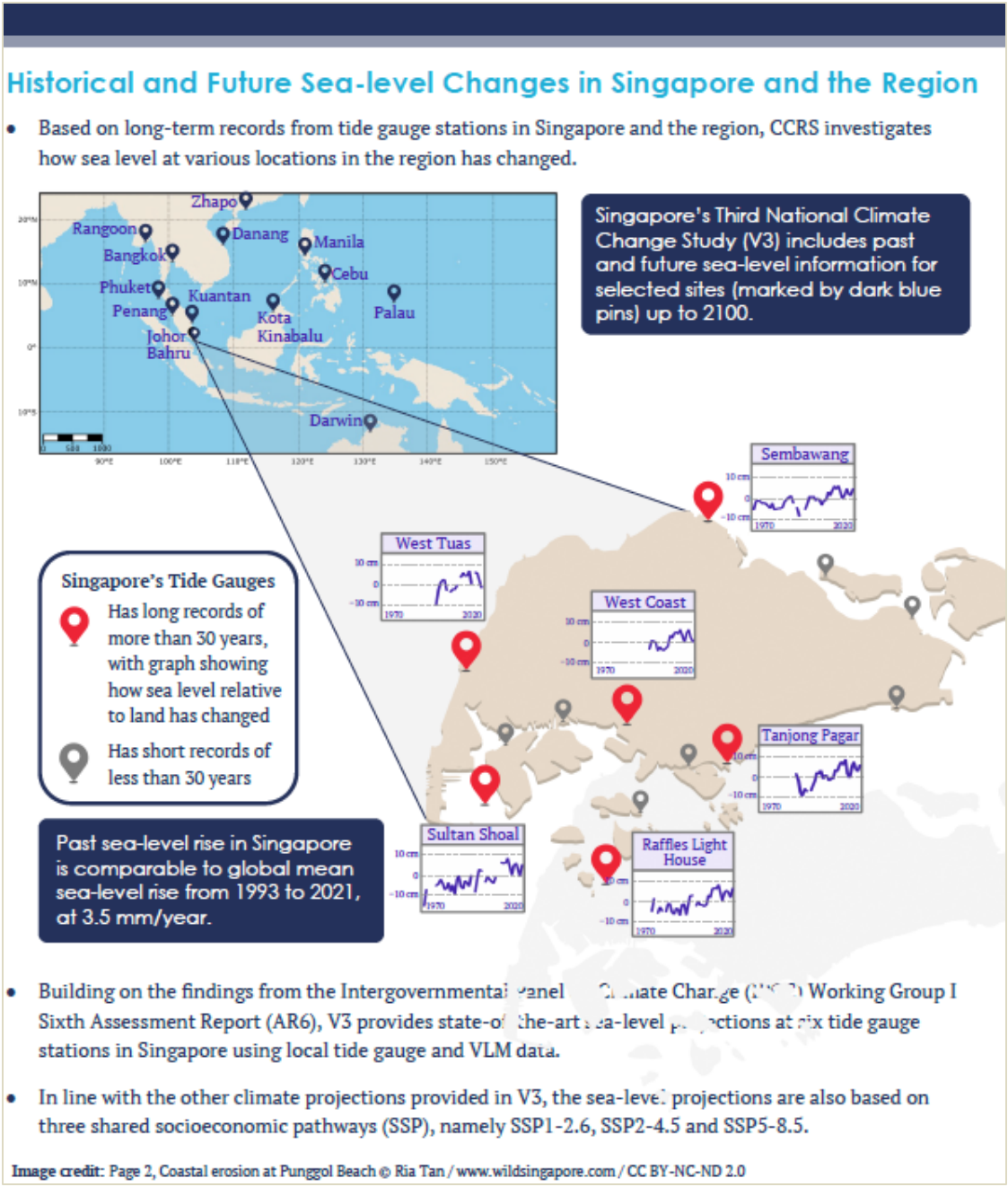

Figure 14.12: The 'Past and Future Sea-level Change' brochure presents the available past and future sea-level information from V3 for Singapore and the surrounding region.

The other brochures and videos are in various stages of preparation.

14.3 Infographics

The findings of the V3 study will be presented in the form of infographics for various climate variables and processes, including some impact-related metrics such as heat stress. One infographic was produced as a part of V2 as well (shown below), but we plan to have multiple infographics conveying various key messages related to physical climate change and impacts as a part of the V3 communications. As a part of this effort, we are also working with the local media

houses to make the infographics more appealing and engaging for the public.

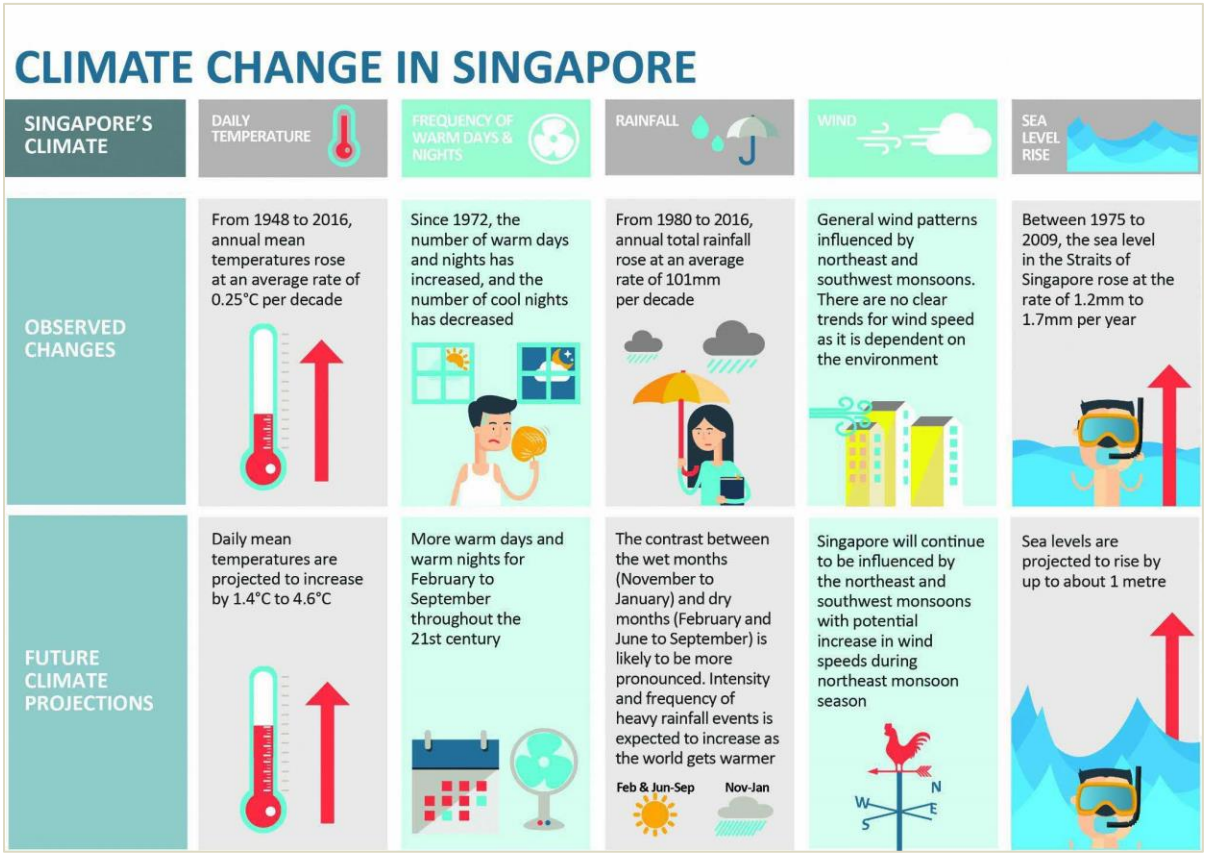

Figure 14.13: Previous V2 infographic

14.4 V3-Data Visualisation Portal (V3-DVP)

The V3-DVP is a key deliverable of the V3 Project and the primary tool for data and products dissemination both nationally and internationally. The design and development of the V3-DVP is an important advancement over the V2 data dissemination method which was primarily done via the Amazon Web Server (AWS) for a duration of 2 years (2015-2017). The data hosted on the AWS had a simple data catalog to display data availability which enabled registered users to select using checkboxes the data they are interested in and download them as Microsoft Excel spreadsheets.

The V3-DVP is intended for local government agencies, researchers in institutes of higher learning (local and abroad) and the general public. The aim of V3-DVP is to present and share future climate change information for Singapore and the wider Southeast Asia region through a custom-built website comprising a visualisation interface and data sharing portal that is 1) easily accessible through any standards-compliant web browser, 2) simple and intuitive to use and 3) highly interactive, in order to engage a wide range of end-users from stakeholder government agencies, institutes of higher learning (local and abroad) and the general public. It also acts as a gateway to facilitate data sharing of standardised, precomputed data products to registered end users, depending on their access credentials.

The following schematic outlines the desired high-level system elements for the V3-DVP. The following capabilities are desired: 1) dedicated

website with a landing page, 2) interactive visualisation and 3) data sharing/download portal.

Through the interactive visualisation functionality users will have the flexibility to select the variable, time period, scenario, time-scale (annual and different seasons) and domain (whole of SEA or individual countries) they are interested in and the corresponding pre-generated figure will be displayed. They will also have the option to download the figure in png format.

In addition, commonly used climate variables will be hosted on the portal and users will be able to search the data catalog and download the desired data after completing a simple registration process. There will be tiered access to data during the initial 2-3 years, before it is made open for all. During the initial phase, the data will be restricted to Singapore Government agencies and local Institutes of Higher Learning and Research Institutions. For advanced users there will also be scope for some data analytics capability.

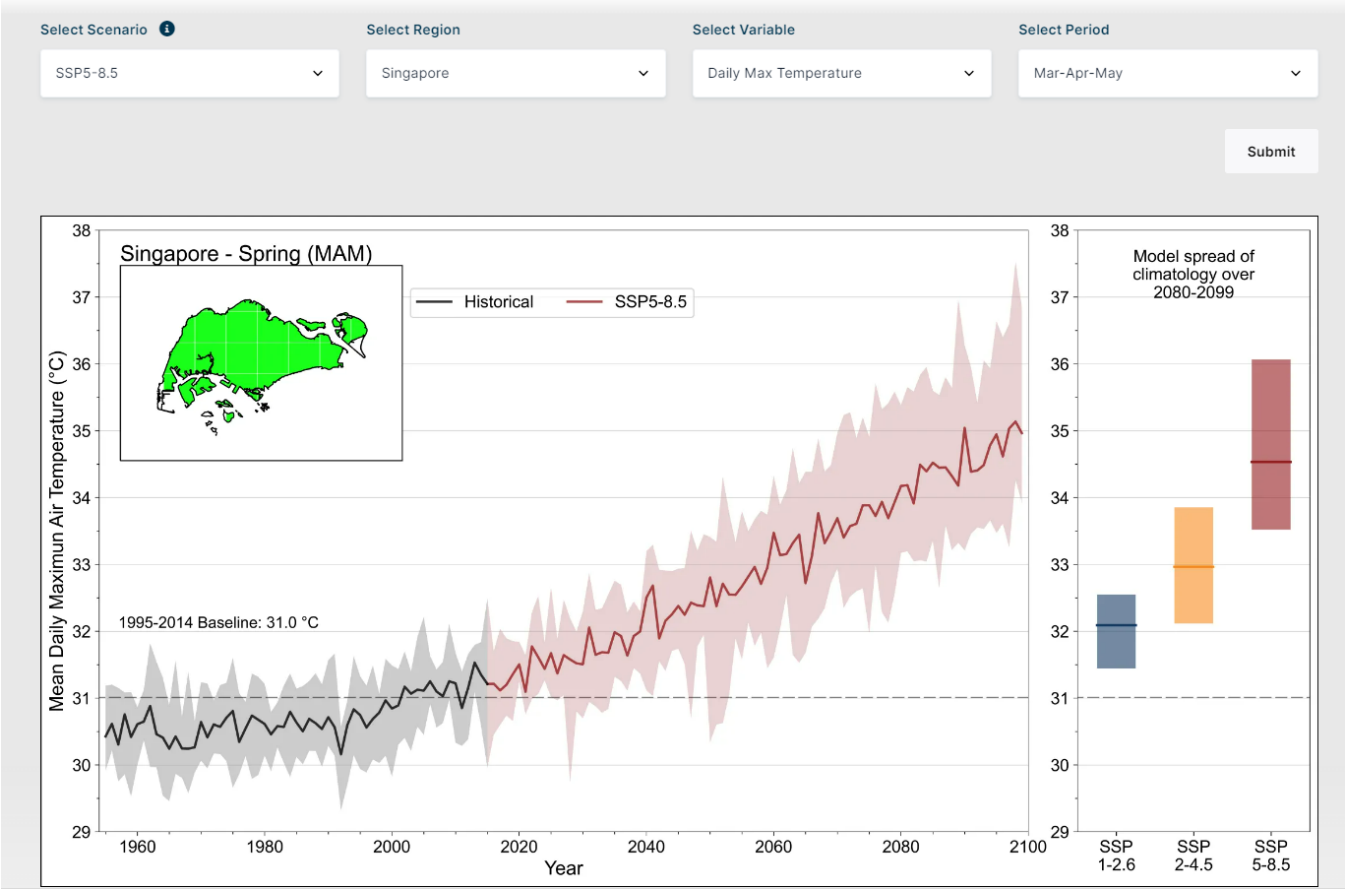

Figure 14.14: Screenshot of the interactive climate visualiser in V3-DVP

The DVP with static and interactive visualisation capability, with around 4000 pre-generated images, will be launched as a part of the V3 release.

14.5 Engagement with Singapore Government Agencies

Engagement with Singapore Government Agencies has been a key strength of the overall V3 planning process. The first Stakeholder

engagement workshop was organised by the Climate Science Research Programme Office (CSRPO) in November 2020, and the second workshop was organised in January 2022. Both these workshops were attended by over 21 Singapore Government agencies from various Ministries, and had over 100 participants. Various aspects of V3 from the V3 workflow were shared with stakeholders along with the data that will be produced and shared with the agencies. Stakeholder inputs were also sought on the various level-2 and level-3 data and products and also aspects on conveying uncertainty of the climate change projections in the V3 technical and stakeholder reports.

In addition to the large annual workshops, there are various ad-hoc engagements with agencies throughout the year by means of working groups, for example, with PUB (Singapore's National Water Agency) and Singapore Food Agency (SFA). CCRS has also been working closely with agencies such as MINDEF and NParks around climate change topics and the uptake of V3 data and products for various impacts and vulnerability studies and adaptation planning. A climate 101 was conducted in June 2023 to share climate science with the Singapore Government agencies.

Agencies are also working with Singapore IHLs on various projects that use V3 data through the 23M SGD Climate Impact Science Research funding, coordinated by the CSRPO. The first CISR SAP meeting concluded in May 2023 that met to finalise the projects that will be funded under the programme.

14.6 Engagement with Singapore Media Houses

Engagement with local media is essential to communicate V3 and its key findings with the public. Supported by NEA Corporate Communications Division (CCD), CCRS has been interacting with media through answering media queries and also being interviewed by news channels on topics of interest. A media technical briefing session was organised in December 2023 to align the media with V3, share what is the kind of information that may be expected at the official V3 launch, and understand the materials needed for media to cover V3 in their news stories. Various media houses such as The Straits Times, Channel NewsAsia, etc. will be invited to the event.

14.7 International Engagement

Singapore organised its inaugural Singapore Pavilion at the 2022 United Nations Climate Change Conference 27th Conference of the Parties (COP27), from 6 to 18 November 2022 in Sharm el-Sheikh, Egypt. Themed around 'Building a Future of Green Possibilities', the Singapore Pavilion showcased how Singapore is actively planting the seeds of change in its economy, environment, and society to achieve a net zero future by 2050: (https://www.nccs.gov.sg/media/press-releases/inaugural-singapore-pavilion-cop27/). V3 was featured under the Green Initiatives as a part of the Singapore pavillion at COP28, held during 30 Nov 2023 – 12 Dec 2023 in Dubai.

Regional engagements will also be happening through the Asean Specialised Meteorological Centre (ASMC). Specifically, the V3 portal, findings from the study and data availability information will be shared with the ASEAN countries through the ASEAN Regional Climate Data Analysis and Projections-4 (ARCDAP-4) workshop. In addition, basic Python-based data analytics training will also be carried out as a part of the workshop to enable some of the ASEAN member countries to use the V3 data in the future for both physical climate change assessment and impact modelling.

The Coordinated Regional Climate Downscaling Experiment-South East Asia (CORDEX-SEA) is an important regional branch of the global CORDEX community focusing on providing regional climate change projections in the SEA region. We are a formal member of the CORDEX-SEA and have been engaging with the research community associated with it. While there are overlaps between the two efforts (CORDEX-SEA CMIP6 regional projections and V3) there are important differences too that make them complement each other for carrying out more robust physical climate change assessment and impact studies over the SEA region.

There are overlaps such as (1) some similar CMIP6 GCMs, (2) similar domain with small differences in latitudinal and longitudinal extents, and (3) some common scenarios (SSP1-2.6 and SSP2-4.5). There are some important differences such as (1) CORDEX-SEA uses SSP3-7.0 as their highest emission scenario, whereas V3 uses SSP5-8.5, and (2) the CORDEX-SEA primary spatial resolution for regional climate change projections is 25 km, whereas for V3 it is 8 km. Thus, the 2 datasets are highly complementary and we are engaging with the CORDEX-SEA community to discuss how to share our high-resolution regional projections data from V3 through the CORDEX-SEA Earth System Grid Federation (ESGF) data nodes.

CCRS has also been engaging with the United Nations Food and Agriculture Organisation (UNFAO) to increase the regional uptake of V2 and V3 data for food security planning over the SEA region. A joint statement by MSE and UNFAO was issued at COP27 around V2/V3 data sharing.

Chapter 15
Glossary of Terms

A

Adaptation Action that helps cope with the effects of climate change - for example construction of barriers to protect against rising sea levels, or conversion to crops capable of surviving high temperatures and drought.

Aerosols Tiny liquid or solid particles of various composition that occur suspended in the atmosphere.

Anomalies Departures of temperature, precipitation, or other weather elements from long-term averages

Anthropogenic climate change Man-made climate change - climate change caused by human activity as opposed to natural processes.

AR4 The Fourth Assessment Report produced by the Intergovernmental Panel on Climate Change (IPCC) published in 2007. The report assessed and summarised the climate change situation worldwide.

AR5 The Fifth Assessment report from the Intergovernmental Panel on Climate Change (IPCC) was published over 2013 and 2014.

AR6 The Sixth Assessment report from the Intergovernmental Panel on Climate Change (IPCC) was published over 2021 and 2022.

Atmospheric aerosols Microscopic particles suspended in the lower atmosphere that reflect sunlight back to space. These generally have a cooling affect on the planet and can mask global warming. They play a key role in the formation of clouds, fog, precipitation and ozone depletion in the atmosphere.

B

Barystatic sea-level change Global-mean sea-level change due to the addition of water that is formerly residing on land or atmosphere, or the removal of water from the oceans.

Bias adjustment of climate change projections. Correcting systematic model simulation errors using observed data.

Business as usual (BAU) A scenario used for projections of future emissions assuming no action, or no new action, is taken to mitigate the problem. WIthin IPCC AR6, the BAU scenario is the SSP585 scenario.

C

Carbon capture and storage The collection and transport of concentrated carbon dioxide gas from large emission sources, such as power plants. The gases are then injected into deep underground reservoirs. Carbon capture is sometimes referred to as geological sequestration.

Carbon dioxide (CO2) Carbon dioxide is a gas in the Earth's atmosphere. It occurs

naturally and is also a by-product of human activities such as burning fossil fuels. It is the principal greenhouse gas produced by human activity.

Carbon dioxide (CO2) equivalent Six greenhouse gases are limited by the Kyoto Protocol and each has a different global warming potential. The overall warming effect of this cocktail of gases is often expressed in terms of carbon dioxide equivalent - the amount of CO2 that would cause the same amount of warming.

Carbon emissions or footprint The amount of carbon emitted by an individual or organisation in a given period of time, or the amount of carbon emitted during the manufacture of a product.

Carbon sink Any process, activity or mechanism that removes carbon from the atmosphere. The biggest carbon sinks are the world's oceans and forests, which absorb large amounts of carbon dioxide from the Earth's atmosphere.

CCRS Centre for Climate Research Singapore and part of the Meteorological Service Singapore (MSS). It was officially launched in March 2013 and aims to advance scientific understanding of tropical climate variability and change and its associated weather systems affecting Singapore and the wider Southeast Asia Region, so that the knowledge and expertise can benefit decision makers and the community.

Climate The prevalent or characteristic weather conditions of a place or region over a period of years.

Climate change A pattern of change affecting global or regional climate, as measured by yardsticks such as average temperature and rainfall, or an alteration in frequency of extreme weather conditions. This variation may be caused by both natural processes and human activity. Global warming is one aspect of climate change.

Climate Driver Global and regional climate drivers influence weather patterns that occur over months and seasons. There are several important climate drivers that help to understand what the general weather pattern might look like (example: ENSO).

CMIP (CMIP5, CMIP6) Coupled Model Intercomparison Project – a global set of model experiments coordinated by the World Climate Research Program (WCRP) every ~7 years. The latest cycle is ‘Phase 6’, e.g. CMIP6.

CO2 See carbon dioxide.

Convection - Vertical air circulation in which cool air sinks and forces warm air to rise.

Contemporary Mass Redistribution (CMR) sea - level change Satellite altimetry sea-level without sterodynamic and GIA-induced sea-level. Composed of barystatic sea-level change and GRD fingerprints.

CORDEX Coordinated Regional Climate Downscaling Experiment. One of the MIPs (Model Intercomparison Projects) forming part of the overall CMIP6 model experiments.

Cyclone A low pressure system with a cyclonic circulation. It is also called a depression and is generally associated with poor or stormy weather. The point of lowest atmospheric pressure marks the centre of the cyclone.

D

Dangerous climate change A term referring to severe climate change that will have a negative effect on societies, economies, and the environment as a whole. The phrase was introduced by the 1992 UN Framework Convention on Climate Change, which aims to prevent "dangerous" human interference with the climate system.

Deforestation The permanent removal of standing forests that can lead to significant levels of carbon dioxide emissions.

Dew Point (also known as Dewpoint) The temperature to which air must be cooled in order to become saturated by the water vapour already present in the air.

Divergence - A wind pattern whereby there is a net outflow of air from some point.

Dynamical Downscaling of global climate models. Running a limited-domain climate model (regional climate model) forced at the domain boundaries by the global model to produce higher resolution climate simulations within the domain.

E

Easterly Wave Also known as tropical wave, they are a type of atmospheric low-pressure trough, oriented north to south, which moves from east to west across the tropics, causing areas of cloudiness and thunderstorms. An easterly wave or tropical wave can develop into a tropical cyclone.

ECS Equilibrium Climate Sensitivity is the global and annual mean near-surface temperature rise that is expected to occur by doubling of CO2 in the atmosphere.

El Niño El Niño can be distinguished when the surface waters in the eastern tropical Pacific extending westward from Ecuador become warmer than average. The changing pattern of the Pacific Ocean causes a shift in the atmospheric circulation, which then influences weather patterns across much of the earth, especially over the Maritima Continent. El Nino is like La Niña's brother, the totally opposite.

ENSO (El Niño/Southern Oscillation) - An episode of anomalously high sea-surface temperatures in the equatorial and tropical eastern Pacific; associated with large-scale swings in surface air pressure between the western and central tropical Pacific.

Evaporation The process by which water changes phase from a liquid to a vapor at a temperature below the boiling point of water.

Evapotranspiration Vaporization of water through direct evaporation from wet surfaces plus the release of water vapor by vegetation.

F

Feedback loop In a feedback loop, rising temperatures on the Earth change the environment in ways that affect the rate of warming. Feedback loops can be positive (adding to the rate of warming), or negative (reducing it). The melting of Arctic ice provides an example of a positive feedback process. As the ice on the surface of the Arctic Ocean melts away, there is a smaller

area of white ice to reflect the Sun's heat back into space and more open, dark water to absorb it. The less ice there is, the more the water heats up, and the faster the remaining ice melts.

G

GCM Global Climate Model (sometimes also called a General Circulation Model).

GIA-induced sea-level change GRD due to ongoing changes in the solid Earth caused by past changes in land ice (i.e., during the Last Glacial Maxima).

Geocentric sea-level change The change in local mean sea level with respect to the terrestrial reference frame. This does not include effects of vertical land movement.

Glacier Sea-ice terminology. Describes a mass of snow and ice that is continuously moving from higher to lower ground or, if afloat, continuously spreading.

Global average temperature The mean surface temperature of the Earth measured from three main sources: satellites, monthly readings from a network of over 3,000 surface temperature observation stations and sea surface temperature measurements taken mainly from the fleet of merchant ships, naval ships and data buoys.

Global energy budget The balance between the Earth's incoming and outgoing energy. The current global climate system must adjust to rising greenhouse gas levels and, in the very long term, the Earth must get rid of energy at the same rate at which it receives energy from the sun.

Global-mean sea-level rise Global-mean sea-level rise for the global mean of relative sea-level change, due to the change in the volume of the ocean.

Global-mean thermosteric sea-level change Global-mean sea-level change due to thermal expansion.

Global warming The steady rise in global average temperature in recent decades, which experts believe is largely caused by man-made greenhouse gas emissions. The long-term trend continues upwards, they suggest, even though the warmest year on record, according to the UK's Met Office, is 1998.

Gravitational, Earth’s Rotational, viscoelastic solid Earth Deformational (GRD) effects Changes in gravitation and rotation alter the geopotential field and hence the geoid, while deformation of the solid Earth changes the sea floor topography through vertical land movement.

Greenhouse gases (GHGs) Natural and industrial gases that trap heat from the Earth and warm the surface. The Kyoto Protocol restricts emissions of six greenhouse gases: natural (carbon dioxide, nitrous oxide, and methane) and industrial (perfluorocarbons, hydrofluorocarbons, and sulphur hexafluoride).

Greenhouse effect The insulating effect of certain gases in the atmosphere, which allow solar radiation to warm the earth and then prevent some of the heat from escaping. See also Natural greenhouse effect.

H

Hadley cell Thermally driven air circulation in tropical and subtropical latitudes of both hemispheres resembling a huge convective cell with rising air near the equator and sinking air in the subtropical anticyclones.

Halosteric sea-level change Steric sea-level change due to changes in salinity in the ocean.

Humidity (also called Relative Humidity) Humidity is the measure of water vapour content in the air. Relative humidity is usually expressed as a percentage of total possible moisture content.

I

Intertropical convergence zone (ITCZ) Discontinuous belt of thunderstorms paralleling the equator and marking the convergence of the Northern and Southern Hemisphere surface trade winds. Associated with the monsoons.

Inverse barometer effects on sea-level change Sea-level change due to atmospheric pressure variations.

IPCC The Intergovernmental Panel on Climate Change is a scientific body established by the United Nations Environment Programme and the World Meteorological Organization. It reviews and assesses the most recent scientific, technical, and socio-economic work relevant to climate change, but does not carry out its own research. The IPCC was honoured with the 2007 Nobel Peace Prize.

ISIMIP3 bias adjustment method in phase 3 of the Inter-Sectoral Impact Model Intercomparison Project (ISIMIP3). This method was employed in V3 bias correction.

J

Jet Stream Relatively strong winds, concentrated within a narrow band in the upper atmosphere.

K

L

La Niña An extensive cooling of the waters in the tropical central and eastern Pacific Ocean. It is the climatic opposite of the El Niño.

Latent Heat Heat that is stored in water vapour in the atmosphere. When water vapour rises, cools and condenses into liquid water, it releases this heat into the surrounding atmosphere. This is the driving mechanism for tropical cyclones.

LULUCF This refers to Land Use, Land-Use Change, and Forestry. Activities in LULUCF provide a method of offsetting emissions, either by increasing the removal of greenhouse gases from the atmosphere (i.e. by planting trees or managing forests), or by reducing emissions (i.e. by curbing deforestation and the associated burning of wood).

M

Manometric sea level Change in the time-mean local mass of the ocean per unit area, assuming the density does not change

Maritime Continent A term commonly used by meteorologists, climatologists, and oceanographers to describe the region between the Indian and Pacific Oceans

including the archipelagos of Indonesia, Borneo, New Guinea, the Philippine Islands, the Malay Peninsula, and the surrounding seas.

Mean sea level The time-mean of the sea surface.

Mesosphere Region of the atmosphere, situated between the stratopause and the mesopause, in which the temperature generally decreases with height.

MICI Marine Ice Cliff Instability

MISI Marine Ice Sheet Instability

Mitigation Action that will reduce man-made climate change. This includes action to reduce greenhouse gas emissions or absorb greenhouse gases in the atmosphere.

Monsoon typically means the rainband associated with the seasonal reversal of winds and progression of the Inter-tropical Convergence Zone (ITCZ) across the equator.

MSS Meteorological Service Singapore. It is Singapore's national authority on the weather and climate. It is an operational pillar under the National Environment Agency (NEA).

N

Natural greenhouse effect The natural level of greenhouse gases in our atmosphere, which keeps the planet about 30C warmer than it would otherwise be - essential for life as we know it. Water vapour is the most important component of the natural greenhouse effect.

NCCS National Climate Change Secretariat. It was established in 2010 under the Prime Minister's Office (PMO) to develop and implement Singapore's domestic and international policies and strategies to tackle climate change.

NEA National Environment Agency is the leading public organisation responsible for ensuring a clean and sustainable environment for Singapore.

O

Ocean acidification The ocean absorbs approximately one-fourth of man-made CO2 from the atmosphere, which helps to reduce adverse climate change effects. However, when the CO2 dissolves in seawater, carbonic acid is formed. Carbon emissions in the industrial era have already lowered the pH of seawater by 0.1. Ocean acidification can decrease the ability of marine organisms to build their shells and skeletal structures and kill off coral reefs, with serious effects for people who rely on them as fishing grounds.

Ocean dynamic sea-level change The local height of the sea surface above the geoid, with the inverse barometer correction applied.

P

ppm (350/450) An abbreviation for parts per million, usually used as short for ppmv (parts per million by volume). The Intergovernmental Panel on Climate Change (IPCC) suggested in 2007 that the world should aim to stabilise greenhouse gas levels at 450 ppm CO2 equivalent in order to avert dangerous climate change. Some scientists, and many of the countries most vulnerable to climate change, argue that the safe upper limit is 350ppm. Current levels of CO2 only are about 380ppm.

Pre-industrial levels of carbon dioxide The levels of carbon dioxide in the atmosphere prior to the start of the Industrial Revolution. These levels are estimated to be about 280 parts per million (by volume). The current level is around 380ppm.

Precipitation Precipitation is a liquid or solid form of water falling from the atmosphere to the earth's surface. Examples include rain, freezing rain, hail, and snow.

Q

R

Radiative Forcing Radiative forcing is what happens when the amount of energy that enters the Earth's atmosphere is different from the amount of energy that leaves it.

Relative Humidity (also called Humidity) Relative humidity is the ratio of water vapour in the air at a given temperature, to the maximum amount which could exist at that temperature. It is usually expressed as a percentage.

Relative sea-level change The change in local mean sea level relative to the local solid surface, i.e., the sea floor. This includes effects of vertical land movement.

Renewable energy Renewable energy is energy created from sources that can be replenished in a short period of time. The five renewable sources used most often are: biomass (such as wood and biogas), the movement of water, geothermal (heat from within the earth), wind, and solar.

RWG Resilience Working Group (Singapore Government).

S

Sea level anomaly (SLA) Deviations of sea surface height from a mean level (i.e., variations from mean sea level).

SINGV, SINGV-RCM The Singapore Variable Resolution weather model and its Regional Climate Model counterpart.

SSP Shared Socioeconomic Pathway. For example SSP126, SSP245, SSP585 are scenarios of future socio-economic pathways used for simulations of future climates in standardised ways.

Steric sea-level change Composed of thermosteric and halosteric sea-level change.

Squall An atmospheric phenomenon characterized by an abrupt and large increase of wind speed within a duration of minutes, that suddenly diminishes. Squalls are usually associated with thunderstorms, and as such are often accompanied by heavy showers, thunder, and lightning. Example: Sumatra Squall Line.

Sterodynamic sea-level change Composed of ocean dynamic sea level and global-mean thermosteric sea-level

Storm Surge The positive or negative difference in sea level from the predicted astronomical tide, due to the forces of the atmosphere. The two main atmospheric components that contribute to a storm surge are air pressure and wind.

Stratosphere The region of the atmosphere extending from the top of the troposphere (the tropopause), at height of 10-17 km to the base of the mesosphere

(the stratopause), at a height of roughly 50 km.

T

Teleconnection A linkage between weather changes occurring in widely separated regions of the globe.

Temperature Anomaly The deviation of temperature in a given region over a specified period from the long-term average value for the same region.

Thermal expansion Thermal expansion happens when water gets warmer, which causes the volume of the water to increase.

Thermosteric sea-level change Steric sea-level change due to changes in ocean temperature.

Thunderstorm A local storm, usually produced by a cumulonimbus cloud, and always accompanied by thunder and lightning.

Tide Sea-level instability/movement in an approximately daily or twice daily period. The movement is caused by the difference of the gravitational attraction between celestial bodies and the centrifugal acceleration of their rotation and is periodic because it is related to the motion of the sun, earth, and moon.

Tide gauge Instrument measuring the sea level height.

Tipping point A tipping point is a threshold for change, which, when reached, results in a process that is difficult to reverse. Scientists say it is urgent that policy makers halve global carbon dioxide emissions over the next 50 years or risk triggering changes that could be irreversible.

Trade Winds (also called Tropical Easterlies) The belts of wind on either side of the equator, blowing from the northeast in the Northern Hemisphere, and from the southeast in the Southern Hemisphere. In both hemispheres the winds become more easterly the closer they are to the equator.

Tropical Cyclone The generic term for the class of tropical low-pressure systems, including tropical depressions, tropical storms, and hurricanes. Tropical cyclone systems typically last a week or more.

Tropical Wave (also called Easterly Wave) A type of atmospheric trough, oriented from north to south, which moves from east to west across the tropics causing areas of cloudiness and thunderstorms. A tropical wave can develop into a tropical cyclone.

Troposphere

The lowermost layer of the atmosphere, in which air temperature falls steadily with increasing altitude. The troposphere begins at ground level and ranges in height from an average of 11 km (at the International Standard Atmosphere) at the poles to 17 km at the equator.

Tsunami A very large wave caused by a shallow submarine earthquake but can also be caused by submarine earth movement, subsidence, or volcanic eruption.

U

UNFCCC The United Nations Framework Convention on Climate Change is one of a series of international agreements on global environmental issues adopted at the 1992 Earth Summit in Rio de Janeiro. The UNFCCC aims to prevent "dangerous" human interference with the climate system. It entered into force on 21 March

1994 and has been ratified by 192 countries.

V

VLM Vertical land movement The change in the height of the sea floor or the land surface.

W

Weather The state of the atmosphere with regard to temperature, cloudiness, rainfall, wind and other meteorological conditions. It is not the same as climate which is the average weather over a much longer period.

Westerlies The dominant west-to-east motion of the atmosphere, centered over the middle latitudes of both hemispheres. In the tropics, monsoon westerlies are a significant feature.

X

Y

Z